Investigation of Local Heat Transfer Phenomena in a Pebble Bed HTGR Core
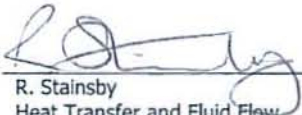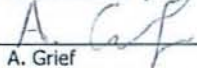
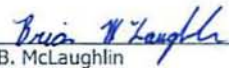NR001/RP/002 R01

May 15, 2009
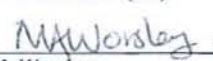
Prepared by:

R. Stainsby
Heat Transfer and Fluid Flow
Consultant
AMEC Nuclear (UK)

Prepared by:

A. Grief
Thermal Hydraulics and CFD
Consultant
AMEC Nuclear (UK)

Prepared by:

M. Worsley
Senior Physicist
AMEC Nuclear (UK)

Prepared by:

F. Dawson
Analyst
AMEC Nuclear (UK)

Prepared by:

M. Davies
Principal Consultant
AMEC Nuclear (UK)

Prepared by:

S. MacIntosh
Senior Analyst
AMEC NSS
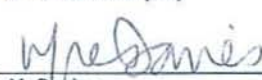
Prepared by:

B. McLaughlin
Analyst
AMEC NSS

Verified & Reviewed
by:

E. van Heerden
Senior Analyst
AMEC NSS

Reviewed by:

A. Dennier
TH Applications and Methods
Manager
AMEC NSS

Approved by:

W. Bowman
Director – Thermal Hydraulics
AMEC NSS

Revision Summary

Rev	Date	Author	Comments
R00	March 2009	R. Stainsby	For U.S.NRC Review
R01	May 2009	R. Stainsby	Incorporate an Executive Summary per U.S. NRC's request.

Executive Summary

This report summarizes the research on Pebble Bed Reactors (PBR) Heat Transfer from the study "Investigation of the Local Heat Transfer Phenomena in an HTGR Core", solicitation number RES-07-087.

The objective of this work is to identify the computational tools and techniques available to resolve local fluid behavior in the core of a high temperature gas reactor (HTGR). This information is needed for U.S. NRC staff to develop the evaluation model that will be used to audit licensee calculations under normal operation and accident conditions. This report summarizes the research performed on local heat transfer phenomena in a pebble bed core. Several models have been developed and sensitivity studies have been performed as part of this research based on the thermal fluids and accidents analysis R&D phenomena tables developed by the U.S. NRC for HTGRs. Based on this research, constitutive models will be developed for inclusion into systems codes (such as the code MELCOR) that are being developed to predict the system-wide thermal fluidic behavior of HTGRs.

This report is structured in thirteen sections. Sections 1 to 3 present an introduction, a discussion of pebble bed HTGRs and a review of the U.S. NRC's Thermofluid and Accident Analysis PIRT exercise. Section 4 presents the scope of the research programme covered by this report and how this is linked to the findings of the aforementioned PIRT exercise.

The investigations were divided into four main themes with each theme targeted on groups of the high-priority PIRT items. These themes were chosen to capture the heat transfer mechanisms from the scale of individual coated particles out to the scale of the whole core, and were identified as:

1.   Mechanisms influencing fuel and moderator temperatures.

2.   Investigation of pebble bed pressure losses and heat transfer mechanisms.

3.   Effective thermal conductivity of the pebble bed in loss of forced circulation (LOFC) conditions.

4.   Production of a whole-core CFD model.

Sections 5 to 9 describe the work and results from the investigation of the first theme. Within Section 5, multi-scale models were developed which are capable of predicting the temperature distributions within individual coated particles and within individual pebbles containing many particles. The multi-scale methods were developed by starting from one-dimensional steady state conduction problems which featured multiple embedded discrete heat sources. Analytical solutions exist for these problems and the bounds of applicability of the multi-scale decomposition were investigated by comparison with these solutions. It is shown that the decomposition of the discrete heat sources into spatial average plus local perturbations resolves the temperature field without approximation. However, averaging of fine-scale material property

variations over longer length scales does introduce approximations and care is required when considering such averaging. Generally, for practical application, the degree of approximation is not large because the packing fraction of particles within pebbles is small.

Section 6 investigates the statistical likelihood of clustering of the coated particles within pebbles. A method was developed by which random arrangements of particles with the correct average packing fraction could be generated and interrogated to determine the frequencies of obtaining different sized clusters of particles. Finite element predictions were made of the temperature enhancement experienced by the centre particle in approximately spherical clusters. The largest such cluster examined contained 14 particles, although a 13 particle cluster was found to be a worse case as it was more spherical. The next largest spherical cluster size that could be considered would contain about 61 particles and it was considered that the occurrence of such a large cluster would be extremely rare. The thirteen particle cluster yielded a temperature enhancement of approximately 4°C for a pebble with average power. In a peak rated pebble, with assumed (paradoxically) highly irradiated graphite, the temperature enhancement is 12°C. From this work it appears, tentatively, that a small margin of about 20°C can be added to a best estimate calculated particle temperature to allow for uncertainties associated with clustering, when considering fission product release. Further work to improve the statistical treatment should be possible – the current method of sampling introduces a scale effect in which the results are influenced by the size of the volumes within which the particles are counted. A scale-independent way of counting to identify the presence and size of clusters should be possible.

Section 7 presented an analytical method, based on Maxwell's method for determining the effective conductivity of a pebble containing a mixture of coated particles and graphite. The predictions of the analytical method were compared with finite element predictions for three different structured arrangements of particles. Also, two alternative treatments of the particles were considered in the finite element simulations. In the first, the multiple layers of a single coated particle were homogenized with a conductivity that was determined by Maxwell's method. In the second treatment, the fuel kernel and each of the coating layers was resolved explicitly within the finite model. The finite element predictions showed that alternative structured arrangements of particles had a negligible influence on the effective conductivity, therefore, it can be concluded that a random arrangement would have given the same result. Further, there was no significant difference in the predicted conductivities between using homogenized and explicitly-layered particles. Finally it was shown that the effective conductivities predicted by Maxwell's method was close to the values obtained from all of the finite element predictions with an accuracy of better than 0.4%.

Section 8 presents a model by which the pebble-to-pebble power and temperature differences that would occur in a multi-batch core can be taken into account. Typically, a CFD calculation of a whole reactor core would calculate a single coolant temperature and a single pebble surface temperature within each computational cell in the core. The multi-batch model starts from these two batch-averaged macroscopic

quantities within a given computational cell. The differences in power developed between different batches, together with estimates of the batch-to-batch and cell-to-cell heat exchange coefficients, are used to "de-average" these temperatures. Thus, it is possible to back-out the pebble and particle temperatures of each of the fuel batches within the given computational cell.

Section 9 is a review of available data and methods for the calculation of thermal properties of irradiated graphite.

Section 10 covers the work of the second research theme, "investigation of pebble bed pressure losses and heat transfer mechanisms". A numerical method for generating random arrangements of pebbles in cylindrical and annular geometries has been developed. This was used to generate a large annular core assembly which has the dimensions of the PBMR-400 core. From this assembly, two smaller assemblies were extracted; a cylindrical assembly from a radial position that was midway between the inner and outer boundaries, and a semi-elliptical assembly taken from the outer edge of the pebble bed corresponding to the location of the outer reflector. Later, a wider semi-cylindrical region was extracted from the outer reflector region to improve the averaging of the results in the circumferential direction. Computational fluid dynamics (CFD) models were developed for these sub-assemblies using the FLUENT code.

Meshing of the domains was not trivial. The point contacts between pebbles led to severely skewed meshes in the vicinity of the contacts and the imposition of planes bounding the models also gave rise to degenerate element shapes. The solution to the contact problem was to build small cylindrical bridges between touching pebbles and to impose a tightly controlled grid around the contacts. The issue with imposing planar boundaries on the model was overcome by using curved boundaries that were free from sharp corners. These methods resulted in high quality elements throughout the entire fluid domain.

The CFD models were used to determine axial pressure drops and heat transfer coefficients for each model. Initially, a Reynolds analogy approach was used to infer the heat transfer coefficients as an alternative to performing thermal calculations. However, problems in determining an appropriate reference velocity led to this being abandoned in favor of modeling the power and temperature distributions directly. Remote from the reflectors, the pressure drop predictions agreed very well with established correlations. Close to the reflectors, the CFD models predicted significantly lower pressure drops than the correlations. This was to be expected as it is known that the phenomenon referred to as wall channeling should yield a lower pressure drop for a given mass flow when compared with correlations derived for complete pebble beds due to the lower packing fraction near the reflector wall. This wall channeling effect was explored further using the semi-cylindrical model and a strong correlation between the radial distributions of axial mass flux with observed oscillations in pebble bed porosity was apparent.

Heat transfer coefficients derived from the Reynolds analogy were generally too high when compared with existing correlations. Conversely, heat transfer coefficients derived from thermal simulations were significantly lower than those obtained from

correlations. It is too early to say that either are in error and more work is required to investigate the influence of turbulence modeling and the methods by which local heat transfer coefficients are determined and then averaged to ensure consistency of approach with the methods used to derive the correlations.

A CFD model of an assembly of pebbles from a multi-batch core was developed to compare with the predictions of the analytical model presented in Section 8. Three different batches of pebbles were simulated with powers of average, 0.5 times average and 1.5 times average power respectively. The temperature spread across the batches of ±16.55°C agreed well with the values predicted by the analytical model of ±16.1°C.

Section 11 addressed the third research theme and attempted to model heat transfer through a pebble bed in the absence of any significant forced or natural convection. This is an important scenario and represents the passive decay heat removal route in a depressurized loss of forced circulation scenario. The intention was to compare the predicted effective conductivity of a section of pebble bed, accounting for solid and gaseous conduction plus thermal radiation heat transfers, with the established correlations of Zehner and Schlünder, and Breitbach and Barthels. However, in the specific case of no fluid flow, severe convergence problems were encountered with the selected thermal radiation model in FLUENT. Many attempts were made to accelerate the convergence and to execute simpler test problems in consultation with the code vendors. Unfortunately, none of these attempts were successful and the investigation was halted.

The fourth research theme is addressed in Section 12. A three-dimensional model of the PBMR core was developed in Section 12. This model was based on the two-dimensional benchmark problem that was part of the IAEA's CRP-5 coordinated research program on high temperature gas cooled reactor performance. Whilst the current model has a three-dimensional representation of the riser and reactivity control channels, the circumferential extent of the model was limited to a 20° sector to remain representative of the two-dimensional benchmark problem and to limit the geometrical description to what could be sourced from the open literature. Whilst the flow channels in the reflector were represented explicitly, the pebble bed was simulated as a porous medium. A simple homogeneous model was chosen as this was adequate for the benchmark calculation which only required a steady state model and had a very simple power distribution. The pebble bed hydraulic resistance was specified using correlations and an analytical version of the multi-scale model of Section 5 was used to determine the fuel and pebble temperatures. The model predicted very similar coolant, fuel and moderator temperatures to the CRP 5 participants, showing a fuel temperature difference of 21oC and an overall coolant temperature rise of 500oC. Further work is required to extend the model to be applicable to more realistic power distributions and to transient conditions. Specifically, a heterogeneous two-phase porous medium model is required so that separate energy equations can be solved for the gas and solid fractions within the bed. Similarly, models for the "geometrical" dispersion of heat and momentum within a packed bed would need to be introduced. Further, the full finite difference form of the multi-scale

model, as presented in Section 5, would need to be implemented to model fast transients.

Overall conclusions and recommendations for further work are presented in Section 13. The work of most of the sections can be extended and refined, but these recommendations focus on two aspects where further work is definitely required. These are:

1. Re-attempting the analysis of Section 11 but using a CFD code that can both handle the large number of degrees of freedom and be able to simulate thermal radiation in the absence of forced flow, and,

2. Further development of the whole-core CFD model to be applicable to realistic power shapes and transient conditions.

Table of Contents

List of Tables and Figures

1.0 INTRODUCTION

This report summarizes the research on Pebble Bed Reactors (PBR) Heat Transfer from the study "Investigation of the Local Heat Transfer Phenomena in an HTGR Core", solicitation number RES-07-087 (Reference 1.1). A study has also been performed looking at heat transfer in a Prismatic Modular Reactor (PMR) core, the results of which are reported in Reference 1.2.

The objective of this work is to identify the computational tools and techniques available to resolve local fluid behaviour in the core of a high temperature gas reactor (HTGR). This information is needed for U.S. NRC staff to develop the evaluation model that will be used to audit licensee calculations under normal operation and accident conditions. This report summarizes the research performed on local heat transfer phenomena in a pebble bed core. Several models have been developed and sensitivity studies have been performed as part of this research based on the thermal fluids and accidents analysis R&D phenomena tables developed by the U.S. NRC for HTGRs. Based on this research, constitutive models will be developed for inclusion into systems codes (such as the code MELCOR) that are being developed to predict the system-wide thermal fluidic behaviour of HTGRs.

This report has been structured in thirteen sections as follows:

Section 1 – "Introduction", this section.

Section 2 – "Pebble Bed Reactor Cores" which gives the background on pebble bed core reactors, and their typical geometries.

Section 3 – "Review of U.S. NRC Thermofluid and Accident Analysis PIRT" with regard to Pebble Bed Cores. This section summarizes the review of the PIRT performed by the U.S. NRC, which led to the selection of the research studies documented in this report.

Section 4 – "Scope of the Current Programme of Research" summarizes the scope of the work documented in the report. Four research themes were identified based on the PIRT and these are described in Sections 5 through 12.

Section 5 – "Models for the prediction of fuel particle and pebble temperatures" summarizes a portion of the first research theme.

Section 6 – "Models for the prediction of the effect of particles clustering on temperatures" summarizes a portion of the first research theme.

Section 7 – "Determination of the effective conductivity of pebbles" summarizes a portion of the first research theme.

Section 8 – "Multi-batch fuel models" summarizes a portion of the first research theme.

Section 9 – "Thermal properties of irradiated graphite" summarizes a portion of the first research theme.

Section 10 – "Models for the Investigation of Pebble Bed Pressure Losses and Heat Transfer Mechanisms" summarizes the second research theme.

Section 11 – "Determination of the effective thermal conductivity of the pebble bed in LOFC conditions" summarizes the third research theme.

Section 12 – "Whole core CFD model" summarizes the fourth research theme.

Section 13 – "Overall Conclusions and Recommendations" provides a summary and conclusion for the research performed for pebble bed cores.

Each section is relatively stand-alone with its own reference list, tables and figures.

1.1 References for Section 1

1.1 U.S. NRC Letter from S. Pool to NSS W. Thompson, "Contract No: NRC-04-07-087, August 31, 2007.

1.2 Stainsby R. et al., "Investigation of Local Heat Transfer Phenomena in a Prismatic Modular Bed HTGR Core", AMEC NSS Report NR001/RP/001 R02, May 2009.

2.0   PEBBLE BED REACTOR CORES

2.1   Purpose of Section 2

Section 2 details the developments of pebble bed HTRs from the early reactors to current designs under development. Early prismatic HTRs and the developments in the design of prismatic cores are discussed in Reference 2.1. The fuel particle properties used in the analysis reported in Sections 5 to 12 are those given in Table 2.4.1 for the Pebble Bed Modular Reactor (PBMR).

2.2   Early Pebble Bed HTRs

2.2.1   AVR

The German AVR (Arbeitsgemeinschaft Versuchs-Reacktor) was the first pebble bed type HTR and operated as an experimental reactor between 1967 and 1988 at Jülich Research Centre with a power output of 15 MWe. The fuel pebble used consisted of TRISO-coated UO_2 fuel particles (of diameter 0.9 mm) embedded in a spherical graphite matrix, which is encased in a fuel-free graphite outer shell of material. The overall pebble diameter was 6 cm (Reference 2.2). A cross section through a sample TRISO particle is shown in Figure 2.2.1.

The porous carbon is designed to accommodate any mechanical deformation that the uranium dioxide kernel may undergo during the lifetime of the fuel, as well as gaseous fission products diffusing out of the kernel. The pyrolytic carbon and silicon carbide layers are designed to provide an impenetrable barrier designed to contain the fuel and fission products (Reference 2.3).

Figure 2.2.1: Cross-Section Through a Sample TRISO Particle

Pyrolytic carbon

Uranium dioxide

Porous carbon

Silicon carbide
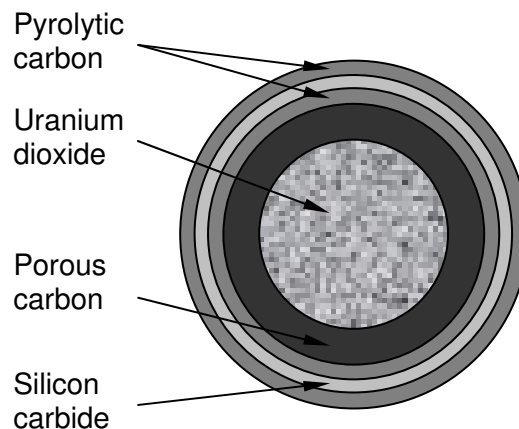
2.2.2   THTR-300

THTR-300 was a 300 MWe thorium high temperature reactor which operated in Germany between 1985 and 1988 as an industrial prototype pebble bed design. The

pebble bed contained 674,200 pebbles. For the initial loading, 358,200 of these were fuel pebbles, 272,500 were graphite pebbles and the rest were absorber pebbles. The fuel pebbles contained TRISO coated particles bonded into graphite spheres (as described in Sub-Section 2.2.1). The fuel particles occupied the inner 25 mm radius of each pebble such that the outermost layer consisted only of graphite. The fuel pebbles contained about 1 g of 93% enriched uranium and 10.2 g of Thorium-232. Thorium enabled the fuel burn-up to be increased through the conversion into Uranium-233 (Reference 2.2).

2.3 Current Operating HTRs

2.3.1 HTR-10

The HTR-10 is a 10 MW pebble-bed high temperature gas-cooled reactor situated at the Institute of Nuclear Energy Technology (INET) of Tsinghua University in Beijing (Reference 2.2). The objective of HTR-10 is to verify and demonstrate the technical and safety features of modular HTGR and to establish an experimental base for developing nuclear process heat applications (Reference 2.4). HTR-10 first achieved criticality in December 2000.

A horizontal cross-section through the reactor is shown in Figure 2.3.1. The core is comprised of the German type spherical elements with TRISO coated fuel particles as well as graphite spheres. The equilibrium core contains about 27,000 fuel elements. As for the AVR and THTR-300, each element is a spherical ball with a diameter of 60 mm. The inner 50 mm contains homogeneously dispersed coated fuel particles with the outer layer being a graphite shell. The fuel particle kernel is a granule of UO_2, with a diameter of 0.5 mm and an initial enrichment of 17% (Reference 2.4).

Figure 2.3.2 shows the configuration of the primary circuit. The reactor core and steam generator are housed in two steel pressure vessels arranged in a 'side-by-side' configuration.

Figure 2.3.1: HTR-10 Reactor Horizontal Cross-Section
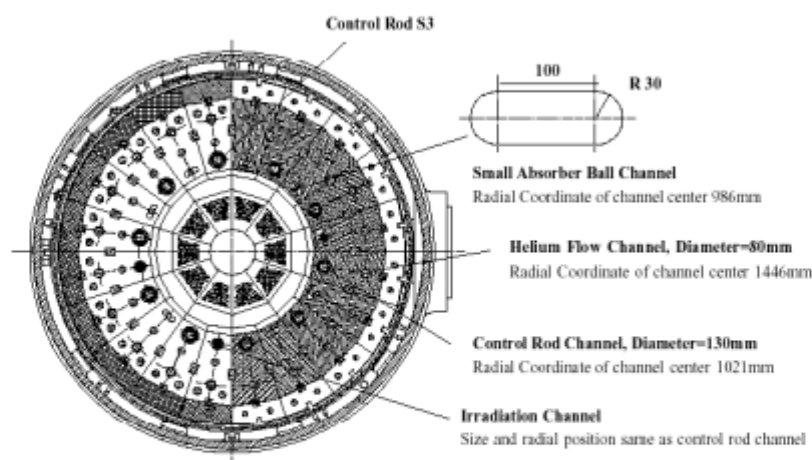
Figure 2.3.2: Cross-Section of the HTR-10 Primary Circuit

Control rod drives
Helium circulator
Absorber balls
Thermal shielding
Top reflector
Cold gas plenum
Steam generator tubes
IHX
Reactor core
Side reflector
Core barrel
Steam generator vessel
Reactor vessel
Bottom reflector

Hot gas duct
Connecting vessel
Hot gas plenum
Core support structures
Fuel discharge
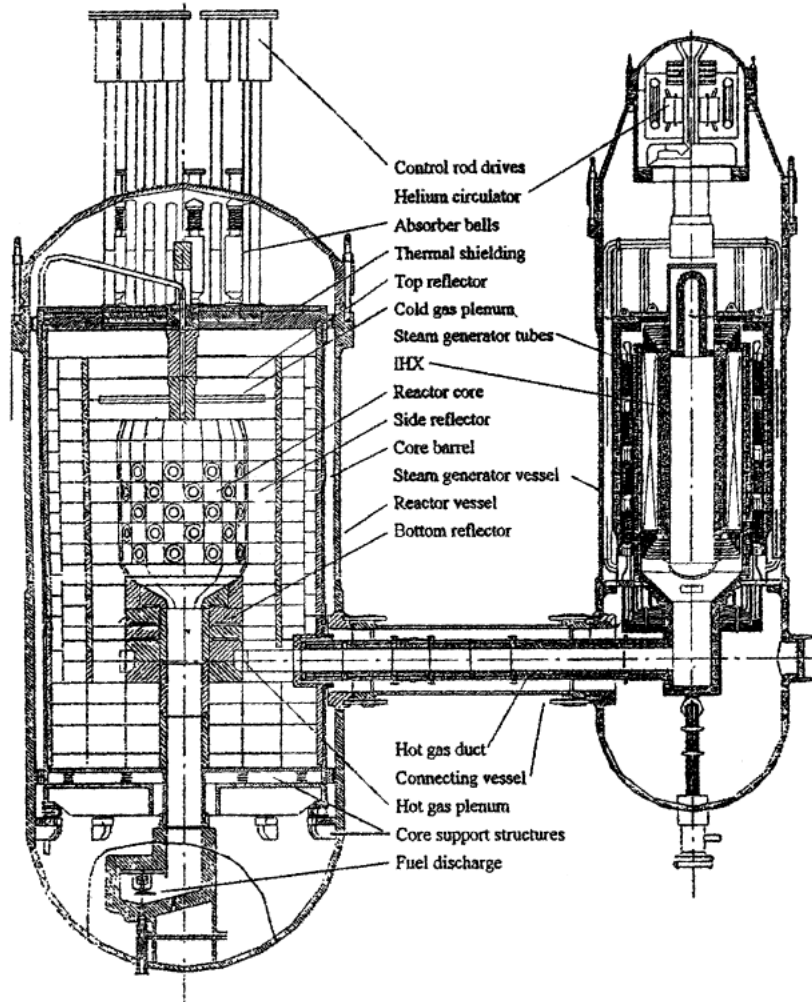
2.4   Pebble-Bed HTR Designs under Development

There are two designs currently under development for pebble-bed HTRs: the PBMR and HTR-PM.

2.4.1   PBMR

The Pebble Bed Modular Reactor (PBMR) is currently under development in South Africa. This incorporates a closed cycle primary coolant system utilizing Helium to transport heat directly from the modular pebble bed reactor to a power conversion unit (direct gas cycle) (Reference 2.4). The design of the PBMR is shown in Figure 2.4.1.

PBMR fuel is based on a German fuel design consisting of low enriched uranium triplecoated isotropic (LEU-TRISO) particles contained in a moulded graphite sphere. A coated particle consists of a kernel of uranium dioxide surrounded by four coating

layers as shown in Figure 2.4.2. The dimensions and thermal conductivities of each layer are shown in Table 2.4.1 taken from Reference 2.5.

Figure 2.4.1: PBMR Design (Courtesy of Reference 2.3)
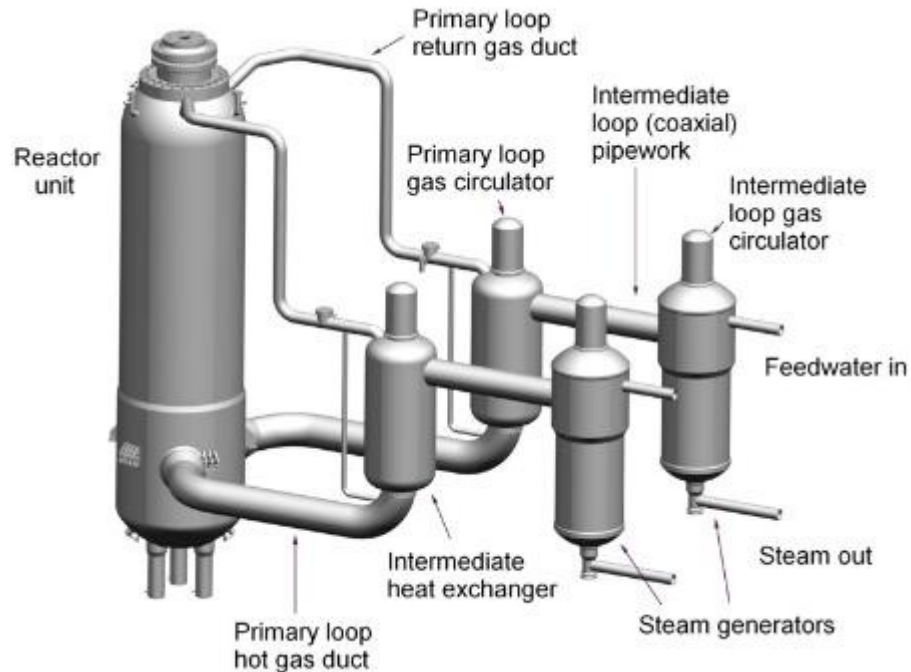
The core comprises of approximately 452,000 fuel spheres (pebbles) with diameters of 60 mm. Each fuel sphere is to contain around 15,000 UO_2 TRISO coated micro-spheres embedded in a graphite matrix. A 5 mm thick outer layer of pure graphite forms a "non-fuel" zone for each sphere. Each fuel pebble is to contain about 9 g of uranium with the total mass of a fuel pebble being approximately 210 g (Reference 2.3).

The core is to be refuelled using a continuous on-line multi-pass method with fresh fuel elements added to the top of the reactor whilst used fuel pebbles are removed at the bottom. Each pebble will on average pass through the reactor six times and last about three years before it is spent, which means that a reactor will use 15 total fuel loads in its design lifetime of 40 years (Reference 2.3).

Figure 2.4.2: Fuel Element Design for PBMR (Courtesy of Reference 2.3)

5mm Graphite layer

Coated particles imbedded in Graphite Matrix

Pyrolytic Carbon 40/1000mm
Silicon Carbide Barrier Coating 35/1000mm
Inner Pyrolytic Carbon 40/1000mm
Porous Carbon Buffer 95/1000mm

Dia. 60mm
Fuel Sphere

Section

Dia. 0,92mm
TRISO Coated Particle

Dia.0,5mm
Uranium Dioxide
Fuel Kernel
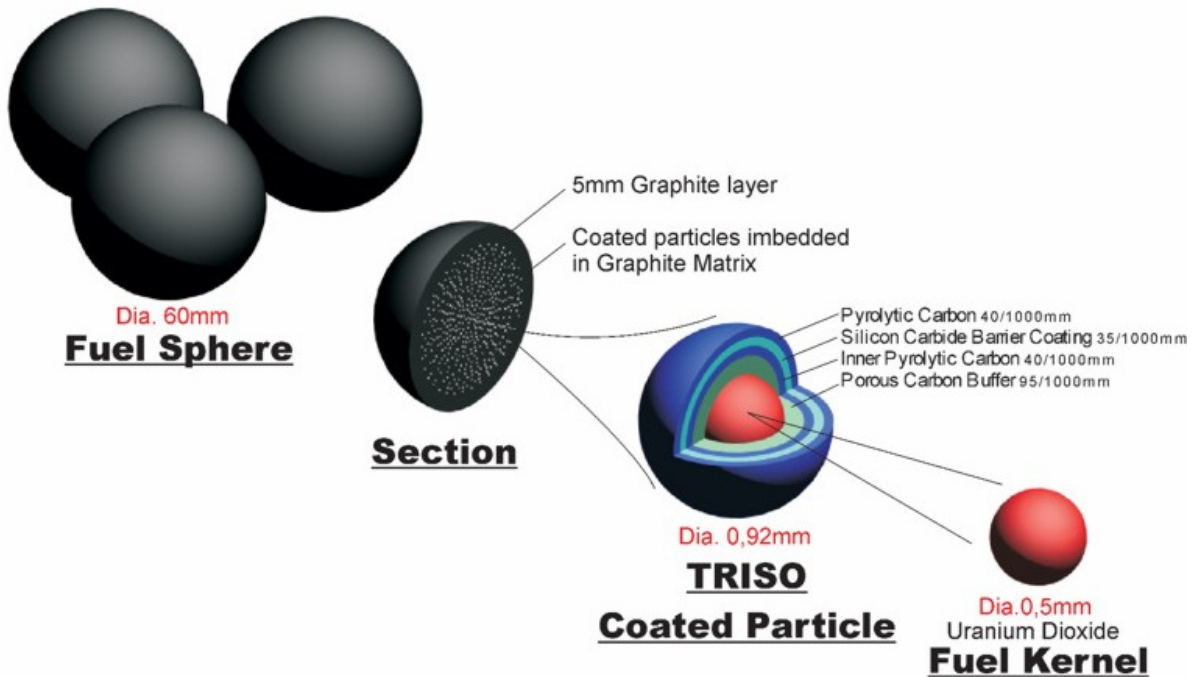
Table 2.4.1: TRISO Fuel Particle Coating Geometry and Material Properties

Region	Material	Outer diameter	Thermal conductivity
Kernel	Uranium dioxide	500×10^{-6} m	3.7 W K^{-1} m^{-1}
Coating 1	Porous carbon	690×10^{-6} m	0.5 W K^{-1} m^{-1}
Coating 2	Pyrolytic carbon	770×10^{-6} m	4.0 W K^{-1} m^{-1}
Coating 3	Silicon carbide	840×10^{-6} m	16.0 W K^{-1} m^{-1}
Coating 4	Pyrolytic carbon	920×10^{-6} m	4.0 W K^{-1} m^{-1}

2.4.2   HTR-PM

The HTR-PM (High Temperature gas-cooled Reactor-Pebble-bed Module) is a demonstration high-temperature gas-cooled reactor, to be built at Shidaowan in the Shandong province of China.

The HTR-PM is based on the design of the HTR-10 with its main objective to research the key technologies of the industrial enlarged scale and engineering experiments for modular HTR, and to accomplish a 200MWe commercial demonstration plant with independent intellectual property rights around 2013 (Reference 2.6). A cross-section of the HTR-PM reactor is shown in Figure 2.4.3.

The design has changed from the initial concept of a 458 MW(th) single module reactor with a two-zone annular core, to a 2x250 MW(th) two module-reactor with a one-zone cylindrical core (Reference 2.6) driving a single steam turbine.

The reactor core consists of approximately 420,000 spherical fuel elements in a pebble-bed with a diameter of 3 m and an average height of 11 m. The mean power density in the core is 3.22 MW/m^3. For each fuel element (of 6 cm diameter), there are about 12,000 TRISO coated particles embedded in the graphite matrix. The fuel elements will reach their proposed maximum burn-up of 100GWD/tU after 15 passes through the core (Reference 2.6).

Figure 2.4.3: Cross-Section of the HTR-PM Reactor (Courtesy of Reference 2.6)
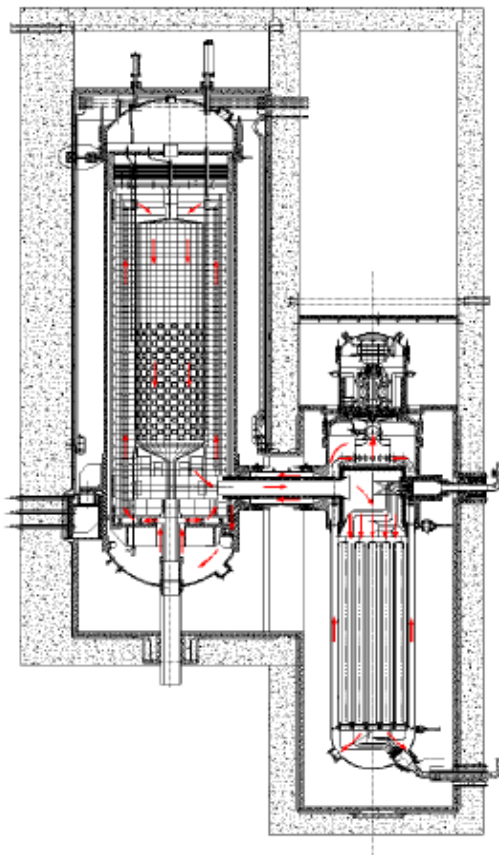
2.5   References for Section 2

2.1   Stainsby R. et al., "Investigation of Local Heat Transfer Phenomena in a Prismatic Modular Bed HTGR Core", AMEC NSS Report NR001/RP/001 R02, May 2009.

2.2   GENIV-NNC-VHTR-TR(04)02, "Review of UK Experience with High Temperature Reactors for the Generation IV VHTR System," D Buckthorpe et al (AMEC), December 2004.

2.3   PBMR website, http://www.pbmr.com, viewed 18 November 2008.

2.4   IAEA CRP 5, Draft TECDOC II, "Evaluation of High Temperature Gas Cooled Reactor Performance", to be published.

2.5   OECD NEA/NSC/DOC2005 (xxx) Draft-V03, PBMR Coupled Neutronics/Thermal Hydraulics Transient Benchmark, The PBMR-400 Core Design, September 2005.

2.6   Y Zhengy and L Shi, "Charteristics of the 250MW Pebble Bed Modular High Temperature Gas-Cooled Reactor in Depressurised Loss of Coolant Accidents," Proceedings of the 4th international topical meeting on high temperature reactor technology, HTR2008-58299, September 28-October 1 2008.

3.0 REVIEW OF U.S. NRC THERMOFLUID AND ACCIDENT ANALYSIS PIRT WITH REGARD TO PEBBLE BED CORES

3.1 Purpose of Section 3

This section discusses the findings from a series of Phenomena Identification and Ranking Tables (PIRT) exercises commissioned by the U.S. NRC examining various aspects of HTGR technology. The findings of relevance to the current study are from the Thermofluids and Accident Analysis PIRTs (Reference 3.1). The PIRT exercise also included neutronics, which is outside of the scope of the current study. However, because of the close coupling between thermal hydraulics and neutronics within HTGR systems, the thermal hydraulic influence on primarily neutronics phenomena are considered within this review.

3.2 Findings of the PIRT

The findings of the PIRT exercise are in line with AMEC's experience of HTGR systems. However, two inconsistencies have been identified as well as some possible omissions. The omissions occur both as missing phenomena and missing linkages between listed phenomena and listed scenarios.

The PIRT could have included the following phenomena, or additional linkages with scenarios, which were omitted from the tables presented.

Normal Operation

1. The influence of dust on performance of the core boundary sealing system. Control of core bypass flow, in a pebble bed reactor, occurring via leakage between the reflector columns is achieved by continuous vertical columns of sealing keys. These keys must be close fitting, but free to slide in their keyways, to limit the leakage flow and accommodate differential growth and thermal expansion between themselves and neighbouring columns of graphite bricks. Accumulation of dust in the keyways could limit the free movement of the sealing keys. The suggested ranking is high importance and low knowledge (H, L).

2. Performance and stability of the core base insulation system. Ceramic insulation materials, such as fused silica, have been researched with a view to forming the insulation layer between the graphite core structures and the metallic core support structure. The main issues with these materials are their thermal and mechanical properties, the dimensional stability at high temperature (avoiding the dimensional changes that occur at the re-crystallisation temperatures) and accommodation of the differential thermal expansion between the ceramic insulator and the steel core support structure. The suggested ranking is high importance and medium knowledge (H, M).

3. Pre-equilibrium (or burn-in) behaviour. Pebble bed reactors have to start, at the beginning of their lives, with clean cores, that behave very differently to the equilibrium cores reached after a few refuelling operations with a multi

batch core. During this transition phase before equilibrium is reached shutdown margins may be degraded and particular fuel element powers and temperatures may be higher than those in an equilibrium core. The suggested ranking is high importance and low knowledge (H, L).

Pressurised Loss of Forced Circulation (PLOFC)

1. Performance of the vessel/core barrel head insulation system. Whilst not subject to the same magnitude of loads as the core base insulation, the vessel head or core barrel top-plate insulation can be exposed to higher temperatures in a PLOFC transient. Maintenance of mechanical properties and dimensional stability are important issues. The suggested ranking is high importance and medium knowledge (H, M).

Depressurised Loss of Forced Circulation (DLOFC)

1. Degradation of heat transfer surfaces due to graphite dust deposition. The core barrel and inner surface of the reactor pressure vessel (RPV) need to maintain high emissivity. The deposition of a layer of graphite dust may change the emissivities and conductivities of the surfaces. The suggested ranking is medium importance, low knowledge (M, L).

2. Influence of core restraint structures and other congestion in the core-to-core barrel gap on radiation view factor. The suggested ranking is medium importance, medium knowledge (M, M).

3. Linkage of the reactivity temperature coefficients and xenon build-up phenomena with the DLOFC scenario. A DLOFC transient without Scram is often cited as being a design basis transient that an HTGR can withstand. Time to achieve re-criticality is an important parameter and depends upon knowledge of the rate of cooling, xenon decay and the reactivity-temperature feedback effects. The suggested ranking is medium importance, low knowledge (M, L).

Air Ingress

1. Inverted siphon effects through breaks occurring in elevated reactor inlet or outlet pipework. Whilst the RPV inlets and outlets may be below the bottom of the graphite core, elevated external pipework may provide a route by which the helium is siphoned out of the vessel and replaced by air. The suggested ranking is high importance, medium knowledge (H, M).

Anticipated Transient Without Scram (ATWS)

1. Reactivity insertion caused by disruption of a pebble bed following a compressor stall/surge event or reactor inlet duct break. If the pressure differential in a direct cycle collapses due to compressor stall or a compressor shaft break, there is a possibility that reverse flows can be set up. Similarly, if a large breach opens in the reactor inlet duct the RPV will blow-down

backwards through the core. If these flows are strong enough to levitate parts of the pebble bed, then there is a mechanism by which a reactivity insertion can occur when the pebble bed slumps back together. The suggested ranking is medium importance, low knowledge (M, L).

The first inconsistency concerns the ranking of the power and flux phenomenon (ID 26) in the normal operation PIRT. In the 4th paragraph of Section 4.4 of the PIRT report (Reference 3.1), this phenomenon is described as having an (H, L) ranking, whereas Table 2.1 in Reference 3.1 shows it as having a (H, M*) ranking. Logically, if the reactivity-temperature feedback coefficients phenomenon has a (H, L) ranking, the power and flux distribution is strongly dependent on local temperature feedback effects, so should have a (H, L) ranking as well.

The second inconsistency concerns the knowledge level associated with the reactivity-temperature feedback coefficients in association with an ATWS. In the ATWS PIRT, the phenomenon has been ranked as having a high importance with a *medium* knowledge level (H, M). However, within the normal operation PIRT, the same phenomenon is ranked as having a high importance with a *low* knowledge level (H, L). The phenomenon is identical in both scenarios, and indeed, is important as mitigation in ATWS sequences. The classification of the knowledge level for this phenomenon in both scenarios should be low (H, L).

3.3   Allocation of Research Priorities

The ranking system of the PIRTs is two-dimensional with importance and knowledge assigned values from high to low. In order to sort the list of phenomena in term of decreasing priority for research, this system has been reduced to a one dimensional ranking system. The highest priority has been given to a phenomenon which is highly important in a given scenario in the reactor, for which the knowledge level is correspondingly low. At the opposite end of the spectrum, the lowest priority is given to phenomena which are well understood and of low importance. In this manner, each phenomena/scenario listed in the PIRTs has been assigned a research priority number between 1 and 6, with 1 being of the highest priority. The mapping between PIRT rankings and research priority is shown in Table 3.3.1.

Table 3.3.1: Mapping of Research Priorities onto PIRT Rankings

PIRT Ranking	Research Priority
H, L	1
H, M	2
M, L	2
M, M	3
H, H	4
L, L	4
M, H	5
L, M	5
L, H	6

3.3.1 Prioritised List of Phenomena and Scenario Pairings

The phenomena and scenario pairings from all of the thermofluids and accident PIRTs that are considered relevant to, or dependent upon, the current study on pebble bed reactors have been ranked according to their assigned research priority and are listed in Table 3.3.2.

3.3.2 High Priority Research Items

The topics chosen for investigation were drawn from the items in Table 3.3.2 ranked as research priority 1 or 2. The selection of the research tasks took into account what was technically feasible and realistically achievable, within the time and budget allocation for this project. In addition, many of the items require the use of coupled thermal hydraulics and neutronics. This has been considered to be beyond the scope of this study, which concentrates on thermal hydraulic aspects only.

The phenomena shown in bold in Table 3.3.2 are those that this research contributes directly towards, and the phenomena shown in italics are those for which this research provides a necessary step towards gaining an understanding.

Potential modeling approaches identified for all of the thermal hydraulic items ranked as research priority 1 or 2 can be found in Reference 3.2. The topics selected for this work and the modeling approaches taken are discussed in Section 4.

**Table 3.3.2: Prioritised Phenomena and Scenario Pairings
from all of the Thermofluids and Accident PIRTs**

PIRT ID	Phenomenon	Ranking	Priority
NO-1	**Core coolant bypass flow**	**H,L**	**1**
NO-8-PBR	**Pebble bed core wall interface effects on bypass flow**	**H,L**	**1**
NO-22	**Reactivity-temperature feedback coefficients**	**H,L**	**1**
NO-2	**Core flow distribution, flow in active core**	**H,M**	**2**
NO-4	*Core flow distribution changes due to graphite irradiation*	*M,L*	*2*
NO-10-PBR	**Coolant heat transfer correlations**	**H,M**	**2**
NO-14-PBR	Pebble flow	H,M	2
NO-16	**Effective fuel element thermal conductivity**	**H,M**	**2**
NO-20	**Shutdown cooling system startup transients during core heatup**	**H,M**	**2**

Table 3.3.2: Prioritised Phenomena and Scenario Pairings from all of the Thermofluids and Accident PIRTs

PIRT ID	Phenomenon	Ranking	Priority
NO-26	**Power and flux profiles (initial conditions for accidents)**	**H,M**	**2**
GL-1	**Core thermal conductivity (effective)**	**H,M**	**2**
GL-4	*Vessel emissivity*	*H,M*	*2*
GL-9	*Reflectors: conductivity and annealing*	*H,M*	*2*
GL-10	*Core barrel emissivity*	*H,M*	*2*
GL-21	*Decay heat (temporal and spatial)*	*H,M*	*2*
PL-1	*Inlet plenum stratification and plumes*	*H,M*	*2*
PL-2	*Radiation heat transfer from top of the core to upper vessel head*	*H,M*	*2*
PL-4	*Core coolant flow distribution*	*H,M*	*2*
PL-5	*Core coolant bypass flow*	*H,M*	*2*
PL-6	*Coolant flow friction/viscosity effects*	*H,M*	*2*
DL-1	**Core effective thermal conductivity**	**H,M**	**2**
DL-2	*Decay heat and distribution versus time*	*H,M*	*2*
DL-5	Hydrodynamic conditions for dust suspension (fluid structure interactions)	H,M	2
AI-5	Core support structures oxidation	H,M	2
AI-6	*Core oxidation*	*H,M*	*2*
AI-7	*Cavity to reactor vessel air ingress*	*H,M*	*2*
AI-8	Phenomena that affect cavity gas composition and temperature with inflow	H,M	2
AI-14	Duct exchange flow	H,M	2
AI-15	*Molecular Diffusion*	*H,M*	*2*
AT-3	*Reactivity insertion due to steam-water ingress accidents*	*H,M*	*2*
AT-5	Reactivity temperature feedback coefficients (fuel, moderator, reflectors)	H,M	2
AT-6	*Control and scram rods, and reserve shutdown worths*	*H,M*	*2*

Table 3.3.2: Prioritised Phenomena and Scenario Pairings from all of the Thermofluids and Accident PIRTs

PIRT ID	Phenomenon	Ranking	Priority
AT-10	*Coolant flow restarts during loss of forced circulation ATWS*	*M,L*	*2*
NO-3	Core flow distribution changes due to temperature gradients	M,M	3
NO-5	Core flow distribution changes due to core barrel geometry changes.	M,M	3
NO-7-PBR	Pebble bed core bridging	M,M	3
NO-11	Core Inlet flow distribution	M,M	3
NO-12	Thermal fluid mixing from separate loops	M,M	3
NO-18	Side reflector - core barrel - vessel heat transfer	M,M	3
PL-7	Impacts (thermal shock) in SCS due to startup flow transient	M,M	3
AI-2	Heat transfer correlations for mixed gases in core	M,M	3
AI-9	Cavity gas stratification and mixing	M,M	3
AI-16	Chimney effects	M,M	3
AT-1	Reactivity insertion due to pebble core compaction (packing fraction) via earthquake	M,M	3
AT-7	Xenon and samarium build-up	M,M	3
NO-9	Coolant properties - viscosity and friction effects	H,H	4
GL-3	Core specific heat function	H,H	4
AI-1	Coolant flow and thermal properties for mixed gases in vessel	H,H	4
NO-15	Effective core thermal conductivity	L,M	5
NO-17	Core specific heat	M,H	5
DL-6	Dust effect on coolant properties and flow in vessel	L,M	5
AT-4a	Phenomena for water or steam ingress from SCS, or PCU coolers	L,M	5
AT-13	Reactivity insertion from core support failure due to air ingress corrosion	L,M	5
GL-11	Stored (Wigner) energy releases	L,H	6

**Table 3.3.2: Prioritised Phenomena and Scenario Pairings
from all of the Thermofluids and Accident PIRTs**

PIRT ID	Phenomenon	Ranking	Priority
AT-12	Reactivity insertion from overcooling transients with ATWS	L,H	6

Key to PIRT ID numbers
General form: Scenario - number of item in relevant PIRT - reactor type (or both if unspecified)
Scenarios: NO – Normal Operation
                  GL – General Loss of Forced Circulation (GLOFC)
                  PL – Pressurised Loss of Forced Circulation (PLOFC)
                  DL – Depressurised Loss of Forced Circulation (DLOFC)
                  AI – Air Ingress
                  AT – Anticipated Transient Without Scram (ATWS)
System specific phenomenon/scenario pairs:
                  PBR – only applicable to pebble bed reactors

3.4   References for Section 3

3.1   Ball S.J., "Next-Generation Nuclear plant Phenomena Identification and Ranking Tables (PIRTs); Volume 1 – Thermofluids and Accident Analysis PIRTs," Draft NUREG/CR-6944 Vol. 1 (ORNL/TM-2007/xxx Vol. 1), September 2007.

3.2   Stainsby R., "Investigation of Local Heat Transfer Analysis in an HTGR Core," NSS Report No. NR001/PL/001 R01, December 3, 2007.

4.0   SCOPE OF THE CURRENT PROGRAMME OF RESEARCH

4.1   Purpose of Section 4

This section discusses the chosen research themes for the pebble bed reactor resulting from the PIRT (see Section 3) and describes how these themes have been addressed.

The approach adopted was to select research themes which generally address multiple PIRT items. A similar study has been performed for prismatic modular reactors (Reference 4.1) and there are common features between both reactor types. Therefore some of the research topics that are applicable to both reactors, such as the microscopic fuel temperature modeling methods, have only been studied for one reactor type.

For the pebble bed reactor, the following research themes were investigated:

1. Mechanisms influencing fuel and moderator temperatures

2. Investigation of pebble bed pressure losses and heat transfer mechanisms- internal and reflector interface effects

3. Effective thermal conductivity of the pebble bed in LOFC conditions

4. Whole core CFD model.

Each theme is discussed in more detail in Sub-Sections 4.2 to 4.5 below.

4.2   PBR Theme 1

The first theme, "Mechanisms influencing fuel and moderator temperatures", is concerned with developing the capability to be able to predict correctly the distribution of fuel kernel, TRISO coating and moderator temperatures in steady state and transient conditions. It was chosen as these temperatures are important for the determination of temperature effects on reactivity, power and flux profiles, and maximum fuel kernel and coating temperatures in normal operation. Further, determination of irradiated graphite properties and the initial conditions for transients, requires the fuel and moderator temperatures to be known. Accurate predictions of these temperatures are also essential to provide input to, or coupling with, neutronics models, to assess fuel particle integrity, and to generate the starting conditions for LOFC and ATWS transients.

This theme specifically addresses some of the PIRT items directly, whilst providing necessary information to others, albeit indirectly. For example, accurate prediction of core temperatures is essential to determine the power and flux distributions; hence the research theme contributes directly to PIRT item NO-22. However, the decay heat distribution (PIRT items GL-21 and DL-2), is not a function of core temperature distribution directly, but it is a function of the power and flux distribution. Following this reasoning, this research theme contributes directly to:

NO-22, AT-5	Reactivity –temperature feedback coefficients
NO-26	Power and flux profiles
NO-16	Effective fuel element thermal conductivity,

and is a necessary step towards gaining an understanding of:

NO-20	Shutdown cooling system startup transients during core heat up
GL-1, DL-1	Core thermal conductivity (effective)
GL-21, DL-2	Decay heat (spatial and temporal)
AT-6	Control and scram rods and reserve shutdown worths
AT-10	Coolant flow restarts during loss of forced circulation ATWS

This theme was split into sub-tasks which are discussed in Sections 5.0 to 9.0. Section 5.0 discusses the development and qualification of the micro and meso-scale fuel particles and pebble temperature models (steady-state and transient). Section 6.0 discusses the examination of particle clustering, that is, the expected size of clusters within a pebble, and the temperature enhancement expected from clustering. Section 7.0 presents an analytical method by which the effective conductivities of TRISO particles in the interior fuelled zone can be interpolated, and a validation of the model. Section 8.0 discusses the development of multi-batch fuel models. Lastly, Section 9.0 summarizes a review of irradiated graphite thermal properties.

4.3 PBR Theme 2

The second theme, "Investigation of pebble bed pressure losses and heat transfer mechanisms – internal and reflector interface effects", is aimed at quantifying the pebble bed internal and edge effects such as coolant flow distribution and edge overcooling (or centre under-cooling) owing to the reduced packing fraction at the pebble bed-reflector interface. Similarly, the local influence on convective heat transfer coefficients and thermal radiation heat transfers is investigated.

This theme is aimed at the development of models to predict how the pebbles interact hydraulically and thermally with their surroundings. These interactions are influenced by whether the pebbles sit internally within a large pebble bed, or alternatively, sit close to or at the edges of the bed in contact with the reflectors. Proximity to the edge of the bed introduces systematic variations in the packing density of the pebbles, which decreases with increasing distance from the edge. Packing densities that are generally close to the average value are only found remote from the reflectors. The packing fraction influences the frictional pressure drop and the surface averaged convective heat transfer coefficients.

Within this research theme, detailed CFD models of limited assemblies of pebbles are set up. Two groups of pebble assemblies are created representing, respectively, pebbles remote from a reflector and those adjacent to reflectors. Each of these models includes convective, conductive and radiative heat transfer. These models are used to obtain:

- Flow distribution and pressure drop
- Local, over pebble surface, and pebble average convective heat transfer coefficient
- Pebble to pebble heat transfer
    - Uniform burn-up
    - Multi-batch fuel – comparison with Theme 1 multi-batch sub-model
- Pebble to reflector heat transfer.

Generation of credible packing arrangements for the assemblies of pebbles is investigated and a suitable technique adopted for creating the models.

This research theme specifically addresses the following PIRT items:

NO-8-PBR	Pebble bed core wall interface effects on bypass flow
NO-22, AT-5	Reactivity –temperature feedback coefficients
NO-26	Power and flux profiles
NO-16	Effective fuel element thermal conductivity
NO-2	Core flow distribution, flow in active core
NO-10-PBR	Coolant heat transfer correlations

and it is a necessary step in gaining an understanding of:

NO-20	Shutdown cooling system startup transients during core heat up
GL-1, DL-1	Core thermal conductivity (effective)
GL-21, DL-2	Decay heat (spatial and temporal)
PL-6	Coolant flow friction/viscosity effects
AT-6	Control and scram rods and reserve shutdown worths
AT-10	Coolant flow restarts during loss of forced circulation ATWS
AI-6	Core oxidation

The methodology used for this research theme is discussed in Section 10.0.

4.4   PBR Theme 3

The third theme is aimed at investigating conduction and thermal radiation heat transfer through the pebble bed in loss of forced circulation conditions. The aim of this is to assess the correctness and applicability of the German correlations commonly used to determine the effective conductivity of a pebble bed, such as the Zehner-Schlunder and Robold correlations.

This theme builds on the work of theme 2, to determine the effective thermal conductivity of the pebble bed at high temperature and in the absence of forced coolant flow.

This research theme specifically addresses the following PIRT items:

GL-1, DL-1   Core thermal conductivity (effective)

and it is a necessary step in gaining an understanding of:

PL-2   Radiation heat transfer from the top of the pebble bed

AI-6   Core oxidation

The work undertaken for this research theme is detailed in Section 11.0.

4.5   PBR Theme 4

The fourth theme, "Whole core CFD models", is aimed at producing a computational fluid dynamics (CFD) model of a pebble bed core and its reflectors. The model is based on a porous medium approximation of the pebble bed and on the published dimensions of PBMR.

The CFD model of a pebble bed HTGR core is set up to act, initially, as host for the sub-models developed in the first three research themes. This model enables the sub-models to be validated using code to code comparisons within the IAEA CRP-5 program. A circumferentially coarse three-dimensional model is set up of the PBMR core, and this is suitable for both steady state and transient conditions. Only the neutronically significant regions of the core and external structures necessary to study passive heat removal are modeled. Some features, such as the exit cones and top surface pebble heaps are omitted. Core bypass flow paths are included in this model. Assignment of the correct hydraulic resistance to these flow paths will only be possible when the relevant design information becomes available.

The model has been developed using the FLUENT CFD code, as this facilitates programming of the sub-models and will be of long-term use to the NRC.

This research theme specifically addresses the following PIRT items:

NO-22, AT-5   Reactivity –temperature feedback coefficients

NO-1   Core coolant bypass flow

NO-2   Core flow distribution, flow in active core

NO-26   Power and flux profiles

and it is a necessary step in gaining an understanding of:

NO-4   Core flow distribution changes due to graphite irradiation

NO-20   Shutdown cooling system startup transients during core heat up

GL-1, DL-1   Core thermal conductivity (effective)

GL-4   Vessel emissivity

GL-9   Reflectors: conductivity and annealing

GL-10	Core barrel emissivity
GL-21, DL-2	Decay heat (spatial and temporal)
PL-1	Inlet plenum stratification and plumes
PL-2	Radiation heat transfer from the top of the pebble bed
PL-4	Core coolant flow distributions
PL-5	Core coolant bypass flow
AI-6	Core oxidation
AI-7	Cavity to reactor vessel air ingress
AI-15	Molecular diffusion
AT-3	Reactivity insertion due to steam-water ingress accidents
AT-6	Control and scram rods and reserve shutdown worths
AT-10	Coolant flow restarts during loss of forced circulation ATWS

Although this model is used to investigate the influence of core bypass flow, a Priority 1 PIRT item, the lack of detailed design information prevents a meaningful study from being achieved. Therefore, the investigation of core bypass flow in a PBR will be deferred to a future study.

4.6   References for Section 4

4.1   Stainsby R. et al., "Investigation of Local Heat Transfer Phenomena in a Prismatic Modular HTGR Core", AMEC NSS Report NR001/RP/001 R02, May 2009.

5.0 MICRO AND MESO-SCALE FUEL PARTICLES AND PEBBLE TEMPERATURE MODELS – STEADY STATE AND TRANSIENT

5.1 Purpose of Section 5

Determination of the fuel temperatures in a pebble bed high temperature gas reactor (HTGR) core requires the temperature field to be modelled over a wide range of length scales. For convenience, these have been classified into three groups and are referred to here as the macroscopic scale, meso-scale and micro-scale, in order of descending length scales.

The largest length scale, the macroscopic scale resolves the temperature distribution on a scale of the whole reactor down to the size of a cell that contains a few tens to a few hundred pebbles – or a few metres down to a few centimetres. A thermal hydraulic solution on this length scale requires the pebble bed to be sub-divided into a number of such computational cells and is able to calculate the mean coolant velocity, pressure and temperature in each cell together with the average surface temperature of the pebbles. Commercial computational fluid dynamics (CFD) codes, or bespoke codes based on standard CFD solution methods, are suitable for solving for the flow and temperature fields on the macroscopic scale. However, the details of the temperature distribution within individual pebbles and in and around the individual TRISO particles within the pebbles are on scales that are too small to be resolved by the CFD code. As such, sub-grid scale models are constructed and applied to re-create these fine-scale temperature fields from the cell-averaged values predicted by the CFD code.

The meso-scale is taken to represent the length scales that range from a collection of a few pebbles down to the size of a collection of a few TRISO particles – or a few centimetres down to a few millimetres. If the heat generation from the particles is smeared over the volume of the heated zone within a pebble, the meso-scale temperature distribution within a pebble can be determined by solving a one-dimensional conduction equation in the spherical co-ordinate system of the pebble. Also on the meso-scale, the pebble exchanges heat with the coolant flowing through the computational cell and with other pebbles in the cell. These heat exchanges are complicated further by the fact the cell contains randomly mixed pebbles with widely different irradiations, possibly different enrichments and, therefore, different power outputs.

The micro-scale resolves the temperature field on the scale of an individual TRISO particle, ranging from a few millimetres down to a few tens of micrometres. The micro-scale temperature field within and around a TRISO particle can be calculated by solving a one-dimensional conduction equation in the spherical co-ordinate system of the particle.

Resolving the temperature field simultaneously on three different length scales is an established technique known as multi-scale modelling. In essence the technique involves successively averaging the behaviour of the smaller scale when progressing upwards through each of the larger length scales. The overall behaviour of the

system is solved for on the largest scale and then each solution on the smaller scales is used as a magnifying glass to progressively zoom-in on the behaviour at the finer scales.

This section concentrates on the development and qualification of the micro and meso sub-grid scale models that enable the fuel kernel and moderator temperatures to be calculated. The first sub-section presents a finite element analysis of a two-dimensional slice through a simplified pebble. This simplified pebble contains the main features of a real spherical pebble, except that the number of particles is greatly reduced and are located based on an ordered arrangement and the geometry is cylindrical rather than spherical. Such a simplified model was chosen as it is both easier to generate and easier to compare with the multi-scale model. This comparison is made in the latter sub-section after the basic concepts and application of multi-scale modelling to a simple one-dimensional linear heated bar problem have been demonstrated. Finally, the development of a multi-scale model in spherical geometry is presented and applied to a realistic pebble geometry that contains coated particles.

5.2   Finite Element Models

This sub-section describes the steady state and transient two-dimensional finite element model that has been produced of a region of a pebble. This simplified model is used for later comparison with the analytical model.

The finite element program code used for this work was Abaqus/CAE version 6.7-1 and the geometry modelled, material properties and boundary conditions applied, and results obtained are described below.

5.2.1   Modelled Geometry

A two-dimensional finite element model was produced of a slice through the centre of an idealised spherical pebble. The slice passes through the centres of 37 fuel particles contained within a graphite matrix. Therefore the two-dimensional representation of the pebble includes a representation of 37 particles as 2-dimensional discs, as shown in Figure 5.2.1. The 37 particles are arranged in a simplified regular manner consisting of a central particle surrounded by three rings containing 6, 12 and 18 particles respectively. The radial distances between rings were equal, at 1.972mm, and within each ring the fuel particles were distributed evenly around the circumference, giving a circumferential pitch of 2.065 mm. The fuel particles were assigned a diameter of 1mm.

Figure 5.2.1: Representative Cross-Section Through an Idealised Pebble
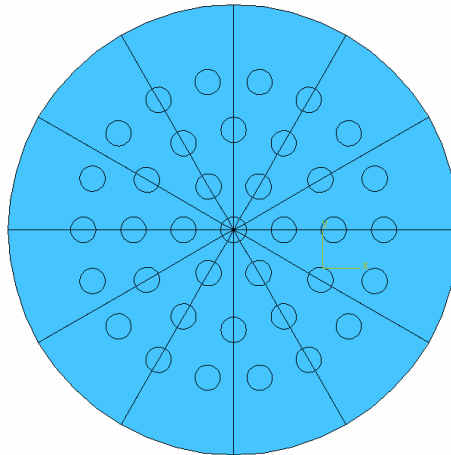
The model used for the finite element analysis is shown in Figure 5.2.2 and together with the radial and circumferential pitches of the particles in Figure 5.2.3. A 30° sector of the overall cross section was modelled taking advantage of symmetry.

Figure 5.2.2: Finite Element Model Domain

Dimensions shown in mm
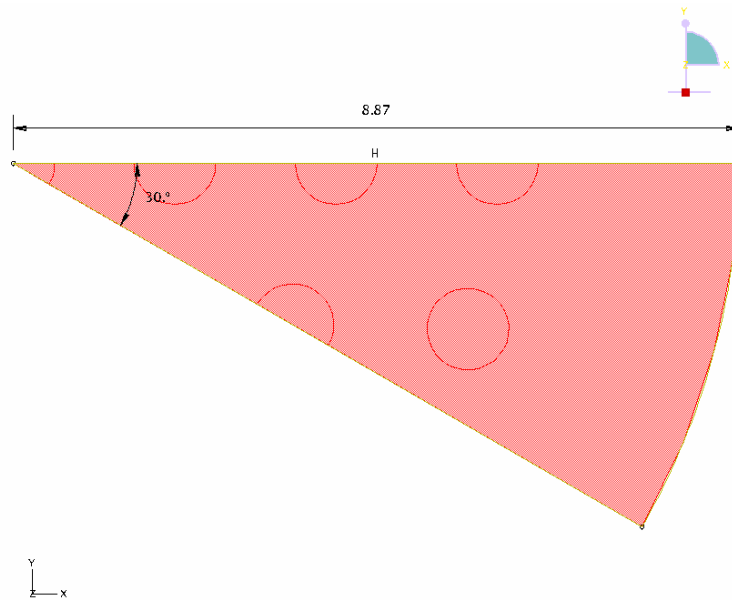
Figure 5.2.3: Finite Element Model Dimensions

Dimensions shown in mm
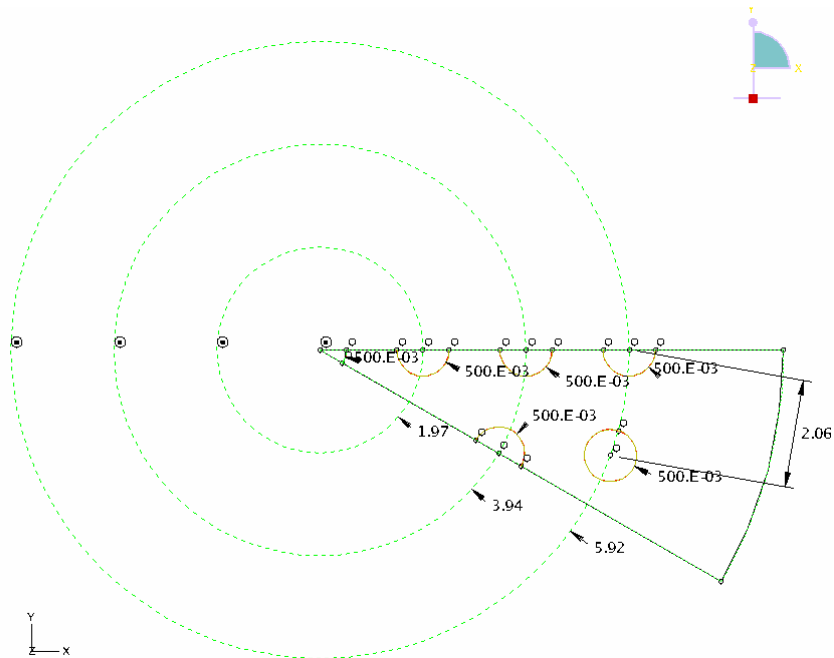
The area ratio of fuel to graphite has been taken to be 20:80. Based on a particle diameter of 1 mm, and with 37 particles, this area ratio was obtained if the radial pitch of the particles was 1.972 mm with a corresponding circular pitch of 2.065 mm.

An extra ring of graphite was added to the model to simulate the particle-free graphite shell of a real spherical pebble, with the width of this ring chosen to be equivalent to one radial pitches of the particles. As the distance between rings of fuel particles is 1.972mm, the overall radial extent of the model is four and a half times this, at 8.874mm.

5.2.2   Material Properties and Boundary Conditions

The finite element model consists of two materials representing fuel particles and graphite. However, the material properties assigned do not represent actual materials, but were simply chosen to compare with the multi-scale solutions of Section 5.3 and the values used are shown in Table 5.2.1. The dimensions of the finite element and multi-scale models were specified in mm and therefore, the units of the properties are based on a length scale of mm.

Table 5.2.1: Material Properties Used in the Model

Material*	Conductivity (W/mm/K)	Density (kg/mm^3)	Specific Heat (J/kg/K)
Graphite	5.0	1.0	1.0
Fuel	5.0	1.0	1.0

* Note: not actual material properties

A power density of 50W/mm^3 was applied to each of the 37 particles.

The boundary conditions along the edges of the model are symmetry planes. A fixed temperature boundary condition was applied to the surface of the pebble, with the surface temperature set to be 20°C (again not a realistic condition but simply for comparison with the multi-scale model of Section 5.3).

The finite element mesh for this model was constructed using 4-node bi-linear quadrilateral elements.

5.2.3 Steady State Results

Figure 5.2.4 shows the steady state distribution of temperature for a particle power density of 50W/mm^3. Temperature profiles along the upper edge and lower edge of the model, relative to the orientation of the sector as shown in Figure 5.2.4, are presented in Figures 5.2.5 and 5.2.6 respectively. A further profile through the centre of the model (at a 15° angle) is presented in Figure 5.2.7.

Figure 5.2.4: Temperature Distribution

Temperatures shown in Kelvin
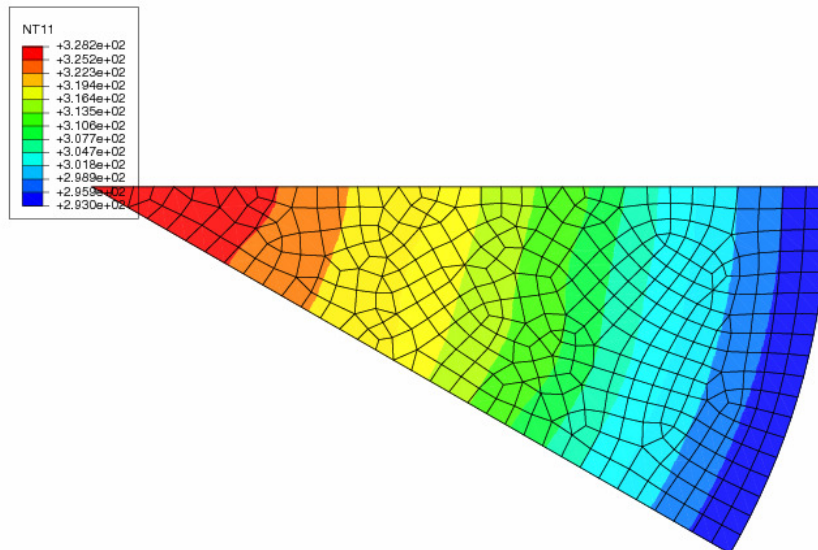
Steady state heat transfer, k=5W/mmk for fuel and graphite
ODB: Steadystate1.odb   Abaqus/Standard Version 6.7-1   Wed Feb 27 10:07:06 GMT 2008

Figure 5.2.5: Temperature Profile Along the Upper Edge of the Model
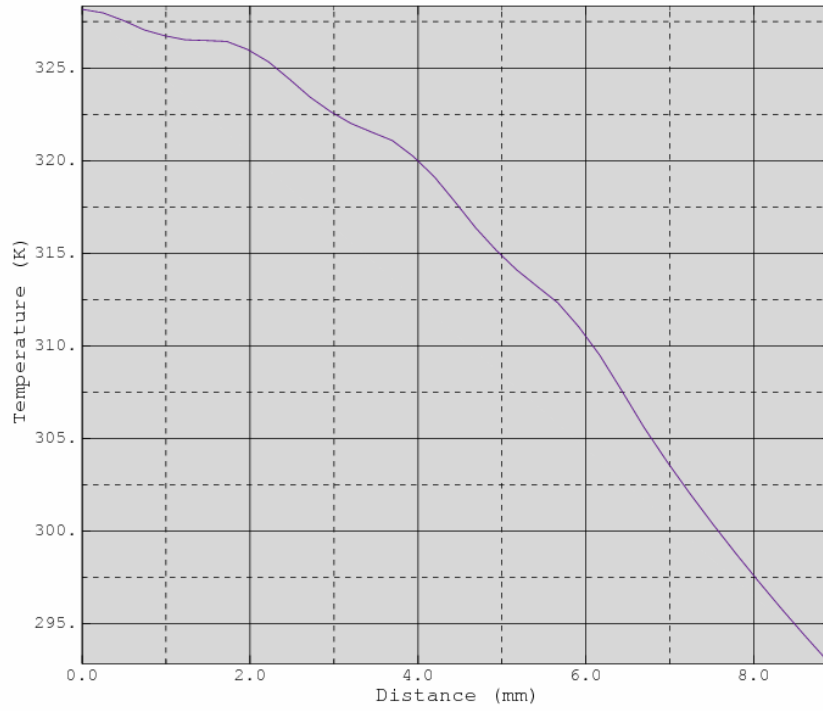
Figure 5.2.6: Temperature Profile Along the Lower Edge of the Model
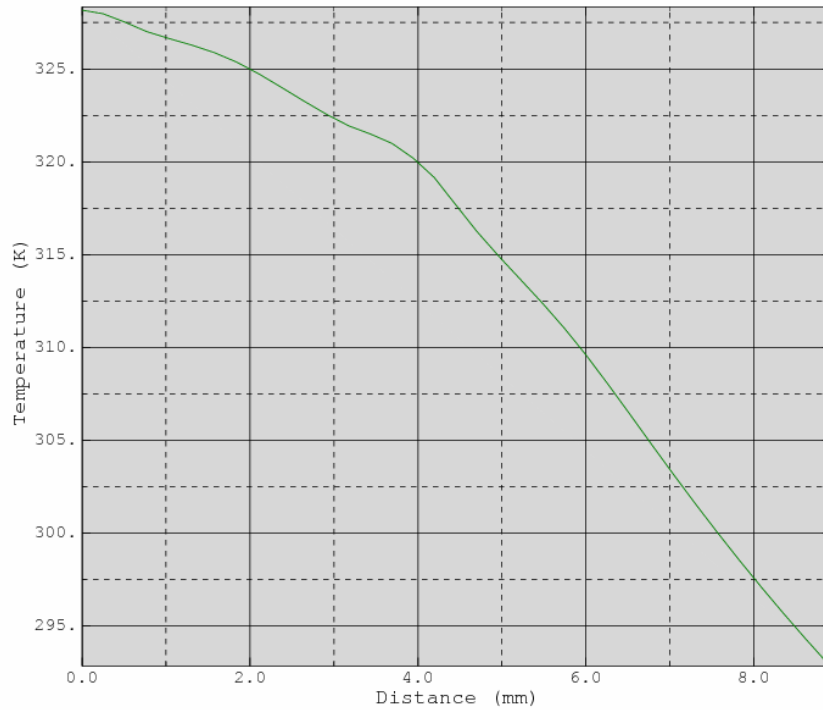
Figure 5.2.7: Temperature Profile Along a 15° Radial Line
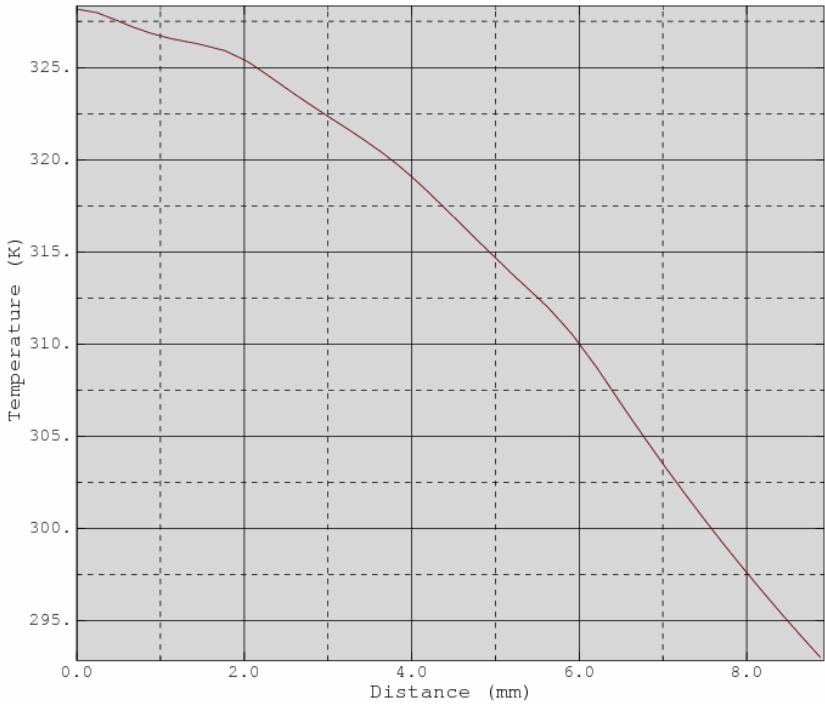
5.2.4 Influence of Material Thermal Conductivities

The fuel conductivity was reduced to 2W/mm/K, with the other properties and boundary conditions unchanged from the initial model. Figure 5.2.8 shows the two-dimensional temperature distribution over the model. Temperature profiles along the upper edge, lower edge and through the centre of the model are shown in Figures 5.2.9 to 5.2.11 respectively. For comparison, the previous results based on a fuel conductivity of 5W/mm/K are shown. It can be seen that, as expected, there is a larger overall radial temperature difference and the fuel particles have a more pronounced effect on the temperature distribution when the fuel thermal conductivity is lower.

Figure 5.2.8: Temperature Distribution with Particle Conductivity of 2W/mm/K

Temperatures shown in Kelvin
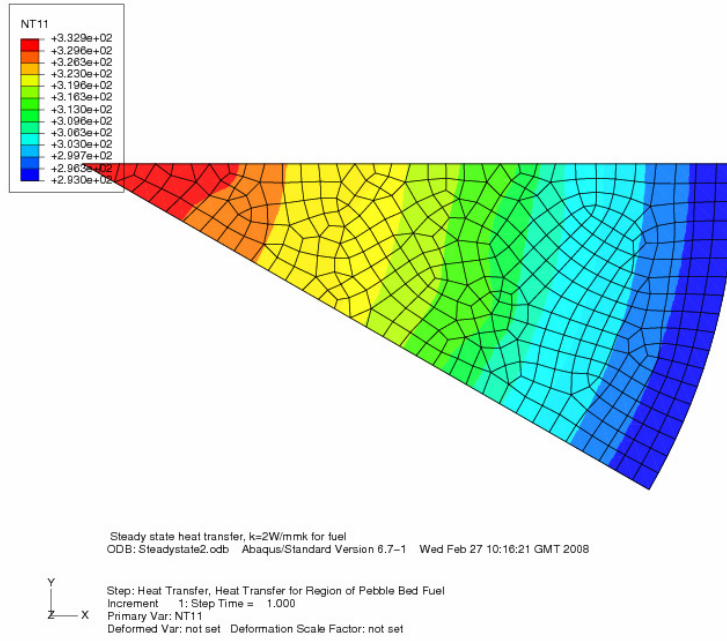
Figure 5.2.9: Temperature Profile Along Upper Edge of Model, with Fuel Conductivities of 2W/mm/K and 5W/mm/K
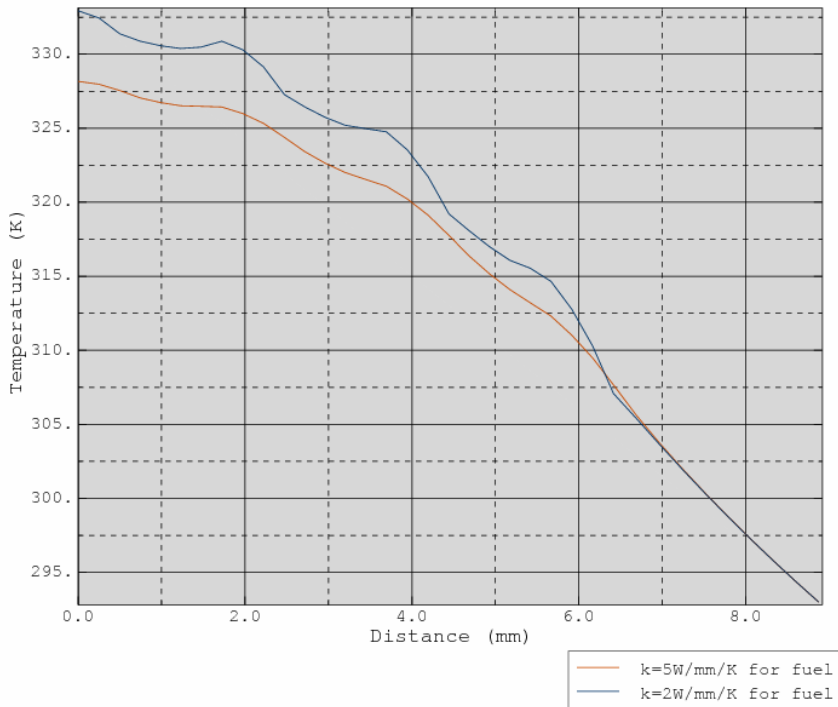
Figure 5.2.10: Temperature Profile Along Lower Edge of Model, with Fuel Conductivities of 2W/mm/K and 5W/mm/K
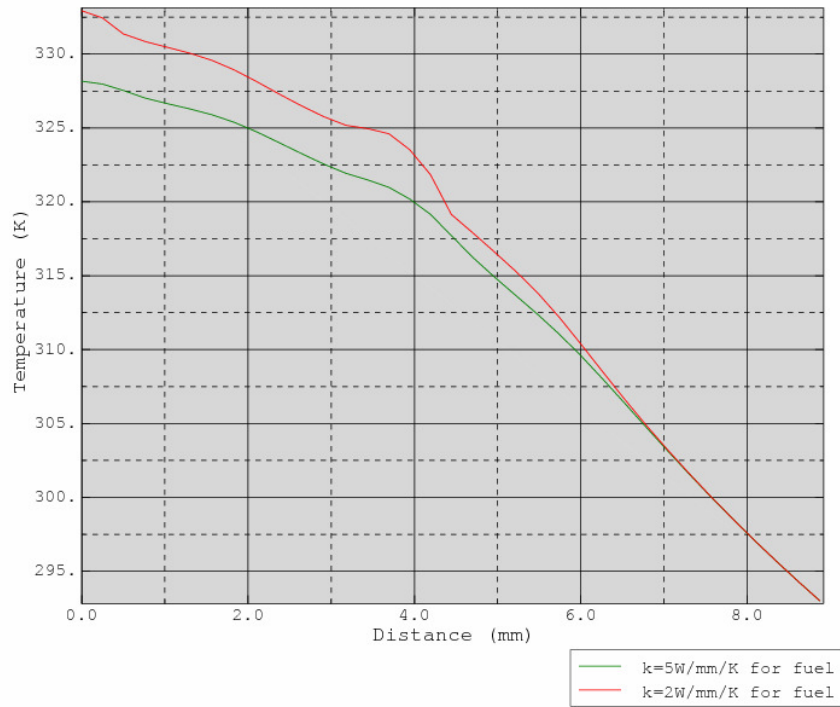
Figure 5.2.11: Temperature Profile Through the Centre of Model, with Fuel Conductivities of 2W/mm/K and 5W/mm/K
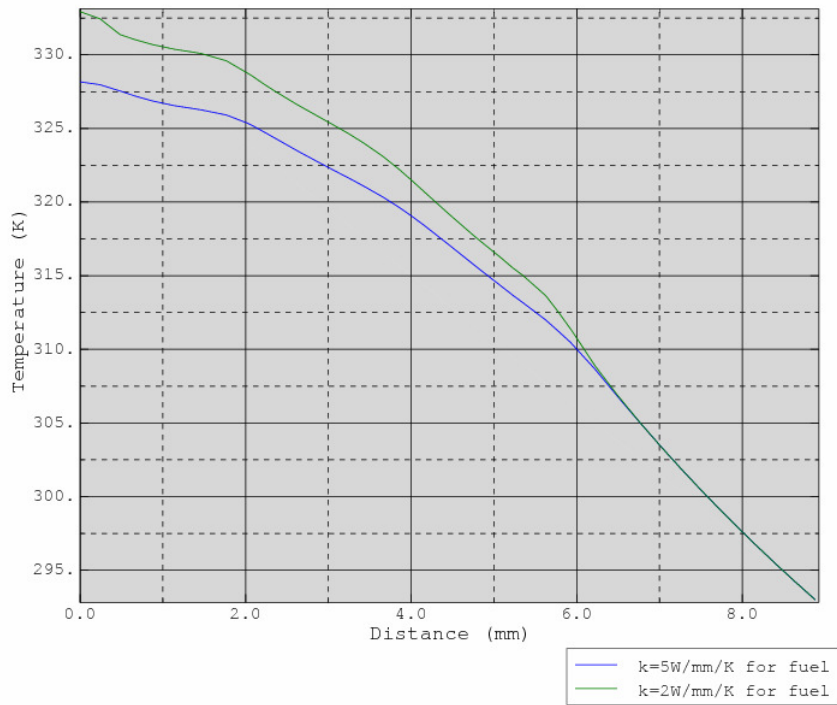
5.2.5   Transient Model

A transient model was set up, with a thermal conductivity of graphite of 5W/mm/K and a thermal conductivity of fuel of 2W/mm/K. The initial temperature was set to 20°C everywhere, to be consistent with the boundary condition in the steady state calculations. The transient begins with zero heat input which is then stepped-up over one time step to the previous steady state value of a power density of 50W/mm^3 in the particles. The boundary condition on the pebble surface was a fixed temperature which was held constant throughout time at 20°C.

Figure 5.2.12 shows the development of the temperature profile along the top edge of the model for a selection of eight time steps with the last time step at 40.49s being negligibly different from the steady state profile. In this figure it can be seen that early in the transient, the particles heat up independently and on a short-timescale without influencing, or being influenced by the temperature of the surrounding matrix material. Later in the transient, the temperature fronts from the separate particles merge and contribute to raising the temperature of the pebble structure, but on a longer timescale.

Figure 5.2.12: Transient Model - Temperature Profile at Various Times Along Upper Edge of Model
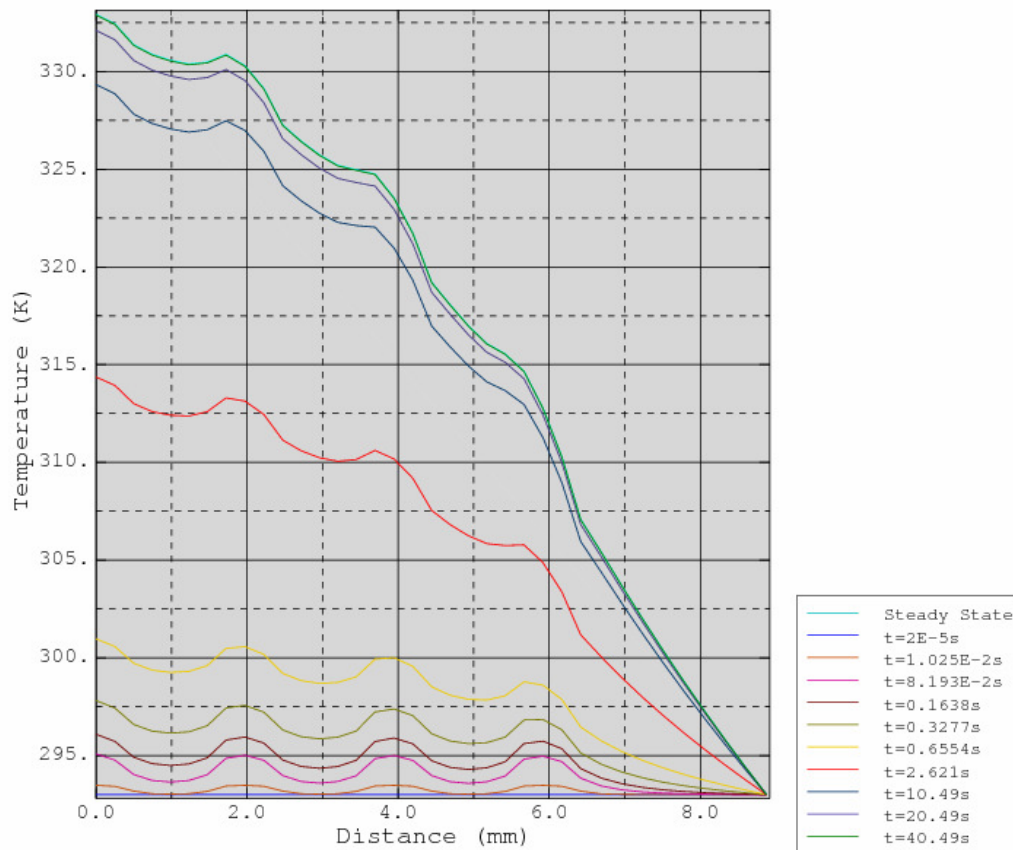
Figure 5.2.13 shows the temperature profiles for the same selection of time steps as in Figure 5.2.12 but along a line through the centre of the model (at 15°). Again, after 40s the transient temperature profile is negligibly different from that of the steady state.

Figure 5.2.13: Transient Model - Temperature Profile at Various Times Along a 15° Radial Path Through the Centre of the Model
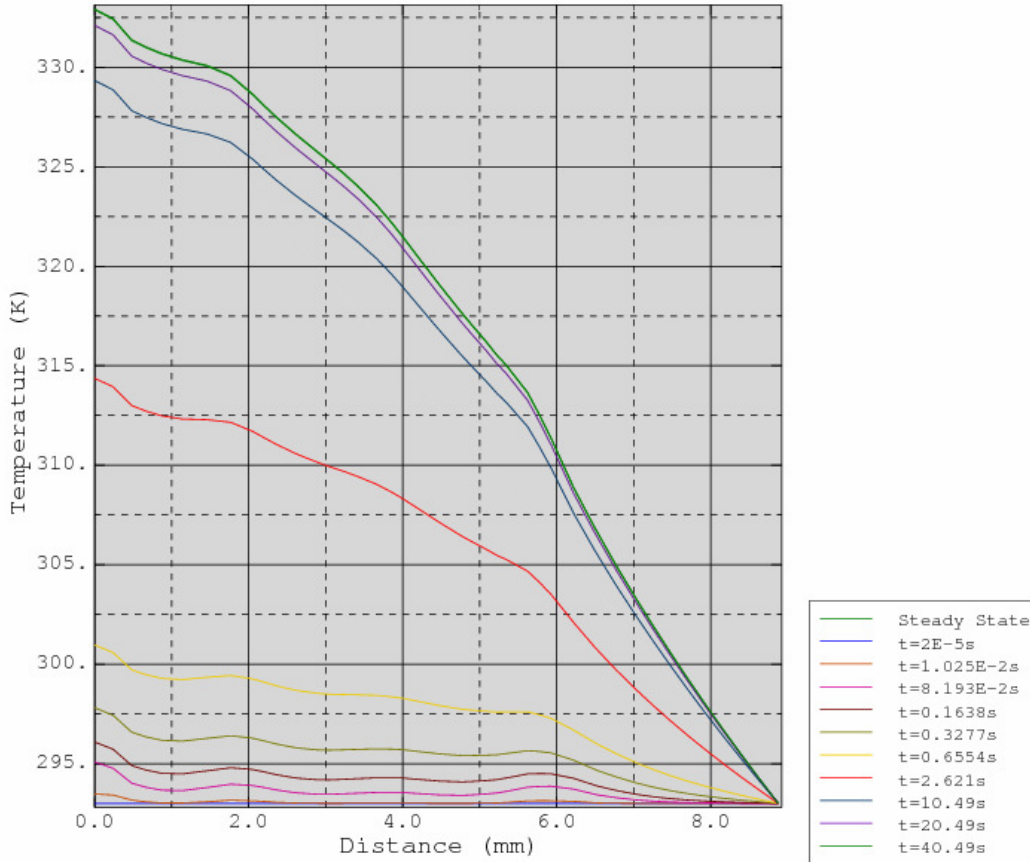
5.3   Micro and Meso-Scale Models

The work presented in this section is directed towards developing and coupling micro and meso-scale models of a pebble and the particles contained therein. In this work, the meso-scale represents length scales from about a tenth of the radius of a pebble up to a few pebble diameters, i.e., the range of length scales that are too small to be represented by a CFD model of the whole reactor but larger than a few particle diameters. The micro-scale length scales range from about 1/10 of a kernel diameter up to a few particle diameters.

Ultimately, the objective of the work is to develop one-dimensional transient models that are able to represent the thermal behaviour of the fuel kernels and the surrounding graphite of the pebble that can be embedded within CFD models of the whole core. The models, therefore, have to be simple and fast running, but also must accurately represent the physics. The technique used to achieve this is known as

multi-scale analysis in which separate differential equations are solved for each of the length scales. In general, detail is progressively smeared out as the length scales become larger, and the spatial extent of the domains are decreased as the length scales becomes smaller. The overall solution is obtained from the addition of all of the solutions on all of the different length scales. In this work, only two length scales are considered, the micro and meso-scales as defined above. In a CFD analysis of the whole core, a third scale is introduced, the macro-scale, whose length scale is that of the reactor core itself and in which the individual pebbles are smeared-out to form a heat generating and heat transmitting porous medium.

The work presented here builds on a method developed by AMEC for coupling thermal hydraulic and neutronic analyses. This method was used in the UK contribution to the IAEA's CRP5 programme within the HTR-10 and PBMR-400 benchmarks. The models developed previously were developed somewhat pragmatically in that they were simple to solve and satisfied the boundary conditions, but were not derived formally by solving the differential equations. This pragmatic method was (and is) believed to be suitable for steady state conditions, but the extension to transient situations requires the differential equations to be solved and, as such, the steady state solutions have to be compatible with the asymptotes of the transient solutions. To this end, the micro and meso-scale solutions have been re-worked, extended to transient situations and mathematical formalism introduced through the use of multi-scale analysis.

5.3.1   Previous Steady State Approach

The derivation of the model used previously to construct pebble and TRISO particle temperature profiles is presented here and expanded further in Appendix A.1.

5.3.1.1   Steady State Temperature Profile in a Pebble

The temperature profile within a pebble is computed using a spherically symmetric heat conduction model. The pebble is divided into two zones: the outer un-fuelled graphite shell and the central fuelled pebble core. The nuclear heating is assumed to be uniformly distributed over the central core region, and non-local heating due to gamma rays, etc. is not modelled.

The steady state temperature within a fuel pebble is governed by the heat conduction equation:

$$-\nabla \cdot \left(k \nabla T_{peb} \right) = \dot{q}'''$$

which, under the assumption of spherical symmetry, reduces to:

$$-\frac{1}{r^2}\frac{d}{dr}\left(r^2 k \frac{d\,T_{peb}}{d\,r} \right) = \begin{cases} 0 & \text{for} & r_{core} < r < r_{peb} \\ \dot{q}'''_{core} & \text{for} & 0 < r < r_{core} \end{cases}$$

where $\dot{q}'''_{core}$ represents the power density within the fuelled core of the pebble element, r_{core} is the radius of the fuelled region within a pebble and r_{peb} is the outer radius of a pebble.

The conduction equation is subject to the boundary condition:

$$T(r_{peb}) = T_{surf} .$$

To simplify the solution of this equation, the conductivity k is assumed to be constant within each of the two regions of the pebble, taking values k_{shell} and k_{core} in the shell and fuelled core region respectively. The conduction equation for the temperature distribution through a fuel pebble can be solved analytically, with the following solution (refer to Appendix A.1):

$$T_{peb}(r) = \begin{cases} T_{surf} + \dfrac{\dot{q}'''_{core} r^3_{core}}{3k_{shell}} \left(\dfrac{1}{r} - \dfrac{1}{r_{peb}} \right) & \text{for} \quad r_{core} < r < r_{peb} \\ \\ T_{surf} + \dfrac{\dot{q}'''_{core} r^3_{core}}{3k_{shell}} \left(\dfrac{1}{r_{core}} - \dfrac{1}{r_{peb}} \right) + \dfrac{\dot{q}'''_{core}}{6k_{core}} \left(r^2_{core} - r^2 \right) & \text{for} \quad 0 < r < r_{core} \end{cases}$$

The thermal conductivities of the graphite in the pebble shell and the pebble core are evaluated using an interpolation scheme to account for temperature and neutron fluence dependence (the dependence of the thermal conductivity of graphite on irradiation is discussed in Section 9). Further, the conductivity of the pebble core should take into account the presence of TRISO fuel particles (see Section 7).

5.3.1.2   Steady State Temperature Profile in a TRISO Particle

The analysis described in Section 5.3.1.1 allows the computation of the graphite temperature within a fuel pebble. However within the pebble there are localised temperature perturbations, caused by the presence of discrete microscopic TRISO fuel particles. In this section the effect of these localised temperature perturbations on the surface temperature of the TRISO particles is considered first. The particle surface temperatures are required for the calculation of the TRISO particle coating and fuel kernel temperatures.

Figure 5.3.1: Temperature Distribution Through a Pebble Consisting of a Long, Meso-Scale, Variation and Short Wavelength, Micro-Scale, Perturbation
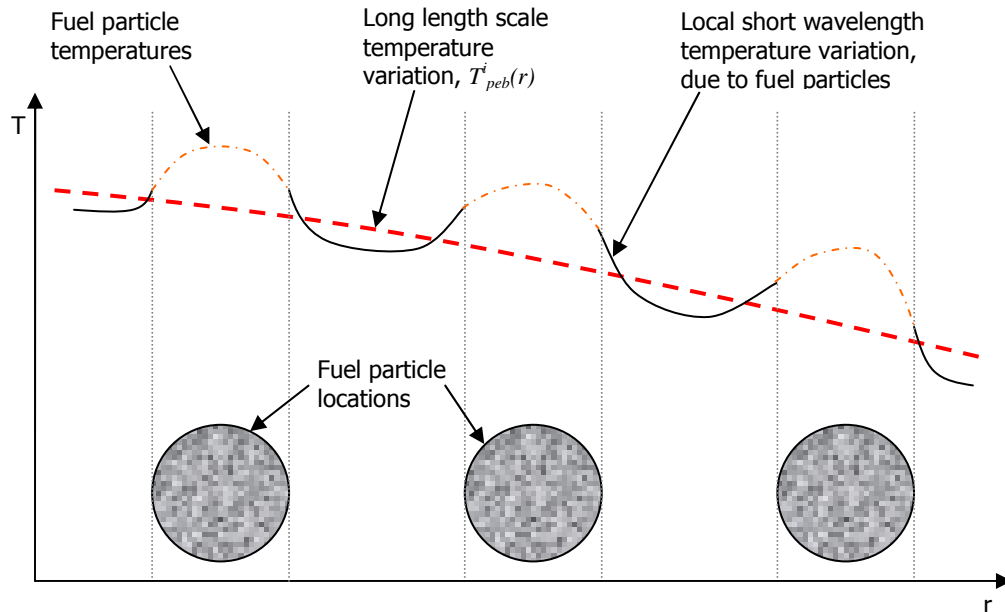
The presence of the fuel particles causes a short wavelength perturbation to the graphite temperature profile $T_{peb}(r)$. The resulting temperature profile is sketched in Figure 5.3.1. The calculation of the exact temperature profile within this region is difficult, requiring a three dimensional computational model. Therefore a simple approximation is used to estimate the particle temperatures, as described below.

Each fuel particle is associated with a representative sphere of graphite, with radius R_{av}, where this radius is determined from the volume of a sphere (a micro-sphere) that contains the particle's share of the pebble core graphite as shown in Figure 5.3.2.

Figure 5.3.2: A 'Micro-Sphere' Consisting of a TRISO Particle and its Share of the Graphite Matrix

The localised perturbation to the background graphite temperature within the representative volume of graphite surrounding a fuel particle is *approximated* by a quadratic profile. A quadratic profile was chosen as being the simplest that fulfils the requirement that the gradient is finite at the surface of the particle and zero between the particles. The second condition comes from the assumption that neighbouring particles are identical on the micro-scale, hence the outer surfaces of the micro-spheres are effectively symmetry surfaces. For a fuel particle centred at radius r within a pebble, this approximation takes the form:

$$T_{core}(r, R) = T_{peb}(r) + \varepsilon(R), \qquad \varepsilon(R) = \alpha R^2 + \beta R + \gamma$$

where R is a local radial coordinate measured from the fuel particle centre, and the local perturbation $\varepsilon(R)$ is assumed to satisfy the following conditions:

1) The temperature perturbation is symmetric about the centre of a fuel particle.

2) The temperature perturbation within the representative volume of graphite has zero mean, such that the average graphite temperature within the volume is equal to the background temperature, $T_{peb}(r)$.

3) The gradient of the temperature perturbation at the particle surface is determined by the heat flux flowing through the particle-graphite contact surface and is proportional to the heat generated within a fuel particle kernel, $\dot{q}_{kernel}^{i}$.

Application of these conditions enables the coefficients α, β, and γ to be determined, leading to the solution for the temperature perturbation at the particle surface, $\varepsilon(R_{part})$, to be:

$$\varepsilon(R_{part}) = \alpha R_{part}^2 + \beta R_{part} + \gamma$$

$$= \frac{\dot{q}_{kernel}}{8\pi k_{core}(R_{av} - R_{part})}\left[1 - \frac{2R_{av}}{R_{part}} + \frac{3R_{part}^3}{(R_{av}^3 - R_{part}^3)}\left[\frac{3}{10}\left(\frac{R_{av}}{R_{part}}\right)^5 - \frac{1}{2}\left(\frac{R_{av}}{R_{part}}\right) + \frac{1}{5}\right]\right]$$

The fuel particle surface temperature is therefore:

$$T_{particle\ surface}(r) = T_{core}(r, R_{part}) = T_{peb}(r) + \varepsilon(R_{part})$$

The temperature profile within a fuel particle, T_{part}, is governed by heat conduction through the particle coatings and fuel particle kernel. In a steady state, the heat flowing through the particle coatings must balance the heat released within the fuel kernel, $\dot{q}_{kernel}$, giving the overall temperature difference across all the coatings as:

$$\Delta T_{coat,total} = \dot{q}_{kernel}\alpha_{coat,eff}$$

where the combined thermal resistance of all of the coatings, $\alpha_{coat,eff}$, is simply the sum of the thermal resistances of the individual coatings.

The temperature at the surface of the fuel kernel is equal to:

$$T_{kernel\,surface} = T_{particle\,surface}(r) + \Delta T_{coat,total}$$

The temperature profile within the fuel kernel is described by the heat conduction equation. The fuel kernel is assumed to be spherically symmetric, and the nuclear heat released within the particle is assumed to be uniformly distributed over the volume of the fuel kernel. This equation, together with the boundary condition:

$$T_{part}(R_{part}) = T_{kernel\,surface}$$

has the unique bounded solution for the temperature profile in the kernel:

$$T_{part}(R) = T_{kernel\,surface} + \frac{\dot{q}'''_{kernel}}{6\,k_{kernel}}\left(R_{kernel}^2 - R^2\right), \quad \text{for} \quad 0 < R < R_{kernel}.$$

where the power density in the kernel is simply the power generated divided by the kernel volume; $\dot{q}'''_{kernel} = \dfrac{\dot{q}_{kernel}}{(4\pi R_{kernel}^3/3)}$.

The above equation is used to determine the temperature at any point within any kernel in the pebble. The average temperature of any single kernel is obtained by integrating this equation over the radius of the kernel. Similarly, the average temperature of all the kernels in a pebble is obtained by a further integration over the radius of the fuelled zone within the pebble.

5.3.2 Extension to Transients

The analytical solutions presented in Section 5.3.1 for the pebble and particle temperature profiles are only applicable to steady state situations. Further, the temperature perturbation over the radius of the graphite micro-sphere is an approximation rather than a solution to the differential equation. Solutions for transients must be obtained by solving the differential equations, therefore, the resulting steady state solution must be a solution to the differential equation so that the transient and steady state solutions are compatible.

5.3.2.1 Revised Steady State Analytical Treatment in One Dimension

In Section 5.3.1, a series of algebraic equations were solved on the meso and micro-scales and the two solutions were coupled by imposing the condition that the average graphite temperature within a micro-sphere in the micro-scale solution must be the same as the local graphite temperature at the radius at which the particle is centred in the meso-scale solution. This constraint introduces a heat sink into the micro-scale solution and represents the heat that flows from the micro-scale up to the meso-scale. The first step in developing the new approach was to provide the coupling between the length scales within the transient differential equations rather than by imposing

this in an ad-hoc way on their solutions and multi-scale analysis was the key to this. The following derivation is developed initially for a one-dimensional Cartesian steady state situation, and then extended to a transient solution before being extended into circular cylindrical and spherical geometries.

In one-dimension, the steady state conduction equation is:

$$\frac{d}{dx}\left(k(x)\frac{dT}{dx} \right) = -\dot{q}'''(x)$$

If we can consider a one-dimensional pebble in the form of a bar, and the bar is divided into a number of heated and un-heated segments, with heated segments being separated by unheated segments, we can decompose the heat generation term into a mean plus a perturbation:

$$\dot{q}'''(x) = \overline{q}''' + \hat{q}'''(x)$$

Integration of the heat generation shows:

$$\frac{1}{L}\int_0^L \dot{q}'''(x)dx = \overline{q}''' \quad \text{, therefore,} \quad \frac{1}{L}\int_0^L \hat{q}'''(x)dx = 0$$

For example, if the power density distribution is as shown in Figure 5.3.3:

Figure 5.3.3: Power density distribution
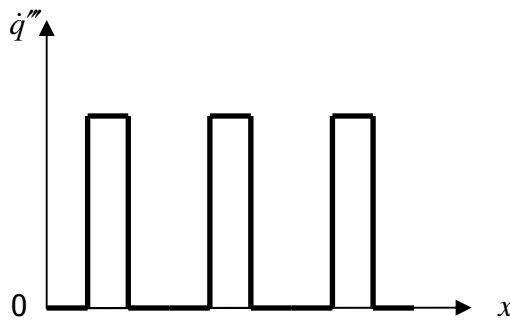
Then this can be decomposed into the two distributions of Figure 5.3.4.

Figure 5.3.4: Power Distribution Decomposed into a Constant Mean Value Plus a Perturbation
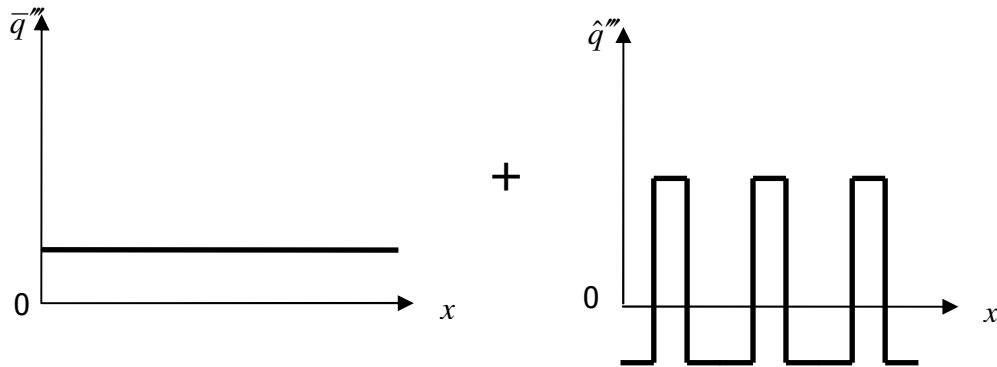
It can be seen, therefore, that over the interval of a heated segment plus its share of the unheated neighbouring segments, the perturbation represents a matched pair of a heat source and a heat sink. This is comparable to the previous approach, but this decomposition introduces the sources and sinks directly into the differential equation, therefore the corresponding source and sink behaviour will be apparent in the micro-scale solution without having to be imposed as an additional constraint.

The temperature field can be similarly decomposed into:

$$T(x) = T_M(x) + T_\mu(\hat{x})$$

Where T_M is the meso-scale temperature variation and T_μ is the micro-scale temperature variation. The micro-scale length co-ordinate is $\hat{x}$, this has the same units as x but has an origin at the centre of each heated segment.

The conduction equation is then decomposed into an equation corresponding to each part of the source term:

$$\frac{d}{dx}\left(k_{eff}\frac{dT_M}{dx}\right) = -\overline{q}'''$$

for the meso-scale, and,

$$\frac{d}{d\hat{x}}\left(k(\hat{x})\frac{dT_\mu}{d\hat{x}}\right) = -\hat{q}'''(\hat{x})\,.$$

for the micro-scale.

The decomposition itself is not an approximation, however, the use of a "smeared" or effective conductivity in the meso-scale equation (but retaining the actual conductivity variation in the micro-scale equation) is an approximation.

For simplicity, the bar and the distribution of heated segments are assumed to be symmetric, with the origin of the length co-ordinate at the mid-span of the bar, as shown in Figure 5.3.5. The bar has a length of *2L*, contains three heated segments and has a cross-sectional area of A. Both ends are held at a constant temperature T_D and each heated segment has a heat input of $\dot{q}_P$.

Figure 5.3.5: One Dimensional Conduction Problem with 3 Discrete Heat Sources
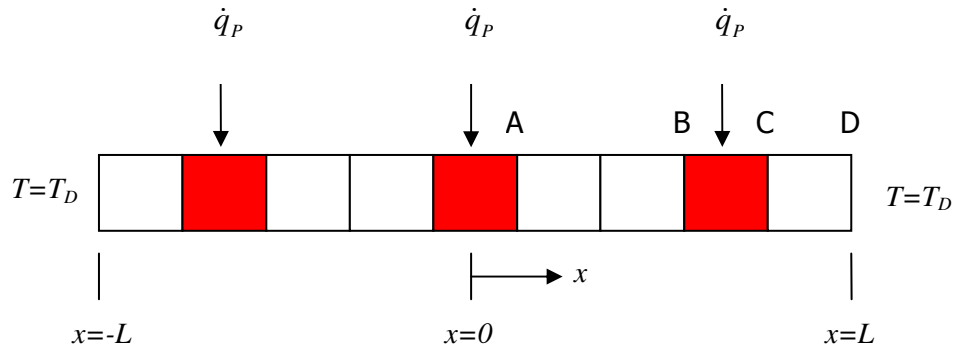
The average power density, which forms the source term for the meso-scale equation is the total heat input divided by the volume of the bar:

$$\overline{q}''' = \frac{3\dot{q}_P}{2AL}$$

Under these conditions, the solution to the meso-scale differential equation is:

$$T_M = \frac{3\dot{q}_P}{4ALk_{eff}}\left(L^2 - x^2\right) + \left(T_D - \delta\right)$$

The term δ is introduced because only the sum of the micro and meso-scale solutions satisfies the boundary condition, so δ is the micro-scale temperature evaluated at the domain boundary D, or

$$T(x_D) = T_D = T_M(x_D) + T_\mu(\hat{x}_s) = T_M(x_D) + \delta ,$$

so, the boundary condition on the meso-scale temperature field is:

$$T_M(x_D) = T_D - \delta .$$

The micro-scale domain is symmetric about the centre of the heated particle, so the differential equation can be solved over half of the domain, as shown in Figure 5.3.6.

Figure 5.3.6: One Dimensional Conduction Problem – Micro-Scale Domain
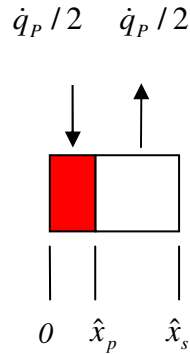
$$\dot{q}_P / 2 \quad \dot{q}_P / 2$$

$$0 \quad \hat{x}_p \quad \hat{x}_s$$

The volume of a heated segment is V_P and is given by:

$$V_P = 2\hat{x}_p A$$

Similarly the volume of the heated segment's share of the unheated material is:

$$V_G = 2(\hat{x}_s - \hat{x}_p)A$$

The average power density expressed in terms of these volumes is:

$$\overline{q}''' = \frac{\dot{q}_P}{V_P + V_G}$$

The source/sink term in the micro-scale conduction equation is then:

$$\hat{q}''' = \frac{\dot{q}_P}{V_P} - \overline{q}''' = \frac{V_G}{V_P + V_G}\frac{\dot{q}_P}{V_P} \qquad \text{for } 0 < \hat{x} < \hat{x}_p$$

and

$$\hat{q}''' = -\overline{q}''' = -\frac{V_G}{V_P + V_G}\frac{\dot{q}_P}{V_G} \qquad \text{for } \hat{x}_p < \hat{x} < \hat{x}_s$$

The boundary conditions on the micro-scale solution are zero temperature gradient at both the centre of the heated segment and at the outer edge of the unheated segment. Therefore, there is no Dirichlet boundary condition (i.e., a fixed temperature) in the model and, as such, an infinite number of solutions exist. However, because we are solving for a temperature perturbation, the temperature field should have a zero mean. In a steady state solution this zero mean has to be imposed as an additional constraint as:

$$\frac{1}{\hat{x}_s}\int_0^{\hat{x}_s} T_\mu d\hat{x} = \frac{1}{\hat{x}_s}\left\{\int_0^{\hat{x}_p} T_\mu d\hat{x} + \int_{\hat{x}_p}^{\hat{x}_s} T_\mu d\hat{x}\right\} = 0$$

Re-arranging gives the constraint as:

$$\int_0^{\hat{x}_p} T_\mu d\hat{x} = -\int_{\hat{x}_p}^{\hat{x}_s} T_\mu d\hat{x}$$

The solution over the heated segment is:

$$T_\mu = \frac{\dot{q}_P}{2 k_P V_P}\left(\frac{V_G}{V_P + V_G}\right)\left(\hat{x}_P^2 - \hat{x}^2\right) + T_{\mu P}$$

And the solution over the un-heated segment is:

$$T_\mu = \frac{\hat{q}_P}{2 k_G V_G}\left(\frac{V_G}{V_P + V_G}\right)\left[\left(\hat{x}^2 - \hat{x}_p^2\right) - 2\hat{x}_s\left(\hat{x} - \hat{x}_p\right)\right] + T_{\mu P}$$

Applying the zero-mean constraint gives the temperature at the junction of the heated and unheated segments as:

$$T_{\mu P} = \frac{\dot{q}_p}{\hat{x}_s}\left(\frac{V_G}{V_P + V_G}\right)\left\{\frac{\left(\hat{x}_s - \hat{x}_p\right)}{2 k_G V_G}\left[\frac{\left(\hat{x}_s^3 - \hat{x}_p^3\right)}{3\left(\hat{x}_s - \hat{x}_p\right)} - \hat{x}_p^2 - \hat{x}_s^2 + \hat{x}_s\hat{x}_p\right] - \frac{\hat{x}_p^3}{3 k_P V_P}\right\}$$

For comparison with the above multi-scale solution, an exact solution was derived. Fortunately, this problem is simple enough to be solved analytically by direct integration over the sub-domains 0-A, A-B, B-C and C-D shown in Figure 5.3.5, and the resulting exact solution is presented in Appendix A.2.

Both the multi-scale and exact solutions were coded into an Excel spreadsheet. The dimensions of the domain were L = 4 units, A = 1 unit^2 , the length of each heated segment was 1 unit (giving V_P as 1 unit^3), there are 3 heated segments with a spacing of 2 units unheated length between each (giving V_G as 2 unit^3). The outermost heated segments are 1 unit from each end of the bar. The conductivity of the heated and unheated sections were set to be equal and equal to 5 W/unit/K. The power density added to each heated segment was 50 W/unit^3.

Figure 5.3.7 shows the predicted micro and meso-scale temperature distributions and the sum of these compared with the exact solution. The addition of the peaks and troughs from the micro-scale solution to the overall quadratic profile from the meso-scale solution recovers the curvature of the profile through the heated segments and the linear temperature variation through the unheated sections. This shows that the multi-scale solution, in one-dimension with constant conductivity reproduces the exact solution.

Figure 5.3.7: Comparison of Predicted Steady State Temperatures from the Multi-Scale and Exact Solutions
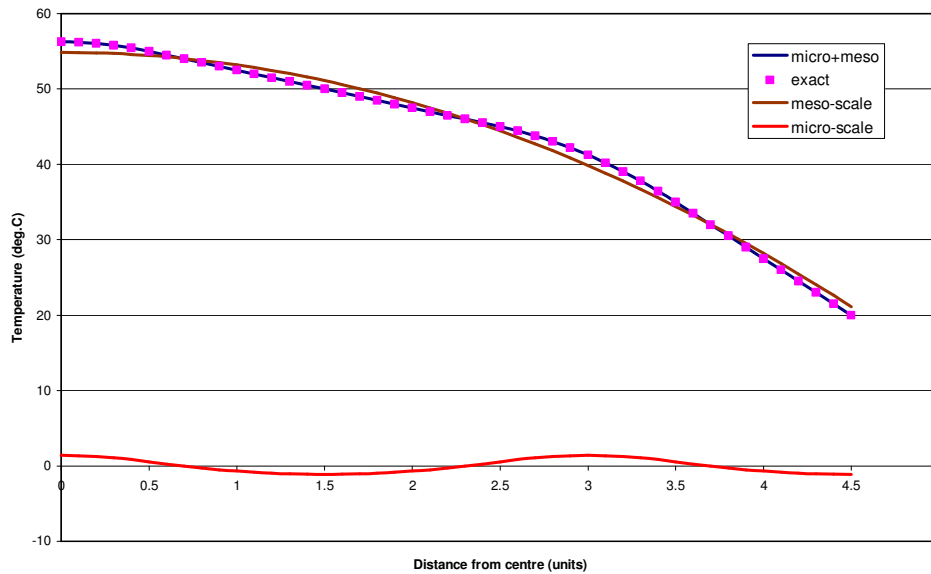
A further calculation was performed in which the conductivity of the heated segments was reduced to 2.5 W/unit/K. In this one-dimensional case, the conductivity was smeared, such that the overall thermal conductivity of the bar remains correct, by taking a harmonic average of the two conductivities following:

$$k_{eff} = \frac{(V_G + V_P)k_G k_P}{V_P k_G + V_G k_P}$$

The corresponding multi-scale solution is shown in Figure 5.3.8. It can be seen that the addition of the micro and meso-scale solutions does not reproduce the exact solution, largely because the latter retains its quadratic shape and, thus, does not capture the underlying shape of the exact solution.

Figure 5.3.8: Comparison of Multi-Scale and Exact Solutions for the Case of Different Conductivities in the Heated and Unheated Regions
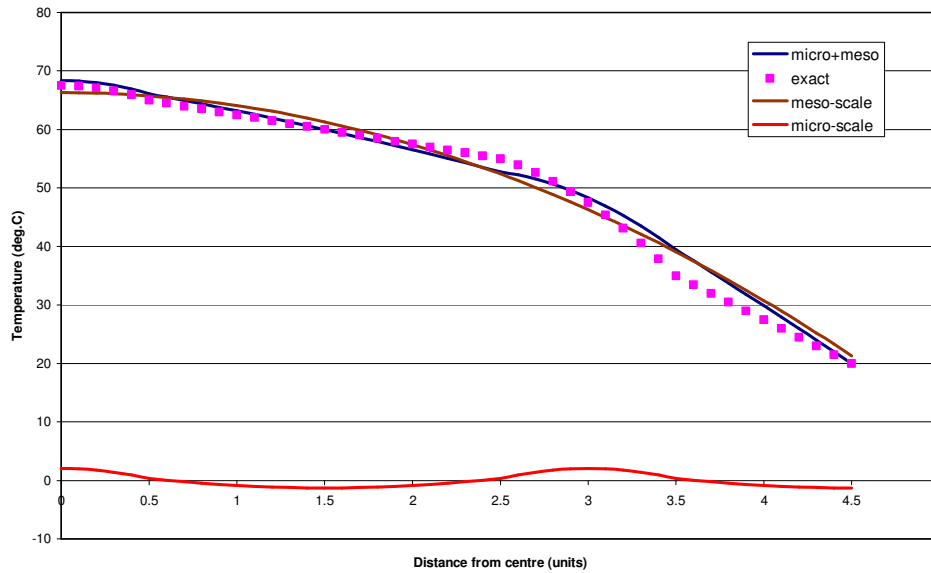
The calculation with different conductivities in the heated and un-heated segments was repeated but with the thermal conductivity variation resolved correctly in the meso-scale solution and the resulting multi-scale solution is shown in Figure 5.3.9.

Figure 5.3.9: Comparison of Multi-Scale and Exact Solutions for the Case of Different Conductivities in the Heated and Unheated Regions – Conductivity Variation Resolved in the Meso-Scale Solution
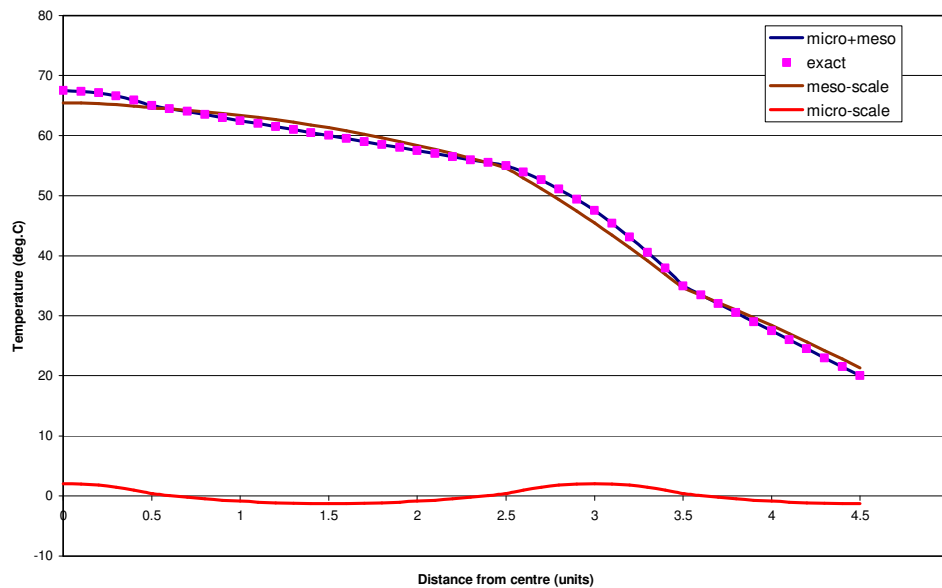
It can be seen from Figure 5.3.9 that the multi-scale solution correctly reproduces the exact solution when the correct conductivity variation is re-introduced into the meso-scale part of the solution. However, in application to pebble fuel elements we do not wish to use property distributions that vary on the micro length scale in the meso-scale solution. In this one-dimensional problem the smeared conductivity approximation is poor because the problem is quite coarse, i.e., not enough length scale difference between the micro and meso-scales and, being 1-dimensional, there are no parallel heat transfer paths, that is, all of the heat flows through the outermost heated segments. In a spherical pebble, the volume fraction of particles is about 10%, there are a large number of particles and they are randomly spaced, all of which make the pebble look much more homogeneous on the meso-scale than does this one-dimensional test problem.

From the above findings, the following can be concluded with regard to multi-scale modelling of the one-dimensional heat conduction equation:

(i) Decomposition of the heat generation into a mean value plus a perturbation, using each of which to solve for two separate temperature fields then summing these to recover the complete solution, is equivalent to solving the original equation directly. This statement is true if the material properties are spatially constant, or if any micro-scale spatial variation in properties is resolved in the meso-scale .

(ii) In practice retaining the abaility to resolve micro-scale material property variations in the meso-scale defeats the purpose of having a multi-scale model. Therefore, if the material properties are not spatially constant, they must be averaged in the meso-scale solution. This averaging of the spatial variation, and variations due to temperature dependence, in the meso-scale equation is an approximation. However, it is believed that this approximation is not significant for practical application of the method to HTGR fuel pebbles because the low packing fraction and random arrangement of the particles make the properties of the pebbles more homogenous on the meso-scale than in the one-dimensional linear problem presented here.

5.3.2.2   Transient Solution in a One-Dimensional Linear Domain

The transient one-dimensional conduction equation with internal heat generation is:

$$\rho c_P \frac{\partial T}{\partial t} = \frac{\partial}{\partial x}\left(k(x)\frac{\partial T}{\partial x}\right) + \dot{q}'''(x,t)$$

Using the same decomposition as for the steady state case, this becomes:

$$(\rho c_P)(x)\frac{\partial T_M}{\partial t} = \frac{\partial}{\partial x}\left(k(x)\frac{\partial T_M}{\partial x}\right) + \overline{q}'''(t)$$

for the meso-scale

$$(\rho c_P)(\hat{x})\frac{\partial T_\mu}{\partial t} = \frac{\partial}{\partial \hat{x}}\left(k(\hat{x})\frac{\partial T_\mu}{\partial \hat{x}}\right) + \hat{q}'''(\hat{x}, t)$$

for the micro-scale.

As in the steady state case, spatial and temperature dependent variations in material properties in the meso-scale must be *approximated* by constant effective values to avoid having to resolve these features on the micro-scale:

$$\overline{(\rho c_P)}\frac{\partial T_M}{\partial t} = \frac{\partial}{\partial x}\left(k_{eff}\frac{\partial T_M}{\partial x}\right) + \overline{q}'''(t)$$

The un-decomposed (i.e., the "original" or "continuous" form) and decomposed forms of the differential equations can both be solved using finite difference approximations. A finite difference scheme to solve the original un-decomposed form of the conduction equation was produced to serve as a reference solution against which the multi-scale solution could be compared. This finite difference solution is presented in Appendix A.2.

Starting with the meso-scale differential equation this is cast in finite difference form using a 1st order forward difference operator to approximate the time derivative and and 2nd order central difference operator to approximate the spatial 2nd derivative:

$$T_{Mi}^{t+\Delta t} = T_{Mi}^t + \frac{\Delta t}{\overline{(\rho c_P)}}\frac{1}{(x_{ei} - x_{wi})}\left(k_{eff}\frac{T_{Mi+1}^t - T_{Mi}^t}{x_{i+1} - x_i} - k_{eff}\frac{T_{Mi}^t - T_{Mi-1}^t}{x_i - x_{i-1}}\right) + \frac{\Delta t}{\overline{(\rho c_P)}}\overline{q}'''(t)$$

Where:

$$x_{ei} = \frac{(x_{i+1} + x_i)}{2} \; ; \; x_{wi} = \frac{(x_i + x_{i-1})}{2}$$

and similarly for the micro-scale differential equation:

$$T_{\mu i}^{t+\Delta t} = T_{\mu i}^t + \frac{\Delta t}{(\rho c_P)_i}\frac{1}{(\hat{x}_{ei} - \hat{x}_{wi})}\left(k_{ei}\frac{T_{\mu i+1}^t - T_{\mu i}^t}{\hat{x}_{i+1} - \hat{x}_i} - k_{wi}\frac{T_{\mu i}^t - T_{\mu i-1}^t}{\hat{x}_i - \hat{x}_{i-1}}\right) + \frac{\Delta t}{(\rho c_P)_i}\hat{q}_i''(t)$$

Where:

$$k_{ei} = k(x_{ei}) \; ; \; k_{wi} = k(x_{wi})$$

These equations are modified at the boundaries to introduce the boundary conditions. For the meso-scale equation, the symmetry boundary condition in the centre of the bar is introduced by reflecting the temperature gradient about the centre of the bar. The fixed temperature boundary condition at the end of the bar is applied to the sum of the meso- and micro-scale temperatures. If the micro-scale temperature at the end

of the bar at time t is $\delta(t)$, then the boundary condition on the meso-scale temperature field is:

$$T_{MN}^{t+\Delta t} = T_D - \delta(t)$$

Finally, the boundary conditions on the micro-scale equation are symmetry at both the centre of the heated segment and at the outer edge of the unheated segment. Both of these are introduced by reflecting the temperature gradients across the boundaries. The modified forms of the micro and meso-scale finite difference equations after introduction of the boundary conditions are presented in Appendix A.2

The finite difference equations were cast in an explicit form to allow solution in a simple Excel spreadsheet. If backward differences had been used for the time derivatives, then the scheme would be fully implicit, requiring a system of simultaneous equations to be solved, but yielding a scheme that is unconditionally stable without a stability limit on the time step size. The explicit scheme is stable when the coefficient of T_i^t is positive and the limit of stability is reached when the time step takes on the value which make this coefficient zero.

The finite difference equations for the un-decomposed (exact) and multi-scale solutions were coded into an Excel spreadsheet. The dimensions of the domain were the same as for the steady state tests, and the conductivities of the heated and unheated segments were equal at 5 W/unit/K. The density-specific heat capacity products for the two type of segments were set to be the equal and to a value of 1 J/unit^3/K. The initial and boundary temperatures were set to 20°C and the power density in the heated segments was increased from zero to 50W/unit^3 at t=0. The initial condition for the micro-scale solution was zero temperature perturbation everywhere. The time step size was constant throughout the calculations at 5x10^{-4} seconds and this was used in both the micro and meso-scale solutions. The length increments were all of equal size and set to be 0.1 units in the micro and meso-scale solutions.

Figures 5.3.10 and 5.3.11 show predicted temperatures from the un-decomposed (exact) and multi-scale finite difference solutions respectively. Temperature profiles on different time steps, with the earliest at 5.5x10^{-3} seconds and the latest at 1 second are shown in both instances. For the special case of identical properties in the heated and unheated segments, both sets of curves are identical, illustrating once again, that decomposing only the power distribution is not an approximation in one-dimension.

Figure 5.3.10: Direct Finite Difference Solution of the Transient Conduction Equation in a 1-Dimensional Linear Domain
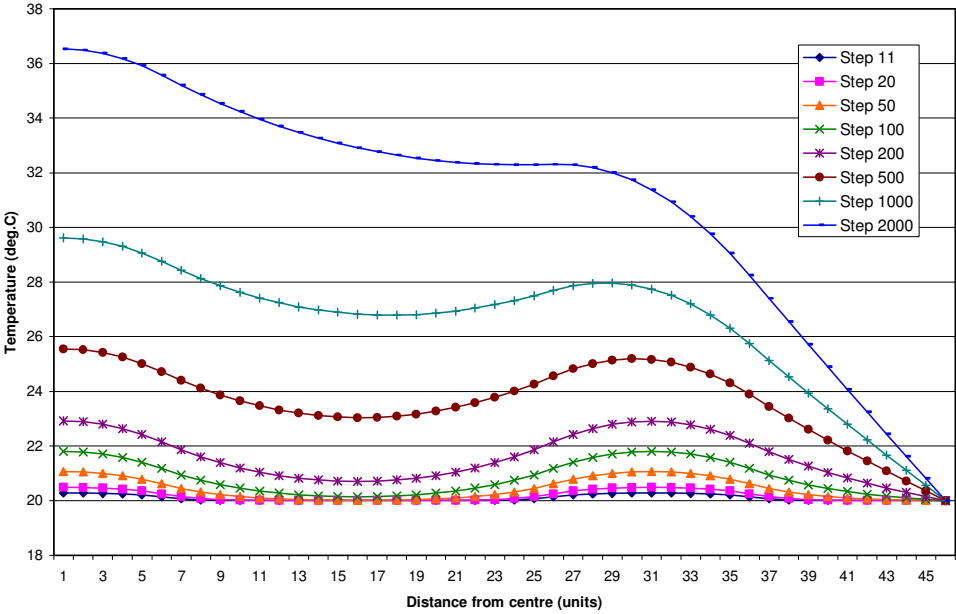
Figure 5.3.11: Multi-Scale Finite Difference Solution – 1-Dimensional Linear Domain
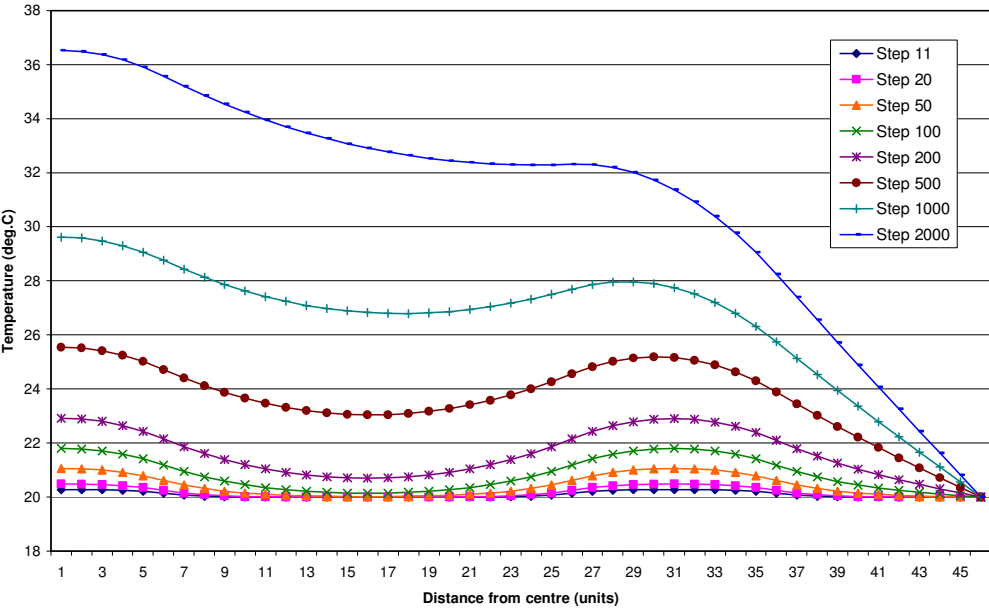
In the above calculation, the micro-scale model reaches a steady solution in about 600 time steps (0.3 seconds), whereas the central segment temperature in the meso-scale solution has only acquired 65% of its steady state value after 1 second. It is clear, therefore, that the multi-scale solutions operate on two different time-scales as well as two different length scales.

The variation of meso-scale temperature with time is shown in Figure 5.3.12. This shows the expected behaviour of transition from a horizontal line towards a parabola. The modification of the temperature boundary condition at the free end of the bar by the subtraction of micro-scale temperature at the boundary can be seen.

Figure 5.3.12: Meso-Scale Solution – 1-Dimensional Linear Domain
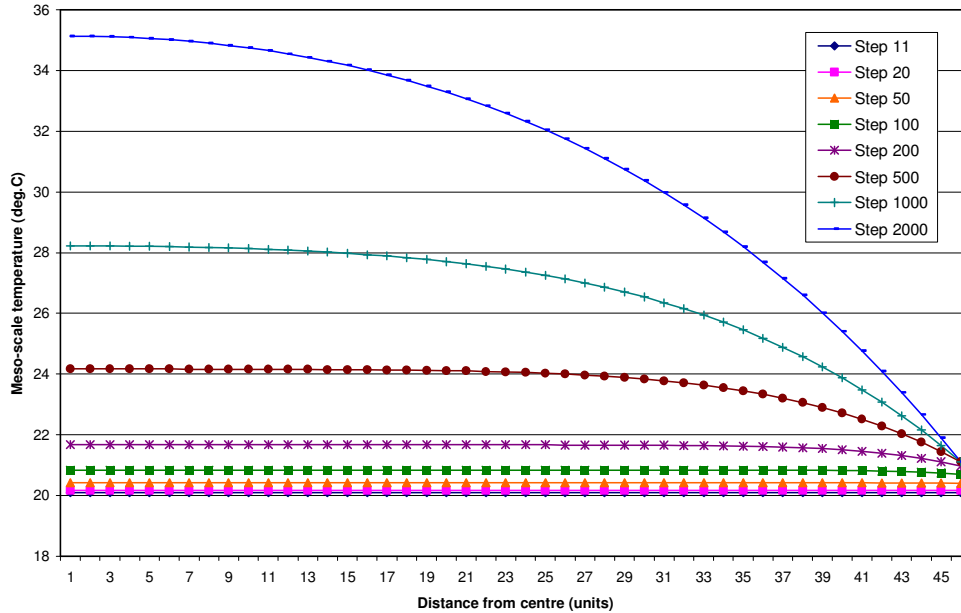
Figure 5.3.13: Micro-Scale Solution – 1-Dimensional Linear Domain
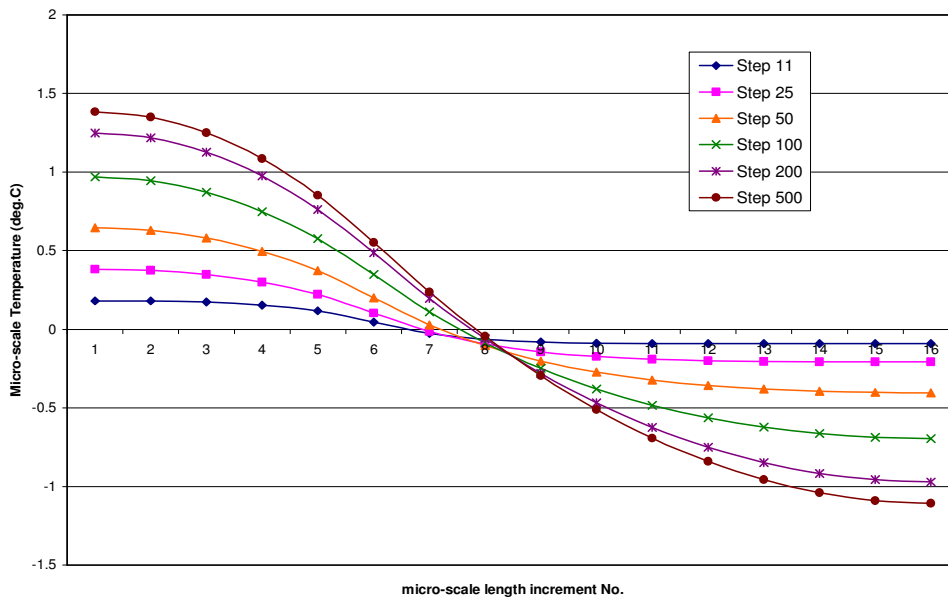
The evolution of the micro-scale temperature distribution is shown in Figure 5.3.13 for time steps 11 to 500 (5.5×10^{-3} to 0.25 seconds). In a transient, the micro-scale solution retains its zero-mean through being coupled to the previous time step. Therefore, as long as the initial guess has a zero mean, the solution retains its zero mean without this having to be enforced as an additional constraint. However, in reality, it will be prudent to add this additional constraint to counteract the accumulation of rounding error which may cause the solution to drift.

5.3.3 Application to a Cylindrical Representation of a Pebble

The multi-scale method of Section 5.3.2 was modified to be applicable to a cylindrical domain in polar co-ordinates (see Appendix A.2). The cylindrical domain is considered to represent a slice through a spherical particle. The domain contains a number of circular particles. The cylindrical domain possesses the same characteristics as a spherical pebble in that the packing fraction of particles is lower. On the meso-scale the domain is more homogeneous and heat can flow around the outside of the particles as well as through them. The use of a cylindrical geometry simplifies the construction of a finite element model to provide a comparison in a more realistic geometry in the absence of a simple-closed form analytical solution.

The transient conduction equation with heat generation in cylindrical co-ordinates is decomposed into meso and micro-scales in an identical manner to that used in Cartesian co-ordinates in Section 5.3.2., giving for the meso-scale:

$$(\rho c_P)(r)\frac{\partial T_M}{\partial t} = \frac{1}{r}\frac{\partial}{\partial r}\left(rk(r)\frac{\partial T_M}{\partial r} \right) + \overline{q}'''(t)$$

and

$$(\rho c_P)(\hat{r})\frac{\partial T_\mu}{\partial t} = \frac{1}{\hat{r}}\frac{\partial}{\partial \hat{r}}\left(\hat{r}k(\hat{r})\frac{\partial T_\mu}{\partial \hat{r}} \right) + \hat{q}'''(\hat{r},t)$$

for the micro-scale.

Again the properties variations are smeared to give effective values and this approximation is introduced in the meso-scale differential equation:

$$\overline{(\rho c_P)}\frac{\partial T_M}{\partial t} = \frac{1}{r}\frac{\partial}{\partial r}\left(rk_{eff}\frac{\partial T_M}{\partial r} \right) + \overline{q}'''(t)$$

Using a forward difference for the time derivative gives an explicit finite difference equation for the meso-scale temperature distribution:

$$T_{Mi}^{t+\Delta t} = T_{Mi}^t + \frac{\Delta t}{(\rho c_P)_i}\frac{1}{r_i(r_{ei}-r_{wi})}\left(r_{ei}k_{eff,ei}\frac{T_{Mi+1}^t - T_{Mi}^t}{r_{i+1}-r_i} - r_{wi}k_{eff,wi}\frac{T_{Mi}^t - T_{Mi-1}^t}{r_i - r_{i-1}} \right) + \frac{\Delta t}{(\rho c_P)_i}\overline{q}_i'''(t)$$

where:

$$r_{ei} = \frac{(r_{i+1} + r_i)}{2} \;;\; r_{wi} = \frac{(r_i + r_{i-1})}{2} \;;\; k_{eff,ei} = k_{eff}(r_{ei}) \;;\; k_{eff,wi} = k_{eff}(r_{wi})$$

Similarly for the micro-scale:

$$T_{\mu i}^{t+\Delta t} = T_{\mu i}^{t} + \frac{\Delta t}{(\rho c_P)_i} \frac{1}{\hat{r}_i(\hat{r}_{ei} - \hat{r}_{wi})} \left(\hat{r}_{ei} k_{ei} \frac{T_{\mu i+1}^{t} - T_{\mu i}^{t}}{\hat{r}_{i+1} - \hat{r}_i} - \hat{r}_{wi} k_{wi} \frac{T_{\mu i}^{t} - T_{\mu i-1}^{t}}{\hat{r}_i - \hat{r}_{i-1}} \right) + \frac{\Delta t}{(\rho c_P)_i} \hat{q}_i'''(t)$$

The results of Section 5.3.2 show that the micro-scale responds on a shorter time-scale than the meso-scale. Therefore, advantage is taken of this by employing smaller time steps in solution of the micro-scale equation, which allows both equations to be solved using their own optimum time step sizes. There is no requirement that the two time step sizes be related to each other, however, practically it is more convenient for re-combining the two solutions if the meso-scale time step size is an integer multiple of the micro-scale time step. The micro-scale finite difference equation is re-cast using its own micro-scale time step:

$$T_{\mu i}^{\hat{t}+\Delta\hat{t}} = T_{\mu i}^{\hat{t}} + \frac{\Delta\hat{t}}{(\rho c_P)_i} \frac{1}{\hat{r}_i(\hat{r}_{ei} - \hat{r}_{wi})} \left(\hat{r}_{ei} k_{ei} \frac{T_{\mu i+1}^{\hat{t}} - T_{\mu i}^{\hat{t}}}{\hat{r}_{i+1} - \hat{r}_i} - \hat{r}_{wi} k_{wi} \frac{T_{\mu i}^{\hat{t}} - T_{\mu i-1}^{\hat{t}}}{\hat{r}_i - \hat{r}_{i-1}} \right) + \frac{\Delta\hat{t}}{(\rho c_P)_i} \hat{q}_i'''(\hat{t})$$

The boundary conditions applied to the meso-scale equation are symmetry at the centre of the pebble and prescribed temperature at the pebble surface. At the pebble centre the finite difference equation, as written above becomes singular because of the 1/r term. To avoid this problem, the equation for the centre node is modified to be written in a finite volume form, in which a cylinder is constructed around the central node. The central symmetry boundary condition is applied by ensuring that heat generation within this central cylinder is balanced by the heat lost from its periphery plus the rate of gain of internal energy within the cylinder. At the surface of the pebble, the contribution from the micro-scale solution has been neglected to avoid having to couple the micro and meso-scale solutions – this is advantageous when using different time step sizes. The contribution from the micro-scale solution is not significant when the volume fraction of the particles in the pebble is small. The boundary conditions on the micro-scale equation are symmetry both at the particle centre and symmetry at the edge of the surrounding cylinder that is particle's share of the graphite (which will be referred to as a "micro-cylinder"). The modified forms of the micro and meso-scale finite difference equations, following application of the boundary conditions, are presented in Appendix A.2.

As with the linear domain, the finite difference equations for the micro and meso-scales have been coded into an Excel spreadsheet. The spreadsheet has been set up to solve for pebble and particle temperatures in a cylindrical domain that contains 37 regularly spaced circular particles, i.e., the same geometry as used for the finite element simulations presented in Section 5.2, and as shown in Figure 5.3.14.

Figure 5.3.14: Geometry of the Cylindrical Representation of a Pebble
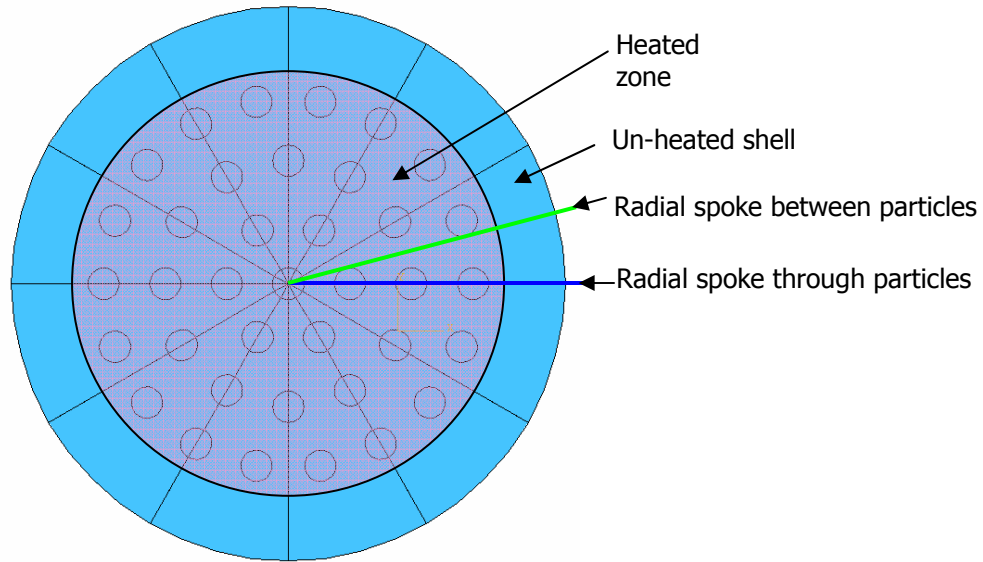
The particles are 1mm in diameter with a 1.972 mm radial pitch, giving a 2.065 mm circumferential pitch. To capture the features of a real pebble, the model was set up to have a particle-free layer of graphite around its periphery. The radius of the pebble is 8.874 mm and, in the meso-scale model, the heat generating zone is assumed to be 3.5 radial pitches in radius (6.902 mm). The volume fraction of particles within the heated zone is 0.1942. The material properties were set to similar values to the linear bar model of Section 5.3.2.1 (although these are not representative of a real pebble) because these gave reasonable temperature variations and a sensible transient response in a model that was on the scale of a few millimetres. The matrix conductivity was set to 5 W/mm/K and the particle conductivity set to 2 W/mm/K – giving an effective conductivity of the matrix and particles of 4.3056 W/mm/K obtained using Maxwell's method (see Appendix A.2). The power density in the particles was stepped up from zero to 50 W/mm^3 at the start of the transient. The density-specific heat capacity product was set to be 1 J/mm^3/K everywhere. The particle and its surrounding micro-cylinder of matrix material was split into 11 radial increments (12 nodes), with 5 increments in the particle of 0.1 mm thickness and 6 increments in the matrix of 0.1058 mm thickness. Based on the volume fraction of 0.1942, the radius of the micro-cylinder was 1.135 mm. In the meso-scale model the radius of the pebble was split into 9 radial increments (10 nodes) of thickness 0.986 mm. The average power density was applied over the innermost 7 increments with the two outermost increments having no internal heat generation. Different time steps were used on the two length scales, with 5×10^{-4} seconds being used on the micro-scale and 1.5×10^{-2} seconds being used on the meso-scale. The initial conditions were a temperature of 20°C with a micro-scale perturbation of 0°C everywhere in the pebble. The outer surface temperature of the pebble was held constant at 20°C.

Figure 5.3.15 shows the comparison of the predicted temperatures along a radial spoke that passes through the centres of four particles (identified by the blue line in Figure 5.3.14) with those obtained from the finite element model of Section 5.2.

Within Figure 5.3.15, the results of the combined micro and meso-scale solutions are plotted together with the solution from just the meso-scale solution and the results of the finite element calculation. Also shown in Figure 5.3.15 is the temperature profile predicted by the finite element solution along a radial spoke that avoids most of the particles (identified as the green line in Figure 5.3.14). It can be seen that the profile between the particles touches the through-particle profile in the troughs between the particles. The temperature gradient at the surface of the pebble is the same in both of the finite element profiles and in the multi-scale models. This shows that the surface heat flux is circumferentially uniform and the total heat flux is the same in both models.

Figure 5.3.15 shows that the particle temperatures are captured well, particularly the temperature of the hottest central particle. However, variations in the effective conductivity are still apparent as abrupt changes in gradient that are not captured in the meso-scale solution. The variation on effective conductivity in the radial direction is due to the regular spacing of the particles by locating them in discrete rings - a random spacing of a large number of particles would have a more homogeneous appearance on the meso-scale.

Figure 5.3.15: Comparison of Predicted Steady State Temperatures
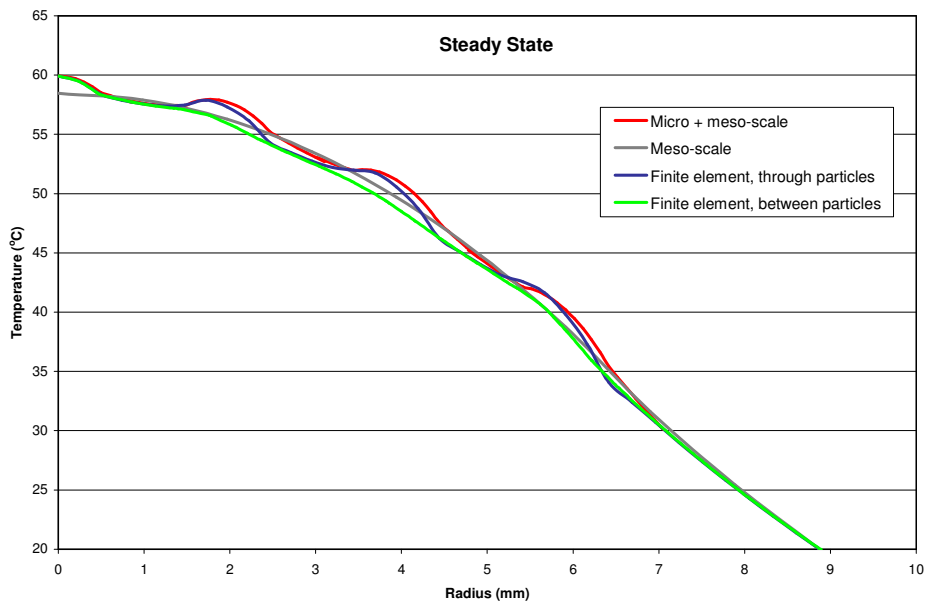
Figure 5.3.16 shows the comparison of the predicted temperatures along a radial spoke that passes through the centres of four particles at 0.165 seconds into the transient. Again the combined micro and meso-scale solutions are plotted (red curves) together with just the meso-scale solution (grey curve) and the finite element results (blue curve). It can be seen that the predicted particle temperatures from the multi-scale and finite element solutions agree quite well again, particularly so for the centre particle.

Figure 5.3.16: Comparison of Predicted Temperatures in the Cylindrical Pebble at t=0.165s
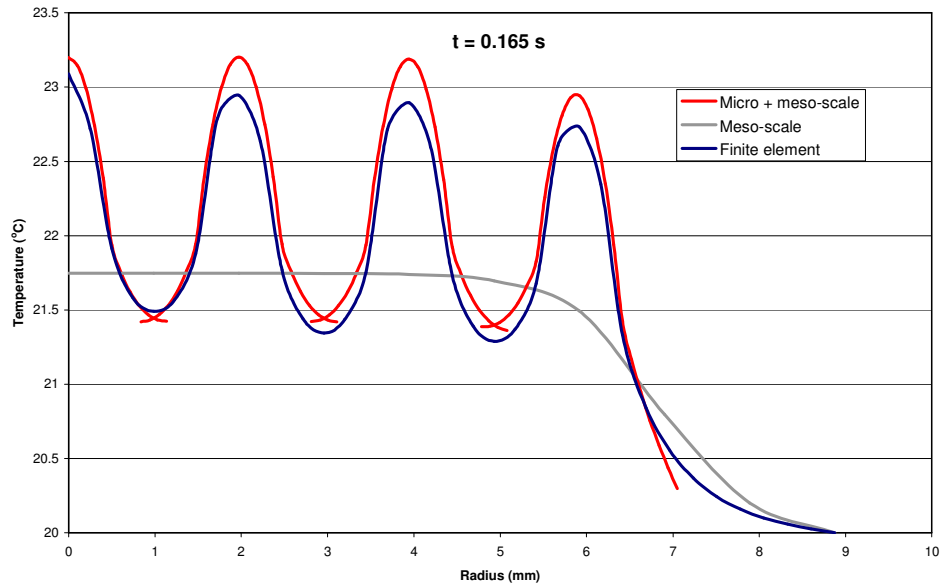
Figure 5.3.17 shows the same solutions plotted half a second later at 0.66 seconds. Again the agreement in the predicted particle temperatures is good and, again, particularly so for the centre particle.

Figure 5.3.17: Comparison of Predicted Temperatures in the Cylindrical Pebble at t=0.66s
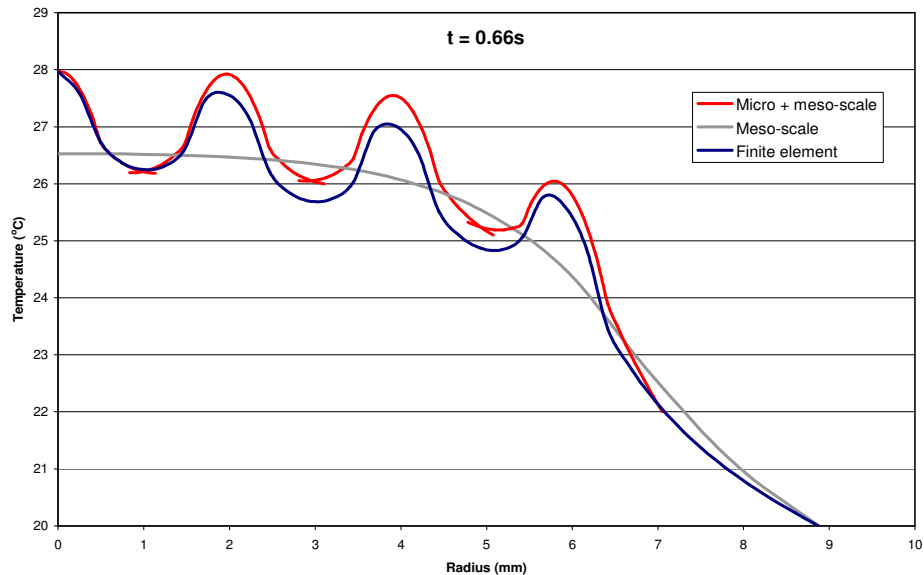
It is believed that the gradient in the peak particle temperatures observed in the finite element results in both Figure 5.3.16 and 5.3.17 is a result of non-uniform packing fraction within the finite element model. The difference in temperature gradient is

also believed to be attributable to non-uniformity of the power distribution in the finite element model, with a larger fraction of the power being deposited closer to the boundary in the multi-scale model. Whilst the surface radial temperature gradients equalise by the time the steady state is achieved, the non-uniformity of heating causes the outer layers of material to heat-up more slowly in the finite element model. The decision to have a fixed radial pitch means that the packing fraction decreases systematically with increasing radial distance, starting at 0.25714 at the centre decreasing to 0.19286 at the 4th ring of particles with an average value of 0.19417. Therefore, it is believed that agreement could be improved by modifying the multi-scale solution to allow the average power density to vary with radial position to reflect the radial variation of the packing fraction in the finite element model, however this has not yet been attempted.

5.3.4 Application to a Spherical Pebble

The multi-scale method of Section 5.3.3 was modified to be applicable to a spherical domain in spherical polar co-ordinates (see Appendix A.2). The domain is considered to represent a spherical pebble and contains a number of spherical particles.

The transient conduction equation with heat generation in spherical co-ordinates is decomposed into meso and micro-scales in an identical manner to that used in Cartesian co-ordinates in Section 5.3.2., giving for the meso-scale:

$$(\rho c_P)(r)\frac{\partial T_M}{\partial t} = \frac{1}{r^2}\frac{\partial}{\partial r}\left(r^2 k(r)\frac{\partial T_M}{\partial r}\right) + \bar{q}'''(t)$$

and

$$(\rho c_P)(\hat{r})\frac{\partial T_\mu}{\partial t} = \frac{1}{\hat{r}^2}\frac{\partial}{\partial \hat{r}}\left(\hat{r}^2 k(\hat{r})\frac{\partial T_\mu}{\partial \hat{r}}\right) + \hat{q}'''(\hat{r},t)$$

for the micro-scale.

As before, the thermal properties variations are approximated by smeared values in the meso-scale equation:

$$\overline{(\rho c_P)}\frac{\partial T_M}{\partial t} = \frac{1}{r^2}\frac{\partial}{\partial r}\left(r^2 k_{eff}\frac{\partial T_M}{\partial r}\right) + \bar{q}'''(t)$$

Using forward difference operators for the time derivatives yields the following pair of finite difference equations for the meso and micro-scales respectively:

$$T_{Mi}^{t+\Delta t} = T_{Mi}^t + \frac{\Delta t}{(\rho c_P)_i}\frac{1}{r_i^2(r_{ei}-r_{wi})}\left(r_{ei}^2 k_{eff,ei}\frac{T_{Mi+1}^t - T_{Mi}^t}{r_{i+1}-r_i} - r_{wi}^2 k_{eff,wi}\frac{T_{Mi}^t - T_{Mi-1}^t}{r_i - r_{i-1}}\right) + \frac{\Delta t}{(\rho c_P)_i}\bar{q}_i'''(t)$$

and

$$T_{\mu i}^{t+\Delta t} = T_{\mu i}^{t} + \frac{\Delta t}{(\rho c_P)_i} \frac{1}{\hat{r}_i^2(\hat{r}_{ei} - \hat{r}_{wi})}\left(\hat{r}_{ei}^2 k_{ei} \frac{T_{\mu i+1}^{t} - T_{\mu i}^{t}}{\hat{r}_{i+1} - \hat{r}_i} - \hat{r}_{wi}^2 k_{wi} \frac{T_{\mu i}^{t} - T_{\mu i-1}^{t}}{\hat{r}_i - \hat{r}_{i-1}} \right) + \frac{\Delta t}{(\rho c_P)_i} \hat{q}_i'''(t).$$

As with cylindrical geometry, the above equations are singular at the centre of the pebble and the centre of a particle for the meso and micro-scales respectively. Again, the equations are converted to finite volume form at these locations with the transient term and heat generation integrated over a spherical control volume that surrounds the centre node whilst the conduction term is integrated over its surface. The boundary condition at both these locations for the respective equations are symmetry conditions. The boundary condition on the meso-scale equation at the surface of the pebble is a fixed temperature and, again, the contribution from the micro-scale solution to the meso-scale boundary condition is neglected to decouple the two solutions. The external boundary condition on the micro-scale solution is a symmetry condition. The modified forms of the finite difference equations, following application of the above boundary conditions, are presented in Appendix A.2.

The finite difference equations for the micro and meso-scales were coded into an Excel spreadsheet. The spreadsheet was set up to solve for pebble and particle temperatures in a spherical domain that represented a PBMR pebble. The pebble contains 15000 spherical particles of 0.920 mm diameter, these particles are modelled as TRISO particles with the 4 layers of coating represented by elements of appropriate thicknesses and conductivities. The model was set with a particle-free layer of graphite around its periphery. The radius of the pebble is 30 mm and the heat generating zone has a radius of 25 mm. The volume fraction of particles within the heated zone is 0.09344. The material properties were set to values representative of those of a PBMR pebble (Reference 5.1). The graphite matrix conductivity was set to 15 W/m/K, this represents an irradiated value and is taken from Reference 5.2 and the particle coating and kernel dimensions and conductivities were set according to those shown in Table 2.4.1 in Section 2.

Maxwell's method was used to determine the effective conductivity of the graphite-TRISO particle mixture and this gave a value of 13.7 W/m/K (see Section 7). The pure graphite value was applied to the pebble shell outside of the heated zone.

The power density in the particle kernel was stepped up from zero to 902.3 MW/m^3 at the start of the transient, this value was chosen because it is the average kernel power in PBMR. The density-specific heat capacity product was set to be 1690 kJ/m^3/K everywhere (note this value implies that the density of the pebble is 1000 kg/m^3, whilst this is of the correct order of magnitude for testing, it is not an accurate value for graphite). The particle and its surrounding micro-sphere of matrix material (see Figure 2.4.2) was split into 20 radial increments (21 nodes), with 5 increments in the particle of 50 microns thickness and 5 increments in the coatings (2 in the porous carbon layer and 1 each in the other three layers) all typically about 40 microns thick and 9 increments in the matrix of 55 microns thickness. Based on the particle volume fraction of 0.09344, the radius of the micro-sphere was 1.012 mm. In the meso-scale model the radius of the pebble was split into 12 radial increments (13 nodes) of thickness 2.5 mm and the average power density was applied over the

innermost 10 increments with the outermost 2 increments having no internal heat generation. Different time steps were used on the two length scales, with 1×10^{-4} seconds being used on the micro-scale and 0.1 seconds being used on the meso-scale. The initial conditions were a temperature of 20°C with a micro-scale perturbation of 0°C everywhere in the pebble. The outer surface temperature of the pebble was held constant at 20°C.

Figure 5.3.18 shows the final steady state temperature distribution through the pebble and through 4 particles centred at distances of 0 mm, 6.667 mm**,** 13.333 mm and 20 mm from the centre of the pebble. Also shown is the analytical meso-scale temperature profile obtained from the pebble temperature equation presented in Section 5.3.1. The temperature from the finite-difference meso-scale model lies slightly below that of the analytical solution (but only a 0.42^{o}C difference at the pebble centre). It is believed that this difference is attributable to a small discretisation error in the finite difference scheme, specifically with regard to the representation of the $1/r^2$ term. If the discrete form of the meso-scale equation is derived by a finite volume method, i.e., by integrating the differential equation over a control volume consisting of a thick shell of a sphere, integration of the $1/r^2$ term gives a slightly different result than the finite difference equation quoted above. In the cylindrical geometry the discrete equations arising from either the finite difference or finite volume routes are identical, whereas in the spherical geometry they are not. The difference can be reduced by refining the grid, but this is already finer than used in the cylindrical case, so the solution to the problem is to re-cast the finite difference equations in finite volume form.

Figure 5.3.18: Predicted Temperature Distribution Through a PBMR Pebble Including the Profiles within 4 Sample Particles
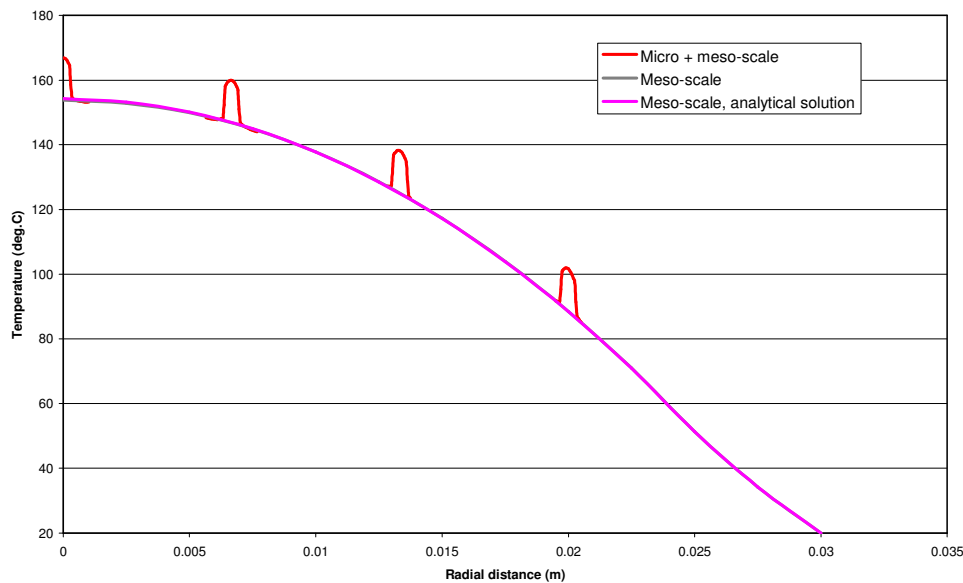
A further test on the model was to look at the initial rates of temperature increase in the particles and in the bulk of the pebble. Early in the transient, external heat loss from a particle or from a pebble are both negligible and all of the heat input goes into raising the temperature of the material. For the pebble this simplification gives:

$$\left.\frac{\partial T_M}{\partial t}\right|_{t=0} = \frac{\overline{q}'''}{\left(\rho c_P\right)}$$

and similarly for a particle:

$$\left.\frac{\partial T_\mu}{\partial t}\right|_{t=0} = \frac{\hat{q}'''}{\rho\, c_P}.$$

Figure 5.3.19: Development of Particle Centre Micro-Scale Temperature with Time
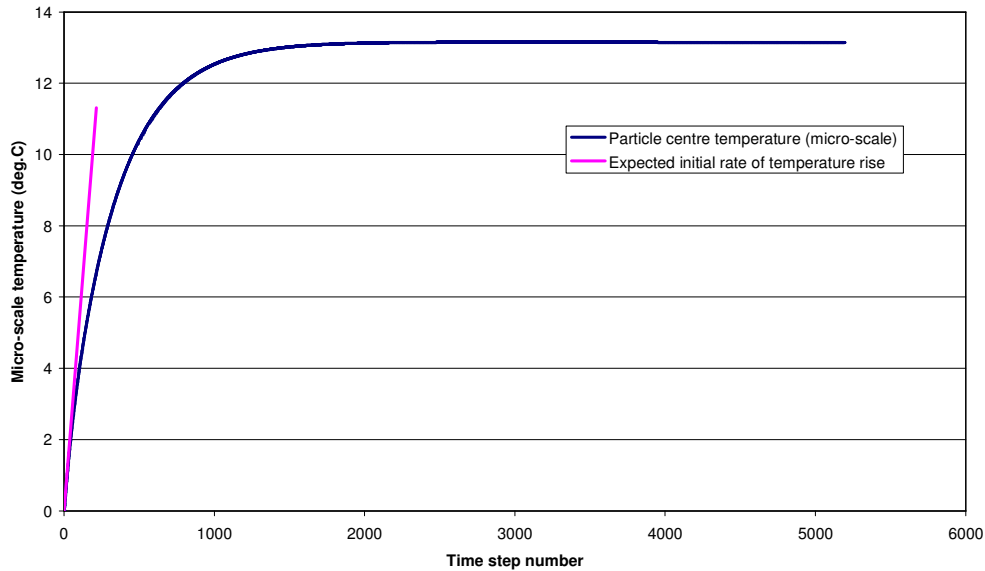
Figure 5.3.19 shows the development of the micro-scale temperature at the particle centre with time. The initial expected rate of change of temperature is also shown. It can be seen that the particle centre micro-scale temperature reaches a steady state after about 2000 time steps (0.2 seconds) and the initial rate of temperature rise agrees with the expected gradient as shown by the magenta line.

Figure 5.3.20 shows the development of the meso-scale temperature at the pebble centre with time. The initial expected rate of change of temperature is also shown. It can be seen that the pebble centre meso-scale temperature reaches a steady state after about 2000 meso-scale time steps (200 seconds) and the initial rate of temperature rise agrees with the expected gradient as shown by the magenta line.

Figure 5.3.20: Development of Pebble Centre Meso-Scale Temperature with Time
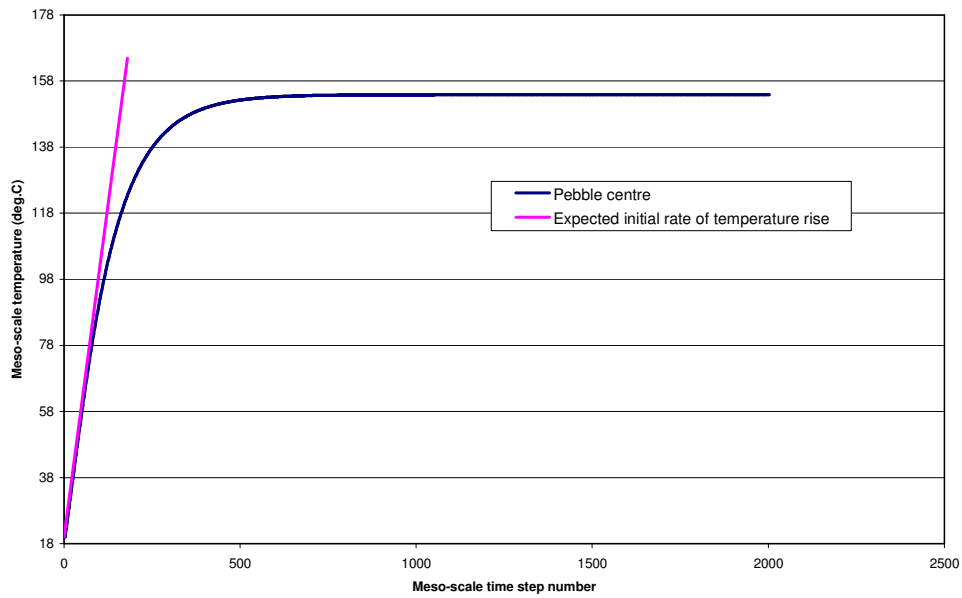
Meso-scale radial temperature profiles for different time steps are shown in Figure 5.3.21.

Figure 5.3.21: Meso-Scale Radial Temperature Profiles for a Spherical PBMR Type Pebble
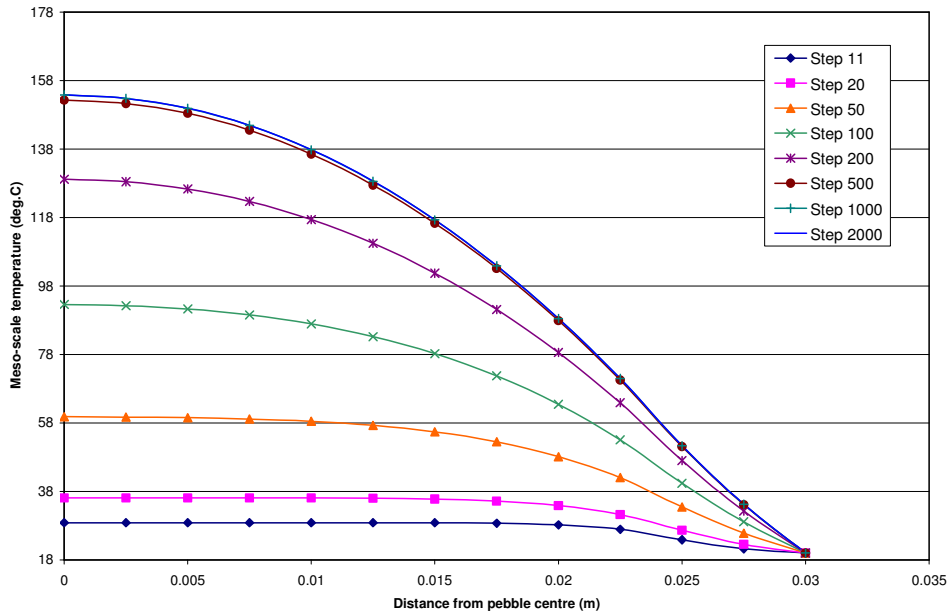
Figure 5.3.22: Micro-Scale Radial Temperature Profiles for a Spherical PBMR Type Pebble
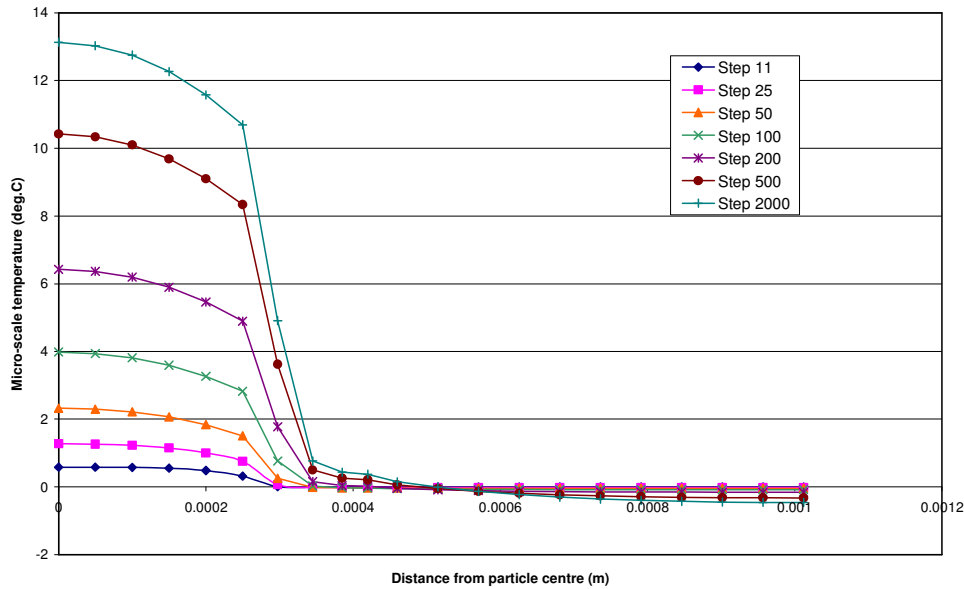
Development of the radial temperature profiles with time through a micro-sphere are shown in Figure 5.3.22. The sharp temperature drop over the inner coating, the porous carbon layer, can be seen clearly. The negative micro-scale temperature over the surrounding graphite outside of the particle is small compared with the particle centre temperature. This justifies decoupling the micro and meso-scale solutions by neglecting the δ term in the meso-scale boundary condition (see Section 5.3.2)

5.4 Closure

This section has presented a multi-scale model that allows the fine-scale detail of the temperature distributions both in the pebbles and in the particles that are within the pebbles to be resolved. The model is based on the solution of a pair of one-dimensional finite difference equations, both of which are uncoupled and computationally efficient to solve.

Comparison of the modelling approach in linear and cylindrical geometries with exact and finite element solutions respectively shows that the multi-scale model gives good results in both steady state and transient simulations.

The model has been applied to a spherical PBMR pebble geometry and compared with a steady-state analytical model on the meso-scale. Comparison of the predicted initial rates of temperature rise, both for the particles and the whole pebbles, in a transient shows good agreement with the values expected from the magnitude of the power density and volumetric heat capacities.

5.5   References for Section 5

5.1   OECD NEA/NSC/Doc(2005)xxx Draft V-03, "PBMR Coupled Neutronics/Thermal Hydraulics Transient Benchmark The PBMR-400 Core Design", September 2005.

5.2   IAEA CRP 5, Draft TECDOC II, "Evaluation of High Temperature Gas Cooled Reactor Performance", to be published.

6.0 PARTICLE CLUSTERING

6.1 Purpose of Section 6

Section 5 presented the development and qualification of sub-grid scale models to enable the fuel kernel and moderator temperatures to be calculated. However, these models are capable only of predicting the temperature distribution within an average pebble at a given location within the reactor and for an average particle at a given location within a pebble. Corrections to the pebble temperatures to account for the variations in burn-up or enrichment between pebbles nominally sitting in the same location within the core are developed in Section 8 on multi-batch fuel models. In the context of particles, an average particle at a given location within a pebble generates the nominal power for that location and is uniformly spaced from all of its neighbours. The spread of possible particle temperature due to the variability of the particle power generation can be estimated deterministically by re-calculating the micro-scale temperature fields for the expected extremes of power generation. However, the spread of temperatures owing to non-uniform particle spacing is more difficult to determine. Firstly, the particles are arranged randomly, therefore random clustering of the particles will occur, with locations and sizes of the clusters also being randomly distributed throughout the pebble. Secondly, clusters of different sizes and geometrical arrangements will influence the particle temperatures differently.

The objectives of the work reported in Section 6 are twofold. The first is to develop a statistical method by which the expected frequencies and corresponding sizes of clusters of particles that occur within a pebble can be predicted. A Monte Carlo method of generating random arrangements of particles has been developed. The statistics of this random arrangement are used to generate the frequency and size data for the particle clusters found therein. The second objective is to predict the temperature enhancement that is experienced by the hottest particle in a cluster of a known size and configuration compared with that experienced by the same particle when surrounded by the same number of particles but with nominal spacing. Finite element models of different sized clusters, both with the particles spaced nominally and with zero spacing have been developed to fulfil this second objective.

6.2 Monte Carlo Modelling of Particles Clusters

This section describes the development and validation of a Monte Carlo code used to simulate the random positioning of TRISO fuel particles as would be found within a fuel pebble.

The TRISO particles have an outer diameter of 0.92 mm (the diameter of the outermost PyC coating). The fuelled region of the fuel pebble is a graphite sphere of diameter 50 mm (the pebble has a fuel-free outer layer giving it a total diameter of 60 mm). Each pebble contains 15,000 TRISO particles, which therefore occupy a volume packing fraction of $\lambda = 15 \times 10^3 \times (0.92/50)^3 \approx 0.09344$. These data are drawn from the South African PBMR design (Reference 6.1).

The statistical modelling consists of two distinct stages. In the first stage, a random arrangement of 15000 particles is packed into a cube of the same volume as the heated zone of a pebble. A cube is used as it is simpler to position the particles randomly in Cartesian geometry. In the second stage, statistical analysis of this arrangement is carried out. Both of these stages are performed by a computer code that was written specifically for the purpose.

The computer code generates a random packing of particles in a region of space according to a prescribed average volume fraction. The region is a cube and is filled with 15,000 TRISO particles randomly positioned at the 0.09344 volume packing fraction typical of PBMR fuel pebbles. This code was designed to run many realisations of the particle packing and to measure various statistical properties of particle arrangement. When the assembly of particles is complete, the code identifies closely-packed "clusters" of particles and stores the particle positions in these clusters to provide data for any potential thermal modelling.

The details of the pebble manufacturing process are not well known enough to attempt to model how the particles become distributed. In the absence of this information, the particles are assumed to be randomly positioned, have a finite size and cannot overlap each other. The part of the code which prevents particle overlapping can be disabled, in which case particles behave as if they are infinitely small and spatial distribution of the particles should reduce to a simple Poisson distribution. Similarly, the nearest neighbour function should reduce to a simple quadratic. If the code is run with particle overlap then the resulting statistics generated can be compared with the above theoretical distributions to check if the code is working properly. This functionality is solely for the purposes of validation – it has no bearing on the real particle distributions.

The statistics measured and reported by the code are the nearest neighbour function and details of particle clustering in terms of the numbers of clusters found in each of a number of size groups. These statistics are explained in the following sub-sections.

6.2.1   Nearest Neighbour Function

The number of particles expected to be found within a certain distance from a given particle is defined by the "nearest neighbour function". Clearly, the number of neighbouring particles that surround a given particle increases as volume of space surrounding it is increased. The nearest neighbour function describes how the number of neighbours increases with radial distance from a given particle.

In the current method the nearest neighbour function is constructed for several particles and these are averaged to obtain a single function for the whole arrangement. A starting particle is chosen at random and chosen to be sufficiently far both from any other starting particles and from the boundaries of the cube. The code steps outwards from the starting particle in successive shells, each with a thickness equal to the particle radius, and records the number of neighbouring particles found within each shell. The process is repeated for a specified number of starting particles

until the averaged counts yield the nearest neighbour function for the whole arrangement with a sufficient degree of accuracy.

If the particles are idealised such that they are allowed to overlap, this function reduces to a simple distribution in which the expected number of particles (each of radius r and volume $V_{particle}$) within a shell of volume V_{shell} is equal to $\lambda V_{shell}/V_{particle}$ where λ is the volume packing fraction. The volume of each shell increases approximately as the square of the distance from the centre of the starting particle, so the expected number of particles in each shell increases approximately proportionately with distance also. More precisely, the number of particles within the shell extending from radius r(n−1) to r(n) is therefore:

$$\lambda(4/3)\pi r^3[(n^3-(n-1)^3]/(4/3)\pi r^3 = \lambda(3n^2-3n+1).$$

For particles that are not permitted to overlap the function will follow a slightly different distribution. The number of neighbouring particles within the first two shells [i.e. the (0 →1).r shell and the (1→2).r shell] are both zero, since the particle centres cannot approach closer than 2r.

6.2.2   Particle Clustering

What constitutes a particle cluster is difficult to define in practice. Whilst clusters are easy to identify visually using judgement, achieving the same process by computer program is more difficult. In this work, clusters were defined as being regions in the arrangement in which the local packing fraction was greater than the average value. This simply indicates that within a given region, the particles are more closely spaced than nominal, but it does not identify if particles are touching. The above definition depends upon what is meant by a *region*, in terms of its shape and its volume. In this work cubical regions of differing sizes were used and the packing fraction was determined by counting the number of particles found in each region.

The cube containing the generated assembly of randomly placed particles was discretised into a sampling grid which consisted of N small, cubic volume elements which are termed voxels. The sampling grid was centred on the centre of the cube with any excess volume ignored (since the grid size may not match the cube size exactly). The number of particles encountered within each voxel are recorded. Any voxel with a particularly high number of particles (relative to a specified threshold value) is considered to contain a cluster of particles. The particle positions are recorded and output for later analysis.

For particles that are allowed to overlap the distribution of the number of particles in a voxel is simply a Poisson distribution (Reference 6.2) with the mean number of particles per voxel given by the volume of a voxel divided by the volume of a particle, scaled by the packing fraction:

$$\alpha = mean = variance = \lambda V_{voxel}/V_{particle} = (3/4\pi)\lambda(x/r)^3$$

where λ is the volume packing fraction and V_{voxel} and x are the volume and side length of a voxel. The probability, therefore, of finding n particles in a voxel is $e^{-\alpha}\alpha^n/n!$. The expected number of voxels (of N in total) containing n particles is therefore $Ne^{-\alpha}\alpha^n/n!$. For particles that are not permitted to overlap the distribution will not be Poisson since there is a practical limit to the number of particles which can be placed within a region.

For convenience, for n ≥ 35, the factorial n! is determined using Ramanujan's approximation (Reference 6.3):

$$\ln n! \approx n \ln n - n + (1/6) \ln \{n[1+4n(1+2n)]\} + (1/2) \ln \pi$$

This is an extremely good approximation, with a relative error of only 1.4×10^{-4} for n=1 which decreases rapidly with n (the relative error is $<1.5 \times 10^{-8}$ for n > 35).

6.2.3   Validation

In addition to independent checking of the code, the correct operation of the program, and the quality of the random number generation, can be validated by showing that the various statistical measurements are equal (within error) to the expected theoretical values when the particles are allowed to overlap.

6.2.3.1   Nearest Neighbour Function

As explained in Section 6.2.1, when particles are allowed to overlap, the expected number of neighbouring particles in a shell around a test particle extending from radius r(n−1) to r(n) is $\lambda(3n^2−3n+1)$; where r is the particle radius and λ is the volume packing fraction.

Figure 6.2.1 shows the measured nearest neighbour function obtained from counting the particles around a test particle in 10^4 independent cases. Each result is the mean of the 10^4 measurements. The error is the expected error in the population mean, i.e.

$$[1/(n−1)] [\Sigma(x_i^2)/n − (\Sigma x_i/n)^2].$$

The measured data points and the expected values are in excellent agreement. The inset plot in Figure 6.2.1 shows the difference between the values for each data point expressed in terms of the estimated error in the measurement. This level agreement shows that the particles are randomly distributed and that, on average, the packing fraction attained is the expected value.

Figure 6.2.1: Nearest Neighbour Function for Overlapping Particles
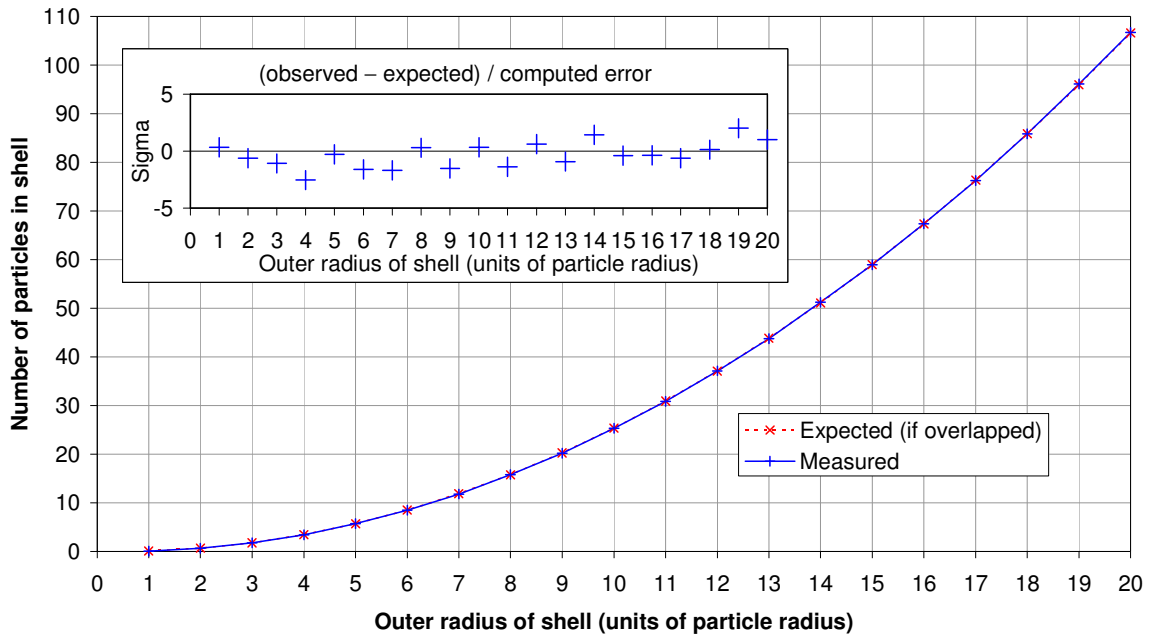
6.2.3.2   Particle Clustering

As explained in Section 6.2.2, when particles are allowed to overlap, the probability of finding n particles in a voxel is:

$$e^{-\alpha}\alpha^n/n!$$

where $\alpha = (3/4\pi)\lambda(x/r)^3$, λ is the volume packing fraction, r is the particle radius and x is the voxel size.

Figure 6.2.2 shows the measured clustering behaviour from counting the number of particles in voxels of size x = 0.25 cm. 1686 grids of 4096 voxels were used in collecting the data, i.e., each data point is the mean of 1686 measurements of the particle distribution into 4096 voxels. Each 4096 voxel grid does not completely cover the interior of the pebble because a 1-radius gap is excluded to avoid edge effects and because the grid does not fit exactly into the remaining space. For the 0.25 cm voxels, 97.8% of the space is sampled and each of the 1686 grids measured contains an average of 14667 particles. Figure 6.2.2 has been re-normalised to present the distribution for a complete pebble of 15000 particles, i.e., it shows the number of clusters of each size which can be expected in a single pebble. The data point errors are the expected error in the population mean.

Again, the measured data points and the expected values are in excellent agreement. The inset plot in Figure 6.2.2 shows the difference between the values for each data point.

Figure 6.2.2: Clustering of Overlapping Particles in Cubic Regions of Side 0.25cm (~5.4 Particle Radii) (Normalised to the 15000 Particles in a Single Fuel Pebble)
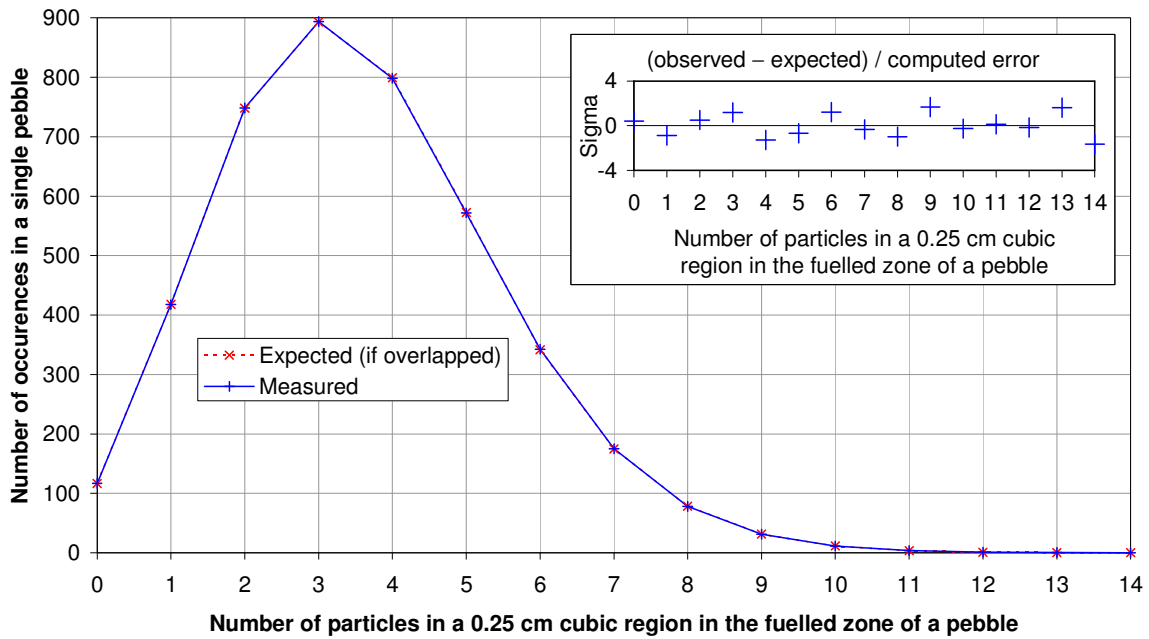
6.2.4 Results

6.2.4.1 Nearest Neighbour Function

Figure 6.2.3 shows the measured nearest neighbour function for the case of non-overlapping particles. The expected nearest neighbour function for the overlapping particle case is also shown for comparison purposes. Since the particles cannot touch, the number of neighbours expected in the first two shells (i.e., 0-1 and 1-2 radii) are zero. Beyond that, the numbers increase just slightly beneath the expected behaviour for particles which can overlap.

Figure 6.2.3: Nearest Neighbour Function for Real (Non-Overlapping) Particles
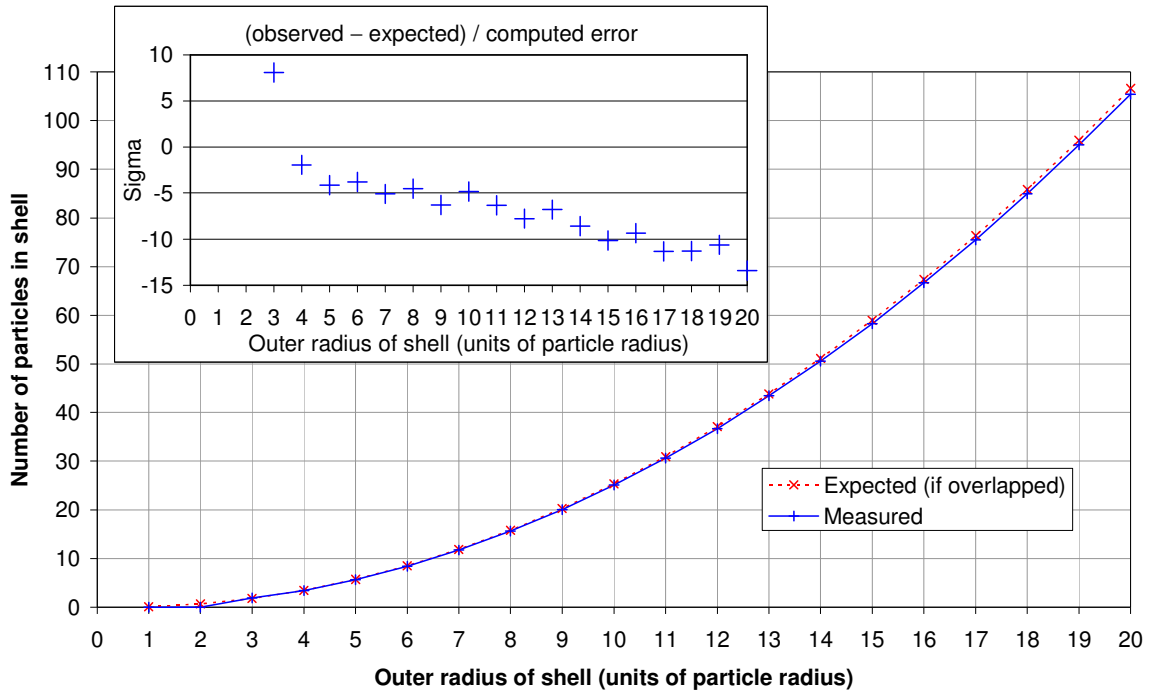
6.2.4.2 Particle Clustering

Table 6.2.1 and Figures 6.2.4, 6.2.5 and 6.2.6 show the measured particle clustering on length scales of 0.15, 0.25 and 0.35 cm (approximately 3.3, 5.4 and 7.6 particle radii respectively). The distributions are clearly different from the overlapping particle validation case. For voxels of size 0.35 cm and larger, the overlapping particle Poisson distribution tends towards a Gaussian (mean = variance). The non-overlapping distribution also appears Gaussian in shape but clearly with a variance less than the mean. The extremes of the distribution are curtailed because the particles cannot overlap.

Table 6.2.1: Number of Occurrences of Different Sized Cluster in a Pebble

Particles per voxel	0.15 cm voxels		0.25 cm voxels		0.35 cm voxels	
	Measured	Error	Measured	Error	Measured	Error
0	7811.507	1.092	38.339	0.149	0.003	0.001
1	8872.332	1.804	258.333	0.342	0.057	0.006
2	2612.108	0.984	712.137	0.536	0.481	0.019
3	283.732	0.412	1090.247	0.692	2.692	0.042
4	12.783	0.091	1042.194	0.696	11.030	0.088
5	0.224	0.012	661.020	0.532	32.862	0.146
6	0.001	0.001	290.696	0.362	76.043	0.211
7	0.000	0.000	90.303	0.213	139.912	0.284
8			20.324	0.111	207.969	0.333
9			3.291	0.044	254.334	0.402
10			0.384	0.015	257.298	0.387
11			0.039	0.005	218.743	0.353
12			0.000	0.000	157.980	0.301
13					96.759	0.238
14					50.737	0.175
15					22.661	0.124
16					8.803	0.078
17					2.917	0.044
18					0.871	0.025
19					0.197	0.012
20					0.049	0.006
21					0.009	0.002
22					0.001	0.001
23					0.000	0.000

Figure 6.2.4: Clustering of Non-Overlapping Particles in Cubic Regions of Side 0.15cm (~3.3 Particle Radii) (Normalised to15000 Particles in a Fuel Pebble)
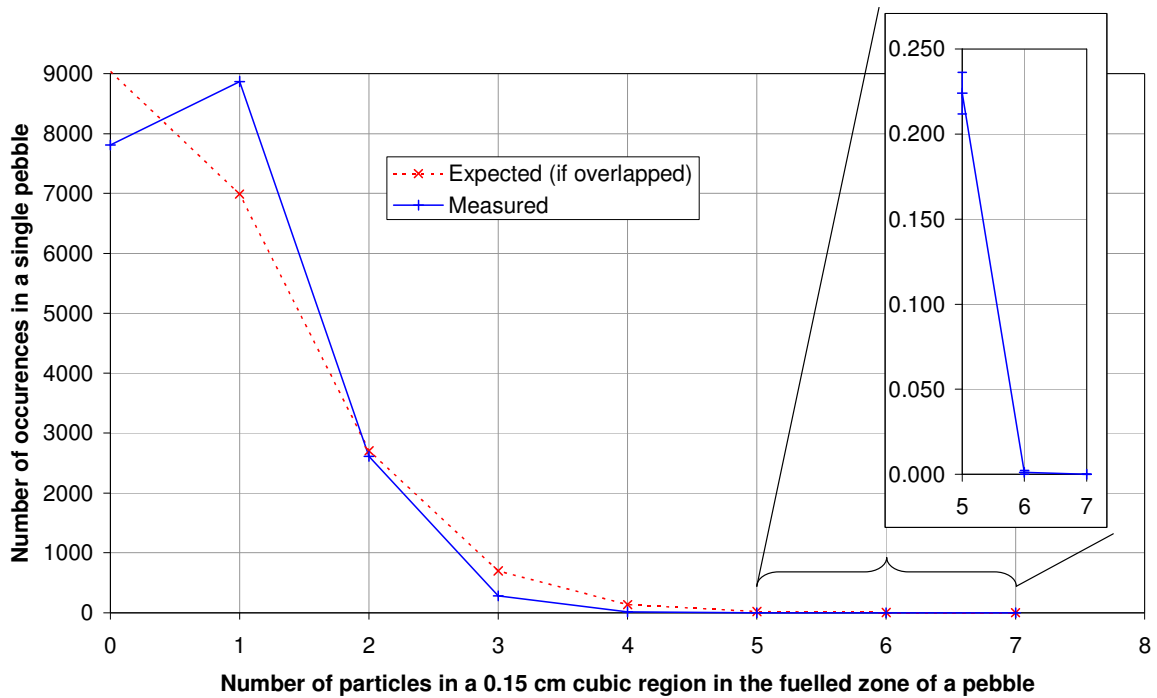
Figure 6.2.5: Clustering of Non-Overlapping Particles in Cubic Regions of Side 0.25cm (~5.4 Particle Radii) (Normalised to 15000 Particles in a Fuel Pebble)
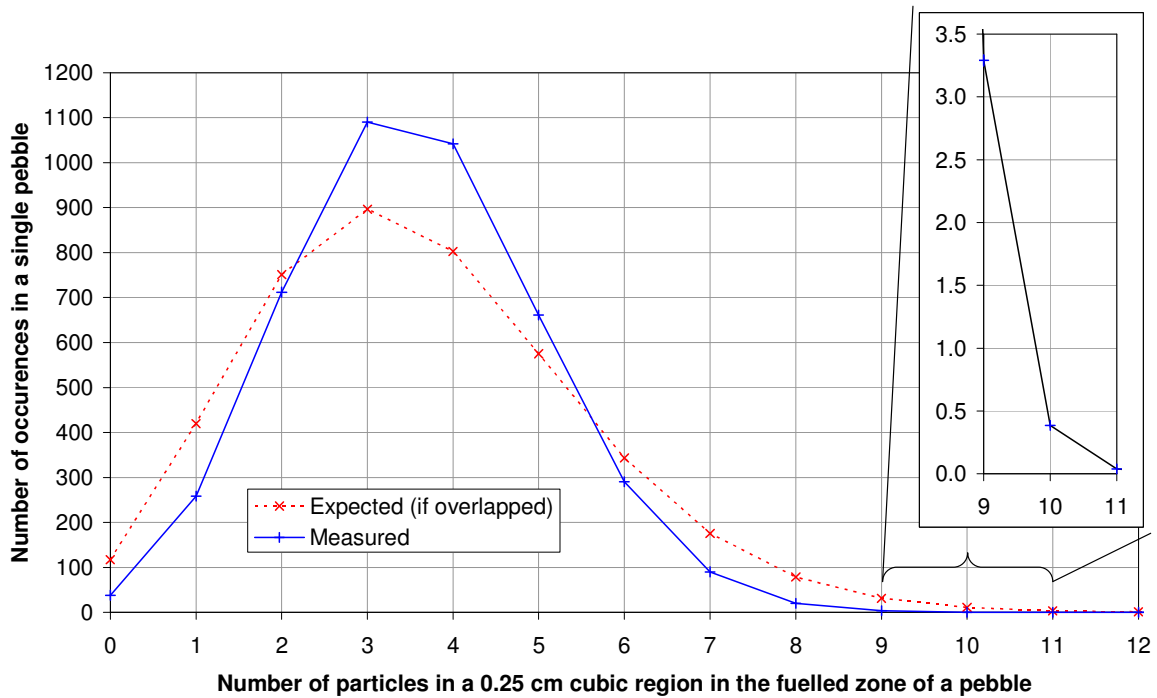
Figure 6.2.6: Clustering of Non-Overlapping Particles in Cubic Regions of Side 0.35cm (~7.6 Particle Radii) (Normalised to 15000 Particles in a Fuel Pebble)
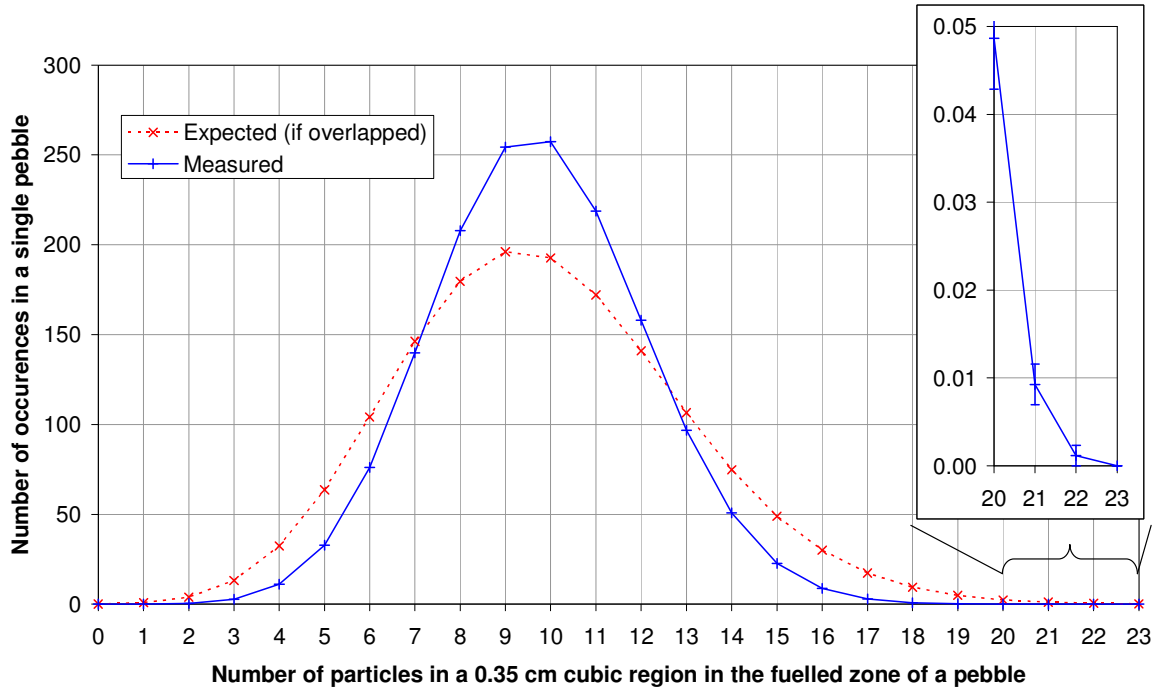
On the 0.15 cm scale, a cluster of 4 particle centres in a 0.15 cm region occurs with a frequency of approximately 13 per pebble, whilst a cluster of 5 or more occurs at only approximately 0.2 per pebble.

On the 0.25 cm scale, a cluster of 9 particle centres in a 0.25 cm region is measured to be approximately 3.2 per pebble, whilst clusters of 10 or more occur at only approximately 0.4 per pebble.

Moving up to the 0.35 cm scale, a cluster of 18 particle centres occurs with a frequency of approximately 0.9 per pebble. Clusters of 19 or more occur at a frequency of only approximately 0.2 per pebble, with clusters of 22 or more occurring in around 1 in 1000 pebbles.

6.3   Finite Element Models of Particle Clusters

To determine the temperature enhancements associated with clusters of particles, finite element models of some cluster arrangements of particles embedded in a graphite matrix were set up using the Abaqus code. In these models it is assumed that within a cluster of particles, the particles touch and the overall shape is compact, i.e., as close to being spherical as the limited number of particles will allow. The largest number of particles in the cluster was limited to 14. Table 6.2.1 showed that a cluster of this size would be expected to be found about 50 times in a typical pebble. The next size of an approximately spherical cluster would contain about 61 particles and Table 6.2.1 shows that the expected occurrence of such a large cluster would be extremely rare.

The approach adopted was to model only the particles that are in the cluster in the pebble and to compare the results of two configurations for each cluster size; one in which all of the particles are touching, and the other in which the particles are spaced at the nominal mean particle separation of 1.2 diameters between their surfaces. Heat generation from all of the other particles in the pebble was neglected in both configurations as this just sets the 'background' temperature fields which are cancelled out when the temperature differences between each pair of configurations are calculated.

The fuel pebble was modelled as shown in Figure 6.3.1 with only the fuel particles that constitute the cluster represented with these located at the pebble centre surrounded by the graphite of the pebble.

Figure 6.3.1: Finite Element Model Domain Showing Loading and Boundary Conditions
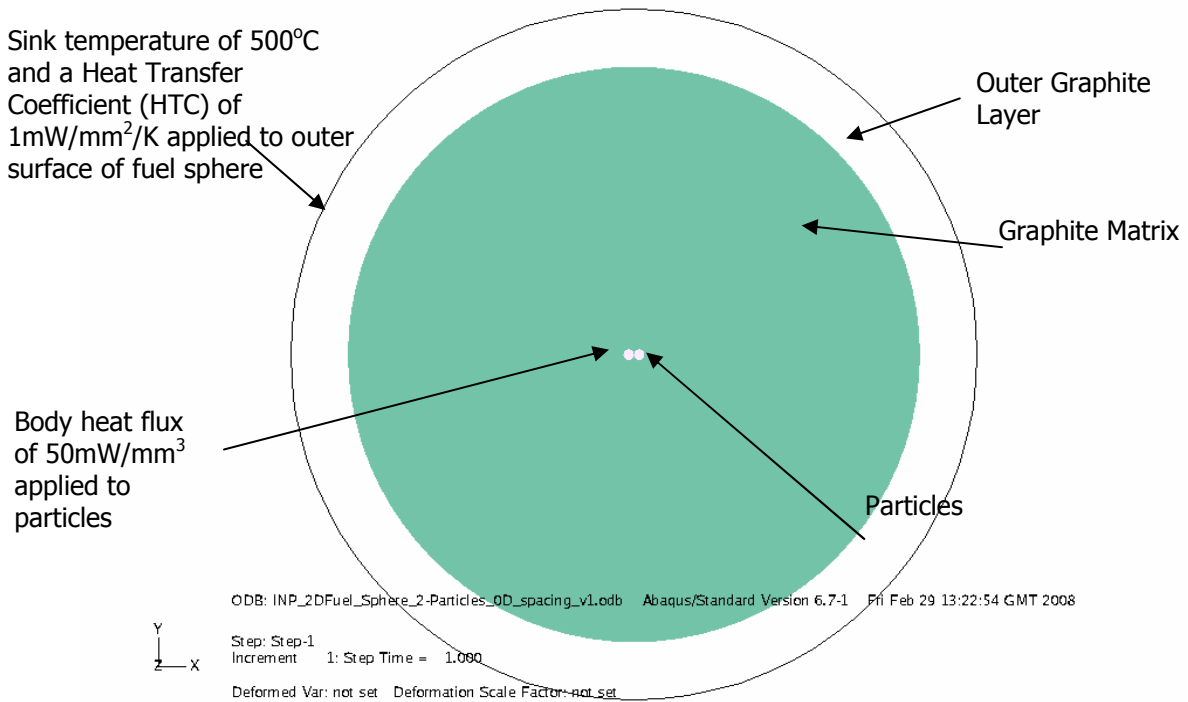
Four pairs of cluster sizes were modelled, each cluster size consisting of a 'touching' and nominally spaced configuration as follows:

- 3 particles with no spacing (distance measured between the surfaces of neighbouring particles)

- 3 particles with a spacing of 1.2 diameters

- 4 particles with no spacing

- 4 particles with a spacing of 1.2 diameters

- 13 particles with no spacing

- 13 particles with a spacing of 1.2 diameters

- 14 particles with no spacing

- 14 particles with a spacing of 1.2 diameters

The diameter of a particle is the standard PBMR size of 0.92mm. The finite element models were set up parametrically, so that the particle spacing could be adjusted without having to re-mesh each cluster size and configuration manually.

The models and meshes that were produced for the 14 particle configurations are shown in Figures 6.3.2 to 6.3.7. The models and meshes for the other particle arrangements are shown in Appendix B.

Figure 6.3.2: Fourteen Particles, No Spacing – Half Model
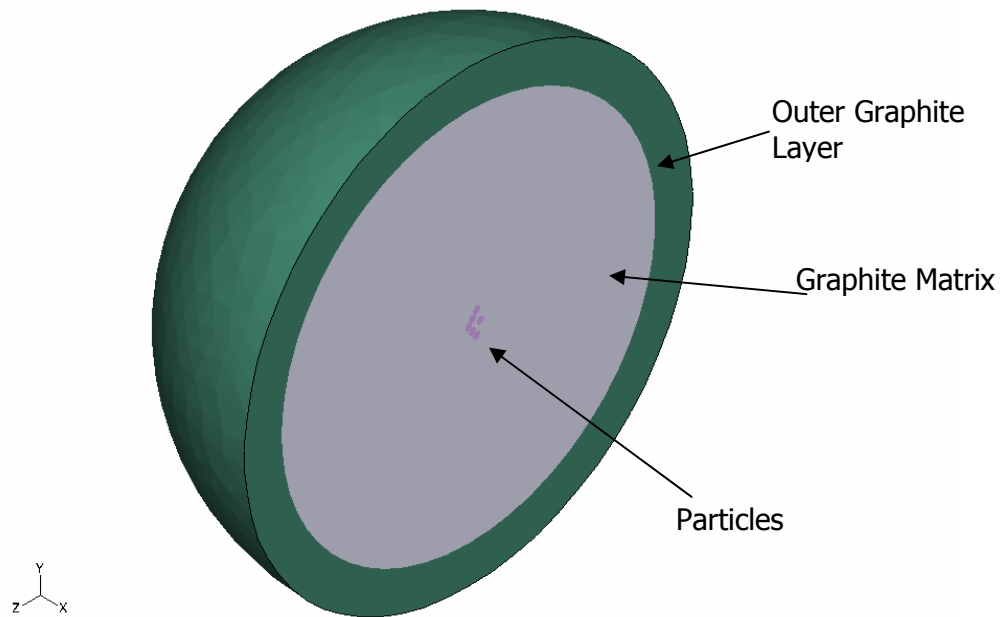
Figure 6.3.3: Fourteen Particles, No Spacing – Pebble Mesh
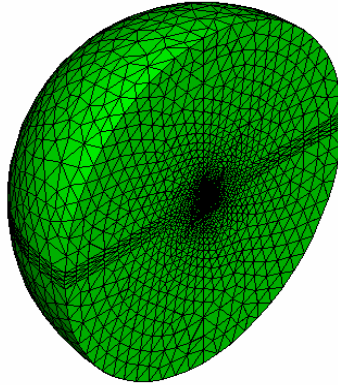
Figure 6.3.4: Fourteen Particles, No Spacing – Close-Up View of Pebble Mesh
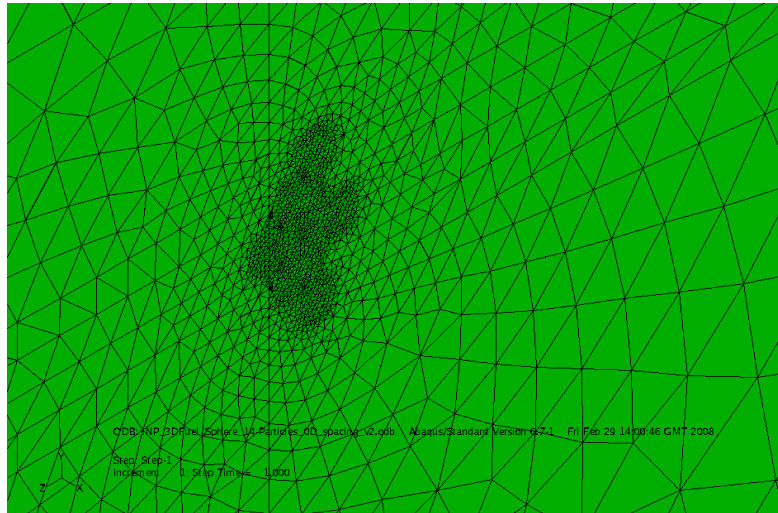
Figure 6.3.5: Fourteen Particles, 1.2 Diameter Spacing – Close-Up View of Mesh
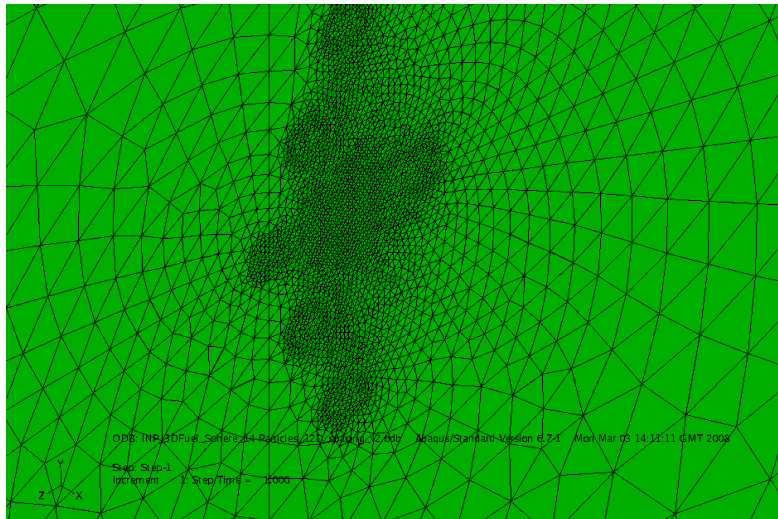
Figure 6.3.6: Fourteen Particles, No Spacing – Isometric View of Cluster

ODB: INP_3DFuel_Sphere_14-Particles_0D_spacing_v2.odb   Abaqus/Standard Version 6.7-1   Fri Feb 29 14:00:46 GMT 2008

Step: Step-1
Increment   1: Step Time =   1.000
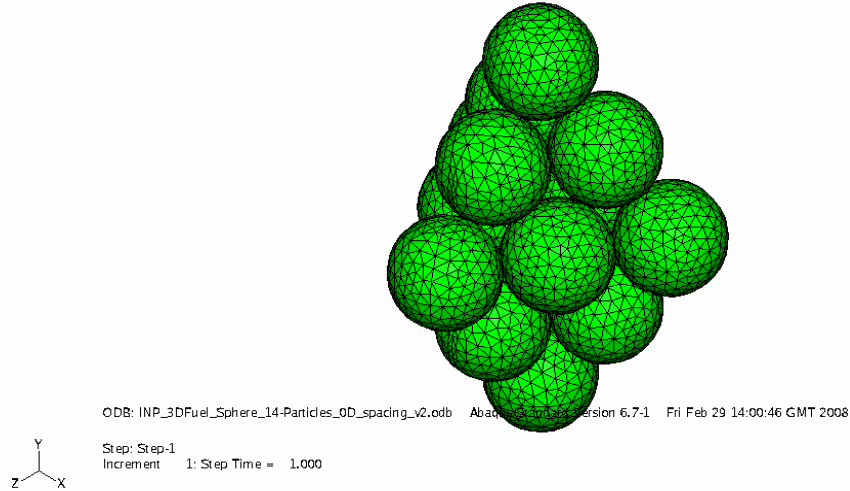
Figure 6.3.7: Fourteen Particles, 1.2 Diameter Spacing – Isometric View of Cluster

ODB: INP_3DFuel_Sphere_14-Particles_12D_spacing_v2.odb   Abaqus/Standard Version 6.7-1   Mon Mar 03 14:11:11 GMT 2008

Step: Step-1
Increment   1: Step Time =   1.000

Deformed Var: not set   Deformation Scale Factor: not set
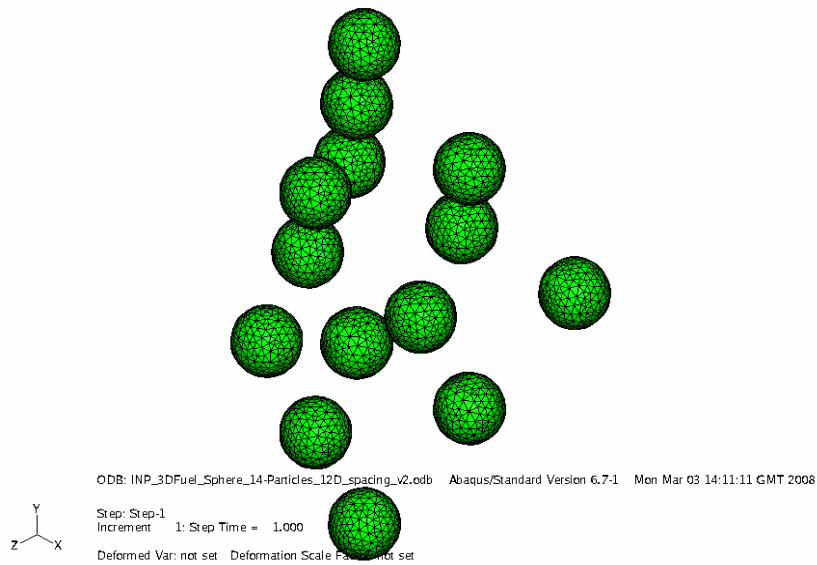
6.3.1   Material Properties

The model is shown in Figure 6.3.1 and contains two materials, fuel particles and graphite. Each TRISO particle is made up of five layers of different materials with different thermal properties. In the current finite element models, a particle was represented as a homogeneous solid, with a smeared effective thermal conductivity. The value used for the effective thermal conductivity of the TRISO fuel particles was determined using the analytical method presented in Section 7.2.

The following thermal conductivities were used:

- Graphite outer layer 15.00 W/m/K

- Graphite matrix   15.00 W/m/K

- Homogenised particles 4.13 W/m/K

The power density in the particles was set to a nominal value of 50 MW/m^3 and this was assumed to be uniformly distributed within a particle and the same for all particles. Whilst this power density is lower than that encountered in an average particle in PBMR, it was simply used as a basis for the models. The resulting temperature differences between the 'touching' and 'separated' configurations were later scaled to correspond to typical PBMR average and peak particle powers of 144.85 MW/m^3 and 449.04 MW/m^3 respectively. These latter values were determined from values given in Reference 6.4, based on an average pebble power of 880 W and a peak-to-mean power density factor of 3.1.

The finite element meshes were made up from 4-node tetrahedral elements.

6.3.2 Results

Figures 6.3.8 and 6.3.9 show the resulting temperature distributions for configurations containing four particles, without and with spacing, respectively. These show the particle surface and internal temperatures in each pair of views. Temperature distributions for configurations containing thirteen particles are shown in Figures 6.3.10 and 6.3.11, again without and with spacing, respectively. The temperature distributions for all four pairs of configurations are presented in Appendix B.

Table 6.3.1 shows the maximum temperature for each cluster taken from the finite model and gives the temperature increase when the particles are touching compared to when they are spaced 1.2 diameters apart.

Table 6.3.1: Temperature Increases Associated with Clustering for Various Numbers of Particles

No. of Particles	Spacing (Particle Diameters)	Maximum Temperature in FE model (°C)	Temperature Increase from FE model (°C)	Temperature Increase for Average Particle Power (°C)	Temperature Increase for Peak Particle Power (°C)
3	0	500.9	0.2	0.58	1.80
3	1.2	500.7			
4	0	501.1	0.3	0.87	2.69
4	1.2	500.8			
13	0	502.5	1.3	3.77	11.68
13	1.2	501.2			
14	0	502.4	1.2	3.48	10.78
14	1.2	501.2			

Figure 6.3.8: Four Particles, No Spacing – Particle Temperature Distributions

Temperatures shown in °C
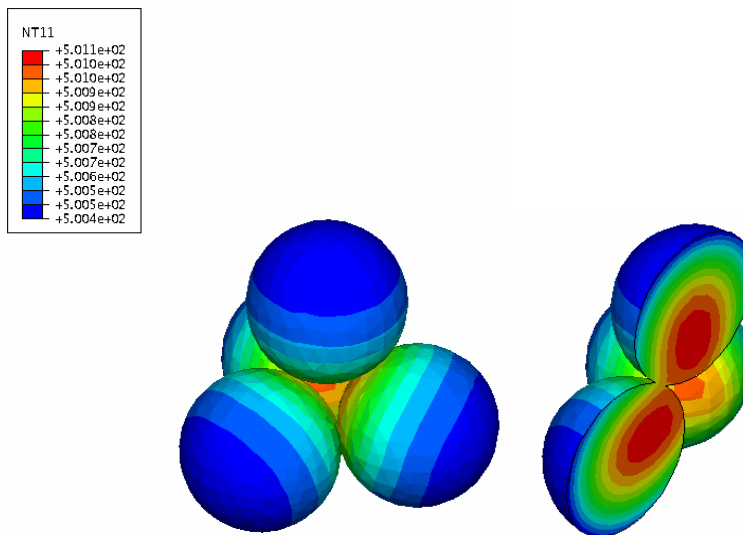
Figure 6.3.9: Four Particles, 1.2 Diameter Spacing – Particle Temperature Distributions

Temperatures shown in °C
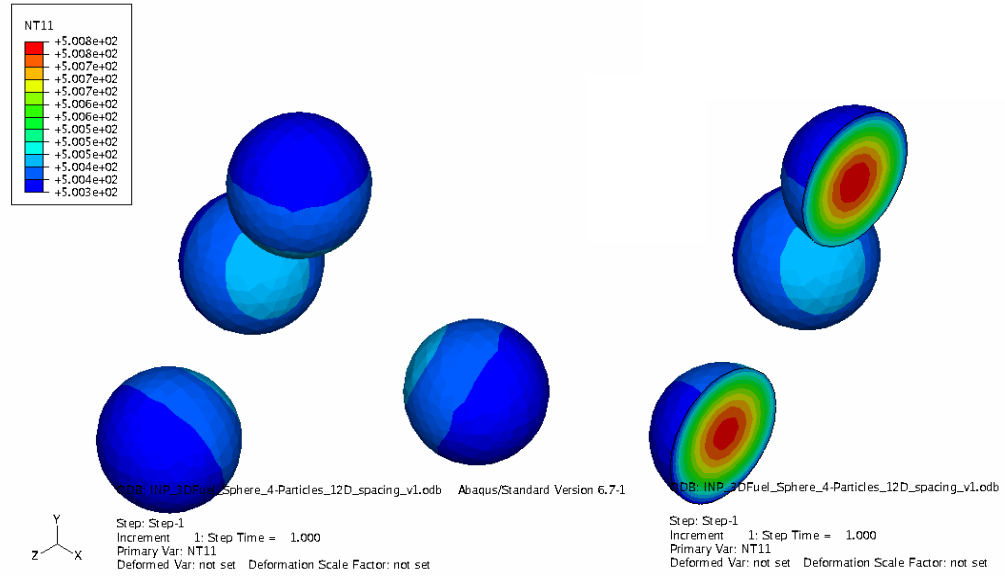
Figure 6.3.10: Thirteen Particles, No Spacing – Particle Temperature Distribution

Temperatures shown in °C
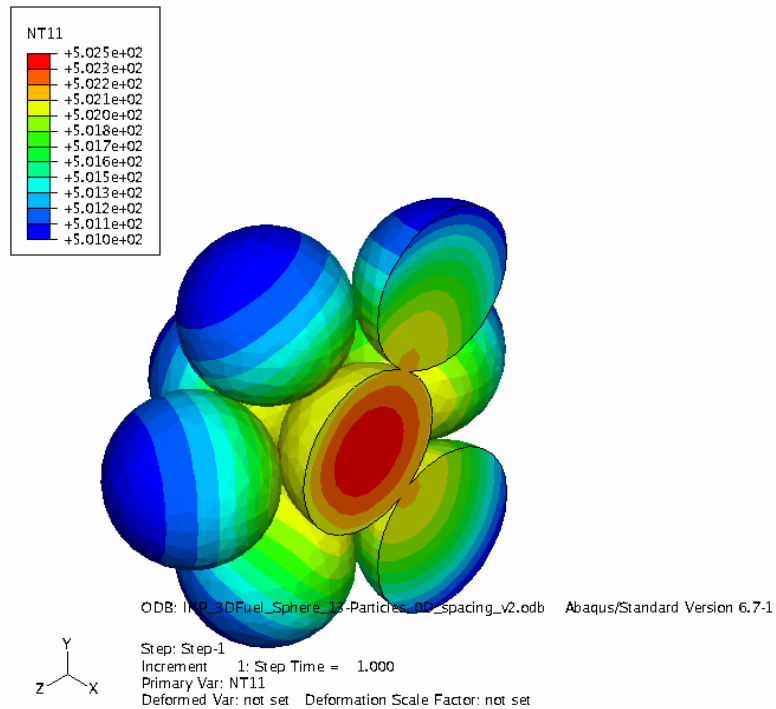
Figure 6.3.11: Thirteen Particles, 1.2 Diameter Spacing – Particle Temperature Distribution

Temperatures shown in °C

NT11
+5.012e+02
+5.012e+02
+5.011e+02
+5.011e+02
+5.010e+02
+5.010e+02
+5.009e+02
+5.009e+02
+5.008e+02
+5.007e+02
+5.007e+02
+5.006e+02
+5.006e+02

ODB: INP_3DFuel_Sphere_13-Particles_12D_spacing_v2.odb   Abaqus/Standard Version 6.7-1   Thu Mar 20 09:23:04 GMT 2008

Step: Step-1
Increment   1: Step Time =   1.000
Primary Var: NT11
Deformed Var: not set   Deformation Scale Factor: not set
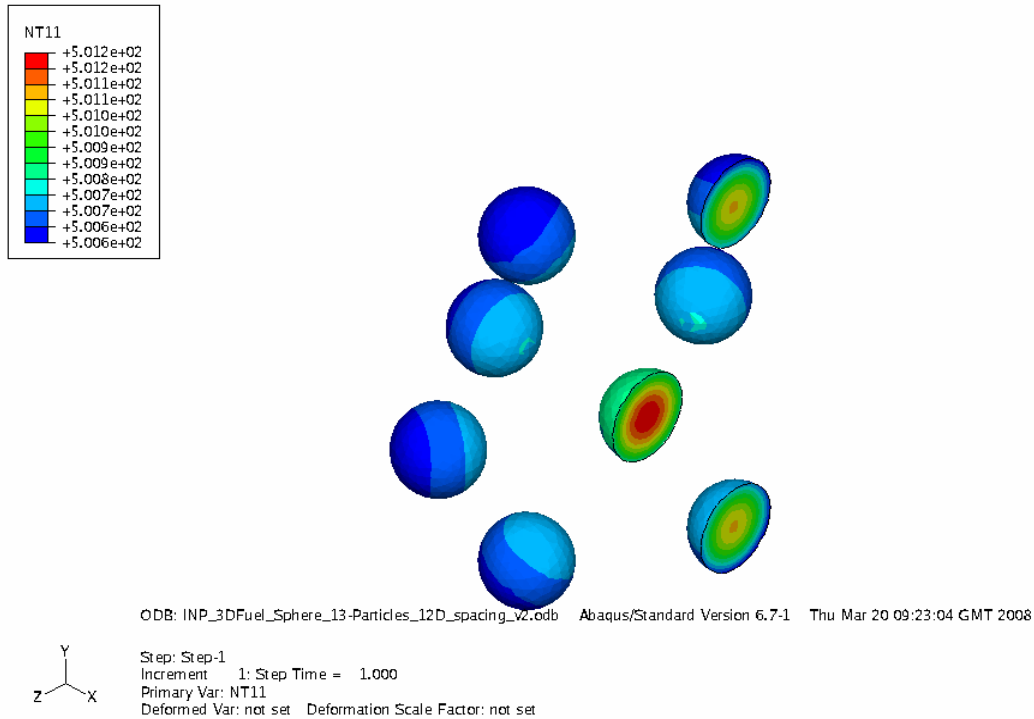
Figure 6.3.12 shows a plot of the temperature increases due to clustering for the average particle power density against the number of particles in each cluster. Two lines are shown; one includes the model results for clusters of 3, 4 and 13 particles and the other for 3, 4 and 14 particles. The 13 particle cluster has one particle in the centre of the cluster whereas each particle in the 14 particle cluster is an external particle and, therefore, the former is a more limiting model even though there are fewer particles in the cluster.

Figure 6.3.12: Temperature Increase due to Clustering for Average Power PBMR Particles
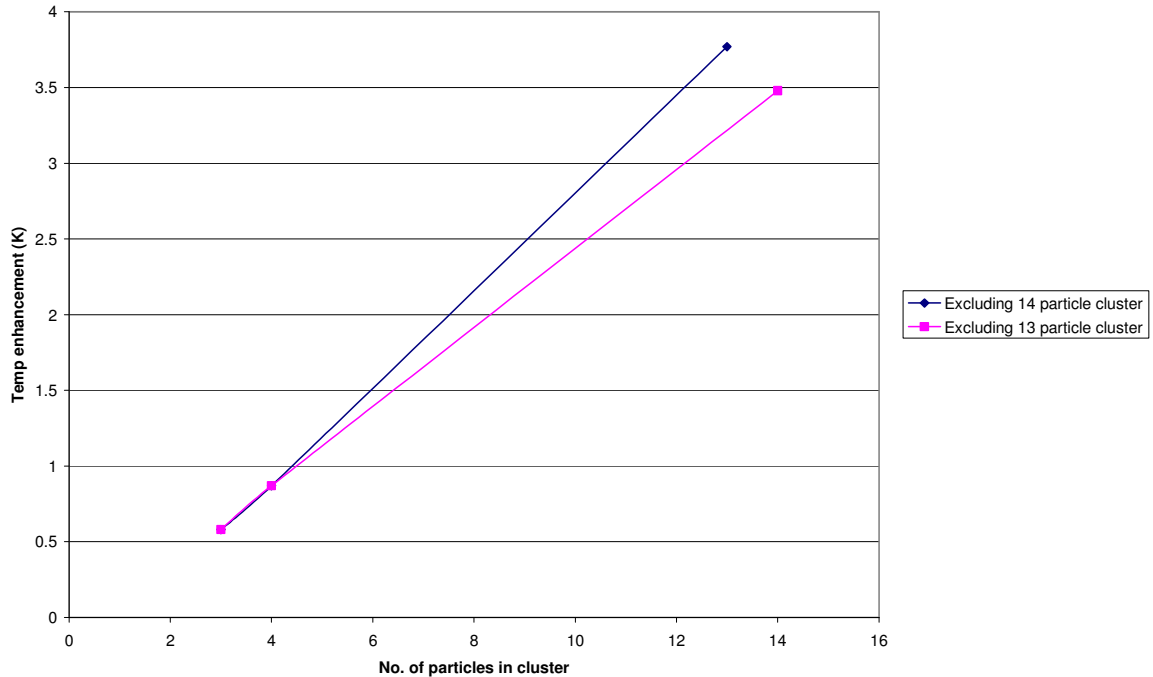
Figure 6.3.12 and Table 6.3.1 show that the increase in particle temperature for an average particle when contained within a reasonably large cluster is quite small, of the order of 4°C. Even for the most highly rated particles in the core the corresponding increase is only of the order of 12°C.

6.4 Closure

This section has presented a study of the likelihood and influence of clustering of the TRISO particles within a fuel pebble. A Monte Carlo method has been created for generating random arrangements of particles and then interrogating these arrangements to derive particle distribution and clustering statistics. Whilst it is believed that the current method for determining the frequency by which given sized clusters occur is sensible - it does introduce a somewhat arbitrary scale effect into the results through the choice of voxel size. Further work is required to develop a more robust method in which results can be obtained that are independent of the scale of the sampling grid. This work has showed that the largest approximately spherical cluster expected will contain of the order of 13 particles, a larger spherical cluster containing about 61 particles will be extremely rare. This work shows that a cluster containing 22 particles should be found in 1 in every 1000 pebbles, so there will be typically 450 such clusters in a reactor of the size of PBMR.

On the basis of this work, a spherical cluster of 13 to 14 particles has been taken to represent the largest credible spherical cluster that will be found. The finite element model of such a cluster that contains 13 touching particles shows that the temperature

increase, compared with nominally spaced particles, is of the order of only 4°C for average power particles. For the same cluster but containing the highest rated particles in the reactor, the temperature increase due to clustering is of the order of 12°C. It appears from the current work that if a margin of, say, 20°C was applied to 'best-estimate' particle temperatures predicted by the multi-scale method of Section 5.3, that this would allow for any enhancement due to particle clustering. However, this statement is a very tentative proposal and requires further work to improve the robustness of the statistics before it can be consolidated.

6.5 References for Section 6

6.1 IAEA CRP5, Draft TECDOC II, Evaluation of High Temperature Gas Cooled Reactor Performance, to be published.

6.2 Jones M.E.M., Statistics, 1988, ISBN 0-7217-2360-8 (Vol 1) and 0-7217-2361-6 (Vol 2).

6.3 www.luschny.de/math/factorial/approx/SimpleCases.html

6.4 PBMR Presentation to the 6th Research Coordination Meeting of IAEA CRP5, Vienna, 6 September 2005, slide 53.

7.0   DETERMINATION OF PEBBLE EFFECTIVE CONDUCTIVITY

7.1   Purpose of Section 7

The temperature distribution within a pebble is influenced by the distribution of thermal conductivity throughout a pebble. Because the pebble is a composite solid, an interpolation scheme must be used to derive the conductivity of the solid as a function of the conductivities of the particles and graphite, and the volume fraction of each.

This section presents an analytical method by which the effective conductivities of TRISO particles in the interior fuelled zone of pebbles can be interpolated. This analytical method is qualified by comparing the predicted effective conductivities with those obtained from finite element models of different arrangements of particles embedded within a graphite matrix. Further, the finite element models were used to examine the influence on the effective conductivity of either representing the individual layers within the TRISO particles explicitly or, alternatively, homogenizing the particles as was done in the clustering calculations of Section 6.3.

In Section 7.2 the analytical model, which is an extension to Maxwell's theory of the conductivity of composites, is developed and applied to predict the effective thermal conductivity of a fuel particle and of the pebble matrix containing the particles. Section 7.3 presents the finite element models that were used to determine thermal conductivities for comparison with the analytical model.

7.2   Determination of Pebble Effective Conductivity using Maxwell's Equation

The fuel pebbles within the pebble bed high temperature gas reactors are formed from TRISO fuel particles embedded in a graphite matrix. The TRISO particles consist of a spherical ceramic fuel kernel, covered by a number of protective coatings, as shown in Figure 2.4.2. The coatings form barriers preventing the escape of fission products from an irradiated fuel particle. However, the low thermal conductivity of some of the coating materials can reduce the effective thermal conductivity of the whole fuel pebble to a level significantly below the conductivity of the graphite matrix material.

Dimensions and properties of fuel pebbles used here are summarized in Section 2 of the report and were taken to be those of PBMR pebbles obtained from the IAEA CRP-5 PBMR benchmark specification described in Reference 7.1.

7.2.1   TRISO Fuel Particle Properties

Particle dimensions and properties were presented in Section 2, but a description of the structure of a particle is repeated here. The TRISO particles consist of a uranium dioxide kernel, of diameter 500 μm, surrounded by four coatings. The innermost coating is formed from porous carbon, to hold fission gases. This is surrounded by a layer of pyrolytic carbon, a layer of silicon carbide, and a final outer layer of pyrolytic carbon, as shown in Figure 2.4.2. The coating diameters, materials and representative thermal conductivity values are shown in Table 2.4.1.

7.2.2 Particle Packing Fraction in PBMR Fuel Pebbles

The volume fraction occupied by TRISO particles within the core of a typical PBMR fuel pebble is 0.09344 (i.e., 9.344% by volume) based on 15000 particles of 0.92 mm diameter contained within the 50 mm diameter fuelled zone of the pebble.

7.2.3 Maxwell's Theory of Conductivity of Composite Materials

The effect of a dilute suspension of homogenous spherical particles on the thermal conductivity of a medium can be modelled using an analysis due to Maxwell (see, for example Reference 7.2). Maxwell's approach makes no assumptions regarding the geometrical configuration of the particles, but does depend on the assumption that the particles are spaced sufficiently far apart that neighbouring particles do not influence the way heat flows through the matrix in the vicinity of any individual particle.

In Maxwell's theory, the temperature field around a single particle within a background temperature gradient is computed analytically. A relationship is obtained between the perturbation to the far-field temperature distribution caused by the particle and the thermal conductivity of the particle itself. This relationship is then used as a basis for calculating the effective conductivity of a suspension of a large number of such particles. The standard form of the equation resulting from Maxwell's theory is (as derived in Appendix C.1):

$$k_{eff} = \frac{3k_m k_p \alpha + (2k_m + k_p)k_m(1-\alpha)}{3k_m \alpha + (2k_m + k_p)(1-\alpha)}$$

Where k_m and k_p are the thermal conductivities of the matrix and the particles respectively and α is the volume fraction of particles in the matrix. Maxwell's method has been extended in this work to allow a value of k_p to be determined for a particle which is, itself, a composite solid. The extension requires twelve unknown coefficients to be determined. These coefficients feature in two equations for the kernel, two for each layer of the coating and two for the surrounding matrix, giving rise to a system of twelve simultaneous equations (since TRISO coatings consist of four layers). Solution of the system of equations allows the conductivity of a particle to be calculated from:

$$\frac{k_P}{k_m} = \left(\frac{1 - 2\, B_{(N_{coat}+2)}}{1 + B_{(N_{coat}+2)}} \right)$$

where $B_{(Ncoat+2)}$ is the last of the unknown coefficients obtained from the solution, in which N_{coat} is the number of coatings (or 4 for TRISO particles). The system of equations required to be solved to calculate $B_{(Ncoat+2)}$ is presented in Appendix C.1. Substituting for the effective particle conductivity into Maxwell's equation gives the effective conductivity of the matrix and particles combined as:

$$\frac{k_{eff}}{k_m} = \left(\frac{1 - 2\,\alpha\,B_{(N_{coat}+2)}}{1 + \alpha\,B_{(N_{coat}+2)}} \right)$$

7.2.4 Analytically Derived Effective Thermal Conductivities

Based on the TRISO fuel particle data given in Section 2 combined with an irradiated graphite thermal conductivity of 15 W/m/K for the matrix, it is found that the effective conductivity of a homogenized single TRISO particle is 4.1328 W/m/K. Using the same properties and a particle volume fraction of 0.09344 gives the effective conductivity of the particle containing zone within a pebble of 13.7 W/m/K, or 8.67% lower than the conductivity of the matrix material.

7.3 Finite Element Modelling

This section presents the finite element models that were produced for comparison with the above theory and shows the results from the finite element analysis.

7.3.1 Geometry Used for 3-D Finite Element Models

Three-dimensional finite element models were produced for three different regular configurations of fuel particles in a graphite matrix. The configurations that were used were:

- Simple cubic (SC)

- Body-centered cubic (BCC)

- Face-centered cubic (FCC).

The simple cubic configuration consists of a unit cell that is a cube with the centre of a particle situated at each of its eight corners. Only one eighth of each particle lies in the volume of the cube giving an equivalent of one particle per unit cell. Figure 7.3.1 shows a simple cubic model consisting of three unit cells stacked on top of each other.

Figure 7.3.1: Finite Element Model of a Simple Cubic Arrangement of Particles
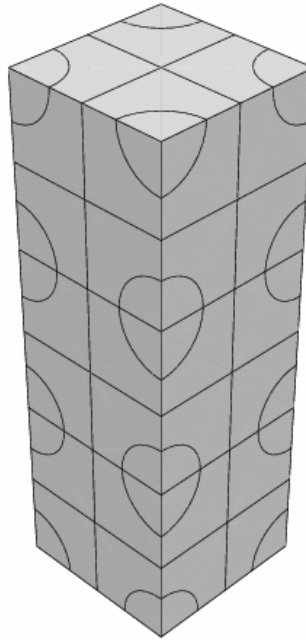
The body-centered cubic configuration has the same arrangement of corner fuel particles as the simple cubic, but with an extra particle located in the centre of the unit cell, giving two particles per unit cell.

The face-centered cubic arrangement has a particle at each of its eight corners, as for the simple cubic, but in addition, it has extra particles centered on each of the six faces. For each of these face centered particles, only half of the particle lies inside the unit cell, giving a total of four particles contained within a unit cell.

Within each of these configurations, two variants of each were produced in which the layered structure of the TRISO particles was represented explicitly or homogenized with an effective conductivity determined using the analytical method of Section 7.2.

7.3.2 Model Unit Cell Dimensions

Each finite element model was set up using different dimensions for the unit cells to ensure that the packing fraction of fuel particles in the graphite matrix was held constant at 9.344% (as stated in Section 7.2.2). As such, the volume of unit cell in the face-centered cubic configuration was four times that in the simple cubic arrangement, as the former contained four times the number of particles. The dimensions of each of the unit cells used in the development of the finite element models are presented in Appendix C.2.

7.3.3 Boundary Conditions and Material Properties

Uniform but different temperatures were applied to the two end faces of the model to set up a prescribed temperature difference of 500°C.

For each particle configuration, two models were created. The first represented the fuel particle as a homogenized solid, with a smeared effective conductivity. The second model represented the particle by explicitly modeling each of its layers, with the correct conductivity assigned to each layer. The conductivity of irradiated graphite was taken to be 15 W/m/K and the effective conductivity of a TRISO particle was taken to be 4.1328 W/m/K (Section 7.2). Figures 7.3.1 and 7.3.2 show the 'smeared' and 'layered' models used for the simple cubic analysis.

Figure 7.3.2: Finite Element Model of the Simple Cubic Configuration (Layered Model)
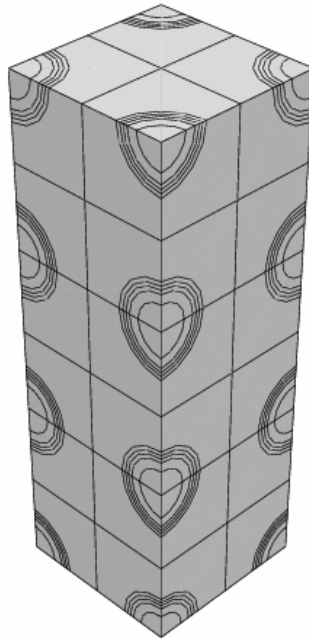
Finite element meshes for each configuration were constructed using 4-node linear tetrahedral elements.

7.3.4   Results

Contour plots of the heat flux and temperature distributions for the 'smeared' and 'layered' variants of the face-centered cubic model are shown in Figures 7.3.3 and 7.3.4 respectively. In both figures, regions of high heat flux lie on either side of the particles as the heat flow lines become squeezed on the passage between the particles. The temperature distributions show that there exist horizontal planes passing through the particle centres upon which the temperature distributions are uniform. Thus, the uniform temperature conditions applied to the ends of the model are legitimate boundary conditions because the end faces are planes that pass through particle centres.

Figure 7.3.3: Face Centred Cubic Smeared Model - Heat Flux and Temperature Distributions

Figure 7.3.4: Face Centred Cubic Layered Model - Heat Flux and Temperature Distributions

From the calculated overall heat flows and imposed temperature difference, effective thermal conductivities were determined using the following equation:

$$k_{eff} = \frac{L\,\dot{q}}{\Delta T\,A}$$

where:

  k_{eff} thermal conductivity (W/m/K)

  L length of model (m)

  $\dot{q}$ total heat flow (W)

  ΔT temperature difference (K)

  A cross-sectional area of model (m^2)

The overall heat flows were calculated by defining a horizontal 2-D surface in the model, and then integrating the heat flux over this surface. The effective thermal conductivities calculated for the 'layered' and 'smeared' variants for each configuration, are shown in Table 7.3.1.

Table 7.3.1: Effective Thermal Conductivities Derived from Finite Element Models

	SC Smeared	SC Layered	BCC Smeared	BCC Layered	FCC Smeared	FCC Layered
Length (mm)	4.902	4.902	6.1764	6.1764	5.188	5.188
Cross Sectional Area (mm^2)	2.670	2.670	4.239	4.239	6.729	6.729
T2 (K)	1273	1273	1273	1273	1273	1273
T1 (K)	773	773	773	773	773	773
ΔT (K)	500	500	500	500	500	500
Heat Flow (W)	3.737	3.738	4.719	4.718	8.926	8.918
Conductivity (W/m/K)	13.72	13.73	13.75	13.75	13.76	13.75

The results of Table 7.3.1 show that the effective thermal conductivity is insensitive to the geometrical arrangement of the particles, with the percentage differences in the predicted values being less than 0.15%. Therefore, a truly random arrangement of a large number of particles with the same packing fraction would yield a very similar

result. Differences in the predicted conductivities determined alternatively with smeared and layered particles are also very small, typically 0.073%.

The analytical treatment of Section 7.2, that is, Maxwell's method extended to cope with multi-layered particles, yielded an effective thermal conductivity of 13.70 W/m/K which is very close to the values predicted here with the maximum difference being 0.36%. Therefore, for the particle packing fraction encountered in PBMR type pebbles with a packing fraction of 0.09344, Maxwell's method gives satisfactory results.

7.4   Closure

This section presented an analytical method for determining the effective thermal conductivities of individual TRISO particles and of the particle containing zone within whole fuel pebbles.

Effective thermal conductivities determined from finite element models of three different arrangements of particles show that the values obtained are largely independent of the geometrical configuration of the particles. Therefore it is concluded that a large enough assembly of randomly spaced particles would yield the same effective thermal conductivities if the particle packing fraction were matched. Further, approximation of the real layered particles by homogenized equivalents has a negligible influence on the predicted conductivities. This latter result is useful should it be necessary to model large assemblies of randomly spaced particles, as was done, to some extent when looking at the influence of particle clusters in Section 6.3.

7.5   References for Section 7

7.1   IAEA CRP5, Draft TECDOC II, Evaluation of High Temperature Gas Cooled Reactor Performance, to be published.

7.2   Carslaw, H.S. and Jaeger, J.C., Conduction of Heat in Solids, 2nd edition, Oxford University Press, 1959, p428.

8.0   MULTI-BATCH FUEL MODELS

8.1   Purpose of Section 8

A medium term objective of this research program is to construct a macro-scale thermal hydraulic model of a pebble bed reactor core which will calculate the pebble, reflector and coolant temperatures in the reactor. The model will be based around a computational fluid dynamics (CFD) code, and within this, the pebble bed will be divided into a large number of discrete computational cells, as shown schematically in two dimensions in Figure 8.1.1.

Figure 8.1.1: Schematic Arrangement of a Macroscopic Computational Grid
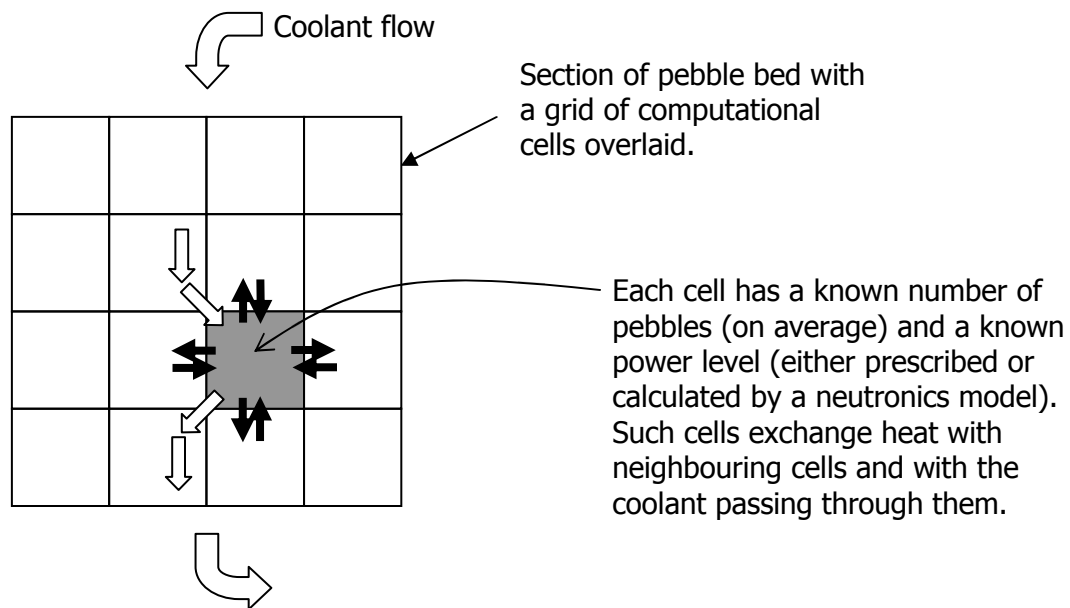
Within each cell of such a macro-scale model, the average coolant temperature and average pebble surface temperature are determined according to the specified distribution of the power density. On a finer scale, the macro-scale model provides the boundary conditions for a meso-scale model which determines the temperature distribution within the interior of an individual pebble. On the finest scale, the contribution from a micro-scale model determines the temperatures of the fuel kernels and their coatings.

Within the macro-scale model, in order to obtain a computational grid that is tractable, the pebbles and coolant must be represented as a porous medium. Within the porous medium, the CFD code solves for the coolant velocities and pressure, and coolant and pebble surface temperatures. It is assumed that all of the pebbles *within* a cell have the same power and surface temperature. In reality, however, the pebble bed consists of pebbles which have different fuel enrichments and/or irradiations, and so, even within a computational cell, a pebble can belong to one of several different, randomly-mixed "batches". Each of these batches generates different power, have different material properties, and consequently, have different surface temperatures.

When coupled to a neutronics model, the CFD solution can be supplied with batch-specific power-levels, i.e., the power level in a pebble of each batch, for each cell, but to achieve this, the neutronics model must be supplied with batch-specific temperatures. Since the macro-scale thermal hydraulic model calculates only the average coolant and pebble surface temperatures, it is necessary to "un-smear" the macro-scale thermal hydraulic model and derive batch-specific surface temperatures. These are then used subsequently by the meso- and micro-scale models to derive all of the batch-specific pebble interior temperatures to supply the neutronics calculation

This section reviews and updates a previously-developed analytical model for re-constructing the batch-dependent pebble surface temperatures from the batch-average value. This model was used in the UK submission to the IAEA CRP-5 PBMR-400 benchmark exercise to provide temperatures to a fully coupled neutronics calculation of the equilibrium core (Reference 8.1).

The review presents the derivation of the existing model, discusses the assumptions made therein, derives an improved term for the contribution of each batch to macroscopic heat conduction and discusses the suitability for extension to model transient behaviour.

8.2 Derivation of the Multi-Batch Model

The thermal hydraulic model of the pebble bed derives the power and temperature of an 'average' pebble at a certain axial and radial position within the core. The pebble is 'average' in the sense that the irradiation history of the pebble is not modelled. Fuel pebbles are designed to pass through the core of the reactor multiple times, e.g., for the PBMR design, each pebble is assumed to pass through the core six times. Pebbles on their first pass are referred to as batch 1, then batch 2 for the second pass, etc.

The irradiation history of a pebble is important for the neutronics calculations to determine the pebble power. Following the thermal hydraulic stage of the iterative solution, the temperatures of the pebble components (fuel, coatings, graphite, etc.) must be passed onto the subsequent neutronics calculation. However, these data must be provided for each batch separately. The aim of the multi-batch fuel temperature model is to 'unsmear' the temperature information calculated for an average pebble, and determine the batch-specific values.

8.2.1 Average Pebbles

Consider a cell containing only one batch of pebbles and that batch has the properties of an average batch in a multi-batch core. The heat transfer paths are as follows:

(a)   Heat production within all the pebbles in a cell: $\dot{q}_{gen}$

(b)   Heat removal via coolant convection: $\dot{q}_{conv}$

(c)   Heat transfer via conduction to/from the pebbles in neighbouring cell: $\dot{q}_{cond}$

These quantities are available from the macroscopic thermal hydraulic solution.

In thermal equilibrium, the heat production is equal to the heat removal:

$$\dot{q}_{gen} = \dot{q}_{conv} + \dot{q}_{cond} .$$ (8.2.1)

The convective heat transfer is given by:

$$\dot{q}_{conv} = \lambda A(\overline{T}_{surf} - \overline{T}_{gas}) ,$$ (8.2.2)

where $\overline{T}_{gas}$ is the average temperature of the coolant in the cell and; $\overline{T}_{surf}$ is the average temperature of the pebble surfaces; A is the surface area of all pebbles in the cell; and λ is the convective heat transfer coefficient. When $\dot{q}_{conv} > 0$, this corresponds to heat transfer away from the pebbles in the cell to the coolant.

The average surface temperature of the pebbles in a given cell is obtained from a macroscopic conduction equation that is solved within the solid phase of a porous medium representation of a pebble bed in a whole-core CFD model. The discretised form of this equation is:

$$\sum_{k=1}^{neighbours} B_k \left(\overline{T}_{surf} - \overline{T}_{surf,k}\right) = \dot{q}_{gen} - \lambda A \left(\overline{T}_{surf} - \overline{T}_{gas}\right)$$ (8.2.3)

Where the summation on the LHS is over all of the neighbouring cells, k, and B_k are the conduction coefficients which comprise an effective conductivity and the grid dependent parameters such as cell surface areas and path lengths to the neighbouring cells. The average surface temperatures in the neighbouring cells are $\overline{T}_{surf,k}$.

8.2.2   Batch-Specific Pebbles

When modelling the pebbles in an individual batch, each batch is additionally assumed to exchange heat with the average pebble. The heat removal rate via this additional path is denoted $\dot{q}_{batch}^{i}$, where i indicates the batch number ($i = 1, 2 \ldots n$) for n batches.

In thermal equilibrium, referring to Figure 8.2.1 to identify the heat flows, balancing the heat production with the heat removal rates for a pebble in the i'th batch leads to the expression:

$$\dot{q}_{gen}^{i} = \dot{q}_{conv}^{i} + \dot{q}_{cond}^{i} + \dot{q}_{batch}^{i} .$$ (8.2.4)

Figure 8.2.1: Heat Flow from Pebbles in the *i*th Batch
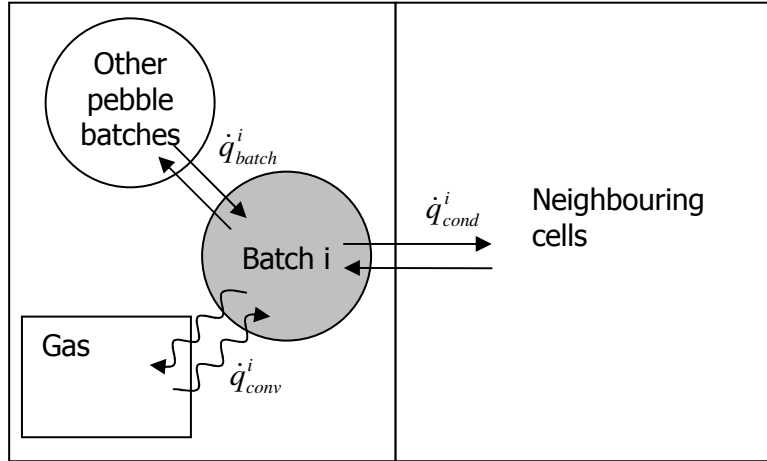
The convective heat removal rate is determined from the surface temperature of the pebble and the average coolant (gas) temperature:

$$\dot{q}^i_{conv} = \lambda A^i (T^i_{surf} - \overline{T}_{gas}) \text{ ,} \tag{8.2.5}$$

where T^i_{surf} is the surface temperature of the pebble in the *ith* batch, and A^i is the surface area of the *ith* batch that is in contact with the coolant where

$$\sum_{i=1}^{n} A^i = A \quad \text{and} \quad A^i = \frac{m_i}{m} A \tag{8.2.6}$$

Where m_i/m is the ratio of the number of pebbles in batch *i* to the total number of pebbles within the computational cell.

The heat exchange rate with the average pebble is *assumed* to be determined from the difference in surface temperatures:

$$\dot{q}^i_{batch} = C^i (T^i_{surf} - \overline{T}_{surf}) \text{ .} \tag{8.2.7}$$

$\dot{q}^i_{batch} > 0$ corresponds to heat transfer away from the *i'th* pebble to the average pebble. The effective heat transfer coefficient C^i depends on the contact area over which the heat conduction may occur and may include additional contributions from heat transfer by thermal radiation and heat transfer via the coolant (this is not included in $\dot{q}^i_{conv}$, which models the total pebble to gas transfer).

Distributing the heat removed via conduction to neighbouring cells amongst the batches is more difficult to determine. Rearranging (8.2.1) gives $\dot{q}_{cond}$ for all pebbles in the cell:

$$\dot{q}_{cond} = \dot{q}_{gen} - \dot{q}_{conv}.$$

(8.2.8)

It is assumed that for a given batch that conduction to neighbouring cells is proportional to the power that it contributes to the cell in which it sits, i.e.,:

$$\dot{q}^i_{cond} = \dot{q}^i_{gen} \left(\frac{\dot{q}_{gen} - \dot{q}_{conv}}{\dot{q}_{gen}} \right).$$

(8.2.9)

Using Equations (8.2.5), (8.2.7) and (8.2.9) to replace the terms on the RHS of Equation (8.2.4) leads to:

$$\dot{q}^i_{gen} = \lambda A^i (T^i_{surf} - \overline{T}_{gas}) + C^i (T^i_{surf} - \overline{T}_{surf}) + \dot{q}^i_{gen} \left(\frac{\dot{q}_{gen} - \dot{q}_{conv}}{\dot{q}_{gen}} \right),$$

(8.2.10)

which can be rearranged into an expression for the batch-specific pebble surface temperature:

$$T^i_{surf} = \frac{C^i \overline{T}_{surf} + \lambda A^i \overline{T}_{gas} + \dot{q}^i_{gen} \left(\dfrac{\dot{q}_{conv}}{\dot{q}_{gen}} \right)}{\lambda A^i + C^i}.$$

(8.2.11)

If the batch-to-batch heat transfer coefficients are all assumed to be zero ($C^i = 0$), then this simplifies to:

$$T^i_{surf} = \frac{\lambda A^i \overline{T}_{gas} + \dot{q}^i_{gen} \left(\dfrac{\dot{q}_{conv}}{\dot{q}_{gen}} \right)}{\lambda A^i}$$

(8.2.12)

This equation enables the surface temperature of each batch of pebbles to be determined from knowledge of the average surface temperature, the local coolant temperature, the convective heat transfer coefficient and the power generated within each batch.

8.2.3 Assumptions

The method relies on two major assumptions, these are discussed below.

8.2.3.1 Batch-to-Batch Heat Exchange

The first assumption is that the heat transfer paths between each pebble of each batch do not need to be explicitly considered but can be represented by instead considering the interaction of each individual batch simply with the average pebble. Consider the interactions of the *i'th* batch pebble with the remaining pebbles. The batch-to-batch heat transfer terms would be:

$$\dot{q}^i_{batch} \propto \sum_{j=1}^{j=n} \left(T^i_{surf} - T^j_{surf}\right) \tag{8.2.13}$$

Introducing heat exchange coefficients between batch *i* and *j*, C_{ij}, gives:

$$\dot{q}^i_{batch} = \sum_{j=1}^{n} C_{ij} \left(T^i_{surf} - T^j_{surf}\right). \tag{8.2.14}$$

The exchange coefficients therefore constitute an *n x n* matrix. So that surface *j* receives the same amount of heat that leaves surface *i*, the following reciprocity condition must hold:

$$C_{ij} = C_{ji} \tag{8.2.15}$$

Therefore, the matrix is symmetrical.

Summing *Cij* along a row and summing down a column gives respectively:

$$C^i = \sum_{j=1}^{n} C_{ij} \quad ; \quad C^j = \sum_{i=1}^{n} C_{ij} \tag{8.2.16}$$

A check on the above equation is that the sum of inter-batch heat exchanges must be zero when summed over all batches in a given computational cell:

$$\dot{q}_{batch} = \sum_{i=1}^{n}\sum_{j=1}^{n} C_{ij}\left(T^i_{surf} - T^j_{surf}\right) = \sum_{i=1}^{n} T^i_{surf}\sum_{j=1}^{n} C_{ij} - \sum_{j=1}^{n} T^j_{surf}\sum_{i=1}^{n} C_{ij} = \sum_{i=1}^{n} C^i T^i_{surf} - \sum_{j=1}^{n} C^j T^j_{surf} = 0 \tag{8.2.17}$$

and this is shown above to be the case.

Using the relationships of (8.2.16), Equation (8.2.14) becomes:

$$\dot{q}^i_{batch} = C^i T^i_{surf} - \sum_{j=1}^{n} C_{ij} T^j_{surf} \tag{8.2.18}$$

So, the original assumed expression for inter-batch heat transfer will be true:

$$\dot{q}_{batch}^{i} = C^{i}\left(T_{surf}^{i} - \overline{T}_{surf}\right)$$

(8.2.19)

only if,

$$C^{i}\overline{T}_{surf} = \sum_{j=1}^{n} C_{ij}T_{surf}^{j}$$

(8.2.20)

However, for this to be true it must be *assumed*:

$$C_{ij} = C^{i}\frac{m_{j}}{m}$$

(8.2.21)

But from reciprocity:

$$C_{ij} = C_{ji} = C^{i}\frac{m_{j}}{m} = C^{j}\frac{m_{i}}{m}$$

(8.2.22)

This is the case if,

$$C^{i} = C\frac{m_{i}}{m} \quad ; \quad C^{j} = C\frac{m_{j}}{m}, \text{ and, therefore, } C_{ij} = C\frac{m_{i}}{m}\frac{m_{j}}{m}$$

(8.2.23)

So the assumption that each batch exchanges heat according to the difference in temperature between itself and the average of all batches is true, provided that the exchange coefficients depend on a conduction coefficient (effective conductivity x area / path length) that is identical for all batches. The total area and path length are independent of the batch, but the effective conductivity will be dose and temperature dependent. Hence, the above treatment only allows one value of effective conductivity and this must be applied to all batches in a given cell. Therefore, the mean surface temperature and fluence within a cell must be used to calculate the effective conductivity using an appropriate correlation, such as Zehner-Schlunder (Reference 8.2) or a modified form thereof.

8.2.3.2 Distribution of the Cell-to-Cell Conductive Heat Transfer between Batches.

Equation (8.2.9) expresses the assumption that, for a given batch, conduction to neighbouring cells is proportional to the power that it contributes to the cell in which it sits, i.e.,:

$$\dot{q}_{cond}^{i} = \dot{q}_{gen}^{i}\left(\frac{\dot{q}_{gen} - \dot{q}_{conv}}{\dot{q}_{gen}}\right)$$

(8.2.9)

This assumption does not appear to be valid under all circumstances. For example, consider a scenario in which there was zero convective heat transfer. In this case:

$$\dot{q}_{cond}^{i} = \dot{q}_{gen}^{i}\left(\frac{\dot{q}_{gen}}{\dot{q}_{gen}}\right) = \dot{q}_{gen}^{i} \tag{8.2.24}$$

That is, for the *i'th* batch, all of the heat generated must be lost by conduction into the neighbouring cells. This then requires zero batch-to-batch heat transfer (see Equation (8.2.1)), and, this in turn would then require that all batches had the same surface temperature. The requirement that all batches have the same temperature even though they are generating different powers is not physical. Therefore, a more physically realistic representation of the contribution-to-conduction heat transfer from individual batches is required.

8.2.4   Revised Distribution of the Overall Conduction Term between Batches

To overcome the problem presented in Section 8.2.3.2, it is proposed that the conductive heat transfer between each individual batch in a given cell and a neighbouring cell depends on the difference between its surface temperature and the average surface temperature of all batches in the neighbouring cell *k*, or $T_{surf}^{i} - \overline{T}_{surf,k}$.

The justification comes from the fact that the total conductive heat flow from batch *i* in a given cell to a neighbouring cell is the sum of the conductive heat flows to or from all of the batches in the neighbouring cell, or:

$$\dot{q}_{cond,k}^{i} \propto \sum_{j=1}^{j=n}\left(T_{surf}^{i} - T_{surf,k}^{j}\right) \tag{8.2.25}$$

By similar logic used in Section 8.2.3.1, but for heat exchange between the batches in neighbouring cells, the following is obtained:

$$\dot{q}_{cond,k}^{i} = B_{k}^{i}\left(T_{surf}^{i} - \overline{T}_{surf,k}\right) \tag{8.2.26}$$

Summing the conduction heat exchanges between batch *i* and all of the neighbouring cells gives:

$$\dot{q}_{cond}^{i} = \sum_{k=1}^{neighbours} B_{k}^{i}\left(T_{surf}^{i} - \overline{T}_{surf,k}\right) = \sum_{k=1}^{neighbours} B_{k}\frac{m_{i}}{m}\left(T_{surf}^{i} - \overline{T}_{surf,k}\right) \tag{8.2.27}$$

The above equation assumes that the macroscopic conduction coefficients, B_k, are distributed amongst the batches according to:

$$B_{k}^{i} = B_{k}\frac{m_{i}}{m} \tag{8.2.28}$$

Summing over all batches demonstrates that the macroscopic conduction term is obtained (c.f. Equation (8.2.3)):

$$\dot{q}_{cond} = \sum_{i=1}^{n} \dot{q}_{cond}^{i} = \sum_{k=1}^{neighbours} B_k \sum_{i=1}^{n} \frac{m_i}{m}\left(T_{surf}^{i} - \overline{T}_{surf,k}\right) = \sum_{k=1}^{neighbours} B_k \left(\overline{T}_{surf} - \overline{T}_{surf,k}\right) \qquad (8.2.29)$$

It is convenient to remove the dependence on the temperatures in the neighbouring cells and to cast the conductive heat transfer from each batch within a given cell in terms of quantities local to that cell. Expanding (8.2.27) gives:

$$\dot{q}_{cond}^{i} = -\frac{m_i}{m} \sum_{k=1}^{neighbours} B_k T_{surf,k} + T_{surf}^{i} \frac{m_i}{m} \sum_{k}^{neighbours} B_k \qquad (8.2.30)$$

Similarly, expanding (8.2.29) gives:

$$\dot{q}_{cond} = -\sum_{k=1}^{neighbours} B_k T_{surf,k} + \overline{T}_{surf} \sum_{k}^{neighbours} B_k \qquad (8.2.31)$$

Rearranging (8.2.31) gives:

$$-\sum_{k=1}^{neighbours} B_k T_{surf,k} = \dot{q}_{cond} - \overline{T}_{surf} \sum_{k}^{neighbours} B_k \qquad (8.2.32)$$

Substituting for the sum of the contributions from the neighbours in (8.2.32) gives:

$$\dot{q}_{cond}^{i} = \frac{m_i}{m}\left(\dot{q}_{cond} - \overline{T}_{surf} \sum_{k=1}^{neighbours} B_k\right) + T_{surf}^{i} \frac{m_i}{m} \sum_{k}^{neighbours} B_k \qquad (8.2.33)$$

And this is re-arranged into:

$$\dot{q}_{cond}^{i} = \frac{m_i}{m}\dot{q}_{cond} + \frac{m_i}{m}\left(T_{surf}^{i} - \overline{T}_{surf}\right) \sum_{k}^{neighbours} B_k \qquad (8.2.34)$$

8.2.5   Determination of Batch Surface Temperatures

Equation (8.2.8) states that $\dot{q}_{cond} = \dot{q}_{gen} - \dot{q}_{conv}$, so substituting this into (8.2.34) and then together with (8.2.5) and (8.2.7) into (8.2.4) gives the heat balance on batch i in tems of quantities local to the cell

$$\dot{q}_{gen}^{i} = \lambda A^{i}(T_{surf}^{i} - \overline{T}_{gas}) + C^{i}(T_{surf}^{i} - \overline{T}_{surf}) + \frac{m_i}{m}\dot{q}_{gen} - \frac{m_i}{m}\dot{q}_{conv} + \frac{m_i}{m}\left(T_{surf}^{i} - \overline{T}_{surf}\right) \sum_{k}^{neighbours} B_k$$

$$(8.2.35)$$

This is simplified by substituting:

$$\frac{m_i}{m}\dot{q}_{conv} = \lambda A^{i}\left(\overline{T}_{surf} - \overline{T}_{gas}\right)$$

Subtracting the two convection terms eliminates the gas temperature from the batch heat balance:

$$\dot{q}_{gen}^i = \lambda A^i \left(T_{surf}^i - \overline{T}_{surf}\right) + C^i (T_{surf}^i - \overline{T}_{surf}) + \frac{m_i}{m}\dot{q}_{gen} + \frac{m_i}{m}\left(T_{surf}^i - \overline{T}_{surf}\right)\sum_k^{neighbours} B_k \qquad (8.2.36)$$

Re-arranging, gives the batch surface temperature as:

$$T_{surf}^i = \frac{\left(\lambda A^i + C^i + \dfrac{m_i}{m}\displaystyle\sum_k^{neighbours} B_k\right)\overline{T}_{surf} + \left(\dot{q}_{gen}^i - \dfrac{m_i}{m}\dot{q}_{gen}\right)}{\lambda A^i + C^i + \dfrac{m_i}{m}\displaystyle\sum_k^{neighbours} B_k} \qquad (8.2.37)$$

and simplifying by using the total convection, diffusion and inter-batch exchange coefficients gives:

$$T_{surf}^i = \overline{T}_{surf} + \frac{\dfrac{m}{m_i}\dot{q}_{gen}^i - \dot{q}_{gen}}{\lambda A + C + \displaystyle\sum_k^{neighbours} B_k} \qquad (8.2.38)$$

The above equation shows that the surface temperature of a batch is simply given by the average surface temperature for all batches perturbed by an amount that is proportional to the difference between the batch power and the power generated by an average batch. Therefore, as expected this equation shows that a batch that generates more power than the average will have a higher than average surface temperature and vice-versa for low power batches. This behaviour is qualitatively the same as Equation (8.2.12), but is mathematically more rigorous and avoids the inconsistencies that were inherent in Equation (8.2.12).

8.3   Extension to Transient Behaviour

The multi-batch heat transfer models (both that described in Section 8.2 and the improved model developed in Sections 8.2.4 and 8.2.5) are based on the pebble surface temperatures, pebble powers and the temperatures of the surrounding cells and coolant. The heat transfer processes from pebble-to-pebble and pebble-to-coolant occur on the surfaces of the pebble. These heat transfers are effectively instantaneous and there is no thermal mass term in these equations. Transient behaviour is modelled in the multi-scale models of the pebble internals (Section 5.3) and these relate the pebble surface temperature to the internal temperatures within the pebble. Further, the pebble internal models determine the heat transferred through the outer surface of each pebble by determining the internal temperature gradients at the pebble surface. Therefore, the transient behaviour of the whole system can be modelled by substituting the heat generation term in Equation (8.2.3) with the sum of the heat transfers through all of the pebble surfaces, as determined by the pebble internal models, for each batch in the computational cell, i.e.:

$\dot{q}_{gen}$ is replaced by the instantaneous heat transfer from all batches:

$$- \sum_{i=1}^{n} A^i k_G^i \left. \frac{\partial T^i}{\partial r} \right|_{r=r_{pebble}}$$

and:

q_{gen}^i is replaced by the instantaneous heat transfer from batch i:

$$- A^i k_G^i \left. \frac{\partial T^i}{\partial r} \right|_{r=r_{pebble}}$$

with both of the above used in Equation (8.2.38) to distribute the average pebble surface temperature amongst the batches. The normal temperature gradients at the pebble surfaces change with time as the temperature fields, both within the pebbles and within the coolant and surrounding pebble bed, change. Similarly, the changing heat outputs that these terms represent change the macroscopic distribution of pebble surface temperatures and the local re-distribution of the surface temperatures amongst the batches. Substituting the sum of the normal gradients into the macroscopic conduction Equation (8.2.3) for exchange of heat between neighbouring cells, leads to:

$$\sum_{k=1}^{neighbours} B_k \left(\overline{T}_{surf} - \overline{T}_{surf,k} \right) = - \sum_{i=1}^{n} A^i k_G^i \left. \frac{\partial T^i}{\partial r} \right|_{r=r_{pebble}} - \lambda A \left(\overline{T}_{surf} - \overline{T}_{gas} \right) \tag{8.3.1}$$

The heat capacity of the coolant in the cell is accounted for by use of the instantaneous fluid temperature obtained from the transient solution of the macroscopic fluid enthalpy equation within the CFD code. The normal temperature gradients at the pebble surface are approximated in the pebble internal models using finite differences. In finite difference form, the sum of the normal gradients is:

$$- \sum_{i=1}^{n} A^i k_G^i \left. \frac{\partial T^i}{\partial r} \right|_{r=r_{pebble}} \approx - \sum \frac{A^i k_G^i}{\Delta r} \left(T_{surf}^i - T_{M,N-1}^i \right) \tag{8.3.2}$$

Where $T_{M,N-1}$ is the nodal temperature on the penultimate node within the meso-scale model of a pebble (see Section 5.3).

Equation (8.3.2) can be expressed in terms of the average surface temperature as:

$$\sum_{i=1}^{n} \frac{A^i k_G^i}{\Delta r} \left(T_{surf}^i - T_{M,N-1}^i \right) = A \frac{\overline{k}_G}{\Delta r} \overline{T}_{surf} - \sum_{i=1}^{n} \frac{A^i k_G^i}{\Delta r} T_{M,N-1}^i + \sum_{i=1}^{n} \frac{A^i k_G^i}{\Delta r} \left(T_{surf}^i - \overline{T}_{surf} \right)_{old}$$

$$\tag{8.3.3}$$

Where $\bar{k}_G$ is the average graphite conductivity at the surface of the pebbles in all batches. The last term in (8.3.3) represents a correction to account for the deviation of the graphite conductivity of an individual batch from the average – the *old* subscript attached to this terms signifies that it will be introduced as a deferred correction using old, or last iteration, values for the temperatures. If all of the graphite conductivities were equal the term would be zero. Substituting Equation (8.3.3) for the heat generation term in the modified macroscopic conduction equation, (8.3.1), gives.

$$
\sum_{k=1}^{neighbours} B_k \left(\bar{T}_{surf} - \bar{T}_{surf,k} \right) =
$$

$$
- A \frac{\bar{k}_G}{\Delta r} \left(\bar{T}_{surf} - \sum_{i=1}^{n} \frac{m_i}{m} \frac{k_G^i}{\bar{k}_G} T_{M,N-1}^i \right) - \lambda A \left(\bar{T}_{surf} - \bar{T}_{gas} \right) + \sum_{i=1}^{n} \frac{A^i k_G^i}{\Delta r} \left(T_{surf}^i - \bar{T}_{surf} \right)_{old}
$$

$$
(8.3.4)
$$

The above form of Equation (8.3.4) is particularly suitable for implementation in a CFD code as the main part of the source term is implemented as gradients which are dependent on the local mean surface temperature. In the solution these terms are split and the terms involving the local mean surface temperature are taken into the matrix on the right hand side to be obtained implicitly when the equations system is solved.

The pebble surface temperatures are the boundary conditions on the transient pebble internal temperature models which, themselves, determine the instantaneous surface normal temperature gradients. The pebble surface heat flux for batch *i* is:

$$
- A^i k_G^i \left. \frac{\partial T^i}{\partial r} \right|_{r=r_{pebble}} \approx - \frac{A^i k_G^i}{\Delta r} \left(T_{surf}^i - T_{M,N-1}^i \right)
$$

$$
(8.3.5)
$$

The finite difference approximations for the average (8.3.2) and batch (8.3.5) pebble surface heat fluxes, are substituted in (8.2.38) to enable the batch surface temperatures to be calculated. Equation (8.2.38) can then be re-arranged to group the unknown batch *i* surface temperatures on the left hand side. However, the right hand side contains terms which feature the mean surface temperature and the surface temperatures of all of the other batches. It should be possible to solve this explicitly using Equation (8.3.3) to weaken the dependence on the surface temperatures of the other batches, or implicitly by inverting a matrix to solve for all the batch temperatures simultaneously – however this implies that the pebble internal temperature models for all batches have to be solved simultaneously also. Various semi-implicit schemes are possible where different combinations of 'old' and 'new' values and/or gradients are used iteratively. The choice and implementation of the scheme will be dictated by the CFD code chosen to solve the macroscopic model.

To summarise, to implement the above model in a transient CFD simulation, a pair of multi-scale equations would be required for each batch of pebbles within each computational cell in the core. A single macroscopic conduction equation (Equation

(8.3.4)) would be required for the whole core and its heat generation term would be determined on a cell-by-cell basis by summing the contributions from each of the pebble batches within the cells. The modified form Equation (8.2.38) (modified by Equations (8.3.2) and (8.3.5)) is used to determine the correct pebble surface temperatures for each batch to feed back to the pebble internal models, either explicitly, implicitly or more likely, semi-implicitly. The ideal solution is to have a coupling that is as implicit as possible so as not to place any limits on the time step size used by the CFD calculation. In principle this should not be difficult as the CFD code will perform a few iterations on each time step, so the surface temperatures and heat fluxes can be exchanged a number of times within each time step. The specifics of the coupling of the models will be left open until more is known about the system codes into which the models are intended to be implemented.

8.4   Closure

This section presented a model by which the fine-scale detail of the surface temperatures of pebbles belonging to different batches, at a given location in core, can be recovered from the average value determined by a macroscopic CFD model of the whole reactor. This model is an improvement of a previous model in which the treatment of contribution of an individual batch of pebbles to the 'long-range' macroscopic conduction heat transfer within the pebble bed has been updated and improved.

The applicability of the multi-batch model to transients has been reviewed and the necessary modifications to the source terms of macroscopic pebble bed conduction equation have been proposed. This equation is normally solved within the solid phase of the porous medium that represents the pebble bed by the CFD code, and the formulation presented is suitable for implementation in commercial CFD codes.

8.5   References for Section 8

8.1   IAEA CRP5, Draft TECDOC II, Evaluation of High Temperature Gas Cooled Reactor Performance, to be published.

8.2   VDI-Wärmeatlas: Berechnungsblätter für den Wärmeübergang, Verein der Deutsche Ingenieure, Düsseldorf, 4th Print, 1984.

9.0 IRRADIATED GRAPHITE THERMAL PROPERTIES

9.1 Purpose of Section 9

In an HTGR core, one of the most important design features is that the reactor is able to remove decay heat by passive cooling alone. The core and reflectors in an HTGR are constructed from graphite components and the removal of the decay heat by conduction depends greatly on the thermal conductivity of the core and graphite reflector.

During reactor operation, many of the graphite component physical properties, including the thermal conductivity, are significantly altered from their initial properties as the graphite is irradiated by fast neutrons, and it is important to include these changes in computational models.

This section carries out a first review of available models for the determination of irradiated graphite thermal conductivity and specific heat capacity and the data upon which these models are based. Suggestions for further assessment of the existing models for later use in thermal analyses are also summarized here.

9.2 Graphites Used in Past/Existing Reactor Cores

There were a number of different graphites developed/selected for the moderator and reflector regions in the range of gas cooled reactors built in the past. In the UK, Pile Grade A (PGA) and Pile Grade B (PGB) graphites were used in the Magnox stations for the moderator and reflector regions respectively. For the Advanced Gas-cooled Reactors (AGRs) different grades of Gilsocarbon graphite were used e.g., GCMB and IM1-24 for the moderator, and GCMC and IM2-24 for the reflector. For the US (prismatic) HTGRs, H-451 graphite was used for the moderator and Stackpole 2020 for the reflector. For the German (pebble bed) HTGRs, ATR-2E was used for the reflector, which is the baseline grade selected for the PBMR. All the above are medium grain, extruded graphites. For the Japanese HTGR, a fine grain, iso-moulded graphite, IG110, was selected.

All the irradiation data on these graphites necessary for designing a core were obtained using Material Test Reactors (MTRs). Properties of interest included dimensional change behaviour, Young's modulus, strength, coefficient of thermal expansion and thermal conductivity. Therefore, a large amount of data exist but only some of these were obtained at temperatures greater than 550°C, which is the lower bound temperature of interest for HTGRs. In addition much of the data are 'restricted' (to the country of origin), and thus not available for third party use. This also applies to the way in which the data were assessed/interpreted and the methods used to determine instantaneous 'point' values of a thermal property as required for example by thermal models of graphite components/structures. The freely available data and methodologies on specific thermal properties, which are the subjects of this note, are covered in Sections 9.4 and 9.5.

The problem for future HTGRs is that none of the previously used graphites, with the exception of IG110, are now commercially available, and so there is a need to qualify candidate graphites which are currently available. The ongoing activities in this area are covered in Section 9.3. Therefore, current designs in progress, which will be built using graphites yet to be qualified, such as PBMR, GT-MHR and ANTARES, can only make use of data from previously used graphites, e.g., ATR-2E as in the case of PBMR. Irradiation data for the actual graphite(s) used will have to be obtained from MTR experiments as in the past.

9.3   Selection/Qualification of Graphites for Future HTGRs

For the European HTGR R&D programme (Raphael), a number of different graphite grades were selected covering the different coke sources available (pitch and petroleum) and the major block forming methods (extrusion, iso-moulding and vibro-moulding). These are listed, along with the manufacturers, in Tables 9.3.1 and 9.3.2. The aim will be to select the 'best' overall graphite(s) based on a number of criteria, including irradiation and oxidation behaviour, cost and long term availability.

Table 9.3.1: Selected Major Grades

Grade	Manufacturer	Coke	Process
PCEA	GrafTech	Petroleum	Extrusion
PPEA	GrafTech	Pitch	Extrusion
NBG-10	SGL	Pitch	Extrusion
NBG-18	SGL	Pitch	Vibro-moulding

Table 9.3.2: Selected Minor Grades

Grade	Manufacturer	Coke	Process
PCIB-SFG	GrafTech	Petroleum	Iso-moulding
LPEB/BAN	GrafTech	Needle	Extrusion
NBG-20	SGL	Petroleum	Extrusion
NBG-25	SGL	Petroleum	Iso-moulding
NBG-17	SGL	Pitch	Vibro-moulding
IG-110	Toyo Tanso	Petroleum	Iso-moulding
IG-430	Toyo Tanso	Pitch	Iso-Moulding

All the above graphites are currently being irradiated in the High Flux Reactor at Petten, in the Netherlands. The selected irradiation temperatures are 750°C and 950°C, although some data will also be obtained at 650°C and 850°C. The first stage of each irradiation will bound the neutron fluences for a prismatic type core, and the

second stage of each irradiation will bound the neutron fluences for a pebble bed type core. Data for the first stage irradiations at both temperatures have been obtained, but data for the second stage irradiations will not be available until 2010. The latter will include data on the thermal conductivity changes.

For PBMR, the selected graphite is NBG-18 which is a vibro-moulded graphite. This differs from ATR-2E which is an extruded graphite. The planned irradiation experiments for NBG-18 have not yet started. Irradiation experiments to be carried out in the US (as part of the NGNP/Gen-IV activities) will concentrate on just two graphites, namely NBG-18 (or NBG-17) and PCEA. NBG-17 is a finer grain version of NBG-18 and is a candidate for the ANTARES reactor, and PCEA is a medium grain extruded graphite, and is also a candidate for the ANTARES reactor.

9.4   Models Used for Predicting Graphite Specific Heat

Reference 9.1 provides a value for the specific heat of reflector graphite in PBMR of 1690J/kg/K at a temperature of 600°C. No temperature dependence or dependence on irradiation is given.

Reference 9.2 presents the properties of Gilsocarbon graphite used in Mk. III Gas Cooled Reactors. This document provides a plot of the mean specific heat of graphite with temperature and states the following:

'*This is a unique relationship which holds for all well graphitised graphites, and there is no variation about the mean curve. It should be assumed that the specific heat is independent of irradiation.*'

A copy of the graph is shown in Figure 9.4.1. The specific heat values vary from between 900J/kg/K to about 2000J/kg/K, with an approximately constant value for temperatures over 1000°C. The value of specific heat at 600°C can be seen to be 1690J/kg/K matching that given in Reference 9.1.

Reference 9.3 also provides a graph showing the variation in specific heat with temperature and states that it has been assumed that there is no change in specific heat with irradiation. This graph is shown in Figure 9.4.2. It has been compared to Figure 9.4.1 and gives very similar values for the specific heat with temperature although it provides results up to a higher temperature of 2500°C compared to 1700°C in Figure 9.4.1.

Figure 9.4.1: Variation of Specific Heat Capacity of Graphite with Temperature (from Reference 9.2)
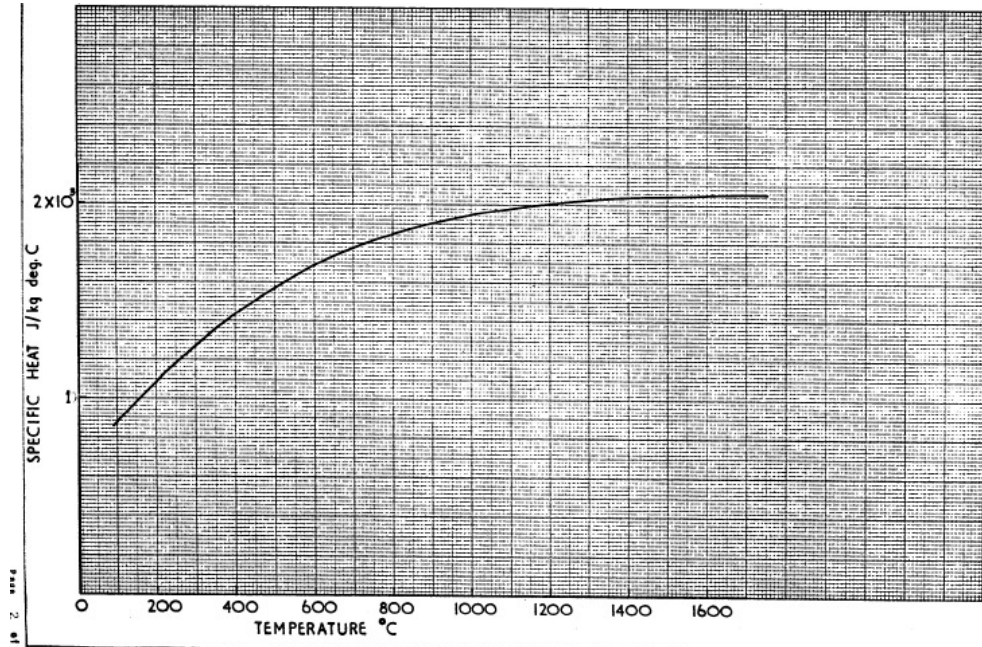
Figure 9.4.2: Variation of Specific Heat Capacity of Graphite with Temperature (from Reference 9.3)
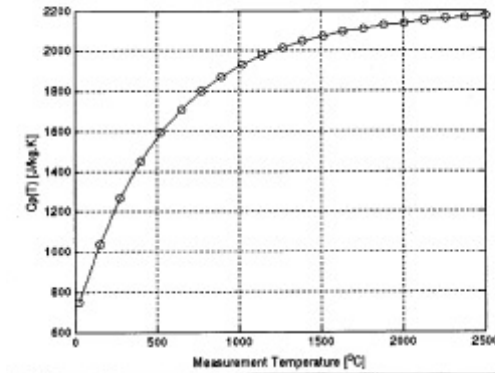
A table of specific heat values (Table 9.4.1) has been produced using the values from Figure 9.4.1.

Table 9.4.1: Specific Heat Variation with Temperature (from Figure 9.4.1)

Temp (°C)	Specific Heat (J/kg/°C)
100	880
200	1080
300	1270
400	1430
500	1560
600	1690
700	1770
800	1840
900	1900
1000	1940
1100	1980
1200	2000
1300	2020
1400	2030
1500	2040
1600	2045
1700	2050

A plot of specific heat against temperature has been produced from the values shown in the Table 9.4.1 with a line of best fit added. A third order polynomial provides a good fit to the data points and the equation for this line is as follows:

$$Cp \ (J/kg/°C) = 3.5023E\text{-}07T^3 - 1.6296E\text{-}03T^2 + 2.5941T + 630.96$$

Where T is specified in °C. This correlation would work well in the temperature range for which it is derived (from 100°C to 1700°C) but it should not be used for extrapolation past 1700°C as the relationship is not based on any physical argument.

The above equation can be compared to the equation for specific heat of graphite given in Reference 9.4 as follows:

$$Cp = (0.54212 - 2.42667E\text{-}6T - 90.2725T^{-1} - 4.34493E4T^{-2} + 1.59309E7T^{-3} - 1.43688E9T^{-4}) \times 4184$$

with T specified in K.

Figure 9.4.3 shows the values of specific heat given in Table 9.4.1 along with the line of best fit and the values calculated using the equation from Reference 9.4. These lines are similar for the lower temperatures, but have a greater variation for temperatures between 800 and 1600°C.

Figure 9.4.3: Modelled Variation of Specific Heat of Graphite with Temperature
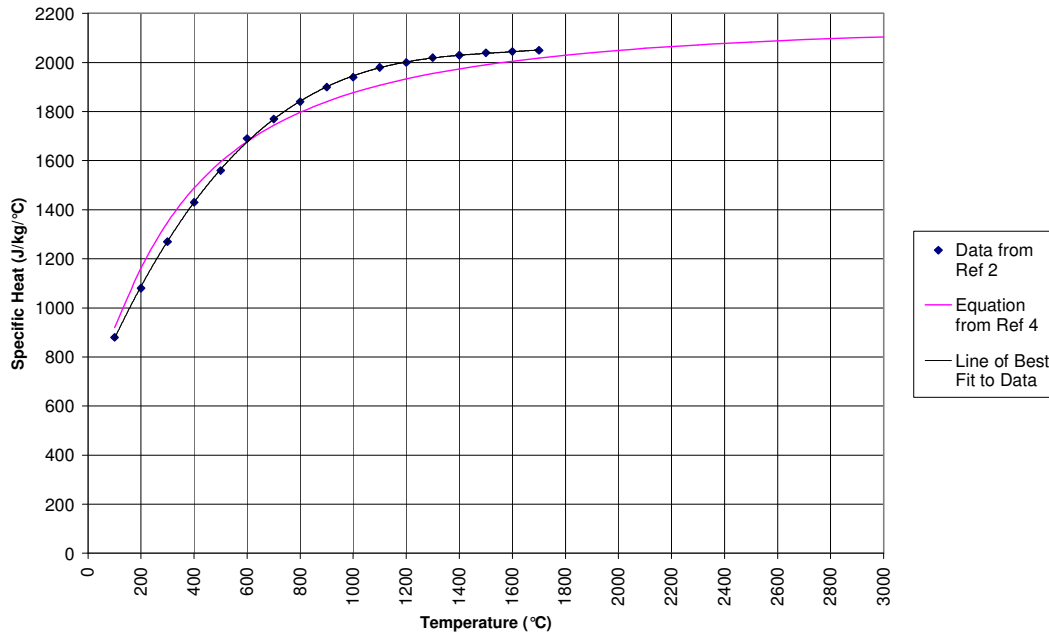
*Note: Ref 2 and Ref 4 in the figure are for References 9-2 and 9-4 respectively.

The above equations and Figures 9.4.1 to 9.4.3 can used to provide values of specific heat for the computational models.

9.5 Models for Predicting Graphite Conductivity

Graphites for HTGRs should be produced with a high level of graphitisation (degree of cystallinity), which generally means they have a high thermal conductivity value. Under the influence of fast neutron irradiation, the thermal conductivity of the graphite initially falls rapidly until the conductivity approaches a saturation level which increases as the irradiation temperature increases (Reference 9.5). At higher fluences (doses), the thermal conductivity again decreases. The changes in thermal conductivity due to fluence and temperature changes need to be taken into account in thermal models of the fuel elements and reflectors.

9.5.1 Terminology

The UK graphite irradiation programme used a number of different MTRs (e.g. DIDO, Pluto, DFR, BR-2), each of which operated at a different flux. There was a need to standardise all the data and so it was decided to use a reference position in the DIDO reactor where the flux was 4×10^{13} n/cm^2. The data from all the MTRs were therefore

expressed in terms of Equivalent DIDO Nickel Dose (EDND). Many other countries also adopted the EDND scale. Nowadays, displacements per atom (dpa) is generally used.

Clearly the MTRs operated at a higher fast neutron flux than conventional reactors, so that the property changes could be determined at an accelerated rate, i.e., there was an accelerated atomic displacement rate. Because the number of atomic displacements depends only on the flux spectrum, and all thermally activated solid state processes depend only on time and temperature, the irradiation of two identical specimens to the same number of atomic displacements (dpa), but one quickly and the other slowly, should give different property changes. It was postulated (Reference 9.12) that if two identical samples are irradiated, one at an atomic displacement rate 'a' for a time 't' and another at a rate 'a*' for a time 't*' such that a.t = a*.t*, then a temperature of irradiation θK exists for the latter sample which will give identical property changes to those obtained for the former sample irradiated at a temperature T_iK and at the displacement rate 'a'. The two temperatures are related by;

$$\frac{1}{\theta} - \frac{1}{T_i} = \frac{k}{E} \log_e\left(\frac{a}{a*}\right)$$

where

θ is the equivalent DIDO temperature (EDT), K
T_i is the irradiation temperature, K
k is Boltzmann's constant (= 8.617×10^{-5} eV.K^{-1})
E is the activation energy (=1.2 eV for mechanical/thermal property changes)

Alternatively:

$$\frac{1}{\theta} - \frac{1}{T_i} = \frac{k}{E} \log_e\left(\frac{\varphi}{4 \times 10^{13}}\right) \quad \text{or} \quad \frac{1}{\theta} - \frac{1}{T_i} = \frac{k}{E} \log_e\left(\frac{END}{1.262 \times 10^{13} \times t}\right)$$

Where

φ is the equivalent DIDO nickel flux (at the point of interest)
t is the time in full power years
EDND is the equivalent DIDO nickel dose at time 't' (at the point of interest)

Note - the concept of equivalent temperature is only relevant at lower irradiation temperatures, where thermally activated processes take place at a slower rate. For the graphite temperature ranges appropriate to HTGRs (i.e. ~550°C to 1050°C) it is generally accepted that the concept of equivalent temperature is not necessary. Therefore the irradiation temperature in the MTR is equivalent to that in the HTGR.

9.5.2   Existing Thermal Conductivity Data

Thermal conductivity data/graphical plots for a limited number of graphites have been obtained from a number of different sources, emanating from a number of different

countries. The main graphites covered are Gilsocarbon and PGA (UK), H-451 and Stackpole 2020 (US) and ATR-2E (Germany). It is found that the variation of thermal conductivity with fluence and temperature for all nuclear grade graphites previously tested is generally of the same form. As mentioned earlier, the thermal conductivity of the graphite initially falls rapidly when subjected to fast neutron irradiation before a saturation level is reached. At higher fluences (doses), the thermal conductivity again decreases. The saturation level increases as the irradiation temperature increases. However there are noticeable differences between graphites, and so in order to conduct an accurate thermal analysis of a graphite component/structure it is important to obtain the appropriate data on the selected graphite(s) from MTR experiments.

A plot of the variation of the thermal conductivity of Gilsocarbon graphite with fluence and temperature as a fraction of the unirradiated thermal conductivity at 40°C is given in Reference 9.2. This plot is shown in Figure 9.5.1. The values are approximately constant above about 650°C and for the largest fluence shown (4.0E21n/cm^2), the graphite has a conductivity of approximately 20% of its original value of 117W/m/K, equivalent to 23W/m/K.

Figure 9.5.1: Fractional Changes in Thermal Conductivity of Gilsocarbon with Fluence and Temperature (from Reference 9.2)
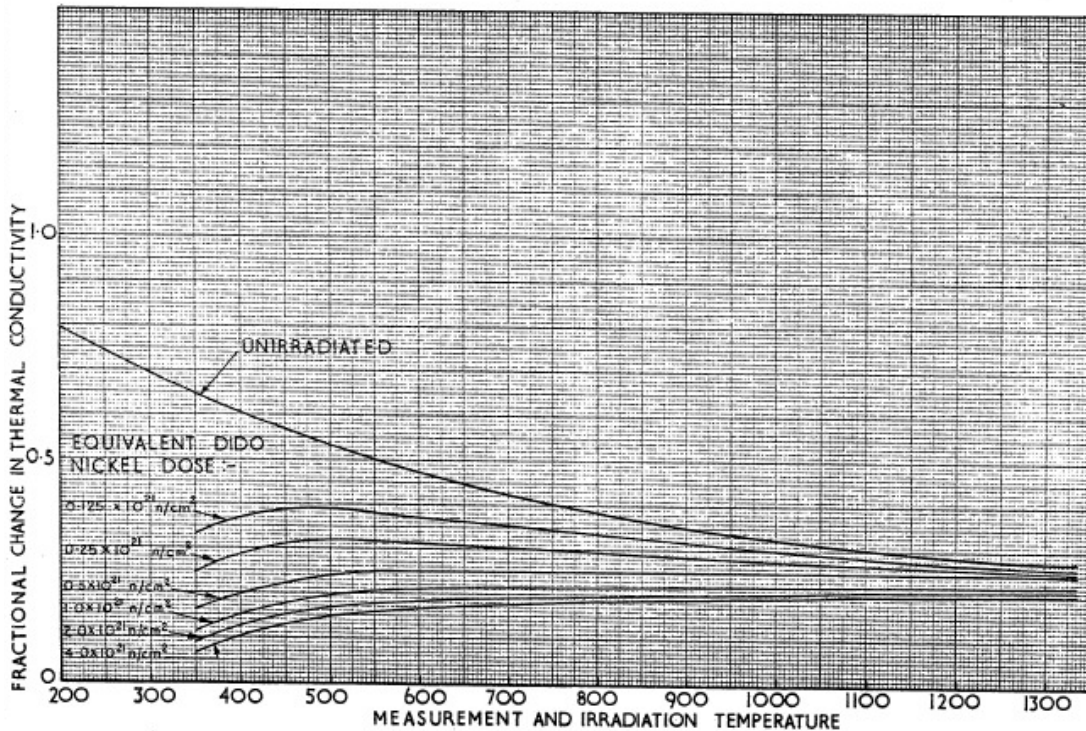
Reference 9.1 provides a plot of thermal conductivity as a function of temperature and neutron fluence for German A3-3 matrix graphite irradiated at 950°C. It also has a graph of the thermal conductivity of two types of German graphite, IE-24 and ATR-2E used for reflectors. IE-24 has been irradiated at 760°C to a fluence of 3.09E21 EDND and ATR-2E has been irradiated at 600°C to a fluence of 17.7E21 EDND. These graphs have been reproduced in Figures 9.5.2 and 9.5.3.

Figure 9.5.2: Thermal Conductivity of A3-3 Graphite as a Function of Temperature and Neutron Fluence Irradiated at 950°C (from Reference 9.1)
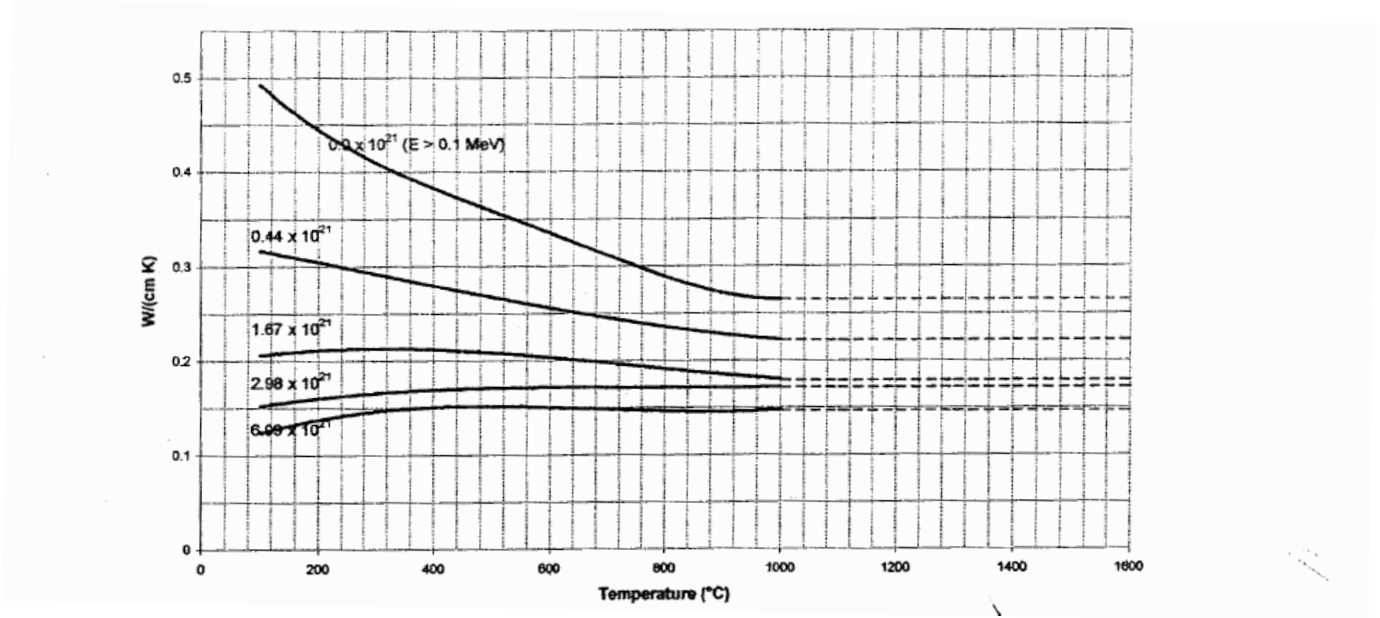
Figure 9.5.3: ATR-2E Graphite Thermal Conductivity as a Function of Temperature and Fluence (from Reference 9.1)
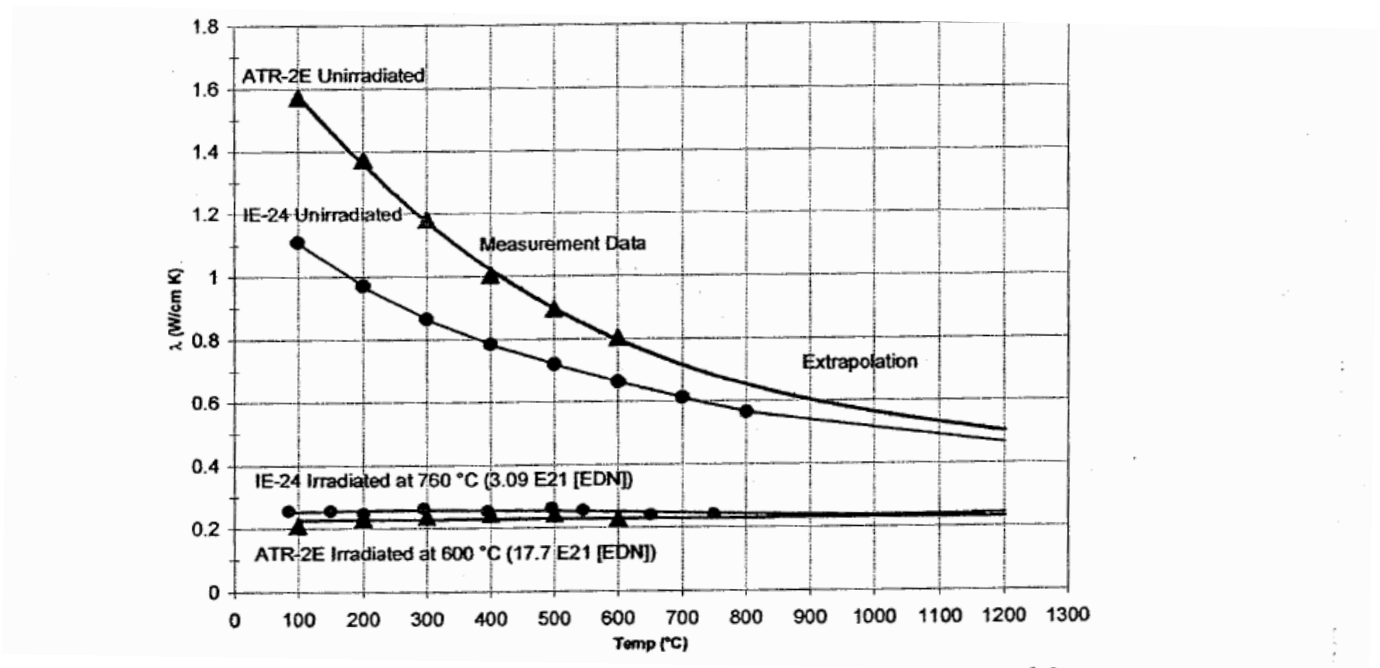
Reference 9.3 provides a graph of the measured ATR-2E thermal conductivity against measurement temperature for various fluences and a plot of the fractional change in measured thermal conductivity against fluence for various irradiation temperatures. These graphs are reproduced in Figures 9.5.4 and 9.5.5 respectively.

Figure 9.5.4: Measured ATR-2E Thermal Conductivity Against Measurement Temperature for Various Fluences (from Reference 9.3)
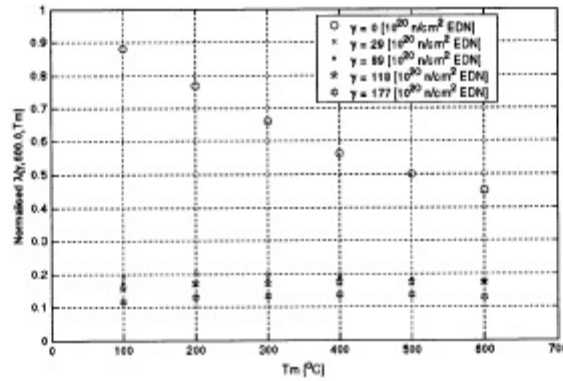
Figure 9.5.5: Fractional Change in Thermal Conductivity Against Fluence for Various Irradiation Temperatures (from Reference 9.3)
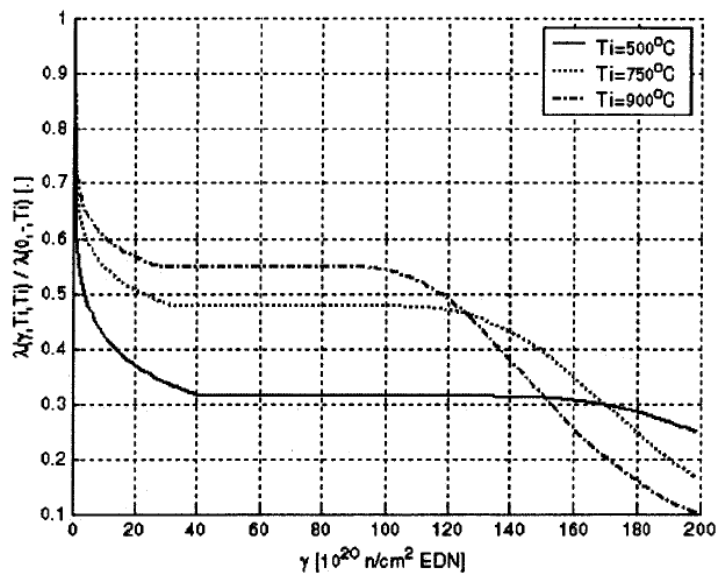
9.5.3   Methodology

Although similar data will have been obtained on the different graphites tested, it is noticeable that the methods used to assess the data, and the subsequent methodology derived to enable the appropriate thermal conductivity at points in a

thermal model of a component to be calculated, differ from one country to another. The methodologies adopted in the UK, for the PBMR and in the US are outline below.

9.5.3.1 UK Methodology

The traditional method of expressing thermal resistance (the reciprocal of thermal conductivity) of irradiated graphite in the UK is given in Reference 9.6 as:

$$\frac{1}{K(T)} = \frac{1}{K_0(T)} + \frac{1}{K_i(T)}$$

Where:

$\dfrac{1}{K(T)}$ - thermal resistance of irradiated graphite at temperature T

$\dfrac{1}{K_0(T)}$ - thermal resistance of unirradiated graphite at temperature T

$\dfrac{1}{K_i(T)}$ - thermal resistance at temperature T introduced by fast neutron irradiation

It has been shown that the thermal resistance parameter $1/K_i(T)$ due to irradiation damage can be separated into two parts. The first part is represented by f;

$$f(\chi, T_i) = \frac{K_0(30)}{K_i(30)} = \frac{K_0(30)}{K(30)} - 1$$

where f is the change in thermal resistance due to irradiation (measured at 30°C) for a given fluence and temperature of irradiation.

The second part is the temperature dependency of the change in thermal resistance due to irradiation. Reference 9.6 states that it has been shown that $1/K_i(T)$ possess a unique relationship to $1/K_i(30°C)$ which is independent of the irradiation damage.

This can be written as:

$$\delta(T)\left[\frac{1}{K_i(30)}\right] = \left[\frac{1}{K_i(T)}\right]$$

So,

$$\delta(T) = \left[\frac{K_i(30)}{K_i(T)}\right]$$

Therefore this represents the temperature dependence of the irradiation induced component of thermal resistance.

Using the above equations to substitute for the thermal resistance introduced by irradiation at temperature T gives:

$$\frac{1}{K_i(T)} = \delta(T)\frac{f(\chi,T_i)}{K_0(30)}$$

An additional factor needs to be introduced to account for structural changes following shrinkage reversal $S_k(\chi,T_i)$, so the final relationship for thermal resistance of irradiated graphite can be defined by the following equation (Reference 9.7):

$$\frac{1}{K(\chi,T)} = S_k(\chi,T_i)\left[\frac{1}{K_0(T)} + \delta(T)\frac{f(\chi,T_i)}{K_o(30)}\right]$$

where:

$K(\chi,T)$ - thermal conductivity of irradiated graphite as temperature T and fluence χ

$K_0(T)$ - thermal conductivity of unirradiated graphite at temperature T

$K_0(30)$ - thermal conductivity of unirradiated graphite at temperature 30°C

$S_k(\chi,T_i)$ - structure factor

The values and relationships needed in order to determine the irradiated thermal conductivity using the above equation are listed in Table 9.5.1 along with the possible available data sources. Some of this data is shown in Figures 9.5.6 to 9.5.15.

Figure 9.5.6 shows values of the structure factor $S_k(\chi,T_i)$ as a function of fluence for various irradiation temperatures.

Figures 9.5.7, 9.5.8 and 9.5.9 show the temperature dependence of the thermal conductivity of unirradiated graphite $K_0(T)/K_0(30)$ for different grades of graphite.

Figures 9.5.10, 9.5.11 and 9.5.12 show the temperature dependency of the irradiated induced component of thermal resistance $\delta(T)$ from different data sources.

Figures 9.5.13, 9.5.14 and 9.5.15 show the fractional change in thermal resistance $f(\chi,T_i)$ as function of fluence for various irradiation temperatures and different grades of graphite.

Table 9.5.1: Data Needed to Determine the Thermal Conductivity of Irradiated Graphite using the UK Methodology

Data	Dependence	Data Sources
$S_k(\chi)$	Fluence and temperature dependent.	The only available information found on the structure factor is in Reference 9.7. This reference provides a plot (Figure 9.5.6) of the variation of S_k with fast neutron fluence for various temperatures. As can be seen from the plot, the structure factor is only needed when the fast neutron fluence is above 125E20n/cm^2.
$K_0(30)$	No dependence. Each graphite has a single value.	Reference 9.2 gives a value for unirradiated gilsocarbon graphite at 40°C to be 117W/m/K and Reference 9.8 gives values for unirradiated graphite between 111 and 138W/m/K. Reference 9.7 has collated thermal conductivities at 30°C for a number of graphites and has calculated a mean unirradiated thermal conductivity to be 125±15W/m/K. Reference 9.9 proposes a specification for HTR graphite and recommends that it should have a high thermal conductivity value of around 145W/m/K when measured at room temperature.
$\dfrac{K_0(T)}{K_0(30)}$	Only dependent on temperature.	Plots of the temperature dependence of unirradiated thermal conductivity against temperature normalised to 30°C can be found in Reference 9.6 and Reference 9.7 (see Figures 9.5.7 and 9.5.8 respectively). Reference 9.10 also has plots of the normalised unirradiated thermal resistances of AGR moderator graphite and CAGR sleeve graphite with temperature (Figure 9.5.9).
$\delta(T)$	Only dependent on temperature.	Reference 9.11 states that $\delta(T)$ is not independent of irradiation temperature but that it shows less temperature dependence for irradiation temperatures greater than 450°C. Plots of the temperature dependence of irradiated thermal conductivity against temperature normalised to 30°C can be found in Reference 9.6 and Reference 9.7 (see Figures 9.5.10 and 9.5.11). Reference 9.8 also provides a plot of $\delta(T)$ versus T up to 600°C (Figure 9.5.12).
f	Fluence and temperature dependent	Reference 9.11 provides a plot of f versus EDN at various irradiation temps for PGA graphite (Figure 9.5.13) and Reference 9.8 provides a plot of f versus fluence for various temperatures up to 550°C (Figure 9.5.14). Reference 9.7 gives various plots of f versus fast neutron fluence for different graphites tested in the PLUTO and DFR MTRs. An overall plot is also provided and is shown in Figure 9.5.15.

Figure 9.5.6: Structure Factor at Different DIDO Equivalent Temperatures (from Reference 9.7)
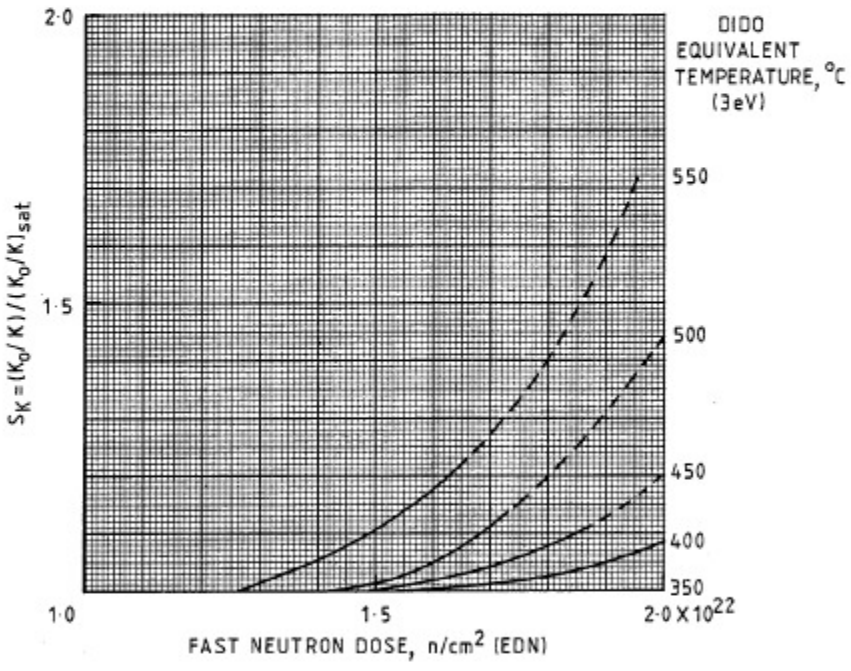
Figure 9.5.7: Conductivity Ratio for Improved Graphite as a Function of Temperature (from Reference 9.6)
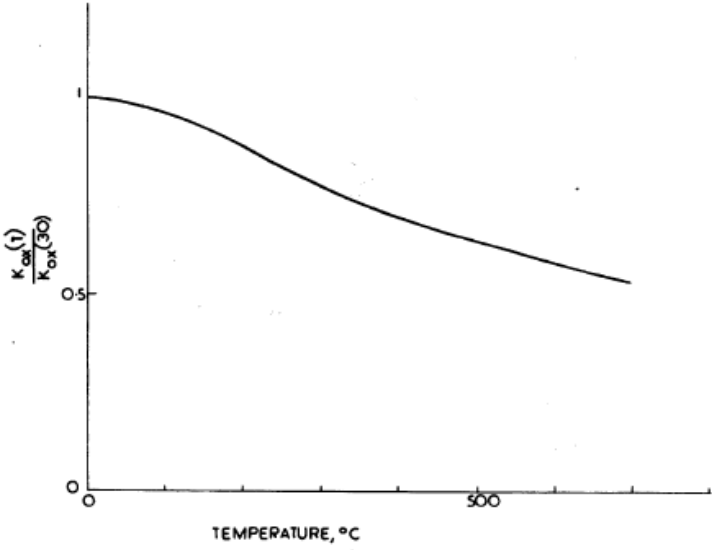
Figure 9.5.8: Conductivity Ratio for Improved Graphite as a Function of Temperature (Reference 9.7)
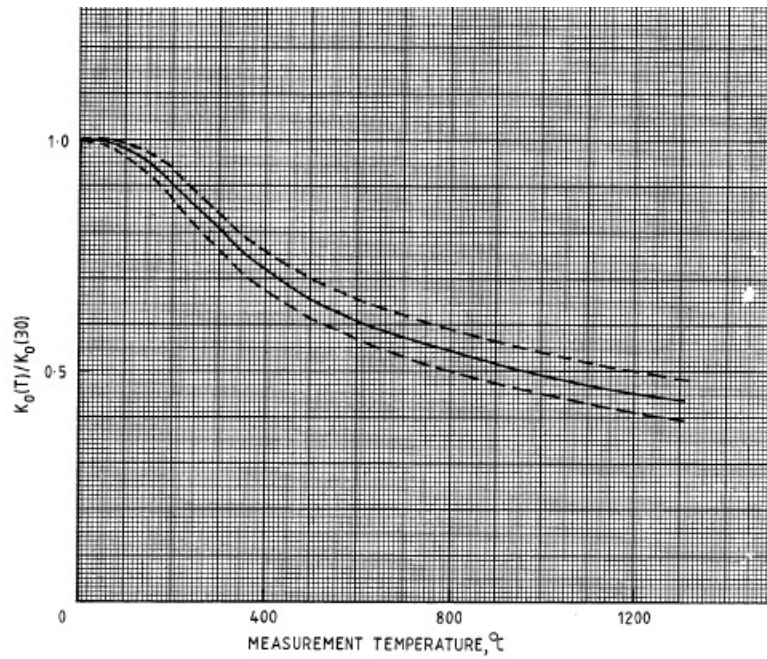
Figure 9.5.9: Normalised Temperature Dependence of Unirradiated Graphite – Comparison of Current Data with Model Curve (from Reference 9.10)
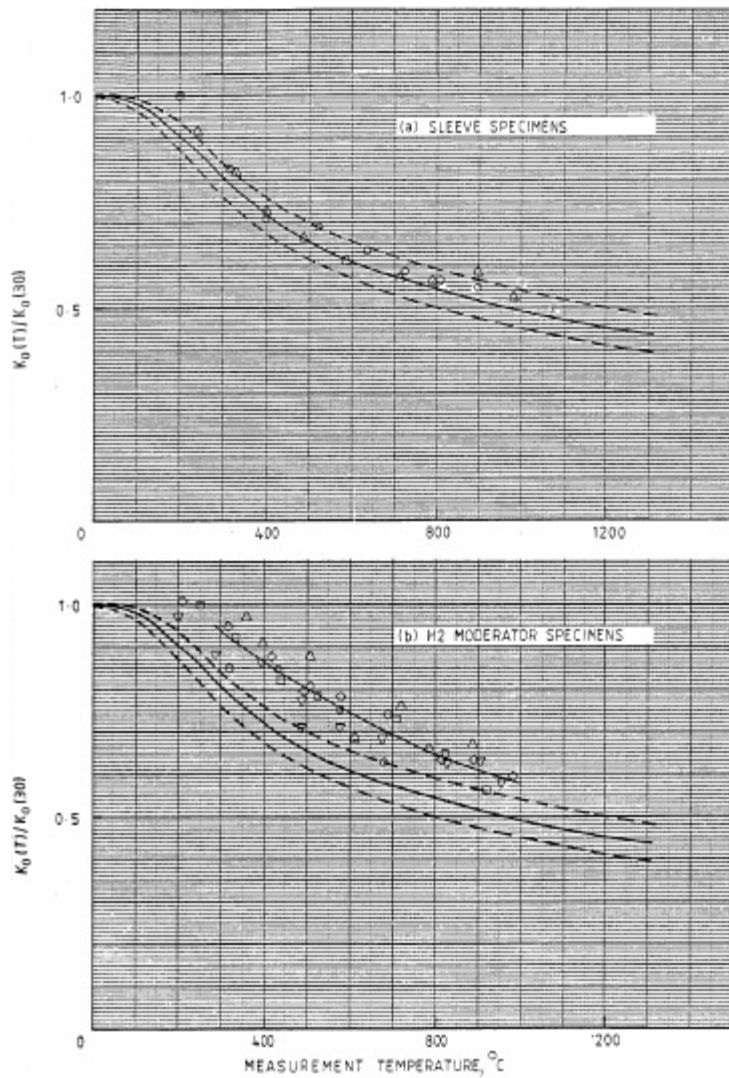
Figure 9.5.10: Thermal Resistance in Irradiated Graphite Normalised to 300K (from Reference 9.6)
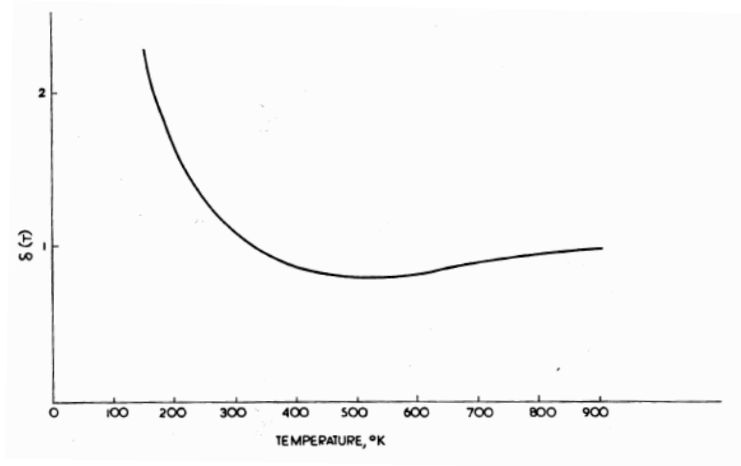
Figure 9.5.11: Thermal Resistance in Irradiated Graphite Normalised to 300K (from Reference 9.7)
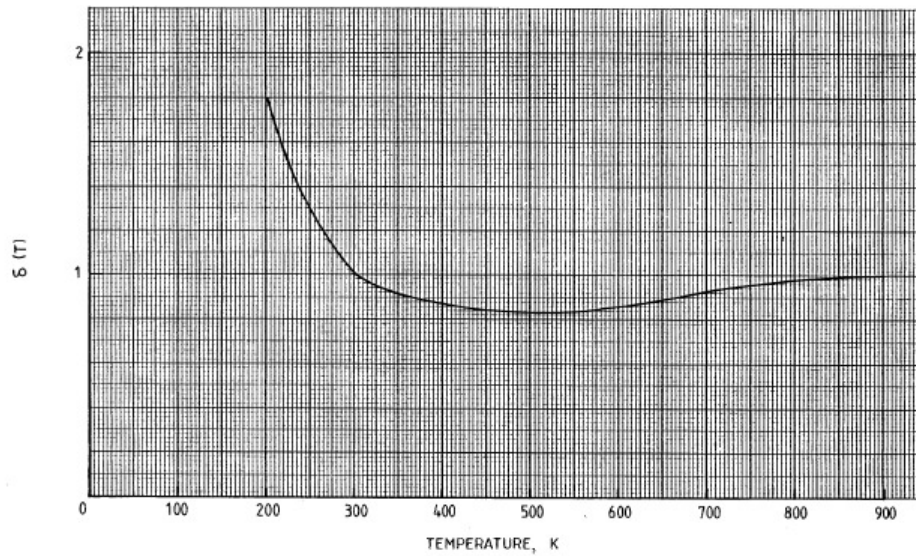
Figure 9.5.12: Temperature Dependence of the Irradiation Induced Resistance (from Reference 9.8)
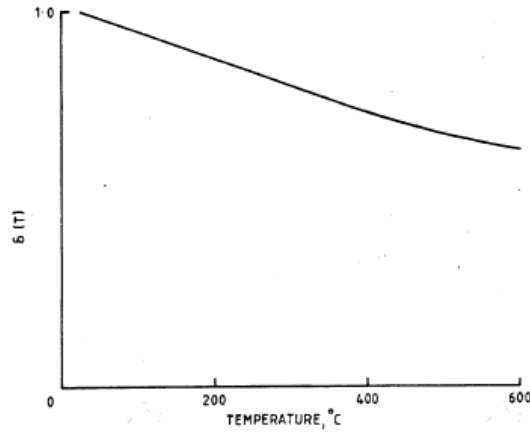
Figure 9.5.13: Fractional Changes in Thermal Resistance of PGA Graphite at Various Irradiation Temperatures (from Reference 9.11)
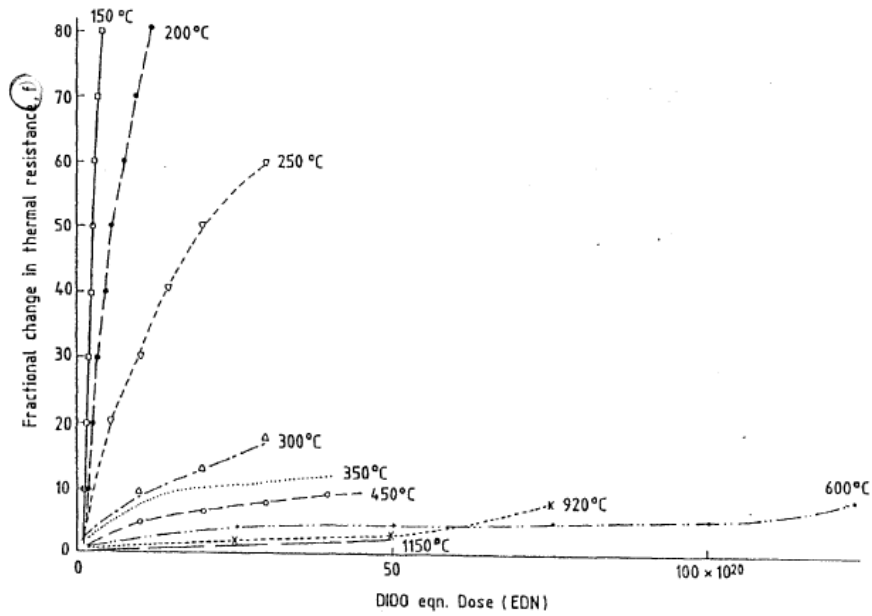
Figure 9.5.14: Fractional Changes in Thermal Resistance of Sleeve Graphite (from Reference 9.8)
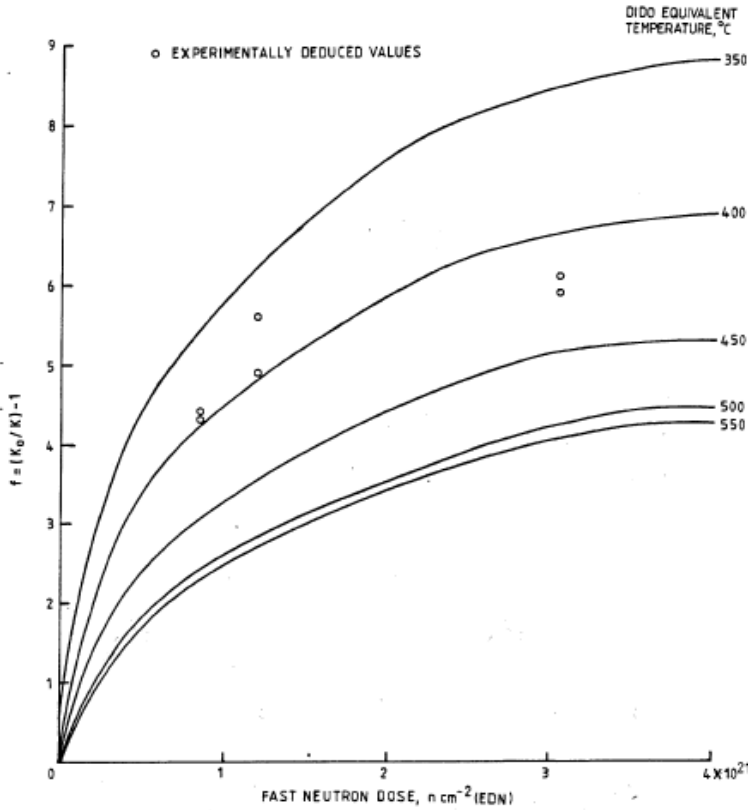
Figure 9.5.15: Fractional Changes in Thermal Resistivity – f Factor (from Reference 9.7)
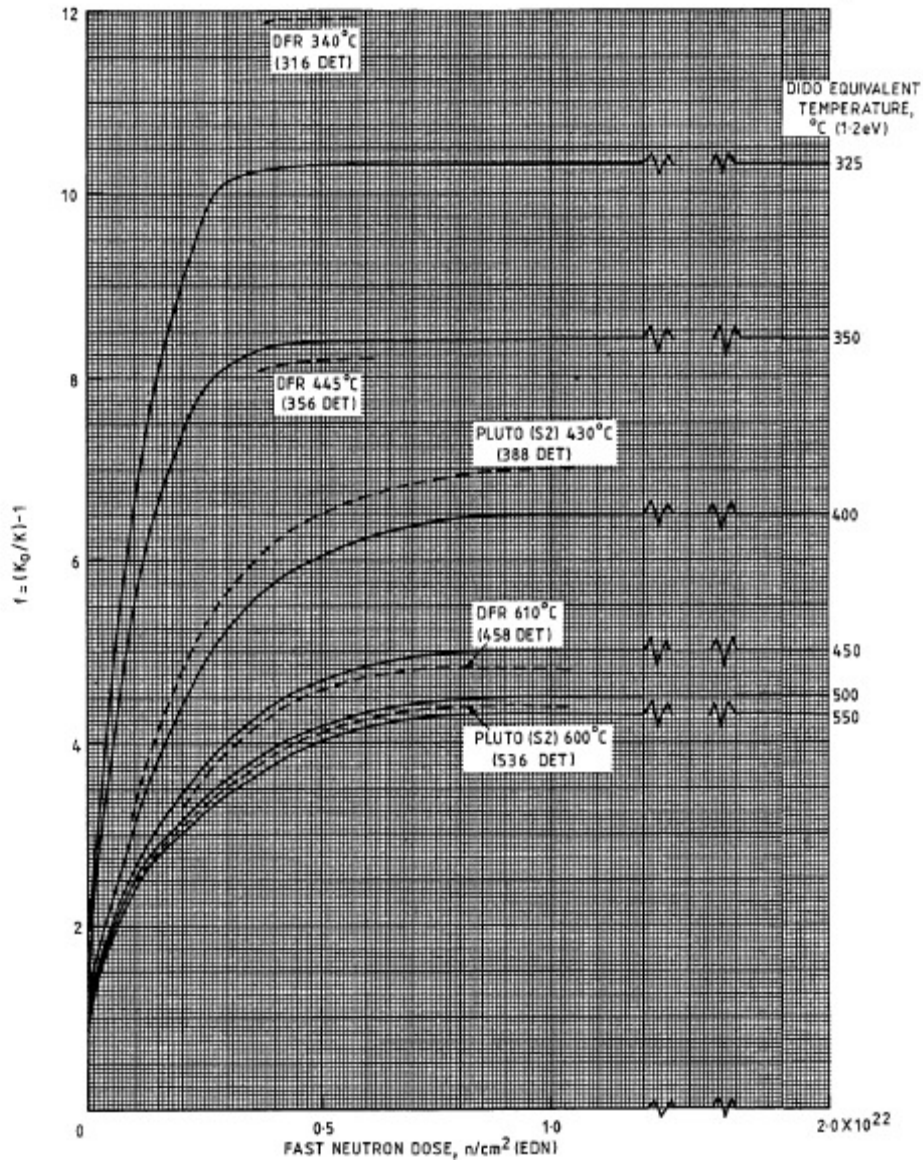
The information on each term can be put into the overall equation to produce tables of values of thermal conductivity for specific temperatures against dose. Care needs to be taken to ensure that the conversion to EDT is correct. Plots can then be made of the thermal conductivity.

This methodology has been tested for three irradiation temperatures and Figure 9.5.16 shows the thermal conductivity curves produced. These can be compared to data from Reference 9.7 as this reference provides tables of values of 'f' for various doses and temperatures along with a value for $K_0(30)$. The data from Reference 9.7 has been input into an Excel spreadsheet and converted into values for the irradiated thermal conductivity. Figure 9.5.17 shows the model curves compared to the data points from Reference 9.7.

Figure 9.5.16: Thermal Conductivity Variation with Fluence for a Range of Temperatures
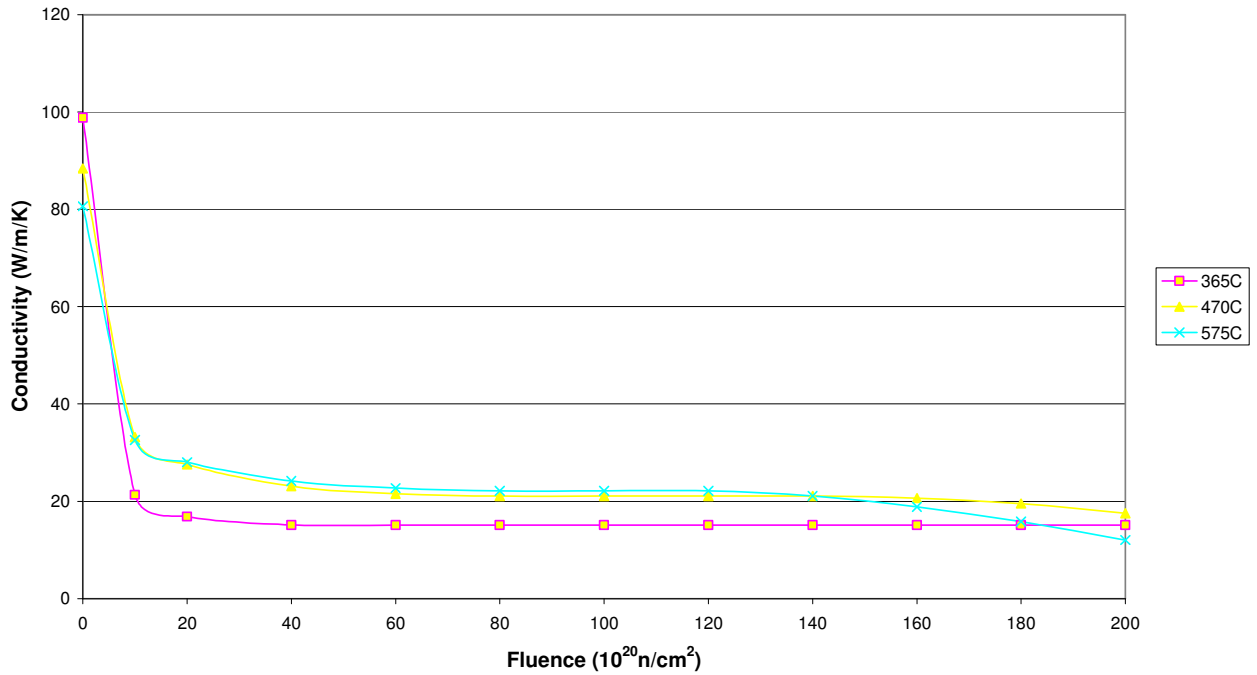
Figure 9.5.17: Thermal Conductivity Variation with Fluence for a Range of Temperatures Compared to Pluto MTR Data
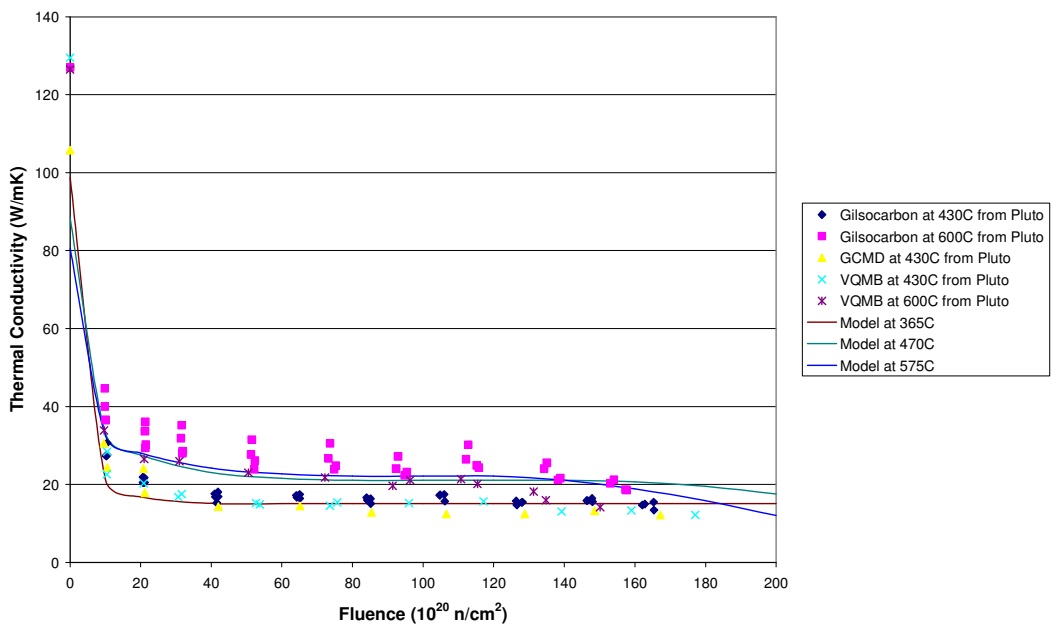
9.5.3.2 PBMR Methodology

The methodology used for the PBMR is given in Reference 9.3 and the information in this sub-section is taken from this reference. It is assumed that this methodology is similar to that used for the German HTGRs.

The PBMR methodology is to split the thermal conductivity curve (against fluence, γ) into four regions/components, and to fit a curve to each region.

The four components are described as follows:

Model Component	Description	Fluence Range (n/cm² EDN)
Virgin Material	Material exposed to these low doses is considered unirradiated.	$\gamma \leq \gamma_0$
Low Dose	The initial breakdown in thermal conductivity occurs in this range.	$\gamma_0 \leq \gamma \leq \gamma_{sat}$
Intermediate Dose	The breakdown in thermal conductivity is saturated in this range.	$\gamma_{sat} \leq \gamma \leq \gamma_{ba}$
High Dose	Secondary breakdown in thermal conductivity occurs in this region.	$\gamma \geq \gamma_{ba}$

The first component of the curve, where the fluence is less than γ_0, is considered to be unirradiated and therefore the thermal conductivity has no dependence on fluence; it can be considered to be at its unirradiated conductivity. The second component is for the region of the curve where there is a rapid decrease in thermal conductivity until it reaches a saturation value γ_{sat}. The third component represents the saturated value up the breakdown value γ_{ba}. This is independent of fluence and dependent on temperature and on the graphite grade. The fourth component represents the region in which the thermal conductivity decreases from γ_{ba}. A representative curve, taken from Reference 9.3 is shown in Figure 9.5.18.

Figure 9.5.18: PBMR Thermal Conductivity Model (from Reference 9.3)
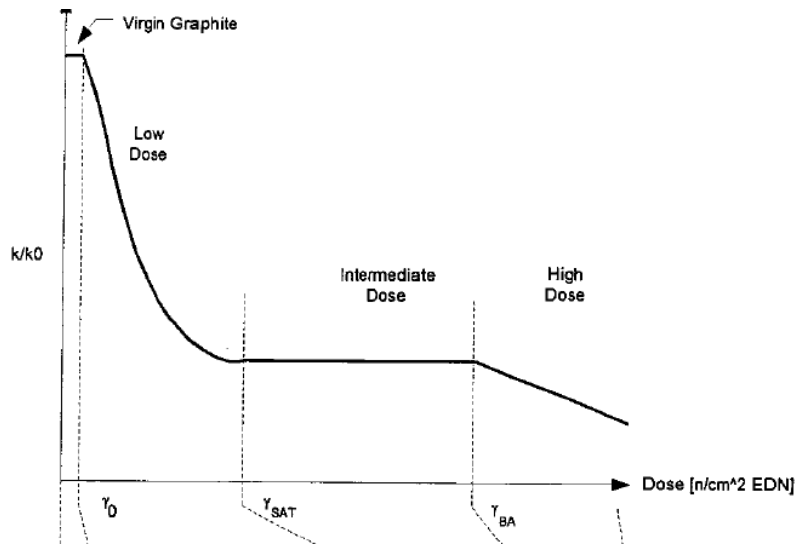
Each region of the curve has been represented by a fitted equation and the complete model is expressed in its four components as follows:

$$\frac{\lambda(\gamma,T_i,T_i)}{\lambda(0,-,T_i)} = \begin{cases} 1 & \gamma \le \gamma_0 \\ K_1 \times \ln(\gamma) + K_2 & \gamma_0 \le \gamma \le \gamma_{sat} \\ 0.4025 \times \ln(T_i) - 2.188 & \gamma_{sat} \le \gamma \le \gamma_{ba} \\ \left(\left(\left(\frac{\lambda(0,-,T_i)}{\lambda(\gamma_{SAT},T_i,T_i)} - 1 \right) + A \cdot V_R(T_i) * (\gamma - \gamma_{ba}) + 1 \right)^{-1} & \gamma \ge \gamma_{ba} \end{cases}$$

With:

$\dfrac{\lambda(\gamma,T_i,T_i)}{\lambda(0,-,T_i)}$ - Change in conductivity due to irradiation measured at the T_i

T_i - Irradiation temperature

A, K_1, K_2 - Constants

It is noted that the function $V_R(T_i)$ is not defined in Reference 9.3, and there are no values given for the constants, A, K_1 and K_2.

To adjust the thermal conductivity value to the measurement temperature the following model is used, which introduces specific heat into the equations:

$$\lambda(\gamma, T_i, T_m) = \frac{\lambda(0,-,20) \times \left(\dfrac{\lambda(0,-,T_m)}{\lambda(0,-,20)} \right)}{1 + \left(\dfrac{Cp(T_i)}{Cp(T_m)} \right) \times \left(\dfrac{\lambda(0,-,T_m)}{\lambda(0,-,T_i)} \right) \times \left(\dfrac{\lambda(0,-,T_i)}{\lambda(\gamma, T_i, T_m)} - 1 \right)}$$

With: T_m -   Measurement temperature

$Cp(T_i)$ -   Specific heat at irradiation temperature

$Cp(T_m)$ -   Specific heat at measurement temperature

Reference 9.3 does not provide much information on the origin of the above equations. It does state that the initial breakdown behaviour has been proposed to follow the above relationship with the constants K_1 and K_2 found such that the initial breakdown point and saturation point are connected. The saturation value with fluence is not known and a simple model has been chosen for the saturation value to be one third of the breakdown value.

Reference 9.3 provides a plot of the fractional change in measured thermal conductivity against dose for three irradiation temperatures. This plot is reproduced as Figure 9.5.5. From this plot, it can be seen that the choice of the saturation value to be one third of the breakdown value does not work for all temperatures but is a reasonable approximation. The curve at 500°C has a saturation value of around 40E20 n/cm^2 and a breakdown value of around 160E20n/cm^2 which does not quite fit with the chosen model.

The PBMR model has been tested against measured data and so far has been reasonably consistent however the model is currently based on ATR-2E data and will therefore need to be reviewed again and changed when data on the new graphite (NBG-18) is available. Reference 9.3 also has one measured value for the thermal conductivity of unirradiated graphite, NBG-10 at room temperature as:

$$\lambda(0, -, 20) = 132.0 \pm 10W/m/K$$

This value will also need to be updated when the new data from the material test reactors is available.

9.5.3.3 US Methodology

The general methodology used in the US (Reference 9.5) is basically the same as that used in the UK with the use of the theoretical work of Kelly (as given in Reference 9.6). Again curves are fitted to experimental data. Reference 9.5 states that for H-451 curves are constructed by assuming that the effects of irradiation on H-451 graphite would be the similar to the effects on Gilsocarbon based graphites.

9.6 Through Life Variations in Density of Graphite

The density of nuclear grade graphites is generally in the range 1.75 to 1.85 g/cm^3. In the UK reactors, the loss of graphite (referred to as weight loss) due to radiolytic

oxidation by the CO_2 coolant is quite significant, and in the AGRs this weight loss can be up to 40% locally. As many properties vary with weight loss (equivalent to a density reduction), it is important to know the variation in weight loss (and hence density) through a component, and specific computer codes have been developed to calculate this. However for HTGRs, with the high purity He coolant, weight loss (and hence density reduction) should be small (less than a few percent) over the lifetime of the reactor.

Irradiation induced graphite shrinkage on the other hand will lead to a slight <u>increase</u> in density. Typically, nuclear grade graphites will undergo a peak linear shrinkage of between 2 and 3%. Thus the volumetric shrinkage could be between 6 and 9%. This will result in an apparent density increase of the same amount.

9.7 Recovery of Thermal Conductivity at High Temperatures

As discussed in Section 9.5, the thermal conductivity of graphite decreases sharply when it is irradiated. However, it is known that some of the conductivity will be recovered if the temperature of the graphite is raised above the irradiation temperature (due to partial annealing). This situation could arise during accident conditions, and the recovery in thermal conductivity as temperatures increase would be beneficial in limiting fuel temperatures. Experiments are being carried out under Raphael to determine the rate of recovery with temperature. However, the recovery with temperature will not be taken into account in this work so the resulting models will determine the most pessimistic fuel temperatures.

9.8 Closure

With regard to specific heat it is quite clear from the available information that there is little difference between the previously used grades of graphite and so a mathematical representation of its variation with temperature can be specified. The representation should also apply to any new candidate graphites. It is also internationally accepted that there is no significant influence of irradiation.

With regard to thermal conductivity it is clear that all the available information shows that previously used grades of graphite show the same trend with regard to irradiation. There is an initial rapid fall to a saturation level, followed by another fall at higher fluences. There is also a temperature dependence. It is known however that there are differences in the variation of thermal (and mechanical) properties with irradiation between the different graphite grades. Thermal conductivity is one such property. In addition, there have been different methodologies developed/used in the past (by different countries) to assess the data and convert them into a usable form for modelling purposes. It is recommended that the different methods be reviewed further and compared, before any recommendations are made for the thermal modelling required for the future licensing stages for HTGRs.

It is also important to note that the graphite data being used for some of the proposed HTGR designs are for previously used grades. There will be a requirement to

determine all the necessary data for the actual selected graphite(s), and the design reassessed accordingly.

With regard to models and data to be used in the current modelling activities, historical data for graphites that are no longer available has to be used before data for contemporary graphite becomes available. Following PBMR's example, data for ATR-2E will be used when modelling the PBR designs. However, there is insufficient data on ATR-2E available in the open literature to fit the model of Section 9.5.3.1 so a combination of polynomial curve fits and linear interpolation will be used to derive thermal conductivities at intermediate temperatures and fluences.

For prismatic cores, H-451 properties will be assumed and Reference 9.5 provides sufficient data for the model of Section 9.5.3.1 to be fitted.

9.9   References for Section 9

9.1   IAEA CRP 5, Draft TECDOC II, "Evaluation of High Temperature Gas Cooled Reactor Performance", to be published.

9.2   UKAEA TRG REPORT 1000(R), List of Data and Conventions for Graphite 'G', Issue 7, 1973.

9.3   Fourth International Nuclear Graphite Specialist Meeting, Marugame, Japan. PBMR Presentation, Graphite Thermal Conductivity and Heat-Removal Paths for PBMR, Mark Mitchell, September 2003.

9.4   General Atomics, DOE-HTGR-88111 Rev 0, Graphite Design Handbook, September 1988.

9.5   Gulf General Atomics, Review of the Thermal Conductivity of Nuclear Graphite under HTGR Conditions, R J Price, Gulf-GA-A12615, 1973.

9.6   TRG memo 4180 (C), JNPC-MWP (GSG)/P(67)69, An Improved Method of Estimating the Thermal Conductivity of Irradiated Graphite at any Temperature, B.T. Kelly, 1967.

9.7   UKAEA ND-R-1117 (S), Irradiation Damage in CAGR Moderator Graphite, J.E. Brocklehurst, July 1984.

9.8   UKAEA NRL-M-2015 (S), Nuclear Research Laboratory Springfields, P Scholfield, R.G. Brown, C.R. Barrett, J.E. Brocklehurst, 1988.

9.9   IAEA TECDOC 1238, Nuclear Graphite for High Temperature Reactors, B.J. Marsden, November 2000.

9.10   UKAEA Northern Division Memo, ND-M-1579 (S) Addendum 2. Thermal conductivity of CAGR graphites – An examination of the temperature dependence, R.G. Brown, J.E. Brocklehurst and N.S.P. Hodgetts, 1990.

9.11 IAEA-TECDOC-1154, Irradiation Damage in Graphite due to Fast Neutrons in Fission and Fusion Systems, April 2000, pg 106.

9.12 AGR/GCWG/P(84)21, ND-M-2655(S), Calculation of DIDO Equivalent Temperatures for AGR Graphites, B.T. Kelly and J.E. Brocklehurst.

10.0 MODELS FOR THE INVESTIGATION OF PEBBLE BED PRESSURE LOSSES AND HEAT TRANSFER MECHANISMS

10.1 Purpose of Section 10

The primary goal of the work presented in this section is to determine the heat transfer coefficients and pressure drop within the core of a pebble bed reactor (PBR). The secondary goals of this section are to investigate the "wall-channeling" phenomena, heat transfer in a multi-batch core and the prediction of pebble surface temperatures. This work is restricted to an examination of a portion of the PBR core ranging from the meso-scale into the macro-scale. The meso-scale ranges from length scales greater than TRISO particles and pebble surface roughness to the immediate surroundings of a pebble. The macro-scale ranges from the upper limit of the meso-scale up to the scale of the whole reactor.

Computational Fluid Dynamic (CFD) models are developed to predict how the pebbles interact hydraulically and thermally with their surroundings. These interactions are influenced by whether the pebbles sit internally within a large pebble bed, or alternatively, sit close to or at the edges of the bed in contact with the reflectors. Proximity to the edge of the bed introduces systematic variations in the packing density of the pebbles, which decreases with increasing distance from the edge. Packing densities that are generally close to the average value are only found remote from the reflectors. The packing fraction influences the frictional pressure drop and the surface averaged convective heat transfer coefficients.

In Section 10.2 a review of available software techniques or packages to generate the geometries of the pebble assemblies is presented and a technique is implemented to generate a collection of randomly distributed pebbles. This is a prerequisite to establish the pebble positions for the CFD mesh generation that is required for the CFD models developed in this section.

The topics common to all the CFD models and runs are discussed in the introduction to the sections on CFD modeling (Section 10.3).

The first CFD model is for an assembly of pebbles remote from the reflector (Section 10.4). Using appropriate turbulence models the flow distribution and pressure losses are determined. The model is also run by solving the energy equation, and a sensitivity study is performed with the power proportional to flow. Local and surface average heat transfer coefficients are determined using a modified Reynolds analogy and from the temperature solution and compared with correlations taken from the German KTA rules.

Next a CFD model of an assembly of pebbles adjacent to a reflector is investigated (Section 10.5). The pressure and flow solution is investigated and compared to previous results. In this model the energy equation is also solved and local and surface average heat transfer coefficients are determined using a modified Reynolds analogy and from the temperature solution and compared to the German KTA rules. Sensitivity studies are performed with the power proportional to flow and with

increased heat transfer to the reflector. An additional study to better investigate the "wall channeling" behaviour near the reflector wall is performed using a larger CFD model of the pebbles adjacent to the reflector (Section 10.6).

A third CFD model is used to investigate pebble-to-pebble heat transfer in multi-batch core to quantify the heat flows between pebbles when the pebbles have differing power outputs (Section 10.7). The results of this model will be compared with those of analytical sub-model of Section 8.0.

Finally error estimates in the CFD modeling and runs are discussed (Section 10.8).

10.2 Random Packing of Spherical Pebbles within a Cylindrical or Annular Pebble Bed

10.2.1 Review of Existing Methods

Packed beds of particles are used within many industries, ranging from the powder processing and petrochemical industries to water treatment plants. This wide field of application has lead to considerable research effort being dedicated to the characterization and simulation of packed beds. A large number of methodologies have been developed to simulate constrained packed beds of uniform spheres. A few of the most widely used methodologies are summarized below.

Monte-Carlo methods: The release of pebbles, one at a time, from a random point above a container is simulated. The pebbles are assumed to fall vertically before colliding inelastically with the container floor or other pebbles. The pebbles then roll, according to a set of predefined rules, until they reach a stable resting position. Once at rest, the pebbles are generally assumed to attain a fixed position, which cannot be altered by the impact of further pebbles. (See for example Reference 10.1 as cited in Reference 10.2 and Reference 10.3 as cited in Reference 10.4).

Full physical simulation: An initial loose packing of non-overlapping pebbles is generated by random placement. A high-fidelity physical model is then implemented, in which gravitational acceleration, friction, slip and inter-pebble forces are integrated to predict the motions of the system of pebbles as they settle from the initial loose packed configuration into a stable, higher density arrangement. See, for example References 10.5 and 10.6.

Modification of a structured packing: In this algorithm, randomly selected pebbles are removed from an initial regular arrangement of pebbles, until the desired packing fraction is achieved. This method is simple to implement, but does not result in an unstructured packing, and the pebble arrangement does not conform to pebble bed boundaries. This method is used by the MONK Monte Carlo neutronics model (Reference 10.7).

Cluster growth model: An initial cluster of pebbles is specified. Further pebbles are added to the edge of the cluster, such that they are in contact with three or more pebbles within the cluster. A variety of methods have been used to identify suitable

stable candidate sites for adding the new spheres (see for example Reference 10.8 as cited in Reference 10.2)

Many variants of these methods have also been reported. For the current study, the following criteria were used to identify suitable packing methods:

- The pebble packing must conform to the shape of the container, such that realistic pebble arrangements can be achieved close to radial reflectors.

- Computational requirements and programming complexity should be low or modest, such that a large assembly of pebbles can be simulated.

- A packing fraction as close as possible to the expected pebble bed value of 61% should be realized.

In view of these considerations, a Monte-Carlo approach was selected, as described below.

10.2.2 Pebble Bed Generation Method Adopted in this Work

The Monte-Carlo code, PEBS, simulates the random packing of spherical particles within a cylindrical or annular pebble bed. The pebble bed has a flat base and a fixed number of pebbles are dropped into the system, one at a time. The code integrates the path of each pebble as it falls into the pebble bed, taking into account the pebbles already present and the walls of the bed.

The pebble path is integrated as it touches and moves over the surface of pebbles already within the system. The path is terminated when the pebble is prevented from moving downhill by its neighbors. The pebbles are frozen into place when they stop moving, which is a significant simplification of the real situation in which a falling pebble could dislodge pebbles already in the bed. This was considered to be far too complex to model within the constraints of this investigation.

The pebbles are also only able to roll downhill and, where a choice exists, the most downhill path is selected. This is also a significant simplification, since a real pebble could potentially roll into and out of a local minimum in the surface formed by the pebbles already within the bed. This effect could be modeled, however, it is instead represented through the use of "simulated annealing", in which a pebble, once it has reached a standstill, is randomly displaced to see if it can fall to a lower position. Several displacements from the final position are tested to see if the resting position is stable.

See Appendix D for a detailed description of the method and its validation.

10.2.3 Generated Assemblies of Pebbles

Datasets have been produced for three different pebble bed geometries using the PEBS code. All use a pebble radius of 0.03 m and all use the following annealing

parameters: an annealing displacement of 1.5 pebble radii horizontally and 0.75 radii vertically, with 10 annealing attempts.

The three different pebble bed geometries are:

1.   A 0.75 m radius cylinder was filled to a depth of ~1.20 m with 11,500 pebbles, each of radius 0.03 m. The tolerance in the calculation (i.e., the maximum amount by which any two pebbles may overlap, or the extent to which a pebble may overlap a wall) is 3 μm (10^{-4} pebble diameters). The data file is a subset of the whole-core data, extracting pebbles that lie within a cubic "shoebox" with a side length 0.30 m and centered on (0.00, 0.00, 0.75) m. The closest approach of shoebox to the wall is 0.54 m (9.0 pebble diameters) diagonally and the top of the shoebox is 0.30 m (5.0 pebble diameters) from the surface of the pebble bed. Both of these are sufficient to avoid edge-effects (which can extend for up to 5.0 pebble diameters).

2.   The specifications for this case are identical to those of the 1st set of data, but the data are extracted from an independent run of the code.

3.   An annular bed of inner and outer radii 1.00 m and 1.85 m was filled to a depth of ~1.20 m with 50,000 pebbles, each of radius 0.03 m. The tolerance remains at 3 μm (10^{-4} pebble diameters). The data file is the complete set of whole-core data, giving pebble centre positions for all 50,000 pebbles. Edge effects are present for up to 5 pebble diameters (0.30 m) from the floor or inner or outer wall of the annulus. Surface effects (i.e., variations in height or incomplete packing) are present within ~3-5 pebble diameters of the upper surface. To exclude effects due to the bottom of the bed, or from the upper surface, it is recommended that only data within an axial position range of 0.30 to 0.90 m are used.

10.3   Introduction to CFD Modeling

The objectives of this and the following four sections are to determine the detailed flow patterns and heat transfer within a random 3 dimensional arrangement of pebbles within a PBR core. No known analytical methods are available for such a problem, however general purpose computational fluid dynamics (CFD) software is available that will allow this problem to be solved discretely.

The problem of determining heat transfer coefficients and pressure drops within the PBR core is addressed by creating a CFD model using the commercial software package ANSYS FLUENT 6.3.26 (Reference 10.10). The models created in this work directly model the pebble geometry, as opposed to relying on a porous medium model. This approach is required to determine the local heat transfer coefficients for a given pebble.

Four distinct models have been used to predict heat transfer and pressure drop:

1.   CFD model of an assembly of pebbles remote from a reflector,

2. CFD model of an assembly of pebbles adjacent to a reflector,

3. A larger (but lower resolution) CFD model of an assembly of pebbles adjacent to a reflector, and

4. CFD model for pebble-to-pebble heat transfer in multi-batch core.

First a literature overview is presented that summarizes some of the work that was done previously. A number of topics common to all four CFD predictions are also discussed upfront. Modeling topics that are specific to a particular CFD model are discussed in the appropriate section. Appendix J discusses a generic process on how to develop a large grid in a packed annular region.

10.3.1 Existing Literature for Explicit Modeling of Packed Beds

An examination of the literature on CFD simulations of pebble bed reactors indicated that many simulations to date have modeled a structured arrangement of pebbles (References 10.11, 10.12, 10.13, 10.14, 10.15, 10.16, 10.17, 10.18). The work of Reference 10.19 models a set of randomly placed pebbles in a narrow container (but does not perform CFD simulations), and Reference 10.20 models a variety of random pebble arrangements (but, not using the finite volume method). Unfortunately the work of References 10.19 and 10.20 are not suitable for the current analysis.

10.3.2 Approach of Current Work

The scale examined in this work ranges from sizes larger than TRISO particles and pebble surface roughness, up to several pebble diameters. In order to create a model of this scale from within the PBR core the locations of pebbles within a large stack of randomly dropped pebbles was first determined (Section 10.2). Regions of interest located in this stack of pebbles were then selected as the solution domain.

When a CFD simulation is performed on structured arrangements of pebbles there is little need to examine large solution domains as the solution is periodic in nature. In the current analysis the dimensions of the solution domain are expected to impact the solution due to the random packing of the pebbles.

In order to determine what appropriate model dimensions were a domain size study was performed (discussed further in Section 10.4.1). The final domains consist of entry regions, allowing the flow to develop before the first pebbles are encountered, regions with pebbles where the pressure and temperature distributions of interest are determined, and outlet regions.

For this work it is assumed that the pebbles are perfectly spherical (except for local contact deformation) and smooth. Any damage to pebbles, such as cracks, is not included in the current geometry. The pebbles in this model are full sized (0.06m diameter) and in direct contact with one another.

10.3.3 Computational Mesh

The mesh applied to the geometry defining the coolant flow between the packed pebbles was constructed using the software ANSYS GAMBIT (References 10.21 and 10.22). The generation of a mesh on the geometry modeled in Sections 10.4, 10.5 and 10.6 poses several significant difficulties, mainly due to the extremely small gap between contacting pebbles. A review of the literature involving the generation of a mesh on discretely modeled packed beds is first presented in this section, followed by the solutions arrived at in this work.

10.3.4 Existing Contact Point Strategies

References 10.13, 10.16, 10.17 and 10.19 attempted to place an unstructured tetrahedral mesh on the fluid between the spheres in an organized arrangement of spheres. These references went to significant lengths to solve turbulent flows using this mesh; however they reported this to be impossible as the tetrahedral elements near the point of contact between spheres were extremely skewed. Extremely skewed elements are known to introduce local errors in CFD simulations and are a primary source of divergent solutions.

The work of Reference 10.13 made several attempts to solve turbulent flow equations on meshes with highly skewed tetrahedral elements near the contact point between pebbles but had no success (using the codes FLUENT or CFX). The work of Reference 10.13 did have several interesting approaches such as changing the physical properties of the skewed elements so that they behave as a solid with the properties of helium. Eventually, Reference 10.13 adopted the approach of spacing pebbles out sufficiently by reducing their size such that a reasonable quality mesh could be placed between pebbles at the contact point (this approach was also used in References 10.11, 10.14, 10.15, 10.16, 10.17 and 10.19).

In the work of Reference 10.18 flow solutions were obtained for a tetrahedral mesh around touching spheres, using the finite element method[1]. The meshes around the contacts were created by manually creating circular guide lines for the mesh near the contact point, however it is unclear how the issue of highly skewed elements at the contact point was resolved and the paper does not provide further details. The work of Reference 10.12 also obtained solutions on a mesh similar to that of Reference 10.18; however no details were provided on how skewed elements at the contact point were treated.

10.3.5 Existing Strategies for Resolving Boundary Layers

A desirable feature of a mesh is to have good near wall resolution such that boundary layers, and derived quantities such as shear stresses and heat transfer coefficients can be accurately predicted. Reference 10.15 creates an extremely fine tetrahedral mesh near the pebble surfaces in order to resolve boundary layers. This approach was

---

[1] FLUENT uses a cell-centred finite volume method for solving flow problems.

possible in Reference 10.15 only because their model contained only 3 partial pebbles. The geometry in the current work contains 129 pebbles and refining the tetrahedral mesh to the degree of Reference 10.15 is beyond conventional computing capacity. Reference 10.19 utilized prismatic layers (5) to resolve the near wall phenomenon. These prismatic layers were applied to a structured arrangement of non-touching pebbles.

10.3.6 Randomly Packed Pebble Arrangements

Limited literature was found involving the simulation of random arrangements of pebbles. Reference 10.19 created geometries for random pebble arrangements, but did not attempt to apply a mesh to these configurations.

Reference 10.19 examines laminar[2] flows through randomly packed beds using the Lattice-Boltzmann simulations. Lattice-Boltzmann simulations are significantly different from finite volume simulations, where in the former, meshing strategies are not relevant. The Lattice-Boltzmann meshes are similar to Chimera grids (overset grids); however, FLUENT does not have facilities to solve problems using these grids.

10.3.7 New Meshing Approach

The goal of the current work with regards to meshing is to develop a strategy to place quality elements in the small gaps near pebble contact points and to resolve boundary layers without placing excessive demands on computational resources. The strategy for the current work could not rely on having a structured arrangement of pebbles, so it must be robust and readily automated.

From a review of the literature many possible meshing strategies have been presented, however no strategy meets all of the goals for this analysis.

Reference 10.18 was found to be the only literature with a documented method of creating meshes near the contact points between pebbles. This approach while successful still has a few issues if it is to be applied to the current work.

1. Pebble contact points in the random assembly have a small tolerance; hence the pebbles may have small gaps between them.

2. Despite the creation of circular rings around the contact point, the use of tetrahedral elements near a contact between pebbles leads to highly skewed elements (See Appendix E). Such elements are known to cause solution divergence in finite volume calculations. As the current work involves a random arrangement of a large number of pebbles a robust meshing strategy is desired.

3. This work does not have highly resolved boundary layers except very near the contact point.

---

[2] Reynolds numbers are on the order of 100.

The approach of Reference 10.13, to disable flow evaluation in skewed elements near the contacts also has merit; however, the authors indicated that the method is not generally successful for solving turbulent flows.

To resolve the near wall effect two meshing strategies are presented. The approach of Reference 10.15, to produce very fine tetrahedral meshes is known to be too computationally expensive, so it is not pursued further. The approach of Reference 10.19, to place prismatic layers on the pebble surfaces is used; however, it must be adapted for use with touching pebbles.

The details of the process to develop a mesh for this geometry are documented in Appendix E. The final meshing solution that was developed for this work is a mixture of mapped quadrilateral elements with a structured appearance in regions near the contacts between pebbles (Figure 10.3.1) and an unstructured mesh composed of wedge tetrahedral elements for the remainder of the solution domain. An important feature of the quadrilateral mesh near the contact between pebbles is that the closer the mesh gets to the contact the smaller the element skew becomes. This result is caused by the geometry of the contact surface. Since the pebble contact area is formed by removing a prismatic region from the model the sides of the contact (vertical surface in Figure 10.3.1) have a finite length.

Figure 10.3.1: Quadrilateral Mesh Near the Contact Point Between Pebbles
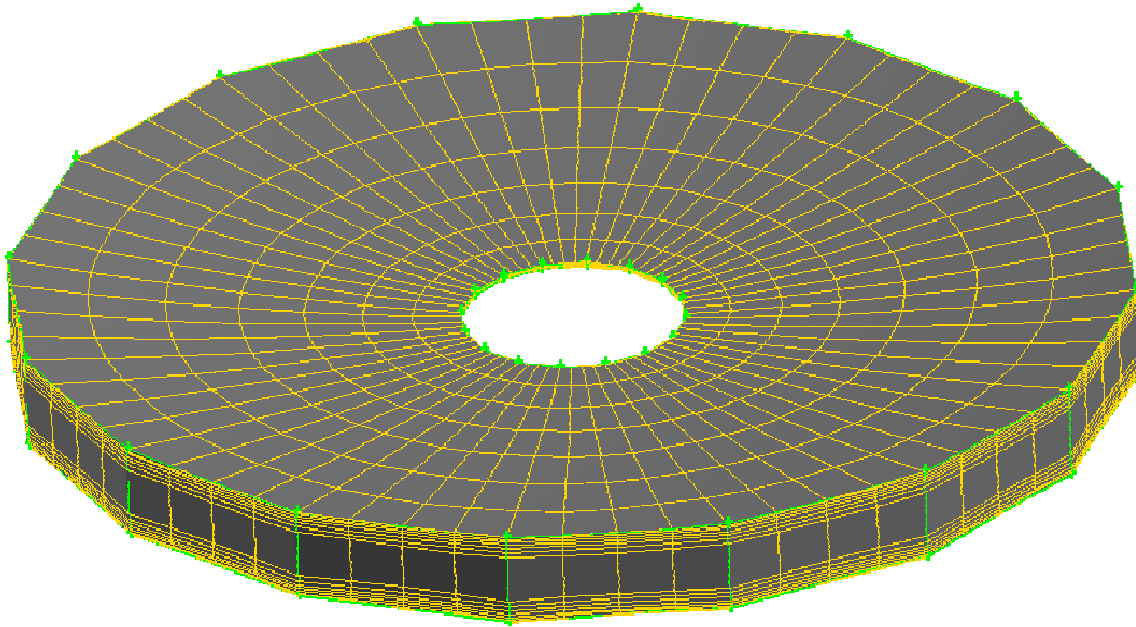
a) Mesh near contact between pebbles
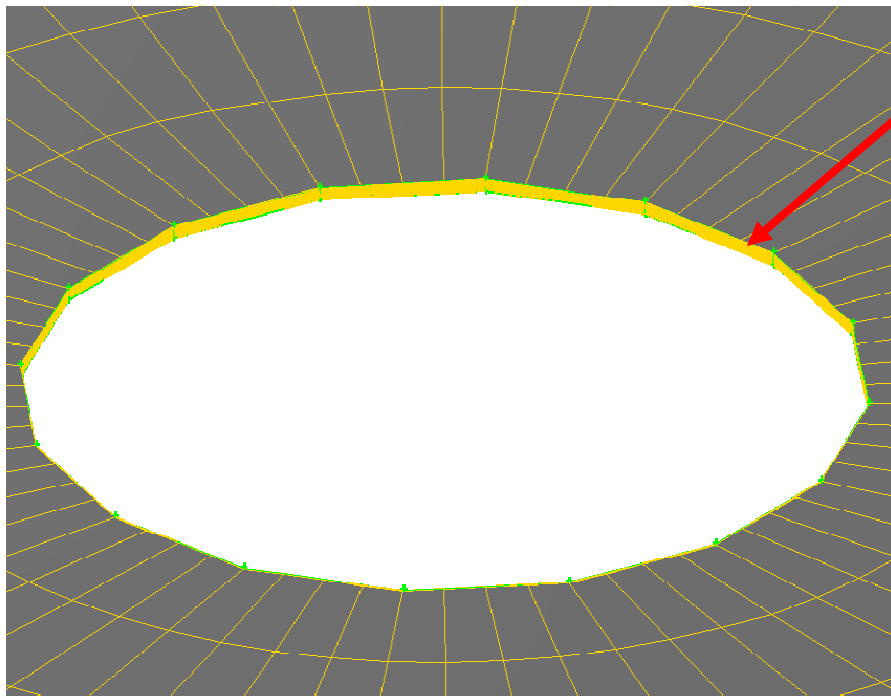
Finite sized faces allow for the elimination of extremely skewed elements

b) Material removed to simulate contact deformation area

The unstructured portion of the mesh contains 6 prismatic layers on the surface of pebbles contained completely within the solution domain. To preserve mesh quality, pebbles that intersect with edges of the solution domain do not have prismatic layers applied to them. These prismatic layers allow for the simulation of boundary layer phenomenon directly without relying on wall-functions. The target first prism height for the model was to have a y+ value of 1.0. As indicated in the results discussion this goal was generally achieved by the mesh.

The mesh is also locally refined wherever pebbles come in close proximity to each other to maintain a high mesh quality. The final surface mesh on the solution domain remote from the reflector (Section 10.4) is shown in Figure 10.3.2. The final mesh contains 11,536,562 cells (of various types). The valid simulation region (Figure 10.3.2c) is estimated to contain approximately 69 pebbles. This model has approximately 160,000 cells per pebble.

In the work of Reference 10.19 it is indicated that 3 million discrete regions are required to obtain a grid independent solution for 16 pebbles (or 187,500 discrete regions per pebble). The 160,000 discretization regions (cells) per pebble that are used in this work is judged to be a reasonable mesh resolution when compared with the recommendation of Reference 10.19.

Figure 10.3.2: Images of Final Mesh
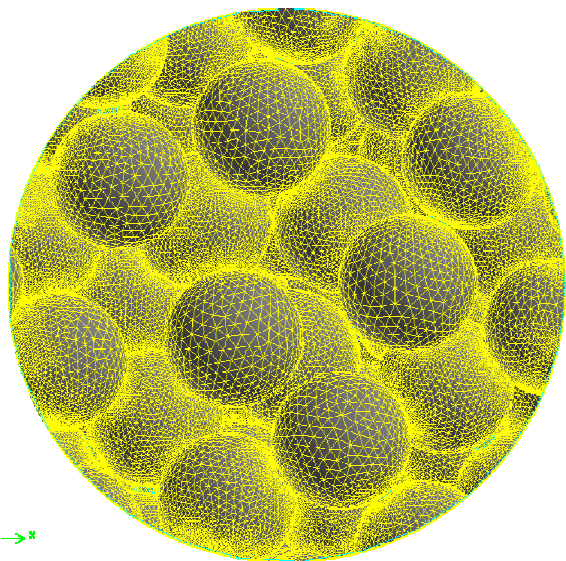
a. Pebble mesh at outlet
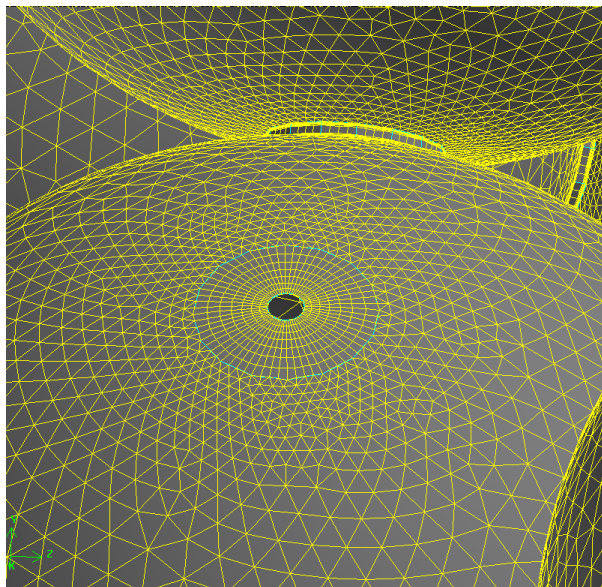
b. Pebble surface mesh in close proximity to another pebble

Exit Region

Valid Simulation Region

Inlet Region
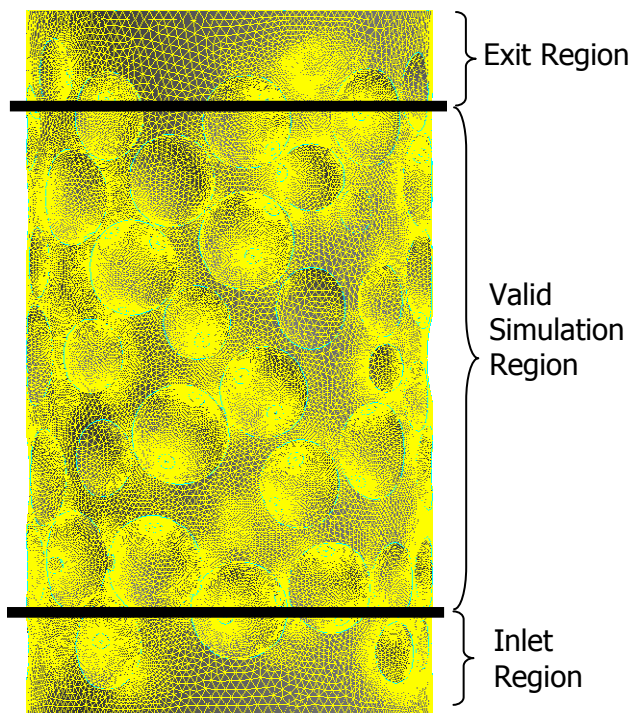
c. Mesh on solution domain
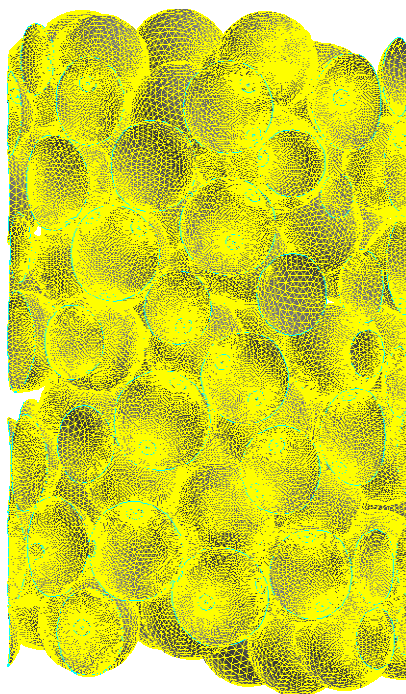
d. Mesh on all pebbles within domain

10.3.8 CFD Methods

The models in this work are solved using the finite volume method with a cell-centered discretization.

- For the model discussed in Section 10.4 all equations are solved using second order discretizations except for the dissipation equation in the turbulence models which is first order. The dissipation equation uses a first order discretization to increase the stability of the problem.

- For the model discussed in Section 10.5 all equations are solved using second order discretizations except for the pressure equation which uses the PRESTO scheme. FLUENT recommends that the PRESTO scheme be used when problems involving buoyancy are solved.

- For the model discussed in Section 10.6, for the 150 kg/s case, convergence was only achieved with first order discretization for all equations with the exception of pressure, which used the standard scheme. For the 75 kg/s and 15 kg/s cases convergence was achieved with the same settings as the 150 kg/s case, except that Second Order Upwind was used for momentum.

- For the model discussed in Section 10.7 it was not possible to solve all of the equations using second order discretizations due to numerical instabilities. Second order discretization was used for the energy and momentum equations and first order for all other equations except for the pressure equation which uses the PRESTO scheme.

All simulations are solved as steady state problems. It is recognized that this type of geometry may produce an oscillating flow pattern; however, the examination of such transient behavior is beyond the scope of this work.

As there is no method to directly solve a set of coupled non-linear discrete equations iterative solution methods are required. The models are solved using FLUENT's coupled solver. The coupled solver uses a pseudo time stepping method to advance the initial guess for the model flow to a final value. The dimensionless time step (Courant number) used in these steady state simulations has a value of 5 for the flow solution remote from the reflector. For the CFD solutions for pebbles adjacent to the reflector the dimensionless time step used in the steady state simulations is initially set to a value between 5 and 100 and final convergence is obtained using a step of 2.5.

In order to solve the non-linear matrix produced for these models the software creates a linear matrix for the problem (based on the current solution), solves this matrix then updates the coefficients in the matrix based on the new solution. Each of these linear matrices are solved using the default iterative matrix solution algorithm in FLUENT.

Since the solution to these models involves an iterative process it is necessary to determine when the iteration should stop. Typically in CFD simulations one can monitor the residual based on the agreement between the current set of equations

and the current solution. FLUENT normalizes its residuals such that they are equal to 1.0 at the first iteration. The problem with this is if the user provides the software with a good initial guess the residual may never drop below 1.0 and if a poor initial guess is given one may see large decreases in the residual in very few iterations, however the solution may not be converged. In order to consider a solution "converged" the following method was adopted:

1. The residuals should not be changing significantly when the solution is converged.

2. The inlet pressure, wall shear stress and pebble surface temperature (when applicable) are monitored throughout the solution. When these quantities have either stopped changing or have settled into an oscillating behavior when the residuals have stopped changing the solution can be considered converged.

In addition for the simulation of Section 10.7 the following was added:

3. The area weighted temperature of the fluid graphite interface was monitored throughout the simulation and at convergence this value was found to be very stable.

10.3.9 Material Properties

A PBR reactor uses helium as the coolant. For the isothermal simulation presented in Section 10.4 helium is treated as an incompressible gas. The properties of helium for this simulation are based on a temperature of 760ºC and a pressure of 89.1 bar and are summarized in Table 10.3.1.

<p align="center">**Table 10.3.1: Properties of Helium**</p>

Property	Value	Evaluation Pressure	Evaluation Temperature	Reference
Density	4.11 kg/m³	89.1 bar	760ºC	10.23
Viscosity	4.73E-5 Pa s	89.1 bar	760ºC	10.23

This temperature and pressure are considered to be characteristic of the conditions within a PBR core (Reference 10.13).

The material properties for the modeling discussed in Sections 10.4.3, 10.5, 10.6 and 10.7 are significantly more complex than those presented in Section 10.4 due to the introduction of the energy equation. In addition, for the model in Section 10.7 properties for radiation are also required. The following sub-sections describe the physical properties of the reflector graphite, pebble graphite and helium coolant in a PBR.

10.3.9.1 Pebble (Fuel) Properties

The outer shell of a PBR fuel pebble is composed of graphite. The thermal conductivity of the type of graphite used in the outer shells of the fuel pebbles is temperature dependent. It is assumed that the graphite in the shells of the fuel pebbles can be represented by A3-3 graphite at a fast dose of 2.98×10^{21} EDN (Effective DIDO Nickel Dose). The temperature dependent thermal conductivity for this material was determined by a polynomial least squares fit to the data in Figure 2 of Section 4.2 of Reference 10.13. The resulting equation is provided below.

$$k = -4.707791 \times 10^{-8} \cdot \left(T^*\right)^2 + 6.953557 \times 10^{-5} \cdot \left(T^*\right) + 1.473090 \times 10^{-1} \quad \text{W/cm K}$$

Where,

$$T^* = \min(1000^\circ C, \text{Graphite temperature} \,^\circ C)$$

The density and specific heat capacity are assumed to be constant quantities for this work, and are taken from Reference 10.13 and as the values have no impact on the steady state simulations the values are not repeated here.

For models that include the effects of radiation the emissivity of the pebbles is required. The value assumed for the graphite layer is 0.8, which although slightly lower than the 0.85 quoted in Reference 10.13 is commonly used for pebble fuel graphite.

10.3.9.2 Reflector Properties

Upon examination of Reference 10.13 it was determined that the physical properties of the graphite in the reflector are approximately constant with respect to temperature. The following value is used for the current model.

Thermal Conductivity, k = 22.8 W/mK

The density and specific heat capacity do not impact the steady state simulations therefore the values are not repeated here.

10.3.9.3 Coolant Properties

The physical properties for the helium coolant are represented by temperature and pressure dependent quantities in the reflector and multi batch CFD models. The correlations that represent the property variations are taken from Reference 10.23 and are restated below. When radiation is modeled it is assumed that the helium does not participate in the radiation heat exchange.

$$\rho = 48.14 \cdot \frac{\left(P/1 \times 10^5\right)}{T}\left(1 + 0.446 \frac{\left(P/1 \times 10^5\right)}{T^{1.2}}\right)^{-1} \quad \frac{kg}{m^3}$$

$$\mu = 3.674 \times 10^{-7} \cdot T^{0.7} \quad Pa \cdot s$$

$$k = 2.682 \times 10^{-3} T^{0.71(1-2 \times 10^{-9} P)} (1 + 1.123 \times 10^{-8} P) \quad W/_{mK}$$

c_p=5195 J/kgK

Where P is the absolute pressure in Pa

             T is the absolute temperature in K

10.4 CFD Model of an Assembly of Pebbles Remote from a Reflector

This section is only concerned with the behavior within the PBR core at a location remote from the reflector region of the core.

The specific outputs of this work are:

1. The pressure drop per unit length within the core of a PBR for three different flow rates.

2. The local surface heat transfer coefficient on the pebbles in the core for three different flow rates.

3. The surface average heat transfer coefficient for sample pebbles in the core.

4. A comparison of predicted pressure drops and surface averaged heat transfer coefficients to the correlations of References 10.24 and 10.25.

5. An examination of pebble surface temperatures.

10.4.1 Approach and Fundamental Assumptions

To create a model within the PBR core at a location remote from the reflector, the locations of pebbles within a large stack of randomly dropped pebbles were first determined (Section 10.2). A cylindrical region centrally located in this stack of pebbles was then selected as the solution domain. To determine appropriate model dimensions, a domain size study was performed and documented in Appendix F.

This study indicated that cylindrical domains with a radius of greater than 2 pebble diameters were able to predict a reasonably smooth pressure drop. The diameter of the solution domain in the final analyses is 4 pebble diameters (0.24 m) across. To compare the model results to the KTA rules (Reference 10.25) for pressure drop it is necessary to have a solution domain at least 5 pebble diameters (0.30 m) in height. The final geometry in this analysis has a solution domain that is 0.42 m in length. This 0.42 m solution domain only contains the full pebble packing fraction over a 0.30 m region, the remainder of the solution domain is to improve the properties of the model boundary conditions (see Section 10.4.2.1 and Appendix E for details).

For this work it is assumed that the pebbles are perfectly spherical (except for local contact deformation) and smooth. Any damage to pebbles such as cracks, are not included in the current geometry. Figure 10.4.1 shows the modeled geometry that was used for all final analyses reported in Section 10.4.

Figure 10.4.1: Model Geometry for Pebbles Remote from the Reflector
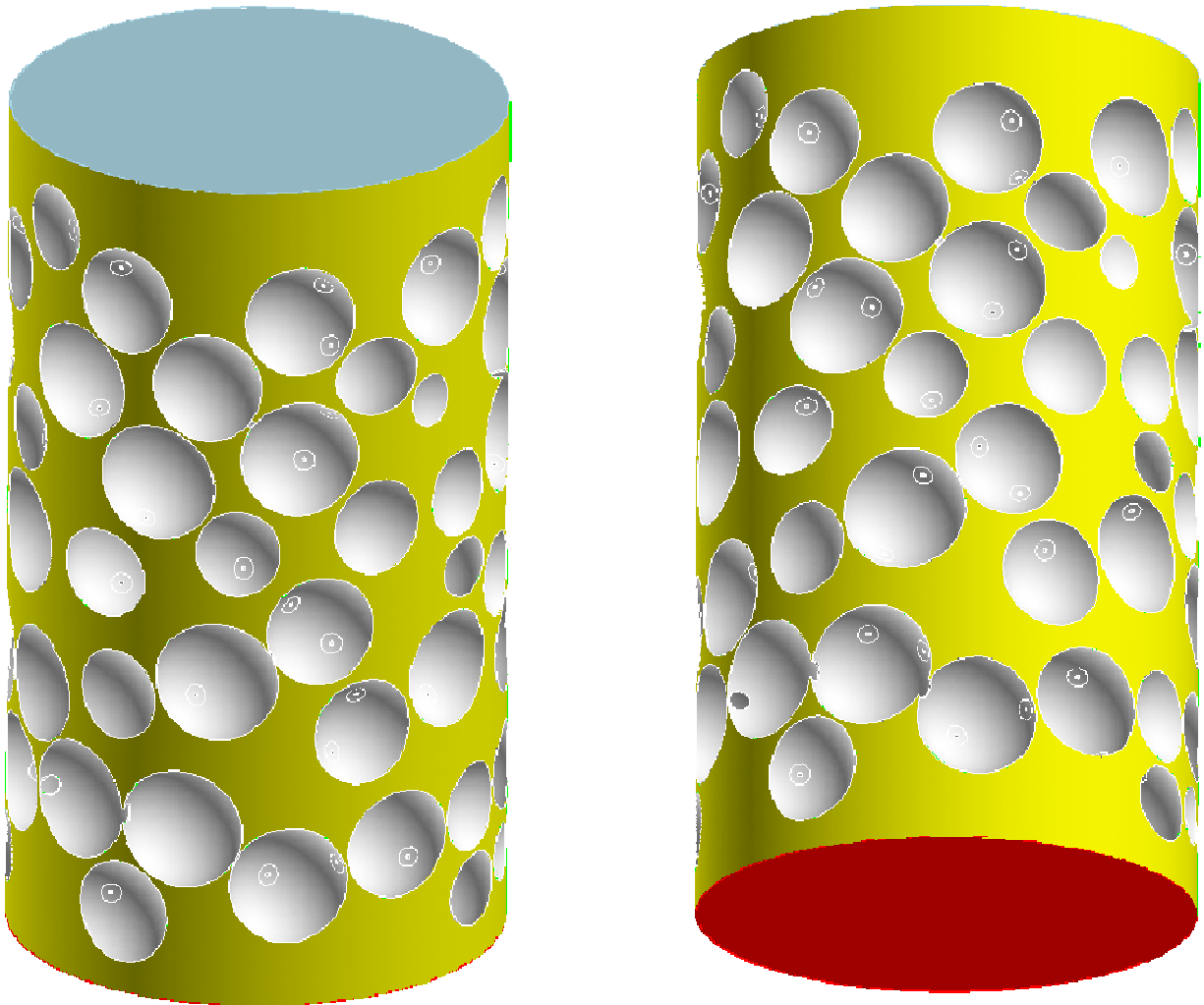
The pebbles in this model are full sized (0.06m diameter) and in direct contact with one another, with a contact area estimated from a contact deformation analysis. The use of a realistic contact area between pebbles will facilitate future analysis for the determination of conduction between pebbles. To produce a consistent contact area between pebbles it was necessary to remove a small amount (< 0.2% of domain volume) to represent the contact deformation. The geometry of the removed fluid is that of a 16 sided prism aligned with the contact point as shown in Figure 10.3.1b.

This model contains 129 pebbles. Of these, 49 pebbles do not touch the boundaries of the solution domain.

In this first study the estimation of pressure drop through the PBR core is based on an isothermal model. It is recognized that the actual flow within a PBR core is not isothermal. In an isothermal model all fluid property variations are neglected. The justification and estimated errors in using an isothermal model are discussed in Appendix G and Appendix I. A second study has been performed which includes the thermal solution for this domain. A third sensitivity study was performed with the power proportional to the coolant flow rate.

The estimation of local and average heat transfer coefficients is based on an isothermal and thermal model. The prediction of heat transfer coefficients using the isothermal model is facilitated through the use of the modified Reynolds or Chilton-Colburn heat transfer analogy. The justification for using this analogy within the current work is discussed in Appendix H. It is recognized that this approach does neglect several effects such as property variations, radiation heat transfer and several other effects; however, this work is still expected to give a reasonable estimate on the value and variation of pebble surface heat transfer coefficients. The Reynolds analogy solution and the thermal model solution are compared with the German KTA rules.

10.4.2 CFD Models Used for the Reference Case

This section describes a three-dimensional CFD model that has been developed to predict the heat transfer and pressure drop within an assembly of randomly[3] packed pebbles. The following sub-sections describe the geometry modeled, material properties, boundary conditions, turbulence closure models and numerical methods used in the model for the prediction of heat transfer coefficients and pressure drop in a PBR core.

10.4.2.1 Boundary Conditions

The model created for this work has four basic types of surfaces that can be seen in Figure 10.4.1. The top surface and bottom surfaces (blue and red) will be described as the "inlet" and "outlet", respectively, throughout this document. The cylindrical boundary of the solution domain will be referred to as the "symmetry" boundary condition. All remaining physical pebble surfaces (white) will be referred to as "walls" or "no-slip walls".

A fundamental assumption for this model is that the coolant flows through the pebble bed from one end to the other; from inlet to outlet. In other words there are no coherent flow patterns moving against the general flow direction that are larger than the vertical height of the solution domain (no large scale swirling motion). This is believed to be a reasonable assumption since the solution domain is approximately 5

---

[3] The assortment is not totally random, but contains random elements. The procedure for generating the pebble positions is documented in Section 10.2.

pebble diameters in height and it is expected that large scale flow structures will be broken up within a very small number of pebble diameters due to the random nature of the pebble packing.

Inlet

The inlet surface was modeled as a constant velocity boundary condition with a constant specified turbulence intensity and length scale. For all simulations the turbulence intensity was set to 2.5% (low fluctuation) at the inlet with a length scale of 0.5 of a pebble diameter (i.e., 0.03 m). There is no information on the turbulence at the inlet so this simplistic approach is accepted. The velocity used for this boundary condition was determined from the flow rate for the entire core divided by the product of the coolant density and total core flow area. For this work total core flow rates of 15kg/s, 75kg/s and 150kg/s are used which translate into velocities of 0.48m/s, 2.4m/s and 4.8m/s.

An important feature of the modeled geometry is that an entrance region is incorporated into the model (See Figure 10.3.2c). Without an entrance region a non-physical shear stress would result when a no-slip wall boundary condition touches an inlet boundary condition. The imposition of both a no-slip and fixed velocity boundary condition to a single cell in the model can produce an infinite velocity gradient (as the mesh resolution increases) and in turn an infinite shear stress. Since the purpose of the current study is to estimate heat transfer coefficients through an examination of the shear stress the inclusion of an entrance region is a key feature in this model.

Outlet

The outlet boundary condition is set to be a plane of constant pressure (on average). In absolute terms the pressure at the outlet is set to a value of 89.1 bar, however in the simulation the relative pressure is set to zero. For an incompressible fluid (as assumed in this simulation) the absolute pressure level is not relevant and any relative pressure may be set at the outlet. The outlet boundary condition in FLUENT allows flow to exit or enter the solution domain as required. All flow that re-enters the solution domain at this boundary condition is specified to enter in a direction normal to the boundary condition and to have a turbulence intensity and length scale of 2.5% and 0.03 m, respectively. The outlet region of the model contains a region of reduced packing fraction that is not included in the final results (see Figure 10.3.2c). The purpose of this exit region is to minimize the influence of the outlet boundary condition and particularly the re-entrant flow that may not match the characteristics of the remainder of the flow.

Symmetry

The outer wall of the cylindrical domain (curved side on the cylinder) in reality has flow entering and exiting the solution domain at various points along it. The pressure distribution along the outer wall of the solution domain is also unknown and will vary significantly locally. It was decided that the most reasonable approximation for this boundary would be to define it as a symmetry plane. The symmetry plane will allow

no flow to enter or exit the solution domain and it will not introduce any artificial pressure drop as would be found if a no-slip wall boundary condition were applied.

In order to assure that the simulation is accurate significant efforts were made to keep the symmetry condition as far away from the pebbles of interest as possible (see Appendix F).

Pebble Surface

The surface of each pebble was modeled as an impermeable no-slip wall. Due to the low Mach number of the flow this is considered to be a reasonable boundary condition. The most significant approximation with this boundary condition may be that the pebbles are modeled as smooth surfaces.

10.4.2.2 Turbulence Model

For the purposes of this work the flow in the bed of pebbles has a Reynolds number of the order 1,000-10,000. Reference 10.18 presented a review of literature on transitional Reynolds numbers for packed beds and this review indicated that a reasonable transition range is between Reynolds numbers of 60-130. It is therefore assumed that all flows in this work will be turbulent. It is also expected that the flow will become laminar at local portions in the packed bed near pebble-to-pebble contact locations.

Based on the assumption that the flow is turbulent (and possibly mixed laminar and turbulent flow), a turbulence model was selected as direct numerical simulation is well beyond the available computational resources.

The study of turbulence and the development of turbulence models is an ongoing research topic and as such there are not many hard rules in selecting a model. Different turbulence models have been shown to offer superior performance depending on the nature of a particular problem. Each turbulence model involves a number of assumptions regarding the nature of the turbulence in a flow. It is not uncommon to apply turbulence models to situations for which the assumptions upon which they were developed are violated. In some situations simplistic turbulence models can perform better than complex models. The only true method of determining what turbulence model is correct is to compare its results against experimental results. There is however limited experimental information on the flow within a large packed bed of pebbles as the experimental setup is difficult.

Reference 10.19 presents the comparison of CFD results to experimental results for a small packed bed. This work shows that reasonable pressure drops can be estimated by both turbulence models examined (k-epsilon and Reynolds Stress Model (RSM)). Reference 10.17 presents a similar comparison as Reference 10.19 where a k-epsilon model is used to predict the flow and heat transfer in a small packed bed with reasonable accuracy. In the work of Reference 10.11 a CFD analysis of the heat transfer and flow over a heated cylinder is performed and compared with experimental data. The results of the comparison are that the k-omega and Large Eddy Simulation

(LES) turbulence models offered superior predictions as compared with the k-epsilon, SST and the Reynolds Stress Models. It is also noted that the SST and RSM perform better than the k-epsilon model in this situation. The work does indicate that the Large Eddy Simulation has a tendency to over predict local temperatures when results are compared with experimental data. This reference argues that the performance of the turbulence models for the prediction of flow over a heated cylinder will reasonably transfer to the prediction of flows through a packed bed.

Based on this brief literature review the SST model with corrections for transitional flows was selected for this work. The SST model is a blend of the k-epsilon and k-omega models. This model is considered to be a reasonable compromise between the proven results of the k-epsilon model in References 10.19 and 10.17, with the more extensive turbulence model study of Reference 10.11 showing advantages to the k-omega model.

The selection of this model requires excellent near wall resolution to get reasonable results. Significant efforts were made in the mesh generation process to facilitate having meshes with average y+ values of 1.0.

10.4.3 CFD Models Used for Sensitivity Cases with Heat Transfer Included

Sensitivity studies were performed using the model described in Section 10.4.2 but solving the energy equation. The solution of the energy equation allows heat transfer coefficients to be calculated directly from the temperature solution and several approximations in Section 10.4.2 related to constant material properties can be removed. The material properties used are described in Section 10.3.9.

While the introduction of the energy equation removes many approximations it also introduces additional modeling complexities. This model does not consider radiation heat transfer or pebble-to-pebble conduction. These details are addressed in Section 10.7. For these sensitivity cases, only the SST turbulence model is used.

The CFD models used for this work are identical to those used in the work documented in Section 10.4.2 with the exception of the changes described in the following sub-sections.

10.4.3.1 Computational Mesh

The computational mesh for this model is identical to that of Section 10.3.7 with the addition of shell elements within the pebbles. Each of these 3 models was modified such that the outer 5 mm of each pebble was represented by shell elements (Reference 10.10).

The mesh was also modified such that all pebble surfaces were then merged into a single surface region. This step is necessary when using shell element as they only allow conduction within a given surface region and not between surface regions.

10.4.3.2 Boundary Conditions

All boundary conditions are the same as the work performed for the reference case and documented in Section 10.4.2, with the exception of the outlet boundary condition, and the heat flux applied to the pebbles, which are described below.

Outlet

The outlet boundary condition is set to be a plane of constant pressure as previously described. A change is made to the temperature of the re-entrant flow, which was set to 1070K, 1100K and 1350K for the 150 kg/s, 75 kg/s and 15 kg/s cases respectively[4]. These values were approximated from the outlet temperatures of the cases documented in Section 10.5.2.3.

Pebbles

A constant heat flux of 147,377 W/m² was applied to the inner surface of the shell elements within all pebbles in the model. This heat flux is taken from Reference 10.13 and is representative of the heat flux remote from the reflector at the same axial location within the core that was used in Section 10.5.2. Refer to Section 10.5.2.3 for details.

10.4.3.3 Buoyancy Model

The model includes buoyancy forces that are generated directly from coolant density variations. The gravitational acceleration vector in this model points in the direction of the flow and has a magnitude of 9.81 m/s².

10.4.4 CFD Models Used for Sensitivity Cases with the Power Proportional to the Coolant Flow

Sensitivity studies were performed using the model described in Section 10.4.2 but varying the reactor power such that it decreases in proportion to the coolant flow rate, which is more reflective of how the reactor would operate. The CFD models are identical to those used in the work documented in Section 10.4.2. Therefore, the modeled geometry, computational mesh, material properties, turbulence and buoyancy model settings are unchanged from the cases previously run at 15 kg/s and 75 kg/s. The only change that was made for these sensitivity cases is that the reactor power is assumed to be proportional to the coolant mass flow rate.

The differences in the boundary conditions used for these cases, compared with the models in Section 10.4.2, are presented in the sub-sections below.

---

[4] The power was held constant in all three models resulting in temperatures for the 75 kg/s and 15 kg/s cases being higher than would be obtained in a real reactor. The actual reduced power at these lower flow rates is examined in Section 10.4.7.

10.4.4.1 Boundary Conditions

All boundary conditions are the same as in the previous work documented in Section 10.4.2, with the exception of the heat flux applied to the pebbles and the outlet boundary condition, which are discussed below.

Pebbles

A constant heat flux of 147,377 W/m² was applied to the inner surface of the shell elements within all pebbles in the model in the work presented in Section 10.4.3. This heat flux corresponds to 100% coolant flow in the reactor (i.e., 150 kg/s). Therefore, 15 kg/s and 75 kg/s correspond to 10% and 50% coolant flow in the reactor, respectively. Assuming that the reactor power is proportional to the coolant mass flow the heat fluxes applied to the pebble interiors in the 15 kg/s case is 14,737.7 W/m^2 and for the 75 kg/s case is 73,688.5 W/m^2.

Outlet

After the pebble heat fluxes were updated the expected temperature increase of the coolant in the model was calculated from a simple heat balance. Using Fluent to calculate the total mass flow and heat addition for the domain used in the model it was found that the increase in the coolant as it passes from the inlet to the outlet of the model is about 32 K. Therefore, the temperature of any fluid that flows back in the outlet region was set to 1065 K (i.e., the inlet temperature from Section 10.3.8, 1033K plus 32 K). Since power is proportional to flow in these cases, and the inlet temperature is the same, the same outlet temperature boundary condition can be applied to the different flow rate cases.

10.4.5 Results of Reference Case

Throughout the discussion of these results the applicable region will be referred to. This region which is shown in Figure 10.3.2 (as Valid Simulation Region), is a 0.30 m vertical region, centrally located on the solution domain that contains a full compliment of pebbles. While there are pebbles outside of this region they are in regions of reduced pebble packing fraction and these pebbles are not considered in the final results.

10.4.5.1 Pressure Drop

This section presents the pressure drop predictions of a flow through the CFD simulation compared with the results of the correlations from the KTA rules of Reference 10.25.

KTA Pressure Drop Correlation

The KTA rules provide the following correlation to give the pressure drop in units of Pa/m through the PBR core (Reference 10.25).

$$\frac{\Delta P}{\Delta H} = \psi \left(\frac{1-\varepsilon}{\varepsilon^3} \right) \left(\frac{1}{d} \right) \left(\frac{1}{2\rho} \right) \left(\frac{\dot{m}}{A} \right)^2$$

Where

$$\psi = \frac{320}{\left(\dfrac{\text{Re}}{1-\varepsilon} \right)} + \frac{6}{\left(\dfrac{\text{Re}}{1-\varepsilon} \right)^{0.1}}$$

and

$$\text{Re} = \frac{\left(\dfrac{\dot{m}}{A} \right) d}{\mu}$$

Further:

> $\Delta P / \Delta H$ is the pressure drop per unit length in units of Pa/m
>
> ε is the void fraction in the packed bed (equivalent to 1-packing fraction)
>
> ρ is the average coolant density in the packed bed in units of kg/m³
>
> $\dot{m}$ is the total core mass flow rate in units of kg/s
>
> A is the core cross-sectional area m²
>
> μ is the coolant viscosity calculated at the average of the coolant and pebble surface temperature in units of (Pa)(s)
>
> d is the pebble diameter in units of m

The correlation predicts the pressure drop within ±15% with 95% confidence if used within its applicable range.

The applicable range for this equation is:

- Reynolds number, Re: $1 < \text{Re}/(1 - \varepsilon) < 10^5$

- Porosity of the bed: $0.36 < \varepsilon < 0.42$

- For Reynolds numbers of 10,000 or greater a (Domain radius)/d ratio of ~4 is suitable.

- For lower Reynolds numbers, larger domains are required.

- Height of bed > 5 d

The models in this work satisfy all of these constraints except for the required (Domain radius)/d ratio for low flow cases.

CFD Model Pressure Drop Predictions

Each point in the data series "Model=XXXkgs-SST" in Figure 10.4.2, Figure 10.4.3 and Figure 10.4.4 represents the area weighted average pressure across the entire solution domain at a fixed vertical location in the model. The figures also include a linear least-squares best fit line for the CFD model data with its corresponding equation. This data only includes points within the valid simulation region. The nominal, upper bound and lower bound on the KTA rules pressure drop correlation are also included in the figures for reference.

Figure 10.4.2: Pressure Drop Prediction for 150kg/s Core Coolant Flow Rate

$$y = -11490x + 1632.4$$

Figure 10.4.3: Pressure Drop Prediction for 75kg/s Core Coolant Flow Rate

$y = -3014.5x + 446.22$

Legend: Model-75kgs-SST · KTA rules nominal · KTA Lower Bound · KTA Upper Bound · Linear (Model-75kgs-SST)
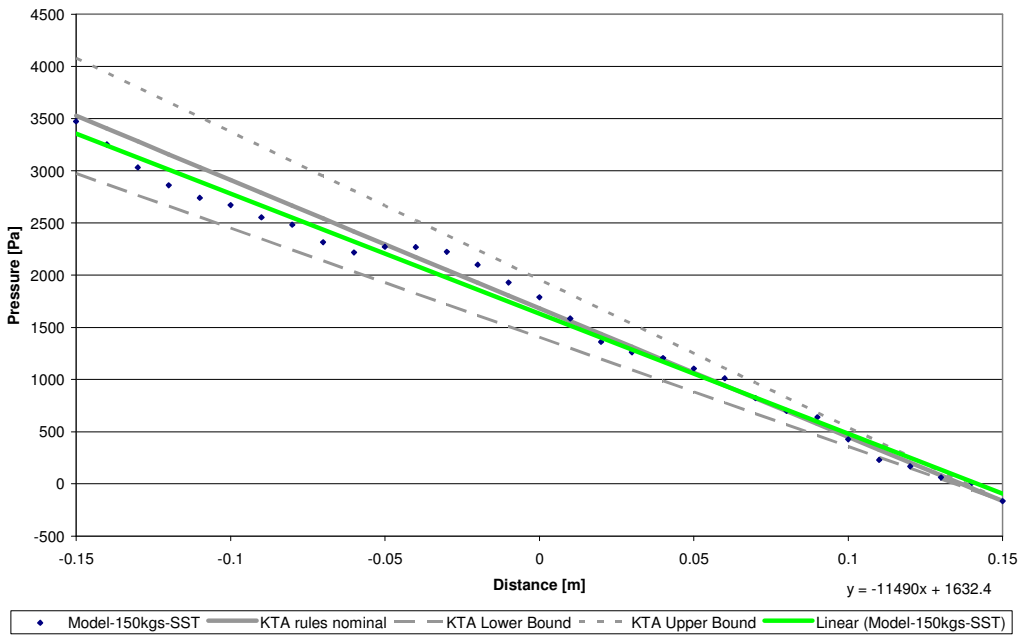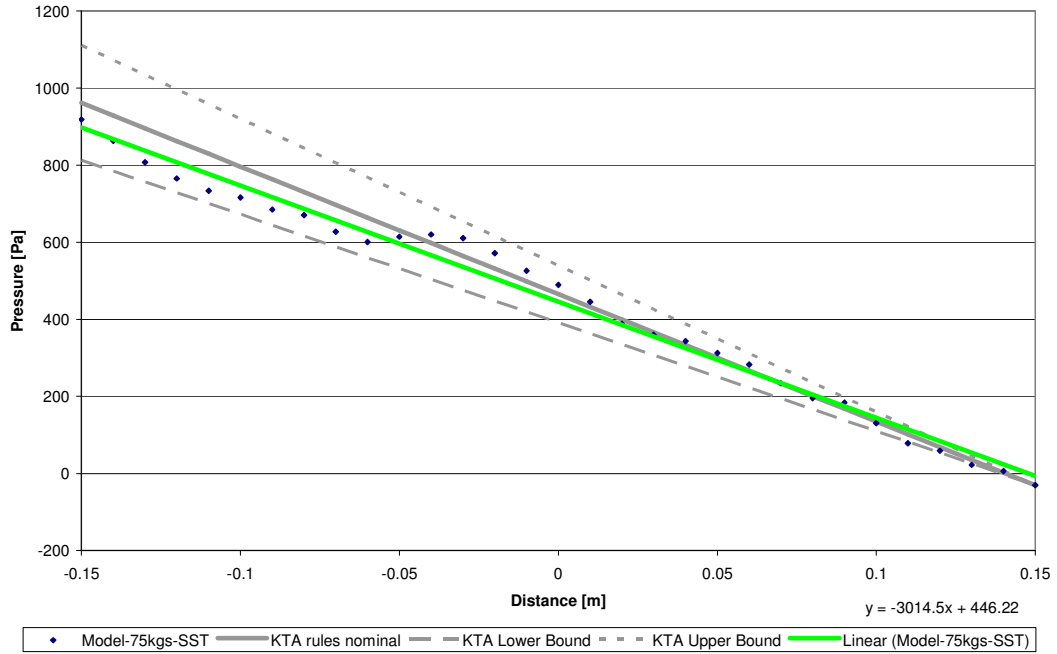
Figure 10.4.4: Pressure Drop Prediction for 15kg/s Core Coolant Flow Rate

$y = -137.57x + 21.287$

Legend: Model-15kgs-SST · KTA rules nominal · KTA Lower Bound · KTA Upper Bound · Linear (Model-15kgs-SST)
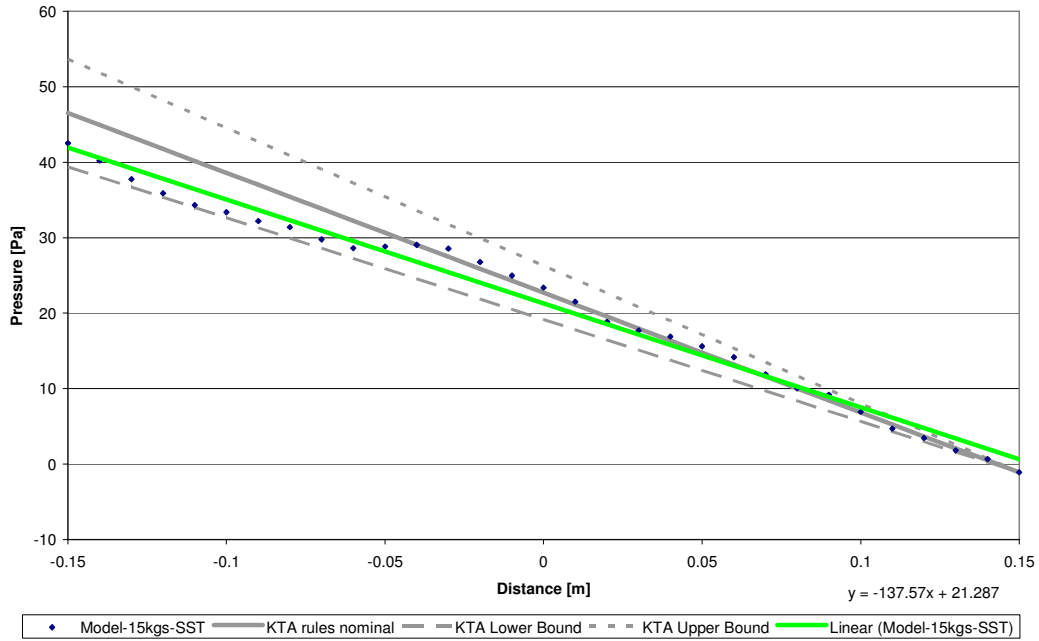
Table 10.4.1 summarizes the results shown in Figure 10.4.2, Figure 10.4.3 and Figure 10.4.4. The pressure drop value in the table is taken from the slope of the least squares best fit line in Figure 10.4.2, Figure 10.4.3 and Figure 10.4.4.

Table 10.4.1: Pressure Drop Prediction Summary

| Flow Rate | Pressure Drop (Pa/m) | | | CFD Model |
| | KTA rules correlation from Reference 10.25 | | | |
	Nominal	Lower Bound	Upper Bound	Nominal
15 kg/s	159	135	183	138
75 kg/s	3308	2812	3804	3015
150 kg/s	12307	10461	14153	11490

It was found that the pressure drop predicted by all CFD models fell within the limits of the KTA rules pressure drop correlation. This result indicates that the CFD model can reasonably predict the pressure drop in the core of a PBR in a location remote from the reflector.

10.4.5.2 Shear Stress

This section examines the shear stress distribution on pebbles within the valid simulation region. The following figures present the shear stress distribution over two selected pebbles for 3 different flow rates.

Figure 10.4.5: Shear Stress Distribution on Selected Pebbles at 150kg/s Core Coolant Flow Rate (top images are viewed from −Y direction, bottom images are viewed from the +Y direction, pebble contacts indicated by dashed lines)
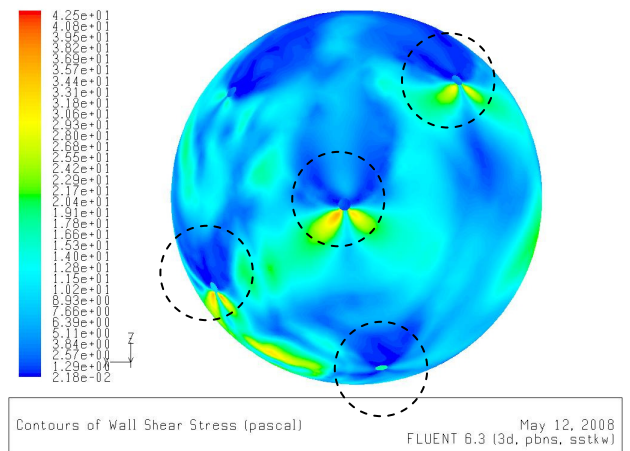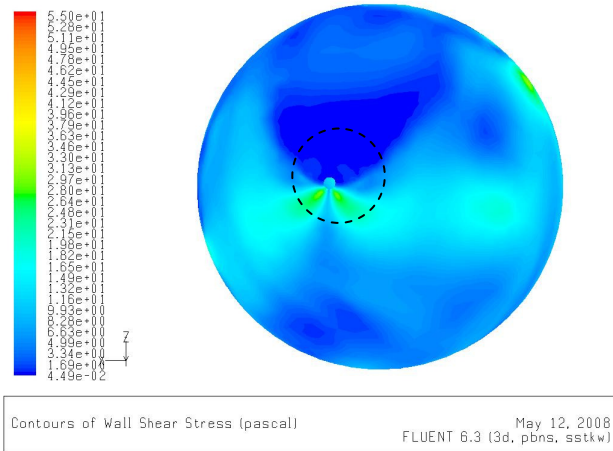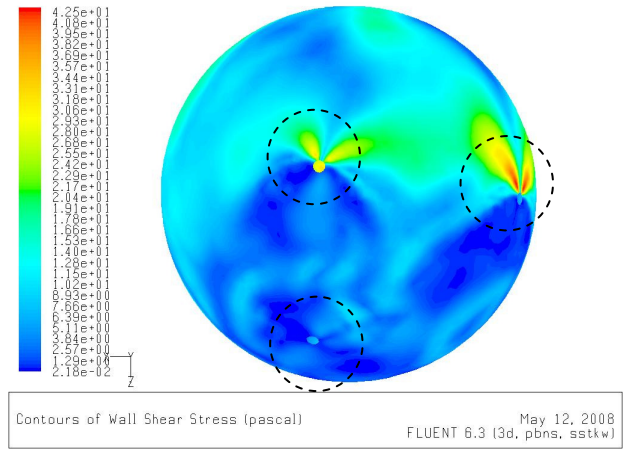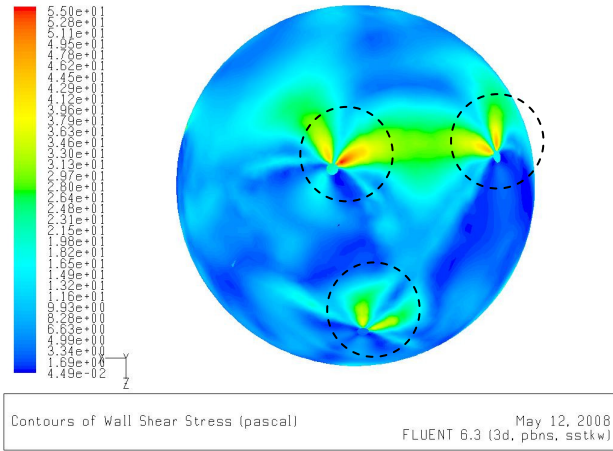
a. Pebble with 5 contacts (pebble post processing label 154)

b. Pebble with 8 contacts (pebble post processing label 160)

Figure 10.4.6: Shear Stress Distribution on Selected Pebbles at 75kg/s Core Coolant Flow Rate (top images are viewed from −Y direction, bottom images are viewed from the +Y direction, pebble contacts indicated by dashed lines)
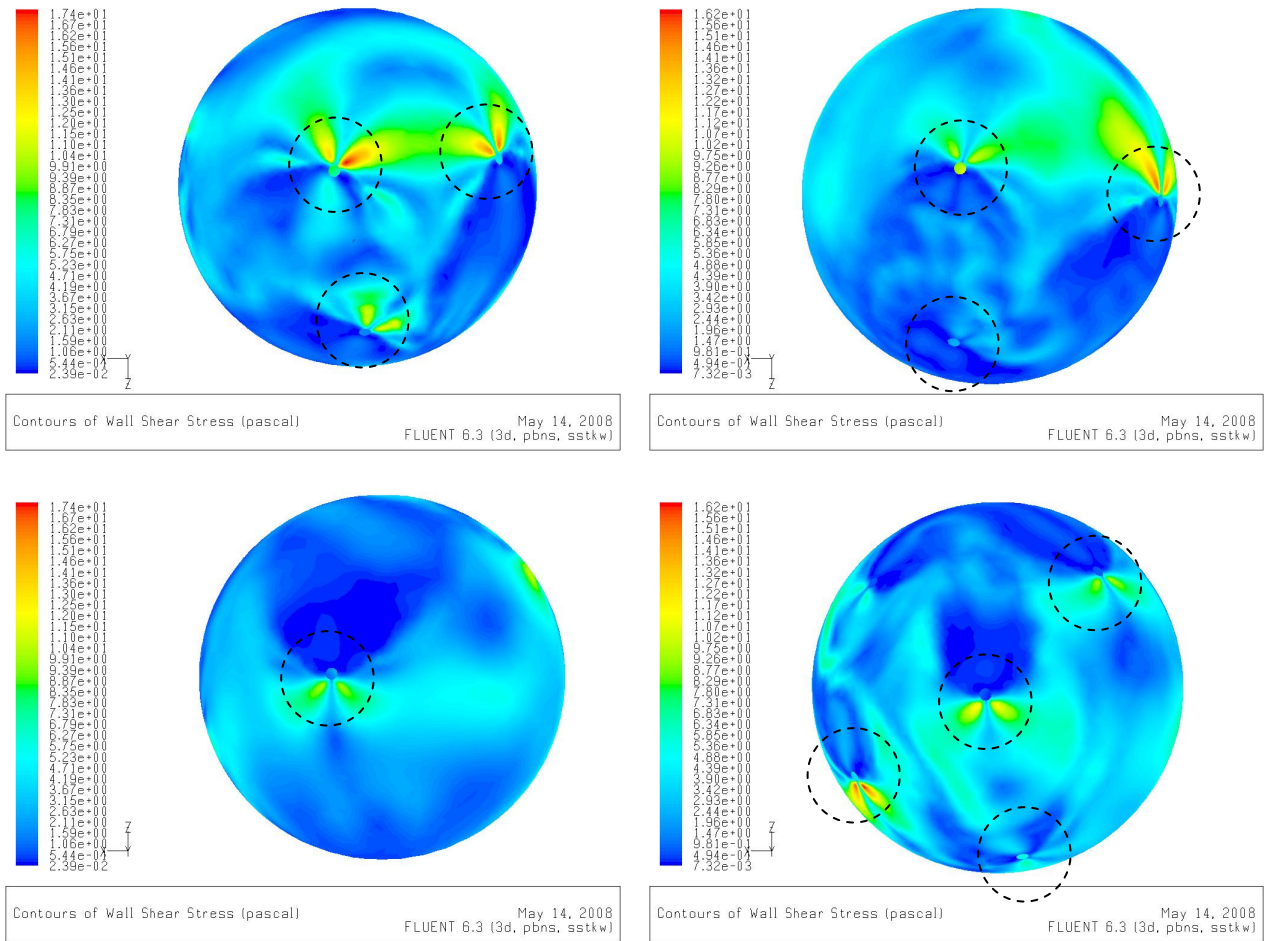
a. Pebble with 5 contacts (pebble post processing label 154)

b. Pebble with 8 contacts (pebble post processing label 160)

Figure 10.4.7: Shear Stress Distribution on Selected Pebbles at 15kg/s Core Coolant Flow Rate (top images are viewed from −Y direction, bottom images are viewed from the +Y direction, pebble contacts indicated by dashed lines)
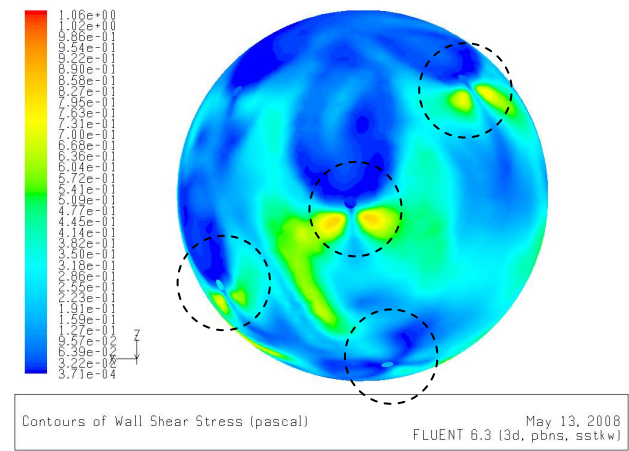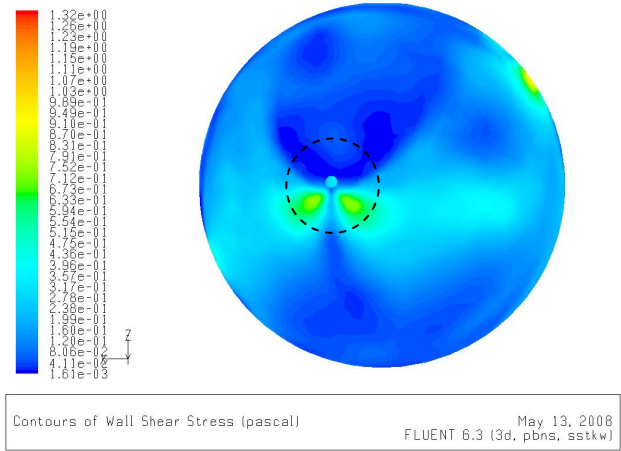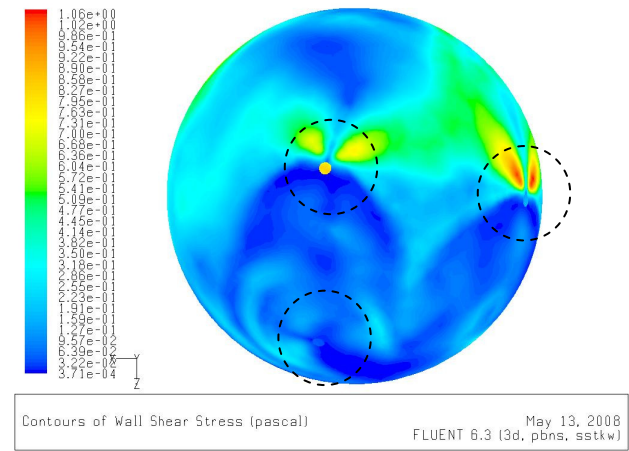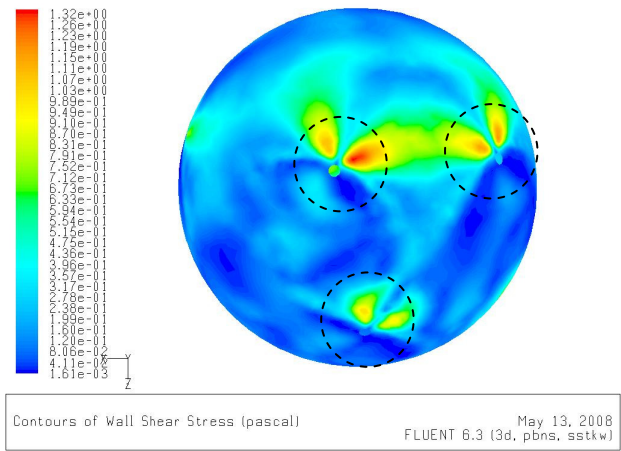
a. Pebble with 5 contacts (pebble post processing label 154)

b. Pebble with 8 contacts (pebble post processing label 160)

An examination of these figures indicates that there is a significant variation in the shear stress over the surface of a single pebble. Figure 10.4.8 show the shear stress distribution near a representative pebble to pebble contact location.

Figure 10.4.8: Representative Shear Stress Distribution in the Vicinity of Pebble-to-Pebble Contact

Contact Area ───→

←5mm→
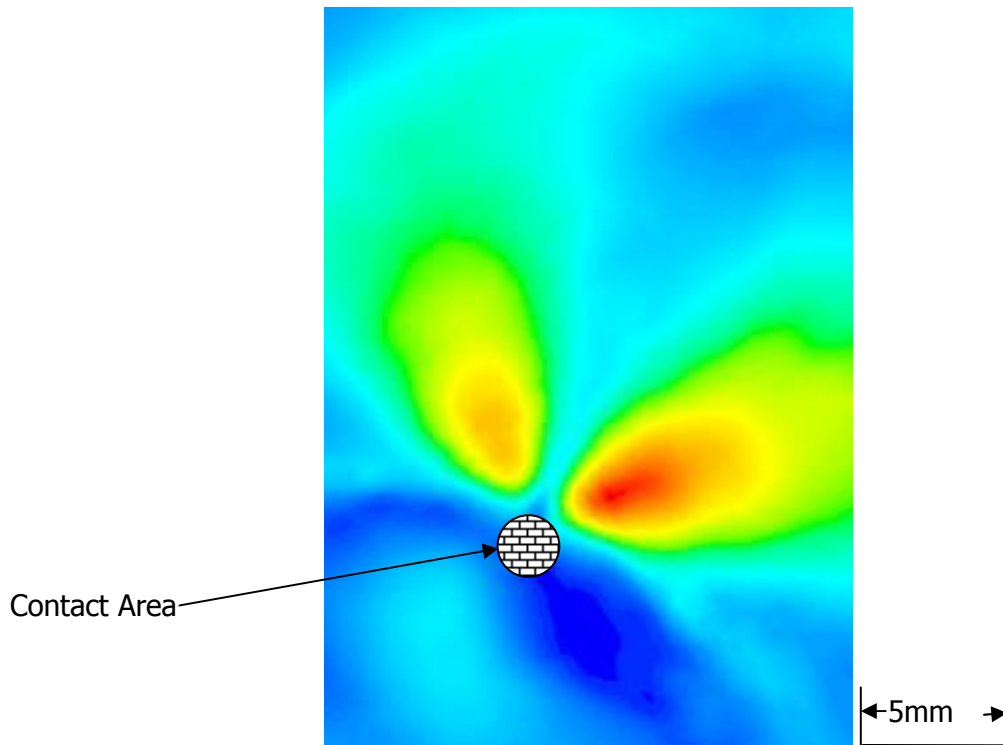
Peak shear stresses are found at locations approximately 2-5mm from the pebble to pebble contact location. At locations within approximately 1mm of the pebble to pebble contact location shear stresses fall off rapidly.

10.4.5.3 Heat Transfer Coefficient

KTA Correlation Heat Transfer Coefficients

The KTA rules correlation for heat transfer within a PBR is defined by the following equations (for Nusselt number and hear transfer coefficients respectively) (Reference 10.24):

$$Nu = 1.27 \left(\frac{Pr^{\frac{1}{3}}}{\varepsilon^{1.18}} \right) Re^{0.36} + 0.033 \left(\frac{Pr^{\frac{1}{2}}}{\varepsilon^{1.07}} \right) Re^{0.86}$$

$$h = \frac{Nu \cdot k}{d} \quad \text{in W/m}^2\text{K}$$

Where: Pr is the Prandtl number, and

k is the thermal conductivity of helium in W/mK.

See Section 10.4.5.1 for the definitions of the other symbols.

The correlation predicts the heat transfer coefficient within ±20%[5] with 95% confidence if used within its applicable region.

The design range for this correlation is within the following constraints:

- Porosity of the bed, $0.36 < \varepsilon < 0.42$

- Diameter ratio (domain radius)/d > 20

- Height of bed > 4 d

- Reynolds number $100 < Re < 10^5$

For the current analysis the diameter ratio criteria can not be met. This correlation will still be used, keeping in mind that it may not be totally applicable to the model.

CFD Model Heat Transfer Coefficients

The heat transfer coefficient can be estimated by utilizing the pebble shear stress and the Chilton-Colburn heat transfer analogy (i.e., modified Reynolds analogy), see Reference 10.26 (details are provided in Appendix H). The analogy equations can be rearranged to yield the following equation for predicting heat transfer coefficients.

$$h = \frac{\tau \cdot c_P}{V_{ref} \cdot \mathrm{Pr}^{2/3}}$$

$$\mathrm{Pr} = \frac{c_P \cdot \mu}{k}$$

Where h is the heat transfer coefficient, τ is the wall shear stress, c_p is the specific heat capacity of helium, Pr is the Prandtl number, μ is the viscosity of helium, k is the thermal conductivity of helium and V_{ref} is a reference velocity.

All quantities in this equation are accurately known except for $V_{ref.}$

The KTA rules heat transfer correlation (Reference 10.24) uses the pebble average surface temperature and subtracts the bulk fluid temperature to define the heat transfer coefficient. Analogous to the KTA heat transfer coefficient is to define V_{ref} as the bulk velocity of the fluid near a given pebble.

---

[5] Reference 10.24 indicates that the uncertainty range is +20%. It was assumed that this was a typographical error and should have been ±20%.

$$V_{ref} = \frac{\dot{m}}{\rho \cdot A \cdot (1-\alpha)}$$

Where, $\dot{m}$ is the full core coolant flow rate, ρ is the density of helium, α is the core model packing fraction and A is the cross sectional area of the PBR core (without pebbles in it).

This reference velocity is an estimate of the average flow velocity through the pebble bed and will differ for each mass flow rate in this work.

Figure 10.4.9, Figure 10.4.10 and Figure 10.4.11 summarize the maximum heat transfer coefficient calculated on each pebble with a centroid within the valid simulation region. Based on the results of the domain size study in Appendix F pebbles with centroids within 0.04 m of the symmetry boundary were also removed from the heat transfer coefficient calculations. This data was constructed by extracting the maximum pebble shear stress (face or facet value) from each of the pebbles in the valid simulation region and converting these values to heat transfer coefficients using the modified Reynolds analogy. The figures present a histogram of the maximum heat transfer coefficient found on the selected pebbles. The frequency axis on these figures represents the number of pebbles with maxima that fall within the specified bins. The "frequency" series on these figures is the probability density function while the "cumulative" series represents the cumulative distribution function.

Figure 10.4.9: Distribution of Maximum Heat Transfer Coefficient on Pebbles at 150kg/s Core Coolant Flow Rate
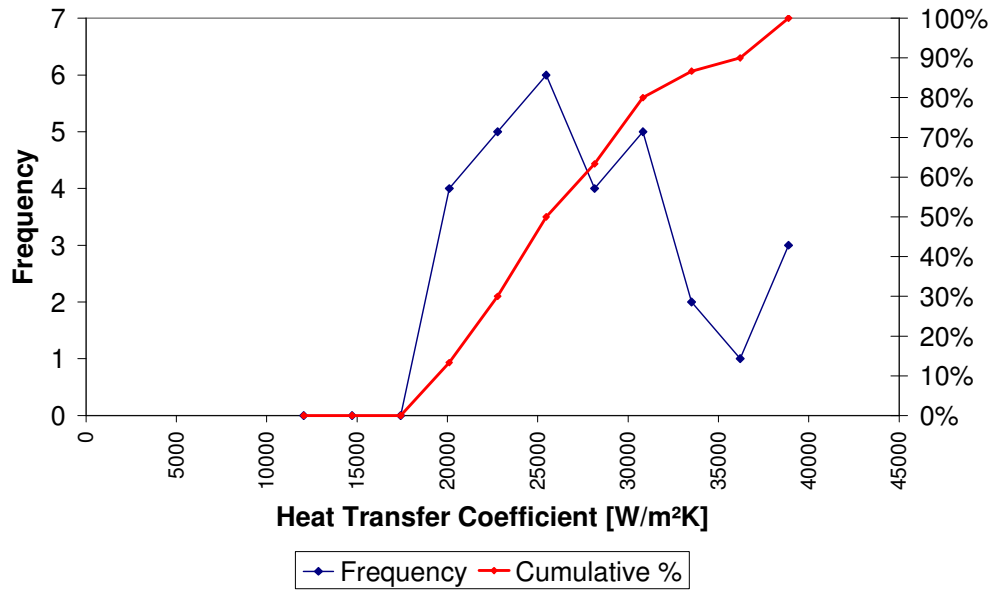
Figure 10.4.10: Distribution of Maximum Heat Transfer Coefficient on Pebbles at 75kg/s Core Coolant Flow Rate
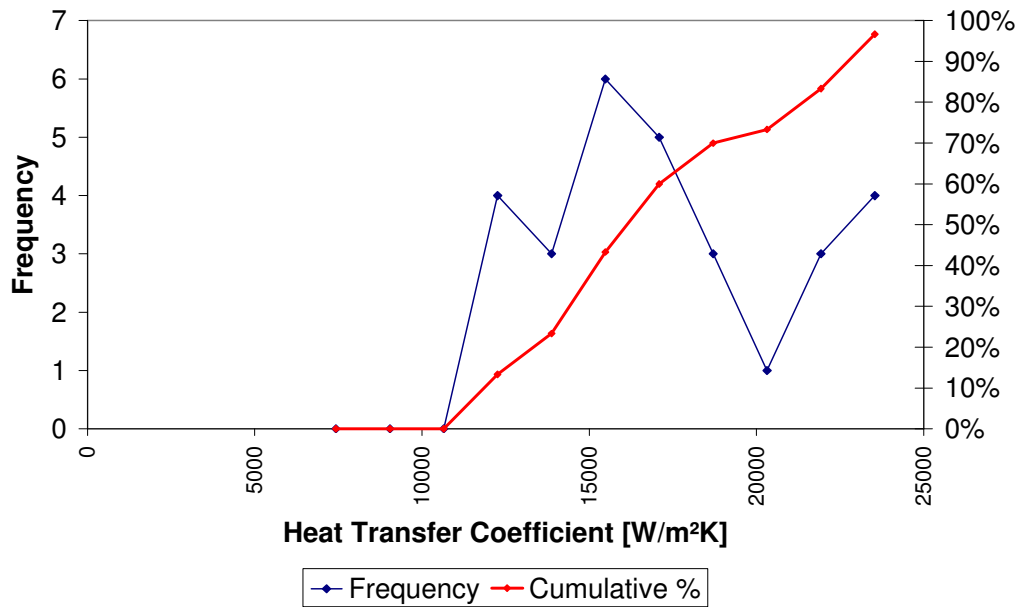
Figure 10.4.11: Distribution of Maximum Heat Transfer Coefficient on Pebbles at 15kg/s Core Coolant Flow Rate
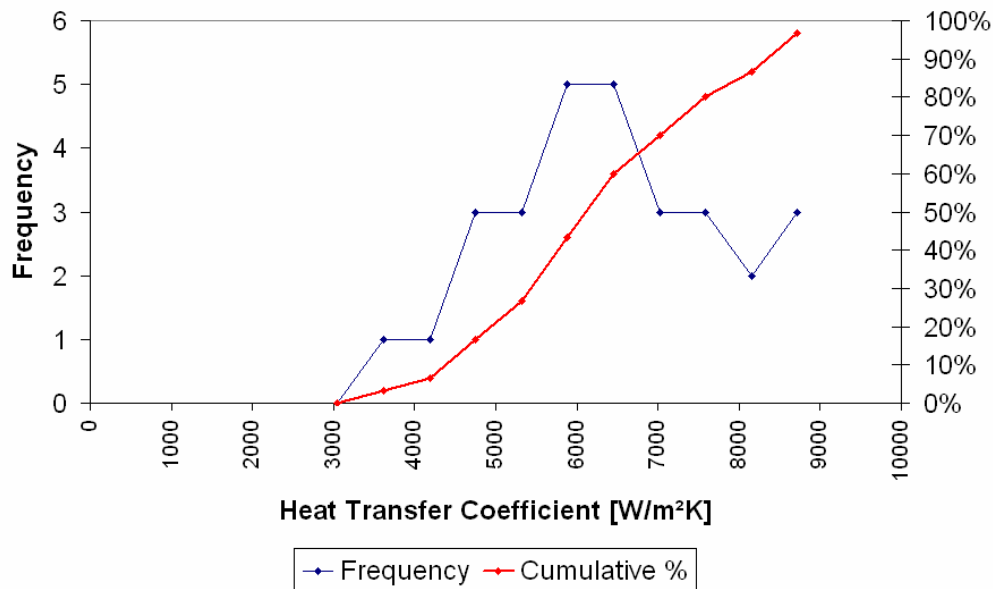
Figure 10.4.12, Figure 10.4.13 and Figure 10.4.14 summarize the area weighted average heat transfer coefficient calculated on each pebble with its centroid within the valid simulation region and more than 0.04m from the symmetry boundary condition. This data was constructed by extracting the area weighted average pebble shear stress (face or facet value) from each of the pebbles in the selected region and converting these values to heat transfer coefficients using the modified Reynolds analogy.

The figures present a histogram of the average heat transfer coefficient found on the selected pebbles. The frequency axis on these figures represents the number of pebbles with maxima that fall within the specified bins. The "frequency" series on these figures is the probability density function while the "cumulative" series represents the cumulative distribution function. The figures also indicate the heat transfer coefficient prediction from the KTA rules correlation including the upper "KTA maximum" and lower "KTA minimum" 95% confidence error bounds.

The domain radius required for the KTA rules heat transfer coefficient correlation to be valid is 10 pebble diameters where the current model has a radius equal to 2 pebble diameters. The KTA heat transfer correlation is still arguably applicable to the current CFD model because the model is actually a representative subset of a domain with a radius significantly greater that 10 pebble diameters.

Figure 10.4.12: Distribution of Average Pebble Heat Transfer Coefficient at 150kg/s Core Coolant Flow Rate
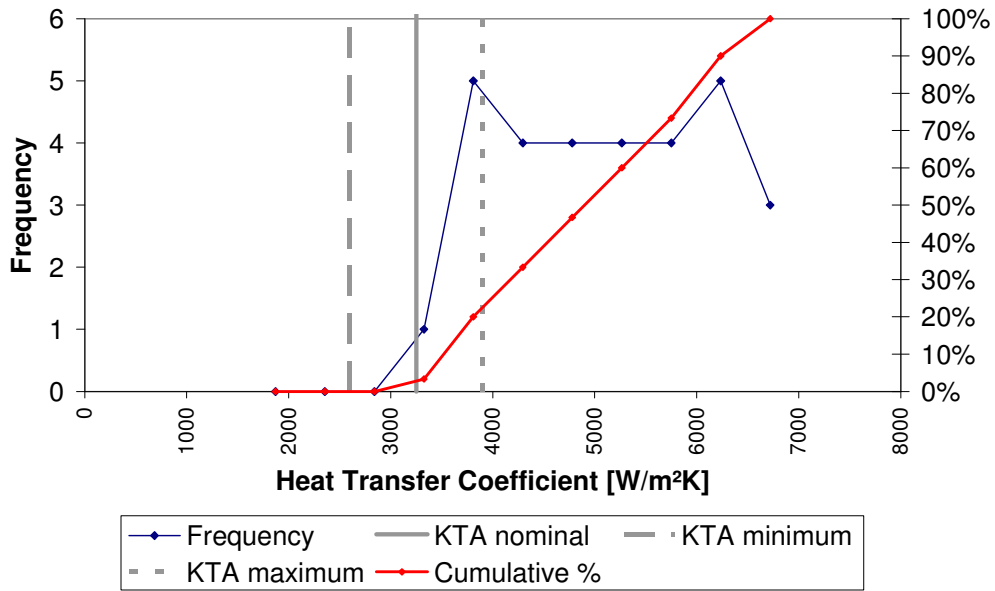
Figure 10.4.13: Distribution of Average Pebble Heat Transfer Coefficient at 75kg/s Core Coolant Flow Rate
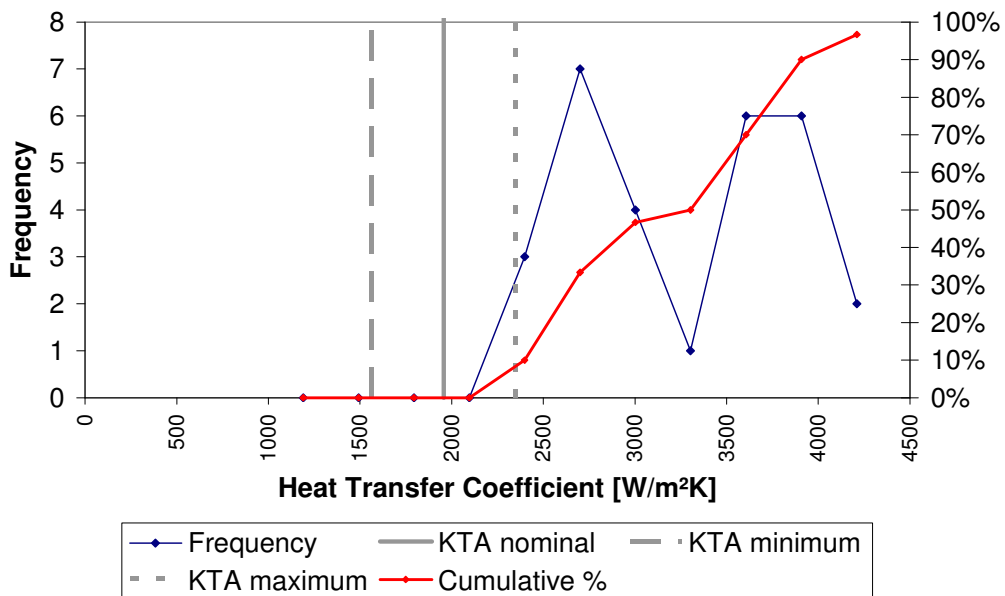
Figure 10.4.14: Distribution of Average Pebble Heat Transfer Coefficient at 15kg/s Core Coolant Flow Rate
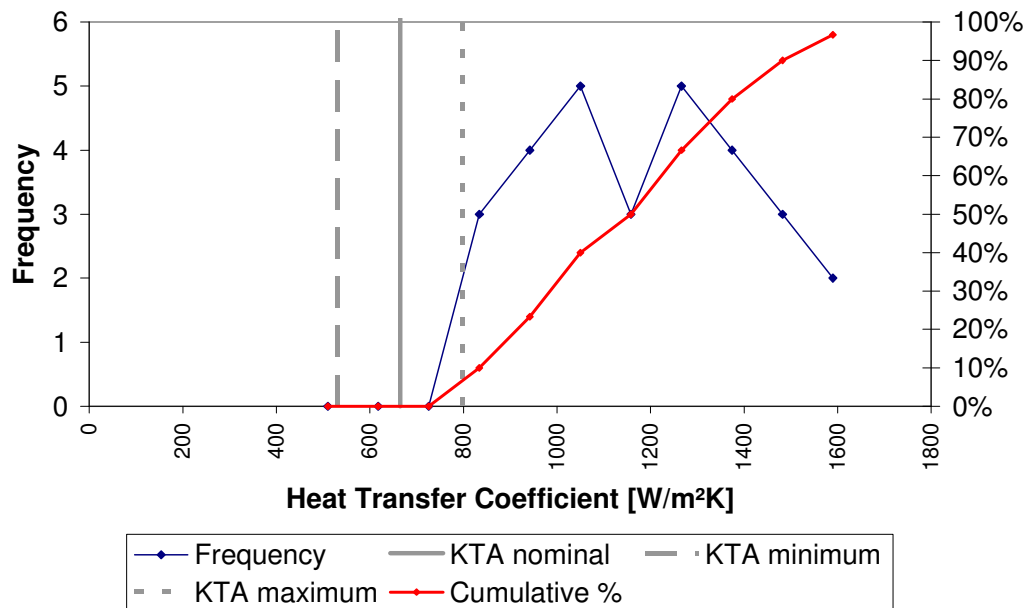
Table 10.4.2 summarizes the results of the preceding figures. This table was created by first extracting the average and the standard deviation of the populations in Figure 10.4.12, Figure 10.4.13 and Figure 10.4.14. The average value is taken as the "nominal value" and the upper and lower bounds of the variation are taken as +/-2 standard deviations (this is consistent with the uncertainty range on the KTA rules correlation, Reference 10.24).

Table 10.4.2: Summary of Average Heat Transfer Coefficient Predictions

Average Heat Transfer Coefficients (W/m²K)							
	KTA rules correlation (Reference 10.24)			CFD Models & Reynolds Analogy			
Flow Rate	Nominal	Lower Bound	Upper Bound	Nominal	Lower Bound	Upper Bound	% Different from KTA
15 kg/s	665	532	798	1155	680	1630	74%
75 kg/s	1956	1565	2347	3156	1932	4381	61%
150 kg/s	3250	2600	3900	4916	2826	7006	51%

An examination of these results indicates that the average CFD predicted heat transfer coefficient is of the same order of magnitude as the KTA rules prediction. It is also noted that the CFD simulation results are consistently higher (approximately 1.5 times)

than the KTA rules prediction. This deviation is postulated to originate primarily from one or more of the following.

1. The selection of the reference velocity in the Reynolds Analogy. If one wished to calibrate the CFD results to the KTA rules prediction an appropriate reference velocity could be determined.

2. The CFD model does not meet the minimum size requirements for the KTA rules heat transfer correlation in Reference 10.24. However, the KTA heat transfer correlation is still arguably applicable to the current CFD model because the model is actually a representative subset of a domain with a radius significantly greater than 10 pebble diameters.

3. Errors discussed in the Appendix I significantly affect the results.

10.4.6   Results of Sensitivity Cases with Heat Transfer Included

As discussed in Section 10.4.3, sensitivity studies were performed solving the energy equation. The solution of the energy equation allows heat transfer coefficients to be calculated directly from the temperature solution and several approximations in Section 10.4.2 related to constant material properties can be removed.

10.4.6.1 Pressure Drop

This section presents pressure drop predictions for the updated remote from reflector CFD model at three different flow rates. Comparisons are made between the current model (i.e., thermal solution) pressure drop predictions; the pressure drop predictions derived using the Reynolds analogy (given in Section 10.4.5.1) and the pressure drop correlation from the KTA rules (Reference 10.25).

CFD Model Pressure Drop Predictions

To estimate the pressure drop within the model a series of axial planes spaced 10 mm apart were created. The area weighted average pressure on each of these planes was calculated within the valid simulation region. These pressure values are plotted in Figure 10.4.15, Figure 10.4.16 and Figure 10.4.17 for each of the three flow rates. The figures also include a linear least-squares best fit line for the CFD model data with its corresponding equation. The nominal, upper bound and lower bound on the KTA rules pressure drop correlation are also included in the figures for reference.

Figure 10.4.15: Pressure Drop Prediction for 150kg/s Core Coolant Flow Rate (Thermal Solution)

$y = -11988x + 1806$

Legend: Model-150kgs-SST | KTA rules nominal | KTA Lower Bound | KTA Upper Bound | Linear (Model-150kgs-SST)
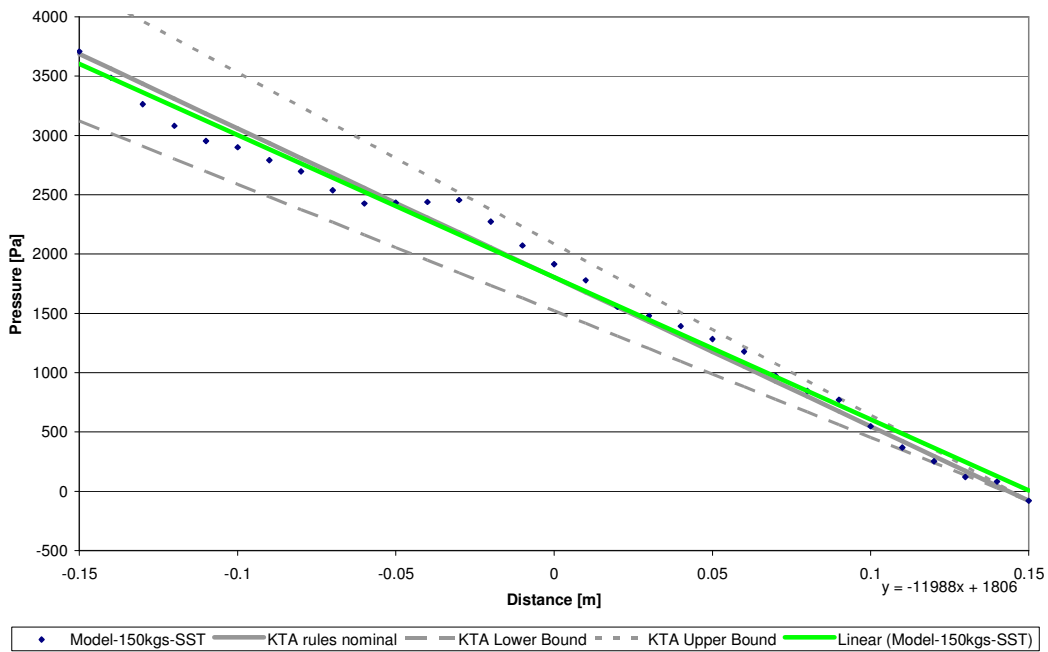
Figure 10.4.16: Pressure Drop Prediction for 75kg/s Core Coolant Flow Rate (Thermal Solution)

$y = -3197.1x + 472.92$

Legend: Model-75kgs-SST | KTA rules nominal | KTA Lower Bound | KTA Upper Bound | Linear (Model-75kgs-SST)
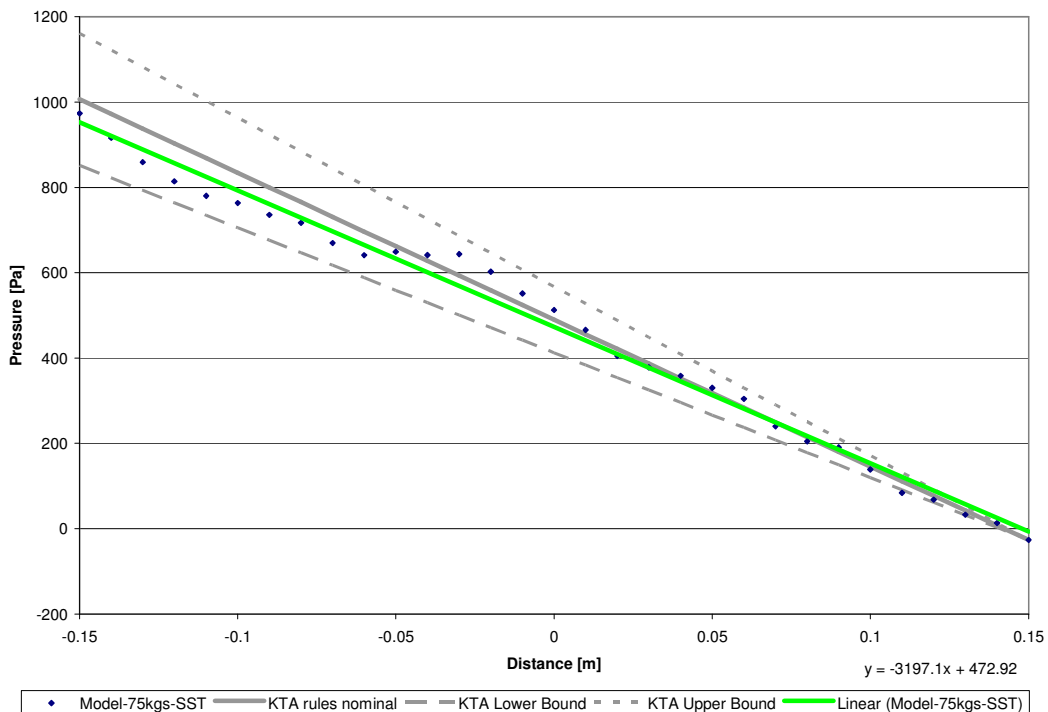
Figure 10.4.17: Pressure Drop Prediction for 15kg/s Core Coolant Flow Rate (Thermal Solution)

$y = -168.09x + 27.36$
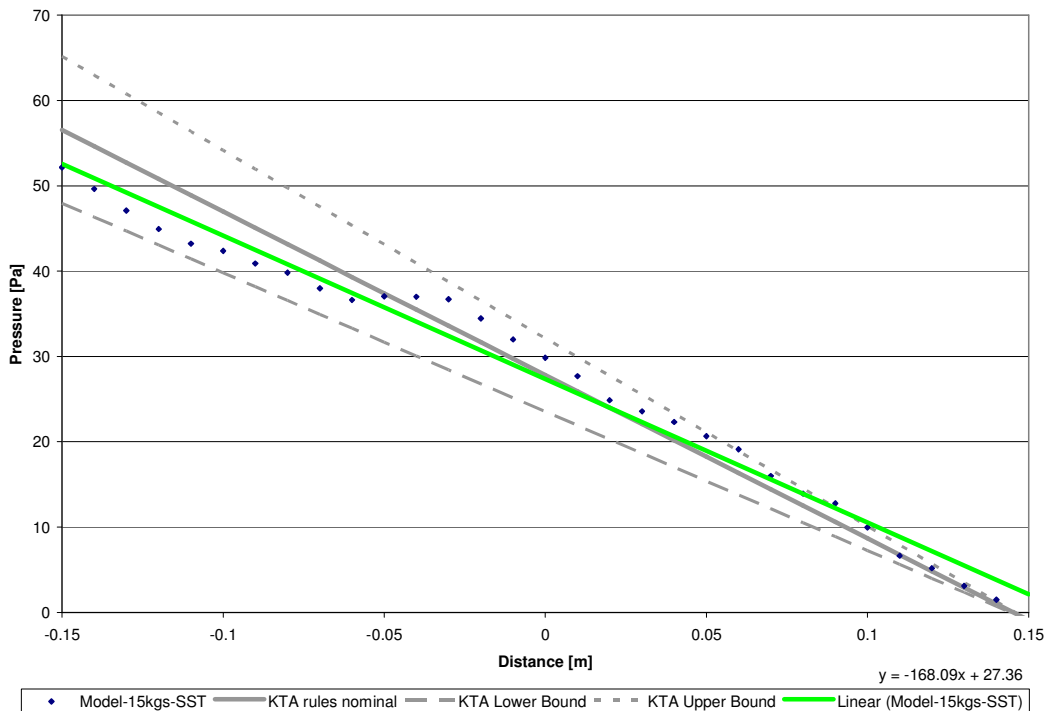
KTA Pressure Drop Correlation

A prediction of the pressure drop from the KTA rules (Reference 10.25) was originally estimated based on the fluid properties evaluated at a constant temperature (of the isothermal model of Section 10.4.5.1). The predictions from the KTA correlations have been updated for these sensitivity studies to use fluid properties based on the temperatures from the CFD model. The resulting predictions based on the updated CFD model temperatures are shown in Table 10.4.3, which can be compared with Table 10.4.2. The only significant change (~22%) in the pressure drop predictions between the updated model and the original model is an increase in pressure drop for the 15 kg/s flow rate. It was expected that if any change was observed it would be for the low flow rate since it has the largest temperature variation, hence the most variation in fluid properties. The 150 kg/s and 75 kg/s cases had changes in pressure drops of 4.3% and 6.8%.

Table 10.4.3: Pressure Drop Predictions – CFD Models Thermal Solution

Flow Rate (kg/s)	KTA Pressure Drop (Pa/m)			CFD Model & Thermal Solution (Pa/m)
	Nominal	Lower Bound	Upper Bound	
15	192	163	220	168
75	3443	2926	3959	3197
150	12556	10673	14439	11988

For both the original and updated model the CFD model prediction for pressure drop falls within the error bounds of the KTA rules. Based on this information it is believed that the KTA rules pressure drop predictions do not need any additional corrections to be applied in regions remote from the reflector.

10.4.6.2 Heat Transfer Coefficient

In Section 10.4.5.3 the pebble surface to coolant heat transfer coefficient was estimated using the modified Reynolds analogy. The pebble surface to coolant heat transfer coefficients for this sensitivity study was estimated using this method and an alternate method based on the thermal solution.

CFD Model Heat Transfer Coefficients

Modified Reynolds Analogy

The justification for the use of the modified Reynolds analogy is presented in Section 10.4.5.3. The values calculated here are based on all fluid properties evaluated at the average fluid temperature for the valid simulation region in the model[6].

The average and ±2 standard deviation bounds on this population of heat transfer coefficients are summarized in Table 10.4.4.

Table 10.4.4: Average Pebble to Coolant Heat Transfer Coefficients For Updated Remote from Reflector Model Estimated with the Modified Reynolds Analogy

Flow Rate (kg/s)	Nominal (W/m²K)	Lower Bound (W/m²K)	Upper Bound (W/m²K)
15	1131	605	1657
75	3020	1812	4228
150	4746	2786	6705

---

[6] The average temperature is determined by calculating the average temperature on 30 equally spaced planes (normals aligned with axial flow) within the valid simulation region, then averaging the temperatures.

Thermal Solution Based

The heat transfer coefficient can also be estimated from the thermal solution to the CFD model using the following definition for the heat transfer coefficient.

$$q^{"}_{pebble} = h\left(T_{pebble} - T_{coolant}\right)$$

where,

$q^{"}_{pebble}$ is the heat flux at the surface of a particular pebble in W/m²

T_{pebble} is the average surface temperature of a particular pebble in K

$T_{coolant}$ is the temperature of the coolant in the vicinity of the pebble under examination in K

h is the heat transfer coefficient between the pebble surface and the coolant in W/m²K.

The surface heat flux for all pebbles in the simulation is 147,377 W/m².

Heat transfer coefficients are calculated for pebbles within the valid simulation region using the area weighted average pebble surface temperature for "T_{pebble}" and the local fluid temperature. To calculate the local fluid temperature the area-weighted average fluid temperature was first extracted on 30 equally spaced planes within the valid simulation region. For calculation of the heat transfer coefficient, the local fluid temperature is defined as the temperature of the plane that is closest to the centroids of the pebble under examination.

The average and ±2 standard deviation bounds on the pebble heat transfer coefficients defined from the thermal solution are summarized in Table 10.4.5.

Table 10.4.5: Average Pebble to Coolant Heat Transfer Coefficients For Updated Remote From Reflector Model Estimated from the Thermal Solution

Flow Rate (kg/s)	Nominal (W/m²K)	Lower Bound (W/m²K)	Upper Bound (W/m²K)
15	572	431	714
75	1280	863	1697
150	2187	1453	2920

KTA Correlation Heat Transfer Coefficients

Heat transfer coefficients between pebbles and coolant may also be estimated using the KTA rules (Reference 10.24). The fluid properties for the correlation are evaluated at the average of the pebble surface temperature and the local coolant

temperature. The local coolant temperature is the same as defined in the CFD thermal solution. A summary of predicted heat transfer coefficients and the 95% confidence bounds on the correlation results is provided in Table 10.4.6.

Table 10.4.6: Average Pebble to Coolant Heat Transfer Coefficients For Remote From Reflector Model Estimated from the KTA rules

Flow Rate (kg/s)	Nominal (W/m²K)	Lower Bound (W/m²K)	Upper Bound (W/m²K)
15	704	563	845
75	1976	1581	2371
150	3266	2613	3919

Comparisons

Figure 10.4.18, Figure 10.4.19 and Figure 10.4.20 show the probability distribution functions (PDF) for the pebble average heat transfer coefficients within the valid simulation region. These figures include PDFs based on the Reynolds analogy and the thermal solution. The KTA rules values are also included on these figures.

Figure 10.4.18: Distribution of Average Pebble Heat Transfer Coefficient for 150kg/s Core Coolant Flow Rate
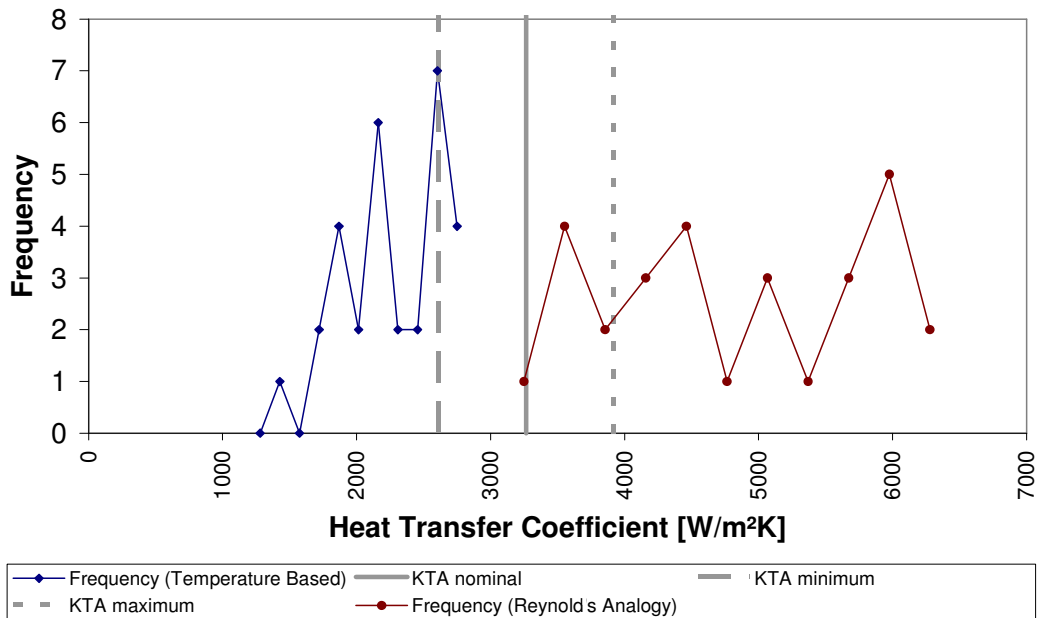
Figure 10.4.19: Distribution of Average Pebble Heat Transfer Coefficient for 75kg/s Core Coolant Flow Rate
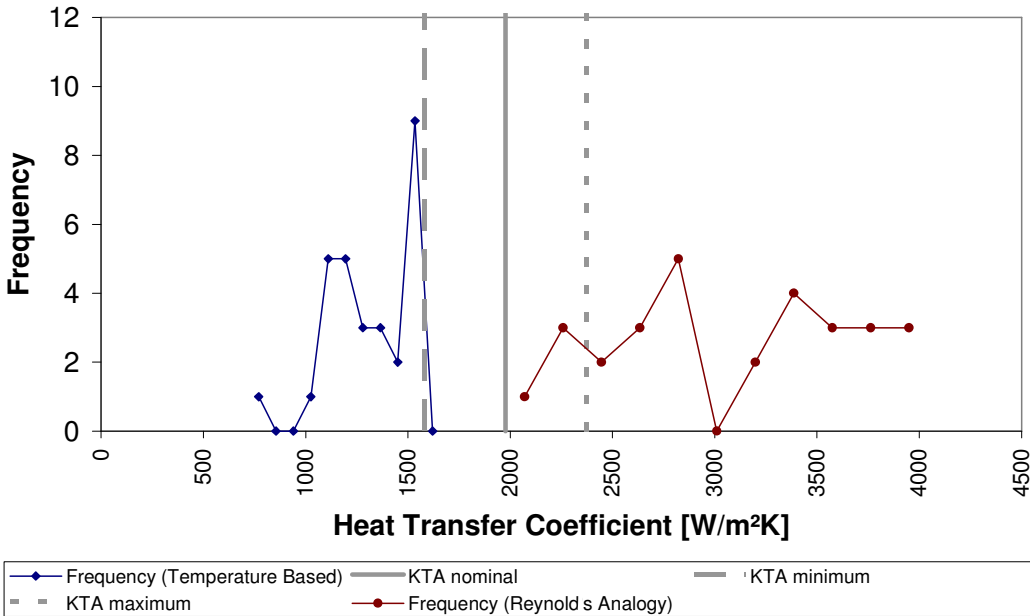
Figure 10.4.20: Distribution of Average Pebble Heat Transfer Coefficient for 15kg/s Core Coolant Flow Rate
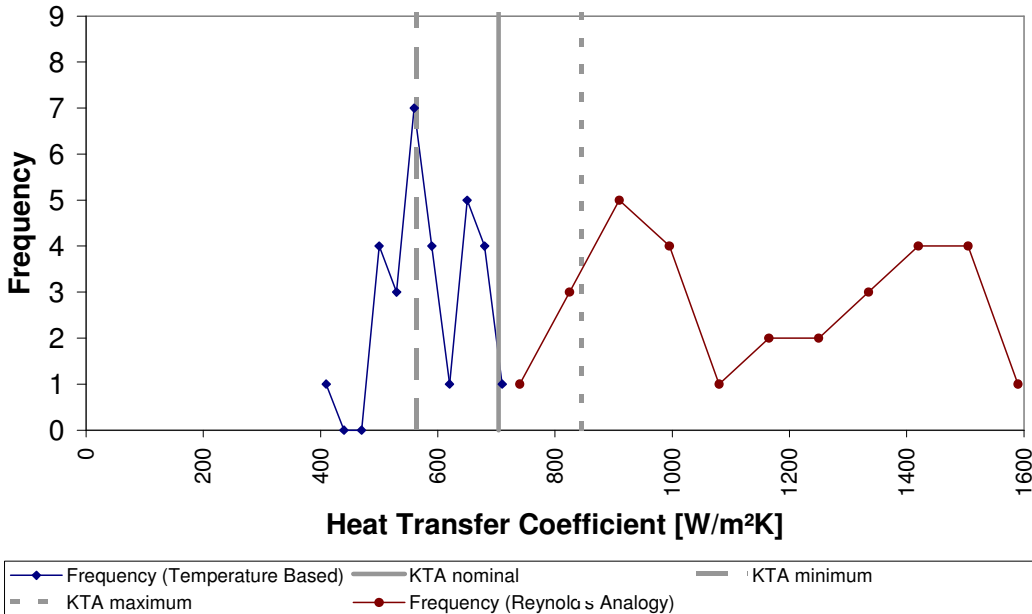
These figures indicate that the heat transfer coefficient from the thermal solution tends to be lower than the KTA correlation and the estimate from the Reynolds analogy tends to be higher than the KTA correlation. Table 10.4.7 summarizes percentage difference between the CFD predictions and the KTA correlation.

Table 10.4.7: Comparison of Average Heat Transfer Coefficient in Updated Remote From Reflector Model

Flow Rate (kg/s)	KTA rules correlation (W/m²K) (Reference 10.24)	CFD Models & Thermal Solution (W/m²K)	% Different from KTA	CFD Models & Reynolds Analogy (W/m²K)	% Different from KTA
15	704	572	-19%	1131	61%
75	1976	1280	-35%	3020	53%
150	3266	2187	-33%	4746	45%

Table 10.4.8 presents the difference between the core center heat transfer coefficients (from Table 10.4.7) and the reflector heat transfer coefficients (from Table 10.5.8, see Section 10.5.5.2 for details) for the KTA rules and the CFD simulations that include thermal solutions.

Table 10.4.8: Comparison of Core Center and Reflector Heat Transfer Coefficients (KTA rules and CFD Thermal Solutions)

Flow Rate (kg/s)	KTA rules correlation (Reference 10.24)			CFD Thermal Solution		
	Core Center (W/m²K)	Reflector (W/m²K)	Difference (%)[7]	Core Center (W/m²K)	Reflector (W/m²K)	Difference (%)[7]
15	704	725	-2.98%	572	529	7.52%
75	1976	1983	-0.35%	1280	1144	10.63%
150	3266	3239	0.83%	2187	1939	11.34%

The KTA rules correlation for the prediction of heat transfer has the following functional form.

$$h = f\left(k, d, \varepsilon, \rho, V, \mu, C_p\right)$$

- k is the thermal conductivity of the helium coolant which is dependent on temperature and pressure in W/m.K

- d is the pebble diameter in m

- ε is the porosity of the pebble bed

- ρ is the density of the helium coolant which is dependent on temperature and pressure in kg/m³

- V is the superficial velocity (same for reflector and core center) in m/s

- μ is the viscosity of the helium coolant which is dependent on temperature in kg.m/s

- C_p is the specific heat capacity of the helium coolant (same for reflector and core center) in J/kg.K

The slight variation that is observed in the KTA rules predictions of heat transfer coefficients between the core center and reflector regions (see Table 10.4.8) can be attributed to differences in porosity (0.424 for core center model and 0.435 for the adjacent to reflector model) and changes in fluid properties. The temperatures

---

[7] (Core Center Value – Reflector Value) / Core Center Value

adjacent the reflector are slightly higher than the temperatures in the core center (higher heat generation rates were applied adjacent to the reflector as indicated in Reference 10.13).

Table 10.4.9 presents the difference between the core center heat transfer coefficients and the reflector heat transfer coefficients for the CFD simulations that use the Reynolds analogy.

Table 10.4.9: Comparison of Core Center and Reflector Heat Transfer Coefficients (CFD Reynolds Analogy Approach)

Flow Rate (kg/s)	Core Center - isothermal solution (W/m²K)	Core Center - Updated (W/m²K)	Reflector (W/m²K)	Difference – type 1 (%)[8]	Difference – type 2 (%)[9]
15	1155	1131	968	16.19%	14.41%
75	3156	3020	2500	20.79%	17.22%
150	4916	4746	3902	20.63%	17.78%

A comparison of values from Table 10.4.7, Table 10.5.8, Table 10.4.8 and Table 10.4.9 yield the following notes:

1. The heat transfer coefficients predicted by the KTA rules are relatively invariant with respect to position in the core. The KTA correlations were not designed to take into account the impact of local variations in heat transfer coefficients induced by the presence of the reflector.

2. The heat transfer coefficients predicted from the thermal solution of the CFD model indicates that the core center heat transfer coefficients are approximately 10% higher than the reflector model heat transfer coefficients.

3. The heat transfer coefficients predicted from the Reynolds analogy indicate that the core center heat transfer coefficients are approximately 18% higher than the reflector model heat transfer coefficients.

4. The heat transfer coefficients based on the thermal solution are fundamentally more correct than the values from the Reynolds analogy[10]. The purpose of the Reynolds analogy was to reduce computational effort.

---

[8] (Core Center Isothermal Value – Reflector Value)/Core Center Isothermal Value

[9] (Core Center Updated Value – Reflector Value)/Core Center Updated Value

[10] The Reynolds analogy is an approximation to the thermal solution. The analogy relates a velocity field solution to a temperature field solution; however it includes several approximations including a zero pressure gradient. The Reynolds analogy was only used originally to reduce solution times for the

10.4.7 Results of Sensitivity Cases with the Power Proportional to the Coolant Flow

As discussed in Section 10.4.4, sensitivity studies were performed by varying the reactor power such that it decreases in proportion to the coolant flow rate, which is more reflective of how the reactor would operate. This section discusses the results of the sensitivity studies.

10.4.7.1 Pressure Drop

This section presents pressure drop predictions for the updated remote from reflector CFD model at two different flow rates and the reactor power proportional to the coolant flow. As previously discussed in Section 10.4.4, 15 kg/s is assumed to correspond to 10% coolant flow and reactor power and 75 kg/s is assumed to correspond to 50% coolant flow and reactor power. Comparisons are made between the current model pressure drop predictions, the predictions previously presented in Section 10.4.6 and the pressure drop correlation from the KTA rules in Reference 10.25.

CFD Model Pressure Drop Predictions

To estimate the pressure drop within the model a series of axial planes spaced 10 mm apart were created, which is the same methodology used in Section 10.4.5. The area weighted average pressure on each of these planes was calculated within the valid simulation region. These pressure values are plotted in Figure 10.4.21 and Figure 10.4.22 for the flow rates examined. The figures also include a linear least-squares best fit line for the CFD model data with its corresponding equation. The nominal, upper bound and lower bound on the KTA rules pressure drop correlation are also included in the figures for reference (the KTA rules pressure drop correlation was previously discussed in Section 10.4.5.1).

---

models. Now that the thermal solutions have been obtained the Reynolds analogy results do not need to be considered.

Figure 10.4.21: Pressure Drop Prediction for 15kg/s Core Coolant Flow Rate (Power Proportional to Flow Rate)

$y = -138.08x + 21.773$
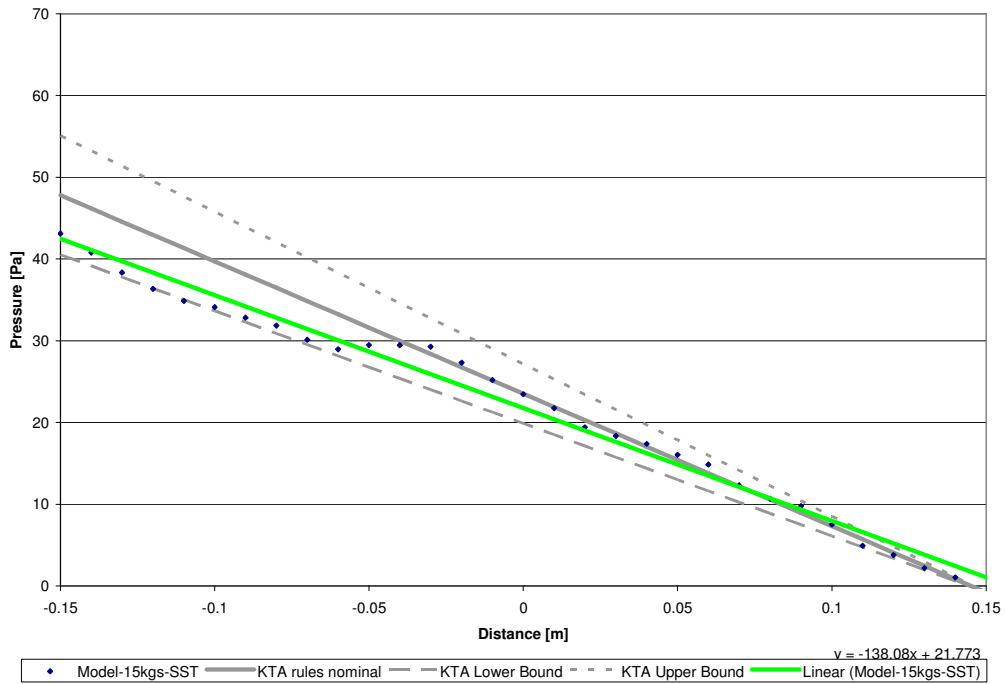
Figure 10.4.22: Pressure Drop Prediction for 75kg/s Core Coolant Flow Rate (Power Proportional to Flow Rate)

$y = -3039.9x + 457.58$
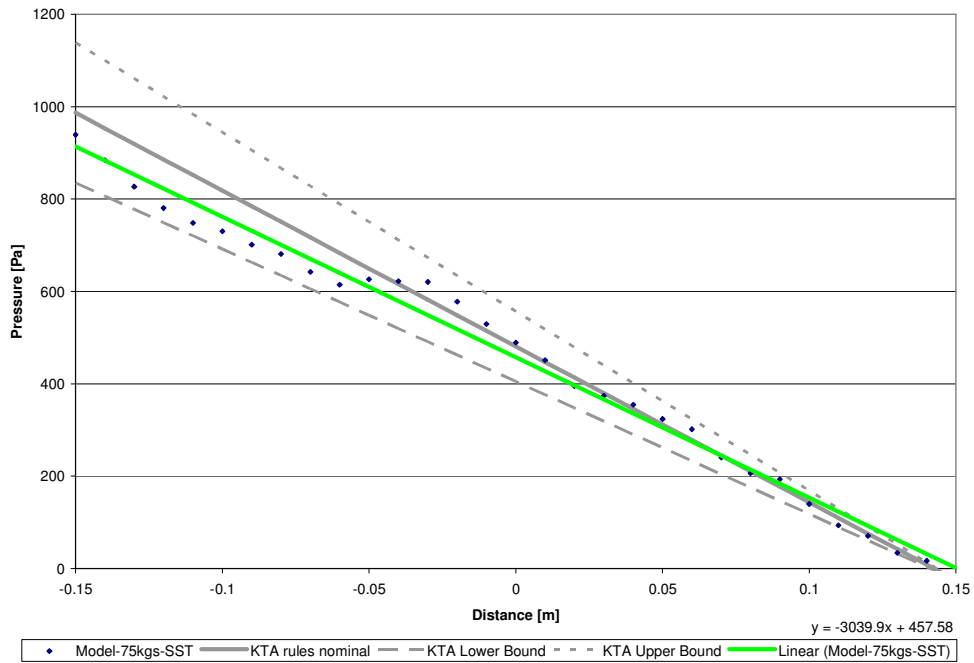
KTA Pressure Drop Predictions

A prediction of the pressure drop from the KTA rules (Reference 10.25) was calculated using fluid properties based on the temperatures from the CFD model, which is the same as the methodology used in Section 10.4.5. The resulting predictions based on the current models are shown in Table 10.4.10, which can be directly comparable to the Table 10.4.3. A comparison of the values in these two tables shows that at a reduced reactor power the KTA pressure drop is lower than what was found for full power. The difference in the KTA pressure drop is on the range of 25-35 Pa/m for the nominal, lower and upper bounds for the 15 kg/s case. For the 75 kg/s case the difference in the KTA pressure drop is on the range of 57-77 Pa/m. These differences largely result from the lower temperatures in the sensitivity cases with the power reduced, which result in a higher helium density.

Table 10.4.10: Pressure Drop Predictions – Remote From Reflector Model with Power Proportional to Flow Rate

Flow Rate (kg/s)	KTA Pressure Drop (Pa/m)			Updated CFD Model (Pa/m)
	Nominal	Lower Bound	Upper Bound	
15	162	138	186	138
75	3375	2869	3882	3040

Based on this information it is believed that the KTA rules pressure drop predictions do not need any corrections to be applied in regions remote from the reflector regardless of whether the power is constant or assumed to be proportional to the flow.

10.4.7.2 Heat Transfer Coefficient

This section presents estimates for heat transfer coefficients between the pebbles and the coolant.

Pebble Surface Heat Transfer Coefficients

In Section 10.4.5.3 the pebble surface to coolant heat transfer coefficient was estimated using the modified Reynolds analogy. The pebble surface to coolant heat transfer coefficients for this updated model is also estimated using this method and an alternate method based on the thermal solution, similar to the approach of Section 10.4.6.2. The heat transfer predicted by the KTA correlations is also calculated for the current simulations.

Comparisons

Figure 10.4.23 and Figure 10.4.24 show the probability distribution functions (PDF) for the pebble average heat transfer coefficients within the valid simulation region for the sensitivity cases performed with the power proportional to the coolant flow. These

figures include PDFs based on the Reynolds analogy and the thermal solution. The KTA rules values are also included on these figures.

Figure 10.4.23: Distribution of Average Pebble Heat Transfer Coefficient for 15kg/s Core Coolant Flow Rate (Power Proportional to Flow Rate)
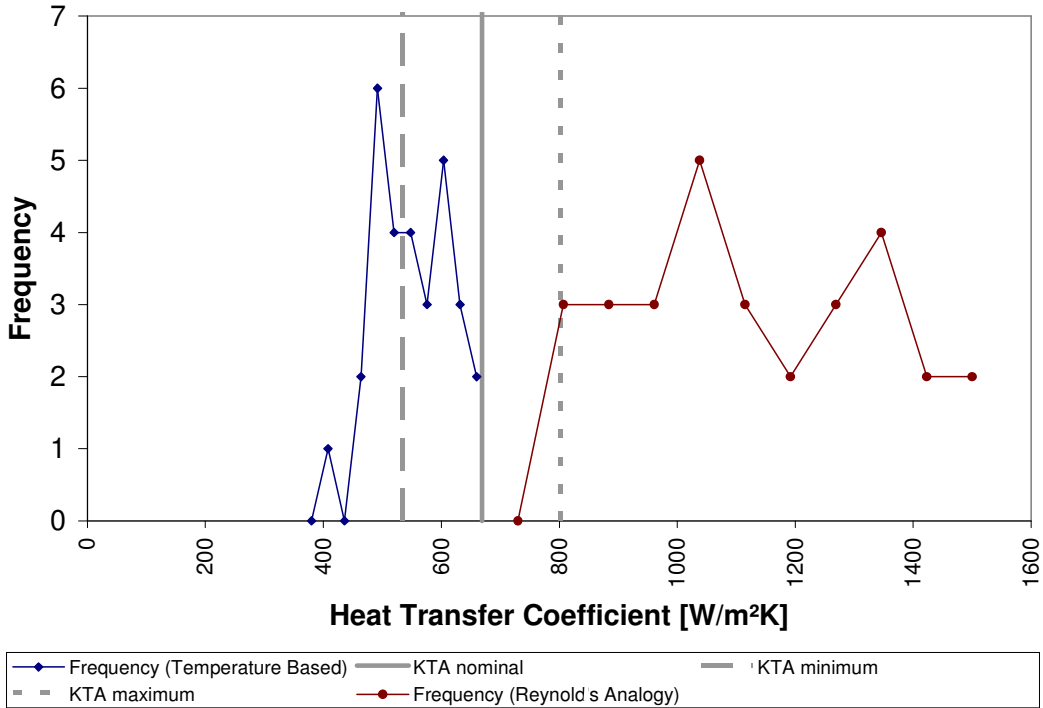
Figure 10.4.24: Distribution of Average Pebble Heat Transfer Coefficient for 75kg/s Core Coolant Flow Rate (Power Proportional to Flow Rate)
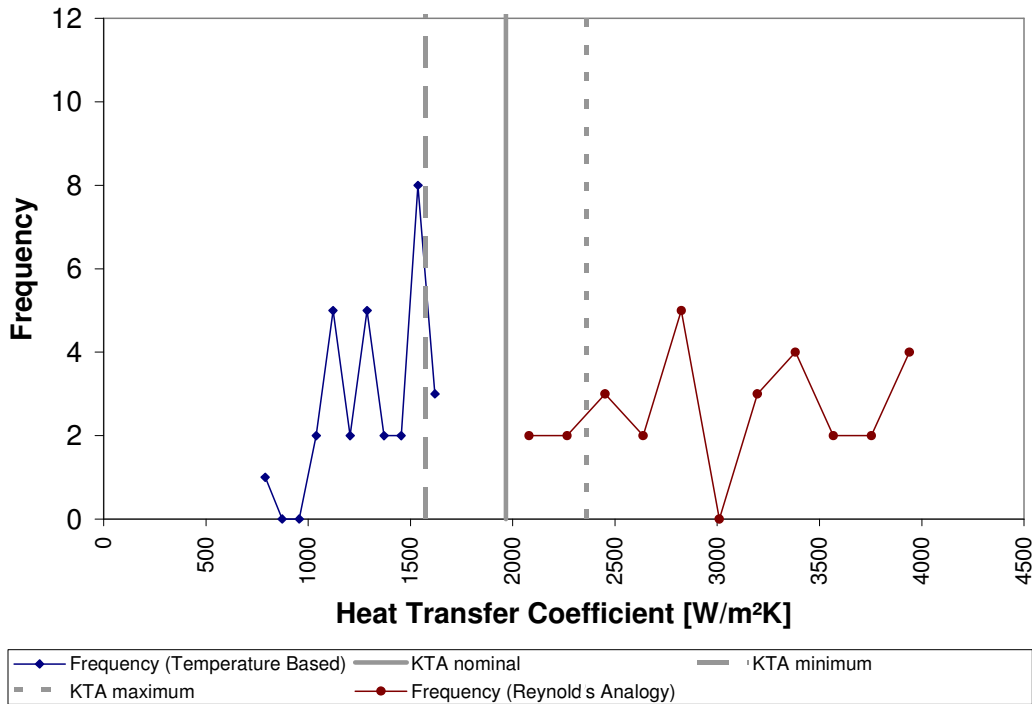
These figures indicate that with the power proportional to the flow the previous trends are still apparent, with the thermal solution predictions tending to be lower than the KTA correlation and the estimate from the Reynolds analogy tending to be higher than the KTA correlation. Table 10.4.11 summarizes percentage difference between the CFD predictions and the KTA correlation. The sensitivity cases produced average heat transfer coefficients that are very close to those of the previous work and the percentage differences between the KTA rules, thermal solution and Reynolds analogy are also very close to those calculated when the power was held constant (see Table 10.4.7).

Table 10.4.11: Comparison of Average Heat Transfer Coefficient in Updated Remote From Reflector Model (Power Proportional to Flow Rate)

Flow Rate (kg/s)	KTA rules correlation (W/m²K)	CFD Models & Thermal Solution (W/m²K)	% Different from KTA	CFD Models & Reynolds Analogy (W/m²K)	% Different from KTA
15	669	538	-20%	1093	63%
75	1966	1296	-34%	3012	53%

10.4.7.3 Pebble Temperature Variations

The variation in the pebble surface temperatures for all three flow rates were also examined as part of the analysis. For the 75 kg/s and 15 kg/s the simulations with the power proportional to flow were used. For the 150 kg/s flow rate the data was extracted from the model discussed in Section 10.4.6. Histograms showing the variation in the pebble temperatures for the various flow rates are presented in Figure 10.4.25, Figure 10.4.26, and Figure 10.4.27.

These figures show that the variation in the maximum and minimum temperatures with regards to average temperature increases at higher powers and flows which is expected[11]. These figures also show that the minimum and average temperatures on the pebbles are much closer than the maximum and average temperatures. Therefore, the hottest spots on the pebbles are likely small and localized near the pebble contacts. This was confirmed by plotting the facet temperatures on a representative pebble with three pebble contacts visible, which is shown in Figure 10.4.28.

Figure 10.4.25: Distribution of Average, Minimum and Maximum Pebble Temperature for 150kg/s Core Coolant Flow Rate (Power Proportional to Flow Rate)

---
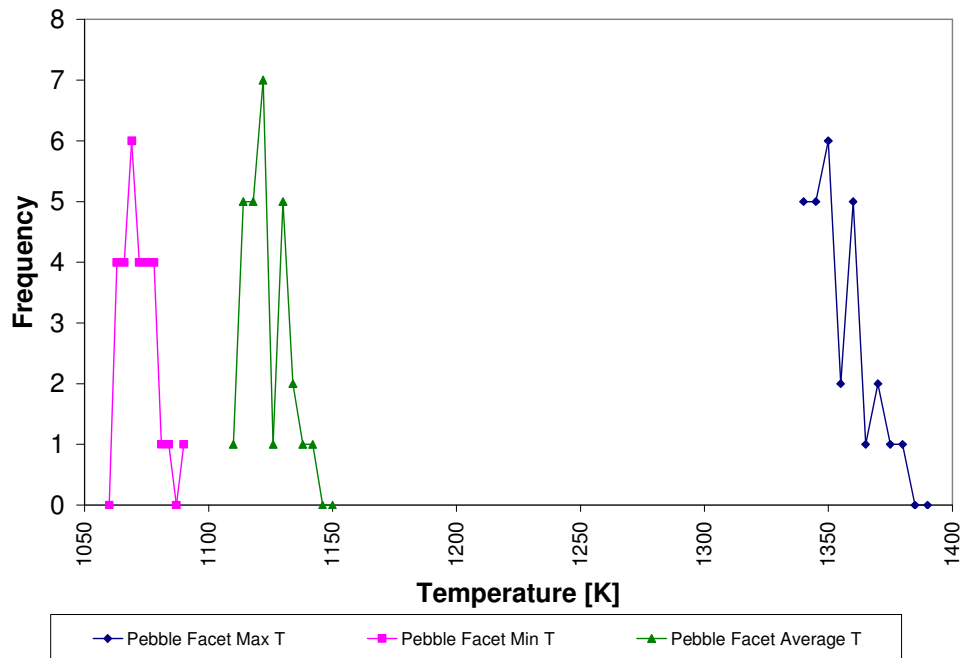
[11] Note that the facet temperatures were used to determine the minimum and maximum values and that the average values are the area-weighted average facet temperature, which is consistent with the average pebble temperature that was used to calculate the heat transfer coefficients for the thermal solution.

Figure 10.4.26: Distribution of Average, Minimum and Maximum Pebble Temperature for 75kg/s Core Coolant Flow Rate (Power Proportional to Flow Rate)
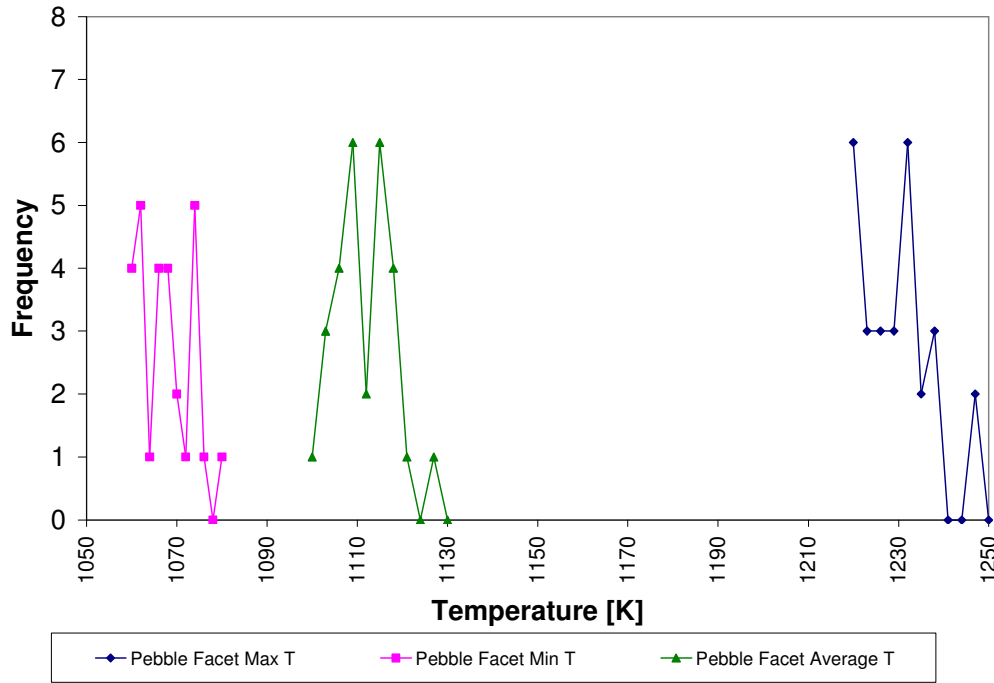
Figure 10.4.27: Distribution of Average, Minimum and Maximum Pebble Temperature for 15kg/s Core Coolant Flow Rate (Power Proportional to Flow Rate)
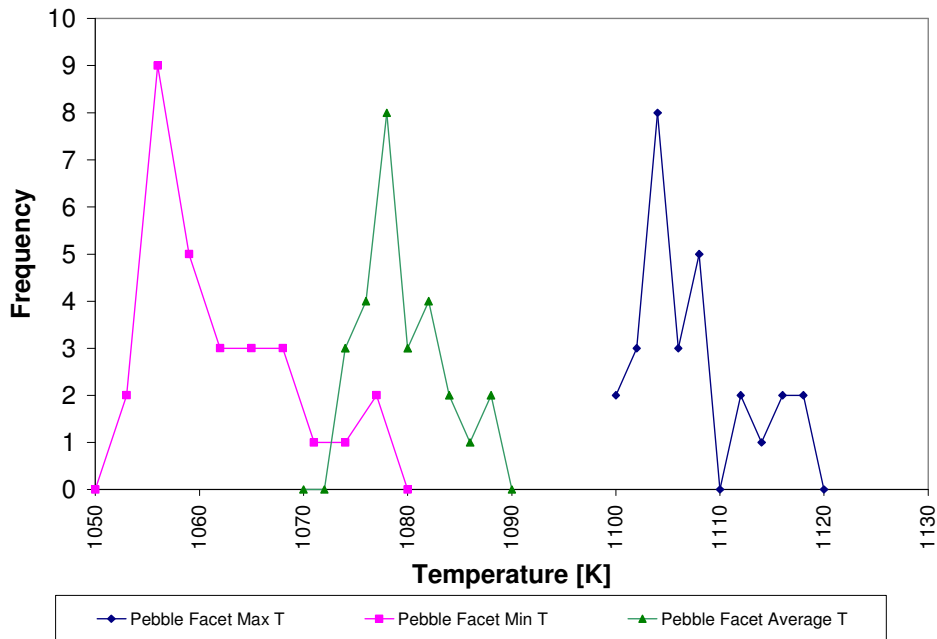
Figure 10.4.28: Facet Temperature Distribution on a Representative Pebble at a Flow Rate of 150 kg/s (Power Proportional to Flow Rate)

Contours of Wall Temperature (Outer Surface) (k)   Feb 25, 2009
                                                      FLUENT 6.3 (3d, pbns, sstkw)
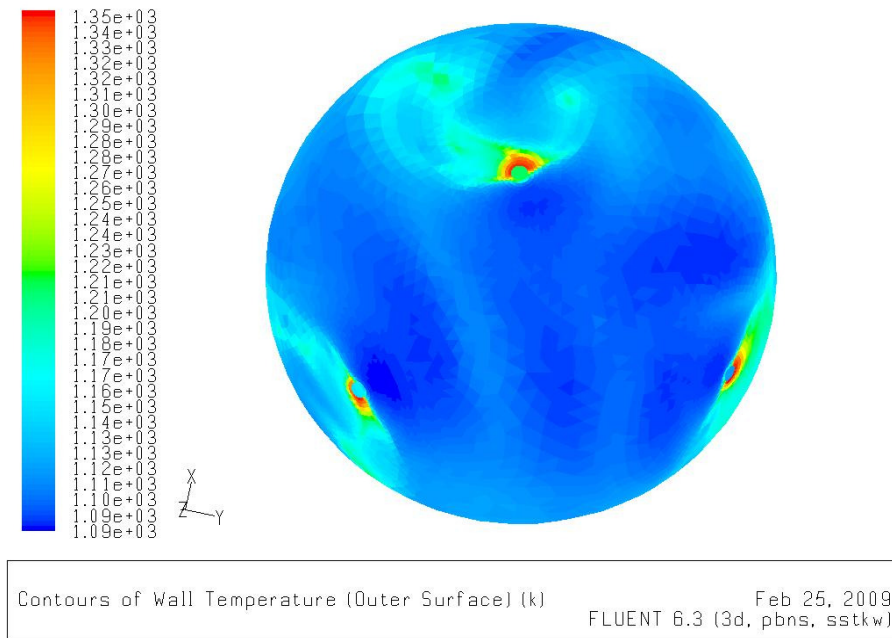
10.5   CFD Model of an Assembly of Pebbles Adjacent to a Reflector

This task examines the details of the flow field and energy distribution around a group of pebbles within a PBR (pebble bed reactor) core adjacent to the reflector.

The goal of this work is to develop correlations or corrections to existing correlations for packed beds such that they are applicable near reflector walls. These new correlations/corrections are arrived at by examining the following quantities.

1. The axial pressure gradient at various distances from the reflector for three different flow rates.

2. The surface average heat transfer coefficient for pebbles near the reflector.

3. The surface average heat transfer coefficient for the reflector wall.

4. The radial speed and porosity distribution near the reflector wall.

10.5.1   Approach and Fundamental Assumptions

The work described in this section is an extension of that in Section 10.4 and, wherever possible, methods described in Section 10.4 are used, unless indicated otherwise. Similar to Section 10.4, a detailed CAD geometry using ANSYS GAMBIT (References 10.21 and 10.22) is used to represent the fluid volume between the

pebbles in a PBR reactor core. The mesh generation strategy developed in Section 10.4 is then used (with appropriate modifications) to create a discretized solution domain. Model boundary conditions are applied to the solution domain using ANSYS FLUENT (Reference 10.10). The ANSYS FLUENT solver is used to solve the mass, momentum and energy conservation equations on this discrete solution domain to obtain the required outputs for this project.

Similar to Section 10.4 the modified Reynolds analogy (Reference 10.26) is used to predict pebble heat transfer coefficients. The energy equation is also solved in the current model, which allows heat transfer coefficients to be calculated directly from the temperature solution.

While the introduction of the energy equation removes many approximations it also introduces additional modeling complexities. This model will not consider radiation heat transfer or pebble-to-pebble conduction. These details will however be addressed in Section 10.7.

10.5.2 CFD Models Used for the Reference Case

This section describes the CFD model used to predict the heat transfer coefficients, pressure drops and velocities through an assembly of randomly packed pebbles near the reflector of a PBR core. The following sub-sections describe the geometry modeled, material properties, boundary conditions, turbulence closure models, buoyancy force treatment and numerical methods used in the model.

10.5.2.1 Modeled Geometry

The geometry generation procedure for the "reflector model" uses a process similar to that outlined in Section 10.4. The locations of pebble centroids were generated using the algorithm of Section 10.2. Figure 10.5.1 illustrates the complete group of pebbles.

Figure 10.5.1: Pebble Location Simulation
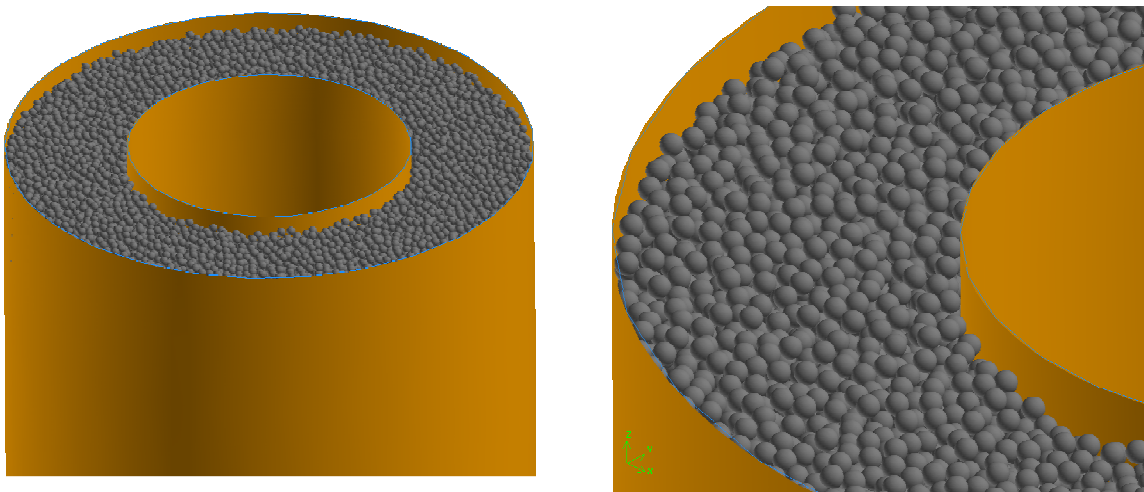
It was illustrated in Section 10.4 that a small group of pebbles (less than 100) requires millions of finite volumes to model accurately, and based on this a complete core model would require excessive computational resources. The reflector model includes a small subset of the pebbles shown in Figure 10.5.1. In Section 10.2 it is indicated that the reflector wall influences the pebble packing fraction within 3 to 5 pebble diameters away from the wall. On the basis of this information the reflector model was sized to contain pebbles 5 pebble diameters away from the reflector. In Section 10.4 it was sufficient to model a cylindrical solution domain however it was realized that this approach was not suitable for the reflector model. Figure 10.5.2 shows the semi-circular solution domain that contains pebbles 5 pebble diameters away from the reflector wall. The model shown Figure 10.5.2 is significantly larger than the model developed in Section 10.4 which already required a large amount of computational resources.

Figure 10.5.2: Circular Solution Domain for Pebbles Adjacent to a Reflector Wall

← Reflector Wall
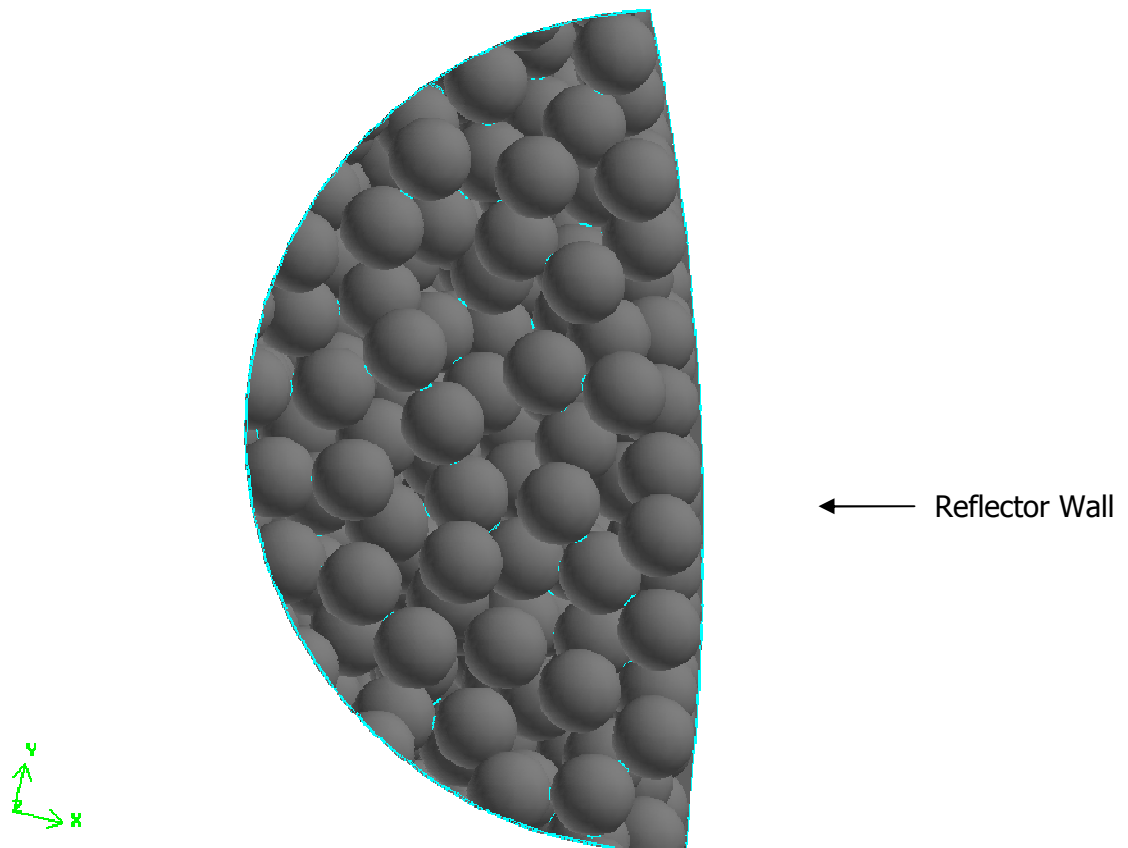
The solution to this problem was to create a model with an elliptical shape. This elliptical region was selected to have a minor radius of 0.12 m (similar to the model of

Section 10.4) and a major radius of 0.3 m[12] (i.e. 5 pebble diameters). The solution domain has a height of 0.42 m. This 0.42 m solution domain only contains the full pebble packing fraction over a 0.27 m region (valid simulation region), the remainder of the solution domain is to be used to improve the behavior of the model boundary conditions. The valid simulation region from this model is from -0.27 m to 0.0 m in the Z (axial) direction. Figure 10.5.3 shows the modeled geometry that was used for all final reported analyses in this section. Figure 10.5.5 illustrates the valid simulation region for pressure drop calculations.

Figure 10.5.3: Geometry of an Arrangement of Pebbles Adjacent to a Reflector

---
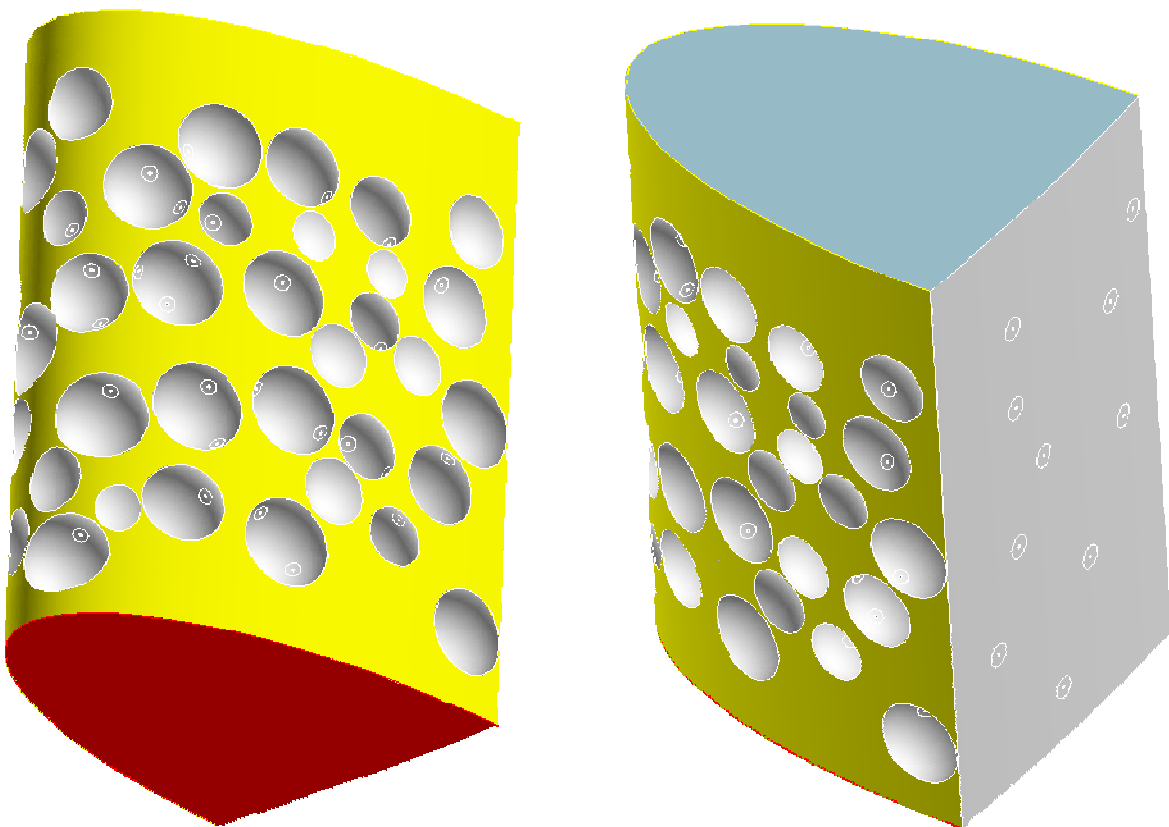
[12] In Section 10.4 it was determined that pebbles located within 0.04 m of the symmetry boundary condition may produce questionable heat transfer coefficients. The solution domain is therefore considered to be valid for an ellipse with a minor radius of 0.08 m and a major radius of 0.26 m for heat transfer coefficient calculations. The entire domain is considered valid for pressure drop calculations as they were shown to be relatively insensitive to the symmetry boundary condition.

Within this geometry the pebble to pebble contacts and the pebble to reflector contacts are modeled using the same contact size and methodology as those used in Section 10.4.

The volumes of the valid simulation region (as defined for pressure drop calculations, see Figure 10.5.4) and the coolant in the valid simulation region were calculated using the volume calculation tools of ANSYS GAMBIT (References 10.21 and 10.22) and the results are summarized in Table 10.5.1.

Table 10.5.1: CFD Model Volume Breakdown

Portion of Valid Simulation Region	Volume (m³)
Total (V_{valid})	15436.5×10^{-6}
Coolant ($V_{coolant}$)	6708.7×10^{-6}
Pebbles	8727.8×10^{-6}

The packing fraction was calculated based on these volumes giving $\alpha = 0.565$.

Figure 10.5.4: Valid Simulation Region (Volume Calculation Model Only)
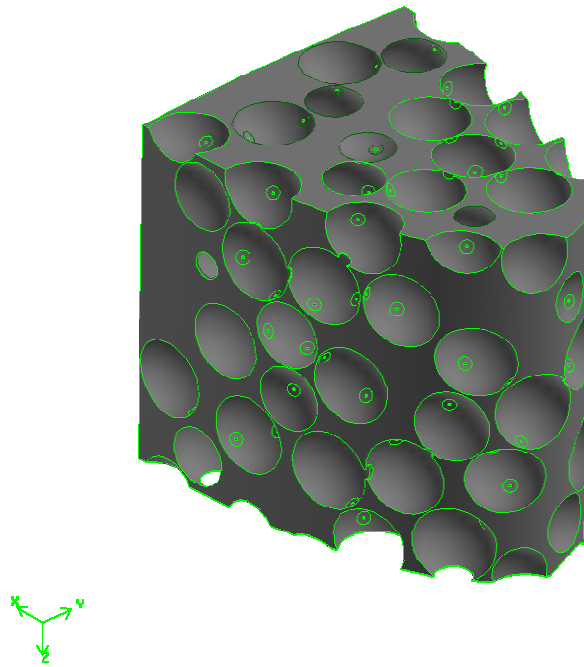
10.5.2.2 Computational Mesh

The reflector model uses the same mesh generation strategy as Section 10.4 with some modifications to allow for mesh generation on the reflector and an elliptical domain. The reflector wall does contain prismatic elements to allow for high near wall resolution. The final surface mesh on the solution domain is shown in Figure 10.5.5. This mesh contains 14,712,914 cells (of various types). The same mesh density is used as in Section 10.4 to ensure a reasonably grid independent solution.

Figure 10.5.5: Images of Final Mesh
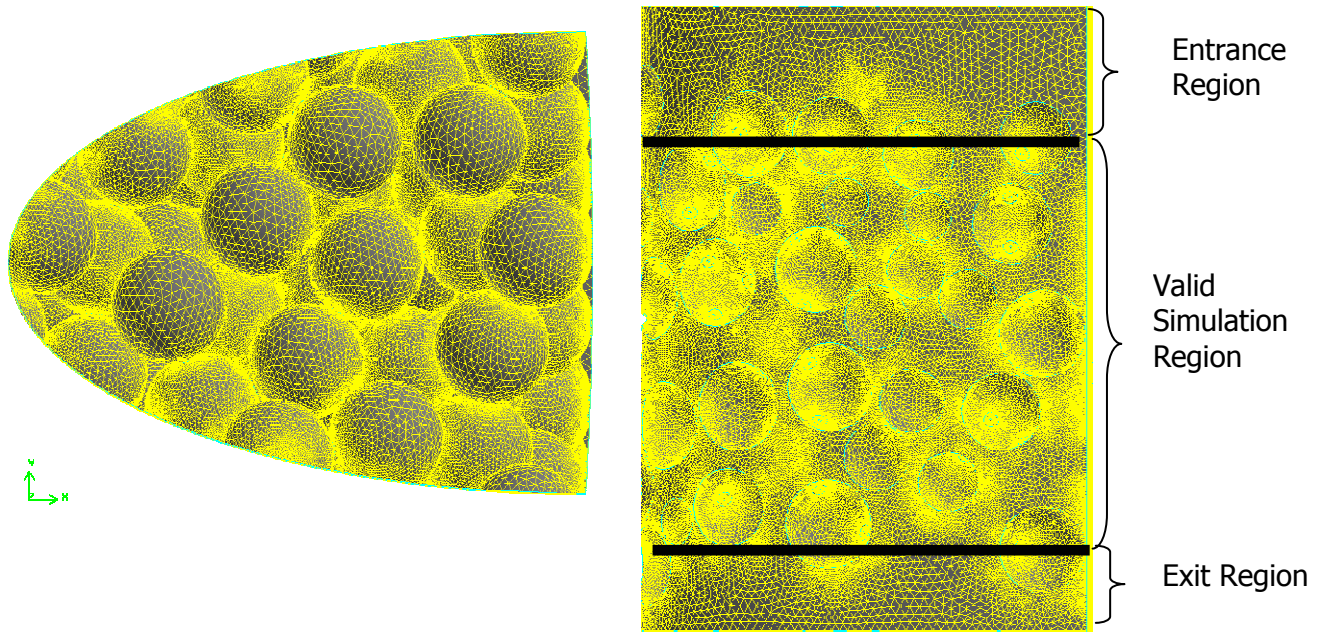
a. Pebble mesh viewed from outlet

b. Mesh on Side of Solution Domain

Entrance Region

Valid Simulation Region

Exit Region
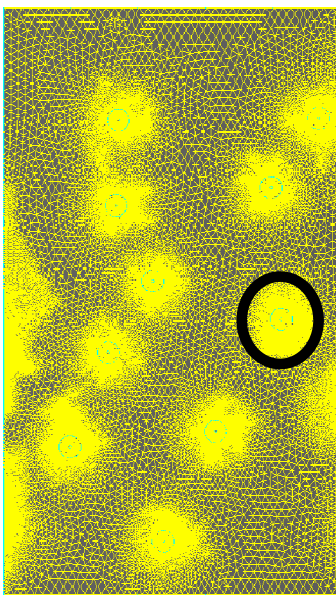
c. Mesh on Reflector Wall
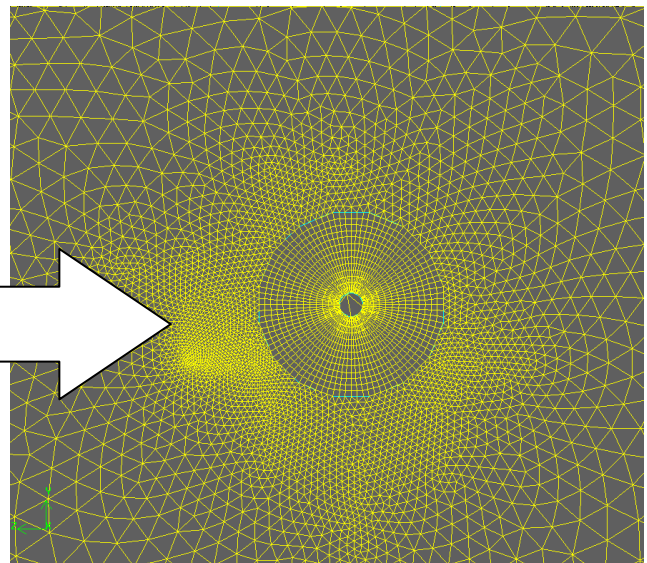
d. Mesh on Reflector contact

10.5.2.3 Boundary Conditions

This sub-section describes the boundary conditions that are used for the reflector CFD model shown in Figure 10.5.3.

Inlet

The inlet surface was modeled as a constant velocity boundary condition with a constant specified turbulence intensity and length scale (see light blue surface in Figure 10.5.3). For all simulations the turbulence intensity was set to 2.5% (low fluctuation) at the inlet with a length scale of 0.5 of a pebble diameter (i.e., 0.03 m) similar to Section 10.4. There is no information on the turbulence at the inlet so this simplistic approach is reasonable. The velocity used for this boundary condition was determined from the flow rate for the entire core divided by the product of the coolant density and total core flow area. For this work total core flow rates of 15 kg/s, 75 kg/s and 150 kg/s are used which translate into velocities of 0.48 m/s, 2.4 m/s and 4.8 m/s.

An important feature of the geometry of the model is that an entrance region is incorporated into the model (See Figure 10.5.5b). This entrance region is 0.09 m in length and contains only a partial compliment of pebbles. This region allows the uniform inlet velocity to develop naturally prior to entering the region of interest in the model.

Outlet

The outlet boundary condition is set to be a plane of constant pressure (see red surface in Figure 10.5.3). In absolute terms the pressure outlet is set to a value of 89.1 bar, however in the simulation the relative pressure is set to zero. The outlet boundary condition in FLUENT allows flow to exit or enter the solution domain as required. All flow that re-enters the solution domain at this boundary condition is specified to enter in a direction normal to the boundary condition. The re-entrant flow is initially specified to have a turbulence intensity, length scale and temperature of 2.5%, 0.03 m and 760 ºC. Once the solution reaches a reasonable level of convergence the average turbulence intensity and temperature at the outlet of the model are calculated. The re-entrant flow properties are altered to reflect these average outlet values. This treatment increases the stability of the problem.

Symmetry

The outer wall of the elliptical domain is modeled as a symmetry plane (see yellow surface in Figure 10.5.3). The work of Section 10.4 indicated that this is a reasonable approach for pressure drop calculations; however heat transfer coefficients for pebbles with centroids within 0.004 m of the symmetry boundary should not be used.

Reflector Wall

The reflector wall (see grey surface in Figure 10.5.3) is modeled as a smooth impermeable no-slip wall. The wall material is represented by shell elements with a

thickness of 0.671 m (difference between pitch circle diameter (PCD) of cooling channels and outer diameter of the core divided by 2). A constant temperature of 763.15 K (490 °C) is applied to the shell elements representing the reflector to simulate the cooling channels within the reflector (Reference 10.13). This modeling approach is depicted in Figure 10.5.6.

Figure 10.5.6: Modeling of Reflector Wall

Pebble Bed

Reflector Material (shell elements)

Constant Temperature Boundary
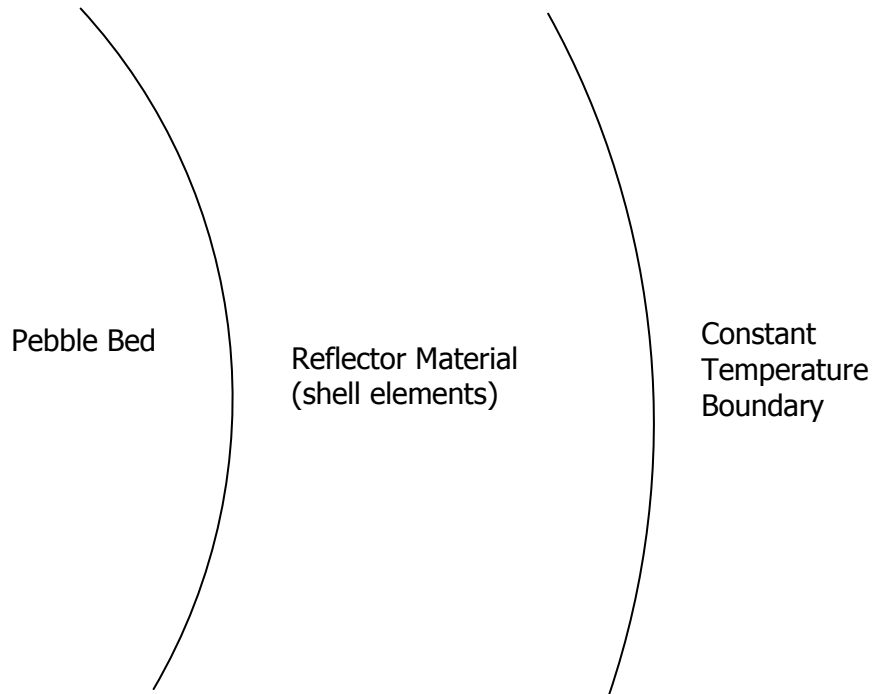
Pebbles

The surfaces of the pebbles are modeled as smooth impermeable no-slip walls.

The heat flux generated within the pebbles would ideally be modeled by a neutronics code coupled to the thermal hydraulic simulation; however this is beyond the scope of the current work. Shell elements are used to model a thin surface layer of the pebbles (0.005 m). A heat flux is applied to the inner surface of the shell elements representing the pebble surface. Shell elements allow for conduction in directions normal and perpendicular to the walls. This heat flux is a function of the distance the pebbles are from the reflector.

The power distribution for this model is calculated based on the peak axial power found in Reference 10.13. The following curve is fitted to the data.

The surface heat flux in (W/m²) is defined as:

$$\text{Surface Heat Flux} = \alpha \cdot r^2 + \beta \cdot r + C \ in \ W/m^2$$

Where: α, β and C are fitting constants

$$\alpha = 204217.5997$$
$$\beta = -619819.9339$$
$$C = 614858.654$$

r is the radial position from the centre of the core

10.5.2.4 Turbulence Model

This model uses the SST turbulence model as discussed in Section 10.4.

10.5.2.5 Buoyancy Model

The model includes buoyancy forces that are represented directly from coolant density variations. The gravitational acceleration vector in this model points in the direction of the flow and has a magnitude of 9.81 m/s².

10.5.3 Sensitivity Cases with the Power Proportional to the Coolant Flow

Sensitivity studies were performed using the model described in Section 10.5.2 but varying the reactor power such that it decreases in proportion to the coolant flow rate, which is more reflective of how the reactor would operate. The CFD models are identical to those used in the work documented in Section 10.5.2. Therefore, the modeled geometry, computational mesh, material properties, turbulence and buoyancy model settings are unchanged from the cases previously run at 15 kg/s and 75 kg/s. The only change that was made for these sensitivity cases is that the reactor power is assumed to be linearly proportional to the coolant mass flow rate.

The differences in the boundary conditions used for these cases, compared with the models in Section 10.5.2, are presented in the sub-sections below.

10.5.3.1 Boundary Conditions

All boundary conditions are the same as in the previous work documented in Section 10.5.2, with the exception of the heat flux applied to the pebbles and the outlet boundary condition, which are discussed below.

Pebbles

The formula used to calculate the heat flux applied to the pebbles as a function of radius was previously presented in Section 10.5.2.3. This heat flux corresponds to 100% coolant flow in the reactor (i.e., 150 kg/s). Therefore, 15 kg/s and 75 kg/s correspond to 10% and 50% coolant flow in the reactor, respectively. Therefore, for these two sensitivity cases the Fluent User Defined Function (UDF) that calculates the heat flux as a function of radius was modified to return values that are 10% and 50% of the value produced by the formula in Section 10.5.2.3. The inherent assumption is that the power profile is not a strong function of the reactor power level.

Outlet

Since the heat load in the model was reduced the temperature specified for flow recirculating back in the outlet had to be reduced accordingly to provide more numerical stability (see Section 10.5.2.3 for details).

10.5.4 Sensitivity Cases with Enhanced Heat Transfer to the Reflector

The heat transfer coefficient for the reflector wall is estimated in Sections 10.5.5.3 and 10.5.6.3. In both cases it was found that using the thermal solution to calculate the heat transfer coefficient to the reflector produces values that are significantly smaller than those predicted using the Reynolds analogy. The heat flux to the wall in the thermal solution was found to be very low, which made it difficult to accurately estimate the heat transfer coefficient. Therefore, a sensitivity study was performed by modifying the boundary conditions and reflector thermal conductivity in order to ensure that there is more heat transfer to the reflector wall. The sensitivity cases assumed that the power is proportional to flow. Flow rates of 150 kg/s, 75 kg/s and 15 kg/s were examined, which translates to Reynolds numbers of approximately 2E+4, 1E+4 and 2E+3, respectively.

The CFD models used for this work are identical to those used in the work documented in Sections 10.5.2 and 10.5.3. Therefore, the modeled geometry, computational mesh, heat generation, turbulence and buoyancy model settings are unchanged from the cases previously run at 150 kg/s (discussed in Section 10.5.2), 75 kg/s and 15 kg/s (discussed in Section 10.5.3). The only changes that were made for these sensitivity cases were to the reflector thickness, reflector conductivity and temperature applied on the helium riser side of the reflector shell elements.

The differences in the materials and boundary conditions used for these cases, compared to the models in Sections 10.5.2 and 10.5.3 are presented in the sub-sections below.

10.5.4.1 Materials and Boundary Conditions

All materials and boundary conditions are the same as in the previous work documented in Sections 10.5.2 and 10.5.3, with the exception of the reflector thickness and temperature and the reflector conductivity. These changes were made for all flow rate cases.

Reflector Conductivity

As presented in Section 10.3.9.2 the thermal conductivity of the reflector used in previous simulations was 22.8 W/mK. In order to increase the heat transfer to the reflector the current sensitivity studies assumed a conductivity of 70 W/mK, which is the conductivity of unirradiated ATR-2E reflector graphite (Reference 10.13)[13].

---

[13] This is the conductivity at ~700°C in Figure 4 of Reference 10.13 for ATR-2E graphite.

Reflector Boundary Condition

As presented in Section 10.5.2.3 the reflector wall thickness is modeled using shell elements. In the sensitivity cases presented here the thickness is reduced to 0.586 m (from 0.671m), which is representative of the distance from the front face of the reflector to the riser channels. The temperature boundary conditions applied to the riser channel side of the reflector was previously 763.15 K, which is the approximate helium inlet temperature. For this sensitivity study the temperature was dropped to an artificially low 563.15 K simply to increase the heat transfer to the reflector.

10.5.5 Results of Reference Case

Throughout the discussion of these results the "valid simulation region" will be discussed. The vertical extents of this region are shown in Figure 10.5.5b (as Valid Simulation Region), and is 0.27 m in length (from Z=-0.27 m to Z=0.0 m in the model). For all pebble surface quantities (i.e., heat transfer coefficients) the valid simulation region includes pebbles with centroids more than 0.004 m away from the symmetry boundary condition as recommended in Section 10.4. The applicable region for all other calculations includes regions across the entire cross section of the model.

10.5.5.1 Pressure Drop

This section presents pressure drop predictions for the near reflector CFD model at three different flow rates. Comparisons are made between the current reflector model pressure drop predictions and the pressure drop correlation from the KTA rules (Reference 10.25). Corrections to the KTA rules correlation are then presented for flows near the reflector.

Domain Average Pressure Drop

To estimate the pressure drop within the model a series of axial planes spaced 0.01 m apart were created. The area weighted average pressure on each of these planes was calculated within the valid simulation region. These pressure values are plotted in Figure 10.5.7, Figure 10.5.8 and Figure 10.5.9 using the labels "Model=XXXkgs-SST", (where XXX represents the core flow rate). The figures also include a linear least-squares best fit line for the CFD model data with its corresponding equation. The nominal, upper bound and lower bound on the KTA rules pressure drop correlation are also included in the figures for reference (details on KTA calculation presented later in this section).

Figure 10.5.7: Pressure Drop Prediction for 150kg/s Core Coolant Flow Rate

$y = -9212x - 192.35$

Model-150kgs-SST   KTA rules nominal   KTA Lower Bound   KTA Upper Bound   Linear (Model-150kgs-SST)
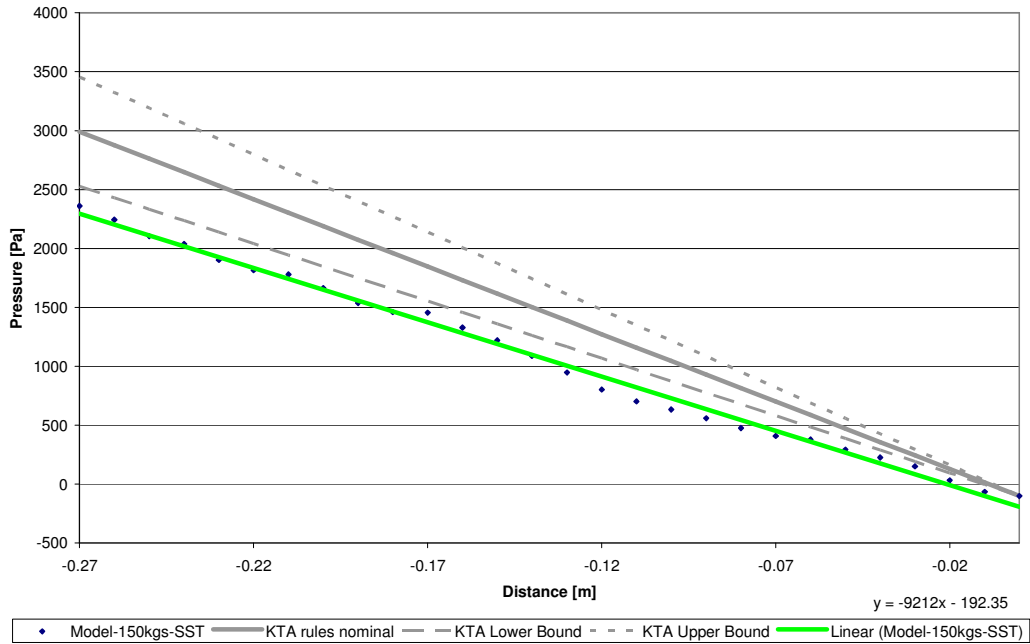
Figure 10.5.8: Pressure Drop Prediction for 75kg/s Core Coolant Flow Rate

$y = -2391.2x - 40.738$

Model-75kgs-SST   KTA rules nominal   KTA Lower Bound   KTA Upper Bound   Linear (Model-75kgs-SST)
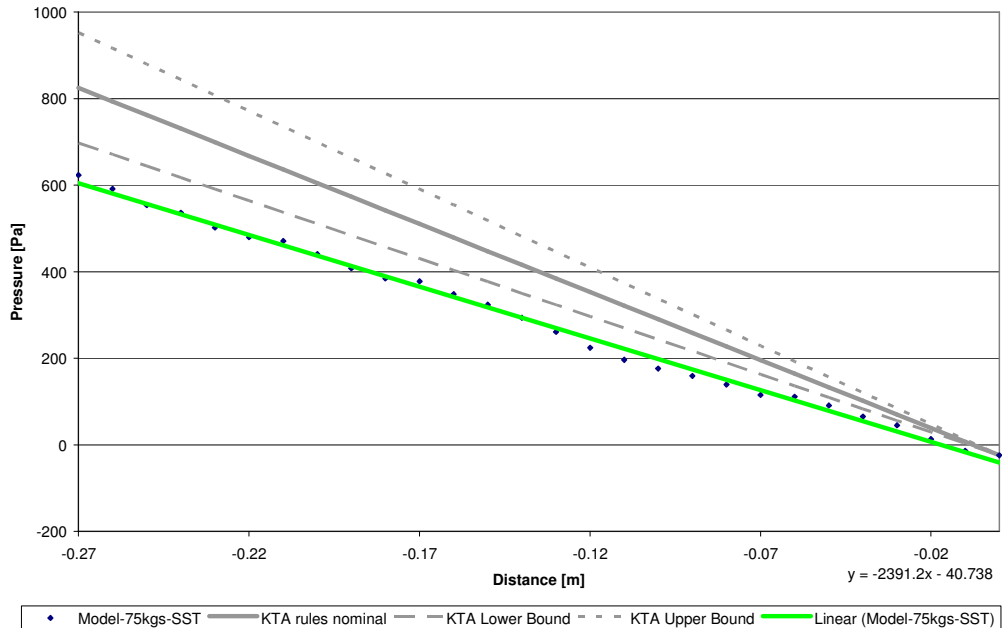
Figure 10.5.9: Pressure Drop Prediction for 15kg/s Core Coolant Flow Rate
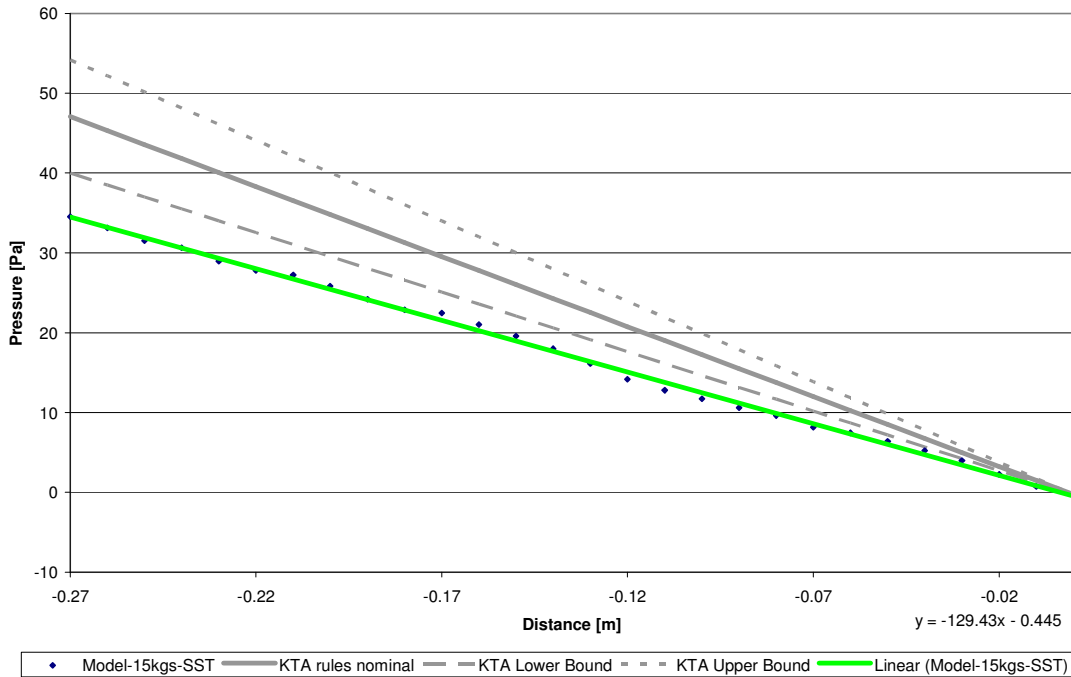
Radial Pressure Drop Variation

The phenomenon referred to as "wall channeling" refers to the increased flow experienced within a PBR near the reflector. This sub-section examines the pressure drop variation within two regions of the reflector model. The first region named "near reflector" contains all materials in the model within 0.1 m of the reflector wall and the second region "away from reflector" contains the remainder of the model. The pressure drop within each of these regions was calculated in a process similar to that of the previous section except that the axial planes are split into a "near reflector" and "away from reflector" region. Figure 10.5.10, Figure 10.5.11 and Figure 10.5.12 show the pressure drop for the three flow rates examined in this analysis for "near reflector" and "away from reflector" regions.

Figure 10.5.10: Pressure Drop Prediction for 150kg/s Core Coolant Flow Rate
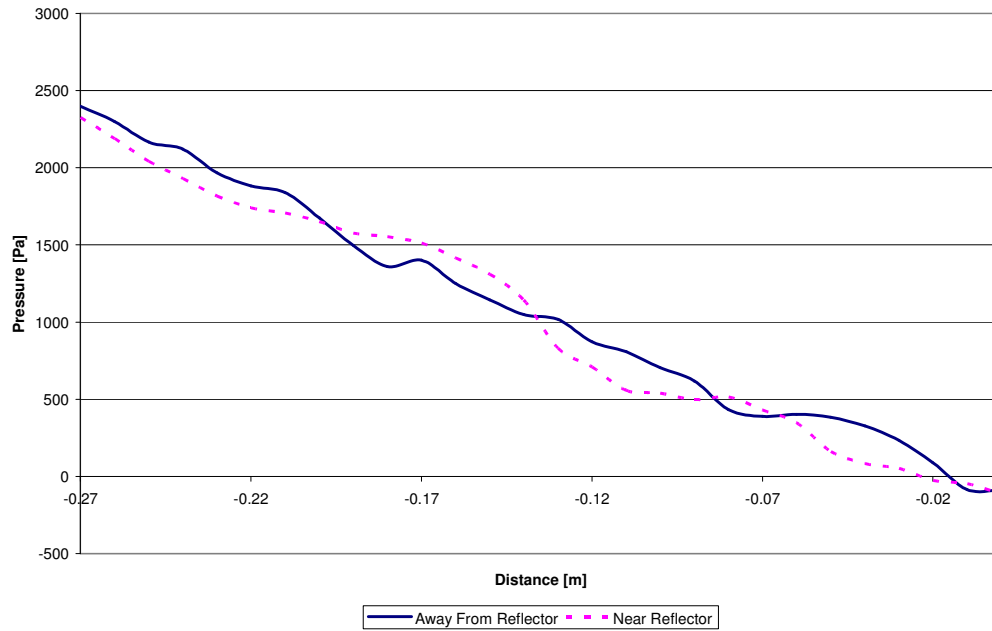
Figure 10.5.11: Pressure Drop Prediction for 75kg/s Core Coolant Flow Rate
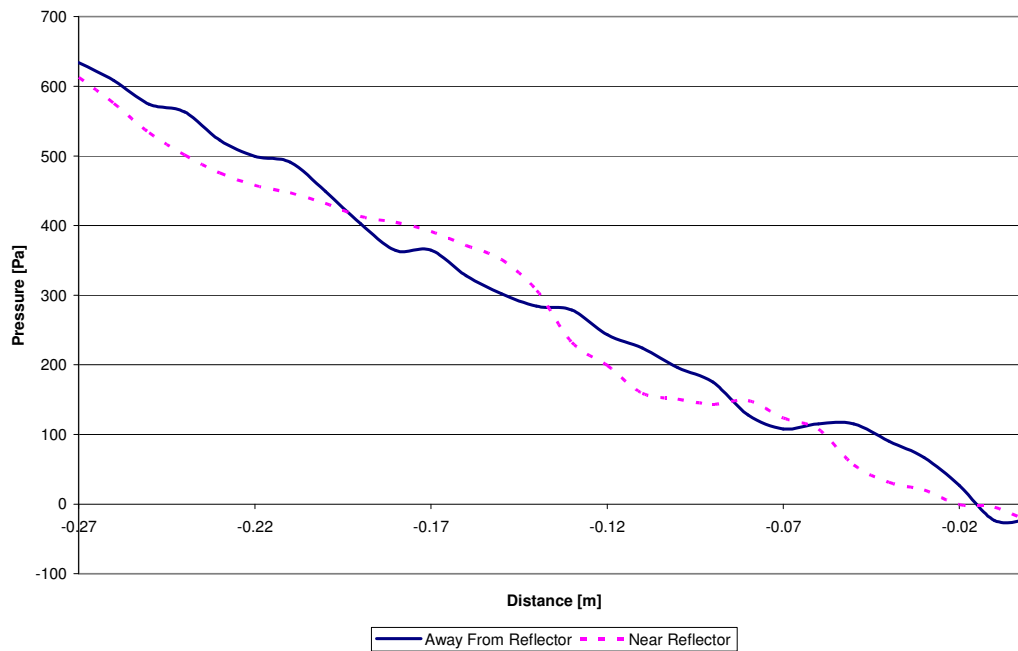
Figure 10.5.12: Pressure Drop Prediction for 15kg/s Core Coolant Flow Rate
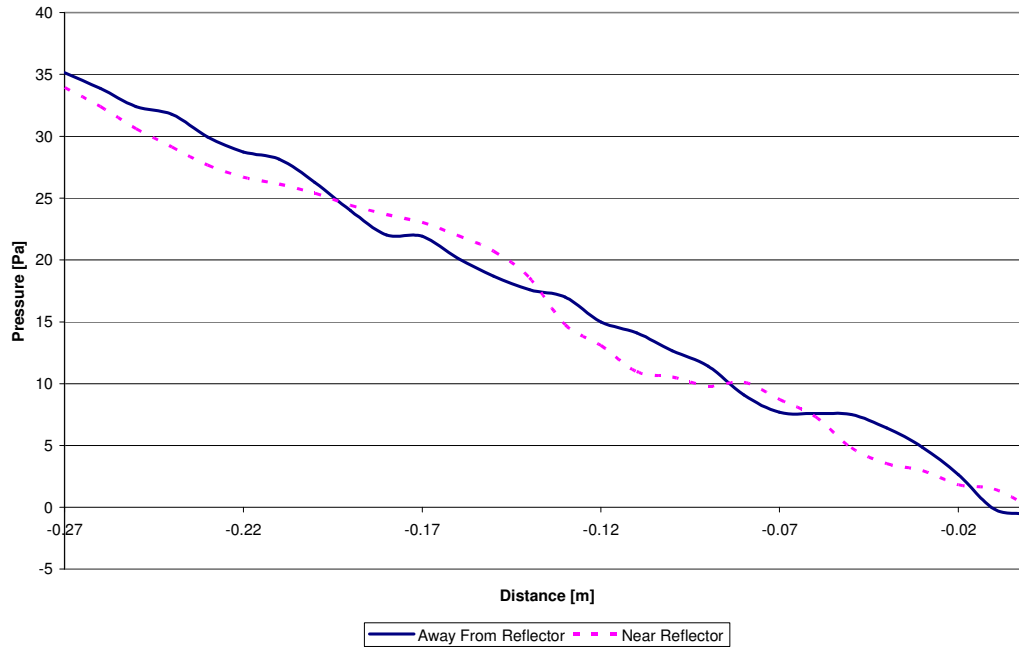
An examination of these figures indicates that no distinguishable change in pressure drop is detected between the inner and outer region.

KTA Pressure Drop Predictions

The KTA rules provide a correlation for predicting pressure drop; however, it is not intended to be applied specifically to near wall regions of a packed bed (Reference 10.25). Knowing that the correlation does not specifically apply to the current model the pressure drop predictions from the KTA correlation are calculated as described in Section 10.4. Density is evaluated at the average fluid temperature and all other properties are evaluated at the average of the surface and coolant temperature as required by the correlation. A summary of predicted pressure drop and the 95% confidence bounds on the correlation results is provided in Table 10.5.2 and plotted in Figure 10.5.7, Figure 10.5.8 and Figure 10.5.9.

Table 10.5.2: Pressure Drop Predictions – Reflector Model

Flow Rate	Pressure Drop (Pa/m)			
	KTA rules Correlation (Based on Reflector Values)			CFD Model
	Nominal	Lower Bound	Upper Bound	Reflector Model
15 kg/s	175	149	202	129
75 kg/s	3144	2673	3615	2391
150 kg/s	11448	9731	13165	9212

A consistent trend observed is that the KTA correlation predicts significantly higher pressure drops than the CFD model. In Section 10.4 the CFD and KTA predictions were in good agreement (i.e., the CFD predictions fell within the error bounds of the KTA correlation). This demonstrates that the near-reflector assembly exhibits a lower hydraulic resistance than an assembly take from the centre of the bed.

Correction to KTA Pressure Drop Correlation

The KTA rules correlation for pressure drop is reproduced in Section 10.4.5.1 based on Reference 10.25.

In FLUENT the pressure drop through a homogeneous packed bed is determined by the following equation.

$$\frac{\Delta P}{\Delta H} = \frac{-\mu \cdot V_{ref}}{C_\alpha} - C_2 \cdot \frac{1}{2} \cdot \rho \cdot V_{ref}^2$$

Where V_{ref} is the superficial velocity in the packed bed, and

C_α and C_2 are user defined constants.

A comparison of the FLUENT porous medium formulation and the KTA rules correlation leads to the following definition of the user defined constants C_α and C_2.

$$\frac{1}{C_\alpha} = \frac{160}{d^2} \cdot \frac{(1-\varepsilon)^2}{\varepsilon^3}$$

$$C_2 = \frac{6}{\left(\frac{Re}{1-\varepsilon}\right)^{0.1}} \cdot \frac{(1-\varepsilon)}{\varepsilon^3} \cdot \frac{1}{d}$$

Optimization Type 1

It was found that by adjusting the value of C_2 much closer agreement between the correlation prediction and the CFD model near the reflector was obtained. Adjusting the value of C_2 to 83.4%[14] of its original value yields the "KTA corrected" values shown in Table 10.5.3.

Table 10.5.3: Comparison of KTA Correlation and Corrected KTA Correlation to CFD Predictions – Optimization Type 1

Flow Rate	Pressure Drop (Pa/m)				
	CFD	KTA	% difference	KTA corrected	% difference
15 kg/s	129	175	35%	162	25%
75 kg/s	2391	3144	31%	2533	6%
150 kg/s	9212	11448	24%	9038	-2%

According to this optimization method it is recommended that if the KTA correlation for pressure drop is used near the reflector (i.e., within 5 pebble diameters) that the C_2 coefficient be adjusted to 83.4% of its original estimate.

Optimization Type 2

A second type of adjustment to the coefficient C_2 was determined by adjusting the exponent on the Reynolds number term in the equation for C_2. It was found that if this exponent is changed from 0.1 to 0.122 the agreement between the KTA correlation and the CFD model were in much better agreement[15] as shown in Table 10.5.4.

Table 10.5.4: Comparison of KTA Correlation and Corrected KTA Correlation to CFD Predictions – Optimization Type 2

Flow Rate	Pressure Drop (Pa/m)				
	CFD	KTA	% difference	KTA corrected	% difference
15 kg/s	129	175	35%	147	14%
75 kg/s	2391	3144	31%	2529	6%
150 kg/s	9212	11448	24%	9057	-2%

---

[14] The optimization used was to hold C_α constant while adjusting C_2 until the sum of the pressure differences between the "KTA corrected" and CFD predictions is zero.

[15] This correction applies only to the near reflector region and should not be used in the core center.

According to this optimization method it is recommended that if the KTA correlation for pressure drop is used near the reflector (i.e., within 5 pebble diameters) that the exponent on the Reynolds number term in the C_2 coefficient equation be changed to 0.122.

10.5.5.2 Heat Transfer Coefficient

This section presents estimates for heat transfer coefficients near the reflector. Estimates of the heat transfer coefficient are provided from:

1. Pebble surface to coolant heat transfer and

2. Reflector to coolant heat transfer

Pebble Surface Heat Transfer Coefficients

In Section 10.4 the pebble surface to coolant heat transfer coefficient was estimated using the modified Reynolds analogy and an alternate method based on the model thermal solution.

Modified Reynolds Analogy

The justification for the use of the modified Reynolds analogy is presented in Section 10.4 and the same arguments generally apply to the reflector model. All fluid properties are evaluated at the average fluid temperature for the valid simulation region in the model[16].

To calculate the average pebble to coolant heat transfer coefficient for a single pebble the average shear stress was extracted from the CFD model and substituted into the modified Reynolds analogy. This process was repeated for each pebble within the valid simulation region (see Section 10.5.2). The average and ±2 standard deviation bounds on this population of heat transfer coefficients are summarized in Table 10.5.5.

---

[16] The average temperature is determined by calculating the average temperature on 27 equally spaced planes (normals aligned with axial flow) within the valid simulation region, then averaging the temperatures.

**Table 10.5.5: Average Pebble to Coolant Heat Transfer
Coefficients For Near Reflector Model Estimated with the
Modified Reynolds Analogy (W/m²K)**

Flow Rate	Nominal	Lower Bound	Upper Bound
15 kg/s	968	595	1341
75 kg/s	2500	1541	3460
150 kg/s	3902	2403	5402

Thermal Solution

The heat transfer coefficient was estimated from the thermal solution to the CFD model using the following definition for the heat transfer coefficient.

$$q''_{pebble} = h(T_{pebble} - T_{coolant})$$

Where:

q''_{pebble} is the heat flux generated within a particular pebble in W/m²,

T_{pebble} is the average surface temperature of a particular pebble,

$T_{coolant}$ is the temperature of the coolant in the vicinity of the pebble under examination, and

h is the heat transfer coefficient between the pebble surface and the coolant in W/m²K.

The power generated in a particular pebble is taken as the integrated heat flux through a pebble surface. Each pebble has a different power output as determined in Section 10.5.2.3.

Heat transfer coefficients are calculated for pebbles within the valid simulation region using the area weighted average pebble surface temperature for "T_{pebble}" and the local fluid temperature. To calculate the local fluid temperature the area-weighted average fluid temperature was first extracted on 27 equally spaced planes within the valid simulation region. For calculation of the heat transfer coefficient, the local fluid temperature is defined as the temperature of the plane that is closest to the centroids of the pebble under examination.

The average and ±2 standard deviation bounds on the pebble heat transfer coefficients defined from the thermal solution are summarized in Table 10.5.6.

Table 10.5.6: Average Pebble to Coolant Heat Transfer Coefficients For Near Reflector Model Estimated from the Thermal Solution (W/m²K)

Flow Rate	Nominal	Lower Bound	Upper Bound
15 kg/s	529	302	757
75 kg/s	1144	774	1513
150 kg/s	1939	1307	2572

KTA Correlation

Heat transfer coefficients between pebbles and coolant may also be estimated using the KTA rules (Reference 10.24) as described in Section 10.4. The fluid properties for the correlation are evaluated at the average of the pebble surface temperature and the local coolant temperature. The local coolant temperature is the same as defined above. A summary of predicted heat transfer coefficients and the 95% confidence bounds on the correlation results is provided in Table 10.5.7.

Table 10.5.7: Average Pebble to Coolant Heat Transfer Coefficients For Near Reflector Model Estimated from the KTA rules (Reference 10.23) (W/m²K)

Flow Rate	Nominal	Lower Bound	Upper Bound
15 kg/s	725	580	870
75 kg/s	1983	1587	2380
150 kg/s	3239	2591	3887

Comparisons

Figure 10.5.13, Figure 10.5.14 and Figure 10.5.15 show the probability distribution functions (PDF) for the pebble average heat transfer coefficients within the valid simulation region. These figures include PDFs based on the Reynolds analogy and the thermal solution. The KTA rules values are also included on these figures.

Figure 10.5.13: Distribution of Average Pebble Heat Transfer Coefficient 150kg/s Core Coolant Flow Rate
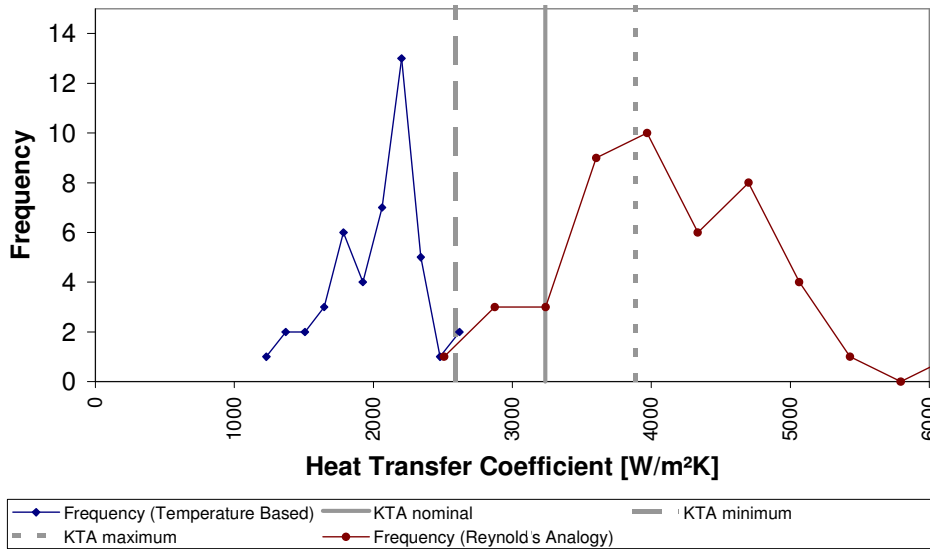
Figure 10.5.14: Distribution of Average Pebble Heat Transfer Coefficient 75kg/s Core Coolant Flow Rate
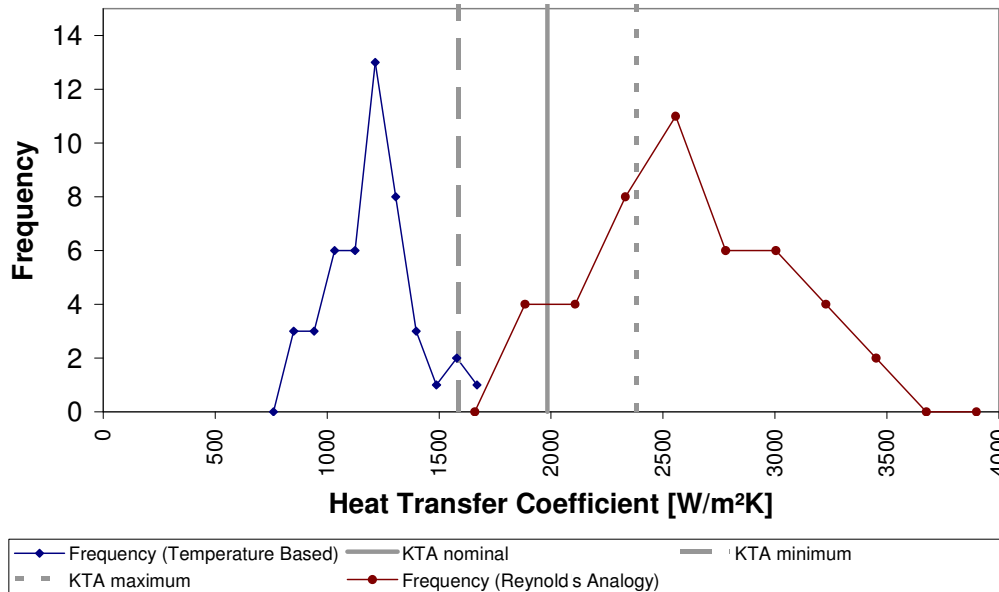
Figure 10.5.15: Distribution of Average Pebble Heat Transfer Coefficient 15kg/s Core Coolant Flow Rate
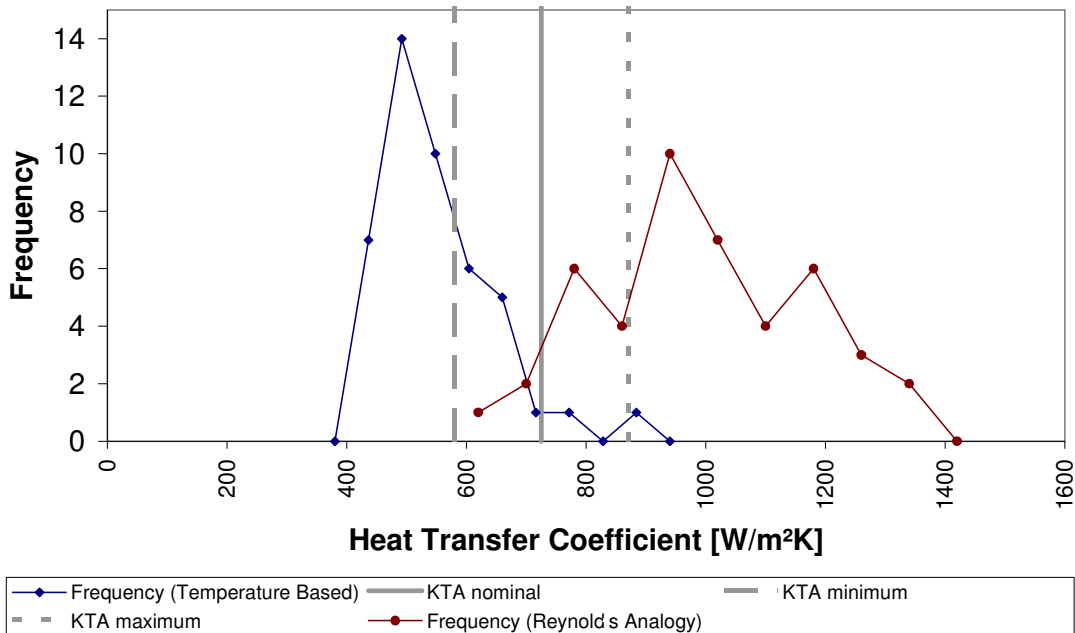
These figures indicate that the heat transfer coefficient from the thermal solution tends to be lower than the KTA correlation and the estimate from the Reynolds analogy tends to be higher than the KTA correlation. Table 10.5.8 summarizes percentage difference between the CFD predictions and the KTA correlation.

Table 10.5.8: Comparison of Average Heat Transfer Coefficient in Reflector Model (W/m²K)

Flow Rate	KTA rules correlation (Reference 10.23)	CFD Models & Thermal Solution	% Difference from KTA	CFD Models & Reynolds Analogy	% Difference from KTA
15 kg/s	725	529	-27%	968	33%
75 kg/s	1983	1144	-42%	2500	26%
150 kg/s	3239	1939	-40%	3902	20%

This result does not conclude that any particular method is superior for calculating the heat transfer coefficient. It is known that the KTA correlation is only intended for large solution domains and gives the average value for the near wall and core central regions. A detailed comparison of predictions near the reflector and remote from the reflector is presented in Section 10.4.7.

It is noted that for the in-core model in Section 10.4 the CFD model using the Reynolds analogy predicted significantly higher (~53%) heat transfer coefficients than the KTA rules correlation (see Table 10.4.7). In the reflector model the Reynolds analogy predictions are much closer to the KTA rules (~26%). The thermal solution has also been shown to under predict the KTA rules correlation (by ~29% in the core centre model, and ~36% in the reflector model).

10.5.5.3 Reflector Heat Transfer Coefficients

This section presents the heat transfer coefficients from the reflector to the coolant derived from the CFD model. Heat transfer coefficients for the reflector were calculated using both the modified Reynolds analogy and the thermal solution from the model.

The approach using the Reynolds analogy is similar to the approach used for the pebble heat transfer coefficients. The shear stress used in the analogy is the area-weighted average shear stress on the reflector wall over the valid simulation region. The reference velocity and fluid properties used are identical those used before.

Heat transfer coefficients derived from the thermal solution were derived based on the following formulation.

$$q''_{reflector} = h\left(T_{reflector} - T_{coolant}\right)$$

Where $q''_{reflector}$ is the total heat flux into the reflector in W/m²K

$T_{reflector}$ is the area weighted average temperature of the reflector surface over the valid simulation region in K

$T_{coolant}$ is the temperature of the coolant 0.01 m away from the reflector in the valid simulation region in K.

The calculated heat transfer coefficients for the reflector using the two approaches are presented in Table 10.5.9.

Table 10.5.9: Reflector Heat Transfer Coefficient Estimates (W/m²K)

Flow Rate	CFD Models & Reynolds Analogy	CFD Models & Thermal Solution
15 kg/s	786	322
75 kg/s	2188	511
150 kg/s	3694	984

An examination of these results shows a large discrepancy between the two methods. The heat transfer coefficients calculated using the Reynolds analogy are very similar to the pebble to coolant heat transfer coefficients using the same method, but the

thermal model predictions are not. This calculation was found to be very sensitive to the reference temperature or $T_{coolant}$. The total heat flux into the reflector is relatively small compared to the flux out of the pebbles and the difference between the coolant and reflector wall temperature is very small. Depending on the definition of the reference temperature the heat transfer coefficient for the reflector can vary by an order of magnitude. The heat transfer coefficient based on the Reynolds Analogy was calculated using the average core velocity as the reference velocity to be consistent with the work of Section 10.4; however it was found that the velocity near the reflector is slightly higher than at locations away from the reflector (See Section 10.5.5.4). The variation in reference velocities is however smaller than the variation in possible temperature differences "$(T_{reflector} - T_{coolant})$". See Section 10.5.7 for additional calculations of the reflector heat transfer coefficients.

10.5.5.4 Velocity Predictions

This section presents the radial velocity distribution encountered in the reflector model. The results in this section present a more complete description of the coolant behavior near the reflector, although the domain is not large enough to produce statistically significant effects. Section 10.6 discusses the "wall channeling" effect near the reflector wall using a larger CFD grid.

To analyze the velocity distribution near the reflector, the reflector model was divided into two regions; one containing all materials within 0.05 m of the reflector and a second containing all remaining materials. The average speed for these regions was extracted at several axial locations and plotted in Figure 10.5.16, Figure 10.5.17 and Figure 10.5.18. These figures indicate that speeds are approximately 30% higher in the region closest to the reflector.

Figure 10.5.16: Axial Speed Distribution for 150 kg/s Core Coolant Flow Rate
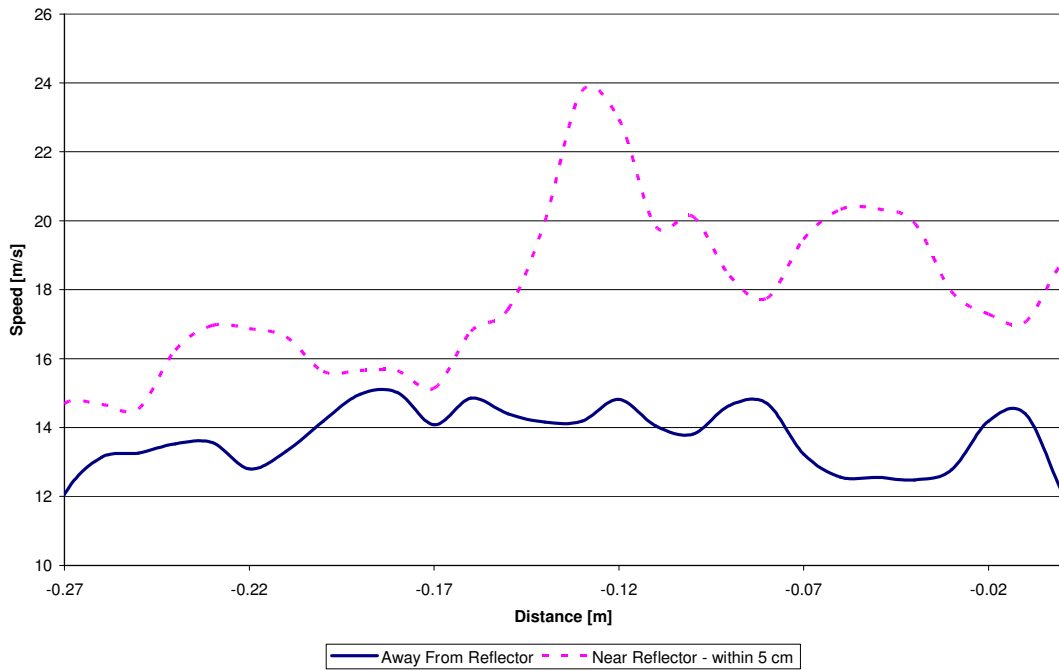
Figure 10.5.17: Axial Speed Distribution for 75 kg/s Core Coolant Flow Rate
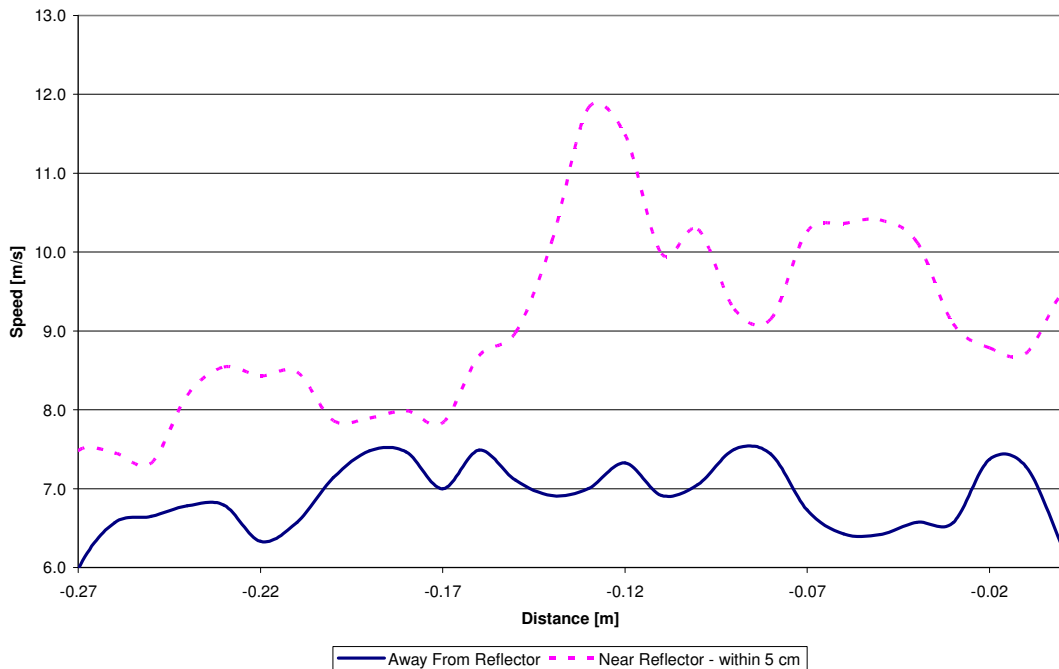
Figure 10.5.18: Axial Speed Distribution for 15 kg/s Core Coolant Flow Rate
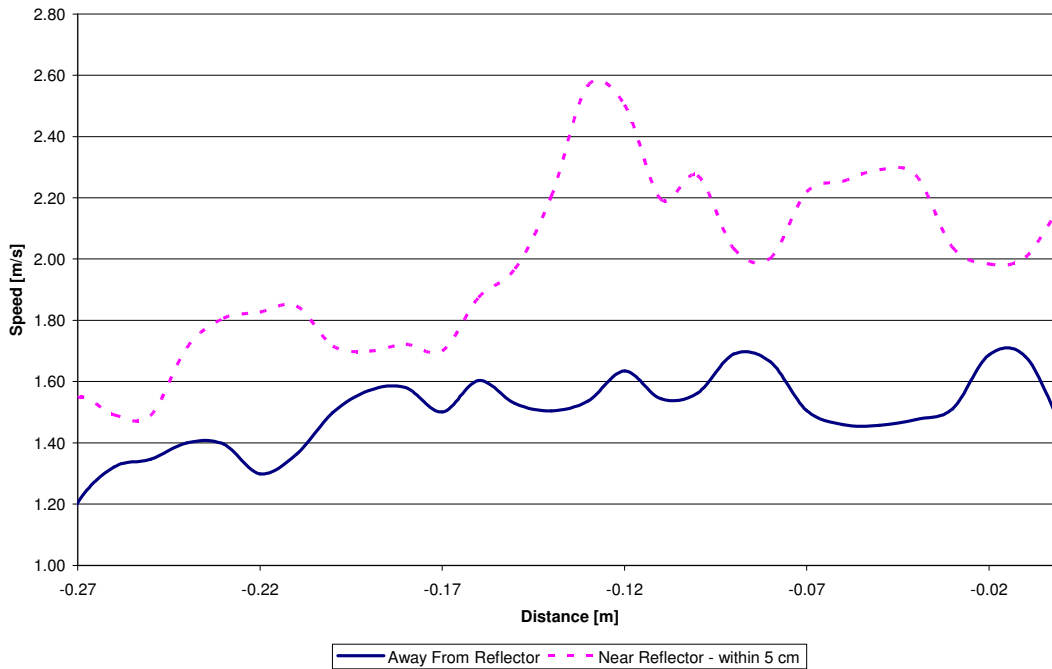
10.5.6 Results of Sensitivity Cases with the Power Proportional to the Coolant Flow

As discussed in Section 10.5.3, sensitivity studies were performed by varying the reactor power such that it decreases in proportion to the coolant flow rate, which is more reflective of how the reactor would operate. This section discusses the results of the sensitivity studies.

10.5.6.1 Pressure Drop

This section presents pressure drop predictions for the updated near reflector CFD model at two different flow rates and the reactor power proportional to the coolant flow. As previously discussed in 10.5.3, 15 kg/s is assumed to correspond to 10% coolant flow and reactor power and 75 kg/s is assumed to correspond to 50% coolant flow and reactor power. Comparisons are made between the current model pressure drop predictions, the predictions previously presented in Section 10.5.5.1 and the pressure drop correlation from the KTA rules in Reference 10.25.

CFD Model Pressure Drop Predictions

To estimate the pressure drop within the model a series of axial planes spaced 10 mm apart were created, which is the same methodology used in Section 10.5.5.1. The area weighted average pressure on each of these planes was calculated within the valid simulation region. These pressure values are plotted in Figure 10.5.19 and Figure 10.5.20 for the flow rates examined. The figures also include a linear least-squares best fit line for the CFD model data with its corresponding equation. The nominal, upper bound and lower bound on the KTA rules pressure drop correlation are also

included in the figures for reference (the KTA rules pressure drop correlation was previously discussed in Section 10.5.5.1. Since the work documented in Section 10.5.5.1 found that the domain was not large enough to adequately study the radial pressure drop this was not examined further during the current sensitivities.

Figure 10.5.19: Pressure Drop Prediction for 15kg/s Core Coolant Flow Rate (Power Proportional to Flow Rate)
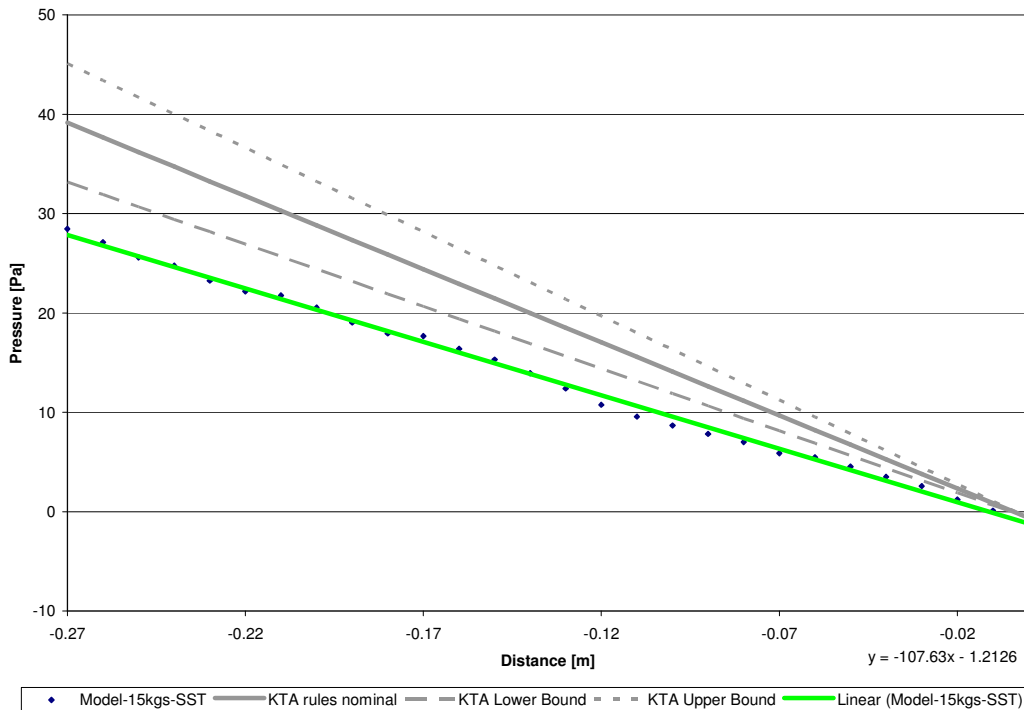
Figure 10.5.20: Pressure Drop Prediction for 75kg/s Core Coolant Flow Rate (Power Proportional to Flow Rate)
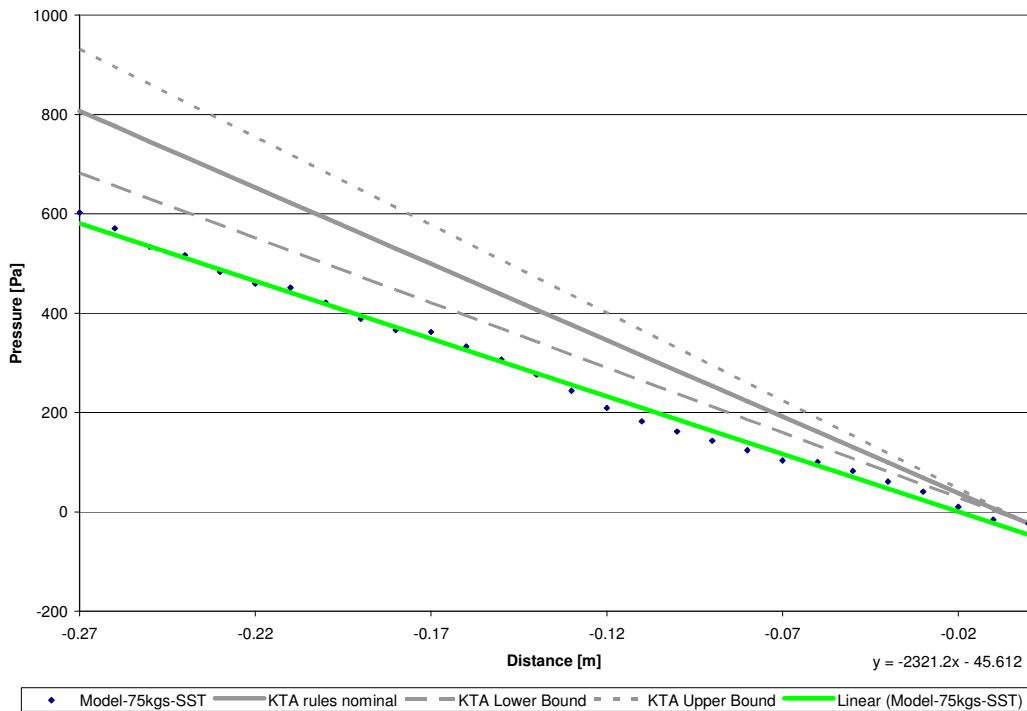
KTA Pressure Drop Predictions

As documented in Section 10.5.5.1 the KTA rules provide a correlation for predicting pressure drop; however, it is not intended to be applied specifically to near wall regions of a packed bed. The KTA pressure drop predictions presented here were calculated in a manner consistent with that reported in Section 10.5.5.1. The results of the sensitivity cases with the power proportional to the flow show the same trends as were previously seen with the pressure drop predicted by the CFD model being less than that predicted by the KTA rules. A summary of predicted pressure drop and the 95% confidence bounds on the correlation results is provided in Table 10.5.10 and plotted in Figure 10.5.19 and Figure 10.5.20.

Table 10.5.10: Pressure Drop Predictions – Reflector Model with the Power Proportional to the Flow Rate

Flow Rate	Pressure Drop (Pa/m)			
	KTA rules Correlation (Based on Reflector Values)			CFD Model
	Nominal	Lower Bound	Upper Bound	Reflector Model
15 kg/s	147	125	169	108
75 kg/s	3075	2614	3537	2321

These values are slightly lower than those found when the power was held constant (see Table 10.5.2).

Based on the similarities between the current and previous models and results where the power was not proportional to the flow, the correction to the KTA pressure drop correlation should also be valid when the power is proportional to the flow.

10.5.6.2 Heat Transfer Coefficient

This section presents estimates for heat transfer coefficients between the pebbles and the coolant with the reactor power proportional to coolant flow rate.

Pebble Surface Heat Transfer Coefficients

In Section 10.5.5.2 the pebble surface to coolant heat transfer coefficient was estimated using the modified Reynolds analogy, CFD thermal solution and the KTA correlations and this is also calculated for the simulations with power proportional to flow.

Comparisons

Figure 10.5.21 and Figure 10.5.22 show the probability distribution functions (PDF) for the pebble average heat transfer coefficients within the valid simulation region for the sensitivity cases performed with the power proportional to the coolant flow. These figures include PDFs based on the Reynolds analogy and the thermal solution. The KTA rules values are also included on these figures and a summary of the heat transfer coefficients calculated using the various methods is presented in Table 10.5.11.

Figure 10.5.21: Distribution of Average Pebble Heat Transfer Coefficient for 15kg/s Core Coolant Flow Rate (Power Proportional to Flow Rate)
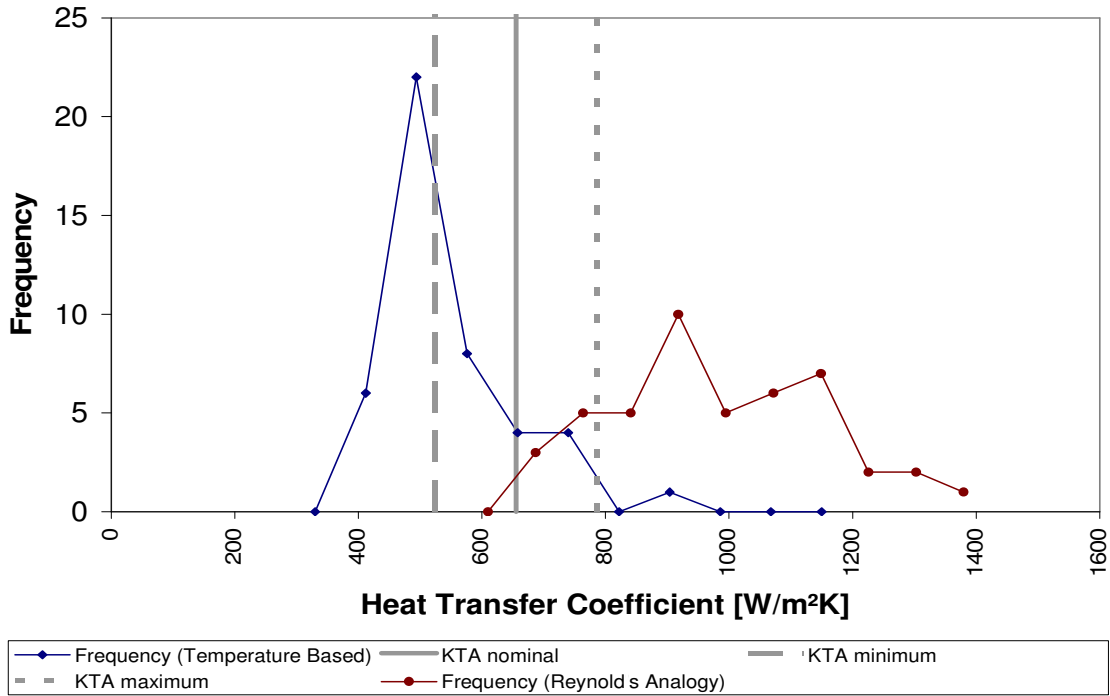
Figure 10.5.22: Distribution of Average Pebble Heat Transfer Coefficient for 75kg/s Core Coolant Flow Rate (Power Proportional to Flow Rate)
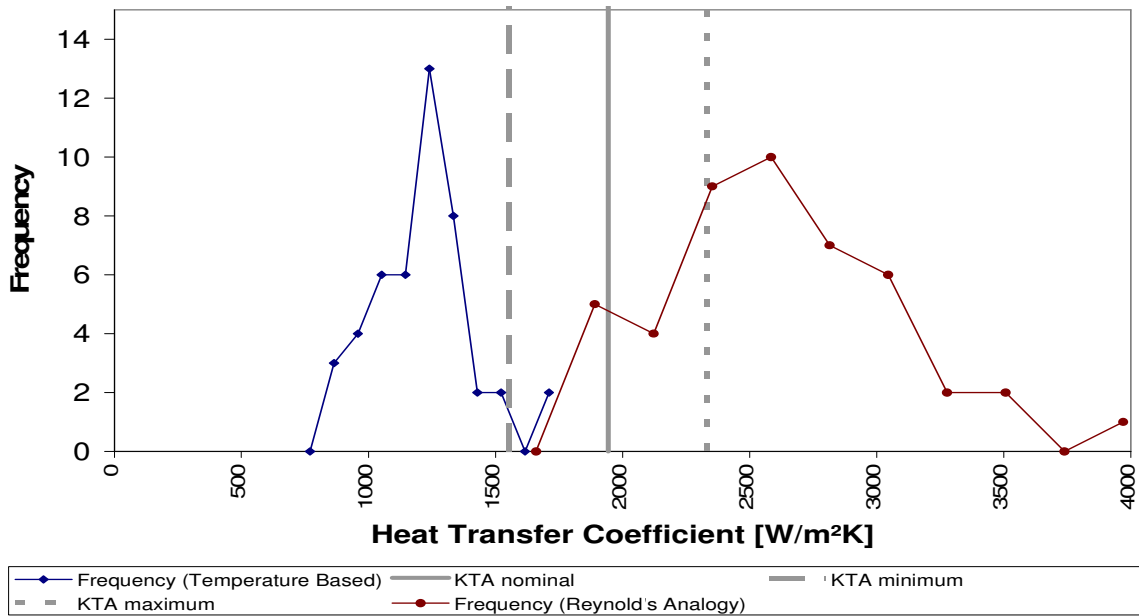
These figures indicate that with the power proportional to the flow the previous trends are still apparent, with the thermal solution predictions tending to be lower than the KTA correlation and the estimate from the Reynolds analogy tending to be higher than the KTA correlation. The sensitivity cases produced average heat transfer coefficients that are very similar to the previous work and the percent difference between the KTA and thermal and Reynolds analogy are also similar to that calculated when the power was held constant (see Table 10.5.8).

Table 10.5.11: Comparison of Average Heat Transfer Coefficient in Reflector Model with Power Proportional to Coolant Flow Rate (W/m²K)

Flow Rate	KTA rules correlation	CFD Models & Thermal Solution	% Difference from KTA	CFD Models & Reynolds Analogy	% Difference from KTA
15 kg/s	655	511	-22%	940	44%
75 kg/s	1944	1162	-40%	2499	29%

As stated in Section 10.5.5.2 it can not be concluded that any one particular method is superior to another for calculating the heat transfer coefficient. The Reynolds analogy over predicts the heat transfer coefficients and the thermal solution under predicts the heat transfer coefficient compared to the KTA rules.

10.5.6.3 Reflector Heat Transfer Coefficients

The heat transfer coefficients for the reflector were calculated for the simulations with the power proportional to the flow and the results are presented in Table 10.5.12. The heat transfer coefficients are similar to those previously calculated without the power reduced to be proportional to the flow with the two methods (i.e., Reynolds Analogy and thermal solution) producing significantly different heat transfer coefficients. A more detailed comparison of the two methods is found in Section 10.5.5.2. An additional sensitivity study was performed to calculate reflector heat transfer coefficients, and the results are presented in Section 10.5.7.1.

Table 10.5.12: Reflector Heat Transfer Coefficient Estimates with the Power Proportional to the Coolant Flow Rate (W/m²K)

Flow Rate	CFD Models & Reynolds Analogy	CFD Models & Thermal Solution
15 kg/s	798	288
75 kg/s	2222	592

10.5.6.4 Pebble Temperature Variations

The variation in the pebble surface temperatures for all three flow rates were also examined as part of the analysis. For the 75 kg/s and 15 kg/s flow rates the simulations with the power proportional to flow were used. For the 150 kg/s flow rate the data was extracted from the model discussed in Section 10.5.5. Histograms showing the variation in the pebble temperatures for the various flow rates are presented in Figure 10.5.23, Figure 10.5.24, and Figure 10.5.25.

These figures show that the variation in the maximum and minimum temperatures with regards to average temperature increases at higher powers and flows which is expected[17]. These figures also show that the most frequent minimum and average temperatures on the pebbles are closer than the maximum and average temperatures. However, at all flow rates, there are some pebbles with minimum temperatures that are much lower than the other pebbles. The pebbles with very low minimum temperatures were found to be touching the reflector wall and this indicates that these low temperatures are likely to due wall channeling and conduction to the cooler reflector. Figure 10.5.26[18] shows that for a pebble that touches the wall the coldest region is small and localized, which is why these very low minimum temperature do not significantly impact the average pebble temperatures. As previously discussed in Section 10.4.7.3 the highest temperature regions on the pebbles are expected to be small and localized near the pebble contacts.

---

[17] Note that the facet temperatures were used to determine the minimum and maximum values and that the average values are the area-weighted average facet temperature, which is consistent with the average pebble temperature that was used to calculate the heat transfer coefficients for the thermal solution.

[18] Note that the center of the contact is actually a cutout on the pebble surface, so the yellow that can be seen in the middle of the blue cold region is actually the temperature on the other side of the pebble and does not mean that center of the contact is much warmer than the surrounding region.

Figure 10.5.23: Distribution of Average, Minimum and Maximum Pebble Temperature for 150kg/s Core Coolant Flow Rate (Power Proportional to Flow Rate)
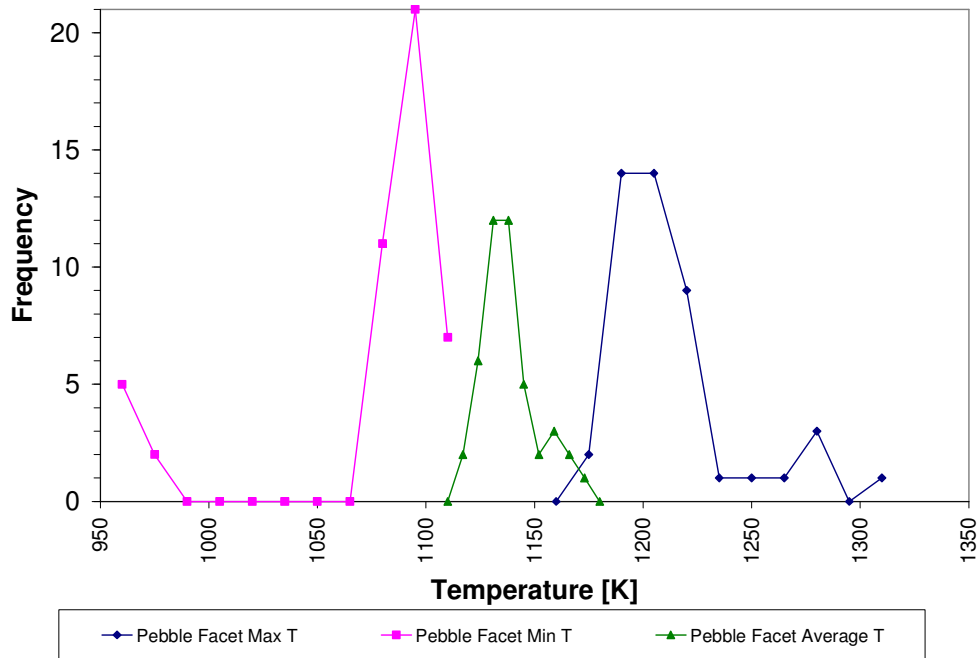
Figure 10.5.24: Distribution of Average, Minimum and Maximum Pebble Temperature for 75kg/s Core Coolant Flow Rate (Power Proportional to Flow Rate)
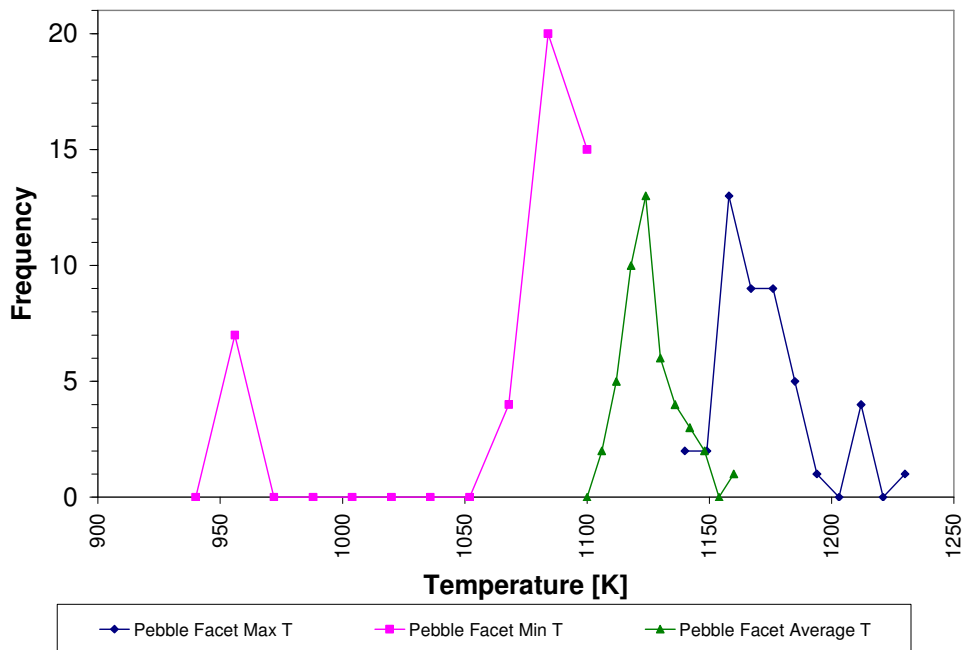
Figure 10.5.25: Distribution of Average, Minimum and Maximum Pebble Temperature for 15kg/s Core Coolant Flow Rate (Power Proportional to Flow Rate)
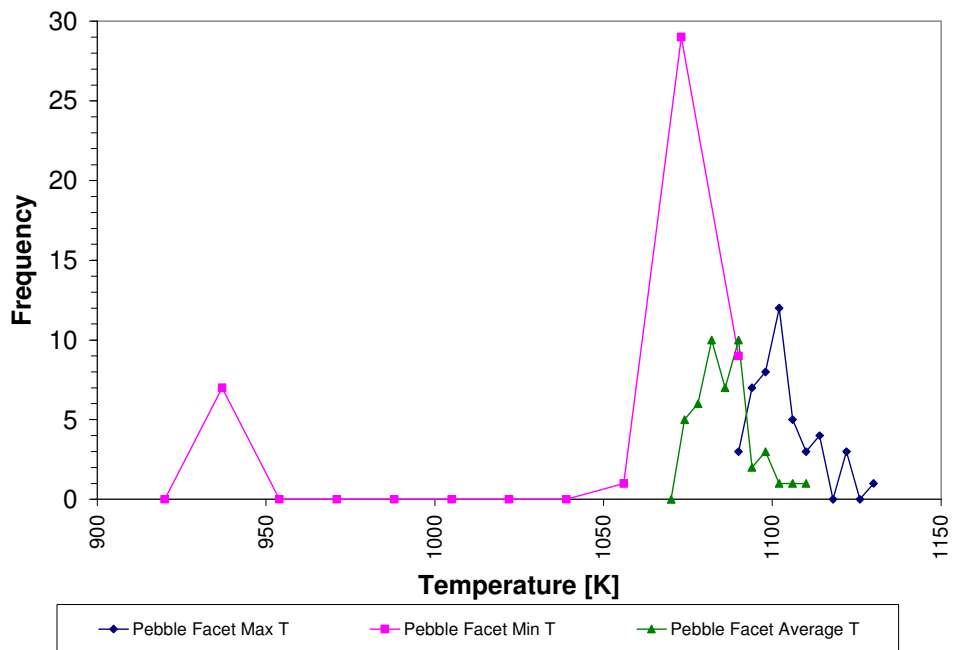
Figure 10.5.26: Facet Temperature on Pebble that Touches the Reflector Wall for a Flow Rate of 150 kg/s
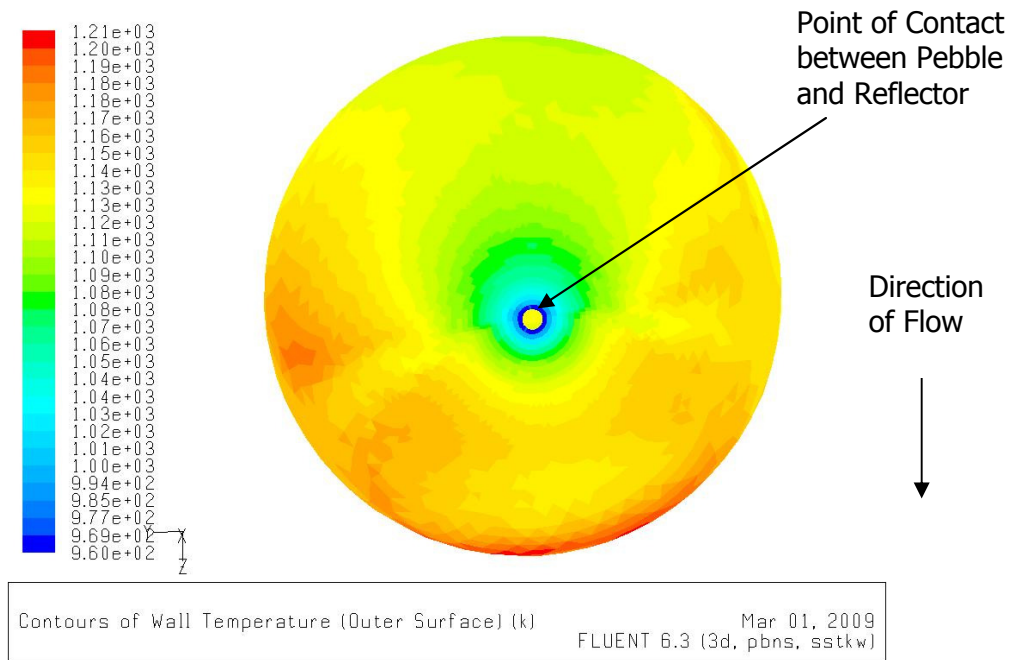
10.5.7 Results of Sensitivity Cases with Increased Heat Transfer to the Reflector

As discussed in Section 10.5.4, sensitivity studies were performed by making modifications to the model in order to increase the heat transfer to the reflector wall. This section discusses the results of the sensitivity studies.

10.5.7.1 Reflector Heat Transfer Coefficients

The heat transfer coefficients for the reflector at the various flow rates are presented in Table 10.5.13. The heat transfer coefficients are similar to those previously calculated without the power reduced to be proportional to the flow with the two methods (i.e., Reynolds Analogy and thermal solution) producing significantly different heat transfer coefficients. A more detailed comparison of the two methods is found in Section 10.5.5, but only the heat transfer coefficients predicted using the thermal solution are calculated for these sensitivity cases. The results in Table 10.5.13 show that the heat transfer coefficients are similar to those previously presented in Sections 10.5.5.3 and 10.5.6.3. The reason for this is that although there is significantly higher heat transfer to the reflector for these sensitivity cases the increase in the heat flux was negated by the cooler reflector surface (which increased the temperature difference between the reflector and the free stream temperature). One point of interest is that the free stream temperature (calculated 0.01 m from the wall) did not change significantly when the results from these sensitivity cases where compared to the simulations previously completed with the power proportional to the flow. For both the 150 kg/s and 75 kg/s simulations the free stream temperature changed by less than 2 K indicating that 0.01 m away from the reflector is a reasonable distance to calculate the free stream temperature.

Table 10.5.13: Reflector Heat Transfer Coefficient Estimates (W/m²K)

Flow Rate	CFD Models & Thermal Solution (Sensitivity Cases with Increased Heat Transfer to the Reflector)	CFD Models & Thermal Solution (Power Proportional to Coolant Flow, from Table 10.5.12)	CFD Models & Thermal Solution (from Table 10.5.9)
15 kg/s	305	288	322
75 kg/s	711	592	511
150 kg/s	1194	984	984

For the 150 kg/s case, contours of temperature in the valid region were plotted on the reflector wall and the reference free stream plane 0.01 m from the reflector wall. As can be seen in Figure 10.5.27 the reflector temperature in the valid region of the domain still shows significant variation in the vertical direction with the flow being between 50-100 K cooler near the entrance of the domain. Figure 10.5.27 also shows that the free stream temperature (measured 0.01 m from the reflector wall) is stable from the top to the bottom of the valid region. Therefore, the reflector heat transfer coefficient is being underestimated when the average reflector temperature (averaged

over the entire valid simulation region) is used. This could also be an artifact of the limited solution domain that has been used for this study. As seen in Figure 10.5.27 near the entrance to the valid simulation region there are very few pebbles touching the reflector, which may be locally enhancing wall channeling effects and locally decreasing the reflector temperature. Similar plots have been generated for the 75 kg/s case (Figure 10.5.28) and 15 kg/s case (Figure 10.5.29) and the same trend is apparent for these cases as well.

Because the reflector temperature profile at the bottom half of the valid simulation region is more uniform, the reflector heat transfer coefficients were calculated using the data for the bottom half and bottom quarter of the valid simulation region as well. These new heat transfer coefficients are shown in Table 10.5.14. The values in this table indicate that there can be significant variation in the heat transfer coefficient along the reflector wall and that the heat transfer coefficient may vary significantly over the height of the pebble bed in the PBMR reactor. Since the reflector heat transfer coefficient in the bottom quarter of the valid region is very similar to that for the bottom half of the reflector it could be that the reflector heat transfer coefficient takes longer to stabilize than the pebble surface temperatures. In order to truly examine the variation in the reflector heat transfer coefficient and determine if they stabilize deeper in the bed the height of the pebble bed would need to be increased. It is expected that similar trends would be seen if the previous simulations were revisited and the reflector heat transfer coefficients were calculated at different depths within the valid region of the pebble bed simulated.

Table 10.5.14: Reflector Heat Transfer Coefficient Estimates: Sensitivity Cases with Increased Heat Transfer to the Reflector (W/m²K)

Flow Rate	CFD Models & Thermal Solution	CFD Models & Thermal Solution (Bottom Half of Valid Simulation Region)	% Diff	CFD Models & Thermal Solution (Bottom Quarter of Valid Simulation Region)	% Diff
15 kg/s	305	346	13%	375	23%
75 kg/s	711	938	32%	957	35%
150 kg/s	1194	1616	35%	1665	39%

Figure 10.5.27: Temperature on the Reflector Wall and 1 cm from the Reflector Wall for the 150 kg/s Case

Reflector Temperature for the Valid Simulation Region
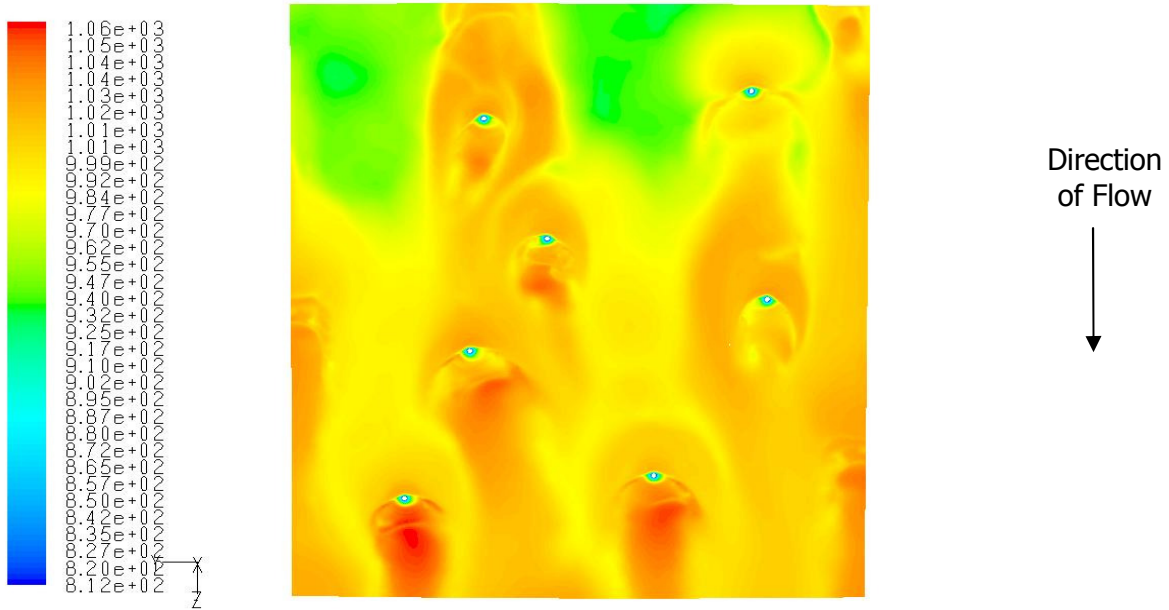
Direction of Flow

Contours of Static Temperature (k)

Feb 19, 2009
FLUENT 6.3 (3d, pbns, sstkw)

Temperature 0.01 m away from the Reflector Wall in the Valid Simulation Region

Direction of Flow
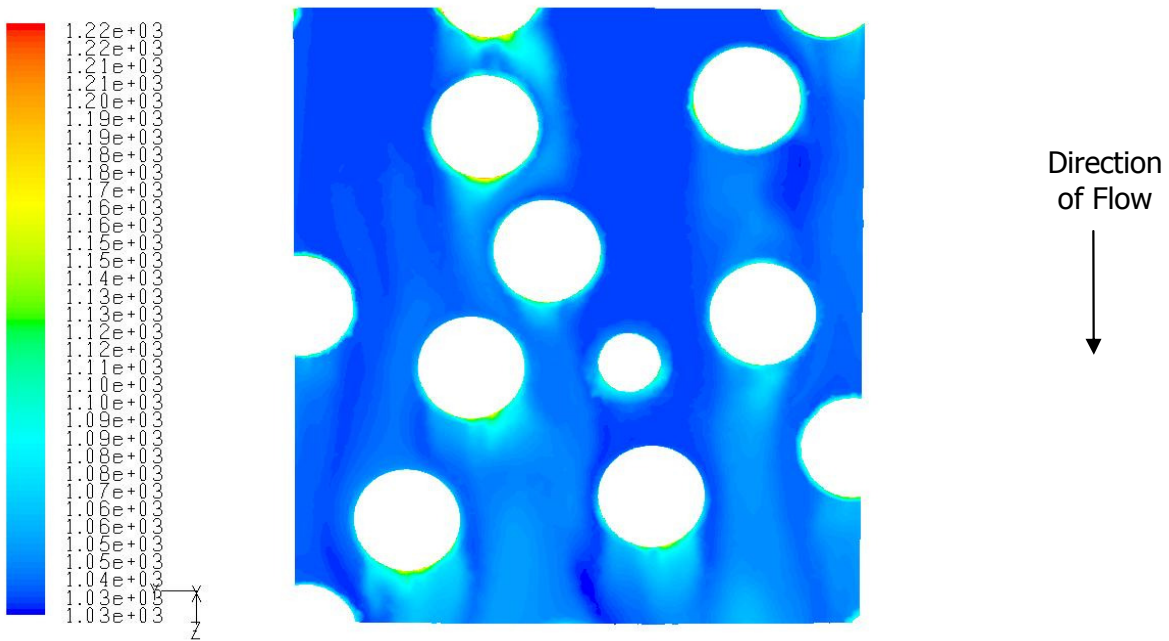
Contours of Static Temperature (k)

Feb 19, 2009
FLUENT 6.3 (3d, pbns, sstkw)

Figure 10.5.28: Temperature on the Reflector Wall and 1 cm from the Reflector Wall for the 75 kg/s Case

Reflector Temperature for the Valid Simulation Region

Direction of Flow

Temperature 0.01 m away from the Reflector Wall in the Valid Simulation Region

Direction of Flow
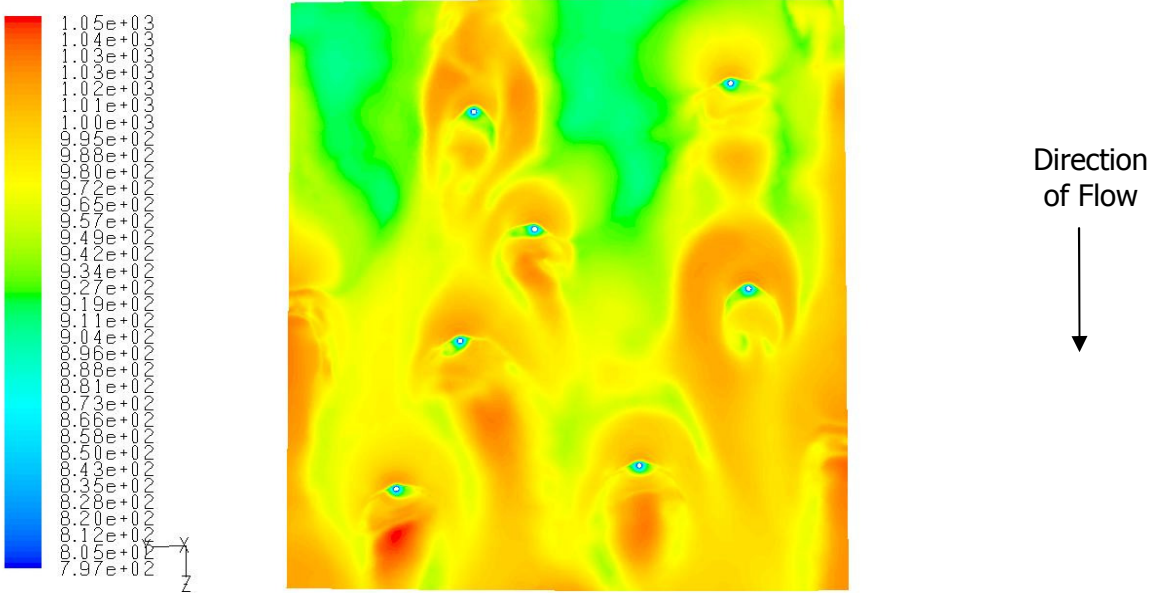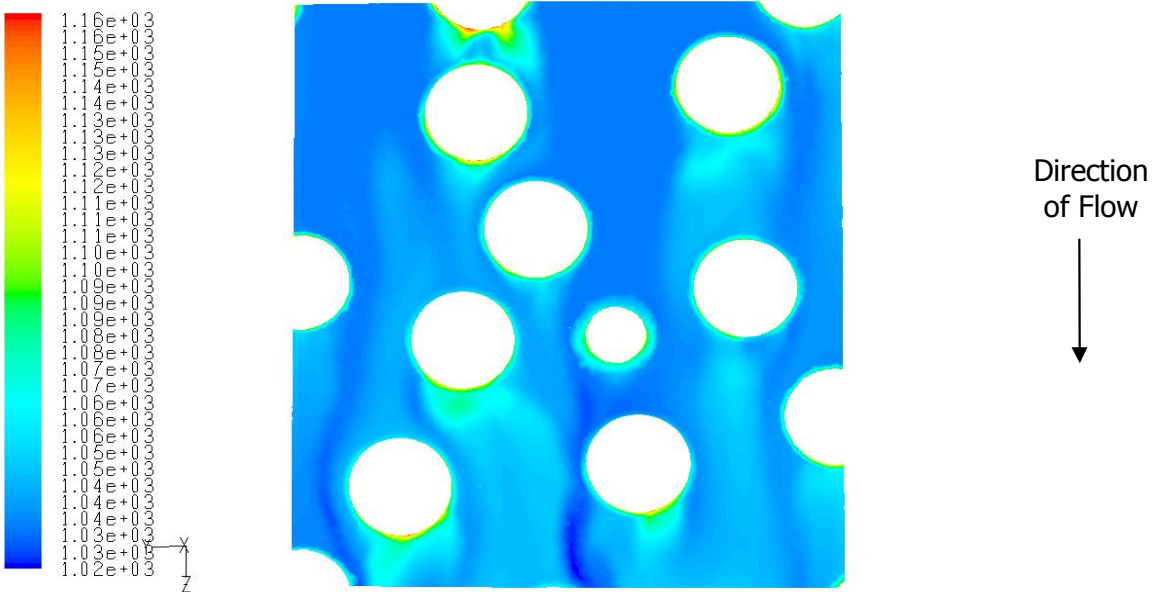
Figure 10.5.29: Temperature on the Reflector Wall and 1 cm from the Reflector Wall for the 75 kg/s Case

Reflector Temperature for the Valid Simulation Region

Direction of Flow

Contours of Static Temperature (k)   Feb 23, 2009
                                                       FLUENT 6.3 (3d, pbns, sstkw)

Temperature 0.01 m away from the Reflector Wall in the Valid Simulation Region

Direction of Flow
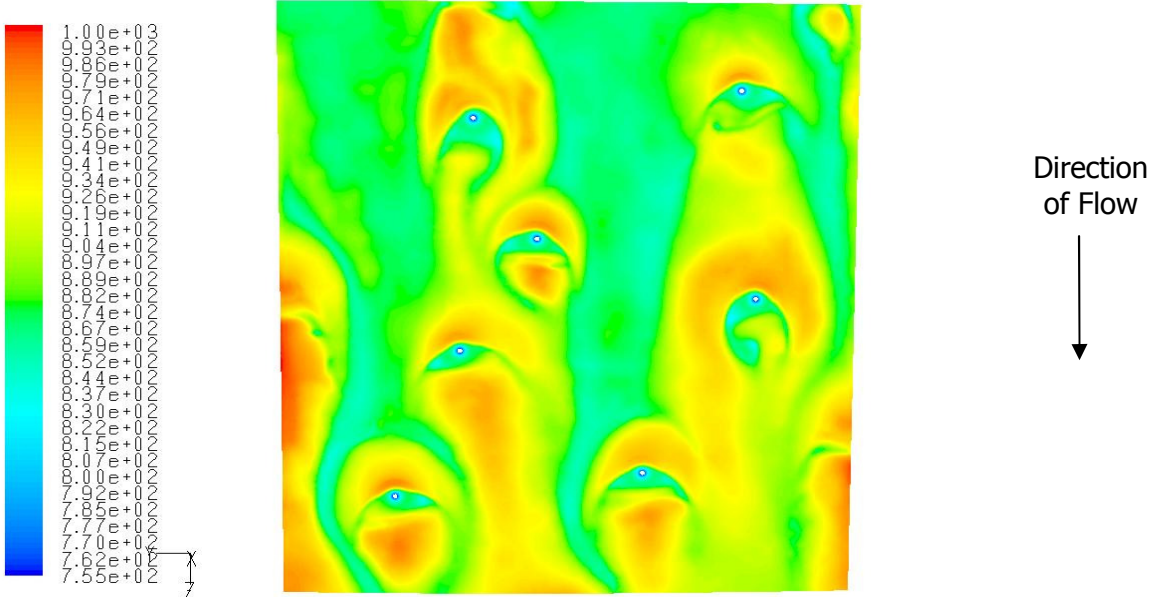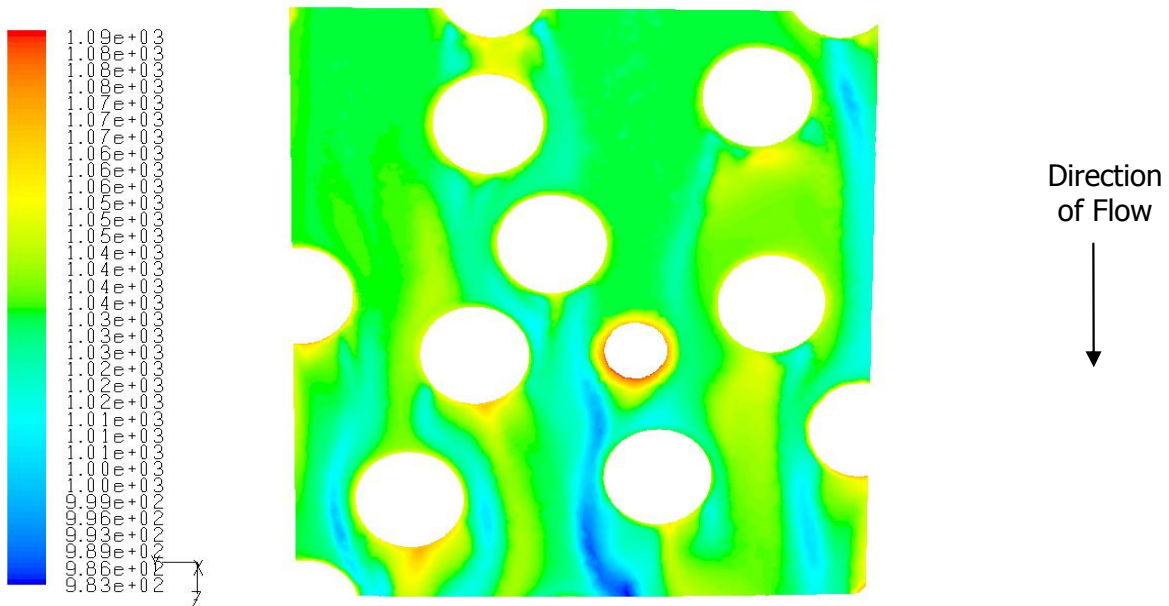
Contours of Static Temperature (k)   Feb 23, 2009
                                                       FLUENT 6.3 (3d, pbns, sstkw)

10.5.7.2 Comparison with Heat Transfer Coefficients from Literature

A literature survey was conducted to obtain fluid to wall heat transfer coefficients for a packed bed. These wall heat transfer coefficients values were compared to those obtained from the detailed CFD analysis discussed in Section 10.5.7.1.

Heat Transfer Coefficients from Literature

A literature search for wall heat transfer coefficients in pebble bed reactors turned up no useful results, however data from the chemical engineering field was available. In general the applications were to packed-bed heat exchangers where there is no heat generation in the pebbles and effective radial temperature distributions are comparatively easy to quantify. For this case the heat transfer coefficient can be quantified in terms of the Biot number or in terms of the Nusselt number. Brief descriptions of four references are provided below.

Correlations for Wall Heat Transfer Coefficients in terms of Biot Number

Dixon and Cresswell (Reference 10.28) found that a theoretically derived relation

$$Bi\left(\frac{d_p}{R}\right) = 3.0 \, \mathrm{Re}^{-0.25} \; for \, \mathrm{Re} > 40$$

predicted the heat transfer coefficient accurately over a wide range of conditions.

Where:

Bi   Apparent Biot number = $h_{w.eff} R / k_{r,eff}$

Re   Reynolds number = $G d_p / \mu$

d_p Particle/pebble diameter, m

R   Cylinder radius, m

$h_{w.eff}$ Effective wall to fluid heat transfer coefficient, $W/m^2 \cdot K$

$k_{r,eff}$ Effective radial conductivity, W/m.K

G   Superficial mass flow rate, kg/s

μ Kinematic viscosity, kg.m/s

One of the problems with this formulation is quantifying $k_{r,eff}$ for a random assembly of pebbles in proximity to a solid surface/fluid domain boundary.

Correlations for Wall Heat Transfer Coefficients in terms of Nusselt Number

Other relations for the wall heat transfer coefficient in terms of Nusselt number have been proposed by various authors:

1.   From Reference 10.28:

$$Nu_{fw} = \frac{h_{wf} d_p}{k_g} = \begin{cases} 0.6 \, \mathrm{Pr}^{1/3} \, \mathrm{Re}^{1/2} & (\mathrm{Re}\ 1-40) \\ 0.2 \, \mathrm{Pr}^{1/3} \, \mathrm{Re}^{0.8} & (\mathrm{Re}\ 40-2000) \end{cases}$$

Where:

Re   Reynolds number $= Gd_p/\mu$

d_p Particle/pebble diameter, m

R   Cylinder radius, m

h_{wf} Wall/fluid heat transfer coefficient, W/m^2·K

k_g Conductivity of the fluid, W/m.K

G   Superficial mass flow rate, kg/s

μ Kinematic viscosity, kg.m/s

2.   From Reference 10.29:

$$Nu = \frac{h_{wf} d_p}{k_g} = 0.17 \left(\frac{G d_p}{\mu} \right)^{0.79}$$

$$0.05 \le d_p / d_t \le 0.3$$

$$20 \le \mathrm{Re}_p \le 7600$$

With same symbol definitions as above, and

d_t tube diameter (reflector outside diameter), m

3.   From Reference 10.30, a relation for the Nusselt number is obtained from analogy to the mass transfer and is given by:

$$Nu = 8.9 \, \mathrm{Re}^{0.34} \, \mathrm{Pr}^{-0.07}$$

With same symbol definitions as above, and

Pr   Prandtl number, $\mu C_p / k_g$

C_p Heat capacity of the fluid, J/kg.K

4.   The references above provide the asymptotic wall heat transfer coefficients whereas Reference 10.31, provides a heat transfer coefficient correlation taking the inlet effects into account.

$$Nu = 0.096 \, \mathrm{Re}^{0.83} (x/d)^{-0.07}$$

With same symbol definitions as above, and:

x Axial distance from the inlet, m

d Particle (pebble) diameter, m

Comparison of Empirical Correlations to Numerically Determined Heat Transfer Coefficients

From the references quoted above it is apparent that the formulation in terms of Biot number provides accurate predictions of the apparent wall heat transfer coefficients over a wide range of conditions. The formulation in terms of Nusselt number versus Reynolds number is not unique and depends on many factors. For the application to a pebble bed reactor it is however not practical to determine $k_{r,eff}$ as in the empirical relation provided for the effective conductivity in Reference 10.28 one parameter needed is the wall heat transfer coefficient. Thus the only practical option was to compare to the remaining correlations.

Figure 10.5.30 shows the value of wall heat transfer coefficients as a function of superficial Reynolds number. The wall heat transfer coefficients were calculated from the Nusselt number using the thermal conductivity of helium at an average core temperature of 1018.5 K (which corresponds to the 75 kg/s flow case with power proportional to flow rate on the bottom quarter of the reflector). The correlations are shown for the range of valid Reynolds number only (note that References 10.30 and 10.31 do not provide limits of applicability of the correlations provided).

A summary of the geometric and fluid properties used in the evaluation of the heat transfer coefficient correlations is provided in Table 10.5.15.

Also shown in Figure 10.5.30 are the wall heat transfer coefficients obtained from the CFD runs summarized in Table 10.5.14 (which have corresponding Reynolds numbers: 2.44E+03, 1.22E+04 and 2.44E+04, for the 150kg/s, 75kg/s and 15kg/s cases, respectively).

Figure 10.5.30: Comparison of the Wall Heat Transfer Coefficients from Literature with the Calculated Heat Transfer Coefficients Using the CFD Models
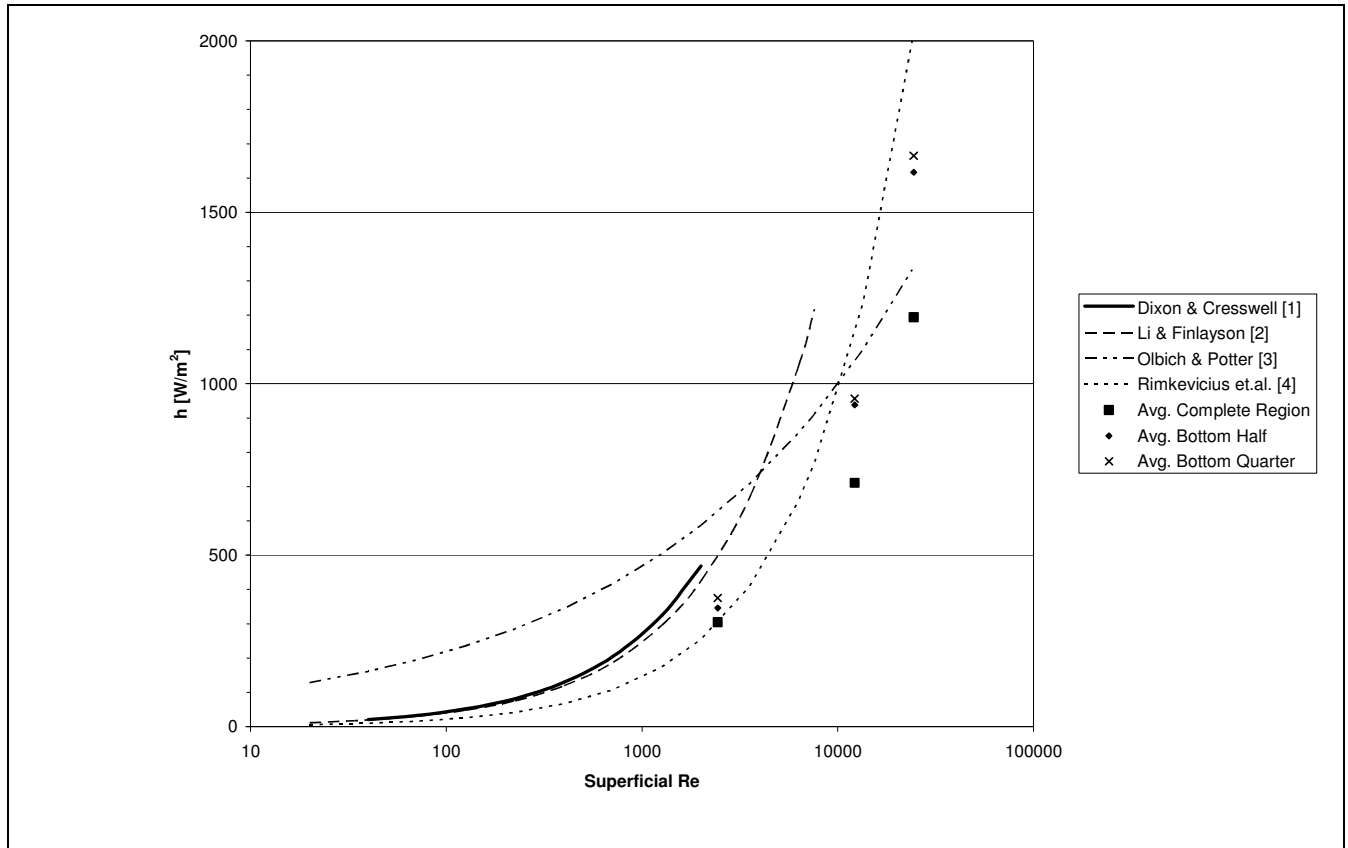
Table 10.5.15: Geometric and Fluid Properties Used in the Evaluation of Heat Transfer Correlations

Description	Value	Units
Pebble Diameter	0.06	m
Distance from inlet	2	m
Pressure	8915000	Pa
Average coolant T	1044.7	[K]
Average Reflector T	992.3	[K]
Reference temperature	1018.5	[K]
Specific Heat Capacity	5195	(J/kgK)
Conductivity at average temperature	0.3694	W/mK
Viscosity at average temperature	4.685E-05	Pa.s
Prandtl number	0.6589	-

Summary

Figure 10.5.30 shows that there is good agreement between the heat transfer coefficients based on averaging over the bottom half and those based on averaging over the bottom quarter of the reflector. This implies that the entrance effects diminish rapidly deeper into the domain. The values obtained for the lower half of the domain are the ones to be used in comparison to the correlations.

The heat transfer coefficients obtained numerically are consistently lower that those predicted by the correlation but follow a comparable trend.

10.6   CFD Model of a Larger Assembly of Pebbles Adjacent to a Reflector

A preliminary investigation of the "wall channeling" effect within a pebble bed reactor core bed was performed using CFD simulations in Section 10.5.5.4. These studies indicated that wall channeling does occur however the CFD model did not contain enough pebbles to produce statistically significant results, unless the results were averaged over large portions of the model (the model was actually split in half and predictions for flows in the inner and outer halves were produced).

The purpose of the model discussed here is to investigate the "wall channeling" phenomenon in further detail. The approach used before is fundamentally sound, however the CFD model needed to be significantly larger. The model in Section 10.5.2 represented an elliptical domain near the reflector wall. This model contained 14,712,914 computational cells. The model that is created in this work uses a solution domain that is virtually identical to the one described in Section 10.5.2 except that the minor radius of the elliptical domain was changed from a value of 0.12 m to 0.30 m and the axial extent of the valid solution region has been increased by 0.03 m (from 0.27 m to 0.30 m). This extension of the solution domain greatly increases the number of pebbles in the model especially near the reflector wall where wall channeling is suspected to be significant.

Core flow rates of 150 kg/s, 75 kg/s, and 15 kg/s were analyzed which lead to model inlet velocities of 4.8 m/s, 2.4 m/s and 0.48 m/s respectively.

10.6.1   CFD Models Used for Larger Reflector Case

10.6.1.1 Computational Mesh

The meshing strategy of Section 10.5.2 was utilized to create a grid for the solution domain using ANSYS Gambit. The mesh created in Gambit has significantly less resolution that the mesh used in Section 10.5.2. The mesh resolution was decreased as it was discovered that Gambit can not create meshes with more than 20 million cells. Once the Gambit mesh was imported into FLUENT and an initial solution was obtained the grid was refined in regions of high wall shear stress and velocity gradients. The resulting mesh has 14,955,101 computational cells.

10.6.1.2 Modeling Assumptions

The only purpose of the current model is to assess the wall channeling phenomenon, hence several effects can be neglected. This analysis assumes that the pebble bed does not generate any heat so the thermal solution was not required. In previous analyses the variation in the properties of the helium coolant in the model was taken into account however it is neglected here. The properties variations are not expected to vary greatly on a local scale when no thermal effects are present.

10.6.1.3 Material Properties

Since the study was isothermal the fluid properties were constant and no solid properties were required. The helium density was set to 4.11 kg/m^3 and the viscosity was 4.73e-05 kg/m-s.

10.6.1.4 Discretization

For the 150 kg/s case convergence was only achieved with first order discretization for all equations with the exception of pressure, which used the standard scheme. For the 75 kg/s and 15 kg/s cases convergence was achieved with the same settings as the 150 kg/s case, except that second order upwind was used for momentum. Although only first order convergence was achieved for momentum for the 150 kg/s case it is not expected that this is introducing any additional significant errors to the solution.

10.6.1.5 Boundary Conditions

This sub-section describes the boundary conditions that are used for the reflector CFD model shown in Figure 10.6.1.

Inlet

The inlet surface was modeled as a constant velocity boundary condition with a constant specified turbulence intensity and length scale (see light blue surface in Figure 10.6.1). For all simulations the turbulence intensity was set to 2.5% (low fluctuation) at the inlet with a length scale of one half of a pebble diameter (0.03 m). The velocity used for this boundary condition was determined from the flow rate for the entire core divided by the product of the coolant density and total core flow area. For this work total core flow rates of 15 kg/s, 75 kg/s and 150 kg/s are used which translate into velocities of 0.48 m/s, 2.4 m/s and 4.8 m/s.

An important feature of the geometry of the model is that an entrance region is incorporated into the model. This entrance region is 0.06m in length and contains only a partial compliment of pebbles. This region allows the uniform inlet velocity to develop naturally prior to entering the region of interest in the model.

Outlet

The outlet boundary condition is set to be a plane of constant pressure (see red surface in Figure 10.6.1). In absolute terms the pressure at the outlet is set to a value

of 89.1 bar, however in the simulation the relative pressure is set to zero. The outlet boundary condition in FLUENT allows flow to exit or enter the solution domain as required. All flow that re-enters the solution domain at this boundary condition is specified to enter in a direction normal to the boundary condition. The re-entrant flow is initially specified to have a turbulence intensity and length scale of 2.5% and 3 cm.

Symmetry

The outer wall of the elliptical domain is modeled as a symmetry plane (see yellow surface in Figure 10.6.1).

Reflector Wall

The reflector wall (grey surface in Figure 10.6.1) is modeled as a smooth impermeable no-slip wall.

Pebbles

Since the simulation was isothermal the boundary condition on the pebbles was simply a no slip wall.

Figure 10.6.1: CFD Solution Domain for Pebble Bed Model Adjacent to the Reflector
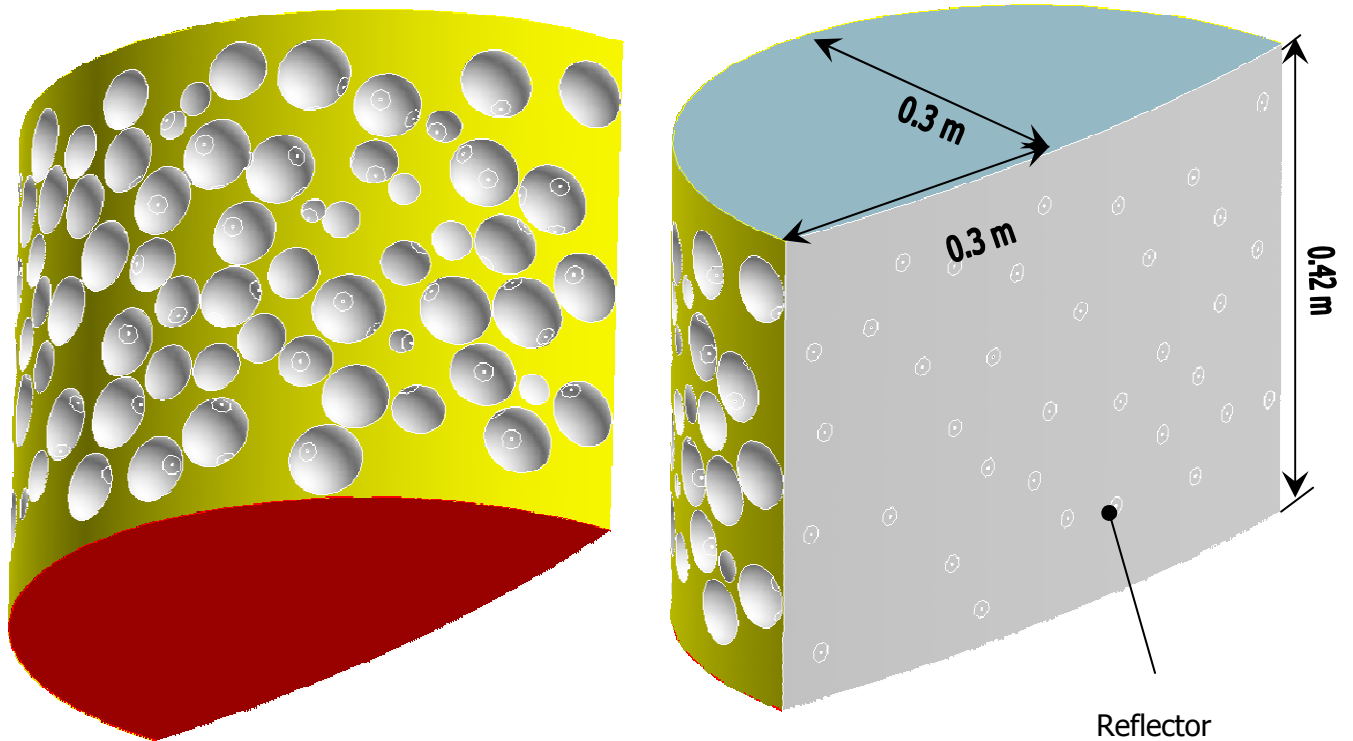
10.6.2 Results

10.6.2.1 Radial Distribution of Axial Velocity

Utilizing methods previously developed, a CFD model was created in FLUENT to predict the flow distribution. Two different methods were used to extract the flow distribution from the model[19]. The radial variation in the z-component (or the axial

---

[19] The first method extracted information approximately every $1/20^{th}$ of a pebble diameter, and the second method extracted information every $1/8^{th}$ to $1/4^{th}$ of a pebble diameter. Although the second method was less rigorous than the first method, it was found to produce very similar results and therefore it was not deemed necessary to evaluate the near wall velocities using both methods.

component) of the velocity is shown in Figure 10.6.2 for all flow rates and this figure shows that both of the methods used to extract the data produce very similar results. Also included in this figure is the porosity that was extracted from the CFD model (using Method 2). This figure clearly shows that the trend in the z-component of the velocity is similar with the peaks and troughs being visible at the same location for all flow rates. When the peaks and troughs are compared to the porosity in the figure it is also clear that these peaks and troughs arise due to the local variations in the packing fraction. The tabular data used to generate Figure 10.6.2 can be found in Table 10.6.1 (for methods 1 and 2).

Figure 10.6.2: Z-Velocity Component and Porosity for Flow Rate Cases of 150 kg/s, 75 kg/s and 15 kg/s Near the Reflector
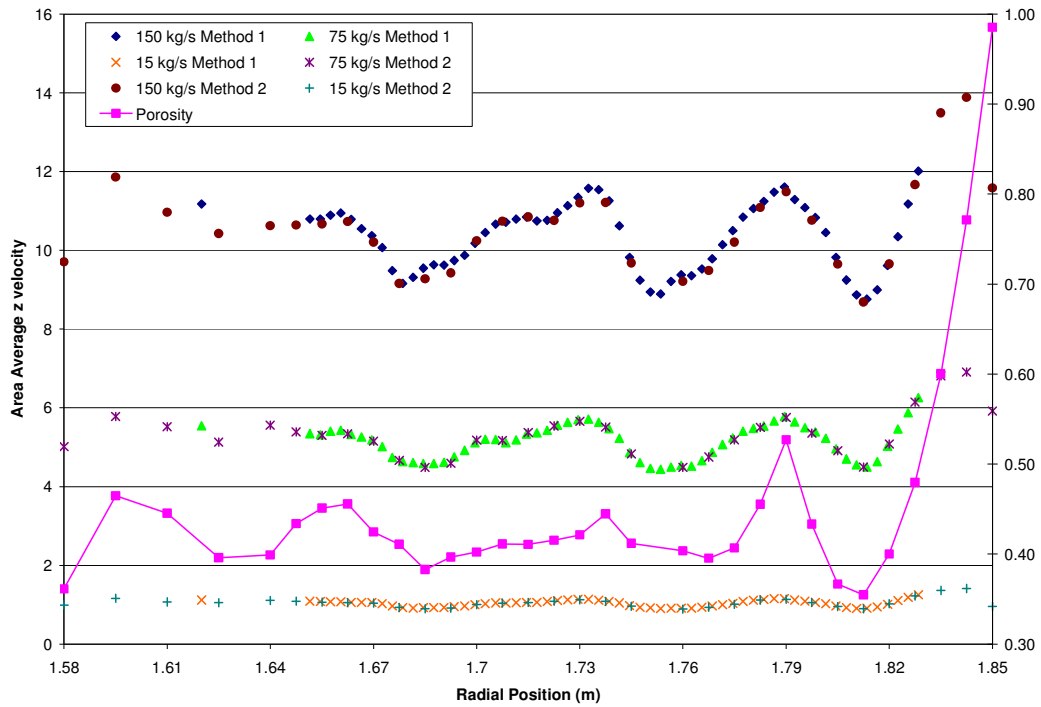
Table 10.6.1: Z-Velocity Component for Flow Rate Cases of 150 kg/s, 75 kg/s and 15 kg/s Near the Reflector

Radius Midpoint (m)	150 kg/s Z Velocity Component (m/s)	75 kg/s Z Velocity Component (m/s)	15 kg/s Z Velocity Component (m/s)	Radius Midpoint (m)	150 kg/s Z Velocity Component (m/s)	75 kg/s Z Velocity Component (m/s)	15 kg/s Z Velocity Component (m/s)
			Method 1				
1.56	10.3681	5.236013	1.007255	1.7625	9.357398	4.518157	0.907387
1.62	11.17731	5.54523	1.12053	1.7655	9.527982	4.656591	0.933292
1.6515	10.79539	5.345597	1.088189	1.7685	9.784999	4.869892	0.968908
1.6545	10.79728	5.316819	1.0799	1.7715	10.14042	5.069081	0.998693
1.6575	10.89346	5.402975	1.073547	1.7745	10.50144	5.237922	1.03674
1.6605	10.94704	5.432891	1.073496	1.7775	10.84641	5.402095	1.083528
1.6635	10.78823	5.322929	1.060524	1.7805	11.06137	5.478347	1.113675
1.6665	10.54697	5.255101	1.060477	1.7835	11.24459	5.536899	1.132558
1.6695	10.37253	5.18808	1.058746	1.7865	11.47953	5.667688	1.150502
1.6725	10.06683	5.012946	1.025167	1.7895	11.60915	5.776235	1.153586
1.6755	9.482358	4.740919	0.96731	1.7925	11.29117	5.640074	1.116834
1.6785	9.156783	4.634421	0.925614	1.7955	11.08447	5.497828	1.088948
1.6815	9.31331	4.611536	0.911898	1.7985	10.83163	5.38977	1.061675
1.6845	9.548035	4.584349	0.923397	1.8015	10.45159	5.22738	1.021917
1.6875	9.631924	4.584774	0.924716	1.8045	9.81816	4.958126	0.96986
1.6905	9.622963	4.614899	0.926612	1.8075	9.24417	4.70429	0.923622
1.6935	9.740616	4.754237	0.948569	1.8105	8.871407	4.551338	0.903571
1.6965	9.872345	4.921142	0.969796	1.8135	8.760592	4.493083	0.907688
1.6995	10.1779	5.116342	0.995515	1.8165	8.994894	4.636484	0.944702
1.7025	10.45321	5.198896	1.019788	1.8195	9.615354	5.024595	1.013688
1.7055	10.66694	5.192011	1.046906	1.8225	10.34283	5.463546	1.105548
1.7085	10.71399	5.115367	1.039014	1.8255	11.17713	5.877157	1.186373
1.7115	10.78963	5.18942	1.051955	1.8285	12.01242	6.257664	1.25111
1.7145	10.84526	5.336634	1.057101				
1.7175	10.74953	5.363223	1.057927				
1.7205	10.76032	5.428694	1.0786				
1.7235	10.9529	5.559023	1.108326				
1.7265	11.13398	5.631918	1.123648				
1.7295	11.3438	5.693813	1.135726				
1.7325	11.57363	5.713444	1.136229				
1.7355	11.53829	5.629376	1.111844				
1.7385	11.25867	5.472212	1.082587				
1.7415	10.61934	5.225458	1.04322				
1.7445	9.820297	4.864919	0.97793				
1.7475	9.237932	4.605104	0.933361				
1.7505	8.942348	4.463416	0.917836				
1.7535	8.890432	4.435609	0.898442				
1.7565	9.210999	4.499633	0.911312				
1.7595	9.374325	4.533023	0.91389				

Table 10.6-1 (cont'd)

Radius (m)	Method 2		
	150 kg/s Z Velocity Component (m/s)	75 kg/s Z Velocity Component (m/s)	15 kg/s Z Velocity Component (m/s)
1.535	8.402336	4.104085	0.764382
1.55	9.892462	4.847197	0.959422
1.565	10.12578	5.117271	0.974701
1.58	9.706591	5.014795	0.990498
1.595	11.86229	5.781301	1.160739
1.61	10.96864	5.52153	1.071565
1.625	10.42786	5.124216	1.052032
1.64	10.6246	5.5566	1.110262
1.6475	10.64037	5.386257	1.091461
1.655	10.67042	5.301531	1.066852
1.6625	10.72914	5.338142	1.051929
1.67	10.20638	5.151491	1.040887
1.6775	9.157501	4.662701	0.927927
1.685	9.274911	4.482209	0.895868
1.6925	9.426987	4.592683	0.915048
1.7	10.24081	5.177355	1.00272
1.7075	10.7399	5.169447	1.039403
1.715	10.84749	5.372905	1.053778
1.7225	10.75903	5.538271	1.091239
1.73	11.20133	5.654206	1.1227
1.7375	11.21493	5.509627	1.0832
1.745	9.678121	4.828487	0.964923
1.76	9.210033	4.488011	0.891244
1.7675	9.487775	4.750705	0.934215
1.775	10.20921	5.191341	1.012535
1.7825	11.08975	5.501535	1.116587
1.79	11.48801	5.752348	1.139698
1.7975	10.7642	5.36085	1.052937
1.805	9.647691	4.914042	0.950862
1.8125	8.686715	4.497731	0.895035
1.82	9.65181	5.079711	1.022725
1.8275	11.66836	6.146	1.220065
1.835	13.48933	6.809024	1.363152
1.8425	13.88255	6.907023	1.4118
1.85	11.5831	5.920229	0.956892

10.6.2.2 Porosity Comparisons

As part of the current work the porosity of the model was extracted every eighth of a pebble diameter[20] and compared to the z-component of the velocity. An additional step was taken to compare the porosities extracted from the model to the radial porosity calculations performed on the entire pebble bed, which is shown in Appendix D. The radial porosity data of the CFD domain and for the entire pebble bed are shown in Figure 10.6.3. This figure shows that there is good agreement between the global data and the much smaller CFD domain. This is especially true near the reflector wall where the packing fraction is noticeably disturbed, but the trend is nearly identical. Although the porosity in the CFD domain is very similar to that for the entire domain near the reflector wall, after about 1.7 m there is more variation about the mean porosity. This could indicate that the results in the CFD domain may be statistically less reliable after this radial location due to the smaller number of pebbles as the elliptical domain tapers inwards.

Figure 10.6.3: Comparison of Porosity for the Entire Pebble Bed and for the CFD Domain (Larger Reflector Model)

---
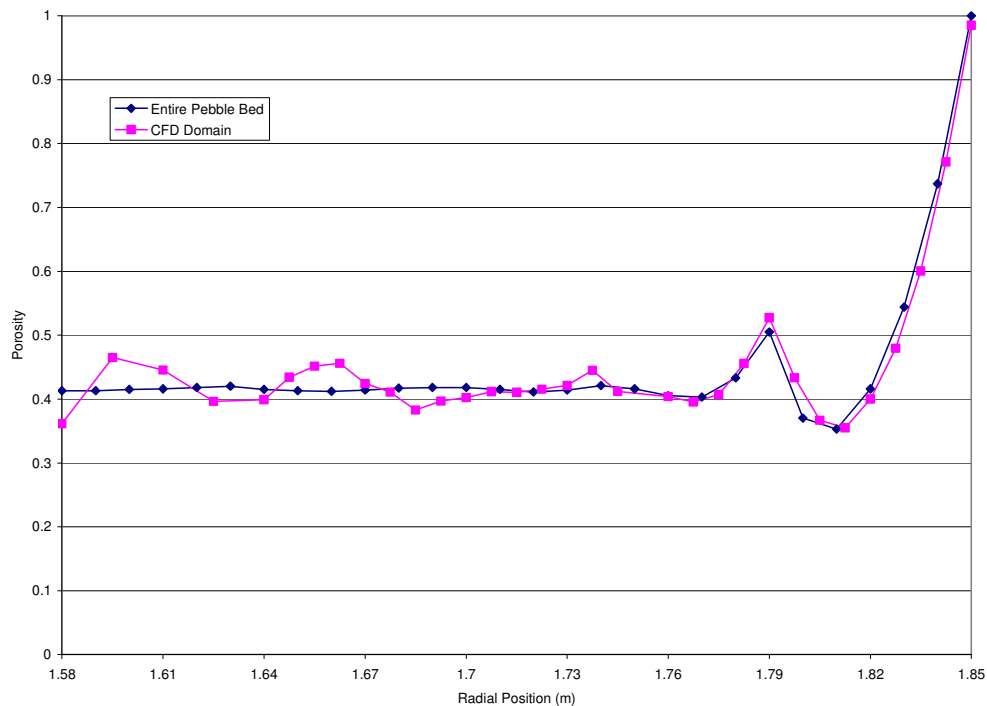
[20] This is true for a radius of 1.85 to 1.64 m and the planes were spaced 0.015 m thereafter.

10.7   CFD Model for Pebble-to-Pebble Heat Transfer in Multi-Batch Core

The goal of the work in this section is to determine through detailed CFD modeling the average surface temperature of individual pebbles remote from the reflector when there are multiple batches of fuel with different powers in the core. The results of this section are compared with those of analytical sub-model of Section 8.0. With this information available for each of the pebbles of interest the following information was obtained regarding the population of pebbles:

1. The average surface temperature of each batch of pebbles, and

2. The variation in the average surface temperatures for a given batch of pebbles.

10.7.1   Approach and Fundamental Assumptions

This work is an extension of the analysis done Section 10.4 and the methods used there are used, unless indicated otherwise. For this work the computational mesh in the fluid zone was identical to that in Section 10.4. An additional mesh was also required to model the solid pebble internals and this mesh was constructed independently of the fluid model of Section 10.4 and attached to the fluid mesh using an ANSYS FLUENT non-conformal interface. In ANSYS FLUENT a non-conformal interface is used to connect two meshes with dissimilar nodal distributions. Dissimilar meshes were used because only the conduction equation needed to be solved in the solid and fewer nodes were needed in the solid portion of the model.

With a portion of the graphite shell of the pebbles modeled it was also possible to incorporate the effects of having different batches of fuel (i.e., pebbles of different powers) included in the model. Model boundary conditions were then applied to the solution domain using ANSYS FLUENT. The ANSYS FLUENT solver was used to solve the mass, momentum, turbulence and energy conservation equations on this discrete solution domain to obtain the required outputs for this project.

In this model a 0.005m graphite shell was modeled for each of the pebbles and the energy equation was solved. The solution of the energy equation allows variations in temperatures in the graphite shell of the pebbles from each of the three different batches as well as temperature variation in the fluid.

While the introduction of the energy equation removes many approximations it also introduces additional modeling complexities which were discussed previously in Sections 10.4 and 10.5. Unlike the models in Sections 10.4 and 10.5, this model also considers radiation heat transfer between the pebbles and pebble to pebble contact conduction. Although radiation could be included in the models in Sections 10.4 and 10.5 pebble to pebble conduction could not be accurately modeled due to the use of shell elements. The current model is capable of accurately modeling pebble to pebble conduction since the graphite layer of the pebble is actually meshed with active cells.

10.7.2 CFD Models

This section describes the CFD model used to predict the pressure drops, velocities and pebble surface temperatures through an assembly of randomly packed pebbles far from the reflector of a PBR core. The following sub-sections describe the geometry modeled, material properties, boundary conditions, turbulence closure models, buoyancy force treatment, radiation model and numerical methods used in the model.

10.7.2.1 Modeled Geometry

The geometry generation procedure for the current model requires that geometry be created for both the fluid and solid portions of the simulation domain. For the fluid domain the model is identical to that outlined in Section 10.4 as the same assembly of pebbles was used (as shown in Figure 10.4.1).

This model contains 129 pebbles, including 49 pebbles that do not touch the boundaries of the solution domain. For each of these pebbles a 0.005m solid graphite shell is included in the model. There were about half a dozen instances where the edge of the domain sliced the pebble such that it was not possible to model the 0.005m thickness of the graphite shell. The solid portion of the pebble was still included in the model.

Within this geometry the pebble to pebble contacts are modeled using the same contact size and methodology as used in Section 10.4, this indicated that the radius of contact between two pebbles is approximately 0.0085 m. In this model, conduction from pebbles of higher temperature to touching pebbles of lower temperature is considered. This contact area plays a more significant role than in the previous model.

10.7.2.2 Computational Mesh

The current model uses the same unstructured tetrahedral and prismatic element mesh for the fluid domain as used in Section 10.4, so the results can be compared more easily. For the solid graphite shell of the pebbles an additional mesh was generated. For the solid graphite internals of the pebbles, only the conduction equation needs to be solved. Therefore, the computational mesh can be significantly coarser and generated using rectangular prism and triangular prism elements. The final surface mesh on the solution domain is shown in Figure 10.3.2 for the fluid mesh and in Figure 10.7.1 for the solid portions of the pebbles. This mesh contains ~11,500,000 cells (of various types) in the fluid zone and ~1,250,000 cells in the solid zone giving a total of ~12,800,000 cells.

Figure 10.7.1: Sample Image of Final Solid Mesh
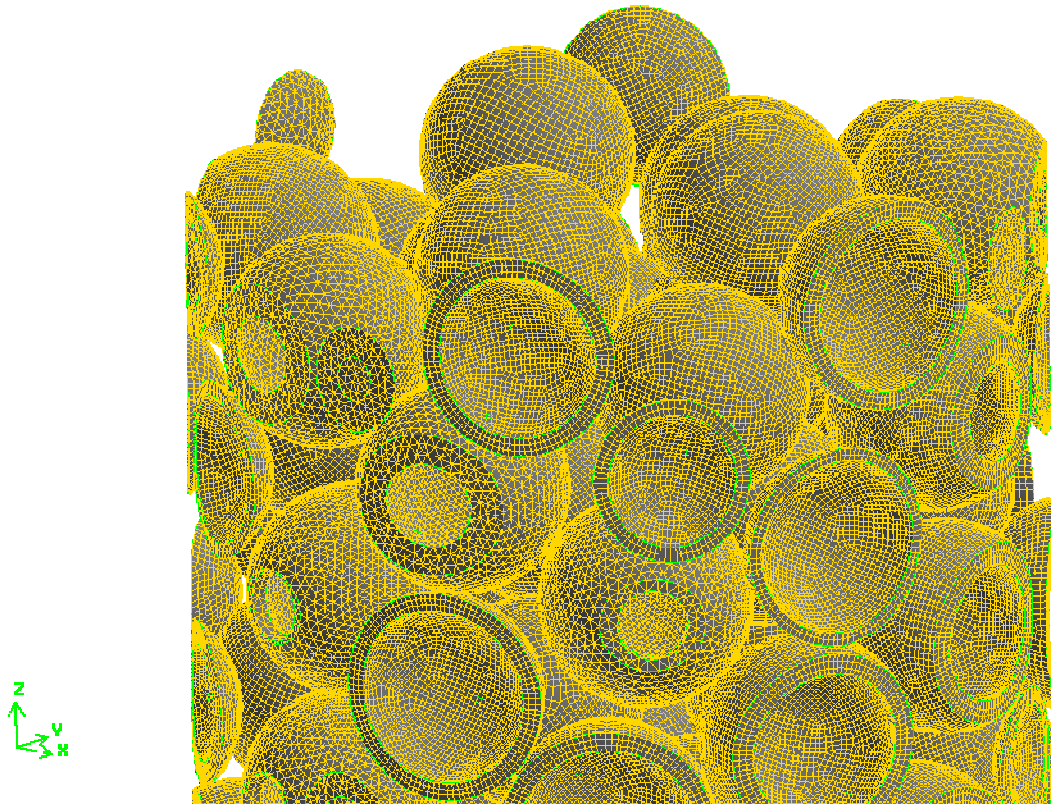
10.7.2.3 Boundary Conditions

This sub-section describes the boundary conditions that were used for the current CFD model.

Inlet

The inlet boundary conditions are the same as in Section 10.4.2.1, and the emissivity of the inlet was set to zero.

Outlet

The outlet boundary conditions are the same as in Section 10.4.2.1, and the emissivity of the outlet was set to zero.

Symmetry

The outer surface of the cylindrical domain is modeled the same as in Section 10.4.2.1.

Pebbles

The outer surfaces of the pebbles are modeled as smooth impermeable no-slip walls. The interior surface of the pebbles is on the inside of the 5 mm graphite shell and it is also modeled as an interior wall within the solid shell.

The heat flux generated within the pebbles would ideally be modeled by a neutronics code coupled to the thermal-hydraulic simulation; however, this is beyond the scope of the current work. For this work the heat load from the fuel is modeled assuming that there are three different batches of fuel in the model as follows:

- Batch 1 – average power
- Batch 2 – 0.5*average power
- Batch 3 – 1.5*average power

These three batches have a different heat flux applied to the interior surface of the pebbles, but first the average heat flux per pebble is calculated. Based on data in Table 4.2-1, Table 4.2-2 and Table 4.2-8 of Reference 10.13 the average pebble power is approximated as being 400MW/451,527 pebbles= 886 W/pebble. The interior surface area of a single pebble is 7.85E-3 m^2, which results in the following fluxes for each of the batches being modeled:

- Batch 1 (average power) – 886 W/pebble/7.85×10^{-3} m^2 = 1.128×10^5 W/m^2

- Batch 2 (average*1.5) – 1329 W/pebble/7.85×10^{-3} m^2 = 1.692×10^5 W/m^2

- Batch 3 (average*0.5) – 443 W/pebble/7.85×10^{-3} m^2 = 5.640×10^4 W/m^2

These heat fluxes were then applied to each of the full pebbles in the domain depending on which batch they belonged to.

Each pebble was randomly assigned to one of the three batches. Since the population of full pebbles is small (a total of 39 full pebbles are contained completely within the domain when the pebbles in the entrance and exit regions of the model are ignored) some constraints were imposed on the random assignment of pebbles to the various batches.

Once the pebbles had been randomly assigned a quick check was completed where the X and Z locations of the pebbles in each batch are plotted to assess if the distribution appeared truly random. Figure 10.7.2 confirms that the assignment of the pebbles to the various batches appears to be random.

Figure 10.7.2: Plot of X and Z Locations of the Pebbles in Each Batch
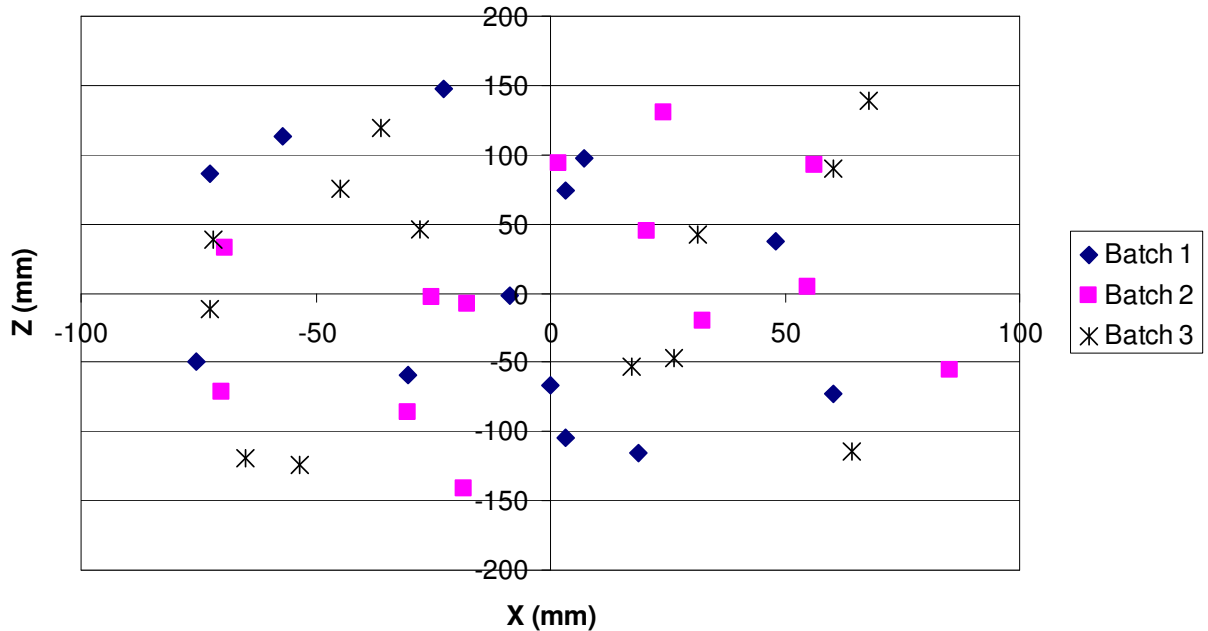
Once the batch assignment process had been completed for the 39 pebbles in the center of the core that are used to sample various solution data the process was repeated for all of the remaining pebbles in the model. There are 86 additional pebbles for which the internals are included in the model. Using the same methodology discussed above, each of these pebbles was assigned to one of the three batches.

10.7.2.4 Turbulence model

This model used the SST turbulence model, which is the same model used in Section 10.4.2.2.

10.7.2.5 Buoyancy model

The model includes buoyancy forces that are represented directly from coolant density variations. The gravitational acceleration vector in this model points in the direction of the flow and has a magnitude of 9.81 m/s² as was used in Sections 10.4.3.3 and 10.5.2.5.

10.7.2.6 Radiation model

Although FLUENT has many different radiation models it was found that many had limitations that made them unsuitable for use in this work. For example some models such as the Discrete Transfer Radiation Model (DTRM) and the Surface-to-Surface (S2S) models can not be used when the model includes non-conformal interfaces (such as the interface used to connect the solid pebble internals to the fluid domain).

Other models, such as the Rosseland and P-1 model were developed for use with optically thick fluids, which helium is not. Therefore, after reviewing the available models in the code the Discrete Ordinates (DO) model was chosen for the simulation and this model is described in Reference 10.10. No additional sensitivity cases were preformed using the other radiation models.

The DO model does not perform ray tracing, but instead includes a transport equation for radiation intensity in spatial coordinates. There are two different implementations of the DO model and the uncoupled version was chosen for the simulation. The FLUENT manual recommends using the coupled version of the DO model if the optical thickness is greater than 10, but this did not apply in this instance. Radiation from surfaces is modeled as diffuse. All pebbles are assumed to be gray bodies (the emissivity is equal to the absorbtivity) with a constant emissivity.

10.7.3 Results

10.7.3.1 Valid Simulation Region

Throughout the discussion of these results the valid simulation region is used to calculate the values of interest. This region is shown in Figure 10.3.2 and is a 0.3 m vertical region, centrally located on the solution domain that contains a full compliment of pebbles. While there are pebbles outside of this region they are in regions of reduced pebble packing fraction and these pebbles are not considered in the final results. Also, as discussed in Section 10.4.5.3 pebbles that have centroids within 0.04 m of the symmetry plane should not be used to calculate quantities of interest. This results in 9 of the 39 full pebbles being excluded from the detailed calculations in the following sections.

10.7.3.2 Batch Temperatures

CFD Batch Temperature Predictions

The primary focus of this work was to examine the variation in the temperatures when the model contained three different batches of pebbles. By following the recommendations of Section 10.4 all pebbles that were not in the valid simulation region were ignored when determining the various temperatures associated with the pebble batches. Therefore valid data was only available for 30 pebbles out of 129 pebbles contained in the model. Information was collected by examining this group of pebbles in detail and is shown in Table 10.7.1. It should be noted that one of the 30 pebbles sampled was found to be a leading edge pebble and was therefore not included in the average temperature calculations[21]. For the remaining 29 pebbles in the valid region the average temperature was found to be 1078.5 K.

---

[21] The highest temperature pebble in this batch was in the first layer of pebbles in the model, which means that it was a leading pebble. The KTA rules indicates that leading pebbles only have about half of the average HTC (References 10.23 and 10.24). Due to this reduced HTC the pebble temperature was found to be about 20°C higher than the next closest pebble in the batch and therefore was neglected.

Table 10.7.1: Batch Temperature Data

Batch Number	Batch Power	Number of Pebbles in Sample	Average Pebble Temperature (K)	Difference Between Average Temperature (K)	Range in Batch Temperature (K)
1	Average	9	1078.6	+.1	13.7
2	1.5*Average	10	1095.0	+16.5	16.0
3	0.5*Average	10	1061.8	-16.6	8.8

Analytical Batch Temperature Predictions

In addition to simulation results the analytical model in Section 8.2 was also used to calculate the different batch temperatures for the equivalent conditions used in the CFD model (see Appendix K for details). Rewriting equation 8.2.38 to ignore heat transfer between computational cells the following equation can be used to calculate the average surface temperature of the various batches of pebbles in a multi-batch core:

$$T_{surf}^i = \overline{T}_{surf} + \frac{\dfrac{m}{m_i}\dot{q}_{gen}^i - \dot{q}_{gen}}{h \cdot A + C}$$

Substituting in the appropriate values based on the inputs used for the current work[22] the equation becomes:

$$T_{surf}^i - \overline{T}_{surf} = \frac{3 \cdot \dot{q}_{gen}^i - 3.46 \times 10^4 W}{2187.0 \dfrac{W}{m^2 \cdot K} \cdot 0.441 m^2 + 109.73 \dfrac{W}{K}}$$

Where $\dot{q}_{gen}^i$ is 1.73x10^{4}W for the highest power batch (Batch 2) and 1.15x10^{4} for the lowest power batch (Batch 3). For the batch with the average power (Batch 1) the surface temperature will simply be the average surface temperature.

Evaluation of this equation indicates that there will be a 16.1 K difference between the surface temperatures of cool (Batch 3) and average (Batch 1) pebbles. Similarly, this equation indicates that there will be a 16.1 K difference between the hot (Batch 2) and average (Batch 1) pebbles. The results of the analytical model are in good agreement with the difference in the batch temperatures predicted by the CFD model, which are shown in Table 10.7.1 to be +16.6 K and -16.5 K when compared to the average

---

[22] The heat transfer coefficient used in the analytical calculation was obtained from Section 10.4.6.2.

pebble temperature. Therefore it was shown that for the single case evaluated the analytical model showed good agreement with the results predicted by the CFD model.

10.7.3.3 Pressure Drop

Although the primary purpose of this simulation was to examine the surface temperatures of the pebbles in the various batches the pressure drop for the model was also examined to ensure that the results were consistent with those documented in Section 10.4. When the solution was converged it was found that the pressure drop for the model agreed with that predicted by the earlier model. This confirmed that the addition of the pebble internals and the effects of radiation did not significantly impact the pressure drop predicted by the model.

10.7.3.4 Pebble Surface Heat Transfer Coefficients

In Section 10.4 the pebble surface to coolant heat transfer coefficient was estimated using the modified Reynolds analogy and in Section 10.5 the heat transfer coefficients were calculated using both the modified Reynolds analogy and the calculated thermal solution. In the current work the heat transfer coefficients were only calculated from the thermal solution.

Thermal Solution Based

The heat transfer coefficient can also be estimated from the thermal solution to the CFD model using the following definition for the heat transfer coefficient, which is the same as in Sections 10.4 and 10.5. The power generated in a particular pebble is taken as the integrated heat flux through a pebble surface.

Heat transfer coefficients are calculated for pebbles within the valid simulation region using the area weighted average pebble surface temperature for T_{pebble} and the local fluid temperature. The average and ±2 standard deviation bounds on the pebble heat transfer coefficients defined from the thermal solution are summarized in Table 10.7.2.

Table 10.7.2: Average Pebble to Coolant Heat Transfer Coefficients For Multi-Batch Model Estimated from the Thermal Solution

Flow Rate (kg/s)	Nominal (W/m²K)	Lower Bound (W/m²K)	Upper Bound (W/m²K)
150	2303	1418	3188

KTA Correlation

Heat transfer coefficients between pebbles and coolant may also be estimated using the KTA rules (Reference 10.23) as described in Section 10.4. The fluid properties for the correlation are evaluated at the average of the pebble surface temperature and the local coolant temperature. The local coolant temperature is the same as defined in Section 10.4. A summary of predicted heat transfer coefficients and the 95% confidence bounds on the correlation results are summarized in Table 10.7.3.

Table 10.7.3: Average Pebble to Coolant Heat Transfer Coefficients for Multi-Batch Model Estimated from the KTA rules Reference 10.24

Flow Rate (kg/s)	Nominal (W/m²K)	Lower Bound (W/m²K)	Upper Bound (W/m²K)
150	3265	2612	3918

Comparisons

Figure 10.7.3 shows the probability distribution functions (PDF) for the pebble average heat transfer coefficients within the valid simulation region. The KTA rules values are also included on this figure. This figure indicates that the heat transfer coefficient from the thermal solution tends to be lower than the KTA correlation. This is consistent with the trend documented in Section 10.5.

Figure 10.7.3: Distribution of Average Pebble Heat Transfer Coefficient for a 150kg/s Core Coolant Flow Rate (Multi-Batch Model)
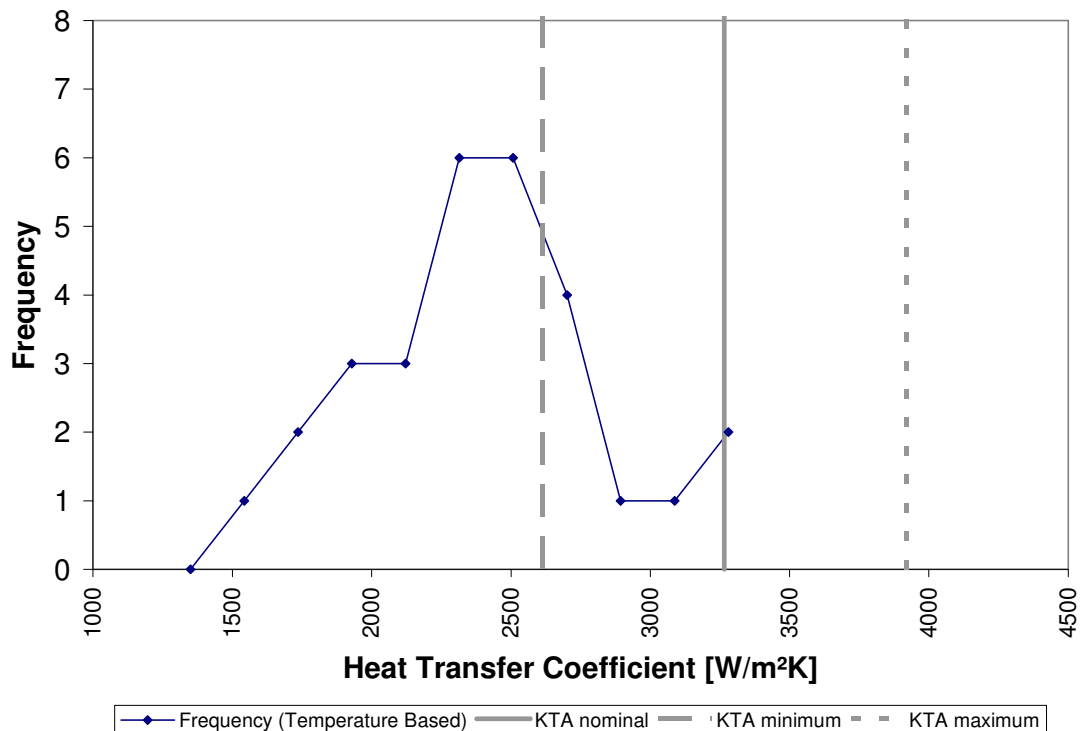
10.8   Error Estimates

Every CFD simulation contains several types of errors, and the goal of a successful analysis is to reduce these errors such that meaningful results may be obtained for the given application. The errors are broken down into the following types:

1. Modeling Errors,

2. Discretization errors,

3. Round off errors, and

4. Solution or convergence errors.

In Appendix I these errors and estimates of their magnitudes for the current work are discussed.

10.9   Assumptions and Limitations of Approach

While this work has made significant efforts to accurately model the behavior within a PBR core there are still several questions related to modeling that could be addressed. The inclusion of radiation heat transfer for Section 10.4 and Section 10.5 would also be valuable additions to the models described in these sections. In the calculation of heat transfer coefficients, it is recommended that more refined calculations are performed, such as using local values for surface and coolant temperatures to calculate local heat transfer coefficients, and then averaging all heat transfer coefficients over each pebble. A similar calculation would likely result in more robust heat transfer coefficients on the reflector walls (i.e., between the reflector and the coolant adjacent to the reflector).

The model in Section 10.7 included the effects of pebble to pebble heat transfer due to radiation. It would be relatively easy to examine the effect of radiation by turning off the radiation model. This would allow for a better understanding of how pebble to pebble radiation affects the batch temperatures in the PBR core during normal operation.

The work in Section 10.7 only looked at one flow rate (150 kg/s). It may be beneficial to look at additional flow rates to examine how the CFD predictions compare to the calculated analytical results at difference flow rates.

10.10   Closure

A method has been developed to create a CFD model to predict the detailed flow through a randomly packed bed of spheres. A mesh generation strategy was developed that allows for high quality meshes near the contact point between spheres, high near wall resolution using prismatic elements and the elimination of "sharp edged" model geometry.

The pressure drop was predicted for a representative group of pebbles remote from the reflector region of the PBR core. The pressure drop predictions were found to be within the limits of the KTA correlation given in Reference 10.25. It was noted that the pressure drop was a fluctuating quantity and the flow inside the arrangement of pebbles may be transient. The models were revisited for the 75 kg/s and 15 kg/s flow cases with the reactor power reduced proportional to the flow. The results for this are very similar to the reference case with the predictions for pressure drop falling within

the error bounds of the KTA rules and the pressure drop being only slightly less than the reference case. This result suggests that the KTA rules are a reasonable approximation for the pressure drop through an assembly of pebbles remote from the reflector when the reactor power is assumed to be proportional to the coolant flow. No corrections to the KTA pressure drop correlation are recommended for an assembly of pebbles remote from the reflector.

For the model remote from the reflector the local and average pebble surface heat transfer coefficients were calculated using the modified Reynolds analogy and a thermal solution. The average surface heat transfer coefficients were compared to the KTA correlation given in Reference 10.24. It was found that the heat transfer coefficients of the KTA correlation and the CFD model only matched within an order of magnitude. It was realized that the prediction of the heat transfer coefficients using the Reynolds analogy relies heavily on the selection of the reference velocity.

For the sensitivity study performed assuming reactor power proportional to coolant flow rate, the calculated heat transfer coefficients predictions showed similar trends to the reference case for the three different methods used. The heat transfer coefficients predicted by the thermal solution were generally lower than those predicted by the KTA correlations and those predicted using the Reynolds analogy were higher than those predicted by the KTA correlations.

The variation in the pebble surface temperatures was also examined and it was found that the spread in the minimum, average and maximum temperatures increases as the flow rate and power increase. It was also found that the minimum surfaces temperatures were closer to the average temperatures than the maximum surface temperatures. This is because the hot spots on the pebbles are small and localized near the pebble contacts.

A second CFD model was created to represent a region in a PBR core within 5 pebble diameters of the reflector.

Axial pressure gradients derived from this model were compared with the predictions of the KTA correlation (Reference 10.25). This comparison led to the derivation of a correction factor to the KTA correlation to allow it to be applicable within 5 pebble diameters of the reflector for core flow rates between 15 and 150 kg/s. The effect of radial position on axial pressure gradients was also examined. As expected no distinct pressure gradient variation with radial position was observed. An examination of the radial variation in velocity did however indicate that the flow within 0.05 m of the reflector was approximately 30% higher than the remainder of the flow.

The surface average pebble-to-fluid heat transfer coefficients for pebbles within 5 pebble diameters of the reflector were calculated using the modified Reynolds analogy, the CFD model thermal solution and the KTA heat transfer correlation (Reference 10.24). These calculations showed that each method predicted heat transfer coefficients of the same order of magnitude however the results based on the modified Reynolds analogy were generally higher than the KTA predictions and the results based on the thermal solution were generally lower than the KTA predictions.

CFD models for an assembly of pebbles adjacent to the reflector were revisited for the 75 kg/s and 15 kg/s flow cases with the reactor power reduced proportional to the flow. The results for this work are very similar to the work previously completed with the predictions for pressure drop falling outside of the range predicted by the KTA rules and it is expected that the correction derived for the KTA pressure drop near the reflector is also valid when the power is proportional to the flow. The heat transfer coefficients for the pebbles and the reflector all showed the same trends as the work completed at full reactor power.

The surface average heat transfer coefficient was calculated between the reflector wall and the coolant with power proportional to flow, and power held constant. These heat transfer coefficients were calculated using the Reynolds analogy and the thermal solution. The heat transfer coefficients between the reflector wall and the coolant calculated using the Reynolds analogy are similar to the pebble to coolant heat transfer coefficient. The heat transfer coefficients between the reflector wall and the coolant calculated using the thermal solution indicated significantly lower values than were predicted for pebble to coolant using the same method. This heat transfer coefficient was found to be extremely sensitive to the reference temperature since the temperature of the reflector was very close to the temperature of the coolant. Generally the heat flux into the reflector was several orders of magnitude lower than the heat flux from the pebbles.

The CFD models for an assembly of pebbles adjacent to the reflector were revisited for the 150 kg/s, 75 kg/s and 15 kg/s flow cases with the reflector conductivity and boundary conditions modified in order to increase the heat transfer to the reflector. Although the reflector heat transfer coefficients were found to be similar to the previous work it was confirmed that the location where the free stream temperatures were extracted from the model (0.01 m from the reflector) was valid. Upon further inspection of the simulation it was noted that the temperature on the reflector wall in the valid simulation region was significantly lower and less uniform near the entrance to the region, and more uniform on the lower half of the valid simulation region. Therefore, calculations for the bottom half and bottom quarter of the valid simulation region were performed, which results in increases in the prediction of the reflector heat transfer coefficients of greater than 30%-40% for the 150 kg/s and 75 kg/s cases and 13%-23% for the 15 kg/s case. This indicates that the local reflector heat transfer coefficients may vary significantly over the height of the pebble bed, but a significantly larger domain would be needed in order to study this in detail. The reflector heat transfer coefficient calculations discussed in the reference cases were not revisited to examine how they would change if only the bottom half or quarter of the valid simulation region were used for the calculation. It is expected that the heat transfer coefficients for these simulations would also increase if this approach was used, although the increase may be less than that observed in these sensitivity studies. The heat transfer coefficients obtained by the CFD simulations are consistently lower that those predicted by the correlations examined in Section 10.5.7.2 but follow a comparable trend.

The variation in the pebble surface temperature was also examined and it was found that at higher flow rates and reactor powers the variation in the surface temperature

was higher. It was also found that the highest frequency minimum temperatures were closer to the average pebble temperature than the maximum temperatures indicating that hot spots are small and localized near the pebble contacts. Some pebbles were found to have much lower minimum temperatures than the other pebbles and the pebbles with the lowest minimum temperatures were found to be those touching the reflector wall. This indicates that the reason for these very low minimum temperatures was a combination of wall channeling and conduction to the cooler reflector wall.

In order to study the effect of wall channeling, a third CFD model was created for the region adjacent to the reflector. The model was generated by including the largest number of pebbles that can practically be built using the GAMBIT mesh generator. The model was run for three coolant flow rates: 150 kg/s, 75 kg/s and 15 kg/s. The results from this work showed that peaks and troughs in the z-component of the velocity exist for all flow rates and coincide with variations in the porosity. Additionally, the packing fraction of the larger reflector CFD model was compared to radial porosity calculations for the entire pebble bed. This comparison showed that although the CFD domain is of a limited size, the trends in the local variation in the porosity are representative of the entire pebble bed.

A fourth CFD model was created to represent a region in a PBR core remote from the reflector assuming multiple batches of fuel with different powers in the reactor and the effects of both pebble to pebble radiation and conduction were included in the model.

This model indicated that when three different batches of pebbles were included in the model that the average pebble surface temperature would be near that of the average surface temperature of the average batch of pebbles. It was found that the average temperature of the pebbles in the average batch was only +0.1 K higher than the average for all of the pebbles (1078.6 K versus 1078.5 K). The average temperature of the remaining two batches of pebbles (one of which was 1.5 times the average power and the other of which was 0.5 times the average power) were found to be 1095.0 K and 1061.8 K, which are +16.5 K and -16.6 K when compared to the overall average temperature of the pebbles in the model.

When the CFD predictions were compared to the results of the analytical model it was found that the difference in the batch temperatures calculated by the analytical model showed good agreement. The analytical model predicted that the difference in the batch temperatures would be -16.1 K for the low power batch (Batch 3) and +16.1 K for the high power batch (Batch 2) with reference to the temperature of the average power batch (Batch 1). Therefore, for the single flow rate examined it was confirmed that the analytical model produced very reasonable values when compared to the more detailed CFD model.

An additional finding was that with a 0.005 m portion of the solid layer of the pebbles modeled and pebble heat transfer due to conduction and radiation included in the model the heat transfer coefficients predicted from the thermal solution tends to be lower than the KTA correlation. This is consistent with the trend documented in Sections 10.4 and 10.5.

10.11   Nomenclature

C_f - Friction coefficient

St - Stanton number

Pr - Prandtl number

Re – Reynolds number

h - Heat transfer coefficient

ρ - Coolant density

V_{ref} - Reference Velocity

k – fluid thermal conductivity

C_p - Specific heat capacity

α - Packing Fraction

A – flow area of reactor when no pebbles are in the core

$A_{reactor}$ – flow area of reactor when no pebbles are in the core

ε - Porosity (equivalent to 1-α)

d - pebble diameter

A- core cross sectional area

$\dot{m}$ - mass flow rate

μ - dynamic viscosity

y^+ - Dimensionless distance from wall

τ - Wall shear stress

10.12   References for Section 10.0

10.1   W.M. Visscher and M. Bolsterli, 'Random Packing of Equal and Unequal Spheres in Two and Three Dimensions', Nature, Volume 239, pp.504-507 (1972).

10.2   A. V.S. Rao, 'Structural Characteristics of Randomly Packed Beds of Spheres', Doctoral Thesis, Dept. of Chemical Engineering, Indian Institute of Science, Bangalore, India, (1994).

10.3   R. Jullien, and P. Meakin, 'Simple Three-Dimensional Models for Ballistic Deposition with Restructuring', Europhysics Lett. 4, pp.1385-90 (1987).

10.4   K. Gopalakrishnan and N. Shashidhar, 'Structural Characteristics of Three-Dimensional Random Packing of Aggregates with Wide Size Distribution', International Journal of Information Technology, Volume 3(3), pp201-208 (2006).

10.5   A.M. Ougouag, J.M. Cogliati and J-L Kloosterman, 'Methods for Modeling the Packing of Fuel Elements in Pebble Bed Reactors', ANS Topical Meeting, Mathematics on Computing, Supercomputing, Reactor Physics and Nuclear and Biological Applications (M&C 2005), Avignon, France (2005).

10.6   J. Cogliati and A. M. Ougouag, 'PEBBLES: A Computer Code for Modeling Packing, Flow and Recirculation of Pebbles in a Pebble Bed Reactor', Proceedings of HTR-2006, 3rd International Topical Meeting on High Temperature Reactor Technology, South Africa, (October 2006).

10.7   M. Armishaw, N. Smith and E. Shuttleworth, 'Particle Packing Considerations for Pebble Bed Fuel Systems', Proceedings of The 7th International Conference on Nuclear Criticality Safety (2003).

10.8   C.H. Bennett, 'Serially Deposited Amorphous Aggregates of Hard Spheres', J. Appl. Phys., Volume 43(6) , p2727 (1972).

10.9   Benenati R.F., Brosilow C.B., "Void Fraction Distribution in Beds of Spheres", American Institute of Chemical Engineers (A. I. Ch. E.) Journal 8, No 3, p359-361 (1962).

10.10 Fluent Inc., "FLUENT 6.3 User's Guide", September 2006.

10.11 J. Lee, S. Yoon, G. Park, W. Lee, "Turbulence-Induced Heat Transfer in PBMR Core Using LES and RANS", Journal of NUCLEAR SCIENCE and TECHNOLOGY, Vol. 44, No. 7, p. 985–996 (2007).

10.12 G. Yesilyurt, "Numerical Simulation of Flow Distribution for Pebble Bed High Temperature Gas Cooled Reactors", Texas A&M University, May 2003.

10.13 "Evaluation of High Temperature Gas Cooled Reactor Performance- Benchmark analysis related to the PBMR-400, PBMM, GT-MHR, HTR-10 and the ASTRA Critical Facility", IAEA-TECHDOC-TBD DRAFT, September 2006.

10.14 M. Kim, H. Lim, W. Lee, "CFD Assessment of the Local Hot Core Temperature in a Pebble Bed Type Very High Temperature Reactor", ICONE16-48316, May 2008.

10.15 M. Mkhosi, R. Denning, "Fluid Flow Analysis in a Pebble Bed Modular Reactor Using RANS Turbulence Models", ICONE16-48947, May 2008.

10.16 M. Nijemeisland, A. Dixon, "CFD Study of Fluid Flow and Wall Heat Transfer in a Fixed Bed of Spheres", AIChE Journal, Vol. 50, No. 5, pp. 906, 2004.

10.17 M. Nijemeisland, A. Dixon, "Comparison of CFD Simulations to Experiment for Convective Heat Transfer in a Gas-Solid Fixed Bed", Chemical Engineering Journal, Vol. 82, pp. 231-246, 2001.

10.18 S.A. Logtenberg, M. Nijemeisland, A. Dixon, "Computational Fluid Dynamics Simulations of Fluid Flow and Heat Transfer at the Wall-Particle Contact Points in a Fixed-Bed Reactor", Chemical Engineering Science, Vol. 54, pp. 2433-2439, 1999.

10.19 H.P.A. Calis, J. Nijenhuis, B.C. Paikert, F.M. Dautzenberg, C.M. van den Bleek, "CFD Modeling and Experimental Validation of Pressure Drop and Flow Profile in a Novel Structured Catalytic Reactor Packing", Chemical Engineering Science, Vol. 56, pp. 1713-1720, 2001.

10.20 R. Hill, D. Koch, A. Ladd, "Moderate-Reynolds-Number Flows in Ordered and Random Arrays of Spheres", Journal of Fluid Mechanics, Vol. 448, pp. 243-278, 2001.

10.21 Fluent Inc., "GAMBIT 2.4 Command Reference Guide", May 2007.

10.22 Fluent Inc., "GAMBIT 2.4 User's Guide", May 2007.

10.23 The Nuclear Safety Standards Commission (KTA), "KTA Program of Standards (14.04.2008), Reactor Core Design for High-Temperature Gas-Cooled Reactor, Part 1: Calculation of the Material Properties of Helium", KTA Standard 3102.1, June 1978. URL <http://www.kta-gs.de/common/regel_prog.htm>.

10.24 The Nuclear Safety Standards Commission (KTA), "KTA Program of Standards (14.04.2008), Reactor Core Design for High-Temperature Gas-Cooled Reactor, Part 2: Heat Transfer in Spherical Fuel Elements", KTA Standard 3102.2, June 1983. URL <http://www.kta-gs.de/common/regel_prog.htm>.

10.25 The Nuclear Safety Standards Commission (KTA), "KTA Program of Standards (14.04.2008), Reactor Core Design for High-Temperature Gas-Cooled Reactor, Part 3: Loss of Pressure through Friction in Pebble Bed Cores", KTA Standard 3102.3, March 1981. URL <http://www.kta-gs.de/common/regel_prog.htm>.

10.26 F. Incropera, D. DeWitt, "Fundamentals of Heat and Mass Transfer 5th Ed.", 2002.

10.27 A. Wheeler, A. Ganji, "Introduction to Engineering Experimentation", 1996.

10.28 A.G. Dixon and D. Cresswell, Theoretical prediction of effective heat transfer parameters in packed beds. AIChE Journal, 25, 663 – 676, 1979.

10.29 C. Li and B.A. Finlayson, Heat transfer in packed beds – a reevaluation. Chemical Engineering Science, 32, 1055 – 1066, 1977.

10.30 W. Olbrich and O. Potter, Heat transfer in small diameter packed beds. Chemical Engineering Science, 27, 1723 – 1732, 1972.

10.31 S. Rimkevicius, J. Vilemas, E. Uspuras, Experimental Investigation of Heat Transfer and Flow Mixing in Pebble Beds, Heat Transfer Engineering, Volume 27, Issue 8, pages 9 – 15, September 2006.

11.0 DETERMINATION OF THE EFFECTIVE THERMAL CONDUCTIVITY OF THE PEBBLE BED IN LOFC CONDITIONS

11.1 Purpose of Section 11

The primary goal of the work presented in this section was to determine the conduction and thermal radiation heat transfer through the pebble bed reactor core in loss of forced circulation conditions. The aim of this work was to assess the correctness of and applicability of the German correlations commonly used to determine the effective conductivity of a pebble bed, such as the Zehner-Schlunder or Breitbach correlations.

As with the work described in Section 10, this work was restricted to an examination of a portion of the PBR core ranging from the meso-scale into the macro-scale. The meso-scale ranges from length scales greater than TRISO particles and pebble surface roughness to the immediate surroundings of a pebble. The macro-scale ranges from the upper limit of the meso-scale up to the scale of the whole reactor.

Computational Fluid Dynamic (CFD) models were developed to predict how the pebbles interact thermally with their surroundings under depressurized loss of forced circulation (DLOFC) conditions. These interactions are influenced by the conductivity of the fluid, the effective conductivity of pebbles, the pebble contact conduction, the radiation between pebbles and to a lesser extent by natural circulation patterns that may evolve. This latter effect was neglected due to the small contribution from convection and the low densities of the helium under DLOFC conditions.

In Section 11.2 the CFD model used for this study is described.

An analytical evaluation of heat transfer coefficients based on the Zehner-Schlunder or Breitbach correlations is presented in Section 11.3.

11.2 CFD Model

The CFD model to be used in the examination of the effective thermal conductivity of a pebble bed reactor (PBR) core during a Depressurized Loss of Forced Circulation (DLOFC) event was based on the cylindrical model developed and described in Section 10, but with no imposed flow and with the internals of the pebbles modeled.

11.2.1 Approach

The intent was to investigate the effective thermal conductivity of a pebble bed under DLOFC conditions at temperatures of 1273K, 1573K, 1873K and 2173K. In efforts to isolate the effects of thermal radiation and pebble to pebble conduction through contacts two sensitivity cases were examined. The first intended sensitivity case would have examined the effective thermal conductivity of the pebble bed in a situation where the thermal conductivity of the helium coolant is approximately zero. The second intended sensitivity case would have examined the effective thermal conductivity of the pebble bed in the absence of pebble to pebble contact conduction and conduction to helium (i.e., only radiation).

11.2.1.1 Preliminary Models

To validate the various correlations used to determine the effective thermal conductivity of a pebble bed during DLOFC conditions a series of computational fluid dynamics (CFD) models was required. Prior to the creation of the final model the following modeling issues were first addressed.

1. How many pebbles need to be modeled to effectively determine the thermal conductivity of the pebble bed?

2. What phenomenon must be modeled?

3. What type of boundary conditions would be appropriate to determine the thermal conductivity of the pebble bed?

Determination of Domain Size

The intent was to determine the effective thermal conductivity of a pebble bed from a sufficiently large sample of pebbles such that local variations induced by individual pebbles are smoothed by an averaging process. The size of this domain was not known beforehand; hence a domain size study was first attempted. Convergence was not achieved for any of the domain size study cases, hence no insight was provided into an appropriate domain size. These issues are described later in this document.

Phenomenon Modeled

The correlations used to determine the effective thermal conductivity of a pebble bed consider the following effects.

-   Solid Conduction

-   Fluid Conduction

-   Thermal Radiation

-   Pebble to Pebble contact conduction

The CFD model developed here to validate the effective thermal conductivity correlations considered each of the above listed phenomena.

Type of Boundary Conditions

The effective conductivity of a group of pebbles was calculated by assuming that the pebble bed is an effectively homogeneous material and that conduction is the only

effective mode of heat transfer.[1] The generalized conduction equation for a motionless effectively homogeneous fluid is represented by the following equation.

$$q = -k_{eff} \cdot \nabla T$$

Where: q is a heat flux vector (W/m²)

k_{eff} is the effective thermal conductivity (W/m²K)

∇T is the temperature gradient (K/m)

Conduction was assumed to be along one coordinate direction (the z Cartesian coordinate for example) therefore the following equation represents the effective conduction through the pebble bed[2].

$$q_z = -k_{eff} \cdot \frac{dT}{dz}$$

Where: q_z is the heat flux in the z direction (W/m²)

$\frac{dT}{dz}$ is the temperature gradient along the z coordinate axis (K/m)

The pebble bed was considered a single homogeneous substance; hence the steady state temperature gradient through the bed will be a constant value. The gradient was estimated by the following equation:

$$\frac{dT}{dz} \approx \frac{T_{z1} - T_{z2}}{z_1 - z_2}$$

Where: T_{z1} and T_{z2} are the temperature at planes located at z= z_1 and z= z_2 respectively.

The effective conductivity is determined by knowing the values of q_z, T_{z1}, T_{z2}, z_1 and z_2.

$$-q_z \cdot \frac{z_1 - z_2}{T_{z1} - T_{z2}} = k_{eff}$$

---

[1] Radiation effects and pebble to pebble conduction are directly incorporated as effective conduction.

[2] This method implies that the effective thermal conductivity is an isotropic property of a pebble bed. This may not be a suitable approximation near the reflector where the packing of pebbles is anisotropic.

11.2.2 Modeled Geometry

The pebbles in the core of a pebble bed reactor are not in any type of ordered lattice structure; hence the first step in the generation of geometry for the CFD model was to determine realistic positions for each pebble. Section 10.2.3 provides the positions of pebbles for various situations.

The CFD model in this chapter contains a group of pebbles within a cylindrical region (where the pebble positions are taken from Section 10.4). Both the helium coolant and fuel pebble materials and pebble contacts are modeled.

11.2.3 Mesh

The meshing strategy for the CFD model in this chapter was similar to that of Section 10.7.[3]

**Figure 11.2.1: View of Outer Surface of Assembled Mesh to Calculate
Effective Thermal Conductivity**

---
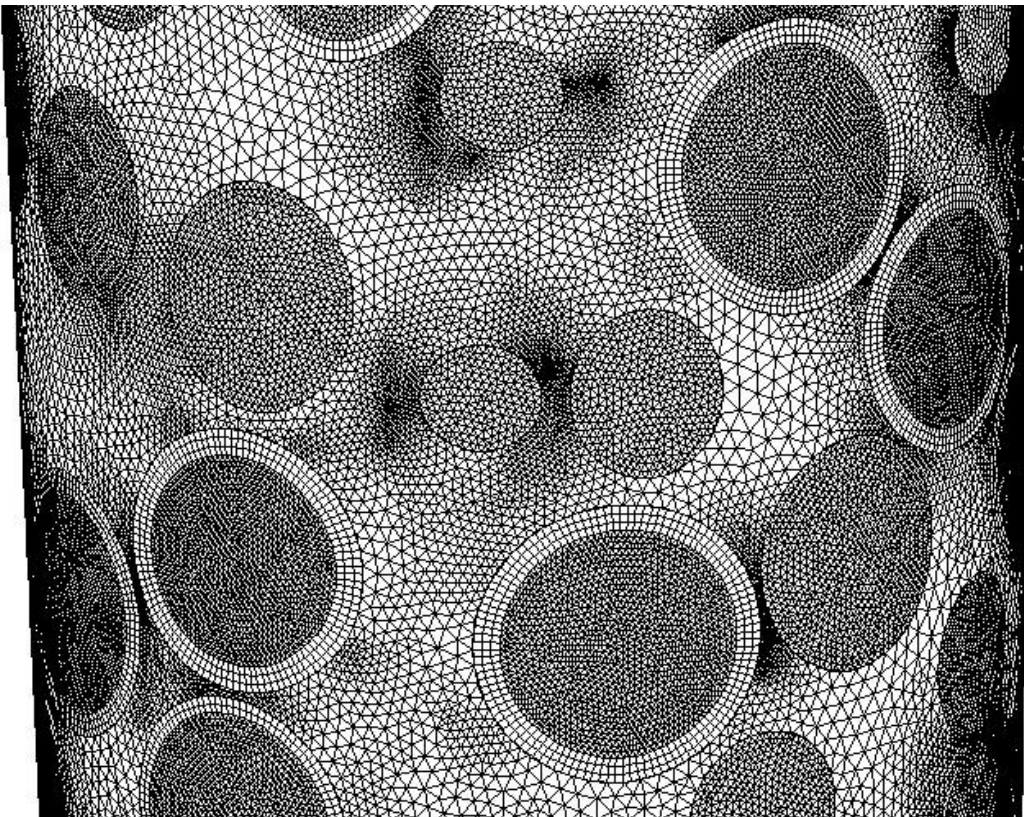
[3] ANSYS GAMBIT was used to generate the meshes in this document.

Figure 11.2.2: View of Solution Domain and Boundary Condition Zones
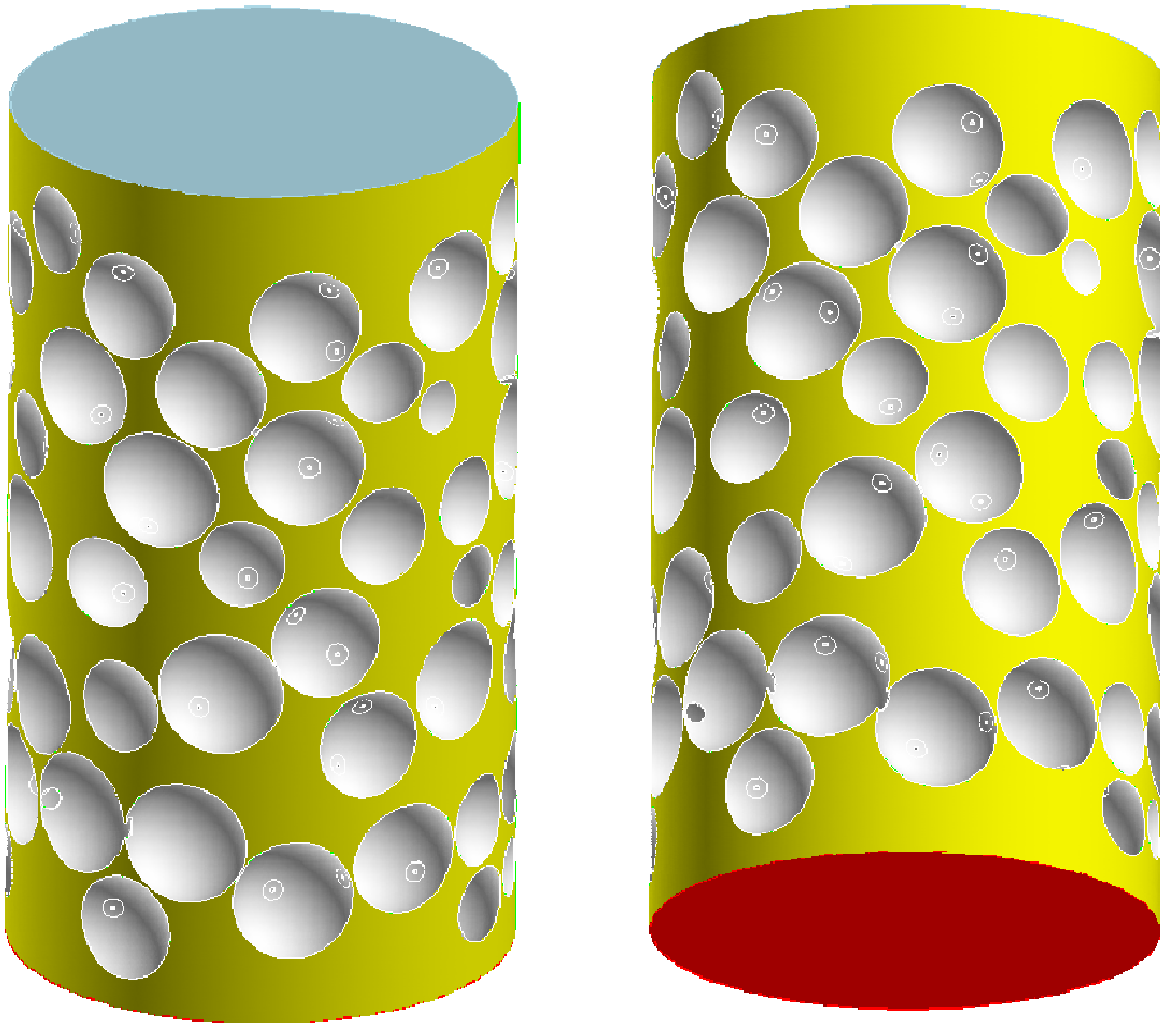
The key features of this mesh are listed below:

1. The coolant portion of the domain had a significantly higher resolution than the solid domain.

2. Contacts were modeled with a hexahedral mesh.

3. The internal volume of the pebbles was modeled with hexahedral elements.

4. The interface between the coolant and solid meshes was done using a non-conformal interface.

The mesh contained 5,125,068 cells to model the fuel and 8,339,307 cells to model the coolant. This contains approximately 30% fewer cells in the fluid zone than the mesh used in Section 10.7. During the course of this work it was discovered that this mesh resolution was significantly too fine to solve this problem, as discussed later in this report.

11.2.4 Material Properties

Material properties can be represented in computational fluid dynamics (CFD) software as variable quantities with values dependent on local fluid conditions. The use of variable material properties removes some assumptions from the model; however, it makes direct comparison with correlations difficult. Constant material properties were selected in this work to facilitate the comparison of correlations and the CFD models.

11.2.4.1 Pebble (Fuel) Properties

A fuel pebble is a multilayered structure composed of various materials. In this chapter the simplifying assumption that the material is homogeneous throughout a pebble and can be represented by constant material properties was made.

Table 11.2.1: Material Properties for Fuel Pebbles

Property	Value	Reference
Thermal Conductivity (W/m/K)	15	11.1
Specific Heat Capacity (J/kg/K)	1690	11.1
Density (kg/m³)	1720	11.1
Emissivity	0.8	11.1

11.2.4.2 Coolant Properties

The KTA correlations provide reference values and correlations for the physical properties of helium in Reference 11.2. Table 11.2.2 summarizes the values of helium properties obtained from evaluating the correlations of Reference 11.2 for temperatures between 1273 and 2173 K at a pressure of 101 325 Pa. [4]

Table 11.2.2: Material Properties for Coolant

Property	Value at Temperature[4] in K				Reference
	1273	1573	1873	2173	
Thermal Conductivity (W/m/K)	0.429	0.499	0.565	0.628	11.2, 11.3
Specific Heat Capacity (J/kg/K)	5195	5195	5195	5195	11.2
Density (kg/m³)	0.038	0.031	0.026	0.022	11.2
Absorption Coefficient[5]	0	0	0	0	n/a

11.2.5 Heat Transfer Models

This work was focused on modeling the effective thermal conductivity of a pebble bed in DLOFC conditions only. Convective heat transfer was not modeled. The helium coolant was treated as a static fluid. The only modes of heat transfer through the helium were conduction and radiation.

FLUENT offers 5 types of radiation models which are listed below.

1.   P-1 Radiation Model

2.   Rosseland Radiation Model

3.   Discrete Transfer Radiation Model (DTRM)

4.   Discrete Ordinates Radiation Model (DO)

5.   Surface to Surface Radiation Model (S2S)

According to Reference 11.4 the S2S and DTRM radiation models cannot be used with non-conformal interfaces, hence they cannot be used for the mesh design used in this work[6]. The Rosseland radiation model is not intended for use in materials with low optical thickness (e.g., helium) and the P-1 radiation model is known to be inaccurate for materials with low optical thickness. The P-1 and Rosseland are the least computationally expensive models. The discrete ordinates (DO) model provided with

---

[4] The KTA correlations provided in Reference 11.2 are not intended for temperatures greater than 1773K, however the correlations are used to determine properties at temperatures up to 2173 K. An examination of Reference 11.3 indicates that the KTA correlation for thermal conductivity continues to provide reasonable values for the thermal conductivity of helium at temperatures of 2173 K.

[5] Reference 11.2 does not provide radiation properties for helium. It is assumed that the absorption coefficient of helium (for radiation transport) is equal to zero.

[6] Basic testing confirms that the S2S model does not function if the solution domain contains solids (i.e. conjugate heat transfer), even if the mesh contains conformal interfaces.

FLUENT is the most general purpose radiation model, however it is computationally expensive.

In this work radiation is modeled using the discrete ordinates model provided with ANSYS FLUENT Reference 11.4. Radiation from surfaces was modeled as diffuse radiation. All pebbles were assumed to be gray bodies (i.e., emissivity=absorbtivity) with a constant emissivity.

11.2.6 Boundary Conditions

In Section 11.2.1.1 the required inputs to determine the effective thermal conductivity of a pebble bed were discussed. The method selected for this study was to set the temperature at opposite ends of the model to different fixed temperatures and calculate the heat flux through the model.

11.2.6.1 Fixed Temperature Conditions

The intent of this research theme was to present CFD models for the effective thermal conductivity through a pebble bed at 4 different mean temperatures. For each of the simulations the end face of the solution domain (flat faces of the cylindrical domain) were set to constant temperatures of 100K above and below the mean temperature.

11.2.6.2 Adiabatic/Symmetry Condition

The model presented in this section considers only axial conduction through a pebble bed. To enforce axial conduction a symmetry boundary condition (which acts as an adiabatic wall) is applied to the outer curved boundary of the cylindrical solution domain[7], see Figure 11.2.2.

11.2.6.3 Interface Radiation Condition

Radiation heat transfer models used in the CFD codes require the application of the pebble surface emissivity. All pebble surfaces in the models used a surface emissivity of 0.8 as specified in Reference 11.1.

11.2.6.4 Special Application of Material Properties

Contact Conductivity

The intent was to conduct a sensitivity study to determine the effective thermal conductivity of the pebble bed in the absence of pebble to pebble contact conduction.

---

[7] This is the same boundary condition that was used in the pressure drop and convective heat transfer studies reported on earlier. Upon further consideration, after the work was essentially completed, it was argued that perhaps a cylindrical symmetrical boundary might give accuracy problems in thermal radiation calculations in which specular reflection is assumed because it represents an unphysical situation. Circular cylinders cannot be clustered without gaps in between them, unlike hexagonal or square prisms. Suggestions for further work include considering hexagonal or square prism domains when dealing with radiation problems.

Originally the CFD grid was not set-up to represent the pebble contacts as separate objects that could be assigned different thermal conductivities. Conduction was disabled through the pebble contacts using an ANSYS FLUENT user defined function. The user defined function sets the thermal conductivity of all cells with centroids within 0.8 mm of the calculated contact position to be equal to 1×10^{-6} W/m/K.

11.2.7 Numerical Treatment

All models in this section used a second order discretisation for the solution of the conservation of energy equation and first order discretisation for the discrete ordinates radiation model. All angular resolution parameters for the discrete ordinates model were maintained at their default values. All simulations were performed using double precision numbers.

The results of the models were only considered converged if the average heat flux at each end of the domain have values within 1% of one another and the residuals were not changing significantly.

11.2.8 Results of CFD Analysis

The cases discussed in Section 11.2.1 are summarized in Table 11.2.3. Unfortunately no results were obtained from modeling attempts described previously due to very slow convergence behavior of the model (the details of this issue and the attempts to resolve them are discussed in Section 11.2.8.1 and Section 11.2.8.2).

Table 11.2.3: Summary of Effective Thermal Conductivity Results.

Temperature (K)	Conduction Through Helium Modeled	Radiation Modeled	Contact Conduction Modeled	Effective Thermal Conductivity [8] (W/m/K)
1273	√	√	√	Not Obtained
1573	√	√	√	Not Obtained
1873	√	√	√	Not Obtained
1873	X	√	√	Not Obtained
1873	X	√	X	Not Obtained
2173	√	√	√	Not Obtained

---

[8] The effective thermal conductivity can be calculated from:

$$k_{eff} = -q_z \cdot \frac{z_1 - z_2}{T_{z1} - T_{z2}}$$

Where q_z is the axial heat flux in W/m^2, the temperatures T_{z1} and T_{z2} are extracted as the area weighted average temperature on planes located at z_1=-0.15 m and z_2=0.15 m.

11.2.8.1 Issues and Initial Attempted Resolutions

This work did not result in any estimates for the effective thermal conductivity of pebble beds due to issues encountered during the solution process. The following attempts were made to solve these cases.

1. Obtain an initial condition by setting the thermal conductivity of the coolant and graphite to 15 W/m/K. Once a converged solution was obtained the radiation model was introduced and the thermal conductivity of the coolant was set to its appropriate value. Figure 11.2.3 illustrates the convergence rate for a simulation with a mean temperature of 1873 K. The curves on this figure represent the heat flux into and out of the system. A converged solution would have these two values equal to each other. This method resulted in an extremely slow convergence rate that indicates a converged solution may possibly require several days or weeks of CPU time.

2. An attempt was made to set the specific heat capacity of the materials in the model to a very small value. This reduction in the specific heat capacity effectively increases the thermal diffusivity of the materials in the model, which may improve the convergence behavior of the model. This change was found to have no effect on the steady state solution process.

3. An attempt was made to solve the model in single precision, however this did not significantly improve the amount of time required to solve a single iteration, hence this approach was abandoned.

4. An attempt was made to solve the radiation models less frequently than the conduction equation. This method did not improve the convergence process.

5. An attempt was made to use the P-1 radiation model from the initial condition provided in point 1 above. It was found that the solution quickly diverged from this solution.

Figure 11.2.3: Convergence Rate for Case at 1873 K with all Conduction and Radiation Transport Modeled
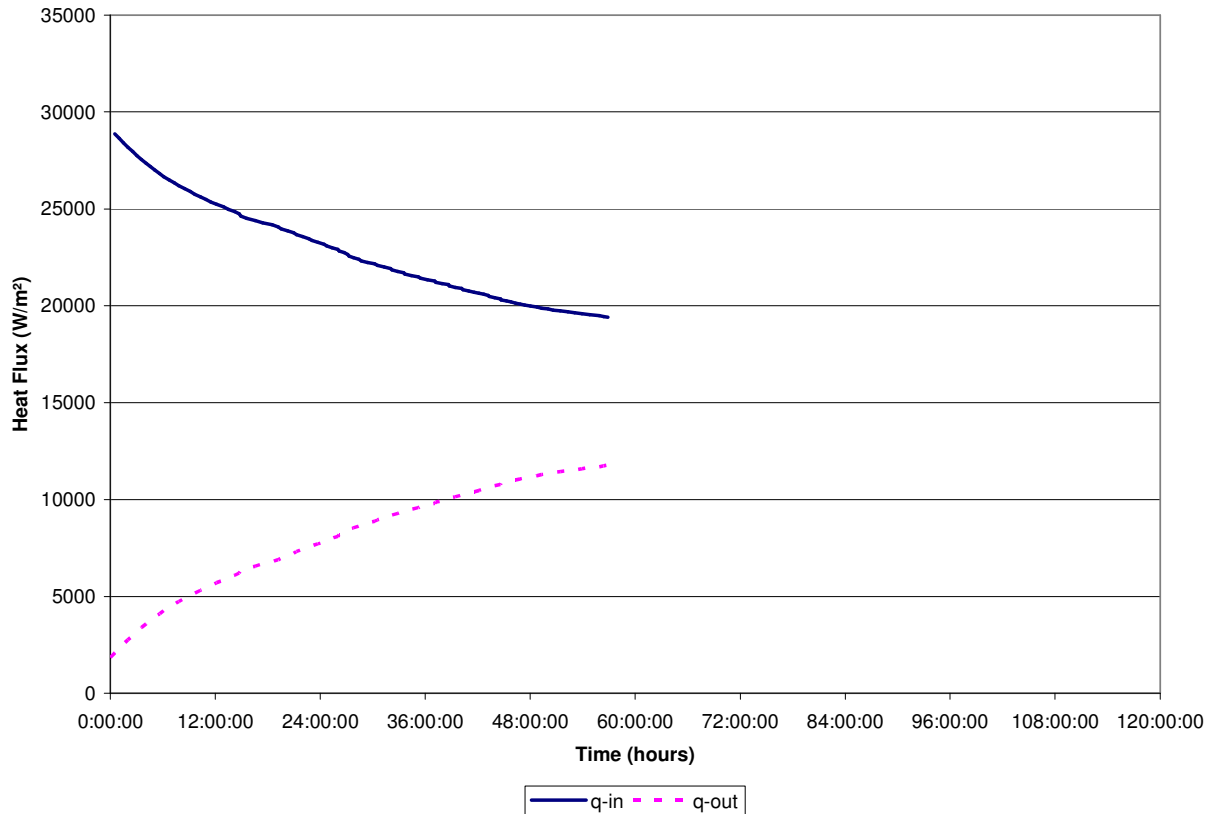
11.2.8.2 Explanation of Issues

The extreme length of the solution process encountered in this work is possibly related to several issues.

The first issue examined was the relative timescales of the radiation model and the conduction phenomena in the models. If the timescales of the various phenomena in the model are significantly different the convergence rate of the model will generally be lower. A method for comparing the relative scales of radiation and conduction was developed in Reference 11.5, for a relatively simple radiation model. The ratio of the scale of radiation to diffusion was estimated using the following equation:

$$RD = \frac{4\varepsilon\sigma A T^3}{\dfrac{kA}{ds}}$$

Where: ε is the emmisivity of the radiating surface

σ is the Stefan-Boltzmann constant, $(5.67\times10^{-8}\ \text{W m}^{-2}\ \text{K}^4)$

A is the face area of a finite volume, m^2

T is the temperature, K

k is the effective thermal conductivity of the problem, W/m.K

ds is the length scale of the finite volume, m.

The timescale for diffusion was represented by:

$$t_d = \frac{\rho \cdot c_p \cdot ds^2}{k}$$

The timescale for advection was represented by:

$$t_a = \frac{ds}{\hat{v}}$$

$\hat{v}$ is the advection velocity.

The timescale for radiation, using a Newton-Raphson linearization was represented by:

$$t_d = \frac{\rho \cdot c_p \cdot ds}{4\varepsilon\sigma \cdot T^4}$$

Table 11.2.4 summarizes the ratio of radiation and conduction scales (RD) for each simulation.

Table 11.2.4: Ratio of Radiation Scale to Conduction Scale				
Temperature -> \ Conductivity	1273 K	1573 K	1873 K	2173 K
0.5 W/m.K (helium)	0.524	0.989	1.669	2.606
15 W/m.K (graphite)	0.017	0.033	0.056	0.087

While the numerical values in Table 11.2.4 are simply rough estimates of the difference in scales they do indicate that there is a significant difference between the time scale of the diffusion equation and radiation equation. In addition to this there are also two distinct conduction timescales in this model; one for conduction in the pebbles and one for the conduction in the helium. Some iterative solvers have difficulties obtaining convergence for plain conduction problems when there are significantly different conduction timescales.

The second possible explanation for the slow convergence is that the problem is highly non-linear and the non-linear terms in the equations are only updated once per

iteration (i.e., a linear multi-grid solution algorithm is being utilized, as apposed to the FAS[9] scheme).

The third possible explanation is that the grid used is simply too large for the computational resources available at AMEC NSS. A single iteration of the models presented in this work can take approximately 30 minutes.

It should be stressed that the discussion in this section is based on suspected sources for the convergence trouble. Without knowing the exact implementation details of the radiation models in FLUENT only these general hypothesis can be offered.

A number of further unsuccessful test were run in an attempt to resolve the slow convergence problems, these are listed in Appendix L.

11.2.8.3 Supplementary Test Models

During this investigation significant difficulties were encountered when attempting to achieve solutions to a problem involving radiation heat transfer with stagnant flow. To further investigate the behavior of the code ANSYS FLUENT several small test models were created. Each test model contained only a few thousand computational cells; hence the models could be solved quickly. On the basis of this study and discussions with ANSYS representatives it was concluded that radiation heat transfer problem can take thousands or tens of thousands of iterations to reach a converged solution, even for models with very coarse meshes.

On the basis of the studies performed in this report and discussions with ANSYS representatives the following conclusion was reached.

The CFD software ANSYS FLUENT was not well suited to applications with stagnant flows and conjugate heat transfer. If the software is utilized for this application, the convergence rate of the solution will be exceedingly slow. For the simplest geometric configurations the software can take thousands to tens of thousands of iterations to reach a solution that conserves energy. ANSYS FLUENT is not a practical utility for solving radiation heat transfer in stagnant flows with conjugate heat transfer and is not recommended for use in this application.

With this, the attempts at finding converged solutions were abandoned and alternative software was investigated. The results of this investigation are documented in Sub-section 11.2.9.

---

[9] The full approximate storage algorithm (FAS) is a multigrid algorithm that performs coefficient updates for non-linear terms on all levels of the multigrid algorithm. A linear multigrid algorithm only updates coefficients on the finest grid level then uses linear solutions on the coarse grid levels to correct the fine grid level. The FAS scheme can offer significant convergence benefits for non-linear problems however the implementation of the method is not straightforward and the method is still being researched.

11.2.9 Potential Alternative Software

11.2.9.1 Commercial Codes

ANSYS CFX

ANSYS CFX is a finite volume based CFD code that is capable of solving conjugate heat transfer problems. CFX supports the use of non-conformal interfaces and contains several radiation models (S2S, DTRM, P-1 and Rosseland). It is not certain as to whether all radiation models work in conjunction with non-conformal interfaces and conjugate heat transfer. Additional research is required.

NX Thermal/NX Flow

NX Thermal/NX Flow is a finite element based CFD code produced by MAYA Heat Transfer Technologies Limited. This code solves fully coupled conduction, radiation and convection heat transfer problems. NX thermal contains extensive radiation modeling capabilities that are based on a view factor approach.

Phoenics

Phoenics is finite volume based CFD code produced by Concentration Heat And Momentum Limited. Phoenics IMMERSOL radiation model is capable of solving radiation problems involving transparent media and conjugate heat transfer. Phoenics contains several other radiation models however they do not function with transparent media and conjugate heat transfer. The main drawback of Phoenics is that is does not support unstructured meshes to date (although the feature is under development), which is a severe limitation for the modeling of an unordered group of pebbles.

Star-CCM+

Star-CCM+ is a finite volume based CFD code produced by CD-adapco. This code contains a surface to surface radiation model and a discrete ordinates model. CD-adapco was contacted and they have confirmed that Star-CCM+ can solve surface to surface radiation problems with conjugate heat transfer and non-conformal interfaces. Star-CCM+ is capable of directly importing FLUENT case files.

Abaqus

Abaqus is a finite element analysis package commonly used for structural and thermal applications; however, the software does contain a cavity radiation model that will solve radiation problems containing either a vacuum or stagnant fluid.

An attempt was made to model a section of pebble bed using the cavity radiation model in Abaqus, starting from two simple test problems of an enclosure and an enclosure containing a single pebble. However it became apparent whilst setting-up and running the test problems that the cavity radiation model had three serious limitations that would preclude its application to a larger assembly of pebbles. First, the model cannot cope with surfaces that are very close to each other (or partially

touching), second the number of radiating faces must be less than 16000 and, third, if isolated objects (i.e., not connected to the cavity wall) were placed within the cavity, the view factor calculation ignored them. The first limitation meant that realistic pebble assemblies could not be modeled, the second, that the assembly could not be large, and the last limitation meant that the whole pebble assembly would have to be artificially connected with bridging volumes, such that all of the be pebbles surfaces were connected to the outer surface of the cavity. Therefore, the application of Abaqus to thermal radiation heat transfer in a pebble bed was not pursued beyond the two test problems.

11.2.9.2 Open Source Codes

Code Saturne

Code Saturne is a comprehensive finite volume based CFD package that contains discrete ordinates and P-1 radiation models. As indicated during the investigation in this report the P-1 radiation model is not suitable for radiation in transparent media. This code should not be immediately dismissed because it uses the DO method, since the implementation of the method and resulting convergence behavior may be significantly different that that of FLUENT.

Open FOAM

Open FOAM is an open source finite volume based CFD package that contains a large number of models. This code does contain a P-1 radiation model (documentation is limited); however, it is unclear as to whether this model will work in conjunction with conjugate heat transfer. Open FOAM is capable of reading in meshes used in FLUENT.

11.3   Analytical Evaluation of Effective Thermal Conductivities

Heat transfer through the pebble bed, in the absence of forced cooling, is commonly modeled as a conduction process. The effective conductivity of the pebble bed models three heat transport mechanisms:

1. Radiative heat transfer between pebbles.

2. Heat conduction through the pebble bed via inter-pebble contacts.

3. Heat transfer across the pebble bed by conduction through the pebbles and coolant gas.

This section summarizes and evaluates published analytical correlations for the three heat transfer mechanisms:

- Section 11.3.1 describes the models for combined conduction and radiation heat transfer due to Zehner and Schlünder, and Breitbach and Barthels,

- Section 11.3.2 reviews models for heat conduction between contacting pebbles,

- Section 11.3.3 reviews models for combined heat conduction through pebbles and heat transfer through (essentially stagnant) coolant gas.

11.3.1 Conduction and Radiation Transfer between Pebbles

Zehner and Schlünder developed a model for heat transfer through an evacuated pebble bed, reported in English in Reference 11.6. This model accounts for radiation between pebble surfaces and heat conduction through pebbles. Breitbach and Barthels state that at high temperature practically all heat transfer across a pebble bed takes place via this mechanism.

The Zehner-Schlünder correlation takes the form of an effective pebble bed conductivity:

$$\lambda_{eff}^{Z-S} = \left\{ \frac{\left[1-(1-\phi)^{1/2}\right]\cdot\phi}{2/\varepsilon-1} + \frac{(1-\phi)^{1/2}}{2/\varepsilon-1}\cdot\frac{B_z+1}{B_z}\cdot\frac{1}{1+\dfrac{1}{(2/\varepsilon-1)\Lambda}} \right\}\cdot 4\cdot\sigma\cdot T^3\cdot d$$

Where:

$$B_z = 1.25\cdot\left(\frac{1-\phi}{\phi}\right)^{10/9}$$

And:

ϕ	Void fraction of pebble bed
d	Pebble diameter (m)
T	Pebble bed temperature (K)
ε	Pebble surface emissivity
σ	Stefan Boltzmann constant (5.67×10^{-8} W m^{-2} K^4)
λ_{peb}	Thermal conductivity of the pebbles (W m^{-1} K^{-1})
$\Lambda = \lambda_{peb}/(4\cdot\sigma\cdot T^3\cdot d)$	Ratio of pebble conductivity to effective black body radiation conductivity

The correlation is based on the analysis of a 'unit cell', as shown in Figure 11.3.1. Within this expression, it is stated in Reference 11.6 that the first term within the brackets represents direct radiative heat transfer across the bed, whilst the second

term represents combined conduction through, and radiation between, pebbles within the bed.

Breitbach and Barthels (Reference 11.6) found improved agreement with a range of experimental data by modifying the first term in the above expression, leading to the modified Zehner Schlünder correlation:

$$\lambda_{eff}^{r} = \left\{ \left[1 - (1-\phi)^{1/2}\right] \cdot \phi + \frac{(1-\phi)^{1/2}}{2/\varepsilon - 1} \cdot \frac{B_z + 1}{B_z} \cdot \frac{1}{1 + \dfrac{1}{(2/\varepsilon - 1)\Lambda}} \right\} \cdot 4 \cdot \sigma \cdot T^3 \cdot d$$

Breitbach and Barthels modification treats the unoccupied sections of the base areas of the unit cell (see Figure 11.3.1) as black surfaces, whereas Zehner and Schlünder originally treated these as grey surfaces with the same emissivity as the pebble surfaces.

Figure 11.3.1: The Unit Cell Considered by Zehner and Schlünder

Unoccupied section of base treated as grey (emissivity ε) by Z&S. Modified to black by Breitbach and Barthels to improve fit with experimental data.

Pebble surface emissivity ε

Pebble conductivity λ_{peb}

"Base areas" partly covered by pebble cross section

Pebble   Pebble

Heat paths across cell:

(a) Conduction – radiation - conduction

(b) Direct radiation across entire cell
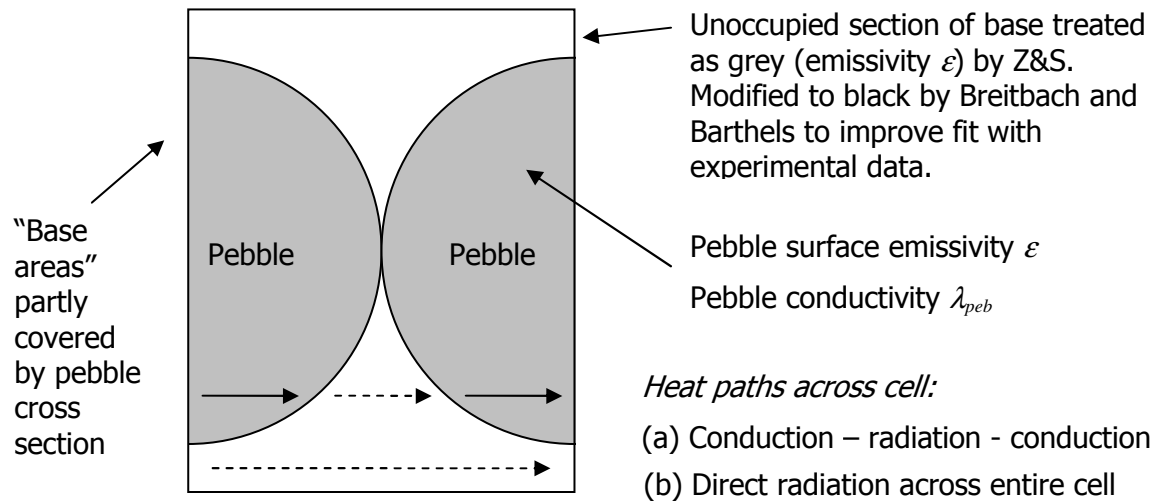
11.3.2 Conduction between Pebbles by Pebble to Pebble Contact

Inter-pebble forces cause pebbles to deform slightly where they contact one another, leading to a non-zero contact area. The contact area depends on the material properties and the magnitude of the inter-pebble forces. Heat may pass between adjacent pebbles by conduction across these contact areas. The effective conductivity of the pebble bed is dependent on both the size of the contact area and the number of contact points between pebbles.

A correlation for the effective pebble bed conductivity resulting from pebble to pebble conduction due to Chen and Tien is quoted in Reference 11.7[10]. The effective conductivity is presented as a fraction of the pebble graphite conductivity, λ_{peb}:

$$\lambda_{eff}^{c} = \lambda_{peb} \cdot \left[\frac{3 \cdot \left(1 - \mu_p^2\right)}{4 \cdot E_s} \cdot f \cdot R \right]^{1/3} \cdot \frac{1}{0.531 \cdot S} \left(\frac{N_A}{N_L} \right)$$

Where:

$$f = p_{peb} \cdot \frac{S_F}{N_A}$$

And:

μ_p, Poisson ratio of the pebble material, 0.136

E_s, Young's modulus of the pebble material, 9.0×10^9 N m^{-2}

R, Pebble radius, 0.03 m

N_L, Number of pebbles per unit length, $1/(2R) = 16.67$ m^{-1}

N_A, Number of pebbles per unit area, $1/(4R^2) = 278$ m^{-1}

S, Parameter describing packing, 1

S_F, Parameter describing packing, 1

p_{peb}, External pressure acting on pebbles

It must be noted that these are representative values for simple cubic packing (Reference 11.8).

The pressure p_{peb} can be estimated from the weight of the pebble bed. However, from the Hertzian contact theory described in Reference 11.9, it may be noted that the expression in square brackets is equal to the cube of the radius of the contact area between two identical elastic spheres in contact. Thus, the correlation presented above may be understood as:

$$\lambda_{eff}^{c} = \lambda_{peb} \cdot \frac{a}{0.531 \cdot S} \left(\frac{N_A}{N_L} \right)$$

---

[10] The original reference could not be obtained in time for the current work.

where a is the radius of the pebble-pebble contacts predicted by Hertzian contact theory.

11.3.3 Heat Transfer across the Pebble Bed due to the Coolant Gas

The presence of the coolant gas in the pebble bed facilitates heat transfer, even in the absence of forced cooling. This is due to heat conduction through coolant gas and the bodies of the pebble fuel element, together with localized convection currents.

Zehner and Schlünder published a correlation for the effective thermal conductivity of a single phase fluid-filled pebble bed, which is reported in Reference 11.8. The correlation states:

$$\lambda_{eff}^g = \lambda_{gas} \cdot \left\{ 1 - (1-\phi)^{1/2} + \frac{2 \cdot (1-\phi)^{1/2}}{1 - \gamma \cdot B} \left[\frac{(1-\gamma)B}{(1-\gamma B)^2} \ln\left(\frac{1}{\gamma B}\right) - \frac{B+1}{2} - \frac{B-1}{1-\gamma B} \right] \right\}$$

Where:

$$\gamma = \frac{\lambda_{gas}}{\lambda_{peb}}, \qquad \text{and} \qquad B = 1.25 \left(\frac{1-\phi}{\phi} \right)^{10/9}$$

And:

ϕ	Void fraction of pebble bed
λ_{peb}	Thermal conductivity of the pebbles (W m^{-1} K^{-1})
λ_{gas}	Thermal conductivity of the coolant gas (W m^{-1} K^{-1})

This correlation was compared to experimental test data by Prasad et al. (Reference 11.8). Prasad et al.'s tests were conducted with three solid materials: glass, steel, acrylic; together with two fluids: water and glycol. The apparatus used is illustrated in Figure 11.3.2.

Figure 11.3.2: Sketch of the Prasad et al. Experimental Setup

Thermofoil heater

Aluminium plate

Plexiglass cylinder, 17.8 cm inner

Insulation surrounds cylindrical sample holder

Test sample region

Aluminium plate

Temperature difference between end plates, ΔT, ranged from 10-50°C

Base

Cooling water inflow (room temperature)

Cooling water outflow
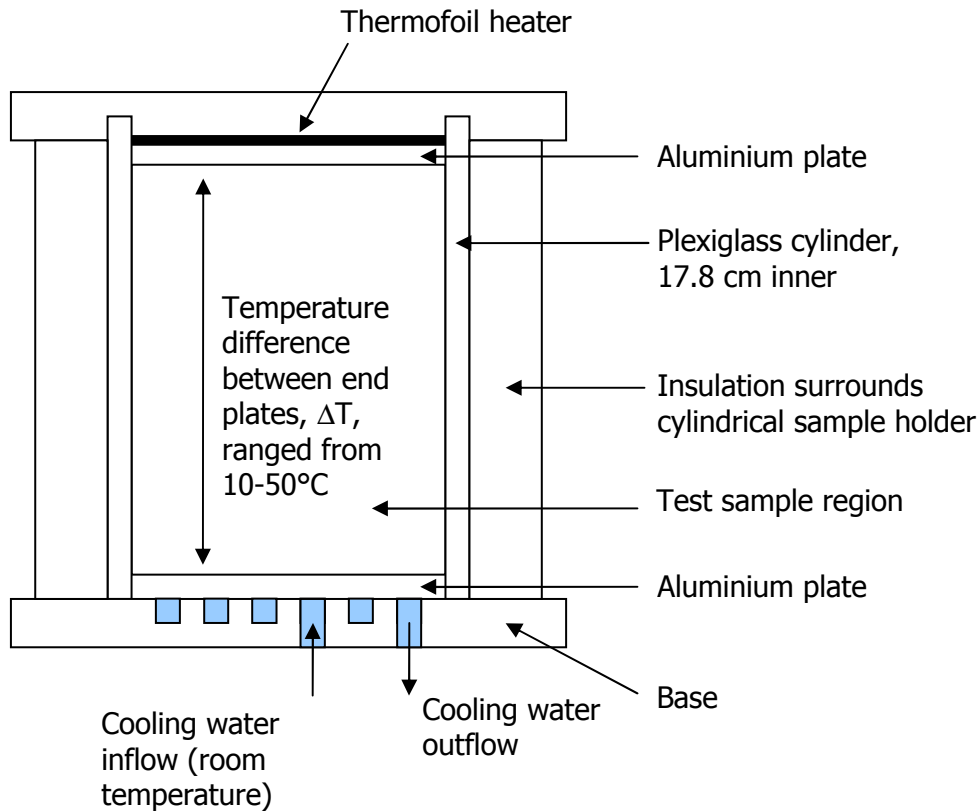
Previously published results based on glass, lead and polypropylene spheres immersed in water and oil were also reviewed. Good agreement between the experimental data and the Zehner-Schlünder correlation was found for combinations of materials satisfying the condition $\gamma<1$, i.e. where the thermal conductivity of the solid material is greater than the conductivity of the surrounding gas. This condition is satisfied by the materials present in a PBR core.

11.3.4 Evaluation of Correlations

The results for all of the cases discussed in Section 11.2.1 are summarized in Table 11.3.1 based on the Breitbach and Barthels formulations for radiation-solid conduction component presented above. It is noted that the total effective thermal conductivity is strictly not a simple sum of the effective conductivities of the different heat transfer mechanisms (radiation, contact conduction and conduction through the gas), since these are not independent parallel heat paths; however, a simple sum of the components is the traditional approach and this is done here for consistency with previous publications on this subject.

Table 11.3.1: Summary of Effective Thermal Conductivities.

Temperature (K)	Effective Conductivity Due To Conduction Through Helium (W/m/K)	Effective Thermal Conductivity Due To Radiation (W/m/K)	Effective Thermal Conductivity Due To Contact Conduction (W/m/K)	**Total Effective Thermal Conductivity (W/m/K)**
1273	2.5	12.8	0.5	**15.7**
1573	2.7	18.0	0.5	**21.2**
1873	3.0	23.4	0.5	**26.8**
1873	not modeled	23.4	0.5	**23.9**
1873	not modeled	23.4	not modeled	**23.4**
2173	3.2	29.7	0.5	**33.3**

11.4   Closure

The conclusion of this work was that the Zehner and Schlünder or Breitbach and Barthels correlations could not be validated by using the software ANSYS FLUENT within a reasonable time period. An attempt to apply the Abaqus finite element code to this problem also proved to be unsuccessful because of limitations with the code's cavity radiation model.

It is suggested that the Star-CCM+ software be used to evaluate the models presented in this study since the developers claim that this problem type can be solved using this software and that the FLUENT case files can be read directly.

In addition, non-cylindrical domains should be considered for future solutions to the radiation problem since cylindrical symmetry surfaces might give accuracy problems in thermal radiation calculations in which specular reflection is assumed because it represents an unphysical situation. Circular cylinders cannot be clustered without gaps in between them, unlike hexagonal or square prisms.

11.5   References for Section 11

11.1   "Evaluation of High Temperature Gas Cooled Reactor Performance-Benchmark Analysis related to the PBMR-400, PBMM, GT-MHR, HTR-10 and the ASTRA Critical Facility", IAEA-TECDOC-TBD DRAFT, September 2006.

11.2   The Nuclear Safety Standards Commission (KTA), "KTA Program of Standards (14.04.2008), Reactor Core Design for High-Temperature Gas-Cooled Reactor, Part 1: Calculation of the Material Properties of Helium", KTA Standard 3102.1, June 1978. URL <http://www.kta-gs.de/common/regel_prog.htm>.

11.3   N. B. Vargaftik and Yu. D. Vasilevskaya, "Thermal Conductivity of Helium at Temperatures from 300 to 6000ºK", Journal of Engineering Physics and Thermophysics, Volume 42, Number 3, March 1982.

11.4   Fluent Inc., "FLUENT 6.3 User's Guide", September 2006.

11.5   B. McLaughlin, "Design of a Non-linear Cell-Centred Multigrid Algorithm", University of Waterloo, 2005.

11.6   G. Breitbach and H. Barthels, "The radiant heat transfer in the HTR core after failure of the afterheat removal systems," Nuclear Technology, Vol 49 Issue 3, pp 392-399, August 1980.

11.7   "INET analysis of SANA-1 experiment benchmark problems," published within "Heat transport and afterheat removal for gas cooled reactors under accident conditions," IAEA-TECDOC 1163, IAEA, January 2001.

11.8   V. Prasad, N. Kladias, A. Bandyopadhaya and Q. Tian, "Evaluation of correlations for stagnant thermal conductivity of liquid-saturated porous beds of spheres," Int. J. Heat and Mass Transfer, Vol 32, Issue 9, pp1793-1796, September 1989.

11.9   Hans-Jürgen Butt, Karlheinz Graf, Michael Kappl, "Physics & Chemistry of Interfaces", 2006.

12.0   WHOLE CORE COMPUTATIONAL FLUID DYNAMICS MODEL

12.1   Purpose of Section 12

The primary goal of the work presented in this section is to set up a computational fluid dynamics (CFD) model of a pebble bed HTGR core to act, initially, as host for the sub-models developed in the first three research themes. This model enables the sub-models to be validated using code to code comparisons within the IAEA CRP-5 benchmark program. The goal of this work is to build a model using the ANSYS FLUENT CFD software package that can be used to simulate a PBMR reactor at a macro level. This model can be compared to the results of the benchmark Case T-1 documented in Reference 12.1 to examine model outputs such as:

1. Average Fuel Temperature
2. Average Moderator Temperature
3. Average Helium Temperature
4. Helium Outlet Temperature
5. Helium Outlet Pressure
6. Maximum Fuel Temperature
7. Maximum Power Density

The approach for this work was to model a slice of the PBMR reactor. As a first step, this model used the standard homogenous equilibrium porous medium model in FLUENT to simulate flow through the core region of the reactor. The inputs for the model were limited to data that was found in the public domain with the majority of the inputs coming from the IAEA CRP-5 documentation (Reference 12.1). Reference 12.1 is currently in draft form only, but the data in this document is considered to be the best available data for benchmarking the FLUENT model. Reference 12.1 includes the results of benchmark analysis that were completed for a variety of cases, some of which included the coupling of neutronics and thermal hydraulics models. The current model is limited to only thermal hydraulics assessments since coupling the model to a neutronics code is outside of the scope of the current work.

Since only a thermal hydraulics assessment was completed at this time there is only one benchmark in Reference 12.1 that is appropriate for comparison with the current model. This benchmark is Case T-1, which is discussed in detail in Section 4.2 of Reference 12.1. Some of the assumptions specific to Case T-1 are discussed in the following subsection.

12.2   CFD Model

12.2.1   Fundamental Assumptions

The standard porous medium model in FLUENT is a homogenous equilibrium model. This means that in the FLUENT model no actual solids are modeled in the core and instead, any solids in the porous medium are in thermal equilibrium with the fluid in

the core. This is clearly a simplification since in the core of a PBMR reactor the pebbles are hotter than the surrounding helium. This is discussed further Section 12.3.7.

A review of the data available in the public domain regarding the geometry of the PBMR reactor found that some of the geometric details of the design are not openly available. For example, the exact dimensions of some of the helium flow paths in the reactor need to be assumed and this is discussed in more detail in Section 12.2.2.

In order to benchmark the current model against Case T-1 in Reference 12.1, the model only contains data that was available at the time that the original benchmark was completed. For example, although work to examine the packing fraction near the reflector walls was completed as part of this project this data was not available during the original benchmark. Therefore the packing fraction will simply be assumed to be 0.61 for the entire core region. It also is not clear in the open literature exactly how the helium bypass flows get from the helium risers to the RCS and RSS channels, or what percentage of the bypass flow goes to each of the RCS or RSS channels. Therefore, only the primary helium flow through the risers (i.e., the nominal flow, reduced by the bypass flow) has been included in the model. The RSS and RCS channels were assumed to contain stagnant helium when the model is benchmarked against Case T-1. Other important modelling assumptions are discussed in the following sub-sections and Sections 12.3 as appropriate.

12.2.2 Modeled Geometry

A 2-D representation of the geometry modelled is shown in Figure 12.2.1. This figure was taken from Reference 12.1 and colours have been added to the figure to make the different regions modelled more obvious. The different colours represent the different regions in the model that have different properties. For example, the supporting graphite bricks have a different porosity and material properties than is found in the pebble filled core of the reactor. Therefore, these two regions are shown in different colours in the figure. Since graphite used in the inner reflector has the same properties as the graphite in the outer reflect they are shown in the same colour.

For the current model, a quasi 3-D geometry is used. The reason that the model constructed is not a true 3-D geometry is because there are no true symmetry or periodic planes in a PBMR 400 reactor as is shown in Figure 12.2.2. This figure shows the following characteristics:

- There are 36 risers channels (one located every 10 degrees).

- 24 Reactivity Control System (RCS) channels (one every 15 degrees).

- 8 Reserve Shutdown System (RSS) channels (one every 45 degrees)

- 3 defuelling chutes (one every 120 degrees).

- The bottom part of the reactor that supports the fuel varies in elevation with the floor being highest in between the defuelling chutes and lowest at the centre of the defuelling chutes.

- The two helium inlets connect to the lower plenum of the reactor and are located 80° apart.

In order to keep the model a reasonable size, a 20° slice of the reactor was modelled and a simplifying assumption used in the model was that the sides of the slices of the reactor can be modelled as symmetry planes.

Although a significant amount of information is available either in the open literature or published within final and draft IAEA and OECD/NEA documents some details of the geometry are not provided. For example, the dimensions required to exactly specify the geometry where the helium flows out of the risers, into the upper torus, through the slots around the RCS channels (shown in Figure 12.2.3) and into the upper plenum over the top of the core are not available. Therefore some simplifying assumptions have been made for this portion of the geometry. These assumptions include:

- Assuming a width of 5 cm for the slot that carries helium from the upper torus to the upper plenum above the core.

- Assuming the width of the channels where the helium flows out of the riser channels and into the upper torus to be 14 cm.

- The depth of the bricks, in the bottom reflector, that support the core and contain the outlet slots were not available. The depth of the bricks was assumed to be 2.2 m. Although Reference 12.1 indicates that the porosity in the region is 0.193 no other details regarding the depth of this area or the dimensions of the outlet slots are provided. Therefore additional assumptions had to be made to model this portion of the model and these are discussed further in Section 12.3.3.

These regions are shown in Figure 12.2.1 and Figure 12.2.3.

The details of the geometrical inputs are tabulated in Section 4.2 of Reference 12.2.

Figure 12.2.1: Side View of Model Geometry
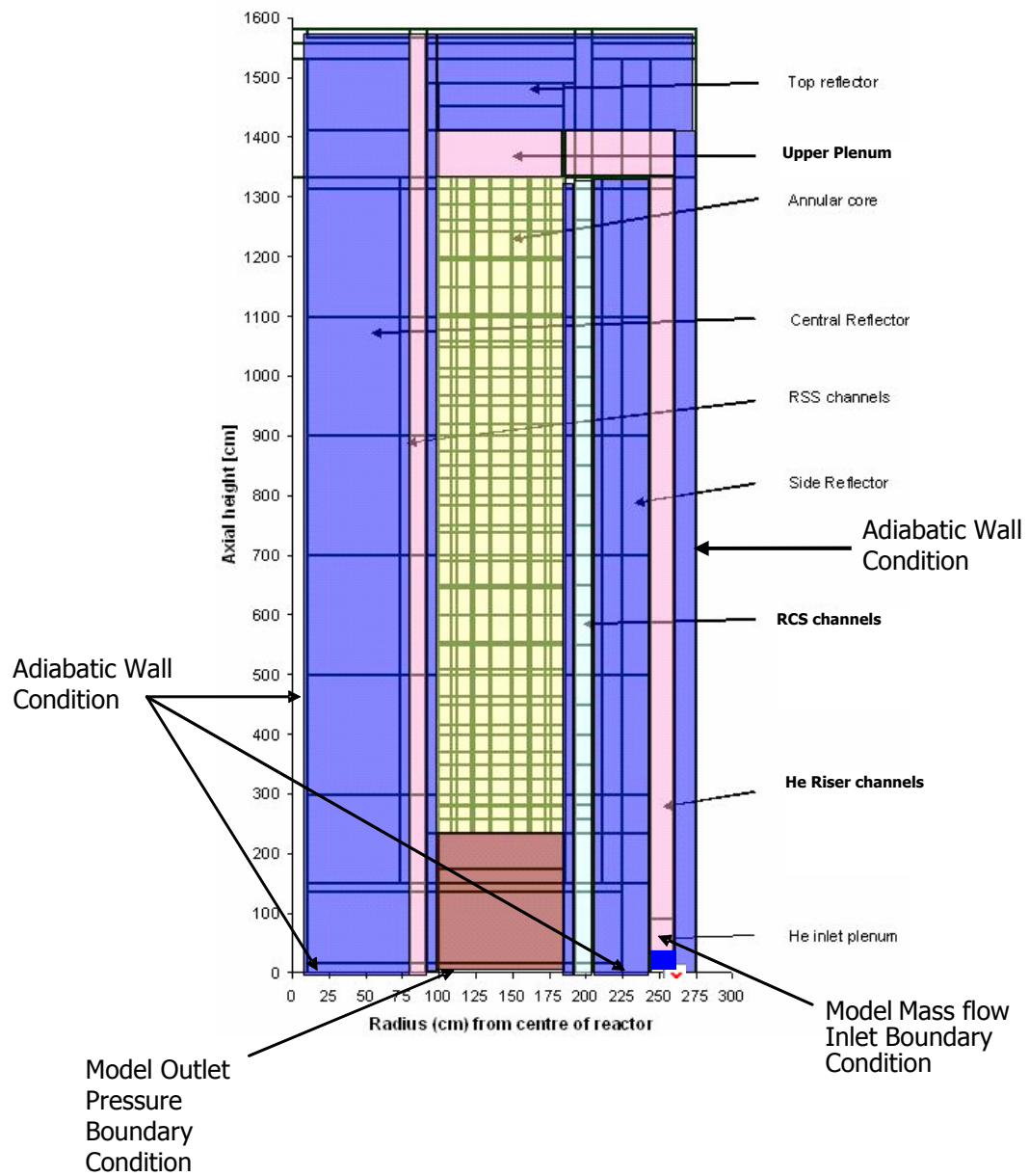
Legend for Figure 12.2.1
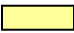
Colour	Region	Notes
	Core Region	Region containing the fuel pebbles. Different properties can be assigned to the core depending on if it is part of the near wall region (within 5 pebble diameters of the reflector walls) or in the centre of the core (greater than 5 pebble diameters from the graphite reflectors).
	Supporting Graphite Bricks	This area was also porous, but the properties and porosity are different than in the pebble core.
	Fluid zone (outside of pebble core)	RSS channels are assumed to be full of circulating helium.
	Graphite reflector	The same properties were used for both the centre and side reflectors. The reflector will be broken up by including a RSS channel as shown in the figure
	RCS	This system is filled with helium and some helium bypass flows through these channels.

Figure 12.2.2: Top view of Reactor Geometry (Reference 12.1)
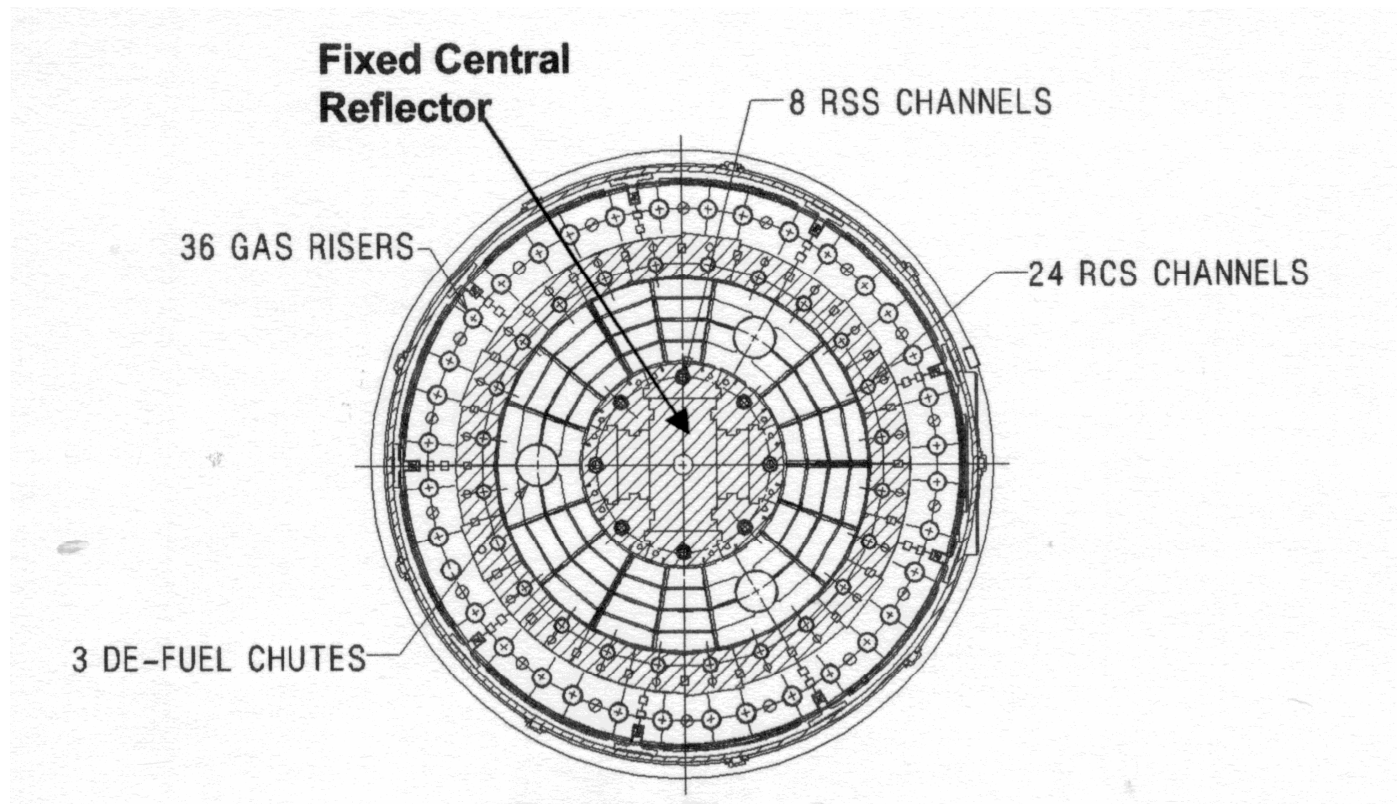
Figure 12.2.3: Images of Model Geometry

Section through the upper plenum showing the helium path from the riser channels to the void region over top of the core in blue.

3-D representation of model geometry with helium path shown in blue.
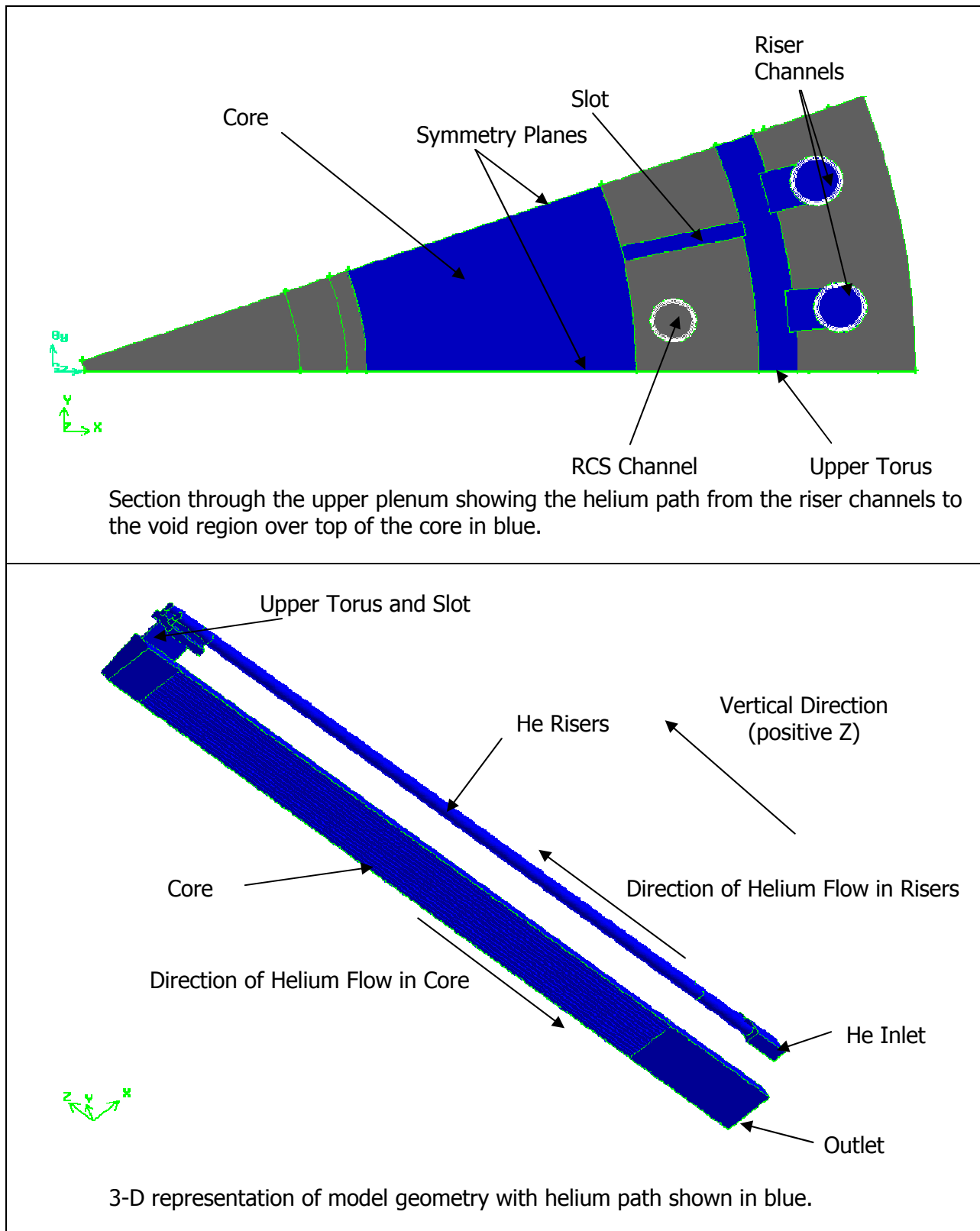
12.2.3 Computational Mesh

The current model uses a computational mesh made up of a variety of element types (including hexahedral, wedge and tetrahedral elements), but the mesh is predominately made up of hexahedral elements. For the solid graphite reflector regions of the model some regions are made up of tetrahedral elements since this makes the meshing easier, although using these lower quality elements would have less of an effect in solid areas where only the conduction equation is solved. There are approximately 1 million elements in the model (including both the solid and fluid regions) and details of the mesh can be seen in Figure 12.2.4.

Figure 12.2.4: Sample Image of Final Mesh in the Solid and Fluid Regions

View of mesh from top of reactor.

View of the inlet plenum region near bottom of the reactor that is constructed of tetrahedral elements.

View of the top region of the reflector over the helium risers that used tetrahedral elements in the solid region.
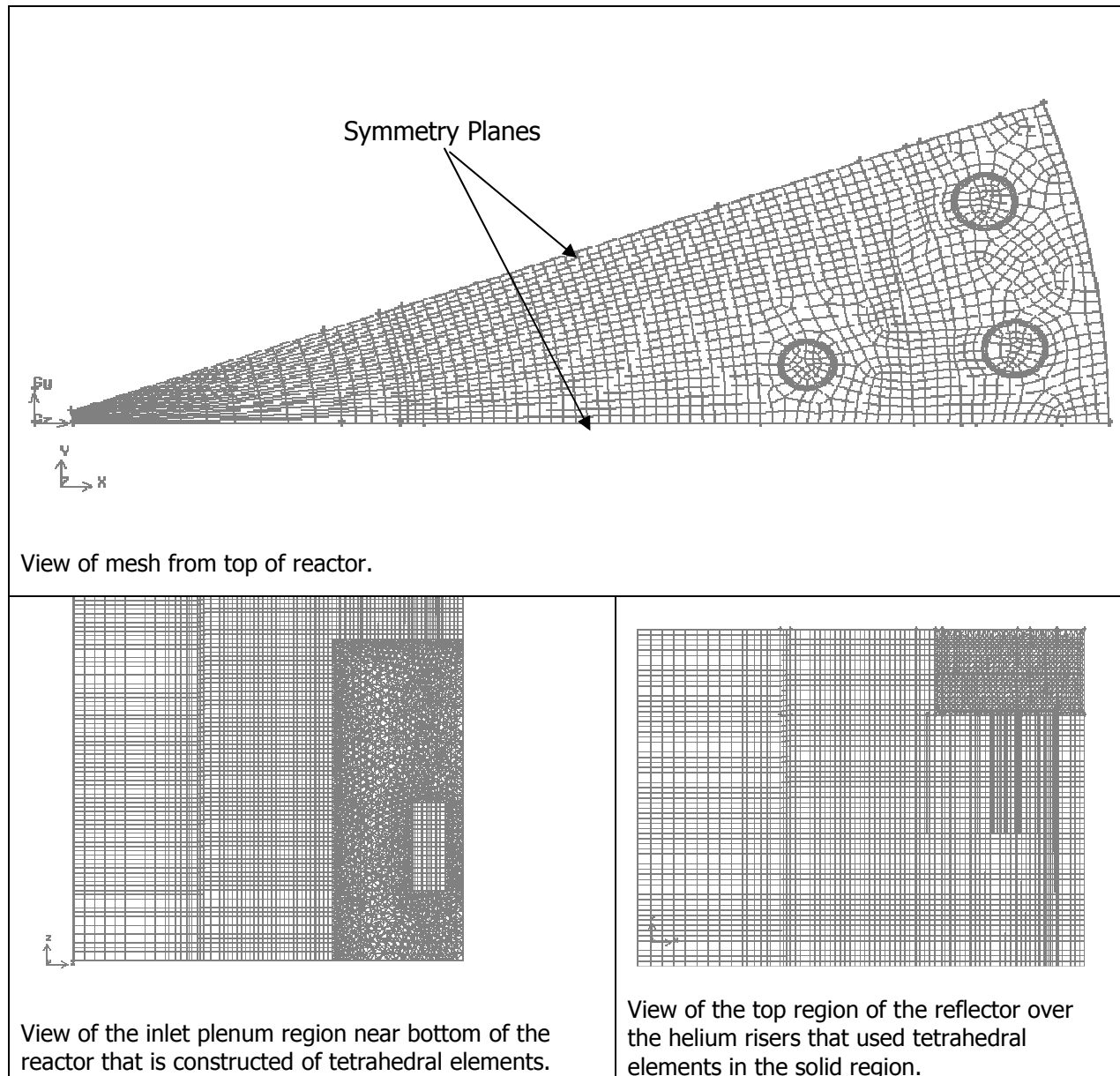
12.3   Material Properties and Boundary Conditions

12.3.1 Material Properties

12.3.1.1 Reflector Graphite Properties

For the current work the central and outer reflector properties were assumed to be made of the same material and the properties used for all reflector regions are shown in Table 12.3.1. These properties were also used for the supporting bricks in the outflow region of the model.

Table 12.3.1: Properties for Reflector Graphite

Property	Value	Reference
Density	1800 kg.m^{-3}	Converted from the 1.80 g.cm^{-3} given in Table 4.2-10 of Reference 12.1.
Specific Heat	1690 J.kg^{-1}K^{-1}	From Table 4.2-12 of Reference 12.1.
Conductivity	Variable	Taken from Figure 4 of Section 4.2 of Reference 12.1[1].

12.3.1.2 Pebble Bed Graphite Properties

Since this model is a macro scale model it is not possible to resolve the individual pebbles in the core. Instead the core was modelled as a porous medium that includes different properties for the solid part of the porous region. For the solid part of the porous region, that is made up of fuel pebbles, the properties are given in Table 12.3.2.

Table 12.3.2: Properties for Pebble in Core

Property	Value	Reference
Density	1720 kg.m^{-3}	Converted from the 1.72 g.cm^{-3} in Table 4.2-9 of Reference 12.1.
Specific Heat	1690 J.kg^{-1}K^{-1}	From Table 4.2-12 of Reference 12.1.
Conductivity	Variable	The conductivity of the pebble bed is calculated based on the Zehner-Schlünder correlation, which is shown in Figure 3 of Section 4.2 of Reference 12.1.[2]

12.3.1.3 Coolant Properties

The physical properties for the helium coolant are represented by temperature and pressure dependent quantities in the CFD model. The correlations that represent the property variations are taken from Reference 12.3 and were coded into FLUENT User

---

[1] The data in Figure 4 of Section 4.2 of 12.1 was digitized and a curve was fit to the data. The data was then coded into a FLUENT User Defined Function. The curve used in the model is the bottom one, which is for highly irradiated graphite.

[2] The curve used in the model is the upper one based on Zehner-Schlünder, which is for unirradiated graphite and the curve used was a curve fit to the digitized data in the figure.

Defined Functions (UDFs). The same FLUENT UDFs are used in the current model and the emissivity of the helium gas is assumed to be zero.

12.3.1.4 RCS Channel Properties

The RCS (Reactivity Control System) channels usually have helium flowing through them in order to provide cooling to the control rods. The helium that flows through these channels is part of the core bypass flow, which is discussed further in Section 12.3.2.1. For the IAEA CRP-5 benchmark problem it is assumed that the channels are filled with helium, but that there is no circulation. A simplification that is made is that the helium in the single RCS channel that is modelled contains stagnant helium, modelled as a solid, using the same properties as are used for the helium coolant (see Section 12.3.1.3 for more details).

An additional simplification is that although there are metal sleeves inside the RCS channels the properties associated with the sleeves are ignored and this simplification will not significantly impact the model predictions. The reason for this is that the Incoloy 800H sleeves are only about 0.01 m thick, which is small compared to the overall thickness of the graphite reflector in the vicinity of the RCS channels.

12.3.1.5 RSS Channel Properties

The RSS (Reserve Shutdown System) channels generally have some helium bypass flow going through them and this provides some additional cooling to the central reflector during normal operation. Since the RSS channels are not explicitly included in the model (due to the lack of symmetry in the reactor) they are instead accounted for by modifying the properties of the annular ring of the central reflector that contains the RSS channels to effectively include them. It is assumed that the helium in these channels is stagnant and is modelled as a solid and the metal sleeves in the channels are ignored, just as was assumed for the RCS channels (see Section 12.3.1.4). It is reasonable to ignore the Incoloy 800H sleeves since they are thin relative to the thickness of the central graphite reflector.

From the data provided in the tables in Section 4.2 of Reference 12.1 the annular region that contains the RSS channels has an inner radius and outer radius of 0.786 m and 0.94 m respectively, which produces an area for this annular region of 0.835 m^2. Within this ring there are 8 RSS channels, each of which is 0.154 m in diameter, which produces a total vertical flow area of 0.149 m^2 for these channels. Therefore, 17.85% of the annular ring is RSS channels (or made of stagnant helium) with the remaining 82.15% of the annular ring being reflector graphite.

The effective properties for this solid section of the reflector is therefore calculated as 17.85% helium (see Section 12.3.1.3) and 82.15% reflector graphite (see Section 12.3.1.1). These new effective properties are coded into FLUENT UDFs and a new material called rss_channels was added to the model.

12.3.2 Boundary Conditions

This sub-section describes the boundary conditions that were used for the current CFD model.

12.3.2.1 Inlet

The inlet surface (which is shown in Figure 12.2.1 and Figure 12.2.3) was modeled as a mass flow boundary condition with a constant specified turbulence intensity and length scale. From Table 4.2-15 of Reference 12.1, the inlet temperature is 488.1°C and the total inlet mass flow rate is 185.31 kg/s. Therefore, for a 20° slice of the reactor the total flow rate is 185.31 *20°/360° = 10.295 kg/s for the current model. Table 4.2-15 also indicates that 19% of the total flow actually bypasses the core (traveling instead down the RCS and RSS channels to provide cooling to the control rods and central and outer reflectors, as well as other leakage paths) and therefore the nominal flow was reduced by 19% to 10.295*0.81 = 8.338 kg/s (or approximately 150 kg/s for the entire core) to account for this. Since this mass flow is split over two different inlet regions, one for each riser, the total mass flow for each riser is 4.169 kg/s.

For the current simulation the turbulence intensity was set to 3.5% (low fluctuation) at the inlet with a length scale of 0.036 m, based on the recommendations for setting these values found in Reference 12.2.

12.3.2.2 Outlet

The outlet boundary condition was set to be a plane of constant pressure. The value chosen for the outlet is 0 Pa(g) (or 0 bar), which is consistent with the values documented in Table 4.2-23 of Reference 12.1 for the IAEA CRP-5 PBMR benchmarks previously completed. In absolute terms the pressure outlet was set to a value of 8,915,000 Pa, as documented in Table 4.2-15 of 12.1, however in the simulation the relative pressure is set to zero and the model operating pressure is set to 8,915,000 Pa. The outlet boundary condition in FLUENT allows flow to exit or enter the solution domain as required. All flow that re-enters the solution domain at this boundary condition was specified to enter in a direction normal to the boundary condition. The re-entrant flow was initially specified to have a turbulence intensity, length scale and temperature of 2.5%, 0.030 m and 1000°C[3]. Once the solution reached a reasonable level of convergence the average turbulence intensity and temperature at the outlet of the model were recalculated. The re-entrant flow properties were altered to reflect these average outlet values. This treatment increased the stability of the problem if there is re-entrainment at the outlet of the model.

---

[3] According to Table 4.2-23 in Reference 12.1 this is the temperature that was predicted in the previously completed IAEA CRP5 PBMR benchmark case T-1.

12.3.2.3 Symmetry

The outer surface of the slice of the domain was modeled as a symmetry plane, as shown in Figure 12.2.3. For this core and central reflector and in the area of the helium risers there is true symmetry in the model due to the way in which the RSS channels are modeled.

Near the RCS channel a symmetry condition is less valid due to the inclusion of only one RCS channel. In this area a periodic boundary condition would be more appropriate, but this simplification is not expected to significantly impact the model predictions since the current analysis is for steady state conditions.

12.3.2.4 Modeling of the Reactor Core

The current model is a macro scale model and therefore it is not reasonable to refine the individual pebbles in the model. Instead, the core is modelled by assuming it is a porous region. At the request of the US NRC the model was developed such that the core region was split in the radial direction into rings that were generally one pebble diameter in thickness (0.06 m). Due to the core actually being 0.85 m thick one of the central regions is actually modelled as 0.07 m thick and the core was split into 14 rings. The locations of the rings can be seen in Figure 12.3.1 and the detailed inputs used for each of the rings in the core is shown in Table 12.3.3.

Although it is known that the actual packing fraction varies as a function of distance from the reflector wall, this data was not available at the time that the T-1 benchmark was originally completed. Therefore in order to compare the current model to the existing T-1 benchmark values a uniform packing fraction of 0.61, or a void fraction of 0.39, was used in the model. The model has been developed to allow the user to easily specify different porosity values for each of the rings if desired.

Equations to determine the viscous and inertial resistances to be used in a porous medium representation of the core were previously developed in the earlier phases of the project (see Section 10.0). These equations were evaluated as part of this work and the values used as input in the current model are shown in Table 12.3.3. The viscous resistance term is only a function of the porosity of the packed bed and the diameter of the pebbles and therefore is straightforward to calculate and it is the same for all of the rings. The inertial resistance term is a function of the porosity, pebble diameter and the Reynolds (Re) number. The Re for the packed bed was calculated as follows:

$$
\mathrm{Re} = \frac{\left(\dfrac{\dot{m}}{A}\right)d}{\mu} = \frac{\left(\dfrac{150 kg/s}{\pi(1.85m)^2 - \pi(1m)^2}\right)0.06m}{4.687x10^{-5} Ns/m^2} = 2.52x10^4
$$

Where:

$\dot{m}$ - is the total mass flow rate through the core (kg/s)

A - is the total nominal cross sectional flow area in the core (m^2)

d - pebble diameter (m)

μ - helium viscosity evaluated at 1019 K (N.s/m^2)

Using this Re the inertial resistances in Table 12.3.3 were calculated.[4]

The pressure drop equation used internally by FLUENT is as follows:

$$\frac{\Delta P}{\Delta H} = \frac{-\mu \cdot V_{super}}{C_\alpha} - C_2 \cdot \frac{1}{2} \cdot \rho \cdot V_{super}^2$$

Where:

ΔP - is the pressure drop in the porous medium (Pa)

ΔH - is the height of porous region (m)

μ - helium viscosity (N.s/m^2)

V_{super} - is the superficial velocity in the porous region (m/s)

ρ - is the helium density (kg/m^3)

The two coefficients in the pressure loss model were derived in Section 10.0 using the KTA pressure drop correlation as:

$$\frac{1}{C_\alpha} = \frac{160}{d^2} \cdot \frac{(1-\varepsilon)^2}{\varepsilon^3}$$

$$C_2 = \frac{6}{\left(\dfrac{Re}{1-\varepsilon}\right)^{0.1}} \cdot \frac{(1-\varepsilon)}{\varepsilon^3} \cdot \frac{1}{d}$$

Where:

d - is the pebble diameter(m)

ε - is the porosity

Re - is the Reynolds number, which was calculated above

The final input required for the annular regions in the core was the heat source terms that represented the heat produced by the fission heating in the core. For case T-1 the

---

[4] It is noted that since the viscosity is actually a function of the temperature, the Re is also a function of temperature. Therefore, the inertial loss term in the momentum sink is actually a weak function of temperature as well. Therefore it may be possible that a constant inertial loss factor could produce a pressure loss that is not identical to the expected KTA pressure drop.

axial power profile was provided in Section 4.2.1.7[5] and Figure 34 of Reference 12.1. The data from Section 4.2.1.7 was used to calculate the heat source. These values were shown for annular rings that were 0.17 m in width, but since the current model had rings that were generally 0.06 m in width the data needed to be modified to apply to the current model. The energy source calculated for each of the rings is shown in Table 12.3.3. Additional information regarding how FLUENT models a porous medium can be found in Section 12.3.7.

The Zehner-Schlünder correlation used for the effective pebble conductivity also includes the effects of pebble to pebble radiation and therefore radiation is implicitly included in the modelling of the core.

Figure 12.3.1: Core Ring Locations in the Model

---
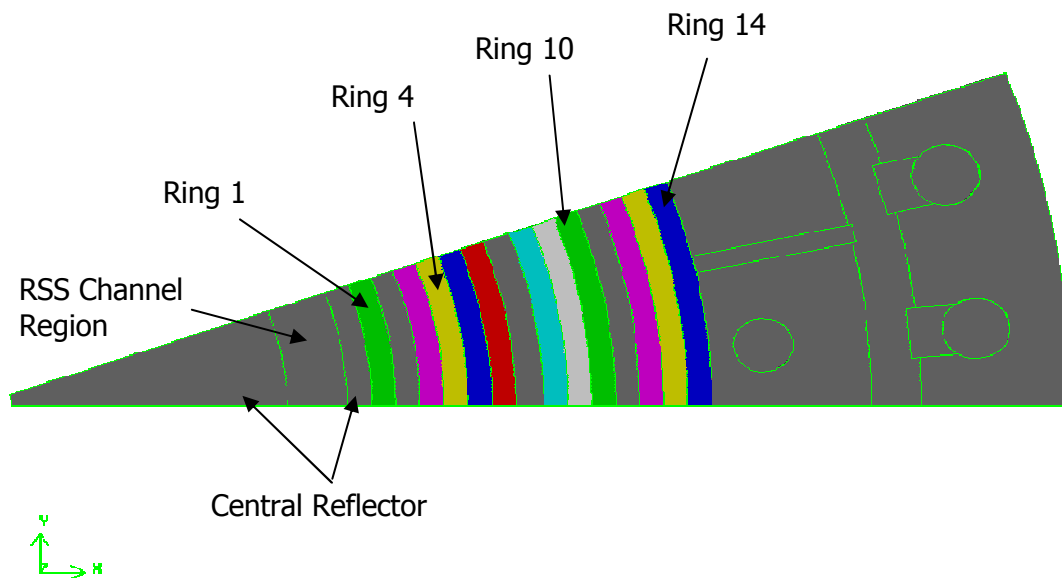
[5] The relative power distribution in five equidistant core axial channels (0.17 m each) where provided. These were 1: 1.119, 2: 1.023, 3: 0.953, 4: 0.957, 5(Fuel nearest outer reflector): 0.945. The interpretation of the data is that the power density in the 1st axial flow channel is calculated as 1.119*(400 MW/83.7156 m3), 1.023*(400 MW/83.7156 m3) in the 2nd, etc.

Table 12.3.3: Inputs for Porous Core Model for IAEA CRP-5 Benchmark Case T-1

Ring Number	Inner Radius (m)	Outer Radius (m)	Ring Width (m)	Porosity	Viscous Resistance (m^{-2})	Inertial Resistance (m^{-1})[6]	Heat Generation Rate (W/m^3)
1	1	1.06	0.06	0.39	278794	355	5403348
2	1.06	1.12	0.06	0.39	278794	355	5403348
3	1.12	1.18	0.06	0.39	278794	355	5326089
4	1.18	1.24	0.06	0.39	278794	355	4939790
5	1.24	1.3	0.06	0.39	278794	355	4939790
6	1.3	1.36	0.06	0.39	278794	355	4827120
7	1.36	1.43	0.07	0.39	278794	355	4601779
8	1.43	1.49	0.06	0.39	278794	355	4601779
9	1.49	1.55	0.06	0.39	278794	355	4614656
10	1.55	1.61	0.06	0.39	278794	355	4621094
11	1.61	1.67	0.06	0.39	278794	355	4621094
12	1.67	1.73	0.06	0.39	278794	355	4572807
13	1.73	1.79	0.06	0.39	278794	355	4563150
14	1.79	1.85	0.06	0.39	278794	355	4563150

12.3.3 Bottom Reflector

In Table 4.2-4 of Reference 12.1 it is stated that the porosity of the bottom reflector that includes the helium outlet slots located directly below the bottom of the core is 0.193. Since the depth of this region is not provided in the open literature it was simply assumed that the depth of the bottom reflector was the distance from the bottom of the core to the outflow plane of the model (2.2 m). Also, there are no details provided regarding the actual geometry of the outlet slots and therefore it was not possible to determine realistic values for the viscous and inertial resistance coefficients for this region of the model.

---

[6] This term is actually a function of the average core temperature since it includes the Re, which is a function of the helium viscosity. The viscosity in the Re calculation was evaluated at 1019 K, which is the average benchmark core temperature listed in Table 4.2-23 of Reference 12.1.

Therefore, in order to simplify the model the supporting bricks were simply modeled as a porous solid with a porosity of 0.193 with reflector graphite properties used for the solid. Since no viscous or inertial resistance coefficients could be determined for the bottom reflector there is no pressure drop in this region. This simplification should not significantly affect the core pressure drop and temperature predictions.

12.3.4 Turbulence Model

This model used the SST turbulence model, which is the same model used in the previous phases of this project.

12.3.5 Buoyancy Model

The model includes buoyancy forces that are represented directly from coolant density variations although these should have a negligible influence at full power conditions. The gravitational acceleration vector in this model points in the direction of the flow in the core (see Figure 12.2.3) and has a magnitude of 9.81 m/s².

12.3.6 Radiation Model

The current work does not require the activation of the radiation model. This is because the effects of radiation heat transfer are already included in the model via the heat conduction correlations used to model the pebble bed and this was discussed in Section 12.3.2.4.

12.3.7 Porous Medium Model

The current work uses the standard porous medium model in the FLUENT Software package. This model only requires that viscous resistance coefficients, inertial resistance coefficients and porosity be entered. Therefore, the model does not by default include any information regarding the surface area of the solid in the porous bed and the solid is in reality not present in the model. This results in some limitation in the model, such as:

- Since the volume blockage that is physically present is not represented in the model, by default FLUENT uses and reports a superficial velocity inside the porous medium, based on the volumetric flow rate, to ensure continuity of the velocity vectors across the porous medium interface.
- The effect of the porous medium on the turbulence model is only approximated.
- When specifying the specific heat capacity, C_p, for the selected material in the porous zone, C_p must be entered as a constant value. The effective Cp of the porous medium will essentially be that of the solid since in this current model the graphite has a density that is 3 orders of magnitude larger than the helium and is a larger percentage of the core. The Cp used will not affect the current benchmark since it is steady state.

In order to solve the energy equation an effective conductivity of the porous medium is calculated based on the properties of the fluid and the solid in the bed. This effective conductivity is simply calculated as follows (from Section 7.19.3 of Reference 12.2):

$$k_{eff} = \varepsilon k_f + (1 - \varepsilon) k_s$$

where:

k_{eff} - the effective conductivity of the porous medium (W/m.K)

ε - the porosity (or void fraction)

k_f - the conductivity of the fluid (W/m.K)

k_s - the conductivity of the solid (W/m.K)

Therefore, the temperature reported by the FLUENT solver is for a homogeneous equilibrium pebble bed. In this model for steady state simulations this temperature will be both the fluid temperature as well as the pebble surface temperature.

In reality, a packed bed of pebbles is a highly dispersive medium. When a jet of helium impinges on a pebble, the jet is split and deflected to flow around the pebble. The branches of the original jet then encounter further pebbles and split again, and so on. As well as jets being split, they are combined with branches of jets split by impacts with neighbouring pebbles. This gives rise to a very strong diffusion mechanism. The diffusivity has a velocity scale that is proportional to the superficial velocity and length scale that is proportional to the diameter of the pebbles. In this work, however, the enhanced diffusion resulting from geometrical dispersion has been neglected. This is not expected to influence the results with the T1 benchmark too strongly because the power density distribution is relatively uniform. However, with more realistic power density distributions, fuel temperatures will be over-predicted if the enhanced diffusivity of momentum and heat is not included in the model.

FLUENT also allows for two different velocity formulations in a porous medium. The default formulation is the superficial velocity, which is the same velocity as would be seen if the medium were not porous. The other formulation is to use the physical (or pore) velocity. Since the viscous and inertial losses calculated for the model in Section 12.3.2.4 were calculated based on the superficial velocity the superficial velocity was used in the model and no cases were completed using the physical velocity model.

Earlier in this sub-section it was noted that the effects of the porous medium on the turbulence model is only approximated. This is because the porous medium model neglects the true geometry, in this case the random pebble arrangement, and does not include information such as pore size, fluid/solid surface area, etc., due to simplifications. Since the superficial velocity formulation was used in the full core model this also results in an average velocity that is significantly lower than the true pore velocity, which increases the fluid residence time in the core region. In a real pebble bed, the influence of turbulence is overwhelmed by the fluid mixing that results from the dispersion of the flow by the pebbles. Such a dispersion mechanism can be described by a simple algebraic model which takes the superficial velocity and pebble

diameter as its velocity and length scales respectively. However, no attempt has been made in the present work to include such a model, or to modify the behavior of FLUENT's built-in SST turbulence model.

Additional information regarding how FLUENT models a porous medium can be found in Section 7.19 of the FLUENT User Manual (Reference 12.2).

12.3.8 CFD Methods

Second order discretization is used for all equations (i.e., Density, Momentum, Turbulent Kinetic Specific Dissipation Rate and Energy) except for the pressure equation which uses the PRESTO! scheme. FLUENT recommends that the PRESTO! scheme be used when problems involving buoyancy are solved. The coupled solver was used with a Courant number of 5 to obtain final convergence.

As with the previous work, in order to consider a solution "converged" the following method was used:

1. The residuals should not be changing significantly when the solution is converged.

2. The core inlet and outlet temperatures and the model inlet and outlet pressures are monitored throughout the simulation and at convergence these values should be stable.

3. The volume average temperature in the innermost and outermost rings (Rings 1 and 14) of the core is also monitored during the simulation and at convergence these values should be stable.

12.4 Results

The primary focus of this work was to generate a model for simulating the whole core of a PBMR that could be compared against the IAEA CRP-5 PBMR benchmark data from Case T-1 documented in Reference 12.1. It should be noted that the model used by South Africa to generate the results in Reference 12.1 was a 2D model. The WIMSTER model developed in the United Kingdom was also a 2D model.

The results of this comparison are discussed in the following sub-sections. It should be noted that IAEA CRP-5 Case T-1 is a benchmarking exercise and that there is no one right answer for this exercise. Comparisons with the existing values are completed simply to ensure that the FLUENT model is producing predictions similar to the other existing models for this case.

12.4.1 Pressure Drop

The pressure drop from the inlet to the outlet of the model was extracted from the converged simulation. IAEA CRP-5 PBMR benchmark case T-1 (Table 4.2-23 of Reference 12.1) found that the pressure drop from predicted Inlet/Outlet Pressures were 1.8133/0.0000 bar and 1.83/0.00. In the FLUENT model the Inlet/Outlet

Pressures were found to be 1.99/0.0000 bar, which is higher than was predicted in the benchmark case. One of the reasons for the higher predicted inlet to outlet pressure drop in the model is due to the slot dimension chosen for the model. As shown in Figure 12.4.1 the slot acts as a significant flow restriction. When the pressure drop from the inlet of the model to the inlet to the core was examined in the model it was found that the pressure drop due to the riser and slot geometry is 0.18 bar. Since the IAEA CRP-5 benchmark was not truly 3D and did not explicitly model the slot this accounts for the different between the predictions in the two models.

The pressure in the core is shown in Figure 12.4.2. In order to verify that the pressure drop through the core is reasonable compared to that predicted by the KTA correlation (Reference 12.5) the pressure drop from the top to the bottom of the core is examined. The model predicted a pressure at the top of the core of about 1.81 bar and essentially 0 bar at the bottom of the core for a core pressure drop of 1.81 bar. Based on the uniform void fraction of 0.39 used in the model the KTA rules predict a pressure drop of:

$$\Delta P = \Delta H \times \Psi \times \frac{(1-\varepsilon)}{\varepsilon^3}\left(\frac{1}{d}\right)\left(\frac{1}{2\rho}\right)\left(\frac{\dot{m}}{A}\right)^2$$

With Ψ defined as:

$$\Psi = \frac{320}{\left(\dfrac{\mathrm{Re}}{1-\varepsilon}\right)} + \frac{6}{\left(\dfrac{\mathrm{Re}}{1-\varepsilon}\right)^{0.1}}$$

Where,

    ΔH - the height of the pebble bed (11 m)
    ε - the void fraction (0.39)
    d - the pebble diameter (0.06 m)
    ρ - the density of the fluid at the average core temperature (evaluated at 1019 K)
    A - the cross sectional flow area ($\pi(1.85m)^2 - \pi(1m)^2$ = 7.61 m^2)
    $\dot{m}$ - the effective helium flow rate (150 kg/s)
    Re - Reynolds number, evaluated at 1019 K

The KTA predicted pressure drop for an 11 m deep core is nominally 1.83 bar (assuming constant properties). Therefore, the FLUENT model currently predicts a pressure drop over the entire core that is slightly less than the KTA correlation. The difference in the pressure drop predictions are largely the results of property variations. Since the viscosity and density of helium are not linear functions of temperature the variations in temperature in the core mean that it is reasonable for the model predictions to differ from a correlation evaluated at the mean temperature.

This finding also indicates that an improvement that could be made to the model would be to calculate the viscous and inertial resistance coefficients dynamically using a FLUENT UDF as this could take into account the density and viscosity variations in the helium as it travels through the core. This modeling improvement would be needed if more realistic power shapes or transients with varying reactor power and/or mass flows were to be simulated. In these cases the viscous and inertial resistance terms will vary as functions of position and time.

Figure 12.4.1: Vector Plot Through Upper Plenum and Slot

Velocity Vectors Colored By Velocity Magnitude (m/s)
Nov 21, 2008
FLUENT 6.3 (3d, pbns, ske)
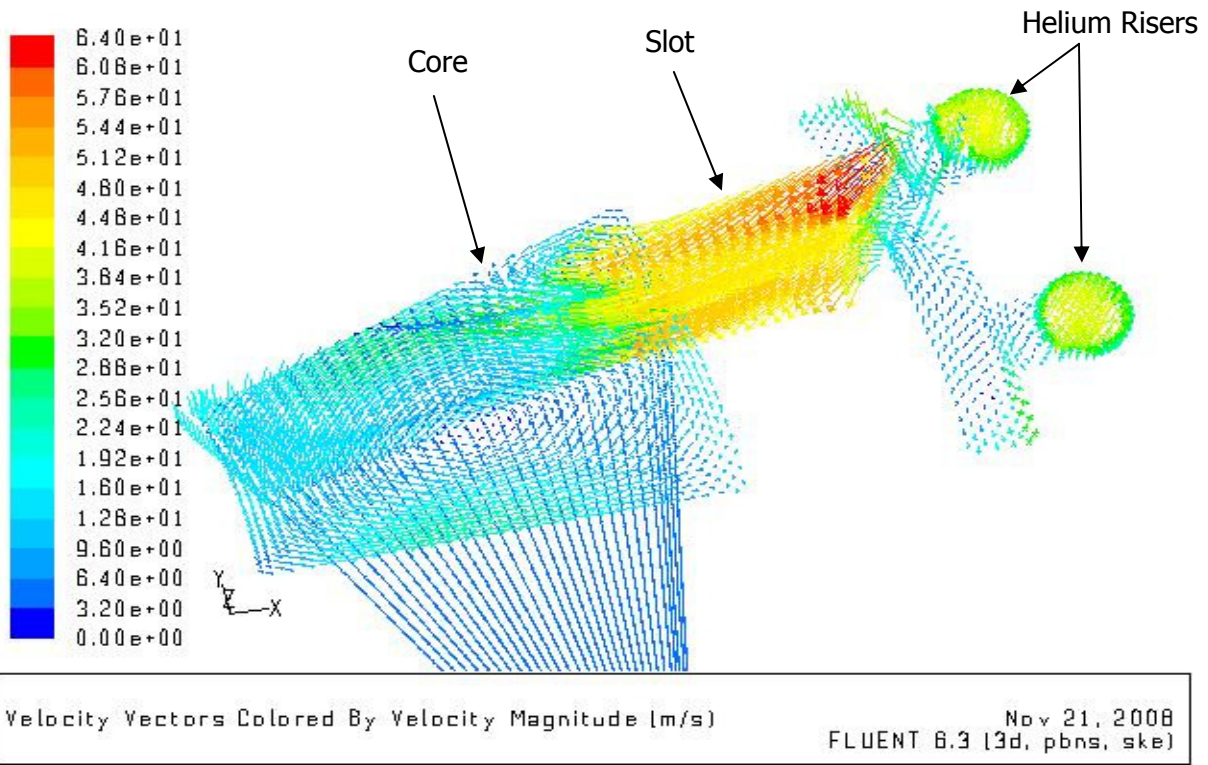
Figure 12.4.2 : Pressure Drop in the Reactor

Contours of Static Pressure (pascal)
Dec 22, 2008
FLUENT 6.3 (3d, pbns, sstkw)
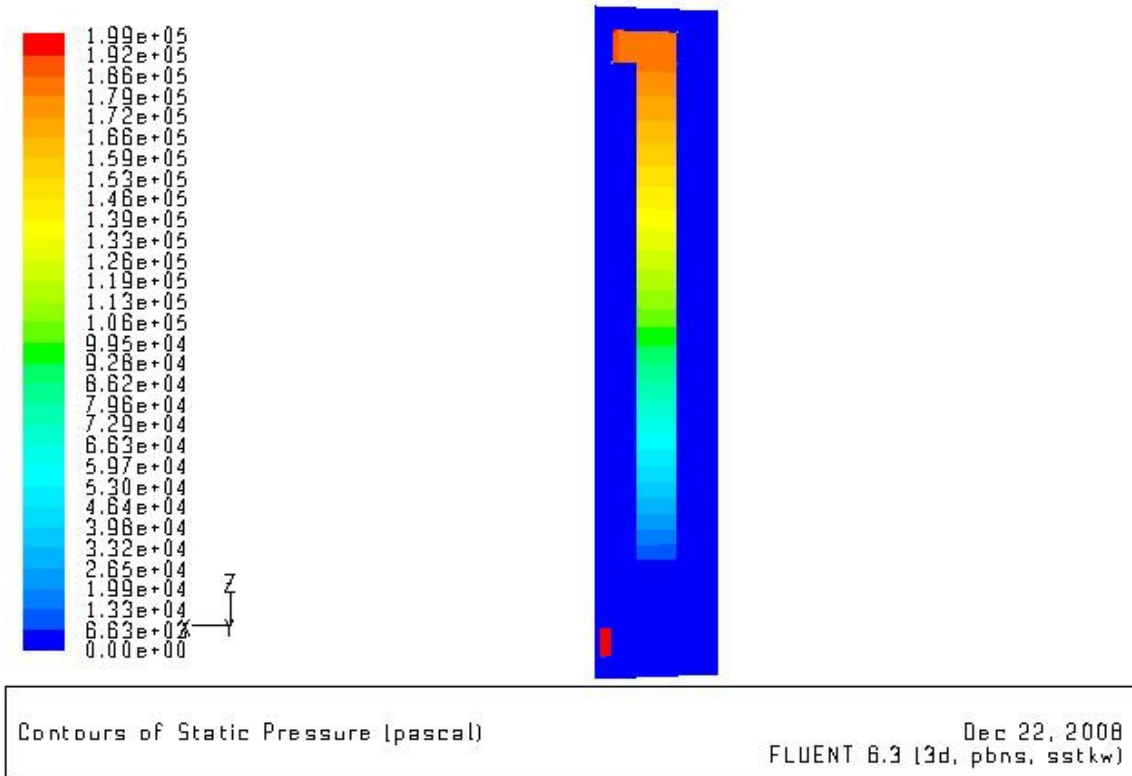
12.4.2 Temperature Predictions

The temperature predictions for IAEA CRP-5 benchmark T-1 can be found in Table 4.2-23 of Reference 12.1 and are reproduced in Table 12.4.1 along side the FLUENT model predictions.

As discussed in Section 12.3.7 the temperature calculated by FLUENT in the porous core region is assumed to be the helium temperature, but the helium temperature is not the only temperature of interest in the core. Using the methodology developed in Appendix M, it is possible to back out the temperature of the moderator and fuel in the reactor. The models in Appendix M were coded into a FLUENT UDF, as discussed in Section M.6, which performed a post processing step after each iteration to calculate the moderator and fuel temperatures from temperatures in the core.

The temperature data for the core region shows that there is good agreement between the volume averaged temperature of the helium in the core for the current model (746°C) and that previously predicted in South Africa and the United Kingdom (745°C and 753°C). There was also good agreement between the average moderator temperatures predicted by the three models, with FLUENT predicting 795°C versus 797°C in South Africa and 799°C in the United Kingdom. The helium, pebble surface and reflector graphite temperatures in the model are shown in Figure 12.4.3.

The predicted average fuel temperatures were about 10-20°C higher in the FLUENT model than in the benchmark (830°C in FLUENT versus 809°C and 823°C). The average fuel temperatures in each cell on a slice plane through the reactor are shown in Figure 12.4.4.

The maximum fuel temperature predicted by the FLUENT model also shows very good agreement with the previous benchmark (1176°C in FLUENT versus 1167°C and 1157°C in the South African and United Kingdom models). Therefore, it has generally been found that the FLUENT model predictions are consistent with the previous benchmark results for IAEA CRP-5 Case T-1. It is not clear from the South African results what properties were used in the simulation. In the current work, the pebbles had the properties of highly irradiated graphite, which has a lower conductivity. If the South African results assumed the pebbles were less irradiated it could help explain why the FLUENT model predicts higher fuel temperatures.

It is also noted that the outlet temperature for both models is virtually identical (1001°C for FLUENT versus 1003°C and 1001°C in the South African and United Kingdom results).

When the maximum power density was calculated for Case T-1 it did not agree with the value listed in Table 4.2-23 of Reference 12.1. Since the Maximum Power Density in MW/m^3 is simply the total power divided by the volume of the core multiplied by the maximum relative power in the profile (1.119 from Section 4.2.1.7 of Reference 12.1) this produces a Maximum Power Density of 1.119*400MW/83.7156 m^3 = 5.35 MW/m^3. Although this value does not agree with the table, it is consistent with Figure 34 of Reference 12.1, indicating that the 10.72 MW/m^3 listed is an error.

Table 12.4.1: Thermal Hydraulics Results for IAEA CRP-5 Benchmark T-1

Parameter	South African Results (from Table 4.2-23 of Reference 12.1)	United Kingdom WIMSTER Results[7]	FLUENT Model Predictions
Average Fuel Temperature (°C)	809.18	822.8	829.6
Average Moderator Temperature (°C)	797.09	798.8	794.8
Average Helium Temperature (in core) (°C)	744.50[8]	753.2	746.4
Total Helium Mass Flow Rate (kg/s)	150.00	150.1	150.0
Inlet/Outlet Temperature (°C)	488.1/1003.0	488.1/1001.1	488.1/1001.2
Inlet/Outlet Pressure (bar)	1.8133/0.0000	1.83/0.0000	1.99/0.00
Maximum Fuel Temperature (°C)	1166.50	1157.4	1175.9
Maximum Power Density (MW/m^3) [9]	10.72	5.4	5.35

---

[7] These values are not shown in the Draft of the IAEA CRP-5 Benchmark documentation, but have been submitted to the IAEA and will be included when the final version of this document is issued.

[8] The value shown in Table 4.2-23 of the draft of Reference 12.1 is actually 727.54°C, but this value is not correct and will be changed to the value in Table 12.4.1 when the final version of the document is issued.

[9] In Table 4.2-23 of Reference 12.1 there are no units for the Maximum Power Density, although they are assumed to be MW/m^3.

Figure 12.4.3: Temperature in the Reactor in °C
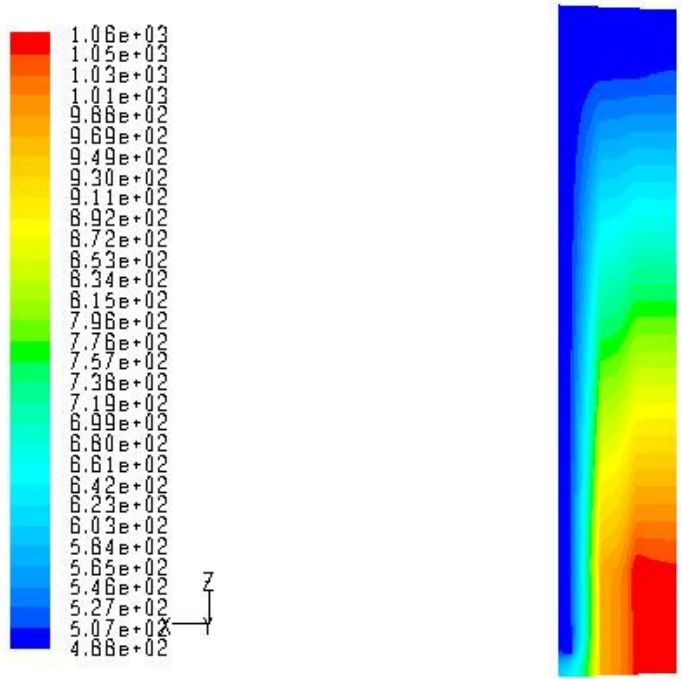
Contours of t_degc

Dec 22, 2008
FLUENT 6.3 (3d, pbns, sstkw)

Figure 12.4.4: Cell Average Fuel Temperatures the Core in °C
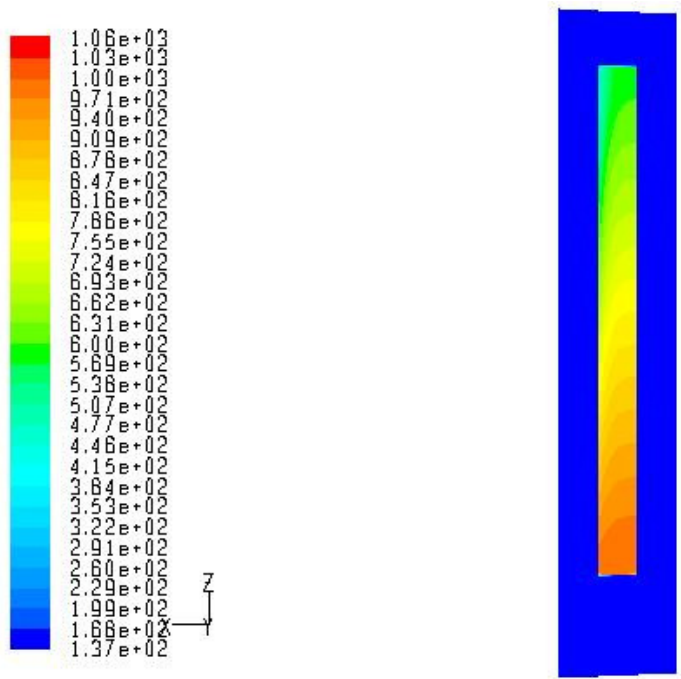
Contours of Ave_Moderator_T_degC

Dec 22, 2008
FLUENT 6.3 (3d, pbns, sstkw)

12.4.3 Error Estimates

Every CFD simulation contains several sources of error, and the goal of a successful analysis is to reduce these errors such that meaningful results may be obtained for the given application. This section discusses the errors and estimates of their magnitudes for the current work. The errors are broken down into the following types: Modelling Errors, Discretization Errors, Solution and Convergence Errors, which are discussed in the following subsections.

12.4.3.1 Modelling Errors

The current analysis uses an equilibrium porous medium model, which oversimplifies the temperature profile in the core (as discussed in Section 12.3.7). It is well known that there are significant temperature differences between the helium and the moderator graphite in the core of PBMR reactors and this was investigated in detail in previous tasks in this project. Since the current work only examined steady state conditions the errors introduced by the homogenous porosity model are not expected to have a significant effect on the solution. The main reason for this is that for steady state conditions with the adiabatic surfaces applied to the outer edges of the model all of the heat generated in the core must go into the helium fluid. For steady state conditions, the required temperature rise in the helium from the inlet to the outlet of the reactor can simply be calculated if the total mass flow and heat source for the system are known. For transient simulations where the mass flow and/or heat generation in the reactor are changing the errors introduced by the homogenous porous medium will be more significant.

If a heterogeneous porous model could be implemented in FLUENT it would give a better estimate of the magnitude of the error introduced by the homogenous porous medium model.

12.4.3.2 Discretization Errors

As previously discussed in Section 12.3.8, for this model all equations were solved using a second order scheme with exception of the pressure equation, which used the FLUENT recommended PRESTO! scheme. In addition, the coupled solver was used for this work.[10] The discretization errors in the model are expected to be small compared to the errors introduced from the porous medium approximation of the core.

12.4.3.3 Solution/Convergence Errors

The current work found that it was possible to achieve a high level of convergence for all of the governing equations. In addition, the porous medium representation, coupled with the simple power profile used appeared very stable. This was evident from the monitored quantities (discussed in Section 12.3.8) which showed little to no fluctuation as the solver neared convergence. Therefore, solution/convergence errors

---

[10] No attempts were made to achieve convergence with the segregated solver.

in the model are expected to be very small compared to the errors introduced from the porous medium approximation of the core.

12.5   Closure

A whole core CFD model has been developed for the PBMR 400 reactor using the FLUENT CFD package. Analytical micro and meso-scale particle and pebble temperature models have also been developed and implemented in the FLUENT model using FLUENT User Defined Functions. The integrated model is a quasi 3D model and the predictions from this model have been compared to the 2D predictions documented as IAEA CRP-5 Case T-1 in Reference 12.1.

The model was found to predict very similar temperatures compared to those documented previously predicted by the South Africans in Reference 12.1. The results also compare well with the predictions by the United Kingdom, which will be issued when Reference 12.1 is updated. The FLUENT model predicted higher temperatures for many quantities of interest, such as the average fuel temperature and the maximum fuel temperature, although the maximum difference between the predictions by the models was no more that 21°C. This is not considered significant given that the temperature rise from inlet to outlet in the models is over 500°C (1001°C at the outlet and 488°C at the inlet).

This work has shown that the analytical micro and meso-scale models presented in Appendix M is adequate for use in macro scale models where it is not possible to model pebbles and fuel particles in detail.

12.6   References for Section 12

12.1 "Evaluation of High Temperature Gas Cooled Reactor Performance- Benchmark analysis related to the PBMR-400, PBMM, GT-MHR, HTR-10 and the ASTRA Critical Facility", IAEA-TECDOC-TBD DRAFT, 2nd Tecdoc from CRP-5, September 2006.

12.2 FLUENT Inc., "FLUENT 6.3 User's Guide", September 2006.

12.3 The Nuclear Safety Standards Commission (KTA), "KTA Program of Standards (14.04.2008), Reactor Core Design for High-Temperature Gas-Cooled Reactor, Part 1: Calculation of the Material Properties of Helium", KTA Standard 3102.1, June 1978. URL <http://www.kta-gs.de/common/regel_prog.htm>.

12.4 OECD NEA/NSC/Doc(2005)xxx Draft V-03, "PBMR Coupled Neutronics/Thermal Hydraulics Transient Benchmark The PPMR-400 Core Design". September 2005.

12.5 The Nuclear Safety Standards Commission (KTA), "KTA Program of Standards (14.04.2008), Reactor Core Design for High-Temperature Gas-Cooled Reactor, Part 3: Loss of Pressure through Friction in Pebble Bed Cores", KTA Standard 3102.3, March 1981. URL <http://www.kta-gs.de/common/regel_prog.htm>.

13.0   OVERALL CONCLUSIONS AND RECOMMENDATIONS

13.1   Purpose of Section 13

This section summarizes the work carried out on pebble bed reactors (PBRs) presented in Sections 5 to 12. Conclusions drawn from this work are presented and topics that would benefit from further investigation are identified.

13.2   Summary of Models Developed and Conclusions

Section 5 was dedicated to the development of a multi-scale model of the heat transfer from the centre of a TRISO particle within a fuel pebble to the coolant surrounding the pebbles. This model was found to be computationally efficient and compared well with finite element simulations within an idealized "cylindrical" pebble, both in steady state and transient conditions.

The solution of Section 5 assumed that all of the TRISO particles within a pebble are uniformly spaced. However, in reality, the particles are randomly arranged, have random spacing and can form closely packed clusters. The work of Section 6 developed a Monte Carlo method to set up random distributions of particles which were interrogated to establish the expected distribution of clusters in terms of the expected frequency of particular cluster sizes. A complementary set of finite element conduction calculations was performed to predict the particle temperature enhancement for the worst-case (center) particle in clusters of given sizes and arrangements.

One aspect of the method used to interrogate the random assemblies of particles could be improved. The arbitrary size of sampling volume used (a voxel) introduces a scale-effect into the results. An improvement would be to devise a method that did not require sampling volumes. However, the finite element results showed that the enhancement to the fuel kernel temperatures for clusters towards the top end of the credible size range, of about 13 to 14 particles, is only of the order of 4°C for average particles, or about 12°C for the most highly rated particles. Therefore, at the moment it appears that further development of the statistical method is not required and that a margin of about 20°C should be applied to the predicted "best-estimate" particle temperatures.

Section 7 presented a method for the determination of the effective conductivities of the TRISO particle-containing region of fuel pebbles. This method is a development of the well-established Maxwell method for predicting the thermal conductivity of a suspension of spherical inclusions in a matrix. Maxwell's method was extended to allow the spherical inclusions to consist of an arbitrary number of layers of dissimilar materials. Comparison with finite element simulations carried out on regular arrangements of particles showed close agreement over ranges of material conductivities that are typical of in-service fuel pebble values. Further, the finite element simulations showed that, at representative particle packing factions, the resulting thermal conductivities are insensitive to the arrangement of the particles, and that the same result is obtained regardless of whether the individual coating layers

within the particle are resolved, or alternatively, all of the materials within the particle are homogenized and replaced by a single material with an overall effective conductivity.

Section 8 presented a method by which the multi-scale model of Section 5 can be extended to cope with a multi-batch fuelled core in which neighboring pebbles will have widely differing amounts of burn-up and power outputs. The model allows for a cascade of heat flows from higher power to lower power pebbles whilst, simultaneously, accounting for the heat transferred to the coolant and the "long-range" macroscopic conduction driven by gradients in the power profile and heat loss through the core boundaries. The values for the fuel particle and moderator temperatures determined for an average fuel batch at a given location in the reactor can be corrected to give the batch specific values that would be required by a neutronics model or for calculating fission product release fractions. Extension of this model to transient scenarios is possible and the steps necessary to achieve this have been proposed.

Section 9 summarizes the available models and data that are available for the determination of the thermal properties of irradiated graphite.

Within Section 10, a method was developed by which the geometry of arbitrarily sized randomly packed beds could be generated and developed into a CFD model. The resulting meshes feature high quality structured zones close to the sphere-to-sphere contact points. The pressure drop predicted by the CFD model is in good agreement with the KTA rules (Reference 13.1). Close to the reflector, and as expected, the pressure drops predicted by the CFD model are lower than those from the KTA rules as a result of the lower packing fraction and more ordered pebble packing adjacent to the wall. Correction factors have been derived that allow the KTA rules to be applied to the near-reflector regions of a whole core CFD model in which the bed is represented as a porous medium.

Heat transfer coefficients for pebbles both remote-from and close-to the reflector have been derived from the CFD simulations. These have been determined by both Reynolds analogy and from thermal solutions. In general, when compared with heat transfer coefficients determined using the KTA rules (Reference 13.2), the Reynolds analogy over-predicts and the thermal solution under-predicts. The thermal solutions are considered to be more representative of the mechanics of the convective heat transfer process. It is now believed that the Reynolds analogy is unreliable in such a complex geometry in which the flow is continually impinging on solids and separating, so fully developed turbulent boundary layers will not exist, or will exist over a small fraction of the area of the heat transfer surfaces.

The under-prediction of the heat transfer coefficients by the thermal solutions is an interesting finding. First, it means that predictions of fuel temperatures using the model will be pessimistically high – assuming that the KTA rules are accurate. However, it could mean that the KTA rules over-predict heat transfer coefficients, but this is a controversial statement that would undermine the status of the KTA rules with regard to their use for licensing PBRs. Therefore, in view of the limited amount of

analysis that has been carried out here, all of which has used a fairly simple two-equation turbulence model, more work is required before seriously challenging the accuracy of the KTA rules.

The heat transfer coefficients between the gas and the surface of the reflector have been extracted from the near-reflector CFD simulations. These values have been compared with correlations found in the literature for packed bed reactors in chemical engineering. The comparison is reasonably close, but again, the CFD values consistently under-predict when compared with the empirically-derived correlations.

A version of the near reflector model with a larger circumferential extent has demonstrated the phenomenon of wall channeling, in which the axial velocities close to the reflector wall are higher (on average) than in the centre of the pebble bed. This work has shown a strong correlation between the radial variation in bed porosity (after being vertically and circumferentially averaged) and the axial velocity. These results will improve porous medium models of the pebble bed by allowing the porosities and hydraulic resistances to be tailored so that the over-cooling of the near-reflector regions are captured correctly.

An assembly has been simulated containing pebbles from three equally-sized batches, with each batch having a different power. The differences in fuel temperatures between the three batches compared well with the batch-to-batch temperature differences predicted by the analytical model of Section 8.

Section 11 presented the development of a CFD model to predict heat transfer through a pebble bed in no-flow conditions. The objective of this work was to predict the effective conductivities of an assembly of pebbles in stagnant helium, or vacuum, and to compare the values with those obtained from the established Zehner-Schlünder or Breitbach and Barthels correlations. Unfortunately, the thermal energy equation in the FLUENT code failed to converge (or to converge within a suitable period of time) in the absence of a flowing fluid. Also, the cylindrical CFD domains adopted for this model, based on those used for the pressure drop and convective heat transfer studies (Section 10), were considered to be a potential source of error as they do not have true reflective boundaries, and therefore cannot be taken to represent a small part of a much larger pebble bed. Prismatic shaped domains, be they triangular, square or hexagonal, tessellate exactly and therefore can represent repeatable elements of a larger domain with true reflective boundaries. Unfortunately, such shapes require the intersections of symmetry planes and, the resulting spear shaped cells, resulting from where these intersections cut through pebbles, gave rise to severe convergence problems in the CFD code when this was tried in the work reported in Section 10. Clearly, more work is required on this topic using a different CFD code (see Section 13.3).

In Section 12, a whole core model, based on a porous medium approximation of the pebble bed, was set up using the FLUENT code. This model is a representation of the PBMR-400 reactor as specified in the IAEA's CRP-5 benchmark exercises (Reference 13.3). The model is based on the homogeneous porous medium approximation within FLUENT coupled with an analytical solution of the multi-scale

heat transfer equations for the fuel pebbles and TRISO particles presented in Section 5. Initial agreement with the participants in the IAEA CRP-5 PBMR-400 thermal hydraulics benchmark is good, although the number of values which can be compared is very small and the boundary conditions for the benchmark are greatly simplified compared with reality.

The limitations of the chosen porous medium model, together with the use of an analytical multi-scale solution, restrict application of the model to steady-state scenarios. Further work is required to allow the model to be applicable with more realistic (less uniform) power distributions and to be able to model transient conditions, and the necessary improvements are detailed below.

13.3   Recommendations for Further Work

The work of Section 11 to determine the effective conductivity of a pebble bed in loss of flow conditions should be repeated using a CFD code that possesses a thermal radiation model that can work in the absence of a forced flow.

The whole-core CFD model, developed in Section 12, is only capable of steady-state thermal hydraulic calculations at this time. However, the multi-scale fuel and moderator temperature model used here was implemented as an analytical model to simplify the coding in the FLUENT user-defined functions. The transient finite difference form of the solution, as presented in Section 5, would be required to permit transient calculations. In the longer term this would allow transient coupled neutronics/thermal hydraulics simulations to be undertaken.

It was identified in this work that the homogenous porous medium model with a superficial velocity formulation in FLUENT introduces significant simplifications with regards to calculating the temperature of the fluid and solid in the core and, by default turbulence is not handled correctly. Although this simplification does not introduce significant errors for the IAEA CRP-5 benchmark Case T-1, as completed, a full heterogeneous model will be needed if more realistic power distributions are to be used or transient simulations are to be run. Such a heterogeneous model would also allow the heat transfer mechanisms, such as conduction through the pebble bed and heat exchange at the interfaces between the pebble bed and the reflector to be represented more accurately. Specifically, the reflectors receive heat directly by thermal radiation from, and through contact with, the pebbles as well as by convection from the coolant. These influences cannot be resolved separately using a homogeneous model.

A model for the dispersion of momentum and heat within the pebble bed by interaction of the flow with the pebbles needs to be introduced. This would be included in the current model by first suppressing the turbulence model within the porous regions of the pebble bed by requesting FLUENT to not apply the turbulence model in these regions. Second, the diffusivities of momentum and energy in the pebble bed region would be modified to include the effects of geometric dispersion. Although this would correct the limitations in the current model for the porous region representing the pebble bed it would also be necessary to supply suitable interface

conditions at the exit of the pebble bed core. This would be required to account for the significant amount of turbulence that is generated by the last few layers of pebbles in the core and would be incorporated into the model by adding turbulent source terms to a thin slice of the domain at the exit of the core.   This would ensure that, after the flow exits the core, the turbulence fields are reasonable in the downstream fluid domains. Therefore, use of the unmodified turbulence model would be restricted to open plenum volumes which do not contain porous regions, resulting in more accurate turbulence levels in all regions of the model.

If the model were coupled to a neutronics code the IAEA CRP-5 PBMR-400 equilibrium core cases could be run using the model. Therefore it would be beneficial to develop an interface to allow the model to communicate with a neutronics code.

13.4   References for Section 13

13.1 The Nuclear Safety Standards Commission (KTA), "KTA Program of Standards (14.04.2008), Reactor Core Design for High-Temperature Gas-Cooled Reactor, Part 3: Loss of Pressure through Friction in Pebble Bed Cores", KTA Standard 3102.3, March 1981. URL <http://www.kta-gs.de/common/regel_prog.htm>.

13.2 The Nuclear Safety Standards Commission (KTA), "KTA Program of Standards (14.04.2008), Reactor Core Design for High-Temperature Gas-Cooled Reactor, Part 2: Heat Transfer in Spherical Fuel Elements", KTA Standard 3102.2, June 1983. URL <http://www.kta-gs.de/common/regel_prog.htm>.

13.3 "Evaluation of High Temperature Gas Cooled Reactor Performance- Benchmark analysis related to the PBMR-400, PBMM, GT-MHR, HTR-10 and the ASTRA Critical Facility", IAEA-TECDOC-TBD DRAFT, 2nd TECDOC from CRP-5, to be published.

Appendix A: Micro and Meso-Scale Models

This appendix presents detailed derivations of the micro and meso scale fuel models.

A.1 Previous Steady State Approach

A.1.1 Pebble Temperature Calculation

The temperature profile within a pebble is computed using a spherically symmetric heat conduction model. The pebble is divided into two zones: the outer unfuelled graphite shell and the central fuelled pebble core. The nuclear heating is assumed to be uniformly distributed over the central core region, and non-local heating due to gamma rays, etc. is not modelled.

The steady state temperature within a fuel pebble is governed by the heat conduction equation:

$$-\nabla \cdot \left(k \nabla T_{peb} \right) = \dot{q}'''$$

which, under the assumption of spherical symmetry, reduces to:

$$-\frac{1}{r^2}\frac{d}{dr}\left(r^2 k \frac{dT_{peb}}{dr} \right) = \begin{cases} 0 & \text{for} \quad r_{core} < r < r_{peb} \\ \dot{q}'''_{core} & \text{for} \quad\quad 0 < r < r_{core} \end{cases}$$

where $\dot{q}'''_{core}$ represents the power density within the fuelled core of the pebble element, r_{core} is the radius of the fuelled region within a pebble and r_{peb} is the outer radius of a pebble.

The conduction equation is subject to the boundary condition:

$$T(r_{peb}) = T_{surf}$$

To simplify the solution of this equation, the conductivity k is assumed to be constant within each of the two regions of the pebble, taking values k_{shell} and k_{core} in the shell and fuelled core region respectively. The conduction equation for the temperature distribution through a fuel pebble can be solved analytically, with solution:

$$T_{peb}(r) = \begin{cases} T_{surf} + \dfrac{\dot{q}'''_{core} r_{core}^3}{3 k_{shell}}\left(\dfrac{1}{r} - \dfrac{1}{r_{peb}} \right) & \text{for} \quad r_{core} < r < r_{peb} \\[3mm] T_{surf} + \dfrac{\dot{q}'''_{core} r_{core}^3}{3 k_{shell}}\left(\dfrac{1}{r_{core}} - \dfrac{1}{r_{peb}} \right) + \dfrac{\dot{q}'''_{core}}{6 k_{core}}\left(r_{core}^2 - r^2 \right) & \text{for} \quad 0 < r < r_{core} \end{cases}$$

For coupling neutronics and thermal hydraulics, the model must report the average temperatures of the pebble components to the neutronics code. The average temperature of the pebble shell and core are computed by volume weighted averaging:

$$\overline{T}_{shell} = \frac{\int_{r_{core}}^{r_{peb}} T_{peb}(r) r^2 \, \mathrm{d}r}{\int_{r_{core}}^{r_{peb}} r^2 \, \mathrm{d}r} = \frac{\int_{r_{core}}^{r_{peb}} T_{peb}(r) r^2 \, \mathrm{d}r}{(r_{peb}^3 - r_{core}^3)/3}$$

$$\overline{T}_{core} = \frac{\int_{0}^{r_{core}} T_{peb}(r) r^2 \, \mathrm{d}r}{\int_{0}^{r_{core}} r^2 \, \mathrm{d}r} = \frac{\int_{0}^{r_{core}} T_{peb}(r) r^2 \, \mathrm{d}r}{r_{core}^3 / 3}$$

Evaluating these integrals shows that:

$$\overline{T}_{shell} = T_{surf} + \frac{\dot{q}_{core}''' \, r_{core}^3}{k_{shell}} \frac{\left(\dfrac{r_{peb}^2}{6} - \dfrac{r_{core}^2}{2} + \dfrac{r_{core}^3}{3 r_{peb}} \right)}{(r_{peb}^3 - r_{core}^3)}$$

$$= T_{surf} + \frac{\dot{q}_{core}''' \, r_{core}^2}{k_{shell}} \frac{\left(\dfrac{\gamma^2}{6} - \dfrac{1}{2} + \dfrac{1}{3\gamma} \right)}{\gamma^3 - 1}, \qquad \text{where} \qquad \gamma = \frac{r_{peb}}{r_{core}}$$

and

$$\overline{T}_{core} = T_{surf} + \frac{\dot{q}_{core}''' \, r_{core}^3}{k_{shell}} \left(\frac{1}{r_{core}} - \frac{1}{r_{peb}} \right) + \frac{\dot{q}_{core}''' \, r_{core}^2}{k_{core}} \frac{1}{15}.$$

Implementation of this model can be simplified if the average shell temperature is approximated by the pebble surface temperature, thus the pebble shell conductivity is evaluated at the temperature $T = T_{surf}^i$. This approximation, which neglects temperature variations within the shell when evaluating k_{shell}, allows the direct evaluation of the average temperature, avoiding the need to solve nonlinear equations to compute $\overline{T}_{shell}$. Because the thermal conductivity varies slowly with changes in temperature the errors introduced by this approximation are small. A similar approximation can be used to compute the average temperature in the pebble core: The temperature at the inner surface of the pebble shell, $T_{peb}^i(r_{core})$, is evaluated using the solution to the conduction equation derived above. The value of k_{core} is evaluated at temperature $T_{peb}^i(r_{core})$.

A.1.2 – TRISO Particle Temperature Calculation

The analysis described in Section A.1.1 allows the computation of the graphite temperature within a fuel pebble. However within the pebble there are localised temperature perturbations within and around the TRISO fuel particles. In this section the effect of these localised temperature perturbations on the surface temperature of the TRISO particles is considered first. The particle surface temperatures are required for the calculation of the TRISO particle coating and fuel kernel temperatures.

The localised perturbation to the background graphite temperature within the representative volume of graphite surrounding a fuel particle is *approximated* by a quadratic profile. A quadratic profile was chosen as being the simplest that fulfils the requirement that the gradient is finite at the surface of the particle and zero between the particles. The second condition comes from the assumption that neighbouring particles are identical on the micro-scale, hence the outer surfaces of the micro-spheres are effectively symmetry surfaces. For a fuel particle centred at radius r within a pebble, this approximation takes the form:

$$T_{core}(r, R) = T_{peb}(r) + \varepsilon(R), \qquad \varepsilon(R) = \alpha R^2 + \beta R + \gamma$$

where R is a local radial coordinate measured from the fuel particle centre, and the local perturbation $\varepsilon(R)$ is assumed to satisfy the following conditions:

1) The temperature perturbation is symmetric about the midpoint of a line connecting the centres of two adjacent fuel particles.

2) The temperature perturbation within the representative volume of graphite has zero mean, such that the average graphite temperature within the volume is equal to the background temperature, $T_{peb}(r)$.

3) The gradient of the temperature perturbation at the particle surface is determined by the heat flux flowing through the particle-graphite contact surface and is proportional to the heat generated within a fuel particle kernel, $\dot{q}^{i}_{kernel}$.

The mathematical formulation of these conditions lead to the following set of equations for the coefficients α, β, and γ :

1) $\left. \dfrac{d\,\varepsilon}{d\,R} \right|_{R=R_{av}} = 0$, implying $2\alpha R_{av} + \beta = 0$

2) $\dfrac{\displaystyle\int_{R_{part}}^{R_{av}} \varepsilon(R)\,R\,\mathrm{d}R}{\displaystyle\int_{R_{part}}^{R_{av}} R^2\,\mathrm{d}R} = 0$, implying $\dfrac{\alpha}{5}\left(R_{av}^5 - R_{part}^5\right) + \dfrac{\beta}{4}\left(R_{av}^4 - R_{part}^4\right) + \dfrac{\gamma}{3}\left(R_{av}^3 - R_{part}^3\right) = 0$

and

3) $\left. -4\pi R_{part}^2\, k_{core} \dfrac{d\,\varepsilon}{d\,R} \right|_{R=R_{part}} = \dot{q}_{kernel}$ implying $-4\pi k_{core}\left(2\alpha R_{part}^3 + \beta R_{part}^2\right) = \dot{q}_{kernel}$

These three simultaneous linear equations for α, β, and γ are solved to obtain:

$$\alpha = \frac{\dot{q}_{kernel}}{8\pi k_{core} R_{part}^2 (R_{av} - R_{part})}$$

$$\beta = -\frac{\dot{q}_{kernel} R_{av}}{4\pi k_{core} R_{part}^2 (R_{av} - R_{part})}$$

$$\gamma = \frac{3\dot{q}_{kernel} R_{part}^3}{8\pi k_{core} (R_{av} - R_{part})} \frac{1}{(R_{av}^3 - R_{part}^3)} \left[\frac{3}{10}\left(\frac{R_{av}}{R_{part}}\right)^5 - \frac{1}{2}\left(\frac{R_{av}}{R_{part}}\right) + \frac{1}{5} \right]$$

Therefore the temperature perturbation at the particle surface, $\varepsilon(R_{part})$, is found to be:

$$\varepsilon(R_{part}) = \alpha R_{part}^2 + \beta R_{part} + \gamma$$

$$= \frac{\dot{q}_{kernel}}{8\pi k_{core} (R_{av} - R_{part})} \left[1 - \frac{2R_{av}}{R_{part}} + \frac{3R_{part}^3}{(R_{av}^3 - R_{part}^3)} \left[\frac{3}{10}\left(\frac{R_{av}}{R_{part}}\right)^5 - \frac{1}{2}\left(\frac{R_{av}}{R_{part}}\right) + \frac{1}{5} \right] \right]$$

The fuel particle surface temperature is therefore computed as:

$$T_{particle\ surface}(r) = T_{core}(r, R_{part}) = T_{peb}(r) + \varepsilon(R_{part})$$

The temperature profile within a fuel particle, T_{part}, is governed by heat conduction through the particle coatings and fuel particle kernel. The heat flux through the particle coatings at a distance R from the particle centre must balance the heat released within the fuel kernel, $\dot{q}_{kernel}$. The particle is assumed to be spherically symmetric and have 4 coatings (i.e., standard TRISO particles). Therefore:

$$-4\pi k_{coat,j} R^2 \frac{dT_{part}}{dR} = \dot{q}_{kernel}, \quad \text{for} \quad R_{inner,j} < R < R_{outer,j}, \quad \text{and } j = 1,2,3,4,$$

where $R_{inner,j}$ and $R_{outer,j}$ represent the inner and outer radii of the jth particle coating, and $k_{coat,j}$ represents the thermal conductivity of the coating. These four differential equations may be integrated to obtain the temperature difference across each of the four coatings, $\Delta T^i_{coat,j}$ as a function of the thermal resistances $\alpha_{coat,j}$:

$$\Delta T_{coat,j} = \dot{q}_{kernel} \alpha_{coat,j} \quad where$$

$$\alpha_{coat,j} = \frac{R_{outer,j} - R_{inner,j}}{4\pi k_{coat,j} R_{inner,j} R_{outer,j}}.$$

The overall temperature difference across the four coatings can be computed as follows:

$$\Delta T_{coat,total} = \dot{q}_{kernel}\alpha_{coat,eff}, \quad where$$

$$\alpha_{coat,eff} = \frac{R_{outer,4} - R_{inner,1}}{4\pi k_{coat,eff} R_{inner,1} R_{outer,4}}$$

and the effective combined conductivity of the four coatings, $k_{coat,j}$, is obtained from the sum of the thermal resistances of the individual coatings:

$$\alpha_{coat,eff} = \sum_1^4 \alpha_{coat,j}, \qquad i.e.$$

$$\frac{R_{outer,4} - R_{inner,1}}{4\pi k_{coat,eff} R_{inner,1} R_{outer,4}} = \sum_1^4 \frac{R_{outer,4} - R_{inner,1}}{4\pi k_{coat,j} R_{inner,j} R_{outer,j}}$$

The temperature at the surface of the fuel particle kernel is equal to:

$$T_{kernel\,surface} = T_{particle\,surface}(r) + \Delta T_{coat,total}$$

The temperature profile within the fuel kernel is described by the heat conduction equation. The fuel kernel is assumed to be spherically symmetric, and the nuclear heat released within the particle is assumed to be uniformly distributed over the volume of the fuel kernel. Therefore:

$$\frac{1}{R^2}\frac{d}{dR}\left(R^2 k_{kernel}\frac{dT_{part}}{dR}\right) = -\dot{q}'''_{kernel}, \quad for \quad 0 < R < R_{kernel},$$

where $\quad \dot{q}'''_{kernel} = \dfrac{\dot{q}_{kernel}}{(4\pi R^3_{kernel}/3)}$

This equation, together with the boundary condition $T_{part}(R_{part}) = T_{kernel\,surface}$, has a unique bounded solution:

$$T_{part}(R) = T_{kernel\,surface} + \frac{\dot{q}'''_{kernel}}{6k_{kernel}}\left(R^2_{kernel} - R^2\right), \quad for \quad 0 < R < R_{kernel}.$$

The volumetric average fuel kernel temperature, is therefore:

$$\overline{T}_{part} = \frac{\int_0^{R_{kernel}} T_{part}(R)R^2\,dR}{\int_0^{R_{kernel}} R^2\,dR} = T_{kernel\,surface} + \frac{\dot{q}'''_{kernel}R_{kernel}}{15k_{kernel}}$$

The value of $\overline{T}_{part}$ is supplied to the neutronics model within the coupled thermal hydraulics – neutronics calculation route.

A.2 New Multi-Scale Model

A.2.1 – Revised steady state analytical treatment in one dimension

In A.1.2, a series of algebraic equations were solved on the meso and micro-scales and the two solutions were coupled by imposing the condition that the average graphite temperature within a micro-sphere in the micro-scale solution must be the same as the local graphite temperature at the radius at which the particle is centred in the meso-scale solution. This constraint introduces a heat sink into the micro-scale solution and represents the heat that flows from the micro-scale up to the meso-scale.   The first step in developing the new approach was to provide the coupling between the length scales within the transient differential equations rather than by imposing this in an ad-hoc way on their solutions and multi-scale analysis was the key to this. The following derivation is developed initially for a one-dimensional Cartesian steady state situation, and then extended to a transient situation before being extended into circular cylindrical and spherical geometries.

In 1D, the steady state conduction equation is:

$$\frac{d}{dx}\left(k(x)\frac{dT}{dx} \right) = -\dot{q}'''(x)$$

If we can consider a one-dimensional pebble in the form of a bar, and the bar is divided into a number of heated and un-heated segments, with heated segments being separated by unheated segments, we can decompose the heat generation term into a mean plus a perturbation:

$$\dot{q}'''(x) = \overline{q}''' + \hat{q}'''(x)$$

Where

$$\frac{1}{L}\int_0^L \dot{q}'''(x)dx = \overline{q}''' \quad \text{, therefore, } \quad \frac{1}{L}\int_0^L \hat{q}'''(x)dx = 0$$

An example of this decomposition is shown graphically in Figures 5.3.3 and 5.3.4.

Over the interval of a heated segment plus its share of the unheated neighbouring segments, the perturbation represents a matched pair consisting of a heat source and a heat sink. This is comparable to the previous approach, but this decomposition introduces the sources and sinks directly into the differential equation, therefore the corresponding source and sink behaviour will be apparent in the micro-scale solution rather than having to be imposed as an additional constraint.

The temperature field is similarly decomposed into:

$$T(x) = T_M(x) + T_\mu(\hat{x})$$

Where T_M is the meso-scale temperature variation and T_μ is the micro-scale temperature variation. The micro-scale length co-ordinate is $\hat{x}$, this has the same units as x but has an origin at the centre of each heated segment.

The conduction equation is then decomposed into an equation corresponding to each part of the source term:

$$\frac{d}{dx}\left(k_{eff}\,\frac{dT_M}{dx}\right) = -\overline{q}'''$$

for the meso-scale, and,

$$\frac{d}{d\hat{x}}\left(k(\hat{x})\,\frac{dT_\mu}{d\hat{x}}\right) = -\hat{q}'''(\hat{x}).$$

for the micro-scale.

The decomposition itself is not an approximation, however, the use of a "smeared" or effective conductivity in the meso-scale equation whilst retaining the actual conductivity variation in the micro-scale equation is an approximation.

For simplicity, the bar and the distribution of heated segments are assumed to be symmetric, with the origin of the length co-ordinate at the mid-span of the bar. The bar has a length of *2L*, contains three heated segments and has a cross-sectional area of A. Both ends are held at a constant temperature T_D and each heated segment has a heat input of $\dot{q}_P$. Refer to Figure 5.3.5 for a graphical representation of the above.

The average power density, which forms the source term for the meso-scale equation is:

$$\overline{q}''' = \frac{3\dot{q}_P}{2AL}$$

Under these conditions, the solution to the meso-scale differential equation is:

$$T_M = \frac{3\dot{q}_P}{4ALk_{eff}}\left(L^2 - x^2\right) + \left(T_D - \delta\right)$$

The term δ is introduced because only the sum of the micro and meso-scale solutions satisfies the boundary condition, so δ is the micro-scale temperature evaluated at the domain boundary D, or

$$T(x_D) = T_D = T_M(x_D) + T_\mu(\hat{x}_s) = T_M(x_D) + \delta,$$

so, the boundary condition on the meso-scale temperature field is:

$$T_M(x_D) = T_D - \delta.$$

The micro-scale domain is symmetric about the centre of the heated particle, so the differential equation can be solved over half of the domain (see Figure 5.3.6).

The volume of a heated segment is V_P and is given by;

$$V_P = 2\hat{x}_p A$$

Similarly the volume of the heated segment's share of the unheated material is:

$$V_G = 2(\hat{x}_s - \hat{x}_p)A$$

The average power density expressed in terms of these volumes is:

$$\overline{q}''' = \frac{\dot{q}_P}{V_P + V_G}$$

The source term in the micro-scale conduction equation is then:

$$\hat{q}''' = \frac{\dot{q}_P}{V_P} - \overline{q}''' = \frac{V_G}{V_P + V_G}\frac{\dot{q}_P}{V_P} \qquad \text{for } 0 < \hat{x} < \hat{x}_p$$

and
$$\hat{q}''' = -\overline{q}''' = -\frac{V_G}{V_P + V_G}\frac{\dot{q}_P}{V_G} \qquad \text{for } \hat{x}_p < \hat{x} < \hat{x}_s$$

The boundary conditions on the micro-scale solution are zero temperature gradient at the centre of the heated segment and zero temperature gradient at the outer edge of the unheated segment. There is therefore no Dirichlet boundary condition (i.e., a fixed temperature) in the model and, as such, an infinite number of solutions exist. However, because we are solving for a temperature perturbation, the temperature field should have a zero mean. In a steady state solution this zero mean has to be imposed as an additional constraint as:

$$\frac{1}{\hat{x}_s}\int_0^{\hat{x}_s} T_\mu d\hat{x} = \frac{1}{\hat{x}_s}\left\{\int_0^{\hat{x}_p} T_\mu d\hat{x} + \int_{\hat{x}_p}^{\hat{x}_s} T_\mu d\hat{x}\right\} = 0$$

Re-arranging gives the constraint as:

$$\int_0^{\hat{x}_p} T_\mu d\hat{x} = -\int_{\hat{x}_p}^{\hat{x}_s} T_\mu d\hat{x}$$

The solution over the heated segment is

$$T_\mu = \frac{\dot{q}_P}{2k_P V_P}\left(\frac{V_G}{V_P + V_G}\right)\left(\hat{x}_P^2 - \hat{x}^2\right) + T_{\mu P}$$

And the solution over the un-heated segment is:

$$T_\mu = \frac{\hat{q}_P}{2k_G V_G}\left(\frac{V_G}{V_P + V_G}\right)\left[(\hat{x}^2 - \hat{x}_p^2) - 2\hat{x}_s(\hat{x} - \hat{x}_p)\right] + T_{\mu P}$$

Applying the zero-mean constraint gives:

$$T_{\mu P} = \frac{\dot{q}_p}{\hat{x}_s}\left(\frac{V_G}{V_P + V_G}\right)\left\{\frac{(\hat{x}_s - \hat{x}_p)}{2k_G V_G}\left[\frac{(\hat{x}_s^3 - \hat{x}_p^3)}{3(\hat{x}_s - \hat{x}_p)} - \hat{x}_p^2 - \hat{x}_s^2 + \hat{x}_s\hat{x}_p\right] - \frac{\hat{x}_p^3}{3k_P V_P}\right\}$$

The 1D problem shown in Figure 5.3.5 can be solved analytically without decomposition over each of the sub-domains shown in the figure, i.e, 0-A, A-B, B-C and C-D. In reverse order, starting at the boundary D, these solutions are:

$$T_{C \to D}(x) = \frac{3}{2}\frac{\dot{q}_P}{k_G A}(x_D - x) + T_D$$

$$T_C = \frac{3}{2}\frac{\dot{q}_P}{k_G A}(x_D - x_C) + T_D$$

$$T_{B \to C}(x) = \frac{\dot{q}_P}{2k_P V_P}\left[(x_C^2 - x^2) - \left(2x_B - \frac{V_P}{A}\right)(x_C - x)\right] + T_C$$

$$T_B = \frac{\dot{q}_P}{2k_P V_P}\left[(x_C^2 - x_B^2) - \left(2x_B - \frac{V_P}{A}\right)(x_C - x_B)\right] + T_C$$

$$T_{A \to B}(x) = \frac{\dot{q}_P}{2k_G A}(x_B - x) + T_B$$

$$T_A = \frac{\dot{q}_P}{2k_G A}(x_B - x_A) + T_B$$

$$T_{0 \to A} = \frac{\dot{q}_P}{2k_P V_P}(x_A^2 - x^2) + T_A$$

The above equations constitute the exact solution presented for comparison with the multi-scale solution in Figures 5.3.7 to 5.3.9.

A.2.2 – Transient Solution in a one-dimensional linear domain

The transient one-dimensional conduction equation with internal heat generation is:

$$\rho c_P \frac{\partial T}{\partial t} = \frac{\partial}{\partial x}\left(k(x)\frac{\partial T}{\partial x}\right) + \dot{q}'''(x,t)$$

Using the same decomposition as for the steady state case, this becomes:

$$(\rho c_P)(x)\frac{\partial T_M}{\partial t} = \frac{\partial}{\partial x}\left(k(x)\frac{\partial T_M}{\partial x}\right) + \overline{q}'''(t)$$

for the meso-scale

$$(\rho c_P)(\hat{x})\frac{\partial T_\mu}{\partial t} = \frac{\partial}{\partial \hat{x}}\left(k(\hat{x})\frac{\partial T_\mu}{\partial \hat{x}}\right) + \hat{q}'''(\hat{x},t)$$

for the micro-scale.

The property variations in the meso-scale can be approximated by constant effective values:

$$\overline{(\rho c_P)}\frac{\partial T_M}{\partial t} = \frac{\partial}{\partial x}\left(k_{eff}\frac{\partial T_M}{\partial x}\right) + \overline{q}'''(t)$$

The un-decomposed (i.e., the "original" or "continuous" form) and decomposed forms of the differential equations can both be solved using finite difference approximations. Starting with the un-decomposed form, using a 1st order forward difference operator to approximate the time derivative and a 2nd order central difference operator to approximate the spatial 2nd derivative gives:

$$T_i^{t+\Delta t} = T_i^t + \frac{\Delta t}{(\rho c_P)_i}\frac{1}{(x_{ei}-x_{wi})}\left(k_{ei}\frac{T_{i+1}^t - T_i^t}{x_{i+1}-x_i} - k_{wi}\frac{T_i^t - T_{i-1}^t}{x_i - x_{i-1}}\right) + \frac{\Delta t}{(\rho c_P)_i}\dot{q}_i'''(t)$$

where

$$x_{ei} = \frac{(x_{i+1}+x_i)}{2}; \ x_{wi} = \frac{(x_i + x_{i-1})}{2}; \ k_{ei} = k(x_{ei}); \ k_{wi} = k(x_{wi})$$

Similarly, the meso-scale differential can be cast into finite difference form using the same finite difference approximations for the time and space derivatives gives:

$$T_{Mi}^{t+\Delta t} = T_{Mi}^t + \frac{\Delta t}{(\rho c_P)}\frac{1}{(x_{ei}-x_{wi})}\left(k_{eff}\frac{T_{Mi+1}^t - T_{Mi}^t}{x_{i+1}-x_i} - k_{eff}\frac{T_{Mi}^t - T_{Mi-1}^t}{x_i - x_{i-1}}\right) + \frac{\Delta t}{(\rho c_P)}\overline{q}'''(t)$$

and for the micro-scale differential equation:

$$T_{\mu i}^{t+\Delta t} = T_{\mu i}^t + \frac{\Delta t}{(\rho c_P)_i}\frac{1}{(\hat{x}_{ei}-\hat{x}_{wi})}\left(k_{ei}\frac{T_{\mu i+1}^t - T_{\mu i}^t}{\hat{x}_{i+1}-\hat{x}_i} - k_{wi}\frac{T_{\mu i}^t - T_{\mu i-1}^t}{\hat{x}_i - \hat{x}_{i-1}}\right) + \frac{\Delta t}{(\rho c_P)_i}\hat{q}_i'''(t)$$

These equations are modified at the boundaries to introduce the boundary conditions. For the un-decomposed form, the boundary conditions are symmetry at the centre of the bar, Node 0,

and fixed temperature ($T=T_D$) at the ends of the bar, Node N. At Node 0, the symmetry condition is introduced by reflecting the temperature gradient:

$$T_0^{t+\Delta t} = T_0^t + \frac{\Delta t}{(\rho c_P)_0} \frac{1}{(x_{e0}-0)} \left(k_{e0} \frac{T_1^t - T_0^t}{x_1 - x_0} - \left(-k_{e0} \frac{T_1^t - T_0^t}{x_1 - x_0} \right) \right) + \frac{\Delta t}{(\rho c_P)_0} \dot{q}_0'''(t)$$

At the free end of the bar, the fixed temperature boundary condition is:

$$T_N^{t+\Delta t} = T_D$$

Similarly in the meso-scale equation, the symmetry boundary condition in the centre of the bar is introduced by reflecting the temperature gradient:

$$T_{M0}^{t+\Delta t} = T_{M0}^t + \frac{\Delta t}{(\rho c_P)} \frac{1}{(x_{e0}-0)} \left(k_{eff} \frac{T_{M1}^t - T_{M0}^t}{x_1 - x_0} - \left(-k_{eff} \frac{T_{M1}^t - T_{M0}^t}{x_1 - x_0} \right) \right) + \frac{\Delta t}{(\rho c_P)} \bar{q}'''(t)$$

and the fixed temperature boundary condition at the end of the bar is set to $T=T_D-\delta(t)$, with $\delta(t)$ being the micro-scale temperature at the boundary of the domain:

$$T_{MN}^{t+\Delta t} = T_D - \delta(t).$$

Finally, the boundary conditions on the micro-scale equation are symmetry at the centre of the heated segment and symmetry at $\hat{x} = \hat{x}_s$. Both of these are introduced by reflecting the temperature gradients, therefore at the centre of the heated segment, $\hat{x} = 0$ (micro-Node 0), the finite difference equation is:

$$T_{\mu0}^{t+\Delta t} = T_{\mu0}^t + \frac{\Delta t}{(\rho c_P)_0} \frac{1}{(\hat{x}_{e0}-0)} \left(k_{e0} \frac{T_{\mu1}^t - T_{\mu0}^t}{\hat{x}_1 - \hat{x}_0} - \left(-k_{e0} \frac{T_{\mu1}^t - T_{\mu0}^t}{\hat{x}_1 - \hat{x}_0} \right) \right) + \frac{\Delta t}{(\rho c_P)_0} \hat{q}_0'''(t)$$

and at $\hat{x} = \hat{x}_s$ (micro-Node n)

$$T_{\mu n}^{t+\Delta t} = T_{\mu n}^t + \frac{\Delta t}{(\rho c_P)_n} \frac{1}{(\hat{x}_s - \hat{x}_{wn})} \left(\left(-k_{wn} \frac{T_{\mu n}^t - T_{\mu n-1}^t}{\hat{x}_n - \hat{x}_{n-1}} \right) - k_{wn} \frac{T_{\mu n}^t - T_{\mu n-1}^t}{\hat{x}_n - \hat{x}_{n-1}} \right) + \frac{\Delta t}{(\rho c_P)_n} \hat{q}_n'''(t)$$

All of these finite difference equations have been cast in an explicit form to allow solution in a simple Excel spreadsheet. If backward differences had been used for the time derivatives, then the scheme would be fully implicit, requiring a system of simultaneous equations to be solved, but yielding a scheme that is unconditionally stable without a stability limit on the time step size. The explicit scheme is stable when the coefficient of T_i^t is positive and the limit of stability is reached when the time step takes on the value which make this coefficient zero.

A.2.3 – **Application to a Cylindrical Representation of a Pebble**

The transient conduction equation with heat generation in cylindrical co-ordinates is decomposed into meso and micro-scales in an identical manner to that used in Cartesian co-ordinates in Section A.2.2, giving:

$$(\rho c_P)(r)\frac{\partial T_M}{\partial t} = \frac{1}{r}\frac{\partial}{\partial r}\left(rk(r)\frac{\partial T_M}{\partial r}\right) + \bar{q}'''(t)$$

for the meso-scale, and

$$(\rho c_P)(\hat{r})\frac{\partial T_\mu}{\partial t} = \frac{1}{\hat{r}}\frac{\partial}{\partial \hat{r}}\left(\hat{r}k(\hat{r})\frac{\partial T_\mu}{\partial \hat{r}}\right) + \hat{q}'''(\hat{r},t)$$

for the micro-scale.

Again the properties variations are smeared to give effective values and this approximation is introduced in the meso-scale differential equation:

$$\overline{(\rho c_P)}\frac{\partial T_M}{\partial t} = \frac{1}{r}\frac{\partial}{\partial r}\left(rk_{eff}\frac{\partial T_M}{\partial r}\right) + \bar{q}'''(t)$$

Using a forward difference for the time derivative gives an explicit finite difference equation for the meso-scale temperature distribution:

$$T_{Mi}^{t+\Delta t} = T_{Mi}^{t} + \frac{\Delta t}{\overline{(\rho c_P)}_i}\frac{1}{r_i(r_{ei}-r_{wi})}\left(r_{ei}k_{eff,ei}\frac{T_{Mi+1}^t - T_{Mi}^t}{r_{i+1}-r_i} - r_{wi}k_{eff,wi}\frac{T_{Mi}^t - T_{Mi-1}^t}{r_i - r_{i-1}}\right) + \frac{\Delta t}{\overline{(\rho c_P)}_i}\bar{q}_i'''(t)$$

where:

$$r_{ei} = \frac{(r_{i+1}+r_i)}{2}\ ;\ r_{wi} = \frac{(r_i + r_{i-1})}{2}\ ;\ k_{eff,ei} = k_{eff}(r_{ei})\ ;\ k_{eff,wi} = k_{eff}(r_{wi})$$

Similarly for the micro-scale:

$$T_{\mu i}^{t+\Delta t} = T_{\mu i}^{t} + \frac{\Delta t}{(\rho c_P)_i}\frac{1}{\hat{r}_i(\hat{r}_{ei}-\hat{r}_{wi})}\left(\hat{r}_{ei}k_{ei}\frac{T_{\mu i+1}^t - T_{\mu i}^t}{\hat{r}_{i+1}-\hat{r}_i} - \hat{r}_{wi}k_{wi}\frac{T_{\mu i}^t - T_{\mu i-1}^t}{\hat{r}_i - \hat{r}_{i-1}}\right) + \frac{\Delta t}{(\rho c_P)_i}\hat{q}_i'''(t)$$

The results of Section 5.3.2.2 show that the micro-scale responds on a shorter time-scale than the meso-scale. Therefore, advantage is taken of this by employing smaller time steps in solution of the micro-scale equation, which allows both equations to be solved using their own optimum time step sizes. There is no requirement that the two time step sizes be related to each other, however, practically it is more convenient for re-combining the two solutions if the meso-scale time step size is an integer multiple of the micro-scale time step. The micro-scale finite difference equation is re-cast using its own micro-scale time step:

$$T_{\mu i}^{\hat{t}+\Delta\hat{t}} = T_{\mu i}^{\hat{t}} + \frac{\Delta\hat{t}}{(\rho c_P)_i} \frac{1}{\hat{r}_i(\hat{r}_{ei} - \hat{r}_{wi})}\left(\hat{r}_{ei}k_{ei}\frac{T_{\mu i+1}^{\hat{t}} - T_{\mu i}^{\hat{t}}}{\hat{r}_{i+1} - \hat{r}_i} - \hat{r}_{wi}k_{wi}\frac{T_{\mu i}^{\hat{t}} - T_{\mu i-1}^{\hat{t}}}{\hat{r}_i - \hat{r}_{i-1}}\right) + \frac{\Delta\hat{t}}{(\rho c_P)_i}\hat{q}_i'''(\hat{t})$$

The boundary conditions applied to the meso-scale equation are symmetry at the centre of the pebble and prescribed temperature at the pebble surface. At the pebble centre the finite difference equation, as written above becomes singular because of the 1/r term. To avoid this problem, the equation for the centre node is written in a finite volume form, in which a cylinder is constructed around the central node. The heat generation within this central cylinder has to be balanced by the heat lost from its periphery plus the rate of gain of internal energy within the cylinder. The resulting modified equation for the central node is thus:

$$T_{M0}^{t+\Delta t} = T_{M0}^{t} + \frac{\Delta t}{(\rho c_P)_0}\frac{1}{r_{e0}^2}\left(2r_{e0}k_{eff,e0}\frac{T_{M1}^{t} - T_{M0}^{t}}{r_1 - r_0}\right) + \frac{\Delta t}{(\rho c_P)_0}\overline{q}_0'''(t)$$

At the surface of the pebble, the contribution from the micro-scale solution has been neglected to avoid having to couple the micro and meso-scale solutions – this is advantageous when using different time step sizes. The contribution from the micro-scale solution is not significant when the volume fraction of the particles in the pebble is small. The prescribed temperature condition is:

$$T_{MN}^{t+\Delta t} = T_{surf}$$

The boundary conditions on the micro-scale equation are symmetry at the particle centre and symmetry at the edge of the surrounding cylinder of the particle's share of the graphite (which will be referred to as a "micro-cylinder"). At the centre of the particle, the finite difference equation is modified to avoid the division-by-zero introduced by the $1/\hat{r}$ term:

$$T_{\mu 0}^{\hat{t}+\Delta\hat{t}} = T_{\mu 0}^{\hat{t}} + \frac{\Delta\hat{t}}{(\rho c_P)_0}\frac{1}{\hat{r}_{e0}^2}\left(2\hat{r}_{e0}k_{e0}\frac{T_{\mu 1}^{\hat{t}} - T_{\mu 0}^{\hat{t}}}{\hat{r}_1 - \hat{r}_0}\right) + \frac{\Delta\hat{t}}{(\rho c_P)_0}\hat{q}_0'''(\hat{t})$$

Similarly at the micro-cylinder surface:

$$T_{\mu n}^{\hat{t}+\Delta\hat{t}} = T_{\mu n}^{\hat{t}} + \frac{\Delta\hat{t}}{(\rho c_P)_n}\frac{1}{(\hat{r}_n^2 - \hat{r}_{wn}^2)}\left(-2\hat{r}_{wn}k_{wn}\frac{T_{\mu n}^{\hat{t}} - T_{\mu n-1}^{\hat{t}}}{\hat{r}_n - \hat{r}_{n-1}}\right) + \frac{\Delta\hat{t}}{(\rho c_P)_n}\hat{q}_n'''(\hat{t})$$

The effective conductivity within the particle containing region of the 2D pebble was determined using Maxwell's equation (from Section 7.2.3):

$$k_{eff} = \frac{3k_m k_p \alpha + (2k_m + k_p)k_m(1-\alpha)}{3k_m \alpha + (2k_m + k_p)(1-\alpha)}$$

For matrix and particle conductivities (k_m and k_p) of 5 W/mm/K and 2 W/mm/K respectively, and particle volume fraction (α) of 0.1942, the above equation gives an effective conductivity of

4.3056 W/mm/K. This was the value used in the multi-scale model in Section 5.3.3. However, because the geometry is cylindrical, a different form of Maxwell's equation should have been used as the above equation assumes that the inclusions (particles) are spherical. The correct form for cylindrical inclusions has been derived for prismatic core HTGR fuel elements and is presented in Reference A.1 (specifically for three materials in that case). For two materials and cylindrical inclusions, Maxwell's equation is:

$$k_{eff} = \frac{2k_m k_p \alpha + (k_m + k_p)k_m(1-\alpha)}{2k_m \alpha + (k_m + k_p)(1-\alpha)}$$

Using the above matrix and particle conductivities and volume fraction in the cylindrical form of Maxwell's equation gives an effective conductivity of 4.2317 W/mm/K. The value from the latter is 1.75% lower than that used in the multi-scale model.

A.2.4 – **Application to a Spherical Pebble**

The transient conduction equation with heat generation in spherical co-ordinates is decomposed into meso and micro-scales in an identical manner to that used in Cartesian co-ordinates in Section A.2.2, giving:

$$(\rho c_P)(r)\frac{\partial T_M}{\partial t} = \frac{1}{r^2}\frac{\partial}{\partial r}\left(r^2 k(r)\frac{\partial T_M}{\partial r}\right) + \overline{q}'''(t)$$

for the meso-scale, and

$$(\rho c_P)(\hat{r})\frac{\partial T_\mu}{\partial t} = \frac{1}{\hat{r}^2}\frac{\partial}{\partial \hat{r}}\left(\hat{r}^2 k(\hat{r})\frac{\partial T_\mu}{\partial \hat{r}}\right) + \hat{q}'''(\hat{r},t)$$

for the micro-scale.

As before, the thermal properties variations are approximated by smeared values in the meso-scale equation.

$$\overline{(\rho c_P)}\frac{\partial T_M}{\partial t} = \frac{1}{r^2}\frac{\partial}{\partial r}\left(r^2 k_{eff}\frac{\partial T_M}{\partial r}\right) + \overline{q}'''(t)$$

Using forward difference operators for the time derivatives yields the following pair of finite difference equations for the meso and micro-scales respectively:

$$T_{Mi}^{t+\Delta t} = T_{Mi}^{t} + \frac{\Delta t}{(\rho c_P)_i}\frac{1}{r_i^2(r_{ei}-r_{wi})}\left(r_{ei}^2 k_{eff,ei}\frac{T_{Mi+1}^{t}-T_{Mi}^{t}}{r_{i+1}-r_i} - r_{wi}^2 k_{eff,wi}\frac{T_{Mi}^{t}-T_{Mi-1}^{t}}{r_i-r_{i-1}}\right) + \frac{\Delta t}{(\rho c_P)_i}\overline{q}_i'''(t)$$

and

$$T_{\mu i}^{t+\Delta t} = T_{\mu i}^{t} + \frac{\Delta t}{(\rho c_P)_i} \frac{1}{\hat{r}_i^2 (\hat{r}_{ei} - \hat{r}_{wi})} \left(\hat{r}_{ei}^2 k_{ei} \frac{T_{\mu i+1}^{t} - T_{\mu i}^{t}}{\hat{r}_{i+1} - \hat{r}_i} - \hat{r}_{wi}^2 k_{wi} \frac{T_{\mu i}^{t} - T_{\mu i-1}^{t}}{\hat{r}_i - \hat{r}_{i-1}} \right) + \frac{\Delta t}{(\rho c_P)_i} \hat{q}_i'''(t).$$

As with cylindrical geometry, the above equations are singular at the centre of the pebble and the centre of a particle for the meso and micro-scales respectively. Again, the equations are converted to finite volume form at these locations with the transient term and heat generation integrated over a spherical control volume that surrounds the centre node whilst the conduction term is integrated over its surface. The boundary condition at both these locations for the respective equations are symmetry conditions, so both equations become at the centres of their respective domains:

$$T_{M0}^{t+\Delta t} = T_{M0}^{t} + \frac{\Delta t}{(\rho c_P)_0} \frac{1}{r_{e0}^3} \left(3 r_{e0}^2 k_{eff,e0} \frac{T_{M1}^{t} - T_{M0}^{t}}{r_1 - r_0} \right) + \frac{\Delta t}{(\rho c_P)_0} \bar{q}_0'''(t)$$

And

$$T_{\mu 0}^{\hat{t}+\Delta\hat{t}} = T_{\mu 0}^{\hat{t}} + \frac{\Delta\hat{t}}{(\rho c_P)_0} \frac{1}{\hat{r}_{e0}^3} \left(3 \hat{r}_{e0}^2 k_{e0} \frac{T_{\mu 1}^{\hat{t}} - T_{\mu 0}^{\hat{t}}}{\hat{r}_1 - \hat{r}_0} \right) + \frac{\Delta\hat{t}}{(\rho c_P)_0} \hat{q}_0'''(\hat{t})$$

The boundary condition on the meso-scale equation at the surface of the pebble is:

$$T_{MN}^{t+\Delta t} = T_{surf}$$

Again the contribution from the micro-scale solution to the meso-scale boundary condition is neglected to decouple the two solutions.

For a micro-sphere, as shown in Figure 5.3.2, the external boundary condition is a symmetry condition and is imposed as;

$$T_{\mu n}^{\hat{t}+\Delta\hat{t}} = T_{\mu n}^{\hat{t}} + \frac{\Delta\hat{t}}{(\rho c_P)_n} \frac{1}{(\hat{r}_n^3 - \hat{r}_{wn}^3)} \left(-3 \hat{r}_{wn}^2 k_{wn} \frac{T_{\mu n}^{\hat{t}} - T_{\mu n-1}^{\hat{t}}}{\hat{r}_n - \hat{r}_{n-1}} \right) + \frac{\Delta\hat{t}}{(\rho c_P)_n} \hat{q}_n'''(\hat{t})$$

This boundary condition completes the equation set that constitutes the multi-scale model in spherical geometry.

A.3 Reference

A.1   Stainsby R. "Investigation of Local Heat Transfer in a Prismatic Modular HTGR Core", AMEC NSS Report NR001/RP/001 R02, May 2009.

Appendix B: Particle Clustering

Finite Element Models for Particle Clustering

This appendix presents a selection of images of the three and four-particle cluster finite element models used for the particle clustering analyses together with the full set of predicted temperature distributions.

Figures B.1.1 to B.1.4 show the geometry and meshes of the pebble and particles in the three-particle cluster.

Figure B.1.1: Three particles, no spacing - fuel pebble and particles
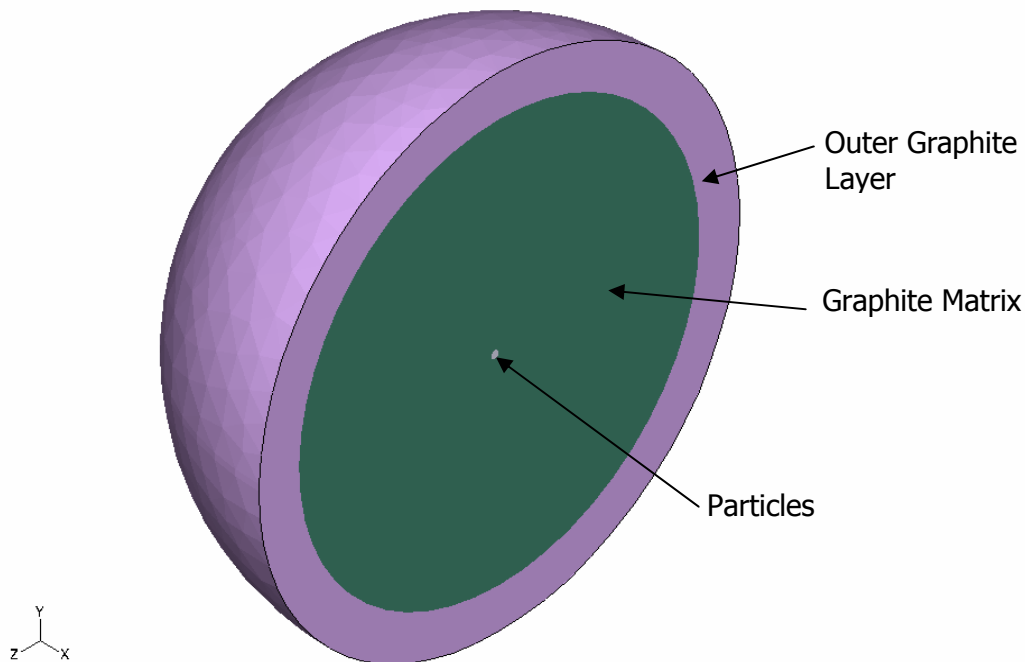
Figure B.1.2: Three Particles, no spacing – view of a half-pebble showing mesh
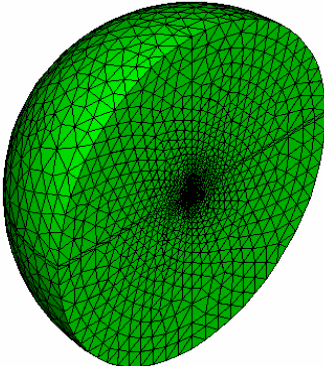
Figure B.1.3: Three particles, no spacing – slice through model of pebble showing mesh around the particles
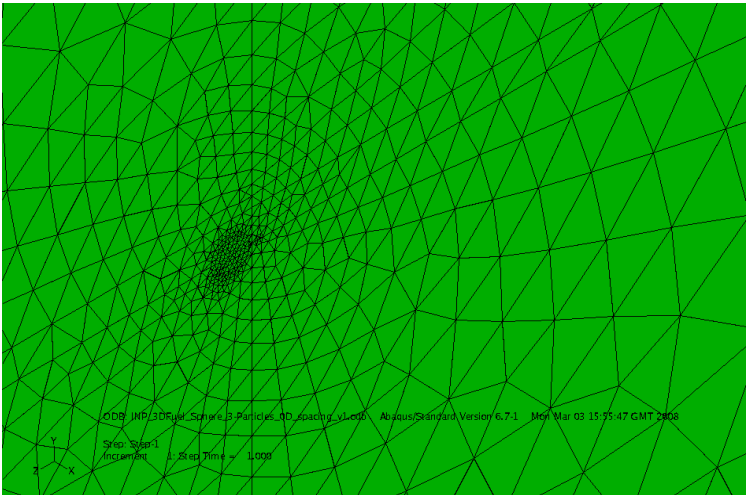
Figure B.1.4: Three particles, no spacing – isometric view of particles
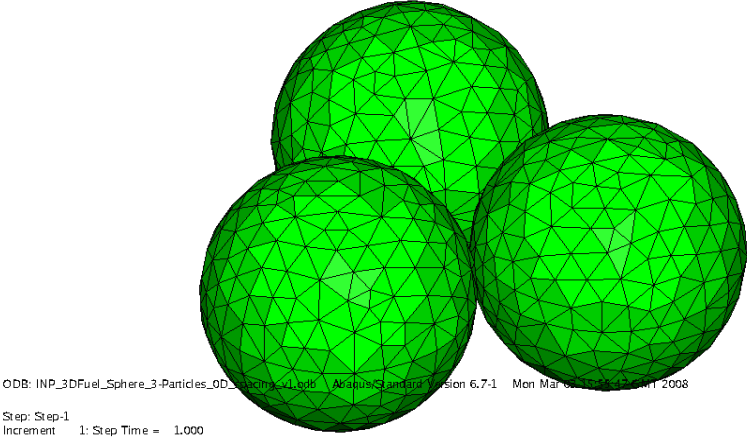
Figures B.1.5 to B.1.7 show the geometry and meshes of the pebble and particles in the four-particle cluster.

Figure B.1.5: Four particles, no spacing – fuel pebble and particles
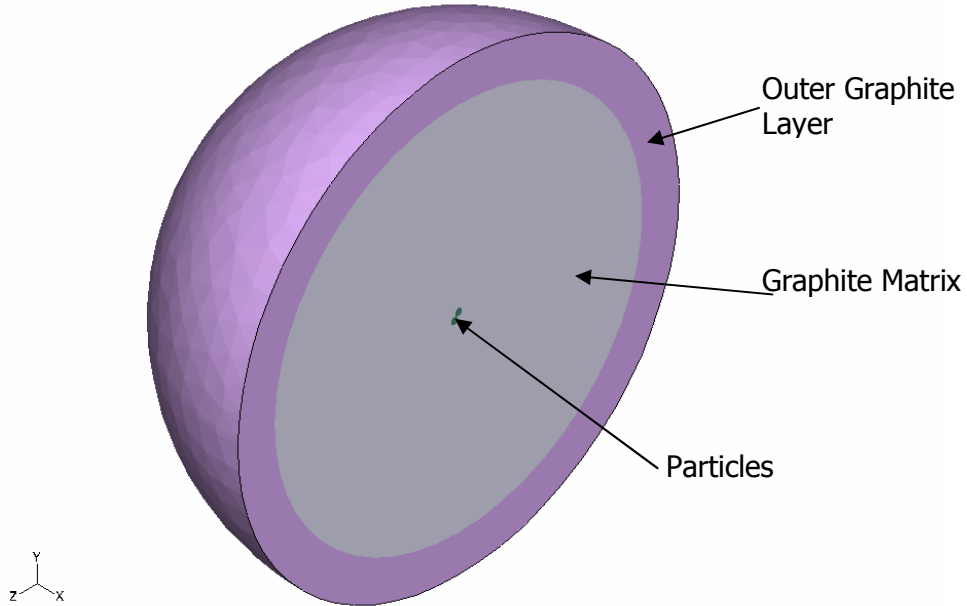
Figure B.1.6: Four particles, no spacing – slice through model of pebble showing mesh around the particles
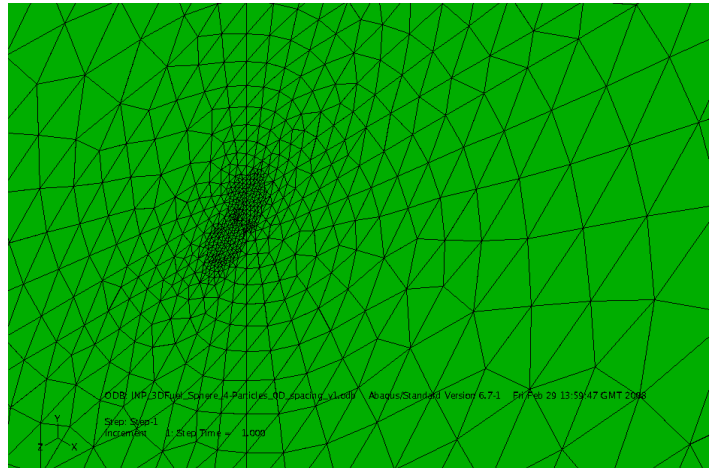
Figure B.1.7: Four particles, no spacing – isometric view of particles
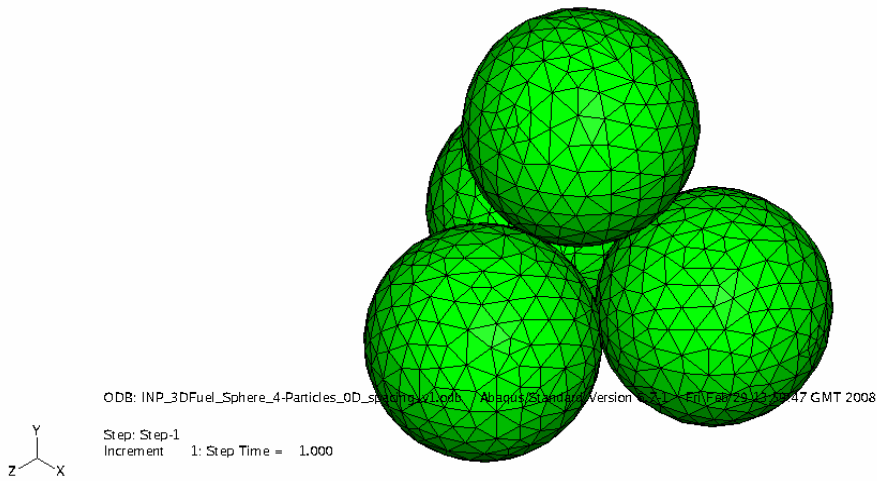
Figures B.1.8 to B.1.13 show the predicted temperature distributions for the three-particle cluster.

Figure B.1.8: Three Particles, no spacing – temperature distribution in graphite matrix and particles
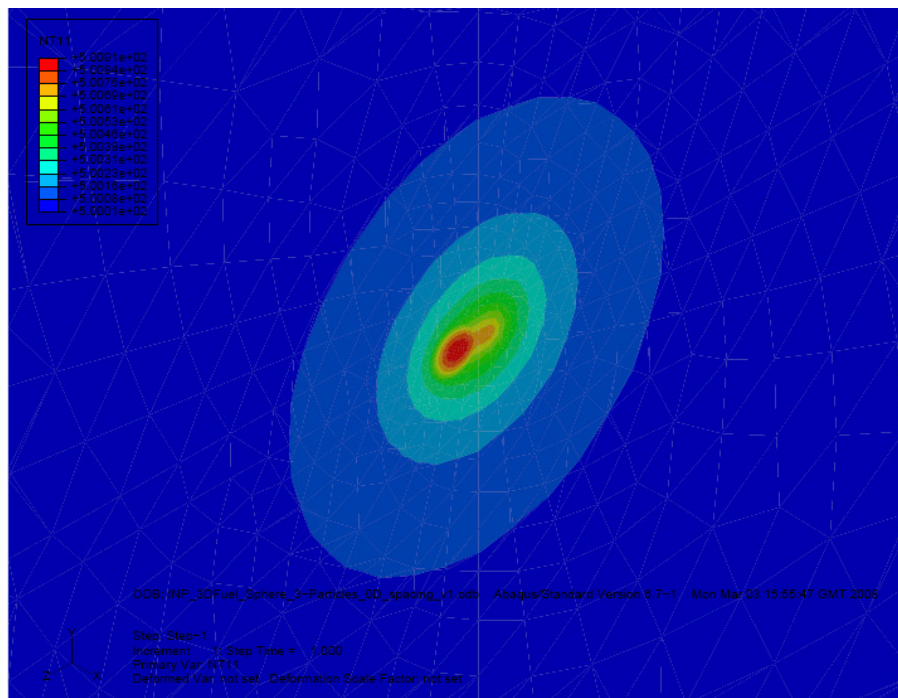
Figure B.1.9: Three particles, no spacing –temperature distribution on particles
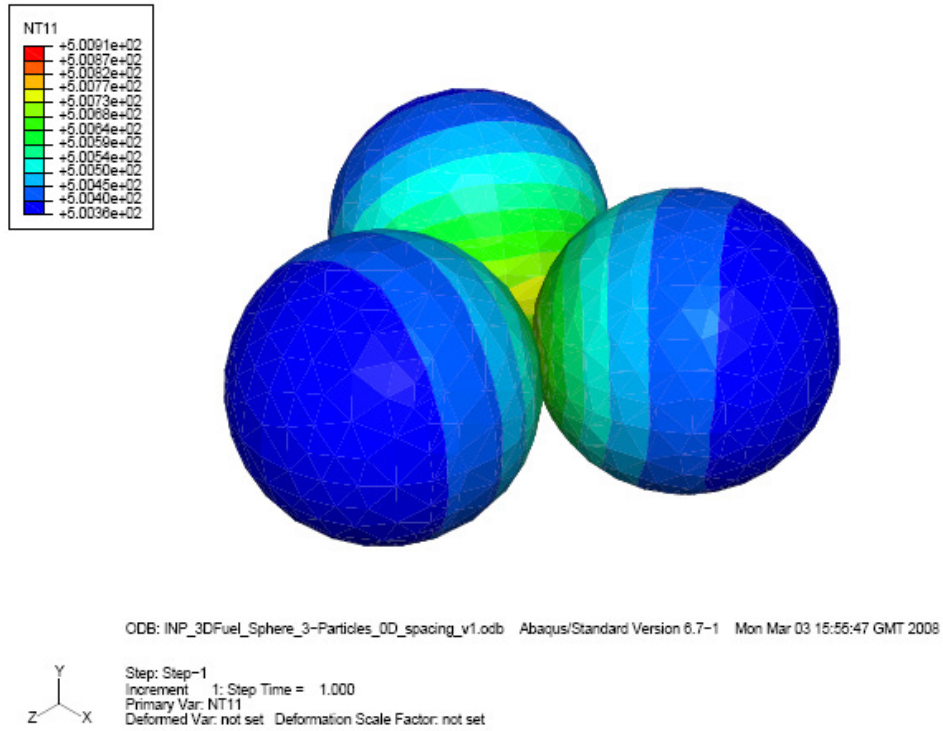
Figure B.1.10: Three particles, no spacing – temperature distribution in particles, interior view
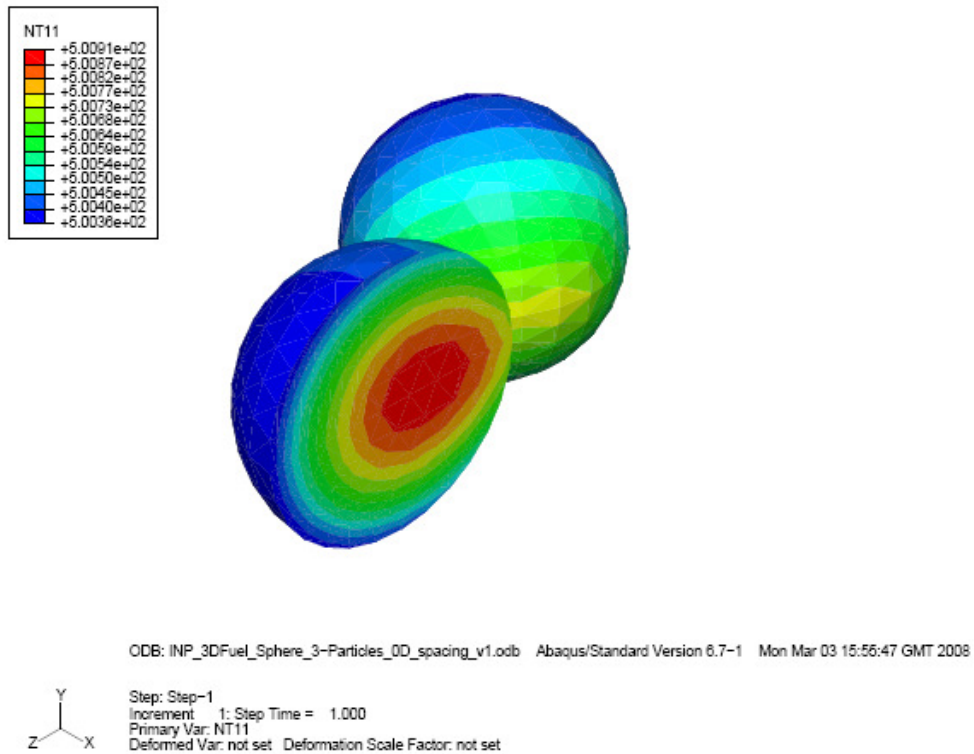
Figure B.1.11: Three particles, 1.2 diameter spacing – temperature distribution in graphite matrix and particles
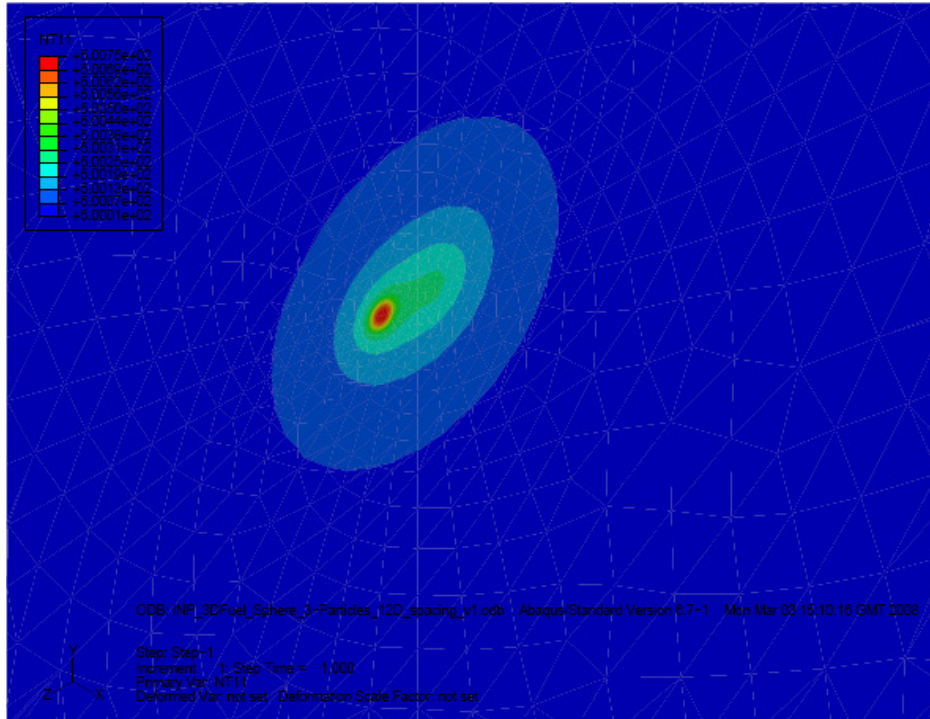
Figure B.1.12: Three particles, 1.2 diameter spacing – temperature distribution on particles
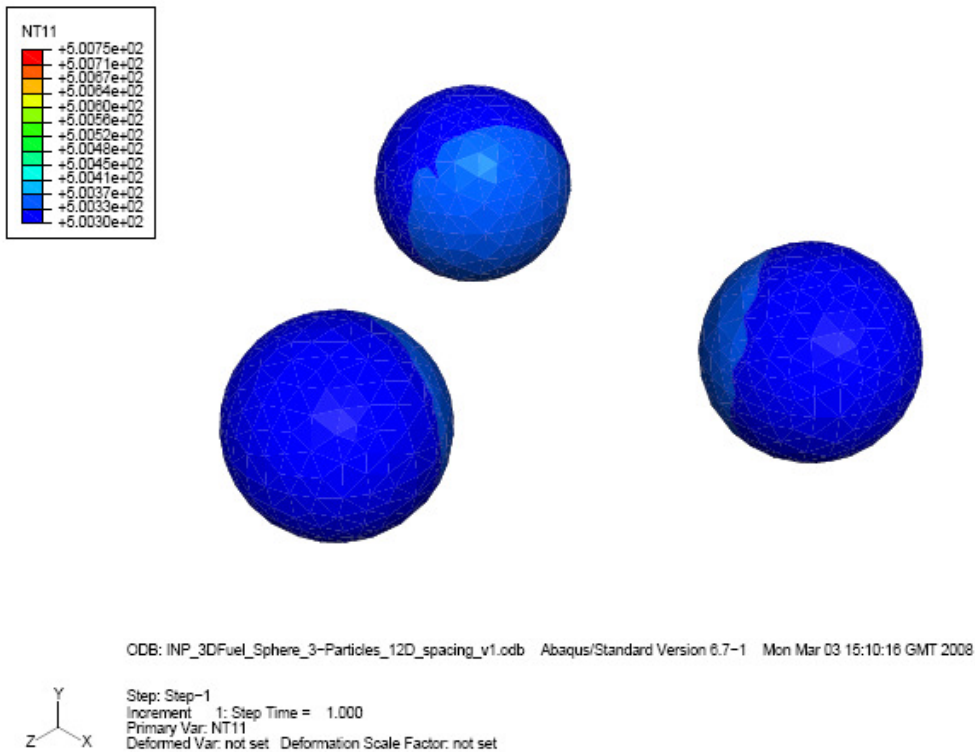
Figure B.1.13: Three particles, 1.2 diameter spacing - temperature distribution in particles, interior view
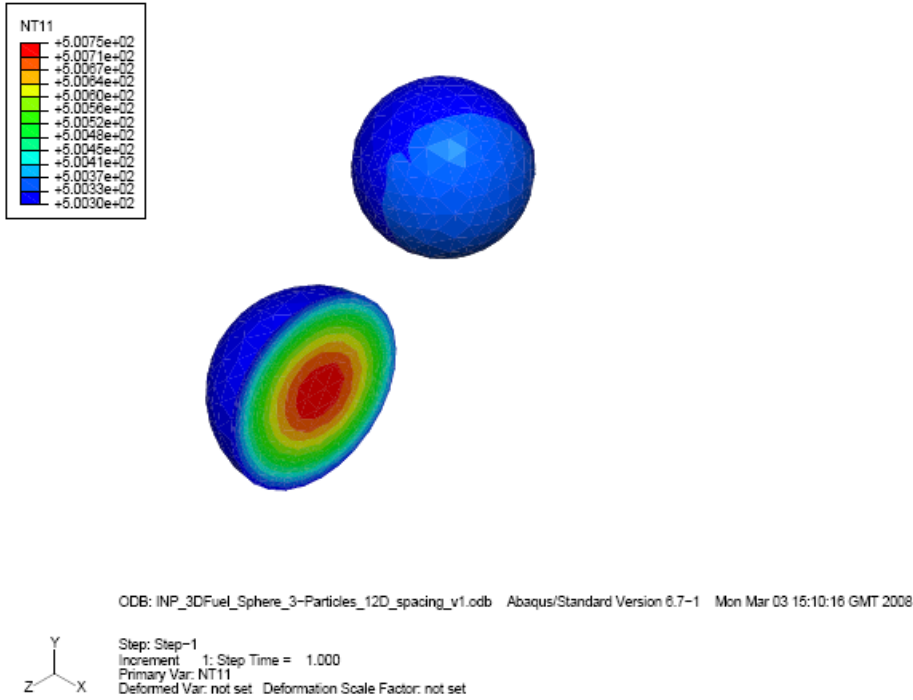
Figures B.1.14 to B.1.19 show the predicted temperature distributions for the four-particle cluster.

Figure B.1.14: Four particles, no spacing – temperature distribution in graphite matrix and particles
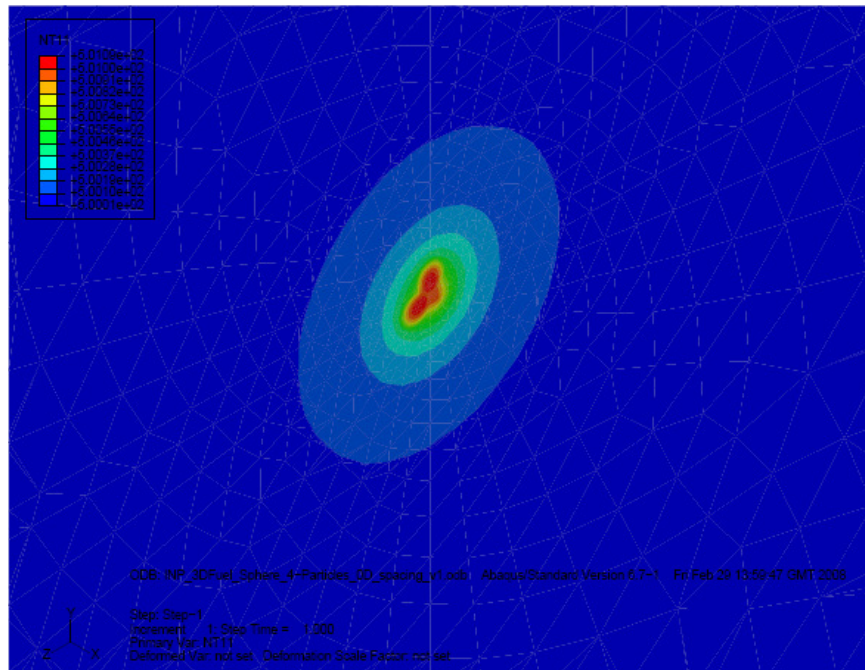
Figure B.1.15: Four particles, no spacing – temperature distribution on particles

ODB: INP_3DFuel_Sphere_4–Particles_0D_spacing_v1.odb   Abaqus/Standard Version 6.7–1   Fri Feb 29 13:59:47 GMT 2008

Step: Step–1
Increment   1: Step Time =   1.000
Primary Var: NT11
Deformed Var: not set   Deformation Scale Factor: not set
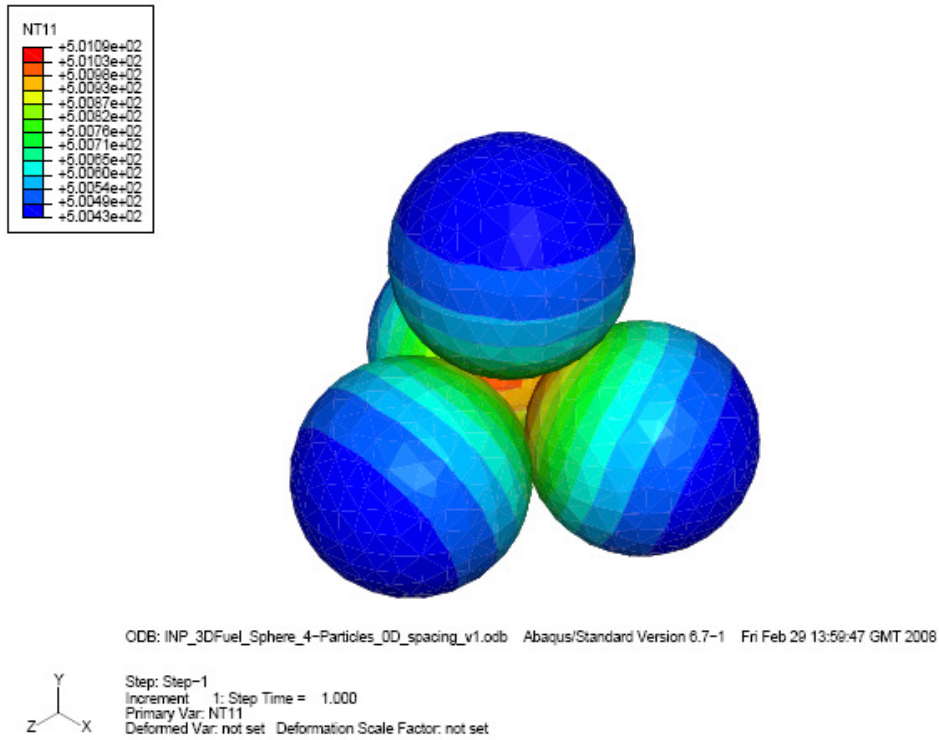
Figure B.1.16: Four Particles, no spacing – temperature distribution in particles, interior view

ODB: INP_3DFuel_Sphere_4–Particles_0D_spacing_v1.odb   Abaqus/Standard Version 6.7–1   Fri Feb 29 13:59:47 GMT 2008

Step: Step–1
Increment   1: Step Time =   1.000
Primary Var: NT11
Deformed Var: not set   Deformation Scale Factor: not set
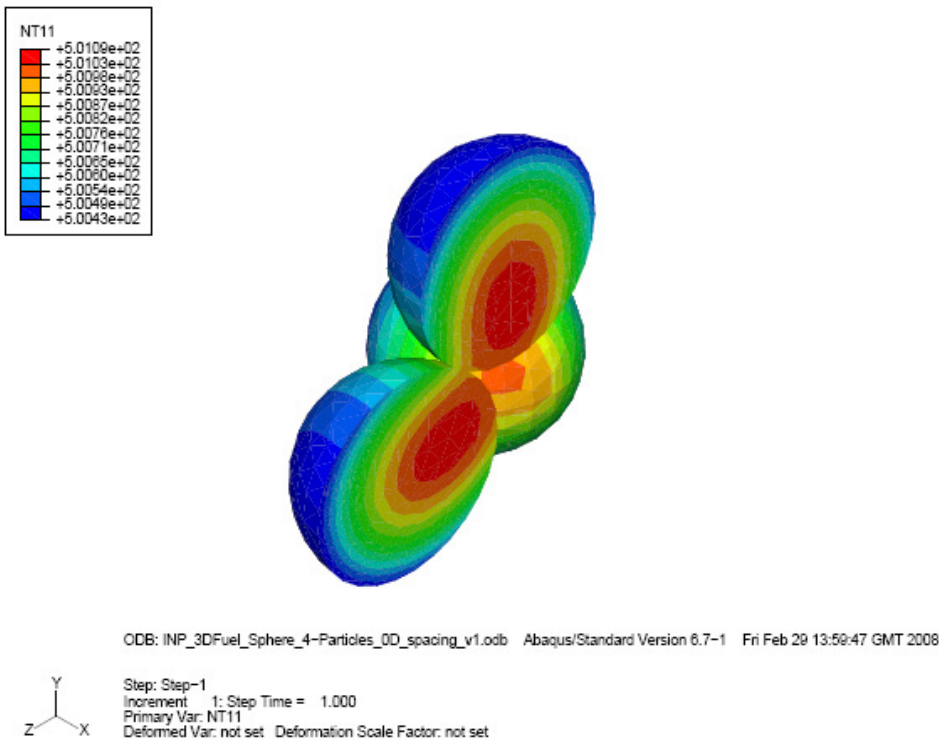
Figure B.1.17: Four Particles, 1.2 diameter spacing – temperature distribution in graphite matrix and particles
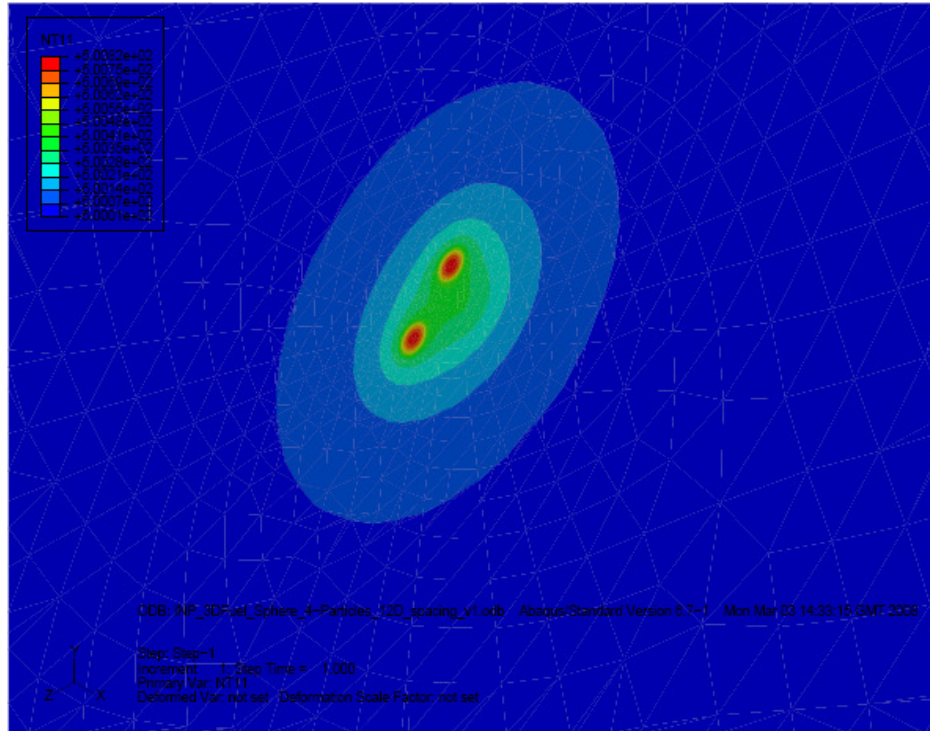
Figure B.1.18: Four Particles, 1.2 diameter spacing – temperature distribution on particles
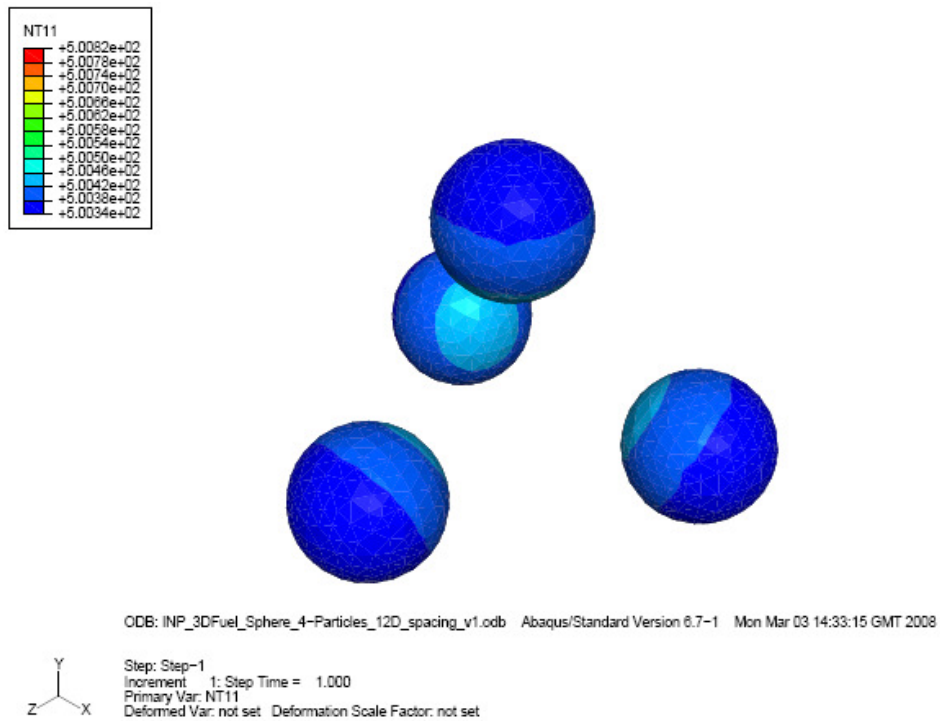
Figure B.1.19: Four particles, 1.2 diameter spacing – temperature distribution in particles, interior view

ODB: INP_3DFuel_Sphere_4-Particles_12D_spacing_v1.odb   Abaqus/Standard Version 6.7-1   Mon Mar 03 14:33:15 GMT 2008

Step: Step-1
Increment   1: Step Time =   1.000
Primary Var: NT11
Deformed Var: not set   Deformation Scale Factor: not set
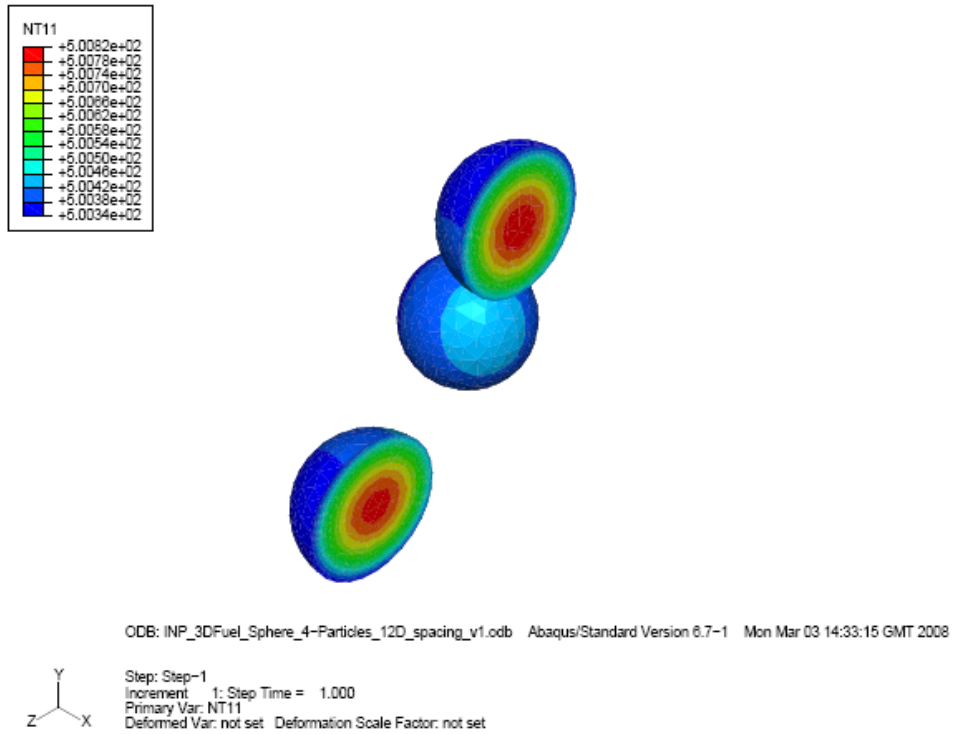
Figures B.1.20 and B.1.21 show the predicted temperature distributions for the thirteen-particle cluster.

Figure B.1.20: Thirteen particles, no spacing – temperature distribution in particles

ODB: INP_3DFuel_Sphere_13–Particles_0D_spacing_v2.odb   Abaqus/Standard Version 6.7–1   Thu Mar 20 10:48:29 GMT 2008

Step: Step–1
Increment   1: Step Time =   1.000
Primary Var: NT11
Deformed Var: not set   Deformation Scale Factor: not set
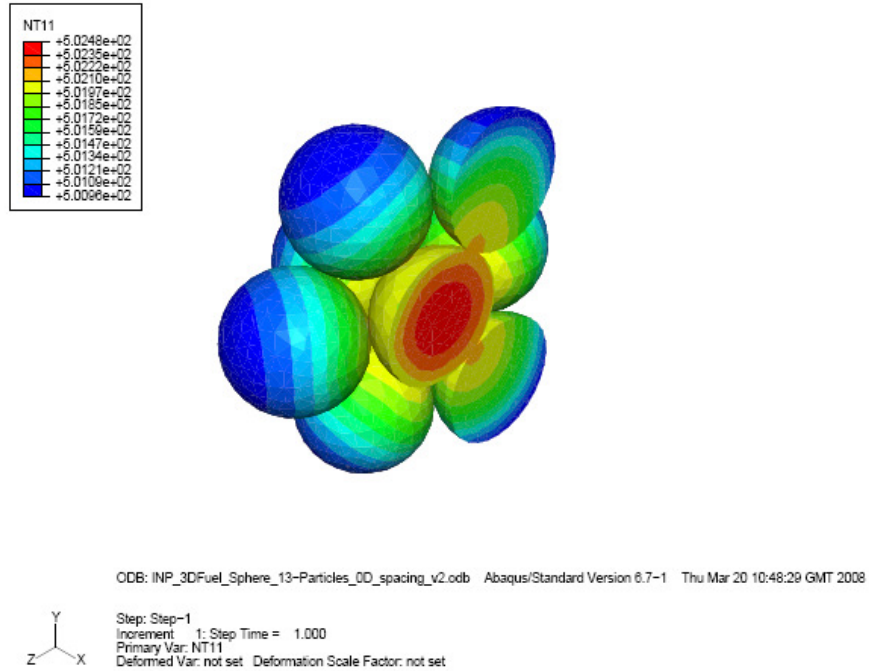
Figure B.1.21: Thirteen particles, 1.2 diameter spacing – temperature distribution in particles

ODB: INP_3DFuel_Sphere_13–Particles_12D_spacing_v2.odb   Abaqus/Standard Version 6.7–1   Thu Mar 20 09:23:04 GMT 2008

Step: Step–1
Increment   1: Step Time =   1.000
Primary Var: NT11
Deformed Var: not set   Deformation Scale Factor: not set
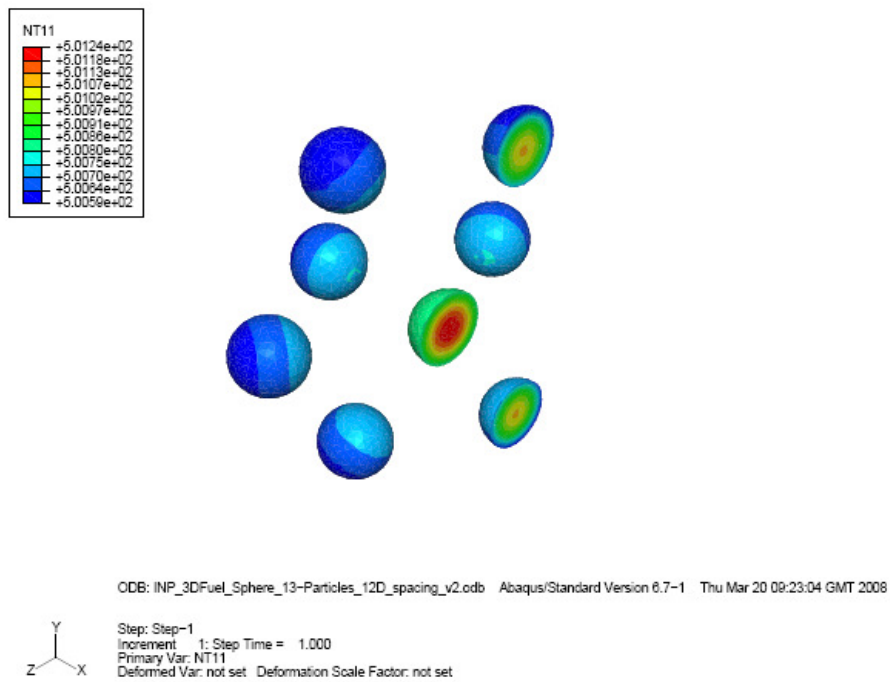
Figures B.1.22 to B.1.25 show the predicted temperature distributions for the fourteen-particle cluster.

Figure B.1.22: Fourteen particles, no spacing – temperature distribution in graphite matrix and particles
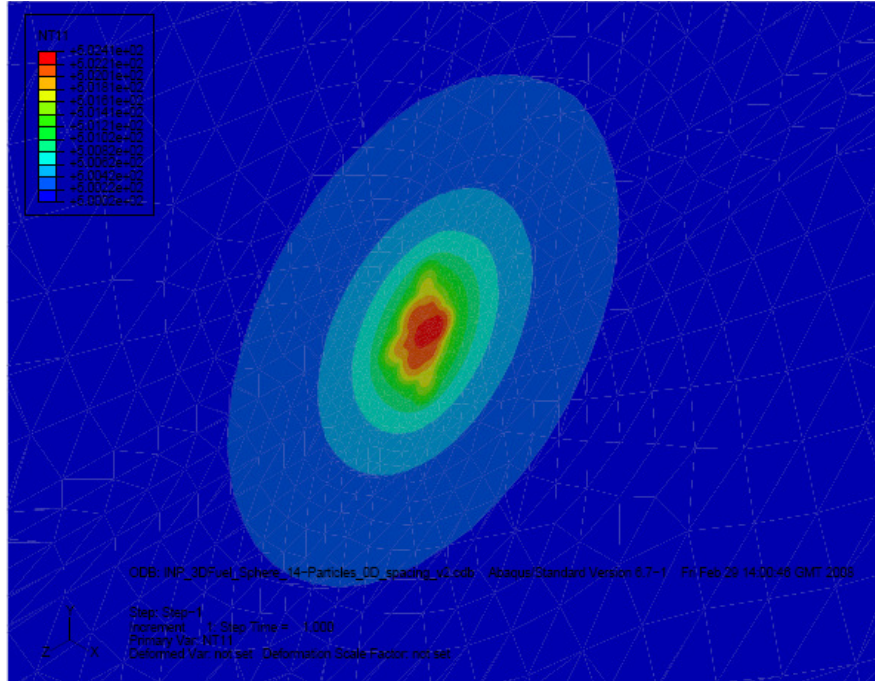
Figure B.1.23: Fourteen particles, no spacing – temperature distribution on particles
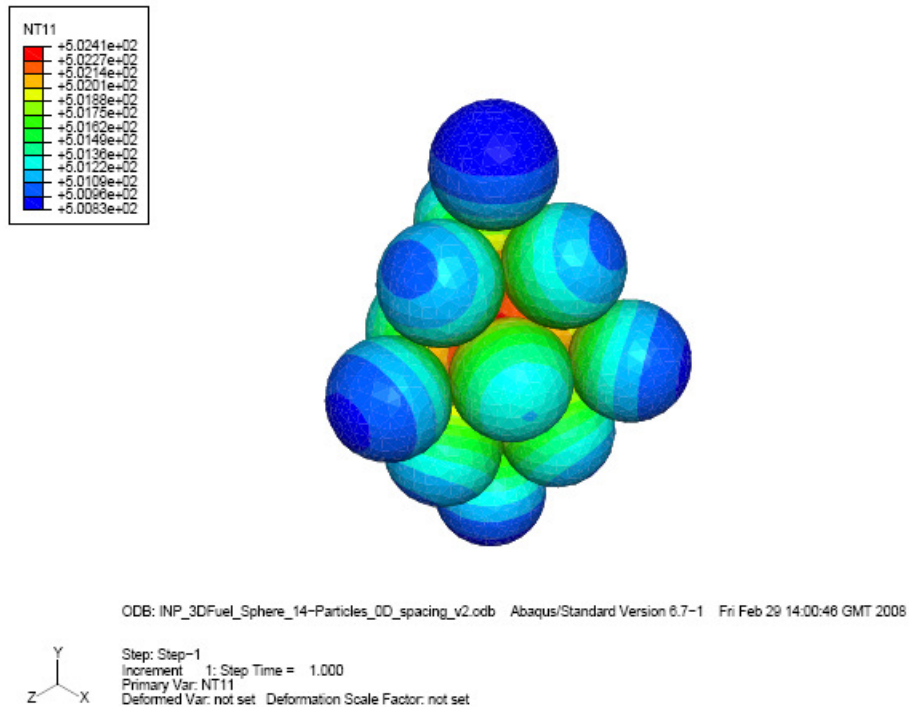
Figure B.1.24: Fourteen particles, no spacing – temperature distribution in particles, interior view
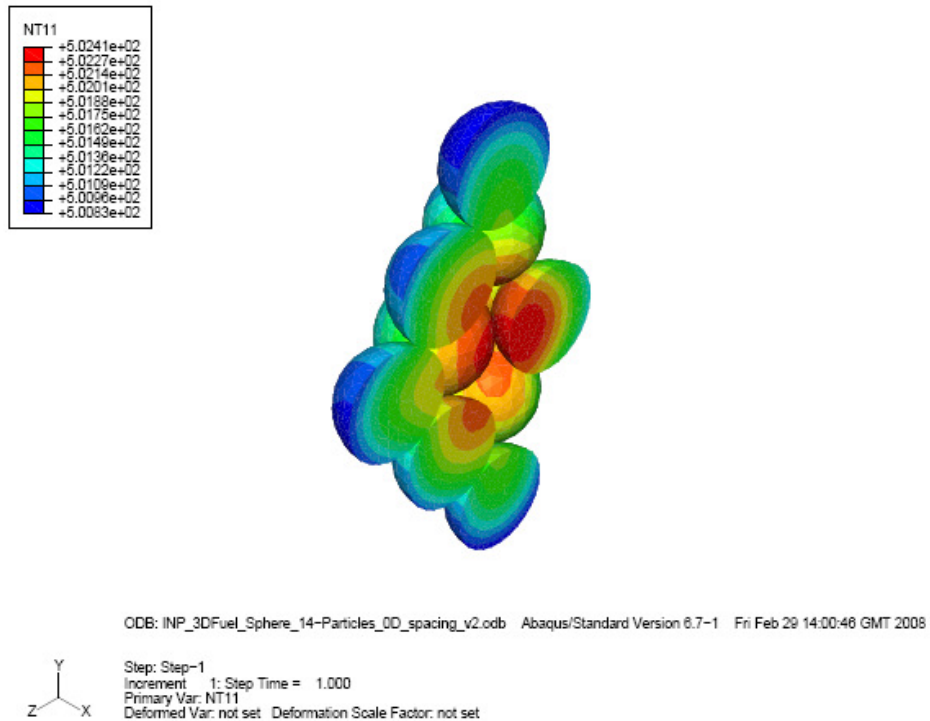
Figure B.1.25: Fourteen particles, 1.2 diameter spacing – temperature distribution in graphite matrix and particles
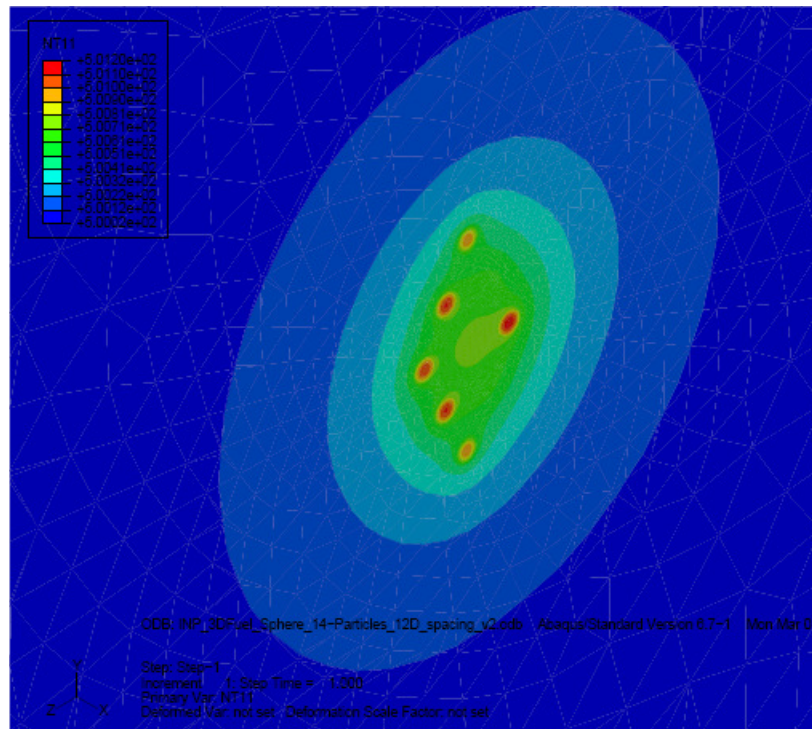
Appendix C: Determination of Pebble Effective Conductivity

This appendix presents detailed working for Section 7. The detailed derivation of the extension to Maxwell's theory to be applicable to multi-layered particles is presented together with the dimensions used for constructing the grids for the finite element models.

C.1 Analytical Models

C.1.1 Temperature Field Around a Single Particle in a Temperature Gradient

A spherical particle of uniform thermal conductivity k_p, and radius a is placed within an infinite uniform material with uniform thermal conductivity k_m. A coordinate system is chosen such that the centre of the particle lies at the origin. A temperature gradient is imposed, such that:

$$T_m \rightarrow V z \quad \text{as} \quad z \rightarrow \infty. \tag{C.1.1}$$

where V is a constant which is equal to the imposed external temperature gradient.

The temperature fields within the particle, T_p, and within the surrounding medium, T_m, are both governed by the heat conduction equation. Spherical polar coordinates are used, and the axial symmetry of the system is exploited, leading to the equation:

$$\frac{1}{r^2}\frac{\partial}{\partial r}\left(r^2 \frac{\partial T_p}{\partial r}\right) + \frac{1}{r^2 \sin\phi}\frac{\partial}{\partial \phi}\left(\sin\phi \frac{\partial T_p}{\partial \phi}\right) = 0 \quad \text{for} \quad 0 \leq r < a \tag{C.1.2}$$

$$\frac{1}{r^2}\frac{\partial}{\partial r}\left(r^2 \frac{\partial T_m}{\partial r}\right) + \frac{1}{r^2 \sin\phi}\frac{\partial}{\partial \phi}\left(\sin\phi \frac{\partial T_m}{\partial \phi}\right) = 0 \quad \text{for} \quad a \leq r < \infty \tag{C.1.3}$$

The system is completed by requiring the temperature and the heat flux to be continuous at the surface of the particle, $r = a$:

$$T_p(a,\phi) = T_m(a,\phi) \tag{C.1.4}$$

$$k_p \frac{\partial T_p}{\partial r}\bigg|_{r=a} = k_m \frac{\partial T_m}{\partial r}\bigg|_{r=a} \tag{C.1.5}$$

The far field boundary condition, (C.1.1), is rewritten in terms of the polar coordinate system, to obtain:

$$T_m \rightarrow V r \cos\phi \quad \text{as} \quad r \rightarrow \infty. \tag{C.1.6}$$

Equations (C.1.2) and (C.1.3) can be integrated using standard mathematical methods, to obtain:

$$T_p(r,\phi) = V \left\{ A_p \, r \cos\phi + B_p \frac{a^3 \cos\phi}{r^2} \right\}$$

$$T_m(r,\phi) = V \left\{ A_m \, r \cos\phi + B_m \frac{a^3 \cos\phi}{r^2} \right\}$$

The coefficients A_p, B_p, A_m and B_m must be determined by applying the continuity conditions, (C.1.4) and (C.1.5), and the boundary condition, (C.1.6). This generates a set of three equations for four unknowns. A fourth equation is obtained by requiring the temperature field within the particle to remain bounded at the origin, which requires $B_p = 0$. These four conditions lead to the equations:

$$\{A_p + B_p\} = \{A_m + B_m\}, \qquad k_p\{A_p - 2B_p\} = k_m\{A_m - 2B_m\}, \qquad A_m = 1, \qquad B_p = 0$$

which may be solved to compute the unknown coefficients. It is found that:

$$T_m(r,\phi) = V \left\{ r - \left(\frac{k_p - k_m}{2k_m + k_p} \right) \frac{a^3}{r^2} \right\} \cos\phi \qquad \text{(C.1.7)}$$

Using equation (C.1.7), it is seen that the particle causes a perturbation to the far-field temperature profile of the form:

$$\Delta T \sim V \, B_m \frac{a^3 \cos\phi}{r^2} = -V \left(\frac{k_p - k_m}{2k_m + k_p} \right) \frac{a^3}{r^2} \cos\phi \qquad \text{(C.1.8)}$$

Note that equation (C.1.8) demonstrates that the thermal conductivity of the region $0 \leq r \leq a$ can be obtained from knowledge of the coefficient of the perturbation to the far-field temperature profile.

Note that equation (C.1.8) demonstrates that if the conductivity of the particle is not known, based on a knowledge of coefficient of the perturbation to the far-field temperature profile, one can deduce the thermal conductivity of the particle.

C.1.2 The Thermal Conductivity of a Dilute Suspension of Homogeneous Spheres

Maxwell noted that if a number of spherical particles, each with conductivity k_p, were placed inside a large spherical region, $0 \leq r \leq a_{\max}$, and a temperature gradient is imposed, such that:

$$T \to V z \quad \text{as} \quad z \to \infty,$$

then the temperature profile in the far-field region, $z \gg a_{\max}$, can be computed by the superposition principle. Using this principle, and equation (C.1.8), it is found that a collection of N such identical particles causes a perturbation to the far-field temperature profile of the form:

$$\Delta T_N \sim - N V \left(\frac{k_p - k_m}{2k_m + k_p} \right) \frac{a^3}{r^2} \cos \phi \qquad (C.1.9)$$

This simple observation allows the effective thermal conductivity of the composite region $0 \leq r \leq a_{max}$, which contains many particles, to be evaluated, as described below.

The large spherical region $0 \leq r \leq a_{max}$ may be viewed as a single macroscopic particle, formed from a composite material with unknown thermal conductivity k_{eff}, embedded within a uniform material with conductivity k_m. The work in the previous section shows that the thermal conductivity of the spherical region, k_{eff}, can be deduced from a knowledge of the perturbation it causes in the far-field temperature profile. Therefore, by equating the far field perturbations due to a single large particle of conductivity k_{eff}, computed from equation (C.1.8), and the far-field perturbation caused by the many small particles within $0 \leq r \leq a_{max}$, described by equation (C.1.9), it is found that:

$$\Delta T_{eff} = \Delta T_N$$

This implies:

$$-V \left(\frac{k_{eff} - k_m}{2k_m + k_{eff}} \right) \frac{a_{max}^3}{r^2} \cos \phi = -N V \left(\frac{k_p - k_m}{2k_m + k_p} \right) \frac{a^3}{r^2} \cos \phi$$

Therefore:

$$\left(\frac{k_{eff} - k_m}{2k_m + k_{eff}} \right) = \left(\frac{k_p - k_m}{2k_m + k_p} \right) \frac{N a^3}{a_{max}^3}$$

From this equation, after some manipulation, it is found that:

$$k_{eff} = \frac{3k_m k_p \alpha + (2k_m + k_p)k_m (1 - \alpha)}{3k_m \alpha + (2k_m + k_p)(1 - \alpha)}$$

where α is the volume fraction of the composite material occupied by the small particles, of radius a:

$$\alpha = \frac{N a^3}{a_{max}^3} = \frac{N \left(4\pi a^3 / 3 \right)}{\left(4\pi a_{max}^3 / 3 \right)} = \frac{\text{Volume occupied by N small particles, radius a}}{\text{Volume of sphere } r \leq a_{max}}$$

The thermal conductivity of the composite material is independent of the material's shape. Therefore the above expression for k_{eff} represents a general formula for a composite material,

formed from a matrix material with thermal conductivity k_m containing a volume fraction $a \ll 1$ of particles of thermal conductivity k_p.

C.1.3 Calculating The Thermal Conductivity Of A Suspension of Coated TRISO Particles

The thermal conductivity of a dilute suspension of coated TRISO particles within a matrix material can be computed using a straightforward extension of Maxwell's theory. The same methodology is used as for the composite material containing homogeneous particles. Initially, the temperature profile is modelled for a single coated particle placed within an external temperature gradient. The perturbation to the far-field temperature profile due to the presence of this particle is then assessed, and this is used to compute the effective conductivity of a suspension of such particles.

C.1.4 The Temperature Around A Single TRISO Particle In A Temperature Gradient

The calculation of the temperature field surrounding a coated particle proceeds in a manner very similar to that for a homogeneous particle. However, for a particle with N_{coat} coatings, there are now $(N_{coat} + 2)$ distinct regions in which the temperature must be modelled (including the matrix material and the fuel kernel region), and $2(N_{coat} + 2)$ boundary and continuity conditions must be applied to determine the final solution.

A coordinate system is chosen such that the centre of the particle lies at the origin. A temperature gradient is imposed, such that:

$$T_m \to V z \text{ as } z \to \infty.$$

The $(N_{coat} + 2)$ distinct regions are indexed from 1 to $(N_{coat} + 2)$, such that the fuel kernel is region 1, the innermost coating is region 2. Moving outwards, the numbering continues, through the coatings, through to index $(N_{coat} + 1)$ for the outermost coating and index $(N_{coat} + 2)$ for the infinite matrix region:

Region	Material	Temperature	Conductivity	Inner radius of region	Outer radius of region
1	Kernel	$T_1(r, \phi)$	k_1	0	a_1
2	Inner coating	$T_2(r, \phi)$	k_2	a_1	a_2
$\vdots$	$\vdots$	$\vdots$	$\vdots$	$\vdots$	$\vdots$
$(N_{coat} + 1)$	Outer coating	$T_{(N_{coat}+1)}(r, \phi)$	$k_{(N_{coat}+1)}$	$a_{N_{coat}}$	$a_{(N_{coat}+1)}$

| $(N_{coat}+2)$ | Matrix | $T_{(N_{coat}+2)}(r,\phi)$ | $k_{(N_{coat}+2)}$ | $a_{(N_{coat}+1)}$ | - |

The temperature in the ith region, $T_i(r,\phi)$, is governed by the heat conduction equation:

$$\frac{1}{r^2}\frac{\partial}{\partial r}\left(r^2\frac{\partial T_i}{\partial r}\right)+\frac{1}{r^2\sin\phi}\frac{\partial}{\partial\phi}\left(\sin\phi\frac{\partial T_i}{\partial\phi}\right)=0 \quad\text{for}\quad a_{(i-1)}\le r<a_i$$

The temperature and the heat flux are required to be continuous at the surface of each region, $r=a_i$, therefore:

$$T_i(a_i,\phi)=T_{(i+1)}(a_i,\phi) \qquad\text{for}\quad i=1,\,2,...,\,(N_{coat}+1)$$

$$k_i\frac{\partial T_i}{\partial r}\bigg|_{r=a_i} = k_{(i+1)}\frac{\partial T_{(i+1)}}{\partial r}\bigg|_{r=a_i} \qquad\text{for}\quad i=1,\,2,...,\,(N_{coat}+1)$$

The differential equations for the temperature fields, $T_i(r,\phi)$, can be solved, to obtain the solutions:

$$T_i(r,\phi)=V\left\{A_i\,r\cos\phi+B_i\,\frac{a_{(N_{coat}+1)}^3\cos\phi}{r^2}\right\} \quad\text{for}\quad i=1,\,2,...,\,(N_{coat}+2)$$

Equations for the unknown coefficients, A_i and B_i, can be obtained by enforcing the continuity conditions. The continuity of the temperature distribution at the boundaries of each coating requires:

$$\left\{A_i+B_i\,\frac{a_{(N_{coat}+1)}^3}{a_i^3}\right\}=\left\{A_{i+1}+B_{i+1}\,\frac{a_{(N_{coat}+1)}^3}{a_i^3}\right\} \qquad\text{for}\quad i=1,\,2,...,\,(N_{coat}+1)$$

The continuity of the heat flux at the boundaries of each coating requires:

$$k_{i-1}\left\{A_{i-1}-2B_{i-1}\,\frac{a_{(N_{coat}+1)}^3}{a_{i-1}^3}\right\}=k_i\left\{A_i-2B_i\,\frac{a_{(N_{coat}+1)}^3}{a_{i-1}^3}\right\} \qquad\text{for}\quad i=2,\,3,...,\,(N_{coat}+2)\,.$$

This provides a system of $2(N_{coat}+1)$ equations for the $2(N_{coat}+2)$ unknown values of the coefficients A_i and B_i. The final two equations are obtained by imposing the far-field boundary condition and insisting that the temperature profile within the kernel is bounded at the origin, $r=0$:

$$A_{N_{coat}+2}=1,\qquad B_1=0\,.$$

These two conditions complete a well-posed system of equations, which may be solved to compute the coefficients A_i and B_i. For a particle with just one or two coatings, these equations can be solved easily by hand. For TRISO particles with four or more coatings, it is more convenient to use a numerical method to compute the coefficients A_i and B_i.

The equation system represented in matrix is:

$$\mathbf{M}\mathbf{x} = \mathbf{b},$$

where, for the specific case of TRISO particles with four coatings ($N_{coat} = 4$), the matrix $\mathbf{M}$ is:

$$
\mathbf{M} =
\left[
\begin{array}{cccccc|cccccc}
1 & -1 & & & & & \dfrac{a_5^3}{a_1^3} & -\dfrac{a_5^3}{a_1^3} & & & & \\[2ex]
& 1 & -1 & & & & & \dfrac{a_{(N_{coat}+1)}^3}{a_2^3} & -\dfrac{a_5^3}{a_2^3} & & & \\[2ex]
& & 1 & -1 & & & & & \dfrac{a_5^3}{a_3^3} & -\dfrac{a_5^3}{a_3^3} & & \\[2ex]
& & & 1 & -1 & & & & & \dfrac{a_5^3}{a_4^3} & -\dfrac{a_5^3}{a_4^3} & \\[2ex]
& & & & 1 & -1 & & & & & 1 & -1 \\[2ex]
& & & & & 1 & & & & & & 0 \\[2ex]
\hline
0 & & & & & & 1 & & & & & \\[2ex]
-k_1 & k_2 & & & & & & -2\dfrac{a_5^3}{a_1^3} & 2\dfrac{a_5^3}{a_1^3} & & & \\[2ex]
& -k_2 & k_3 & & & & & & -2\dfrac{a_5^3}{a_2^3} & 2\dfrac{a_5^3}{a_2^3} & & \\[2ex]
& & -k_3 & k_4 & & & & & & -2\dfrac{a_5^3}{a_3^3} & 2\dfrac{a_5^3}{a_3^3} & \\[2ex]
& & & -k_4 & k_5 & & & & & & -2\dfrac{a_5^3}{a_4^3} & 2\dfrac{a_5^3}{a_4^3} \\[2ex]
& & & & -k_5 & k_6 & & & & & -2 & 2 \\
\end{array}
\right]
$$

The first N_{coat+2} rows in the vector $\mathbf{x}$ correspond to the unknown values of A_i and the second N_{coat+2} rows correspond to the unknown B_i values. Vector $\mathbf{b}$ only contains one non-zero entry of 1.0 in row N_{coat+2} as a result of the application of the boundary condition on $A_{Ncoat+2}$.

Following solution of the equations, the perturbation to the far-field temperature distribution due the presence of the coated particle is found to be:

$$\Delta T \sim V\, B_{(N_{coat}+2)} \frac{a_{(N_{coat}+1)}^3 \cos\phi}{r^2}.$$

C.1.5 The Effective Thermal Conductivity of A TRISO Particle In An External Temperature Gradient

When assessing heat flow around and through a TRISO particle, due to an external temperature gradient, it is convenient to work with an effective particle conductivity instead of directly resolving the multilayer structure.

An appropriate effective conductivity can be calculated by comparing the temperature perturbation surrounding a TRISO particle, as calculated in Section C.1.4, with the temperature perturbation surrounding a single material particle as calculated in Section C.1.1.

Solution surrounding TRISO particle, outer radius $a_{(N_{coat}+1)}$:	$T = Vr\cos\phi + VB_{(N_{coat}+2)}\dfrac{a^3_{(N_{coat}+1)}\cos\phi}{r^2}$
Solution surrounding solid particle of radius a, conductivity k_p in a matrix of conductivity k_m:	$T = V\left\{r - \left(\dfrac{k_p - k_m}{2k_m + k_p}\right)\dfrac{a^3}{r^2}\right\}\cos\phi$

Comparing these solutions, we see that an identical matrix temperature profile, and hence the correct division of the heat flow between the matrix and particle, is obtained if:

$$-\left(\frac{k_p - k_m}{2k_m + k_p}\right) = B_{(N_{coat}+2)}\;.$$

The equality of these expressions allows an effective conductivity to be evaluated for the TRISO particle. Simple algebraic manipulation shows that:

$$k_p = k_m\left(\frac{1 - 2\,B_{(N_{coat}+2)}}{1 + B_{(N_{coat}+2)}}\right)$$

Note that, if required, this method could be extended to account for thermal interface resistances at boundaries of each coating. However, as no data is available, this has not been pursued to date.

C.1.6 The Thermal Conductivity of a Dilute Suspension of TRISO Particles

Using Maxwell's methodology, if a number of coated TRISO particles are placed inside a large spherical region, $0 \le r \le a_{max}$, then the temperature profile in the far-field region, $z \gg a_{max}$, can be computed by the superposition principle. Using this principle, it is found that a collection of N identical TRISO particles causes a perturbation to the far-field temperature profile of the form:

$$\Delta T_N \sim N V B_{(N_{coat}+2)} \frac{a_{(N_{coat}+1)}^3 \cos\phi}{r^2} \qquad (C.1.10)$$

However, the whole region $0 \le r \le a_{max}$ may be viewed as a single (not coated) macroscopic particle, formed from a composite material with unknown thermal conductivity k_{eff}, embedded within a uniform matrix material with conductivity $k_{(N_{coat}+2)}$. The far field perturbations due to a single such particle can be computed from equation (C.1.8). Comparing the result of equation (C.1.8) with the far-field perturbation caused by the many TRISO particles within the region $0 \le r \le a_{max}$, described by equation (C.1.10), it is found that:

$$\Delta T_{p,eff} = \Delta T_N$$

This implies that:

$$-V\left(\frac{k_{eff} - k_m}{2k_m + k_{eff}}\right)\frac{a_{max}^3}{r^2}\cos\phi = N V B_{(N_{coat}+2)} \frac{a_{(N_{coat}+1)}^3}{r^2}\cos\phi$$

Therefore,

$$-\left(\frac{k_{eff} - k_m}{2k_m + k_{eff}}\right) = B_{(N_{coat}+2)} \frac{N a_{(N_{coat}+1)}^3}{a_{max}^3}.$$

Manipulating this expression, it is found that (recall that $k_{(N_{coat}+2)} = k_m$):

$$k_{eff} = k_m\left(\frac{1 - 2\alpha B_{(N_{coat}+2)}}{1 + \alpha B_{(N_{coat}+2)}}\right)$$

where α is the volume fraction occupied by the TRISO particles:

$$\alpha = \frac{N a_{(N_{coat}+1)}^3}{a_{max}^3} = \frac{N\left(4\pi a_{(N_{coat}+1)}^3/3\right)}{\left(4\pi a_{max}^3/3\right)} = \frac{\text{Volume occupied by TRISO particles}}{\text{Volume of sphere } r \le a_{max}}.$$

TRISO particles contain four coatings, resulting in a system of $2(N_{coat}+2) = 12$ linear equations for the coefficients, A_i and B_i. Although only the coefficient $B_{(N_{coat}+2)} = B_6$ is required to evaluate k_{eff} and k_p, the whole linear system must be solved to compute these values.

C.2 Finite Element Models

The dimensions of each of the finite element models used for the determination of the effective thermal conductivity of a pebble are given here for each arrangement of particles.

For a PBMR TRISO coated particle, the diameter of a single particle is 0.92 mm and its corresponding volume is 0.40772 mm^3. In each arrangement of particles the volume fraction of particles is 0.09344.

Three arrangements were studied, simple cubic, body-centered cubic and face-centered cubic, the dimensions for each of which are given below.

Simple cubic

A unit cell contains the equivalent of one particle, distributed as eight 1/8ths of a particle centered on each of the eight corners of a cubic unit cell. The volume of the cubic unit cell is therefore:

Volume of unit cell   = 0.40772/0.09344 = 4.363 mm^3

Length of an edge of the cube = (4.363)$^{1/3}$ = 1.634 mm

The finite element model consists of three cells stacked in a column which is 4.902 mm high by 1.634 mm wide by 1.634 mm deep.

Body-centered cubic

A unit cell contains the equivalent of two particles, distributed as eight 1/8ths of a particle centered on each of the eight corners and one in the center of the volume of a cubic unit cell. The volume of the cubic unit cell is therefore:

Volume of unit cell   = 2 x 0.40772/0.09344 = 8.726 mm^3

Length of an edge of the cube = (8.726)$^{1/3}$ = 2.0588 mm

The finite element model consists of three cells stacked in a column which is 6.1764 mm high by 2.0588 mm wide by 2.0588 mm deep.

Face-centered cubic

A unit cell contains the equivalent of four particles, distributed as eight 1/8ths of a particle centered on each of the eight corners and six 1/2 particles centered on the centres of each of the six faces of a cubic unit cell. The volume of the cubic unit cell is therefore:

Volume of unit cell   = 4 x 0.40772/0.09344 = 17.4538 mm^3

Length of an edge of the cube = (17.4538)$^{1/3}$ = 2.5940 mm

The finite element model consists of two cells stacked in a column which is 5.188 mm high by 2.594 mm wide by 2.594 mm deep.

APPENDIX D : METHOD DEVELOPMENT FOR RANDOM PACKING OF SPHERICAL PEBBLES AND ITS VALIDATION

This appendix documents the development of a method to generate a random packing of pebbles, the validation of the method, and the comparison with experimental results.

D.1 Method for Generating Random Arrangement of Pebbles

D.1.1 Integration

Initially, the pebble falls vertically at a fixed speed, but if the pebble moves into contact with either the walls or floor of the pebble bed, or with a pebble already present, then the velocity vector is modified accordingly and the integration proceeds. For the purposes of the code, "contact" is deemed to be when a pebble overlaps with another pebble or a wall. The extent of the overlap effectively determines the spatial tolerance of the solution. Once the velocity has reached zero, an adjustable number of annealing steps are performed to ensure the pebble is stable. This is done by slightly perturbing the pebble from its final position (by a small random amount in the horizontal plane plus a fixed amount in the vertical plane) and testing to see if any of the perturbed positions allow the pebble to fall to a lower height within the system. Following the annealing, the pebble position is frozen into position, i.e., a falling pebble cannot disrupt the position of any pebbles already present in the system.

A pebble begins with a fixed velocity. This is an adjustable parameter in the code, but for these calculations is set to $[0,0,-1]$, i.e., movement in the negative z-direction with a speed of 1 m.s^{-1}. Note that the code uses SI units throughout. The starting position is randomly chosen in the horizontal plane and the initial height is set to be the maximum height of the pebbles already in the bed plus two pebble radii (to ensure that the pebble cannot be in contact with a pebble at the start of the integration). The pebble path is integrated in a series of discrete time steps, ending when the pebble has come to rest (with an upper limit to prevent an infinite loop). At each time step the velocity vector is re-calculated based on any contacts between the pebble and the pebble bed walls, floor or with other pebbles. The pebble position is then updated:

$$\underline{x}(t + \Delta t) = \underline{x}(t) + \underline{v}\Delta t \qquad \text{(D.1.1)}$$

where $\underline{x}$ is the pebble position, $\underline{v}$ is the velocity vector, t is the time of the last integration and $t + \Delta t$ is the time of the new integration (Δt clearly being the time step).

D.1.2 Pebble Contacts

Contact with the floor of the pebble bed is tested for explicitly. Contact between the falling pebble and the pebbles already present within the bed is tested at each integration time step. If the falling pebble is the nth pebble and has a central position $\underline{x}_n$, then an overlap with the ith pebble clearly corresponds to the condition:

$$\left| \underline{x}_n - \underline{x}_i \right| \le 2r_{peb} \qquad \text{(D.1.2)}$$

where $\underline{x}_i$ is the position of the centre of the ith pebble and r_{peb} is the radius of a pebble. Contact between the falling pebble and the vertical walls of the pebble bed are also tested at each time step. This is achieved by placing two "fictional" pebbles in the system at the same height of the current pebble but positioned so that they lie r_{peb} beyond the surface of the vertical walls (the outer wall and, if applicable, the inner wall).

Testing for the Equation D.1.2 contact condition against the $n-1$ pebbles already in the bed can be computationally very intensive. The majority of pebbles are located deep within the pile already in the bed and have a very low probability of interacting with the nth pebble. A very simple method has been employed to limit the contact testing to only those pebbles close to the top of the bed. Preliminary investigations showed that only pebbles lying within the uppermost ~5 layers of the bed had any appreciable probability of interacting with a freshly-dropped pebble, where the term "layer" refers to a depth of $2r_{peb}$. Within an annular bed, with inner and outer radii of r_i and r_o, a region with a depth of σ pebble layers has a volume of

$$2\pi\sigma\, r_{peb}\left(r_o^2 - r_i^2\right)$$

and contains, assuming a packing fraction α,

$$N_{likelycontacts} \quad = \quad \frac{2\alpha\pi\sigma r_{peb}\left(r_o^2 - r_i^2\right)}{\frac{4}{3}\pi r_{peb}^3} \quad = \quad \frac{3\alpha\sigma\left(r_o^2 - r_i^2\right)}{2r_{peb}^2} \tag{D.1.3}$$

pebbles. The expected value of the packing fraction for a random arrangement is $\alpha \approx 0.61$ (Reference D.1) and $\sigma \approx 5$ is known from the preliminary investigations.

When dropping the nth pebble, rather than testing for contact with all of the $i = 1\ldots(n-1)$ pebbles, is restricted to testing the $i = \left(n - N_{likelycontacts}\right)\ldots(n-1)$ recently dropped pebbles. Note that, in the code, testing is always carried out against the fictional pebbles representing the walls of the pebble bed.

D.1.3 Velocity Adjustment

Figure D.1.1: Schematic of Pebble Arrangement Showing Velocity Definitions
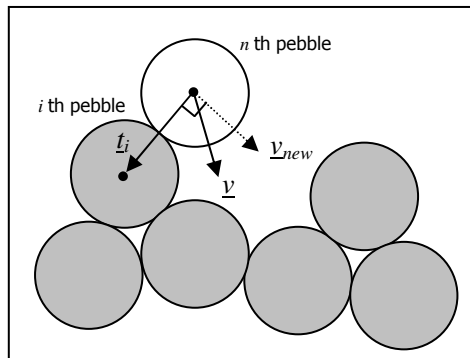
If the nth pebble is in "contact" with any other pebbles (including the two fictional pebbles representing the walls) then the velocity vector $\underline{v}$, as shown in Figure D.1.1, is modified before the integration is allowed to proceed. The new velocity vector $\underline{v}_{new}$ must not allow the pebble to continue to approach any other pebble with which it is in contact. In other words, the component of $\underline{v}$ in the direction of a unit vector, $\hat{\underline{t}}_i$, from the centre of the nth pebble, $\underline{x}_n$, to the centre of the ith pebble, $\underline{x}_i$, with which it is in contact, must be zero or negative, i.e.,:

$$\underline{v} \bullet \hat{\underline{t}}_i \leq 0 \qquad\qquad\qquad (D.1.4)$$

where $\hat{\underline{t}}_i = \dfrac{\underline{x}_i - \underline{x}_n}{\left| \underline{x}_i - \underline{x}_n \right|}$.

This condition must be met for all of the $\hat{\underline{t}}_i$ associated with all of the pebbles in contact.

Single contact

The case in which the nth pebble is in contact with only one other pebble is a common situation and is dealt with specifically in the code. The new velocity, $\underline{v}_{new}$, is given by:

$$\underline{v}_{new} = \underline{v} - \tfrac{1}{2}\left(\underline{v} \bullet \hat{\underline{t}}_i + \left| \underline{v} \bullet \hat{\underline{t}}_i \right| \right) \hat{\underline{t}}_i .$$

This means that, if $\underline{v} \bullet \hat{\underline{t}}_i > 0$ (i.e., condition Equation D.1.4 is not met), then

$$\underline{v}_{new} = \underline{v} - \left(\underline{v} \bullet \hat{\underline{t}}_i \right) \hat{\underline{t}}_i ,$$

i.e., the component of $\underline{v}$ in the direction $\hat{\underline{t}}_i$ is subtracted.

However, if $\underline{v} \bullet \hat{\underline{t}}_i \leq 0$ (i.e., condition Equation D.1.4 is satisfied), then $\underline{v}_{new} = \underline{v}$, and the velocity remains unchanged.

Multiple contacts

If the nth pebble is in contact with more than one other pebble a more general approach is taken to find an acceptable new velocity (which may be $\underline{v}_{new} = \underline{0}$)

Step 1 involves determining whether, despite being in contact with multiple pebbles, the nth pebble is free to move unopposed, i.e., that $\underline{v} \bullet \hat{\underline{t}}_i \leq 0$ (condition Equation D.1.4) holds for all of the contacting pebbles. If $\underline{v} \bullet \hat{\underline{t}}_i \leq 0$ is found to hold for all of the contacting pebbles, then the velocity can be left unchanged (i.e., $\underline{v}_{new} = \underline{v}$) and the integration can proceed. If not, then a

candidate new velocity, $\underline{v}_{trial}$, is calculated by finding a velocity compatible with just one of the contacts (using the method described under Single contact), and the code exits from Step 1.

Step 2 takes $\underline{v}_{trial}$ from Step 1 and checks whether or not this would be compatible with the other contacting pebbles. If so, then a valid new velocity has been found ($\underline{v}_{new} = \underline{v}_{trial}$) and the integration can proceed. If $\underline{v}_{trial}$ is not consistent with one or more of the remaining pebble contacts then the multiple contacts must be examined in more detail in order to determine a valid new velocity.

Step 3 is only reached if the falling pebble is in contact with multiple neighbours and is constrained from free-fall. The code initially presumes that there is no valid new velocity, i.e., $\underline{v}_{new} = \underline{0}$. It then loops over each possible pair of contacting pebbles and determines a unit vector, $\underline{\hat{p}}_{ij}$, perpendicular to the plain in which each pair lies:

$$\underline{\hat{p}}_{ij} = \frac{\underline{\hat{t}}_i \times \underline{\hat{t}}_j}{\left|\underline{\hat{t}}_i \times \underline{\hat{t}}_j\right|} .$$
(D.1.5)

The direction of the cross product $\underline{\hat{p}}_{ij}$ is then aligned so that $\underline{\hat{p}}_{ij} \bullet \underline{v} \geq 0$ to give a candidate new velocity, $\underline{v}_{trial}$, that lies within $\frac{\pi}{2}$ of the original velocity but is tangential to the surfaces of the pair of contacting pebbles considered. This trial velocity is then checked against all of the other contacting pebbles (testing condition Equation D.1.4 in each case). If the candidate velocity is acceptable to the other candidate velocities then it is adopted as a valid, non-zero new velocity $\underline{v}_{new}$, provided that it is "more downhill" than the existing value of $\underline{v}_{new}$ (which could be zero if no suitable velocity has been found, or could be a non-zero velocity if another contacting pebble pair has generated a valid vector). In this determination, "more downhill" corresponds to a larger value of the $\underline{v}_{new}$ component in the $[0,0,-1]$ negative z-direction.

If the velocity is not acceptable then the code abandons the $(i, j)^{th}$ contacting pair and moves on to derive a candidate velocity from the $(i, j+1)^{th}$ pair. At the end of the step, if a valid non-zero velocity has not been found, then $\underline{v}_{new}$ will have retained its initial value of zero and the pebble is unable to fall any further into the pebble bed.

The final new velocity calculated in any of Steps 1 to 3 is renormalized according to the tolerance-based prescription which is explained in Section D.1.4.

D.1.4 Tolerance

The initial pebble direction is set to $[0,0,-1]$ (referred to in the code as the gravity vector). This is the pebble direction presumed at every integration step unless contact with other pebbles or the walls forces a different direction or zero (indicating that the pebble cannot move downhill).

The integration time step, Δt, is set to unity within the code and is essentially redundant. The pebble velocity, $\underline{v}_{new}$ (as determined by considering the interaction with any contacting pebbles

and/or the pebble bed walls), is renormalized so that the pebble moves as quickly as possible whilst ensuring that it could not end up overlapping with another pebble or a wall and does not become so small that the movement would be smaller than the problem tolerance. The velocity is renormalized to:

$$\underline{v}_{new}^{renormalised} = \frac{\underline{v}_{new}}{\left|\underline{v}_{new}\right|} \cdot \max\left(d - 2r_{peb} ; \varepsilon\right),$$

where ε is the spatial tolerance of the problem and d is the minimum distance between the nth pebble and another pebble or a wall. The minimum distance is the minimum value of the distance from the nth to the ith pebble and the minimum distance to either the inner wall, outer wall or floor of the pebble bed.

This treatment results in pebble movement steps demonstrated in Figure D.1.2 through Figure D.1.5.

Firstly, the pebble will fall, with a step size determined by the distance to the nearest pebble (or wall if applicable) as shown in Figure D.1.2.

Figure D.1.2: Schematic of Pebble Arrangement Showing Time Step Progression
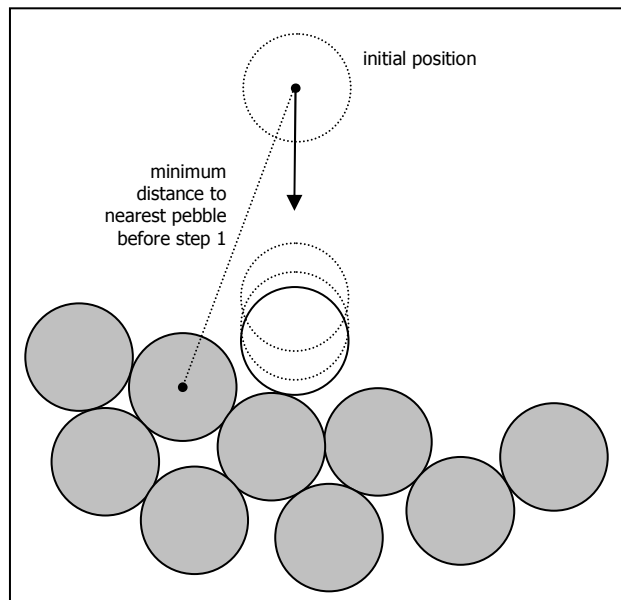
Once the surface-to-surface distance decreased to below the problem tolerance, the step size remains fixed at the tolerance whilst the pebble rolls into a stable position; Figure D.1.3.

Figure D.1.3: Schematic of Pebble Arrangement Showing Pebble Rolling into Stable Position
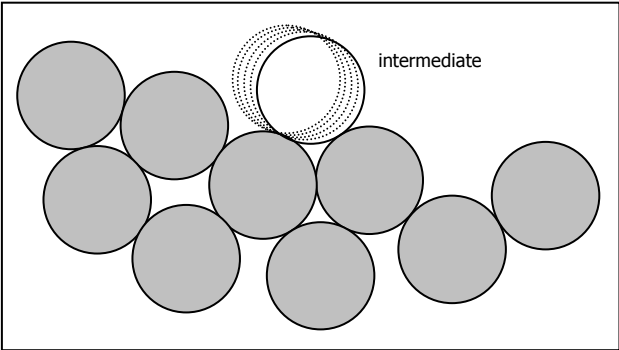
The simulated annealing then attempts to "jostle" the pebble into a more stable final resting place by re-starting the pebble with a random horizontal displacement and fixed upwards displacement; Figure D.1.4.

Figure D.1.4: Schematic of Pebble Arrangement Showing Pebble Rolling into Stable Position
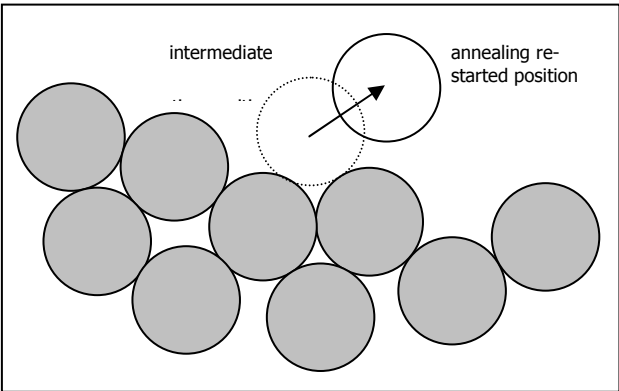
Following the re-started position, the pebble falls and/or falls to achieve a new stable position. If the pebble is now at a lower height than has been achieved before, then the new position will be adopted as the final resting position; Figure D.1.5.

Figure D.1.5: Schematic of Pebble Arrangement Showing Pebble Rolling into Final Position

final resting
position
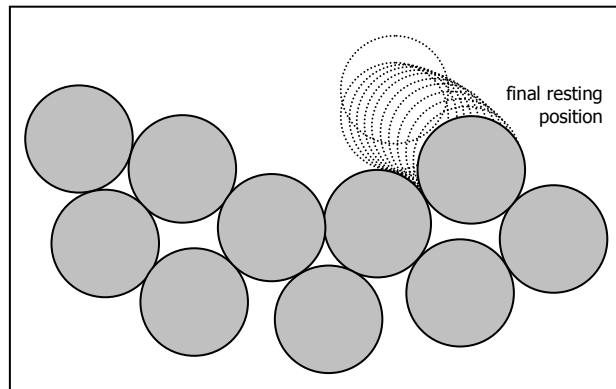
D.2 Validation

The pebbles code is fairly complex, and the integrated-path method leads to a considerable number of individual calculations. Whilst it is conceivable that checking could be performed by manually mimicking the trajectory of a pebble dropped into the bed, the best validation approach lies with validating the resulting pebble distribution produced by the code, i.e., treating the code itself as a "black box" and verifying the quality of the results.

If the code is working correctly, then the pebble arrangement it generates should satisfy the following conditions:

1. The mean (x,y) position of the collection of pebbles should be (0,0), i.e., that the distribution is symmetric in the horizontal plane.

2. The upper surface of the collection should be approximately flat, i.e., the average height of the pebble bed (measured over a suitable region away from the walls to avoid edge effects and of sufficient size to be statistically significant) should not vary with position.

3. The pebbles should lie entirely within the pebble bed (to within the problem tolerance), i.e., that the minimum pebble height $z \geq r_{peb}$; the maximum radial position satisfies $r = \sqrt{x^2 + y^2} \leq r_o - r_{peb}$; and (where applicable), the minimum radial position satisfies $r = \sqrt{x^2 + y^2} \geq r_i + r_{peb}$.

4. The pebbles should overlap each other by up to the problem tolerance.

5. The average packing fraction (measured over a suitable region away from the walls to avoid edge effects and of sufficient size to be statistically significant) should be approximately 0.61, which is the experimentally-derived value for a

random collection of spheres (see Reference D.1).

6. That, when dropped onto a layer of pebbles specifically placed into a close packed configuration (see Section D.2.3 of this Appendix), that the pebbles fall into the local minima in the surface to enable the close packed arrangement to continue in the subsequent layers.

Conditions 1 and 2 are concerned with the quality of the random numbers and the azimuthal symmetry of the problem.

Conditions 3 and 4 validate the pebble contact methods used – if the approach failed then this would most likely result in one or more pebbles which: are either not in contact with each other and the walls and/or overlap by more than the tolerance and/or do not lie completely within the pebble bed.

Condition 5 validates the pebble contact method including the simulated annealing used to overcome the simplifications in which pebbles are frozen into position once they have finished falling, and the assumption that a pebble always falls downhill. This condition is unlikely to be satisfied perfectly, since the quality of the annealing will not be perfect. A further demonstration is therefore required to show that the pebble contact method successfully allows a pebble to reach a local minimum.

Condition 6 tests whether or not pebbles dropped onto a layer in which the pebbles are already in a close packed configuration, are able to successfully enter the correct close packing positions in the subsequent layers.

Together, if the solution can satisfy all of these six conditions, then it is argued that, regardless of the method used, the resulting pebble arrangement is a valid, randomly-packed collection of touching spheres.

The next five sections describe the validation that was performed on the program that was developed to generate a random collection of pebbles.

D.2.1 Cylindrical Domain

133,000 pebbles were randomly dropped into a cylindrical bed of radius 1.85 m. A computational tolerance of 3×10^{-5} m was used (i.e., 0.1% of the pebble radius). Assuming an ideal packing fraction of ~0.61, this results in a depth of ~2.3 m of pebbles and is designed to allow a "shoebox" of randomly-packed pebbles to be extracted from deep within the core as shown in Figure D.2.1. The shoebox, assumed to be of side 0.3 m (5 pebble diameters), can have its centre located 1.85 m from both the outer wall and the floor of the reactor, whilst lying ~0.45 m from the upper surface. The ~0.45 m (~7.5 pebble diameters) should be sufficiently far from the upper surface to be certain that the shoebox is filled. The 1.85 m from the walls (~38 pebble diameters) should be more than sufficient to be free from edge-effects.

Figure D.2.1: Cylindrical Domain Filled with 133,000 pebbles

cylindrical bed (viewed from the side), randomly filled with 133,000 pebbles of 0.03 m radius (not drawn to scale)
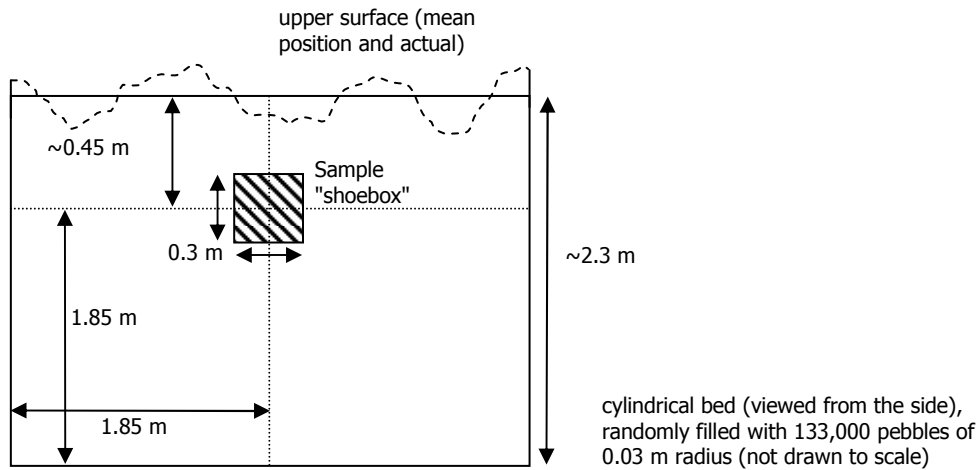
Figure D.2.2 plots the positions of the pebble centers and clearly show that the pebbles lie (within the tolerance) within the bounds of the pebble bed and do not overlap by more than the tolerance (i.e., that the minimum centre-centre distance from a pebble to its nearest neighbor lies between $2r_{peb} - \varepsilon$ and $2r_{peb}$, which is 0.05997−0.06 m in this case).

Figure D.2.2: Various Metrics for Cylindrical Domain of Randomly Packed Pebbles
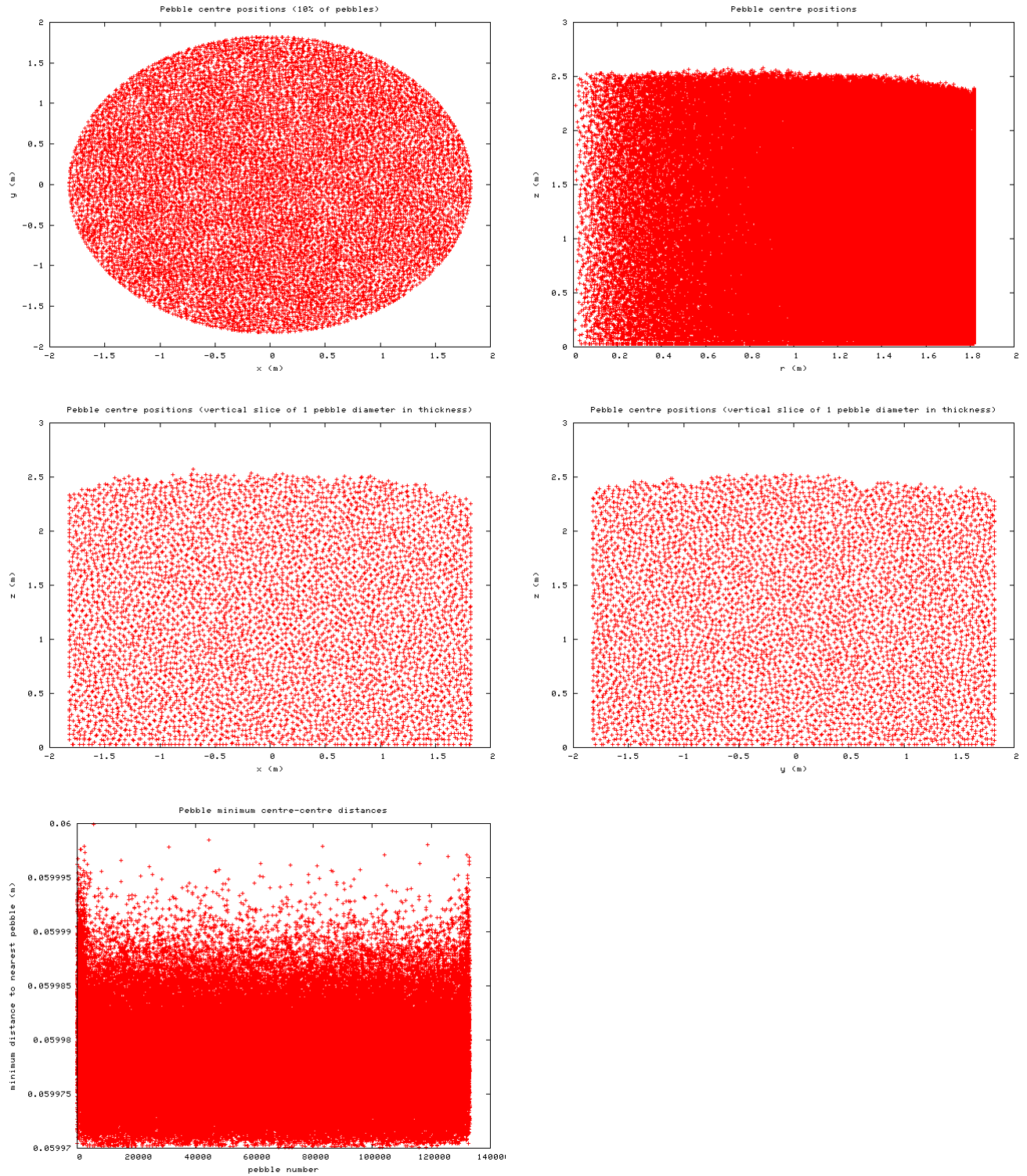
Interestingly, there appears to be a slight edge effect in the upper surface of the pebble bed, with a slight downward slope in the surface towards the edges of the cylinder. This is only apparent in the outer ~0.5 m of the cylinder – the centre of the bed appears (within the statistical variation) to be a level surface.

The packing fraction in the sample shoebox located at (0, 0, 1.85) m with side 0.3 m is 0.591. This was calculated by simply counting the number of pebble centers located within the shoebox volume and estimating the packing fraction from:

$$\varphi \approx \frac{4N_{centres}\pi r_{peb}^3}{3L^3} \; .$$

Where $N_{centres}$ is the number of pebble centers in the shoebox and L is length of the side of the shoebox.

To obtain a value based on better statistics and drawn from several different shoeboxes, packing fractions have been calculated for eight shoeboxes located at (±0.35, ±0.35, 1.30±0.35)m each of side 0.7 m. The sides of the shoeboxes remain at least 10 pebble diameters (0.6 m) from the floor and ~14 diameters from the outer wall, which should still be more than enough to eliminate edge effects. The top of the shoeboxes are all also at least 5 diameters below the upper surface of the bed, which ensures they are properly filled with pebbles. The measured packing fractions are shown in Table D.2.1.

Table D.2.1: Measured Packing Fractions at Various Locations in the Cylindrical Domain

position	measured packing fraction	mean packing fraction
(−0.35, −0.35, +0.95)	0.57802	0.5814 ± 0.0019
(+0.35, −0.35, +0.95)	0.58659	
(−0.35, +0.35, +0.95)	0.57967	
(+0.35, +0.35, +0.95)	0.58131	
(−0.35, −0.35, +1.65)	0.58461	0.5810 ± 0.0013
(+0.35, −0.35, +1.65)	0.58131	
(−0.35, +0.35, +1.65)	0.57868	
(+0.35, +0.35, +1.65)	0.57934	

The packing fraction produced by the code, as measured over all 8 shoeboxes in the two datasets, is 0.5812 ± 0.0011. This is slightly below the 0.61 measured experimentally (Reference D.1), but is close enough to demonstrate the code is replicating random packing well.

D.2.2 Annular Domain

94,000 pebbles were randomly dropped into an annular bed of inner and outer radii 1.00 and 1.85 m respectively (the dimensions of the South African PBMR design). A computational tolerance of 3×10^{-5} m was used (i.e., 0.1% of the pebble radius). This results in a depth of ~2.3 m of pebbles and will allow a shoebox of pebbles to be extracted from a position 1.85 m from the bottom of the core and 0.425 m from both the inner and outer walls of the annulus, as shown in Figure D.2.3. It also allows the packing fraction to be carefully examined in a model based on the PBMR dimensions.

Figure D.2.3: Annular Domain Filled with 94,000 pebbles
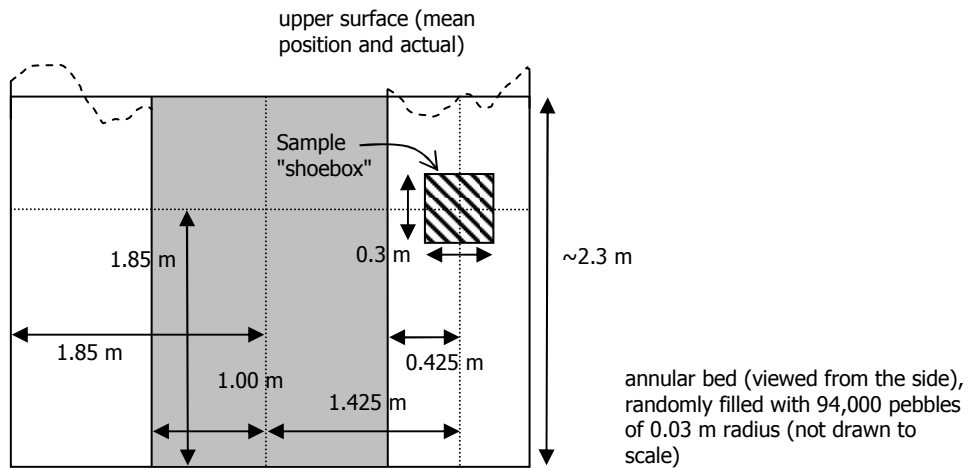
Figure D.2.4 plots the positions of the pebble centers and clearly show that the pebbles lie (within the tolerance) within the bounds of the pebble bed and do not overlap by more than the tolerance (i.e., that the minimum centre-centre distance from a pebble to its nearest neighbor lies between $2r_{peb} - \varepsilon$ and $2r_{peb}$, which is 0.05997 to 0.06 m in this case).

Figure D.2.4: Various Metrics for Annular Domain of Randomly Packed Pebbles
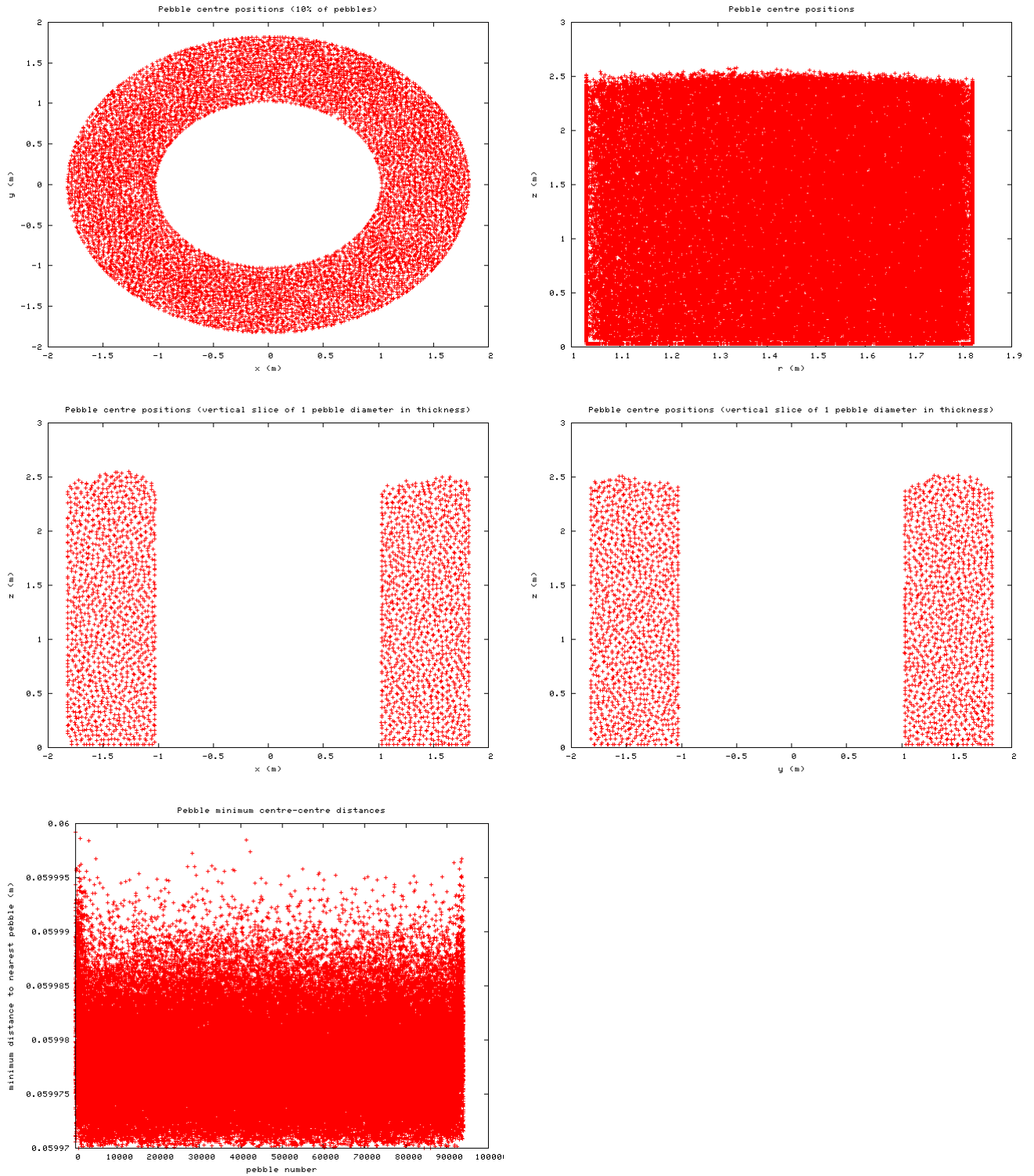
The packing fraction was determined from twelve different shoeboxes of side 0.25 m. The outside of the shoeboxes lie ~5 pebble diameters (0.275 m) from the walls and the bottoms lie at least 21 diameters from the floor. The top of the shoeboxes are at 5 diameters below the upper surface of the bed, which ensures they are properly filled with pebbles. The measured packing fractions are shown in Table D.2.2.

Table D.2.2: Measured Packing Fractions at Various Locations in the Annular Domain

position	measured packing fraction	mean packing fraction
(0, −1.425, +1.375)	0.58630	0.5791 ± 0.0057
(0, +1.425, +1.375)	0.56458	
(−1.425, 0, +1.375)	0.59353	
(+1.425, 0, +1.375)	0.57182	
(0, −1.425, +1.625)	0.59353	0.5772 ± 0.0070
(0, +1.425, +1.625)	0.57182	
(−1.425, 0, +1.625)	0.58630	
(+1.425, 0, +1.625)	0.55734	
(0, −1.425, +1.875)	0.55734	0.5664 ± 0.0110
(0, +1.425, +1.875)	0.53563	
(−1.425, 0, +1.875)	0.59353	
(+1.425, 0, +1.875)	0.57906	

The packing fraction produced by the code, as measured over all 8 shoeboxes in the two datasets, is 0.5742 ± 0.0050. This agrees with the 0.5812 ± 0.0011 measured in the cylindrical data.

D.2.3 Cubic Close Packed Test Variant

This variant has been produced specifically to satisfy the 6th validation test. If a number of pebbles are deliberately placed in the first layer of a face-centered cubic (FCC) lattice (refer to Section D.2.5 of this Appendix), then any pebbles falling onto this arrangement must either settle in the close-packed positions on the next layer up, or they must fall off the edge of the arrangement and land on the base of the bed. Pebbles subsequently falling onto the second layer should again settle in the close-packed positions and the FCC arrangement should continue to grow.

In the test case, the PEBS code was modified to pre-place 25 pebbles in the first layer of the face centered cubic lattice (described in Section D.2.5 of this Appendix), as shown in Figure D.2.5.

Figure D.2.5: Twenty Five Pre-Placed Pebbles in the First Layer of the Face Centered Cubic Lattice
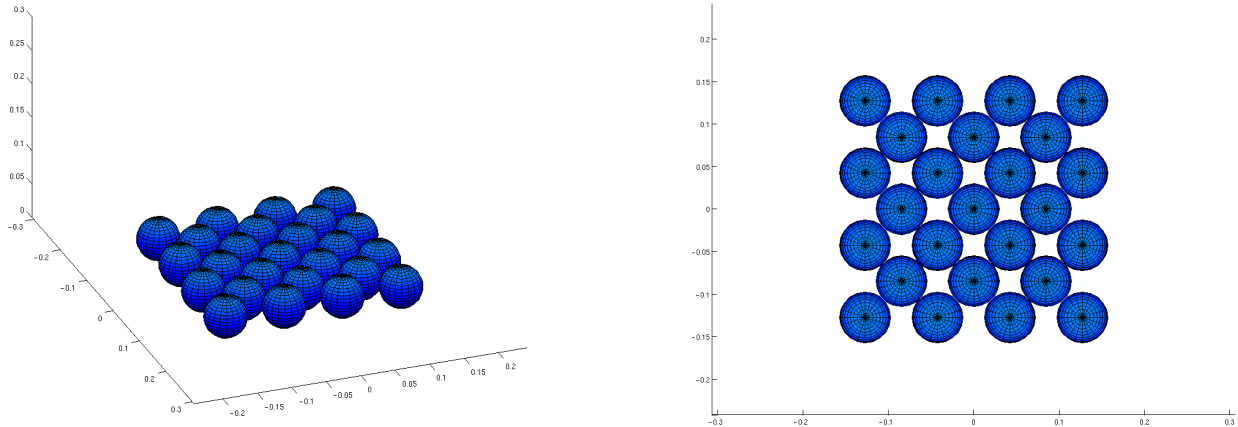
A further 75 pebbles (*i.e.,* 100 in total) were then dropped onto the centre of the arrangement (the code was modified to drop the pebbles randomly within 1 pebble radius of the centre of the bed) as shown in Figure D.2.6. A very high computational tolerance of 10^{-7} m was used:

Figure D.2.6: Arrangement of Pebbles after 75 Additional Pebbles are Dropped
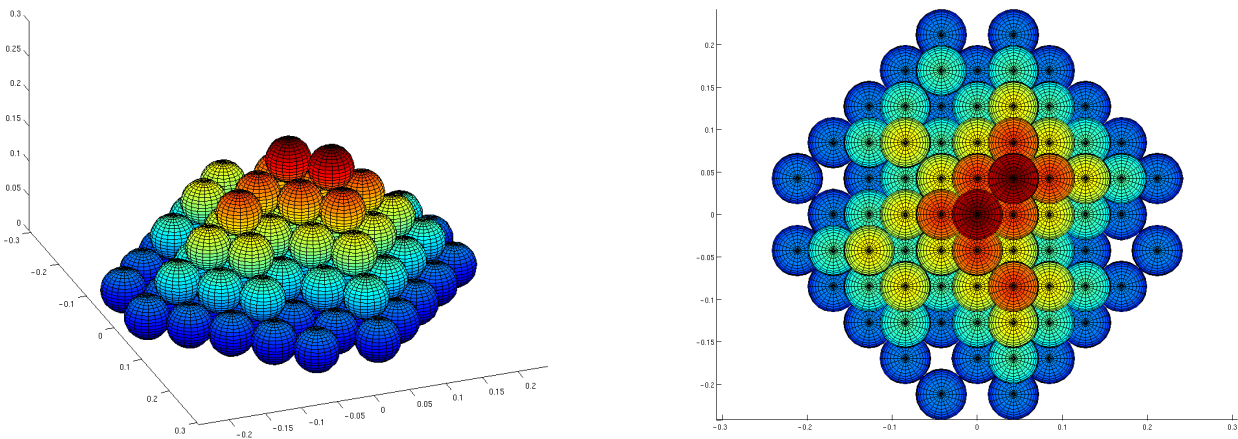
The figure shows the arrangement after a further 75 pebbles were randomly dropped onto the arrangement by the code. The close-packing arrangement clearly continues to grow as expected. In fact, pebbles which roll off the original 25-pebble arrangement continue to grow

the close-packed structure horizontally. This is also to be expected, since the pebbles are channeled into the minima in the surface and roll off the edge of the arrangement straight into another FCC lattice position on the floor of the pebble bed. Annealing has no effect since, once on the floor, the vertical position can be reduced no further. Consider a pebble landing as shown in Figure D.2.7 (after, for example, an annealing following an initial landing in a minima close to the central pebble):

Figure D.2.7: Final Position of Pebble Ended on the Floor
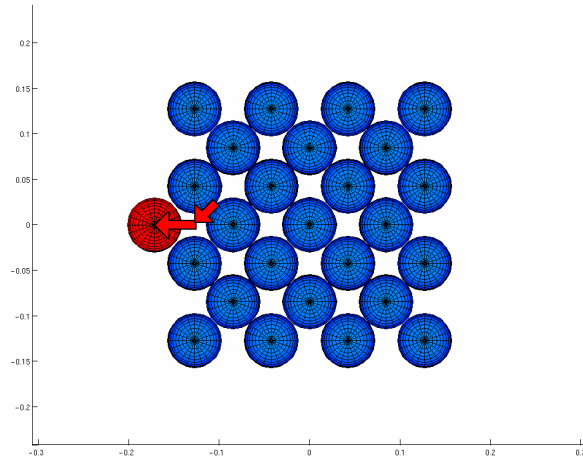
This behavior would not be seen if the pebbles were not dropped from close to the centre of the bed.

Figure D.2.8: Pebble Centre Positions showing Resulting Face Centered Cubic Lattice
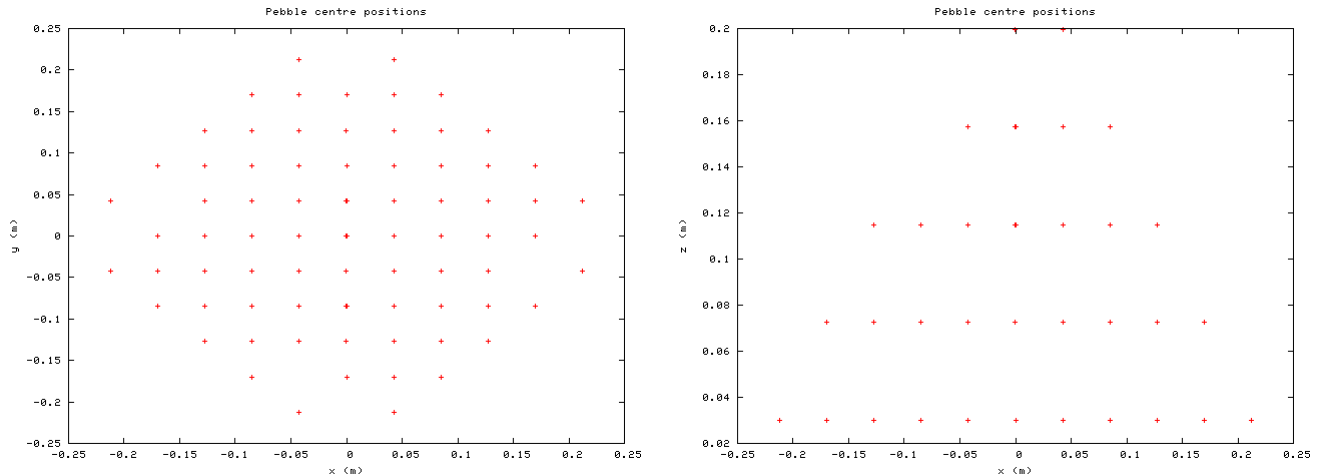
Figure D.2.8 shows that when looking down onto the x-y plane, the pebbles continue to land in the FCC positions shown in Section D.2.5 of this Appendix. Looking from the side, the pebble layers are seen to occur (measured at the centre of the pebbles) at 0.03, 0.0724263, 0.1148527 and 0.1572790 m. These correspond exactly to the theoretical positions which should occur at $(1 + n\sqrt{2})r_{peb}$ for the nth layer. This expression gives heights of: 0.03, 0.0724264, 0.1148528 and 0.1572792 m. As expected, since the pebbles in a layer overlap those beneath by somewhere between 0 and the tolerance (10^{-7} m), the measured positions slowly decrease, by approximately 0.5×10^{-7} m, below the theoretical position, for each layer in height.

This test case clearly shows that the code is successfully placing falling pebbles in the local minima of the surface formed by the pebbles already in the bed. The perfect arrangement is unlikely to continue indefinitely: as the positional errors increase, the packing will return back to a random arrangement.

D.2.4 Hexagonal Close Packing

The unit cell of a hexagonal lattice is as shown below which also gives Cartesian coordinates for the sphere centers. The spheres are packed into an AB arrangement (2-layer repeats) in the vertical $[0,0,1]$ direction.
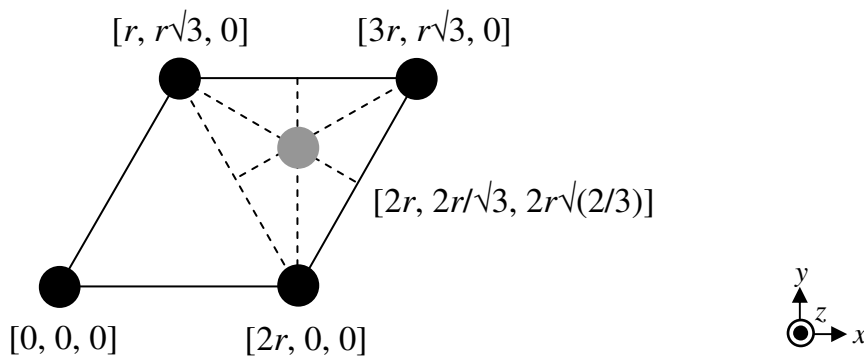
Each unit cell contains the volume of two spheres, leading to the close-packed packing fraction of:

$$\frac{V_{spheres}}{V_{cell}} = \frac{2 \cdot \frac{4}{3}\pi r^3}{2r \cdot r\sqrt{3} \cdot 4r\sqrt{\frac{2}{3}}} = \frac{\pi}{3\sqrt{2}} \approx 0.74048$$

D.2.5 Face Centered Cubic Close Packing

The face centered cubic lattice is as shown below. The arrangement is of close-packed layers of spheres in an ABC arrangement (3-layer repeats) in the $[1,1,1]$ direction.

[0, 2r√2, 0]   [r√2, 0, r√2]   [2r√2, 2r√2, 0]

[r√2, r√2, 0]

[0, r√2, r√2]   [0, r√2, r√2]

[0, 0, 0]   [r√2, 0, r√2]   [2r√2, 0, 0]
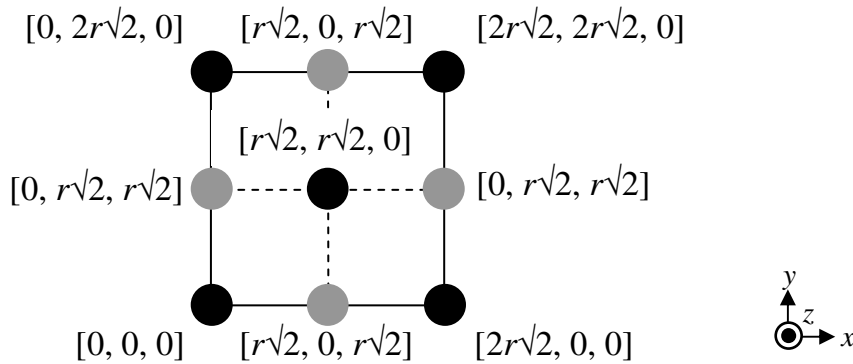
Each unit cell contains the volume of four spheres, leading (again) to the close-packed packing fraction:

$$\frac{V_{spheres}}{V_{cell}} = \frac{4 \cdot \frac{4}{3}\pi r^3}{\left(2r\sqrt{2}\right)^3} = \frac{4 \cdot \frac{4}{3}\pi r^3}{8r^3 2\sqrt{2}} = \frac{\pi}{3\sqrt{2}} \approx 0.74048$$

The results in the previous five sections indicate that the code can successfully generate a random pebble collection.

D.3 Packing Fraction Variation as a Function of Radius for a Cylindrical and an Annular Pebble Bed

An analysis of the pebble bed packing fraction as a function of radial distance away from the outer walls of the bed has been performed. The resulting packing fraction functions are compared to independent numerical and experimental investigations.

D.3.1 Data

The cylindrical data set and annular data set used are described in Sections D.2.1 and D.2.2 respectively where they were used to validate the pebble dropping code.

In both cases, the radial variation in packing fraction will only be calculated using data from an axial position of 0.3 to 2.0 m within the beds. This avoids edge-effects from the flat bottom of the bed and from the irregular surface. These effects are conservatively assumed to extend for 5 pebble diameters (0.3 m). These constraints reduce the effective size of the data sets to 120,371 and 65,004 pebbles respectively.

D.3.2 Packing fraction equations and script

A short Python script has been written to extract the packing fraction data. For a series of 2D cylinders at the radial sampling points, the script calculates the packing fraction from the area of intersection between the pebbles and the plane. Only pebbles with a centre within 1 pebble radius of the cylinder will have an intersection – other pebbles are ignored.

Intersecting area

The area of the saddle shape formed by the intersection of a cylinder and a sphere is not trivial. If the pebble radius is small compared to the cylinder radius then the problem can be approximated to intersection of a flat plane and a sphere.

Figure D.3.1 shows a radial slice through the centre of a pebble at radial position r. In Cartesian coordinates, the pebble is chosen to be at $(x, y, z) = (r, 0, 0)$. The figure shows the intersection (coloured green) with the cylindrical surface at radius R. The pebble is of radius a. Figure D.3.2 shows a axial slice taken at an axial position of z_*. At this height, the line of intersection (coloured red) lies along an arc along the circumference of the cylinder, bounded by the circular outline of the pebble (which has a radius of $\sqrt{a^2 - z_*^2}$).

Figure D.3.1: Radial Slice Through the Centre of the Pebble
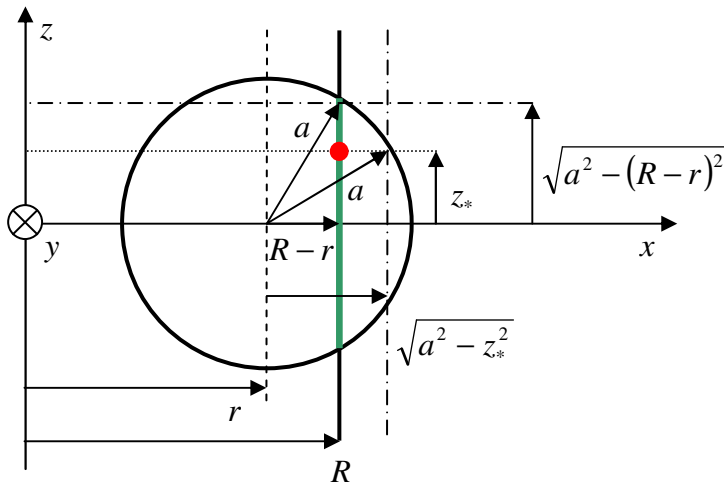
Figure D.3.2: Axial Slice at Height z_*
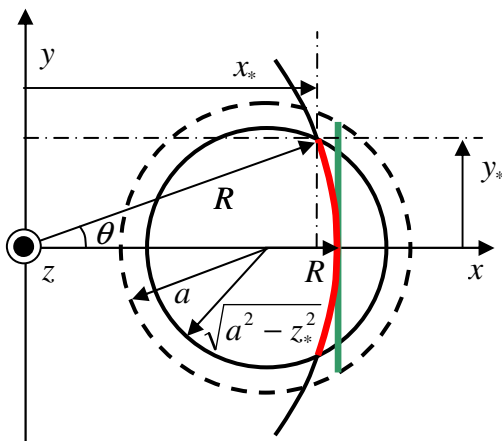
In Figure D.3.2, for a height z_*, the equation for the cylinder is $x^2 + y^2 = R^2$ and the equation for the circular outline of the pebble is $(x-r)^2 + y^2 = a^2 - z_*^2$. The intersection occurs at $(x_*, \pm y_*)$, where $x_* = \dfrac{R^2 + r^2 + z_*^2 - a^2}{2Rr}$. From this, the angle θ can be shown to be:

$$\theta = \cos^{-1}\left[\frac{R^2 + r^2 + z_*^2 - a^2}{2Rr}\right],$$ and the length of the intersecting arc $L(z_*)$ (shown in red) is

therefore given by $L(z_*) = 2R\cos^{-1}\left[\dfrac{R^2 + r^2 + z_*^2 - a^2}{2Rr}\right].$

Integrating the arc lengths between the axial limits of $\pm\sqrt{a^2 - (R-r)^2}$ leads to the following expression for the total intersecting area $A(R, r, a)$:

$$A(R,r,a) \quad = \quad \int_{-\sqrt{a^2-(R-r)^2}}^{\sqrt{a^2-(R-r)^2}} L(z_*)\,dz_* \quad = \quad 2 \int_{0}^{\sqrt{a^2-(R-r)^2}} L(z_*)\,dz_* \quad .$$

$$A(R,r,a) \quad = \quad 4R \int_{0}^{\sqrt{a^2-(R-r)^2}} \cos^{-1}\left[\frac{R^2 + r^2 + z_*^2 - a^2}{2Rr}\right] dz_*$$

Numeric integration
There is no simple analytic solution to this equation and the result is evaluated by the script using Simpson's Rule for numeric integration.

Simpson's Rule, for a function $f(z)$ between the limits of $z = [\alpha, \beta]$ and with n strips (n must be an even number), is:

$$\int_{\alpha}^{\beta} f(z)\,dz \quad \approx \quad \frac{h}{3}\left(f(z_0) + 4\sum_{j=1}^{j=\frac{n}{2}} f(z_{2j-1}) + 2\sum_{j=1}^{j=\frac{n}{2}-1} f(z_{2j}) + f(z_n)\right),$$

or alternatively:

$$\int_{\alpha}^{\beta} f(z)\,dz \quad \approx \quad \frac{h}{3}\left(f(z_0) + 4f(z_1) + 2f(z_2) + 4f(z_3) + ... + f(z_n)\right)$$

where $z_j = \alpha + jh$ for $j = 0, 1, ... n$ and $h = \dfrac{\beta - \alpha}{n}$ is the strip width.

Preliminary investigations indicate that a value of just $n = 100$ results in a calculated packing fraction with an error of $<10^{-4}$.

Limits

It can be shown that, in the limit of $R = r$ and for $R \gg a$, i.e. in which the cylinder tends to a flat plane bisecting the pebble, that the equation for the intersecting area reduces to πa^2, the area of the disc formed by bisecting the sphere:

$$A(R,r,a) = 4R \int_0^{\sqrt{a^2-(R-r)^2}} \cos^{-1} \left[\frac{R^2 + r^2 + z_*^2 - a^2}{2Rr} \right] dz_*$$

Setting $R = r$ leads to:

$$A = 4R \int_0^a \cos^{-1} \left[1 - \frac{a^2 - z_*^2}{2R^2} \right] dz_*$$

Since $\dfrac{a^2 - z_*^2}{2R^2} \ll 1$ we can use $\cos^{-1}[1-\varepsilon] \approx \sqrt{2\varepsilon}$ for small ε (see Figure D.3.3) to simplify this to:

$$A = 4R \int_0^a \sqrt{\left(2 \frac{a^2 - z_*^2}{2R^2} \right)} \, dz_*$$

$$A = 4 \int_0^a \sqrt{\left(a^2 - z_*^2 \right)} \, dz_* = \pi a^2$$

which is as expected.

Figure D.3.3: Geometry to Illustrate cos⁻¹[1-ε]≈(2 ε)⁻½

$$\cos^{-1}\left[\frac{1}{\sqrt{1+\delta^2}} \right] \approx \tan^{-1}\left[\frac{\delta}{1} \right] \approx \delta$$

$$\cos^{-1}\left[1 - \tfrac{1}{2}\delta^2 \right] \approx \delta$$

$$\cos^{-1}\left[1 - \varepsilon \right] \approx \sqrt{2\varepsilon}$$
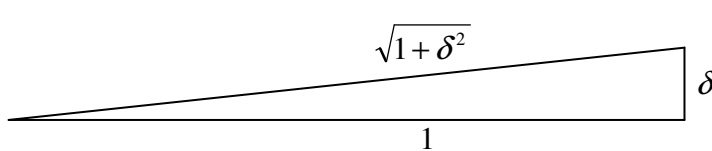
D.3.3 Results

Figure D.3.4 shows a plot of packing fraction measured in the annular pebble bed (green line). The packing fraction was determined using a radial resolution of 1 mm. Within the centre of the beds, i.e. away from the walls, the packing fraction settles around a steady value of ~0.58. The variations observed here indicate the statistical variation from the finite depth of the bed.

Figure D.3.4: Annular Pebble Bed Packing Fraction as a Function of Radius
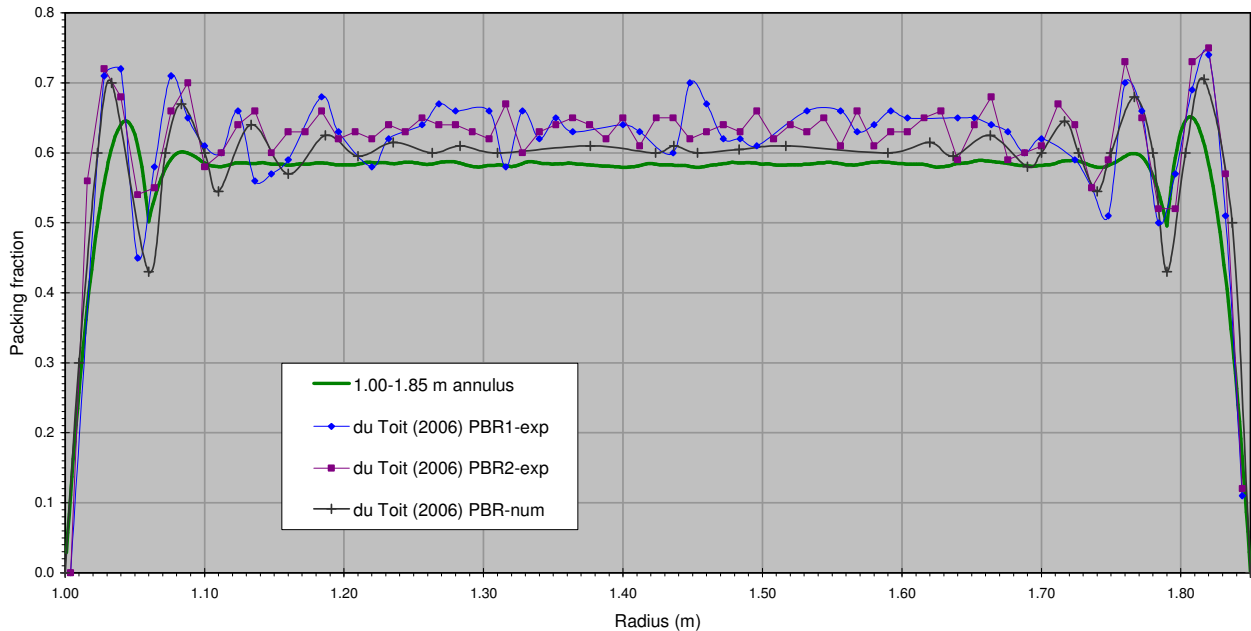
Strong oscillations in the packing fraction are observed close to the walls of the pebble bed. Moving away from a wall, the packing fraction rises sharply from 0 towards a peak at 1 pebble radius away from the wall. The fraction then decreases towards a minimum at ~2 pebble radii from the wall before rising and falling to progressively smaller maxima and minima.

The plot also shows the results (blue diamonds and purple squares) from two experiments which attempted to measure the packing fraction in scale models of the PBMR annulus (refer to Reference D.2 for details). The black crosses indicate the predicted packing fraction from a numerical simulation (again, refer to Reference D.2 for details). Unfortunately, in the absence of the raw data, the results reproduced from Reference D.2 have been manually measured from the plot on p. 3 of the reference. This will be sufficiently accurate (within ~0.01 in packing fraction and ~0.01 m in radial position) for the comparison here.

For the annular pebble bed, the predicted packing fraction compares reasonably well to the experimental data and to the independent numerical simulation. The model has a lower bulk packing fraction of ~0.58, compared to the ~0.63 in the experiments and ~0.61 in the independent numerical simulation. This lower fraction is likely to be due to the limited annealing and approximations in the modelling (particularly the freezing of pebble positions once placed in the bed). The strength of the oscillations near the wall is noticeably stronger in the independent numerical simulation, with both experimental and our model showing weaker variations. If the annular model data are upscaled by 8% (Figure D.3.5) so as to have a similar bulk packing fraction comparable with the experimental data, then the model shows a good fit to the experimentally observed form of the near-wall oscillations.

Figure D.3.6 shows the cylindrical data along with the annular data for comparison. It can be seen that the data agree well, although obviously the cylindrical data extends inwards of the

1.00 m present in the annular bed. The data become noisier toward the centre of the cylinder as the number of pebbles sampled decreases with decreasing radius.

Figure D.3.5: Annular Pebble Bed Packing Fraction as a Function of Radius
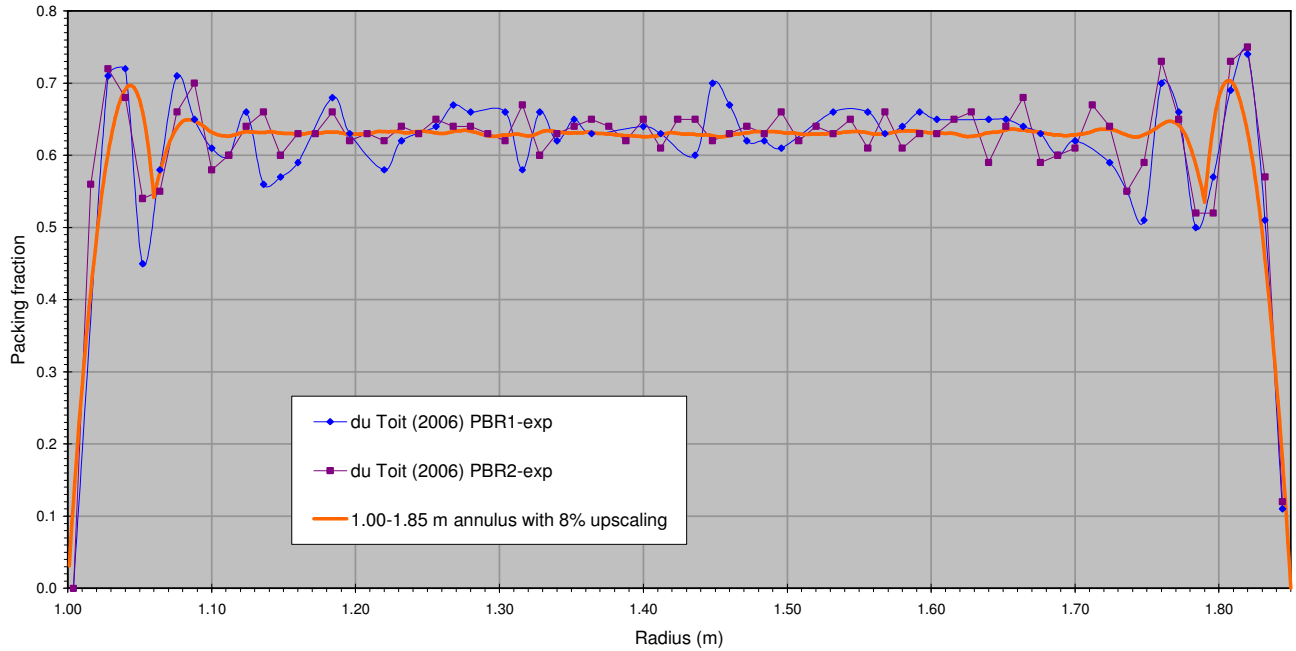
Figure D.3.6: Cylindrical and Annular Pebble Bed Packing Fraction as a Function of Radius
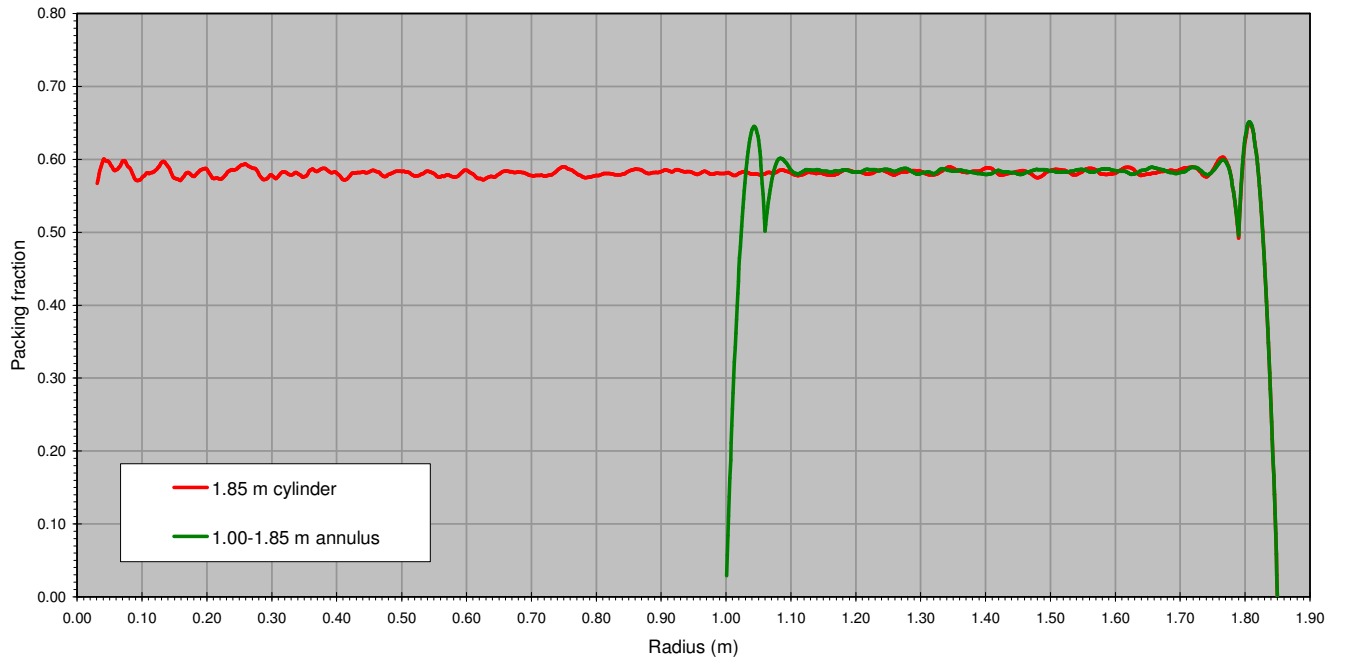
D.4 References

D.1   Benenati R.F., Brosilow C.B., "Void Fraction Distribution in Beds of Spheres", American Institute of Chemical Engineers (A. I. Ch. E.) Journal 8, No 3, p359-361 (1962).

D.2   du Toit, C.G., Analysis of the radial variation in the porosity of annular packed beds, Proceedings of HTR2006, Johannesburg, South Africa (2006 October).

APPENDIX E : CFD MODEL DEVELOPMENT FOR A RANDOM ARRANGEMENT OF PEBBLES

The purpose of this appendix is to document the development of a process for creating the geometry and mesh to represent a fluid within a PBR core. An iterative process of geometry cleanup and meshing was performed to arrive at the final geometry/meshing solution. This appendix is arranged by presenting problems encountered followed by the solutions.

The following issues were encountered during the mesh/geometry generation process:

- How to efficiently create a geometry potentially containing over 100 pebbles.

- How to deal with slightly overlapping or slightly spaced (non-touching) pebbles.

- Mesh elements near the point of contact between pebbles are always highly skewed.

- Limitations of prism layer generation algorithms in GAMBIT/TGRID.

- Some pebbles may not touch but are close causing the generation of highly skewed elements.

- Slicing a set of pebbles with perpendicular symmetry planes can create sharp edged geometry and highly skewed elements.

- Slicing the pebbles at the outlet boundary conditions creates solution divergence and accuracy issues.

- Slicing the pebbles at the inlet creates non-physical quantities in the solution.

- Peak shear stresses located near artificial cutouts.

- Lower than expected packing fraction in model.

E.1 How to Efficiently Create a Geometry Potentially Containing Over 100 Pebbles

ANSYS GAMBIT can be used to create a geometry through either a graphical user interface (GUI) or a text user interface (TUI). It would be possible to create the equivalent geometry through either interface. The GUI interface allows the user to interactively create geometry and visual feedback is provided. This approach is useful for creating a "one off" geometry, but is tedious and time consuming if any variation on the geometry is required.

GAMBIT keeps records of operations in a stack structure, so to modify an early step in the geometry generation process the user must unwind the entire stack to make the modification. The inability to modify intermediate geometry creation steps without recreating all subsequent steps does not lend itself well to parametric studies through the GUI. The only method to create "parametric" models is to record journal files (a list of TUI commands) and feed them into GAMBIT. This still requires the complete recreation of the geometry for any modification; however, limited user input is required.

Due to the random nature of the geometry created for this project and the large number of pebbles desired in the model the only reasonable approach to geometry creation is to use GAMBIT journal files.

The language used to create GAMBIT journal files is documented in References E.1 and E.2.

While the GAMBIT journal files do allow for the definition of variables and various control structures such as loops, they do not have utilities for reading and parsing data. The locations of pebbles in the PBR core are provided in the form of an ASCII text file. As GAMBIT journal files can not read and parse data from external files a PERL wrapper program is created that translates pebble locations into a GAMBIT journal file that will create the pebble geometry. All decision making code is performed in the PERL wrapper and the GAMBIT journal file has no control structures (if and do loops).

Before describing the PERL code for creating the journal files the geometry creation paradigm that is used in GAMBIT is first described.

GAMBIT has the capability of performing geometric Boolean operations, to subtract, add or intersect multiple independent volumes (*i.e.,* constructive solid geometry, CSG). The Boolean operations are only valid if the volumes actually overlap (*i.e.,* two non-touching volumes cannot be subtracted from each other), attempting to do so will result in a failure of the Boolean operation in GAMBIT.

GAMBIT also has the ability to create basic primitives such as spheres and cylinders. The geometry created for this work will use these basic primitives and CSG to form the volume between pebbles in a packed bed. The actual pebbles are not modeled as part of this work only the fluid between them. The following is the general process that is followed for geometry creation.

1. Create spheres representing pebbles: requires the input of the pebble centre in Cartesian coordinates and the pebble diameter (Section 10.2).

2. Create a large volume representing the fluid between the pebbles. The pebble volumes are removed from this.

3. Remove all pebbles that are not touching the large volume as this will produce errors during the Boolean operation.

4. Use the subtraction Boolean operation to remove pebble volumes from the solution domain.

5. Perform additional geometry cleanup.

The PERL program that creates journal files is required to perform the following basic functions:

1. Extract geometric data for the pebbles (Section 10.2).

2. Convert the pebble data into GAMBIT journal file commands that will create pebbles.

3. Based on user input create a GAMBIT journal file command to create the solution domain from which pebbles will be removed.

4. Subtract pebbles from the solution domain volume.

There are several subtleties to this process.

1. Only pebbles that touch the solution domain should be created in GAMBIT. Boolean operations will fail if pebbles do not touch the domain and it will decrease the efficiency of the geometry generation process.

2. It was found that the logic for determining whether pebbles are inside a solution domain becomes somewhat complex in certain areas (*e.g.,* the corners of a rectangular solution domain). Rather than create a detailed logic for selecting pebbles, it is accepted that most pebbles selected on a simple criteria will lie inside the domain and a few may lie outside. An extra step is added to the CSG procedure. First a very large solution domain encompassing all possible pebbles is created. All pebbles are subtracted from this volume. Next the desired solution domain is created and the volume intersecting between it and the existing volume is extracted. This process is relatively simple and maintains the efficiency of the geometry creation process.

This process allows one to create the geometry representing the volume between pebbles in a packed bed with minimal user input. While this process creates a valid geometry it is not always possible to apply a mesh to this geometry.

E.2 How to Deal with Slightly Overlapping or Slightly Spaced Pebbles

The data provided from the geometry developed in Section 10.2 contains the positions of the pebble centers with a small tolerance. This means that touching pebbles do not form a point contact but a very small surface or face contact (shown as Section A-A in Figure E.2.1).

Figure E.2.1: Slightly Overlapping Pebbles
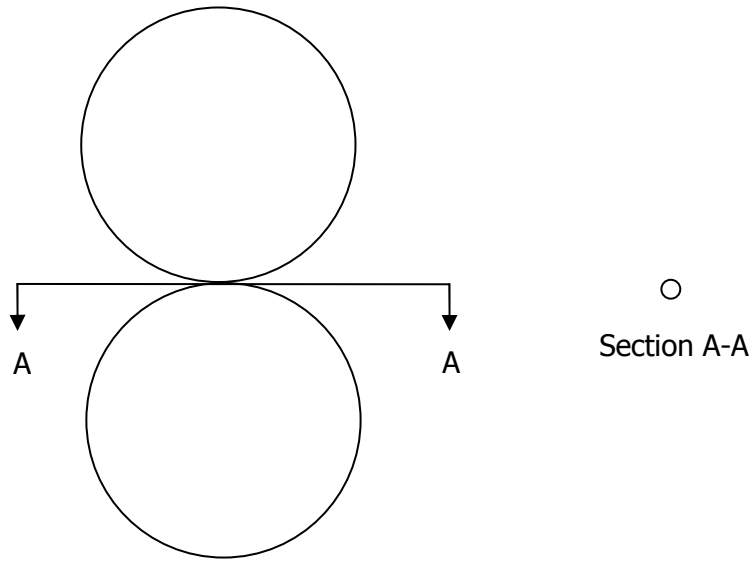
The problem with this face contact is that the mesh resolution must be extremely high to resolve this contact, since the edge of the face must be divided at least 3 times to form a valid surface. If the mesh size is set by the size of this contact the number of elements required becomes extremely high and computational resources will be quickly consumed.

GAMBIT includes a set of tools called size functions. Size functions control the distribution of mesh entities on the geometry. The proximity size function is of particular interest in this situation as it can increase the number of elements when surfaces are close together. For the geometry presented in this work several important parameters for the proximity size function must be set.

Parameter	Description
Maximum Element Size	Maximum size of element that will be set by the size function
Minimum Element Size	Minimum size of element that will be set by the size function
Elements per Gap	Number of elements expected between close surfaces
Growth Rate	Controls the transition between small and large element sizes
PROXIMITY_REFINE_SMALL_GAP	If this flag is on, the proximity algorithm is extended to detect gaps surfaces that approach a distance of zero from each other
PROXIMITY_VIEW_ANGLE	The angle from a face normal in which to search for another surface in close proximity (maximum allowed is 89º)

Though a set of preliminary testing the following notes were constructed regarding these parameters:

- The minimum element size should be set to a size on the scale of the smallest face in the model (contact face in this case).

- As the contact point is approached the maximum number of elements in the gap will reduce to 1 regardless of what this parameter is set to.

- A growth rate of 1.1 was found to create a mesh with a smooth transition.

- The PROXIMITY_REFINE_SMALL_GAP parameter results in meshes that are much smaller than the minimum element size in attempts to fit smaller and smaller elements as the surfaces get closer together. The number of elements added becomes extremely large. The mesh generation time also increases significantly.

- The PROXIMITY_VIEW_ANGLE controls the range over which surface proximity is examined. It was found that the maximum value of 89º produces meshes with a more continuous change in element size than the default value. With lower angles, clustering of elements in unexpected locations was found to occur, and the maximum angle is recommended.

E.3 Mesh Elements near the Point of Contact between Pebbles are Always Highly Skewed

The proximity size function was found to be capable of creating a high quality surface mesh on the touching pebbles. It was found that it is not possible to create a valid volume mesh with this surface mesh. As one approaches the contact face the volume elements are essentially forced between two parallel plates infinitely close together. Attempts to place volume elements on this type of geometry will result in highly skewed elements, which in turn do not allow a stable system of equations to be found for the CFD model. Best efforts must be taken to reduce the number of skewed elements so that a valid solution can be found. Figure E.3.2 shows how the pebble surfaces approach becoming touching parallel plates as the point of contact is approached. Putting finer elements in this region only brings the mesh closer to the parallel plate situation.

Figure E.3.1: Enlargement of Contact Point Between Two Pebbles
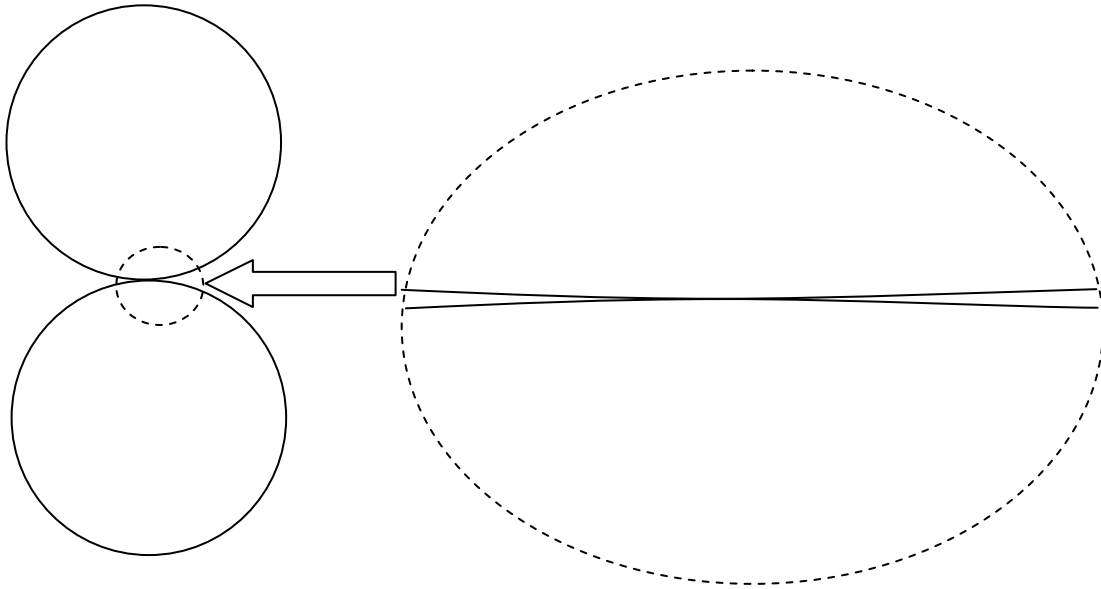
The alternative to making elements smaller in the interface is to make them larger. According to the TGRID user's manual, element skew should be less than 0.75 if possible to be considered a "fair" quality mesh. The definition of skew based on the smallest angle in an element is:

$$skew_{min\_angle} = \frac{60° - (\text{minimum angle in cell in degrees})}{60°}$$

To achieve an element quality of 0.75 the minimum angle in the cell must be greater than 15°. If a single element is to fit into the contact region between two pebbles and a maximum skew of 0.75 is to be maintained the minimum size of such an element can be calculated.

Figure E.3.2 shows the geometry of the contact point.

Figure E.3.2: Geometry for Determining Minimum Element Size to Ensure Cell Angles Larger than 15°
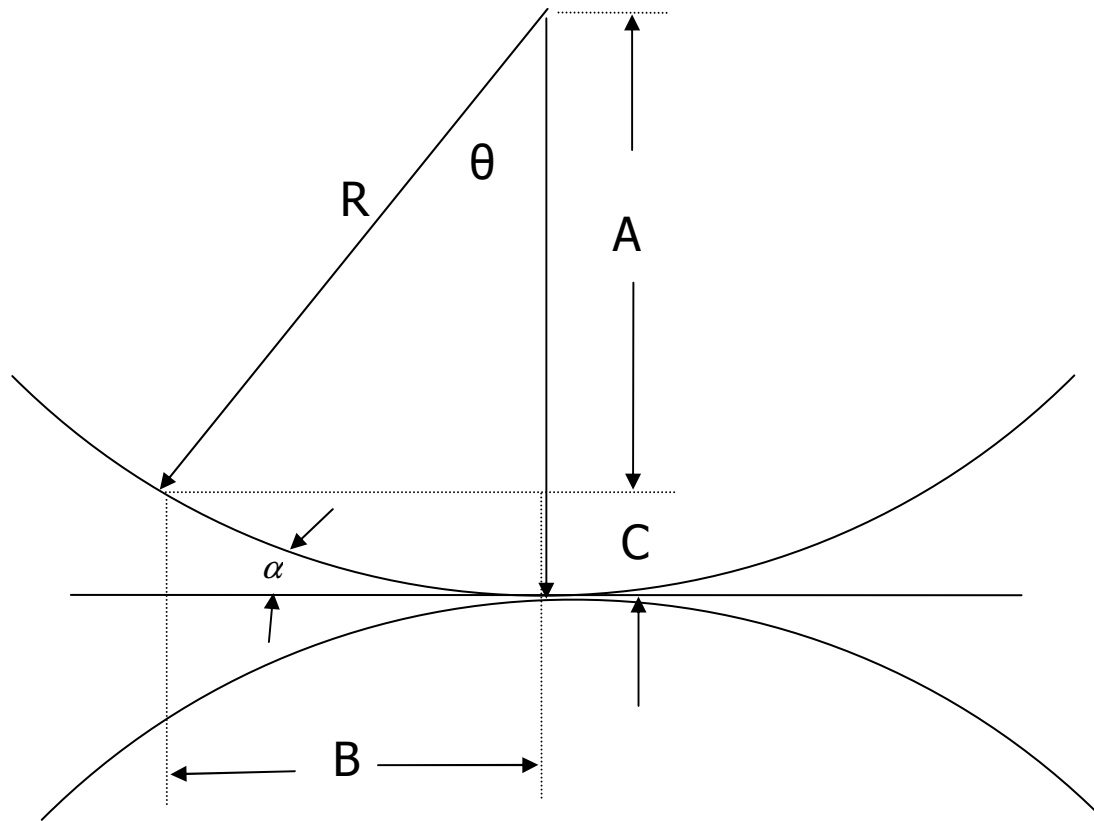
$$A = R\cos(\theta)$$

$$B = R\sin(\theta)$$

$$C = R(1 - \cos(\theta))$$

$$\tan(\alpha) = \frac{C}{B} = \frac{1 - \cos(\theta)}{\sin(\theta)}$$

$$\alpha = 7.5°$$

$$\Rightarrow \theta = 15.1°$$

$$B = 3cm \cdot \sin(15.1) = 0.78cm$$

An element would be required to have a side length of 0.0078 m. This would result in an extremely coarse mesh on a pebble with a radius of 0.03 m, which could not be refined to resolve flow details. Transitioning between such a coarse mesh and a finer mesh would be difficult to achieve smoothly over the surface of a pebble, considering that multiple contact points can exist on any given pebble. This approach was not pursued further due to these limitations.

E.4 Limitations of Prism Layer Generation Algorithms in GAMBIT/TGRID

Setting the problem of tetrahedral mesh generation aside for the moment a second type of meshing problem was examined. Since the purpose of this work is to estimate the shear stress/heat transfer rate at the surface of a pebble, steps must be taken to ensure the mesh is suitable for the estimation of these parameters. Heat flux at a surface is found using Fourier's law (due to the no slip condition there is no fluid motion at a wall, hence only conduction applies) and shear stress is found using Newton's law of viscosity. The simplified versions of these laws are shown below.

$$q = -k \frac{dT}{dn}\bigg|_{surface}$$

$$\tau = \mu \frac{dV_{tangent}}{dn}\bigg|_{surface}$$

The key point to note is that the heat flux, q, or the shear stress, τ, are determined based on the derivative of velocity or temperature at the surface. In order to achieve reasonable estimates of these quantities the near wall gradients must be solved accurately. If tetrahedral elements are used to mesh the near wall region there must either be an extremely large number of elements or the elements must be very skewed. The solution to this problem is to introduce a number of extruded prismatic layers on the surface of the pebbles. The extruded layers may have high aspect ratios since they are well aligned with the flow (tangent to the surface) in the near wall region. The introduction of prism elements greatly reduces the number of elements required to resolve near wall gradients.

In addition, introducing prismatic cells on the surface of the pebble eliminates false diffusion of momentum and energy that would be associated with tetrahedral cells.

The initial attempt to apply prismatic layers to all surfaces in the model resulted in a mesh containing overlapping volumes, which have no physical meaning, as shown in the following image.

Figure E.4.1: Example of Prism Layers Overlapping
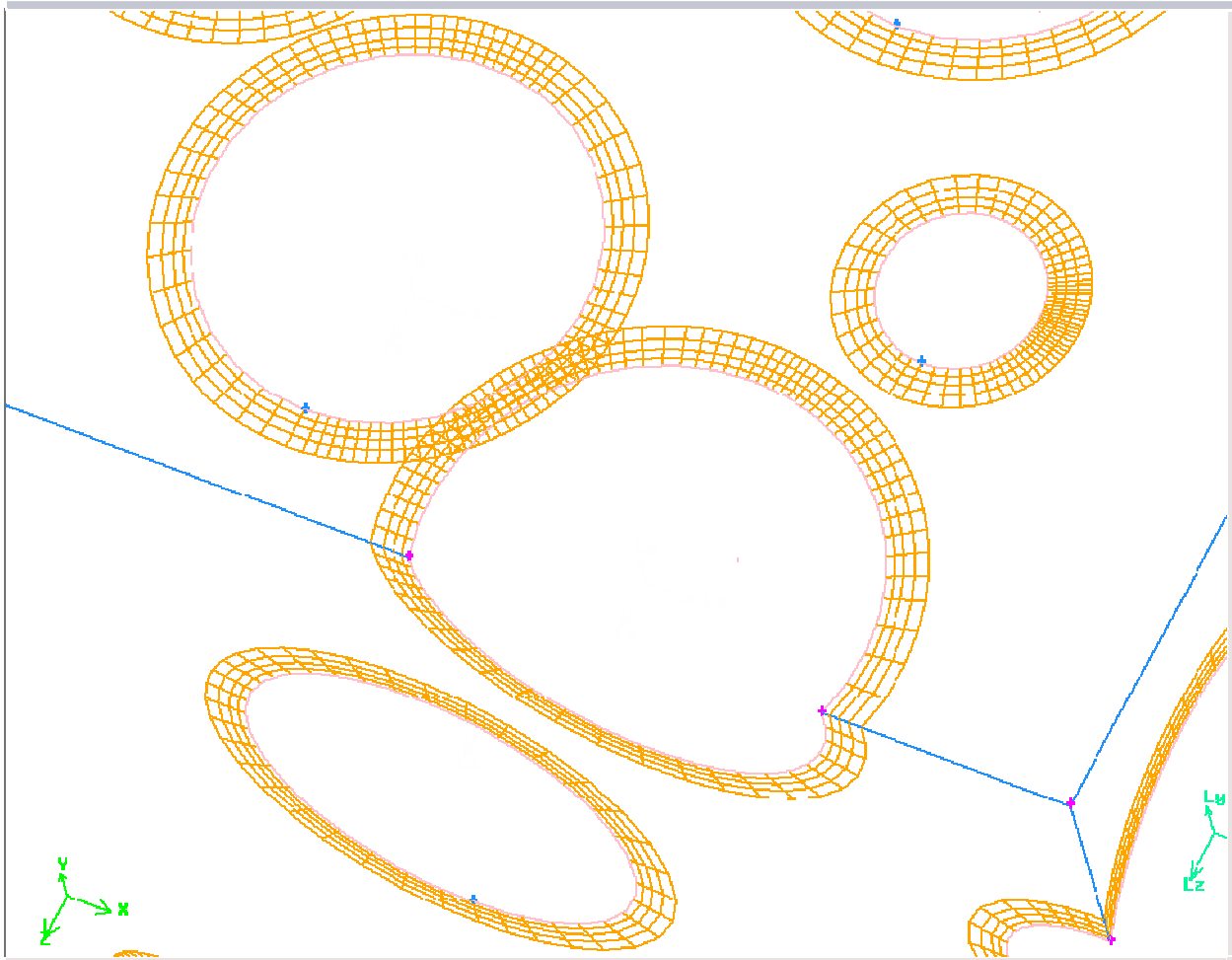
FLUENT includes an algorithm for detecting the collision of prism layers, which was enabled in the above setup. However it was found that the prism layers had a tendency to overlap, as shown in Figure E.4.1. After contacting ANSYS technical support it was discovered that prism layer collision of the external surfaces of objects is not supported, only internal (3D) prism layer detection is available.

There was limited success in placing prismatic layers on pebbles that were entirely internal to the solution domain. Figure E.4.2 and Figure E.4.3 show prism layers applied to the surface of a pebble near the point of contact.

Figure E.4.2: Prism Layers Applied to the Surface of a Pebble Near the Point of Contact
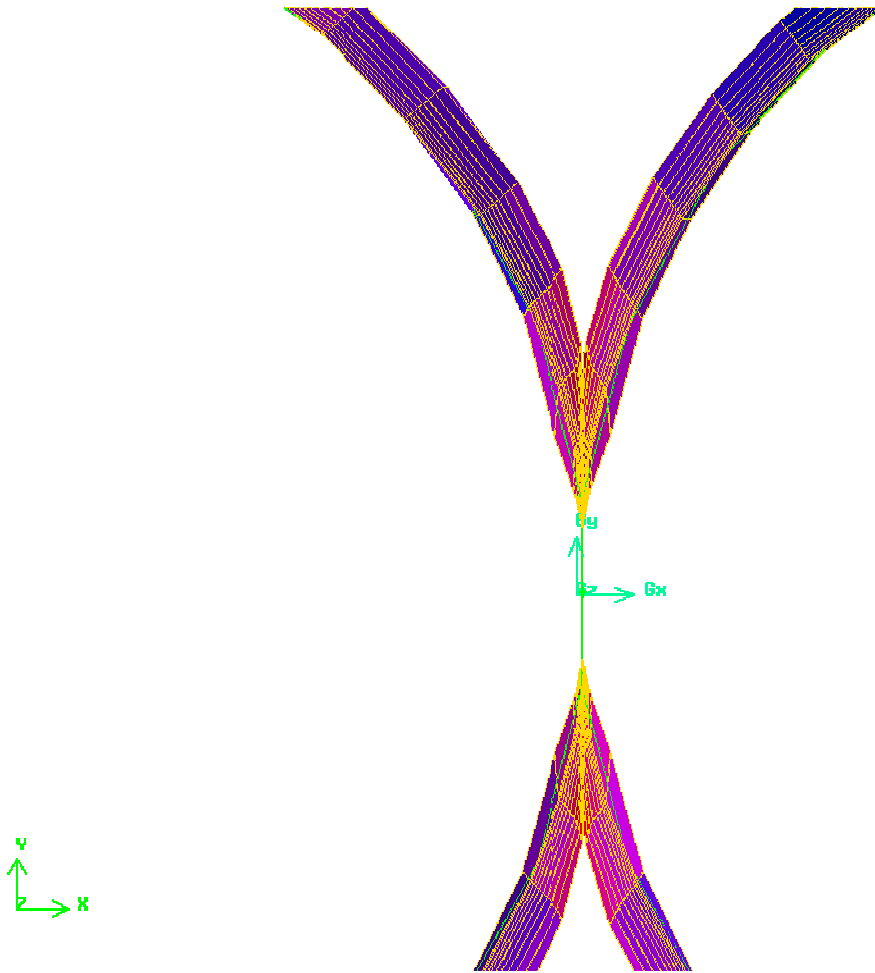
Figure E.4.3: Close-up of Prism Layers Applied to the Surface of a Pebble Near the Point of Contact
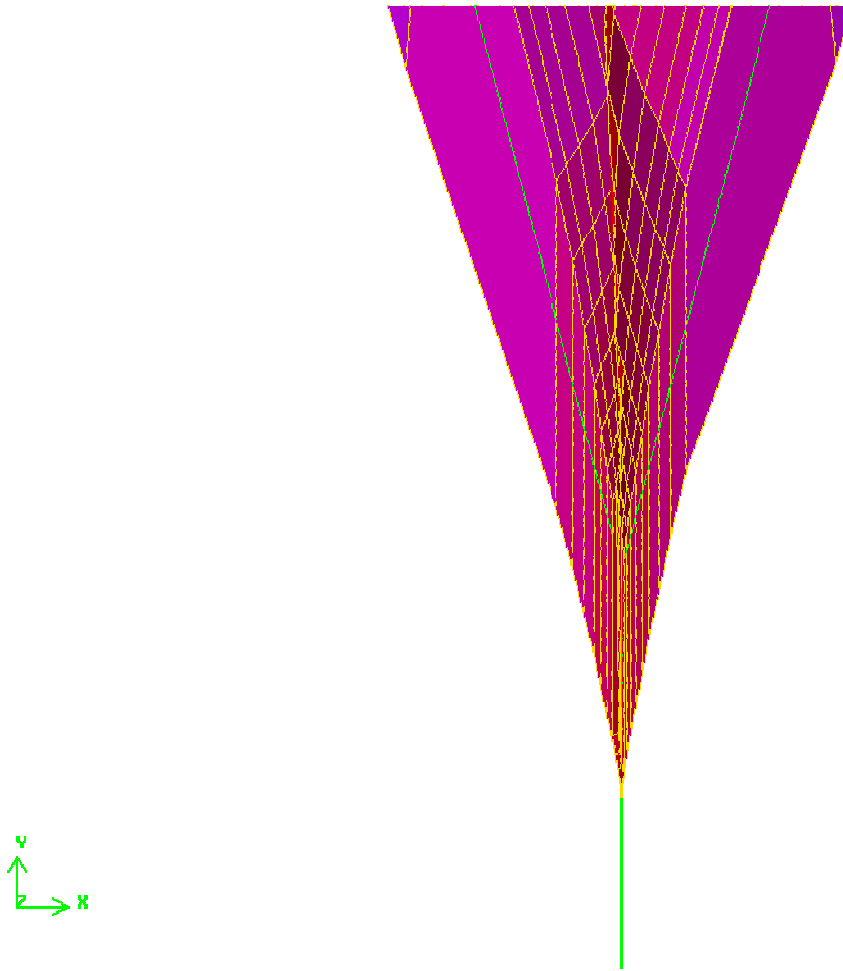
In the situation shown in Figure E.4.3 the prism layers do not overlap but elements located on the front where the prism layers collide and the elements next to the contact face have extremely high skew angles.

If the overlap between the pebbles is increased to reduce the angle at the contact point a more reasonable mesh is produced, as shown in Figure E.4.4. The pebble radii must be increased significantly to allow this, so this option was abandoned.

Figure E.4.4: Increased Overlap between Pebbles to Reduce the Angle at the Contact Point
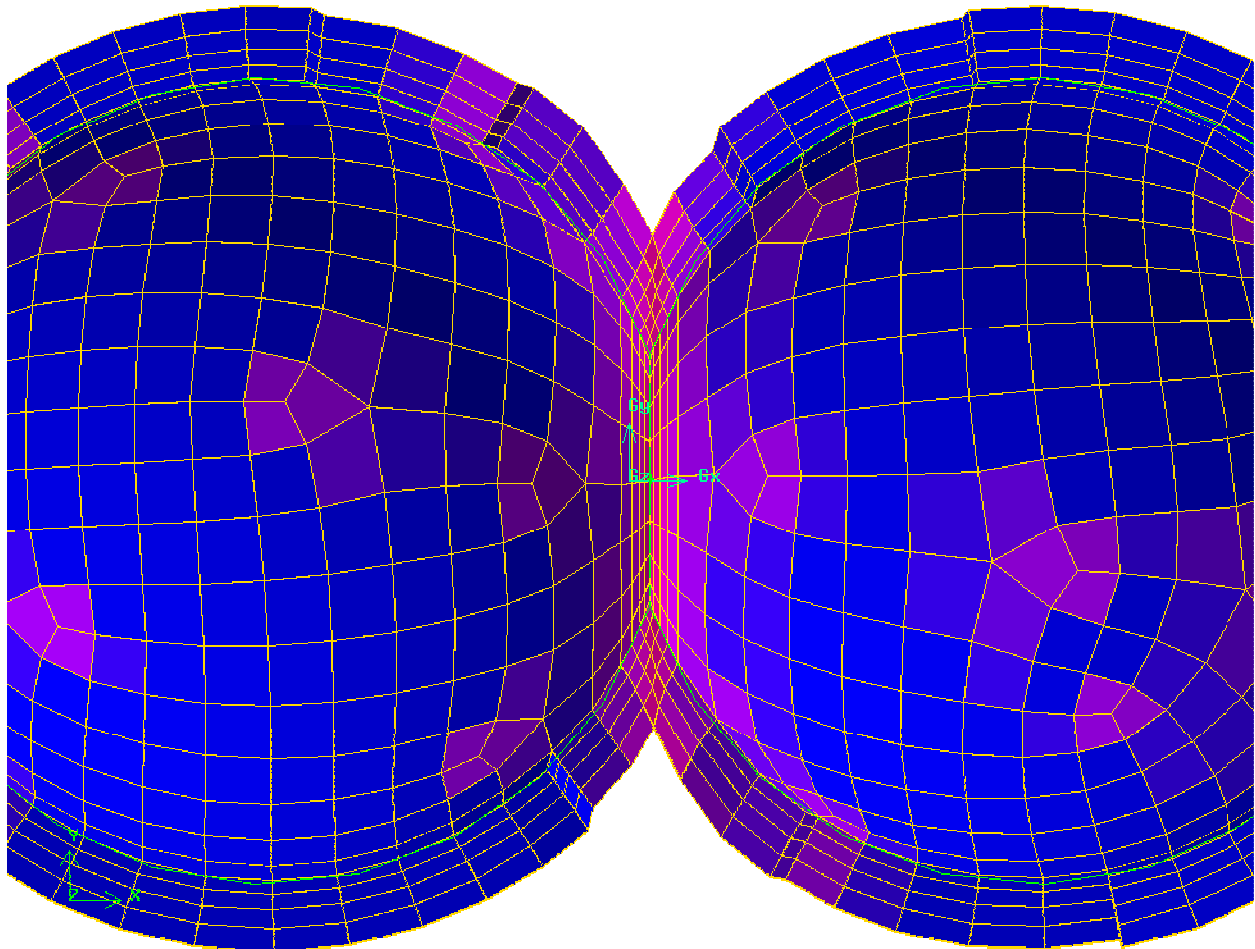
The volume meshing program TGRID has the ability to stop prism layers from going into sharp angled corners. This keeps the prism layers from becoming extremely skewed. TGRID was used to produce the meshes shown in Figure E.4.5.

Figure E.4.5: Meshes Generated using TGRID
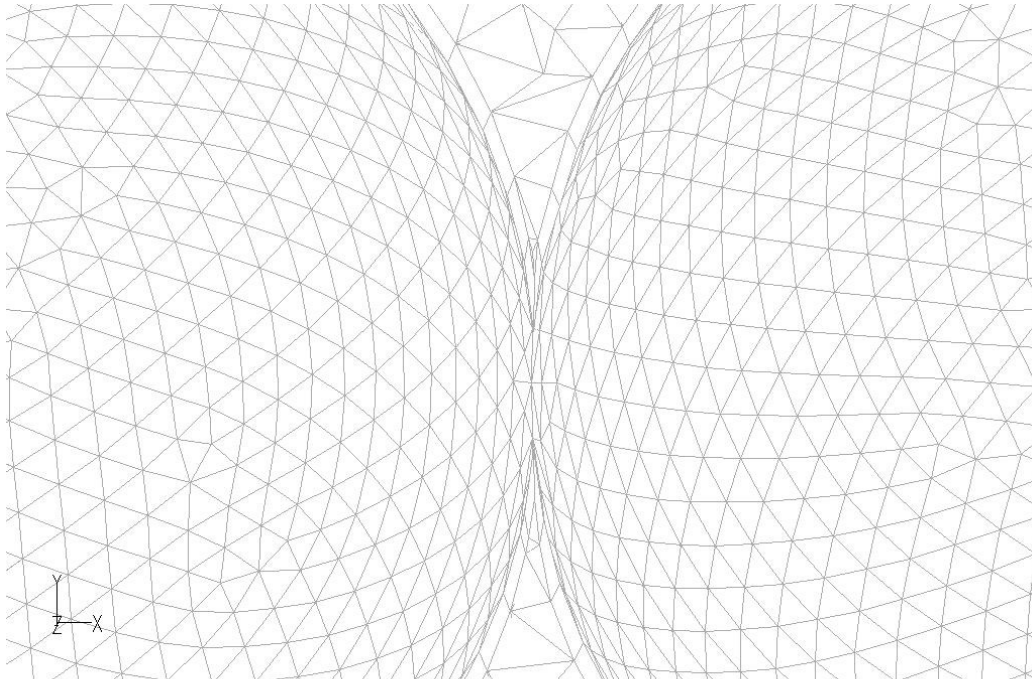
Mesh   Apr 04, 2008
Restrictions: z-range   TGrid 4.0 (3D)
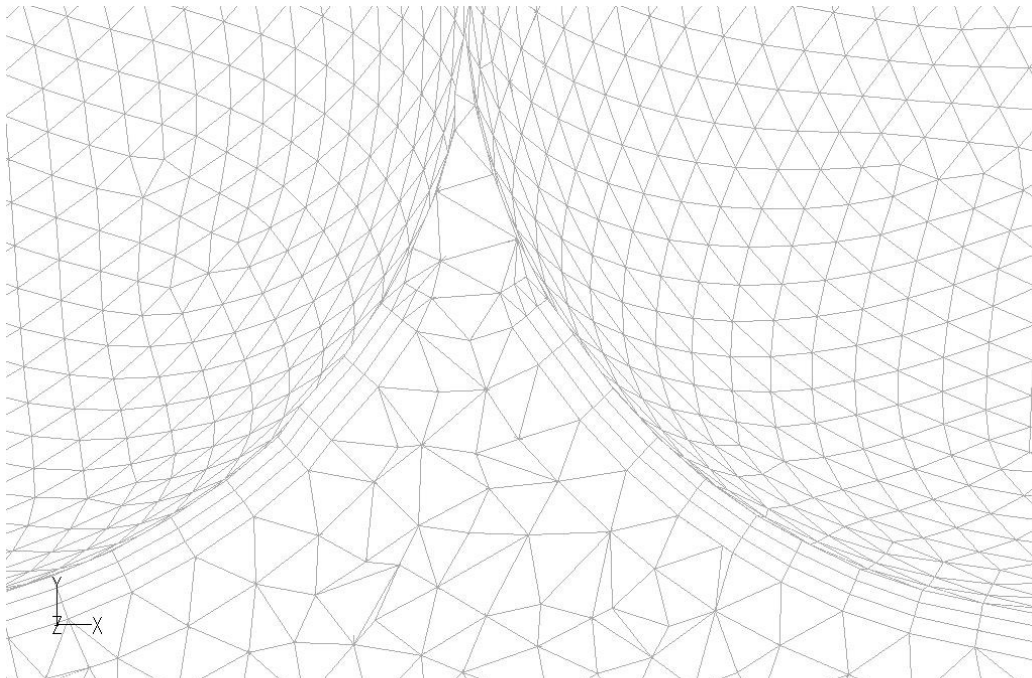
Mesh   Apr 04, 2008
Restrictions: z-range   TGrid 4.0 (3D)

This feature works as expected allowing a high quality prism layer to be created. The remaining issues are that a series of skewed element result where the prism layer ends and highly skewed tetrahedral still exist next to the point of contact between the pebbles.

E.5   Some Pebbles May Not Touch but Are Very Close to Each Other

The next point to note is that some pebbles inside the pebble assembly may be located very close together but not touching. In this case the GAMBIT prism layer (and TGRID) collision detection algorithm does not work as expected allowing the layers to overlap as shown in Figure E.5.1.

Figure E.5.1: Failure of GAMBIT Prism Layer Collision Detection Algorithm
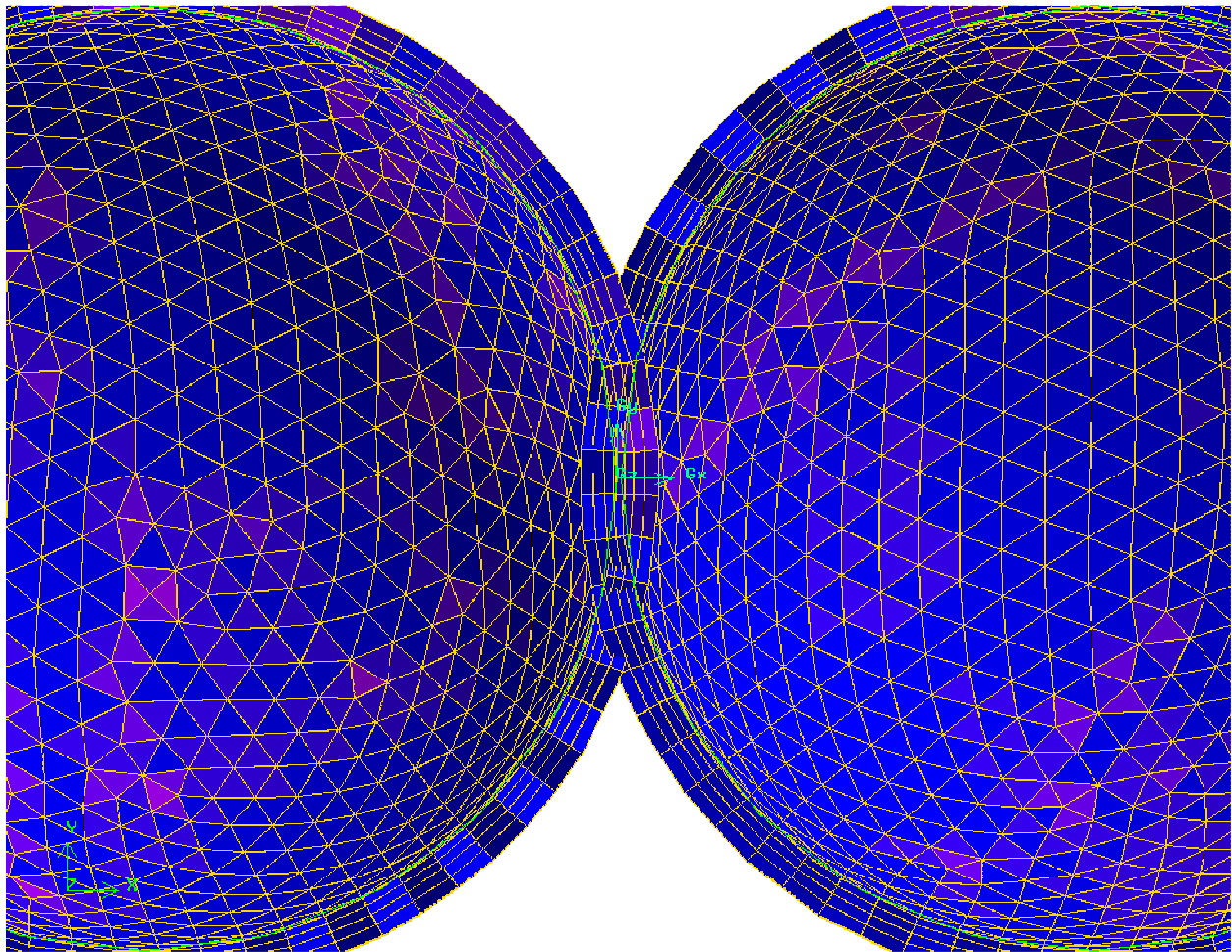
This limitation of the prism layer generation algorithm was noted and taken into consideration in the creation of subsequent meshes.

E.6 Mesh Elements near the Point of Contact between Pebbles are Always Highly Skewed (Revisited)

The problem of skewed elements at the point of contact is a persistent problem to this point so possible methodologies to eliminate this problem were considered. The following options were conceived:

- Reduce the pebble diameters so that the pebbles do not touch and a point of contact does not exist between any two pebbles.

- Maintain full sized pebbles but create a separately meshed region for the contact point.

- Maintain full sized pebbles but remove a small region around the contact point so that sharp angles are removed.

Each of these alternatives has pros and cons which are discussed below.

Reduction of Pebble Diameters

The first approach was to reduce the diameters of the pebbles such that they do not have a contact surface (*i.e.,* a very small, yet finite space exists between pebbles). This approach involved the following two setups:

1. Use a slightly reduced pebble diameter such that the pebbles never touch, but do come within a "hair" of each other. Pebble radius = 0.02975m, 2.5% volume reduction.

2. Use a more reduced pebble diameter such that there is a significant gap between the pebbles. Pebble radius = 0.02925m, 7.3% volume reduction.

The first approach attempted to use the proximity size function with pebbles with a radius of 0.02975m. No prism layers were applied to this situation as the pebbles come very close and the maximum prism layer thickness is extremely small. The results of this mesh generation approach were a valid volume mesh with extremely low quality elements in the small gaps. Attempts to solve flows on this type of mesh resulted in extremely slow convergence and divergence issues.

The next step was to model smaller pebbles (R=0.02925m) that would allow tetrahedral elements near the contact points to have a reasonable size and a low element skew. The approach works producing a high quality mesh on which solutions can generally[1] be found within an acceptable number of iterations. The problem with this method is that it significantly reduces the packing fraction of the model (7.3%) which will have adverse effects on the solution. It was decided that although this approach is reasonable better solutions should be investigated.

---

[1] Divergence issues were encountered in some cases that were unrelated to the elements near the contact points. These issues are discussed later in this appendix.

Plug Cut Out and Meshing of Plugs

Returning to full sized pebbles the next approach considered for dealing with low quality elements near the contact face was to separate a volume of material around the contact face. This separated volume is to have a structured mesh applied to it. This approach was found to produce a more consistent mesh however extremely skewed elements still existed at the contact face

Plug Removal

It was next conceived that it may not be a bad approximation to remove a small amount of fluid from the solution domain near the pebble contacts. This was accomplished by removing a cylindrical volume around the contact points as shown in Figure E.6.1.

Figure E.6.1: Cylindrical Volume Removed around Contact Points
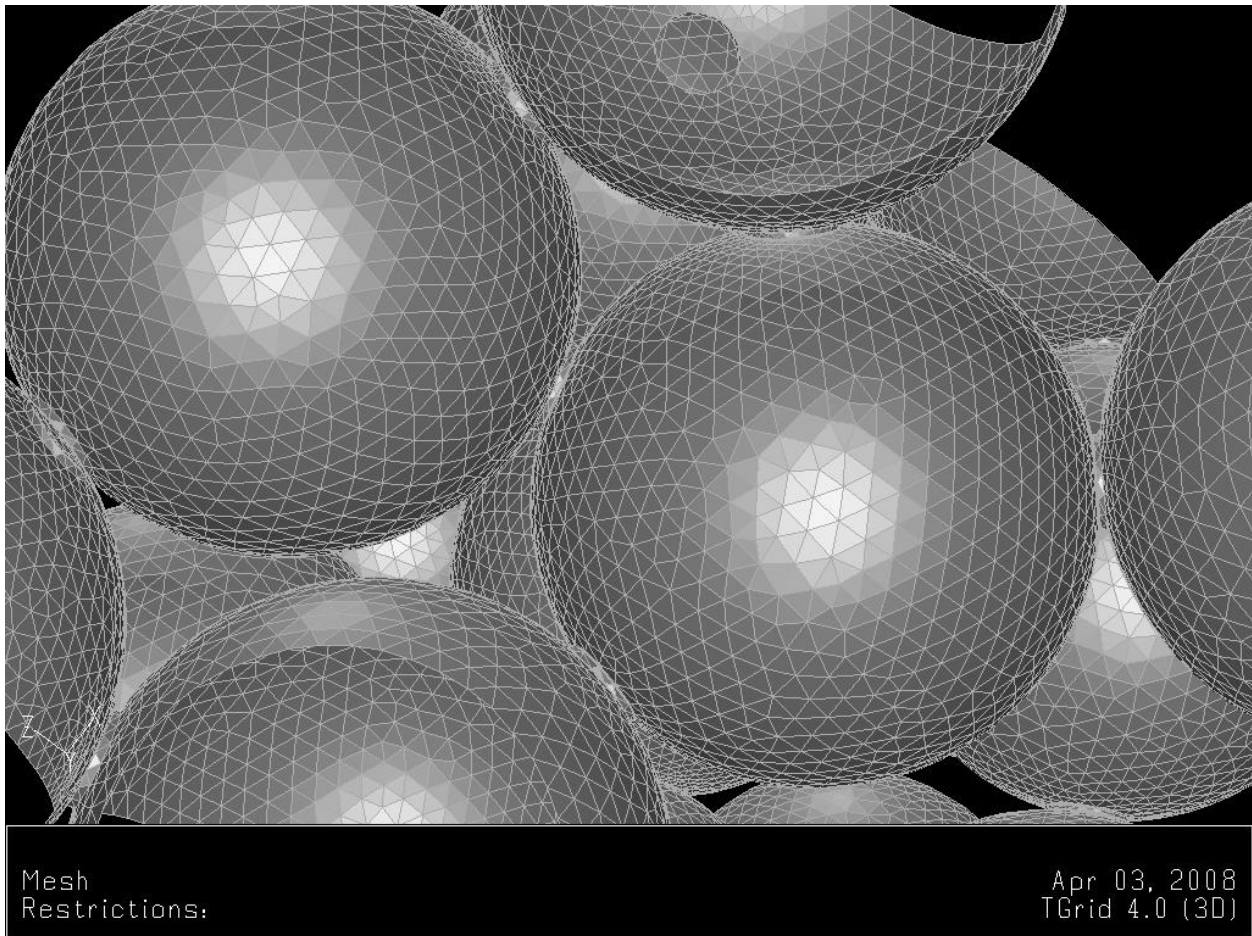
This contact cutout cylinder was created such that it would be large enough to allow two prism layers and a layer of quality tetrahedral elements to fit on it as shown in Figure E.6.2.

Figure E.6.2: Cylindrical Contact Cutout
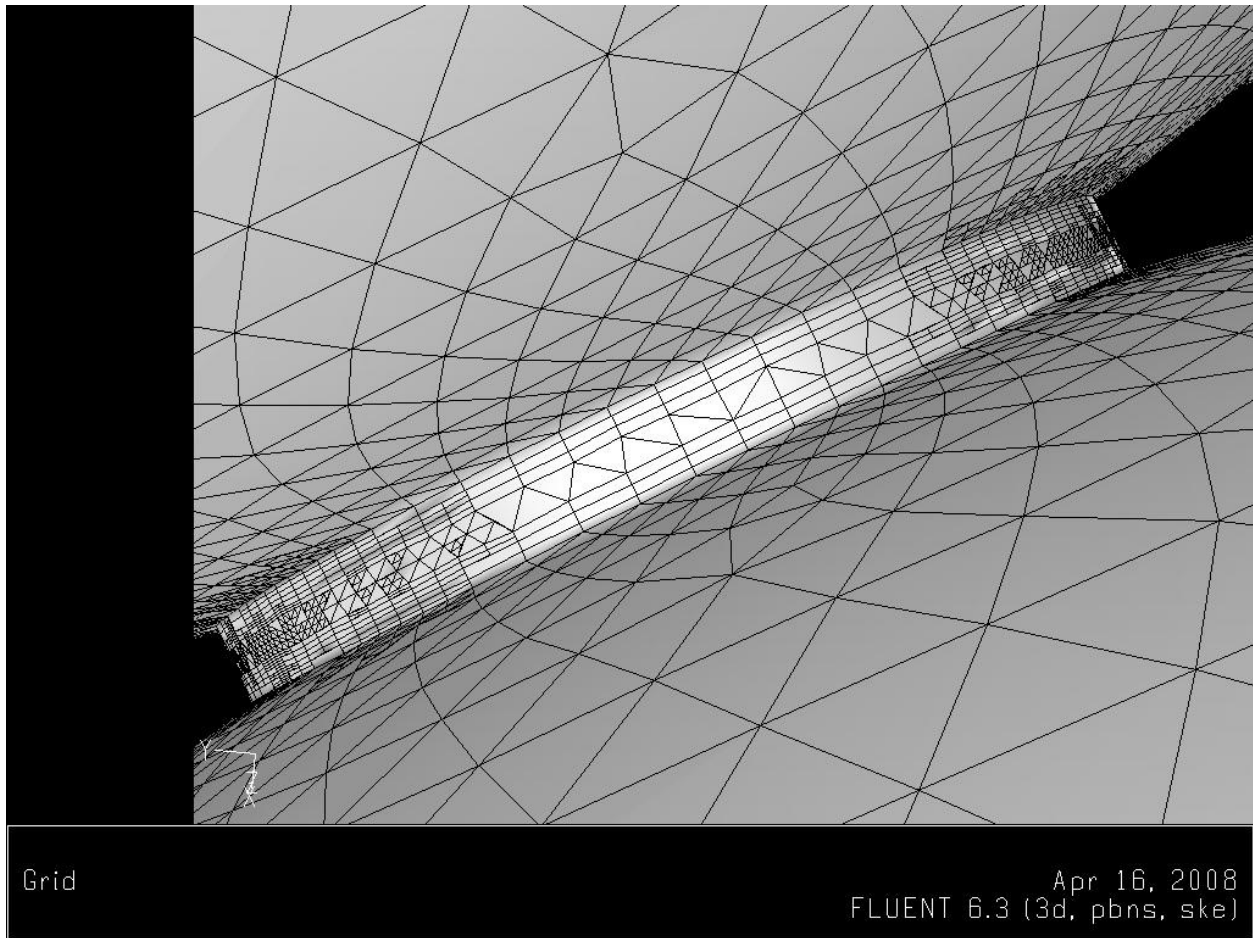
This was considered an acceptable compromise. For a minimal loss of volume the model can now have high quality prism layers and the low quality elements caused by pebble contact points have been eliminated.

E.7   Slicing a Set of Pebbles with Perpendicular Planes Can Create Sharp Edged Geometry and Highly Skewed Elements

Using full sized pebbles and contact cutouts, a set of pebbles was modeled within a rectangular prism solution domain, as shown in Figure E.7.1, from which a laminar flow solution could readily be obtained.

Figure E.7.1: Rectangular Solution Domain
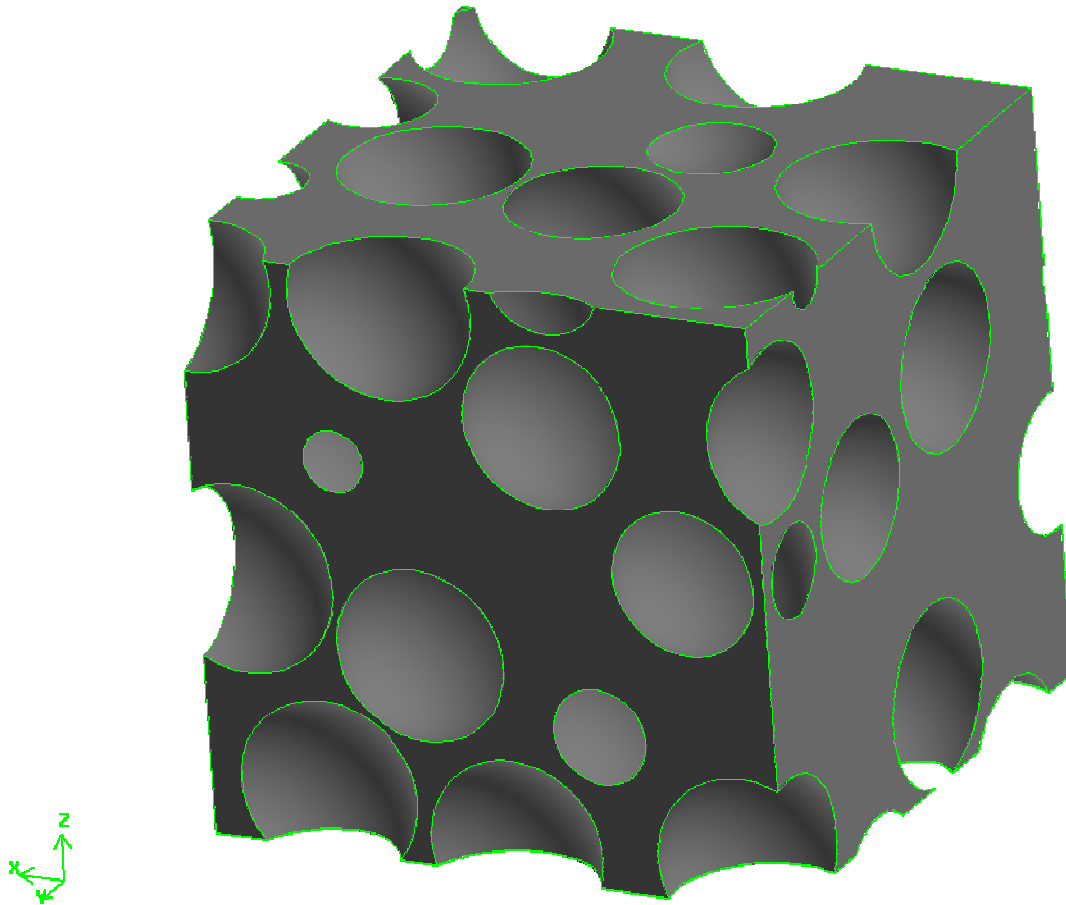
Following the laminar flow solution, attempts were made to solve for the flow with the standard k-epsilon turbulence model. The introduction of the turbulence model immediately caused the solution to diverge. It was found that the solution was diverging at a sharp point that was formed from a sphere cut by two planes. This situation is shown in Figure E.7.2.

Figure E.7.2: Diverging Solution at a Sharp Point Formed From a Sphere Cut by Two Planes

Contours of Static Pressure (pascal)   Apr 03, 2008
FLUENT 6.3 (3d, pbns, skw)
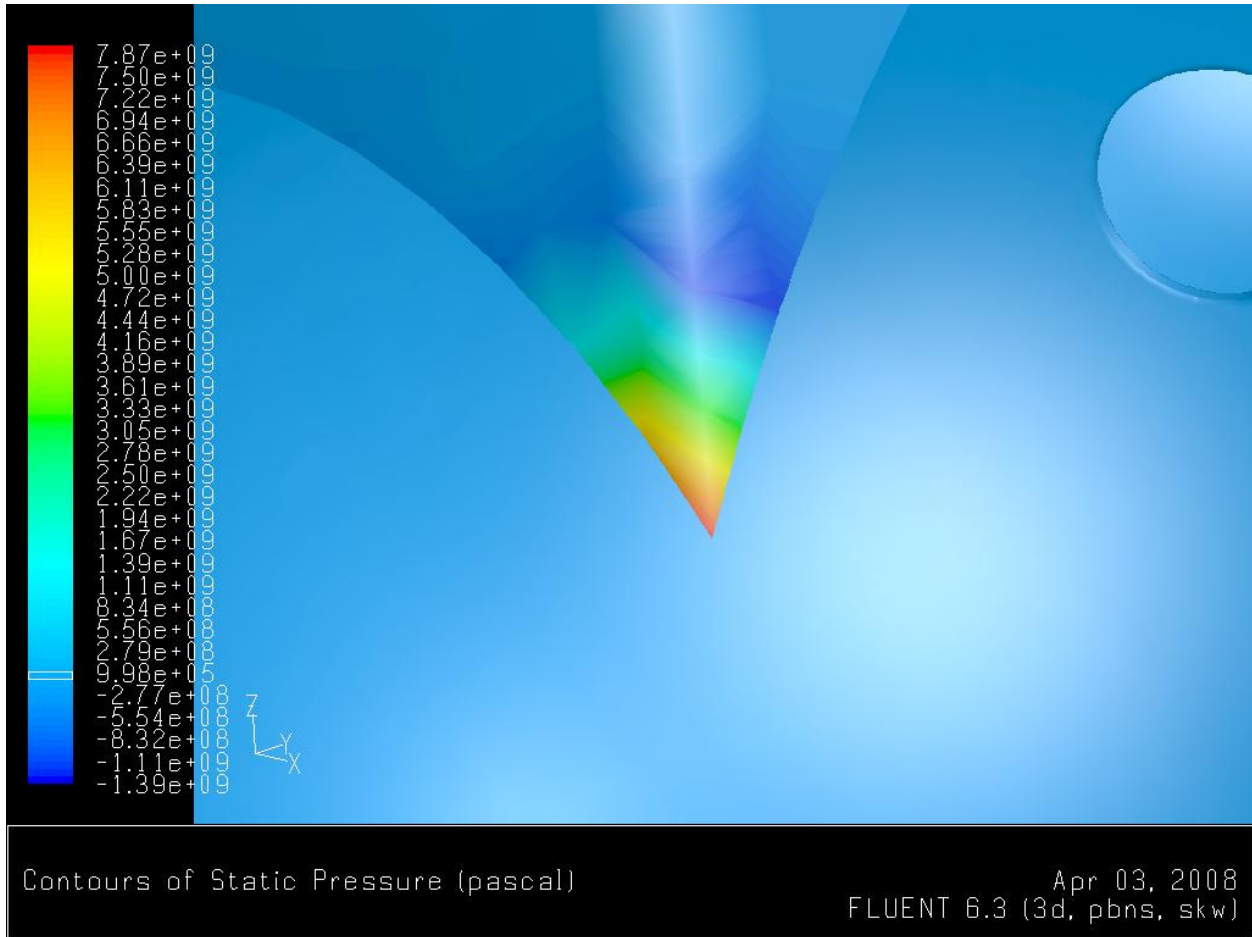
At this point the case of a cylindrical solution domain was considered to avoid the sharp edges formed by a rectangular solution domain. A cylindrical domain does not form sharp edges as a cylinder does not contain any corners.

E.8   Slicing the Pebbles at the Outlet Boundary Conditions Creates Solution Divergence and Accuracy Issues

In the next step of the work an arrangement of pebbles was found that did not contain sharp edges caused by the shape of a rectangular solution domain and a mesh was created on this assembly (see the Figure E.8.1).

Figure E.8.1: Rectangular Solution Domain Containing no Sharp Edges
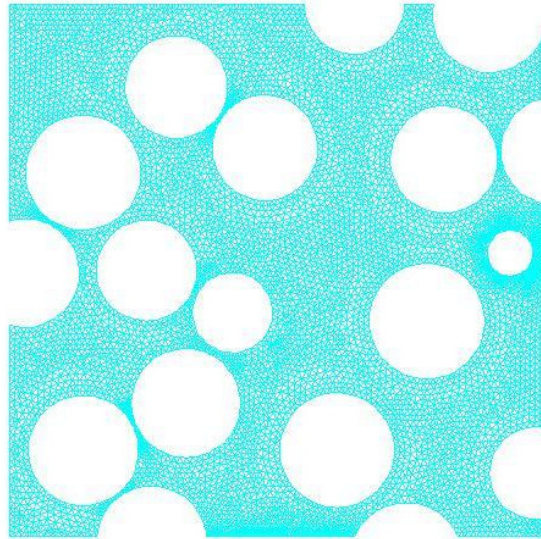
Once again a laminar flow solution was obtained however all attempts to find a turbulent solution resulted in immediate solution divergence. It was postulated that these difficulties were resulting from a high amount of reversed flow at the outlet plane. While reversed flow is allowed at outlets it does introduce some approximations into the solution. Reversed flow at the outlet is assumed to flow into the solution domain normal to the outlet surface and all turbulence properties of this re-entrant flow are manually set by the user. It is critical that the user provides accurate turbulence information for the re-entrant flow if there is interest in the flow near the outlet.

To resolve the issue of reversed flow, or at least reversed flow near the pebbles being modeled the outlet face of the solution domain was extruded as shown in Figure E.8.2.

Figure E.8.2: Solution Domain with Extruded Outlet Face
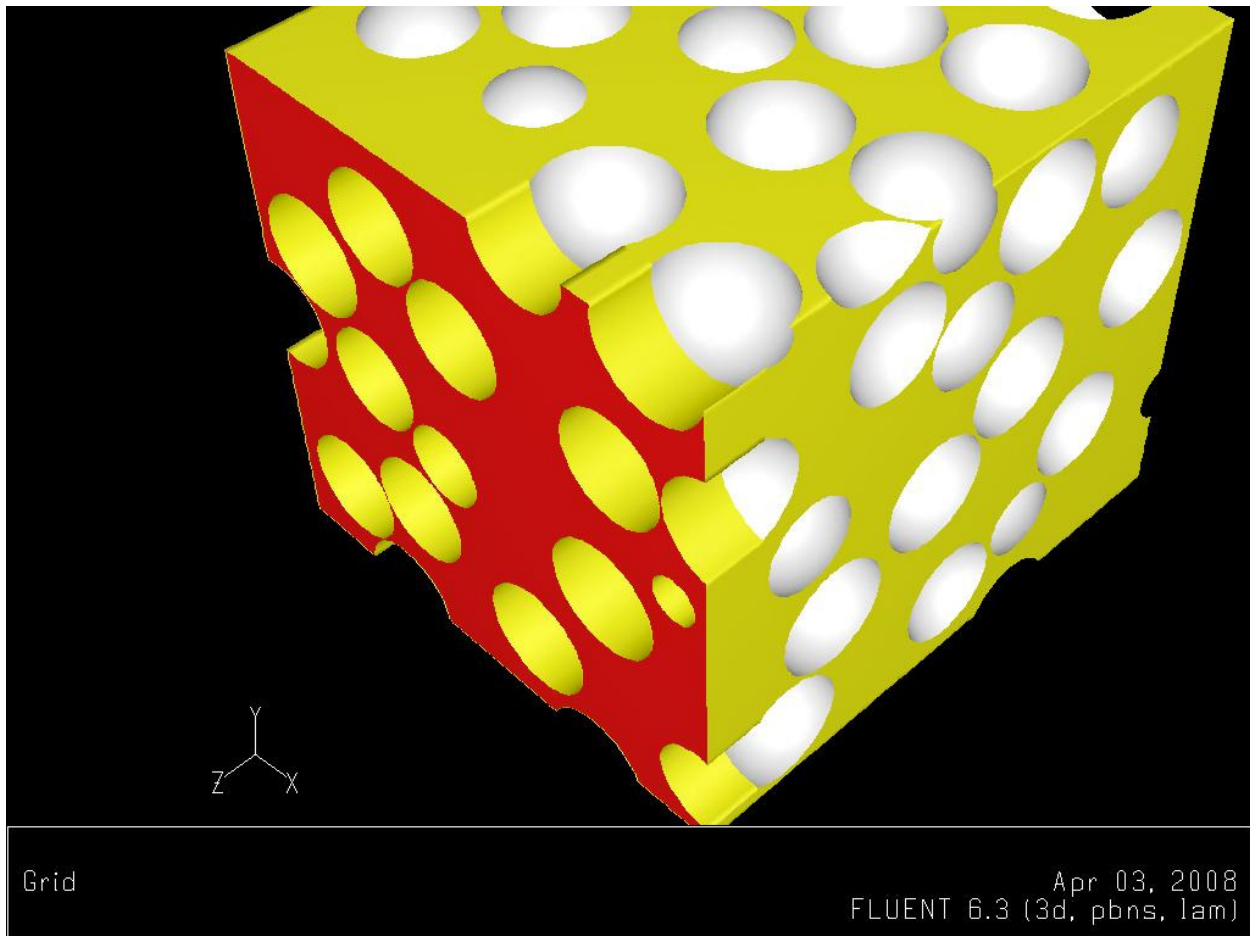
The extrusion of the outlet face allows the flow to straighten out and move any minor flow reversal away from the pebble bed.

Various extrusion lengths were examined; however, convergence difficulties persisted. It was found that the solution was calculating unrealistic/divergent values at a knife edge located on the outlet face.

The resolution to this problem is to extend the solution domain such that no pebbles are sliced by the outlet plane. This problem also reaffirmed the idea that a cylindrical solution domain may be a better solution. An example of this type of solution domain is shown in Figure E.8.3.

Figure E.8.3: Cylindrical Solution Domain
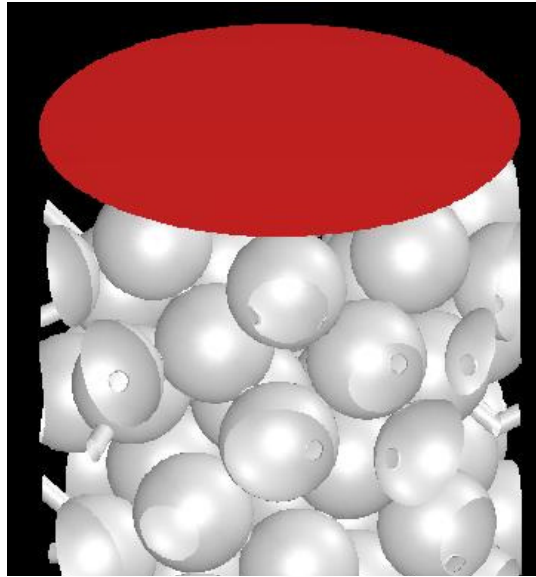
It was found that both laminar and turbulent flows could be solved on a geometry with this configuration. This extended portion of the domain has a significantly reduced packing fraction and should not be used in shear stress and pressure drop results.

E.9   Slicing the Pebbles at the Inlet Creates Non-Physical Quantities in the Solution

Upon noting the success of not cutting pebbles at the outlet, the impact of cutting pebbles at the inlet plane was more closely considered. The arguments in Section 10.4.2.1 demonstrate why it is not desirable to cut the pebbles with the inlet surface, especially since this simulation is attempting to accurately predict shear stress. The geometry was modified so that the inlet boundary does not cut any pebbles. This extended region is not included in the model results.

E.10 Peak Shear Stresses Located Near Artificial Cutouts

At this point it was believed a reasonable model was created using a cylindrical domain that did not cut pebbles at the inlet and outlet boundaries, and with a small volume of fluid removed around the contact points between pebbles. A series of simulations were carried out using this strategy; however, upon looking at the final results it was noted that the highest shear stresses in the model were next to the contact cutouts (see Figure E.10.1). This may be reasonable since the flow is throttled through the small gaps; however, there was some concern that this may be an artifact caused by the cutouts themselves.

Figure E.10.1: Shear Stress Distribution close to Cutouts
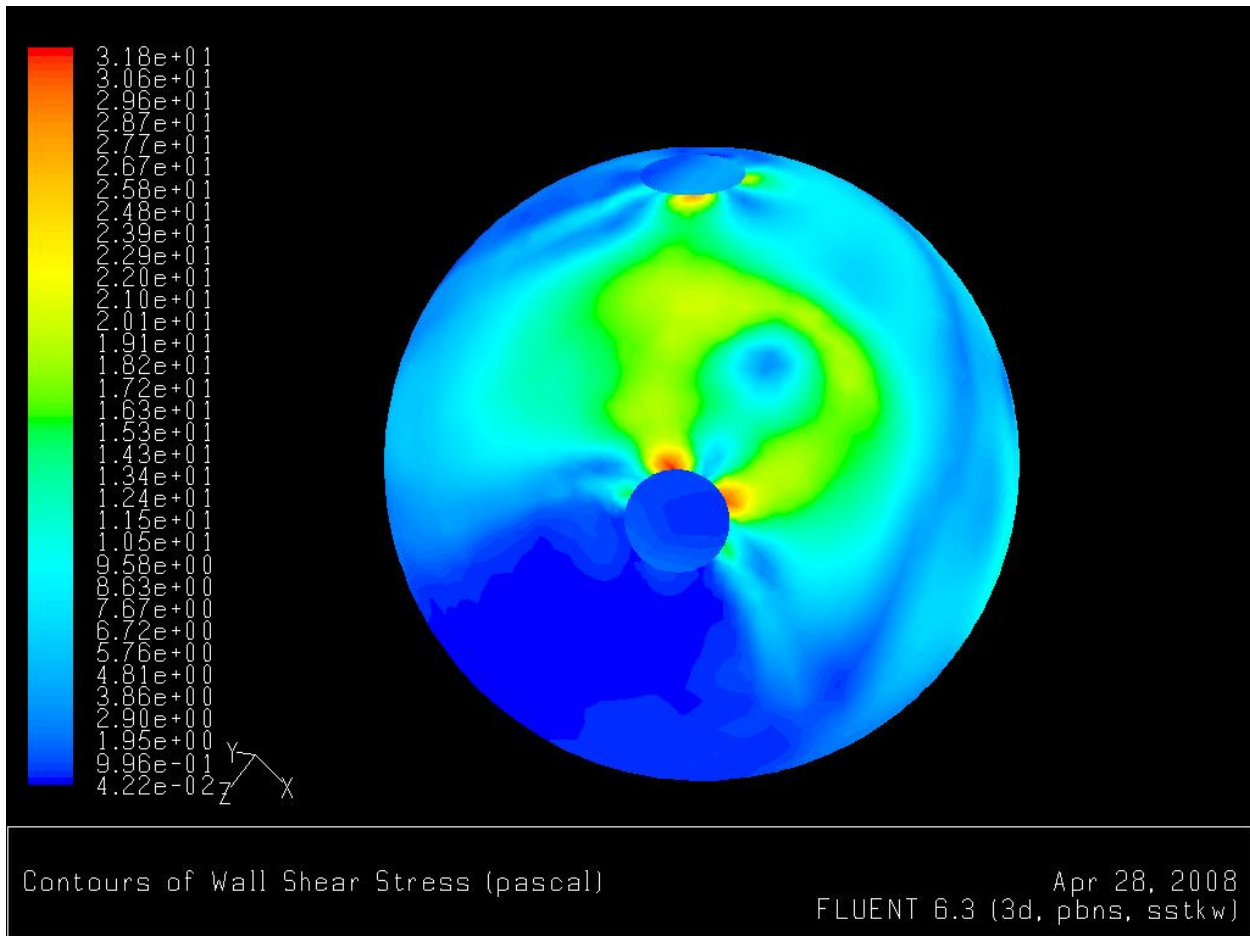
Since the size of the cutouts is set by the thickness of the prism layers a reduction in the cutout size would require a reduction of the number or size of the prism layers. In order to get a smaller contact cutout, maintain the size and number of prism layers, and have them not overlap the following approach was conceived.

A very small contact cutout (a realistic size for the deformation of a pebble) would be removed from the solution domain. Around this cutout the fluid would be split again using an object with a radius equal to the original contact cutout. This new region would then have a structured mesh applied to it to ensure that the prism layers do not overlap. The cutouts are not cylindrical but 16-sided figures to allow for easy generation of a structured mesh, as shown in Figure E.10.2.

Figure E.10.2: Contact Cutout for Resolving Near Contact Point Effects
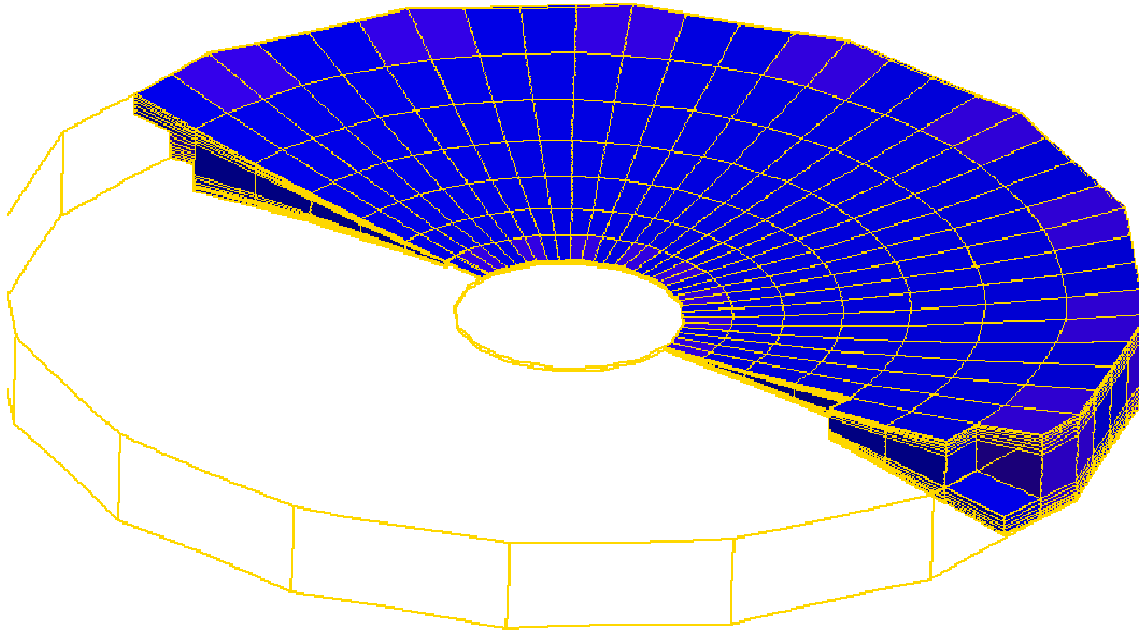
This geometry/mesh generation process is significantly more complex; however, it is also more realistic. The following figures show the results from a test simulation using the full cut-outs (Figure E.10.3) and the cutout meshed with a structured style grid (Figure E.10.4).

Figure E.10.3: Impact of Meshing Contact Cutouts
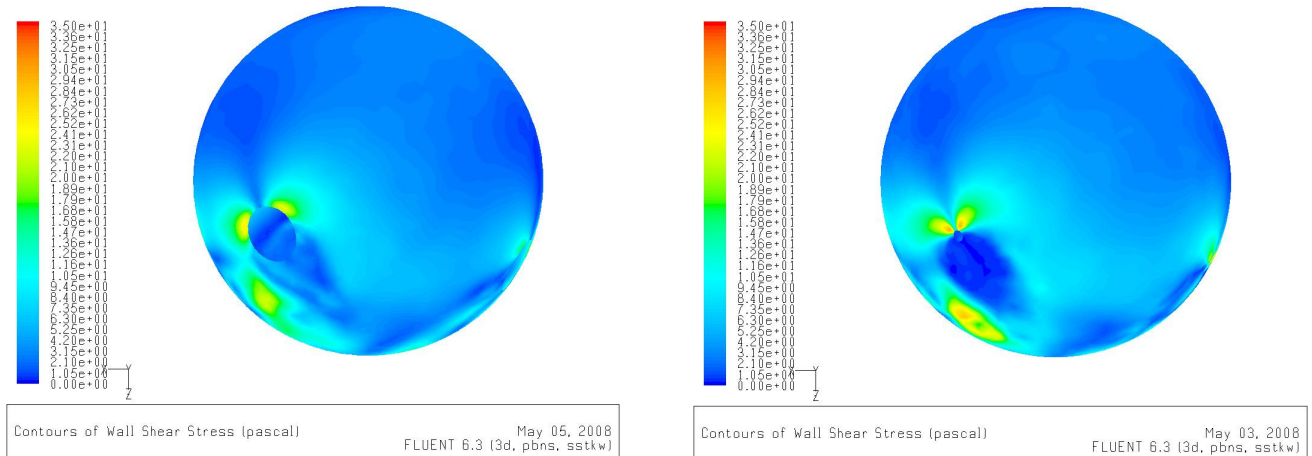
Figure E.10.4: Impact of Meshing Contact Cutouts
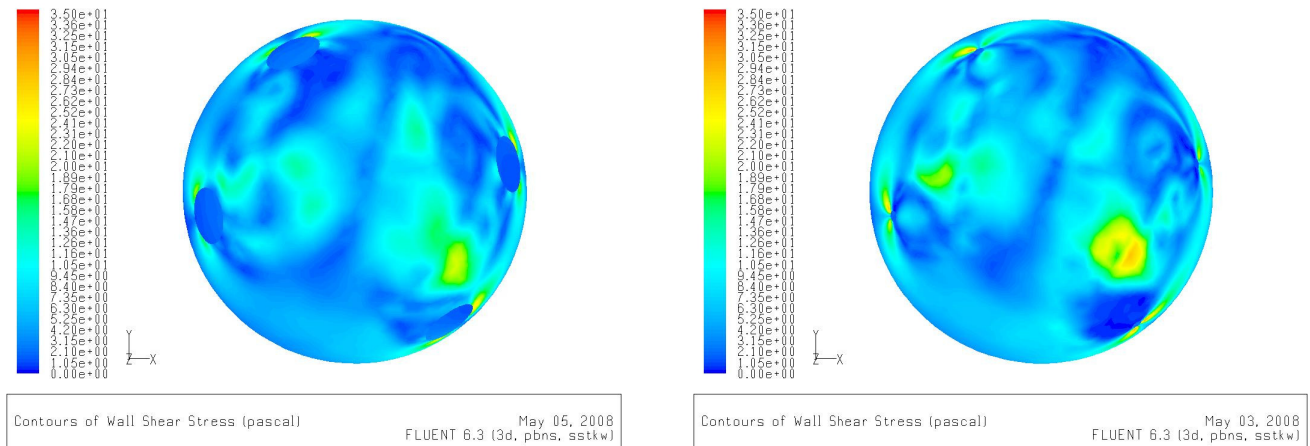
From the results in Figure E.10.3 and Figure E.10.4 the shear stress distribution is very similar overall. The only significant impact of modeling the full cutout region is that shear stress values are obtained closer to the contact point.

E.11 Lower than Expected Packing Fraction in the Model

During the mesh/geometry generation process it was noticed that contact cutouts on the outside surface of the solution domain caused sharp edged geometry (even in cylindrical domains). In order to avoid this issue, one of the pebbles in the pair that is in contact with the surface of the domain was removed. This was considered acceptable since there was little interest in the pebbles closest to the symmetry boundary of the solution domain. Upon examination of results and the application of the KTA rules correlations (Reference E.3) for pressure drop it was discovered that the pressure drop is very sensitive to packing fraction. Since the removal of problematic pebbles results in a reduction in packing fraction there may be some impact on the solution. To limit this effect it was decided that the pebbles should not be removed but simply be recreated with a reduced radius. A reduced radius pebble can readily be meshed without contact cutouts and it maintains the packing fraction and geometry significantly better than the removal of the pebble.

A solution domain with a radius of 0.12 m extending from -0.15 m to 0.15 m (with reference to the coordinate system provided in Section 10.2) was constructed with the removal of problematic pebbles and with the reduction of size in problematic pebbles. The resulting packing fractions are presented in Table E.11.1.

Table E.11.1: Packing Fraction of Sample Model

Model	Volume of Fluid (mm³)	Volume of Domain (mm³)	Packing Fraction
1. Removal of problem pebbles	5931377	13571680	0.563
2. Reduction in radius (5%) of problem pebbles	5746590	13571680	0.577
3. Reduction in radius (5%) of problem pebbles, including structured contact region	5753689	13571680	0.576
4. Ideal model – (not possible to mesh)	5701478	13571680	0.580

Results were produced using the improved contact cutouts and this reduced size approach to problematic pebbles.

E.12 References

E.1   Fluent Inc., "GAMBIT 2.4 Command Reference Guide", May 2007.

E.2   Fluent Inc., "GAMBIT 2.4 User's Guide", May 2007.

E.3   The Nuclear Safety Standards Commission (KTA), "KTA Program of Standards (14.04.2008), Reactor Core Design for High-Temperature Gas-Cooled Reactor, Part 3: Loss of Pressure through Friction in Pebble Bed Cores", KTA Standard 3102.3, March 1981. URL <http://www.kta-gs.de/common/regel_prog.htm>.

APPENDIX F : CFD MODEL DOMAIN SIZE STUDY

A significant question in the development of the CFD model presented in this report was the impact of edge effects on the solution. Edge effects include any geometric approximations made to the pebbles near the edge of the domain and the application of a symmetry boundary condition.

To address this question a series of solution domains were created using the same grid generation methodology but using increasingly large solution domains. The same pebble arrangement was used for each of these cylindrical domains so each smaller domain is a subset of the pebbles from the larger domains.

The meshes used in this appendix do not use the quadrilateral meshes near the contact points between pebbles (see Section E.10), but remove a 5mm radius cylinder of fluid around the contact point. This approach is cruder than the final model but is considered justified for the purposes of this study. The models in this section have "problematic" pebbles located on the symmetry plane removed. The final model used in this report uses a more refined approach of slightly shrinking these problematic pebbles. It is expected that edge effects demonstrated in this appendix will be more significant than the edge effect in the final model due to the treatment of problematic pebbles on the symmetry plane. It is assumed that the results of this domain size study are a bounding estimate on the impact of edge effects.

It should also be noted that all meshes in this study use prismatic elements on the surface of pebbles. They utilize proximity size functions and they include the additional entrance and exit regions discussed in Sections E.8 and E.9. The mesh resolution in this study is comparable to the final model in this report.

F.1   Geometry/Mesh Generation Details

Table F.1.1 presents the dimensions of and the number of pebbles in the three different domains. The numbers in brackets are the actual number of pebbles after problematic pebbles are removed. The "total number of pebbles" represents the ideal number of pebbles that should be in the model.

Table F.1.1: Number of Pebbles in Various Domain Sizes

Radius (m)	Height (m)	Number of Whole Pebbles	Total Number of Pebbles
0.05	0.30	1	33 (23)
0.10	0.30	26	94 (67)
0.12	0.30	49	129 (105)

F.2   Assessment of Pressure Drop Predictions

The first assessment performed was to examine the pressure drop over a cylinder with a radius of 0.05 m. The area weighted average static pressure was extracted from 40 planes within each model. At each plane average values are calculated over an area with a radius of 0.05 m.

Figure F.2.1 shows the pressure drop from -0.15 m to 0.15 m in the model. This range of values does not include the entrance and exit regions with reduced packing fractions.

Figure F.2.1: Pressure Drop Predictions for a Cylindrical Region at a 0.05 m Radius
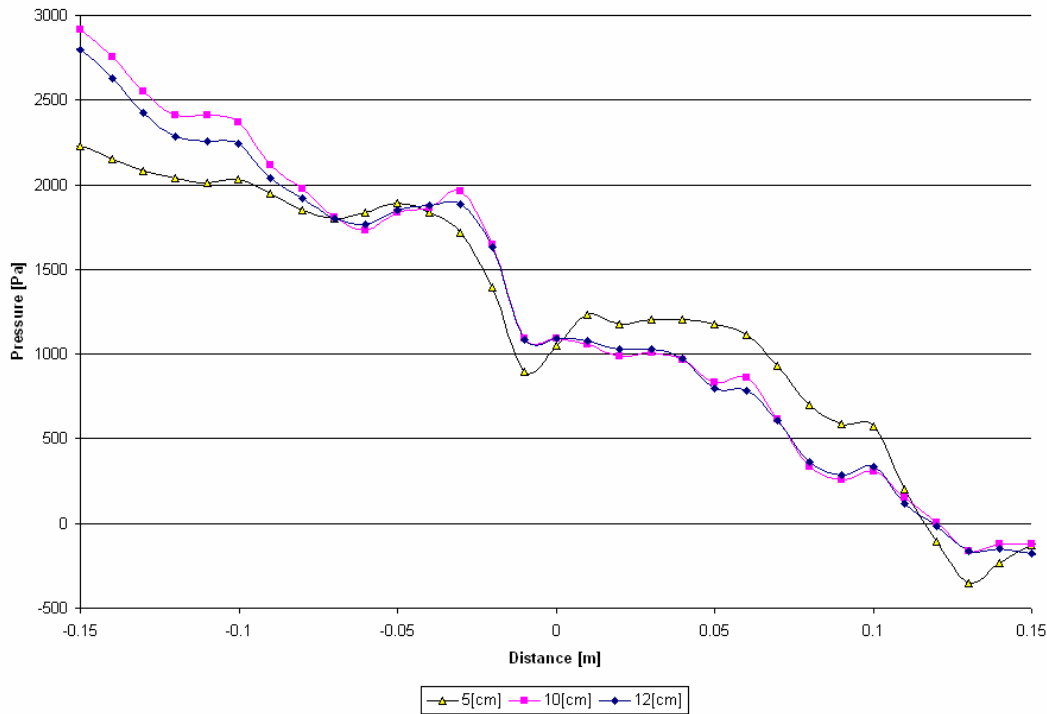
The results from Figure F.2.1 clearly show that the pressure decreases as the flow moves through the pebble bed. This pressure drop is reasonably linear considering that the pressure values are averaged over a 0.05 m radius. It is also clear from these results that while there is some similarity between the three models, the model with a radius of 0.05 m is predicting values significantly different than the other two larger models.

The next comparison was to examine the pressure drop over a cylindrical region with a radius equal to 0.10 m. In this case, the model with a radius of 0.05 m can not be included in the comparison. The results of this comparison are shown in Figure F.2.2.

Figure F.2.2: Pressure Drop Predictions for a Cylindrical Region at a 0.10 m Radius
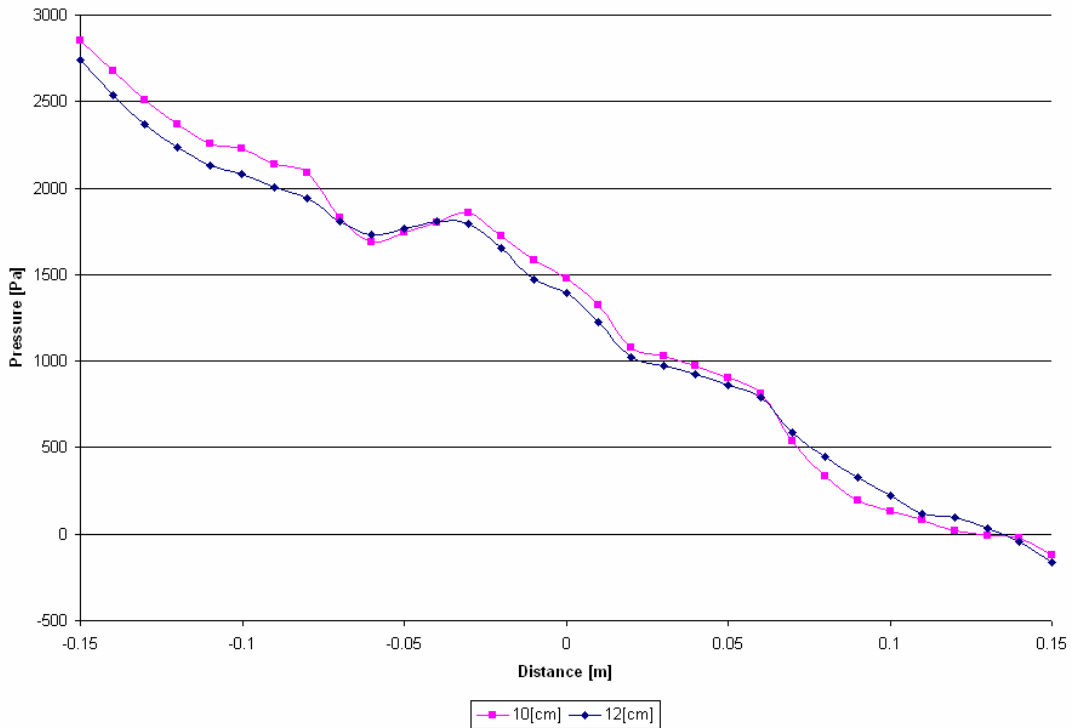
These results show a much more smoothed out and approximately linear pressure drop across the model. There are still some minor fluctuations present but these are significantly less severe that the results of Figure F.2.1. It is also noted that the pressure drop for each the 0.10 m and 0.12 m radius models are very similar. While studies with larger domains would be desirable these models are prohibitively large. On the basis of these three models it is believed that the 0.12 m radius model is large enough to remove most of the impact of the symmetry boundary condition and other edge effects.

The next comparison was to examine the pressure drop averaged over a variety of radii, but only for the model with a 0.12 m radius. The results of this study are shown in Figure F.2.3.

Figure F.2.3: Pressure Drop Predictions for Averaging Over Various Cylindrical Regions within the 0.12 m Radius Model
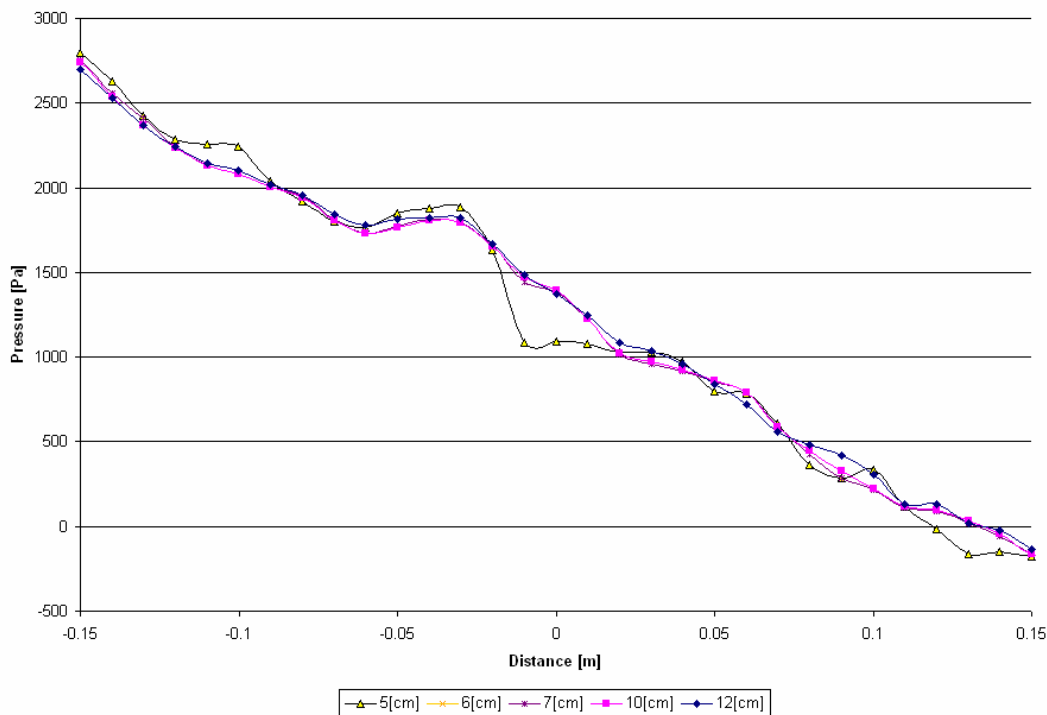
These results show that when averaging the pressure over a radius of 0.06 m the results are very similar. The only significant deviation is found when the pressure is averaged over a 0.05 m radius. This result would indicate that a majority of the radial pressure variation can be smoothed out for cylinders larger that 0.06 m or one pebble diameter.

F.3 Supplementary Domain Size Study

Since the results from the first part of this appendix were based upon the initial meshing strategy of removing problematic pebbles from the model, the next study was to examine how applicable these results were to the final model using an improved meshing/geometry strategy. In order to further investigate the impact of the domain size on the results of the final model a model with a domain radius of 0.09 m was created using the same methodology as the final models in this work[2]. This 0.09 m radius model can be directly compared with the 150 kg/s flow rate model using the SST turbulence model. Figure F.3.1 shows the pressure drop estimated by the model with a 0.09 m radius solution domain. The data points in this figure are taken as the area averaged static pressure over cross-sectional planes spanning the entire solution domain.

---

[2] The final meshing/geometry generation procedure shrinks problematic pebbles slightly as opposed to removing them from the solution domain.

Figure F.3.1: Pressure Drop Predicted from 0.09 m Radius Model

$y = -12362x + 1676.5$
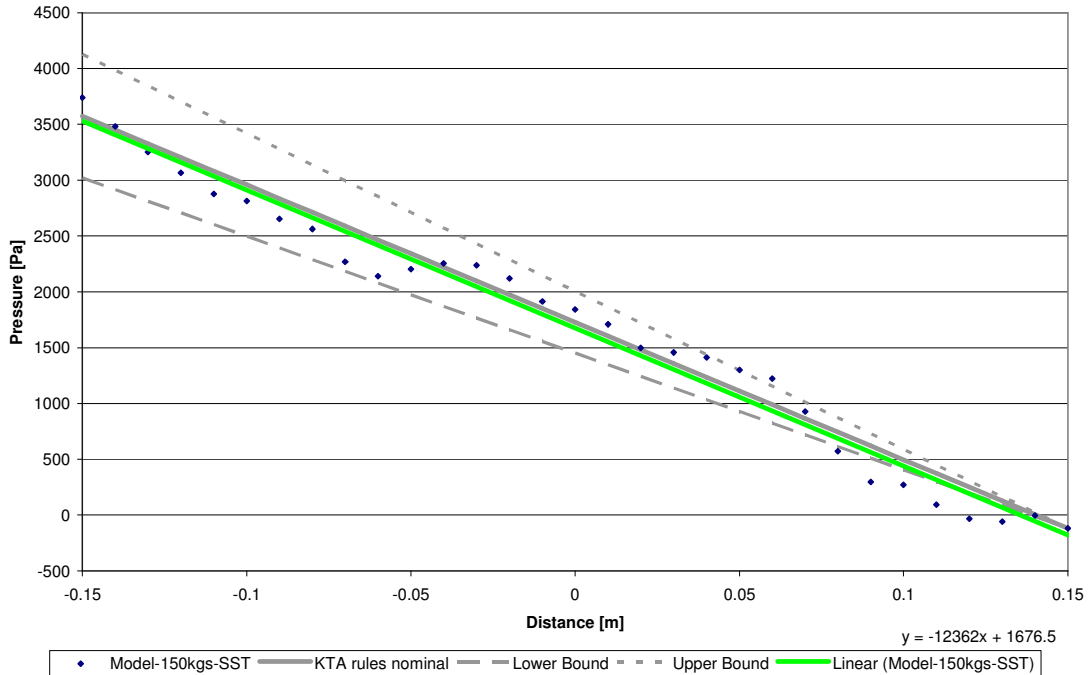
This 0.09 m model predicts a pressure drop of 12362 Pa/m (least squares fit line) as opposed to the pressure drop of 11490 Pa/m predicted by the larger 0.12 m radius model. This 7% difference between the pressure drops is considered to be very good since this difference is approximately the same as the fluctuations observed in the final solution (See Section 10.7.4 for details).

The average shear stress was also extracted from the 0.09 m radius model, for pebbles that are totally contained within the domain (*i.e.,* pebble centroids with radii less than 0.06 m from the centre of the domain). The percentage difference between the shear stress predictions for these pebbles and the same pebbles in the 0.12 m radius model were then calculated and used to create a population of data points. Figure F.3.2 shows the percentage difference between the shear stress calculations of the models versus distance from the centre of the domain.

Figure F.3.2: Difference in Shear Stress Predictions between 0.09 m and 0.12 m Solution Domain Radii
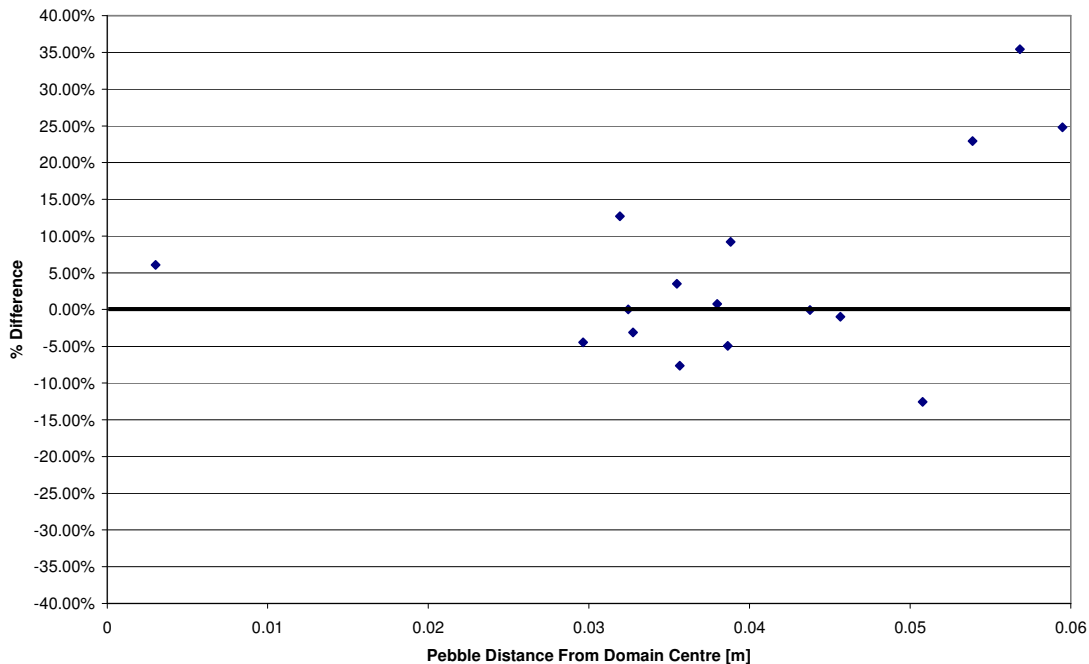
This figure shows that for pebbles with centroids less than 0.05 m (0.04m from domain symmetry wall) the difference between the two models is generally less than 10%. The average percentage difference for all data points in Figure F.3.2 is 4.2%. The average percentage difference for all pebbles with centroids more than 0.04 m from the symmetry wall was calculated to be 0.719%. While individual values of shear stress do vary between these models the average value is not greatly affected, especially for pebbles more than 0.04 m from the edge of the domain.

F.4 Conclusions of Domain Size Study

The results of this domain size study have indicated the following.

- A reasonably smooth pressure drop profile can be predicted by taking average pressures on planes with radii greater than 0.06 m as indicated in Figure F.2.3.

- The pressure drop in the PBR core can be predicted well (as compared with KTA rules predictions (Reference F.1)) for domains with radii greater than 0.09 m.

- The prediction of pebble shear stress is significantly affected by the symmetry boundary condition for pebbles closer than 0.04 m to the boundary.

- The average shear stress is relatively unaffected by the symmetry boundary condition if only pebbles with centroids more than 0.04 m (or 0.667 pebble diameters) from the domain edge are considered.

F.5 References

F.1   The Nuclear Safety Standards Commission (KTA), "KTA Program of Standards (14.04.2008), Reactor Core Design for High-Temperature Gas-Cooled Reactor, Part 3: Loss of Pressure through Friction in Pebble Bed Cores", KTA Standard 3102.3, March 1981. URL <http://www.kta-gs.de/common/regel_prog.htm>.

APPENDIX G : NEGLECTED PROPERTY VARIATION IN ISOTHERMAL PRESSURE DROP CFD MODEL

G.1 Helium Properties

Reference G.1 provides the following formulations for the properties of density and viscosity of helium.

$$\rho = 48.14 \cdot \frac{P}{T}\left(1 + .446\frac{P}{T^{1.2}}\right)^{-1}$$

$$\mu = 3.674 \times 10^{-7} \cdot T^{0.7}$$

In these equations the pressure P and temperature T are in units of bars and Kelvin, respectively. The units of density and viscosity are in units of kg/m³ and Pa•s. Assuming a temperature variation of 500ºC over the 11 m height of the PBR core, the temperature change over a 0.30 m model would be approximately 15ºC. To evaluate the impact of this temperature change on the properties of the fluid relevant to predicting pressure drop these properties were evaluated at 745ºC, 760ºC and 775ºC and 89.1 bar, as presented in Table G.1.1.

Table G.1.1: Material Property Variation with Temperature

Temperature (ºC)	Density (kg/m³)	Viscosity (Pa•s)
745	4.17488	4.6839E-05
760	4.110423	4.7321E-05
775	4.056792	4.78008E-05

The pressure impact was also evaluated. It is estimated that the pressure drop in a PBR core may be 1.9 bar for a flow rate of 150kg/s. It is estimated that the pressure drop over the CFD model should be approximately 0.1bar. The coolant properties were evaluated over 3 pressure levels at 760ºC, as presented in Table G.1.2.

Table G.1.2: Material Property Variation with Pressure

Pressure (bar)	Density (kg/m³)	Viscosity (Pa•s)
89.0	4.105855	4.7321E-05
89.1	4.110423	4.7321E-05
89.2	4.11499	4.7321E-05

G.2 Discussion

Based on these calculations the average property variation is less than 2%, and is neglected in the isothermal model.

It is recognized that temperature and pressure levels may have local values outside of these calculated ranges. In the work of Reference G.2 a CFD analysis of a packed bed with a regular pebble arrangement was performed and this analysis predicted maximum surface temperature 300ºC higher than the mean coolant temperature. This analysis also indicates that the surface temperature of a pebble can vary locally by approximately 30ºC.

The shear stress in a simulation is directly related to the properties of the coolant at the pebble surface; hence it is argued that only variations over the pebble surface are critical to the prediction of shear stress and through the Chilton-Colburn analogy heat transfer coefficients. Based on a 30ºC surface temperature variation it is expected that the coolant properties on a pebble's surface will vary by amounts similar to that shown in the table above (~2%). This 2% property variation will be applied as a direct uncertainty on the heat transfer coefficient.

A secondary implication of the above argument is that the simulation in this document is valid for surface temperatures equal to the temperature at which the coolant properties were evaluated.

Irreversible pressure loss is primarily caused by viscous drag and turbulence. As indicated previously, viscous forces are expected to have a 2% uncertainty caused from property variation and a similar effect would is assumed for the pressure drop.

There will also be secondary errors introduced to the shear stress calculation due to local changes in coolant density. Changes in coolant density will change the ratio of inertial and viscous forces, which will in turn alter the flow patterns in the model.

G.3   References

G.1   The Nuclear Safety Standards Commission (KTA), "KTA Program of Standards (14.04.2008), Reactor Core Design for High-Temperature Gas-Cooled Reactor, Part 1: Calculation of the Material Properties of Helium", KTA Standard 3102.1, June 1978. URL <http://www.kta-gs.de/common/regel_prog.htm>.

G.2   J. Lee, S. Yoon, G. Park, W. Lee, "Turbulence-induced Heat Transfer in PBMR Core Using LES and RANS", Journal of NUCLEAR SCIENCE and TECHNOLOGY, Vol. 44, No. 7, p. 985–996 (2007).

APPENDIX H: JUSTIFICATION FOR CHILTON-COLBURN ANALOGIES FOR DETERMINING HEAT TRANSFER COEFFICIENTS FROM AN ISOTHERMAL PRESSURE DROP CFD MODEL

To simplify this work it is desirable to utilize the Chilton-Colburn analogies to determine the local heat transfer rate. Use of these analogies implies that an isothermal flow solution is sufficient to determine the local heat transfer rate. The full details of the analogy will not be presented here, the interested reader should refer to Reference H.1. The analogy for heat transfer is stated below.

$$\frac{C_f}{2} = j_H$$

$$j_H = St \cdot Pr^{2/3}$$

$$St = \frac{h}{\rho V_{ref} C_p}$$

$$Pr = \frac{C_P \mu}{k}$$

$$C_f = \frac{2\tau}{\rho V_{ref}{}^2}$$

Where:

C_f friction coefficient,

j_H Chilton-Colburn j-factor

St Stanton number

Pr Prandtl number

h heat transfer coefficient, W/m^2K

ρ fluid density, kg/m^3

V_{ref} reference velocity, m/s

C_p specific heat capacity, J/kgK

μ dynamic viscosity, Pa·s

k thermal conductivity W/mK

τ shear stress N/m^2

In order to use the analogy the following conditions must be satisfied:

1. Buoyancy effects are not significant especially in the boundary layer;

2. Prandtl numbers must be between 0.6 and 60;

3. There is negligible viscous dissipation; and

4. The flow is either completely turbulent or the pressure drop through the pebble bed is zero.

Criteria i)

Buoyancy effects in the boundary layer can be quantified using the Grashof number which is defined in Reference H.1.

$$Gr = \frac{g\beta(T_s - T_\infty)L^3}{v^2}$$

If the Grashof to Reynolds squared ratio is much less than 1 then buoyancy effects are negligible (Reference H.1).

$$\frac{Gr}{Re^2} << 1$$

The coolant density used in the current analysis was estimated at 760°C and 89.15 bar and has a value of 4.1 kg/m³.

The inner and outer diameters for a PBR core are 3.7 m and 2.0 m, respectively. Based on these dimensions and a mass flow rate of 150 kg/s, the superficial velocity through the core is approximately 4.8 m/s.

The length scale "L" was selected as the pebble diameter.

For an ideal gas, Beta can be simply calculated as given in Reference H.1:

$$\beta = \frac{1}{T} = 9.7 \times 10^{-4}$$

Also,

$$g = 9.81 \text{m/s}^2$$

$$T_\infty \approx 760°C = 1033.15K$$

$$v = \frac{\mu}{\rho} = 1.15 \times 10^{-5} \text{ (see Reference H.2)}$$

$$\text{Re} = \frac{\rho V L}{\mu} = 25044$$

$$Gr = 15541 (T_s - T_\infty)$$

$$\frac{Gr}{\text{Re}^2} = \frac{15541 (T_s - T_\infty)}{25044^2} = 2.5\text{e-}5 (T_s - T_\infty) << 1$$

The temperature difference required for buoyant effects to become important in the boundary layer is an order of magnitude higher than the melting temperature of graphite; hence, buoyant effects can reasonably be neglected.

Criteria ii)

The Prandtl number must be greater that 0.6 for the analogy to apply. The Prandtl number can be readily estimated from the properties of the coolant.

$$k = 2.682\times10^{-3} T^{0.71(1-2\times10^{-9} P)} (1 + 1.123\times10^{-8} P) \quad {}^{W}\!/_{mK} \text{ (Reference H.2)}$$

$$C_p = 5195 \quad {}^{J}\!/_{kgK} \text{ (Reference H.2)}$$

$$\mu = 3.674\times10^{-7} \cdot T^{0.7} \text{ (Reference H.2)}$$

For the simulation performed for this work the coolant temperature and pressure were 760ºC (or 1033.15K) and 89.15 bar (or 8915000 Pa).

$$\mu = 4.73\times10^{-5} \quad Pa \cdot s$$

$$k = 0.373 \quad {}^{W}\!/_{mK}$$

$$\text{Pr} = 0.66$$

At 760ºC and 89.15 bar the Prandtl number satisfies the constraints of the Chilton-Colburn heat transfer analogy.

Criteria iii)

The ratio of viscous dissipation to convection is described by the ratio of the Eckert to Reynolds number or the Brinkman number (Reference H.3).

$$E_c = \frac{V^2}{C_P (T_s - T_\infty)} = \frac{(4.8 {}^{m}\!/_{s})^2}{(5195 {}^{J}\!/_{kgK})(T_s - T_\infty)} = \frac{4.43\times10^{-3}}{(T_s - T_\infty)}$$

$$\frac{E_c}{\text{Re}} = \frac{1.77\times10^{-7}}{(T_s - T_\infty)}$$

$$Br = \frac{\mu V^2}{k(T_s - T_\infty)} = \frac{4.73 \times 10^{-5}\, Pa \cdot s \cdot (4.8\mathrm{m/s})^2}{0.373\, ^W\!/_{mK} \cdot (T_s - T_\infty)} = \frac{2.9 \times 10^{-3}}{(T_s - T_\infty)}$$

Using either criteria, for the viscous dissipation to become significant the temperature difference between the surface of the pebbles and the average coolant temperature must become extremely small. This examination is considered sufficient to show that viscous dissipation will be negligible in the current simulation and the Chilton-Colburn analogy constraint is satisfied.

Criteria vi)

The final constraint to be satisfied is to confirm that the flow has either a minimal pressure gradient or is turbulent. Reference H.4 presented a review of literature on transitional Reynolds numbers for packed beds and this review indicated that a reasonable transition range is between Reynolds numbers of 60-130. Since the Reynolds number in this work is on the order of 1×10^4 the assumption that the flow is turbulent seems justified.

H.1   References

H.1   F. Incropera, D. DeWitt, "Fundamentals of Heat and Mass Transfer 5th Ed.", 2002.

H.2   The Nuclear Safety Standards Commission (KTA), "KTA Program of Standards (14.04.2008), Reactor Core Design for High-Temperature Gas-Cooled Reactor, Part 1: Calculation of the Material Properties of Helium", KTA Standard 3102.1, June 1978. URL <http://www.kta-gs.de/common/regel_prog.htm>.

H.3   R. Bird, W. Steward, E. Lightfoot, "Transport Phenomena 2nd Ed.", 2002.

H.4   S.A. Logtenberg, M. Nijemeisland, A. Dixon, "Computational fluid dynamics simulations of fluid flow and heat transfer at the wall-particle contact points in a fixed-bed reactor", Chemical Engineering Science, Vol. 54, pp. 2433-2439, 1999.

APPENDIX I ERROR ESTIMATES FOR THE CFD SIMULATIONS

Within a CFD simulation there are several sources of errors, and the goal of a successful analysis is to reduce these errors such that meaningful results may be obtained for the given application. This appendix discusses the errors and estimates of their magnitudes for the current work. Not all the errors are applicable to all the CFD runs, but it should be obvious from the context which ones apply to a specific analysis. The errors are broken down into the following types:

1. Modeling Errors,

2. Discretization errors,

3. Round off errors, and

4. Solution or convergence errors.

I.1 Modeling Errors

The modeling errors are generated from approximations introduced by the analyst's assumptions during an analysis. The current analysis contains the following types of modeling errors.

I.1.1 Use of Perfect Pebbles

All simulations in this work assume that pebbles are perfectly spherical and contain no surface defects or roughness. Actual pebbles in a PBR core will be slightly deformed (due to the weight of the packed bed) and may contain scratches and other surface defects from movement through the core. Unfortunately there is no data available to assess these pebble variations, however the effects of these imperfections/variations will be insignificant compared to other approximations made for this work.

I.1.2 Use of a Simulated Random Packing Arrangement of Pebbles

In this simulation the pebble packing arrangement generated in Section 10.2 was used however it is known that this arrangement is not the exact arrangement found in a PBR core. The packing fraction found in a PBR core is estimated to be 0.61 (Reference I.1) and the packing fraction in the arrangement generated by the procedure described in Section 10.2 over the range of the current model was found to be 0.580. This variation in packing fraction will significantly change the pressure drop through the packed bed, so one should use caution in applying the CFD results in this work directly to a PBR core with a packing fraction of 0.61. It should be noted that a packing fraction of 0.58 is still within the range of applicability of the KTA correlations (Reference I.2).

I.1.3 Neglecting Property Variations for Pressure Drop Calculations

In the simulations described in Section 10.4 all variations of coolant properties were neglected. Appendix G discusses the impact of neglecting this variation for purposes of comparing the current results to PBR results.

I.1.4 Using the Modified Reynold's Analogy

Appendix H discusses the applicability of using the Chilton-Colburn Analogies for predicting heat transfer. It was generally found that all conditions for the analogies to be used are satisfied and the use of this analogy is not expected to introduce additional errors. The neglect of the variation in property values is expected to be the more significant error term as discussed in the previous section.

I.1.5 Use of Symmetry Boundary Conditions and Special Edge Treatments

This simulation uses a symmetry boundary condition at the edge of the modeled region. The use of this condition implies that no flow may enter or exit the domain at this radial coordinate; which is an unlikely situation. It is however expected that the net flow through a radial surface in the solution domain will be zero. In order to minimize this impact the solution domain was made as large as was reasonably allowable within computing resource constraints.

To mesh this model some pebbles that touch the symmetry plane had to be reduced in size. This reduction in size reduces the packing fraction by 0.7% from the target packing fraction (see Appendix E). This local reduction in packing fraction has the potential to cause "wall channeling" or increase mass flow near the wall of the solution domain. It was considered that since the packing fraction was changed by a minimal amount this effect would be minimized.

The results of Appendix F indicate that wall shear stress prediction for a pebble with its centroid within 0.04 m of this boundary condition is significantly affected by this boundary condition. Pebbles located more than 0.04 m from the symmetry boundary condition were not found to be significantly affected by the boundary condition.

I.1.6 Use of a Constant Velocity Inlet Boundary Condition

The inlet boundary condition in this model is a fixed constant velocity plane. In the actual PBR core the velocity distribution may not be so uniform, however for lack of any information to the contrary this condition is considered reasonable. It would not be expected that a large velocity variation is present for this model as the process of pushing the flow through the packed bed is expected to break up any large scale flow structures/velocity gradients.

I.1.7 Use of a Pressure Specified Boundary Condition

The use of a constant pressure boundary condition at the outlet is an approximation however this approximation is not expected to have a great impact on the solution for the following reasons:

1. From the study in Appendix F it is shown that the average pressure on a particular plane within the model is relatively insensitive to size of the averaging region on that plane. This would imply that a constant pressure on a given plane in the model is a reasonable approximation.

2. The model contains a region around the outlet that is not included in the analysis. The purpose of this region (beyond increasing solution stability) is to minimize the impact of approximations applied at the outlet boundary conditions. This

effectively moves the outlet away from the region of interest in the model, hence reducing the importance of the precise details of the outlet boundary condition.

I.1.8 Selection of Turbulence Model

The quantification of uncertainties associated with a turbulence model can be assessed by comparison of the model results to experimental or direct numerical simulation results. A review of the literature yielded the following two applicable experimental results that can be compared to the current CFD model for estimating the accuracy of the turbulence model used in this simulation.

1. Reference I.3 demonstrates the performance of various turbulence models for prediction of velocity and temperatures around an isolated heated cylinder

2. Reference I.2 and I.4 provide correlations for average heat transfer coefficients and pressure drops within a PBR core.

The work of Reference I.3 indicates that at high Reynolds numbers ($> 3.6 \times 10^4$) SST, k-omega, RSM and LES turbulence models predict the temperature distribution around a single heated pebble with reasonable accuracy. At low Reynolds numbers ($< 1.2 \times 10^4$) k-omega and LES models exhibit the best predictions; however the LES model tended to over predict temperatures at particular locations. At a Reynolds number of 1.2×10^4 the normalized temperature error is approximately ~0.012.

The normalized temperature error is defined here as:

$$\hat{T}_{error} = \left(T_{experiment} - T_{model} \right) / T_{experiment}$$

Where: $\hat{T}_{error}$ is the normalized temperature error,

$T_{experiment}$ is the experimental temperature measurement, and

T_{model} is the CFD model temperature prediction.

The standard deviation of the normalized temperature error is the square root of the variance or 0.11. The heat transfer coefficient is defined by the following equation.

$$h = \frac{Q}{\Delta T}$$

Where, h is the heat transfer coefficient, Q is the surface heat flux and ΔT is the temperature difference between the surface and fluid.

If one assumes that the heat flux is perfectly known then the variance in the heat transfer coefficient is only attributable to the variance in the temperature difference, ΔT. If one further assumes that the normalized temperature error is comparable to the variation in the

temperature difference the uncertainty in the heat transfer coefficient can be calculated from the normalized temperature error (Reference I.5).

$$\frac{h_{uncertainty}}{h} = \left(\frac{\sigma_{temperature}}{\Delta T_{average}} \right) = 0.11$$

The standard deviation of the error in the heat transfer coefficient introduced by the SST turbulence model for low Reynolds numbers is estimated to be 11%. It is worth noting that based on the data presented in Reference I.3 the uncertainty in the heat transfer coefficient introduced by the k-omega model is approximately half of the SST model for low Reynolds numbers.

To further examine the impact of the turbulence model on results a set of sensitivity models were created. These models use the identical geometry and flow rate (150kg/s) but use different turbulence models. The three turbulence models used were the SST model, the k-omega model and the Reynolds Stress Model.

Table I.1.1 summarizes the impact of the turbulence model on the pressure drop and average heat transfer coefficient through the model. These numbers are defined analogous to those provided in Section 10.4.3.1 and 10.4.3.3.

Table I.1.1: Turbulence Model Effect on Results (150 kg/s)

Model	Pressure Drop (Pa/m)	Average Heat Transfer Coefficients (W/m²K)		
	Nominal	Nominal	Lower Bound	Upper Bound
SST	11490	4916	2826	7006
K-omega	11643	4836	3146	6526
RSM	11116	4528	2939	6117

These results indicate that the different turbulence models predict very similar pressure drops. The differences between the models are on the same order of magnitude as the convergence error so no definite conclusion can be drawn about the turbulence model impact on the pressure drop prediction other than it is relatively insignificant. There is a more noticeable variation in the heat transfer coefficients where the RSM predicts heat transfer coefficients approximately 10% lower than the other two models. These impacts will not significantly change the findings reported in Sections 10.4.3.1 and 10.4.3.3.

In order to quantify the impact the turbulence model has on local heat transfer coefficients plots of the shear stress (which is directly related to the heat transfer coefficient through the Reynold's analogy) are extracted from the same pebble for each of the three turbulence model sensitivity cases. Figure I.1.1 shows the variations in shear stress over a selected pebble for illustrative purposes.

Figure I.1.1: Shear Stress Distribution For Various Turbulence Models (SST, k-ω, RSM respectively) at Flow Rates of 150kg/s on First Selected Pebble

Contours of Wall Shear Stress (pascal)   May 12, 2008
                                              FLUENT 6.3 (3d, pbns, sstkw)

Contours of Wall Shear Stress (pascal)   May 12, 2008
                                              FLUENT 6.3 (3d, pbns, skw)

Contours of Wall Shear Stress (pascal)   May 14, 2008
                                              FLUENT 6.3 (3d, pbns, RSM)
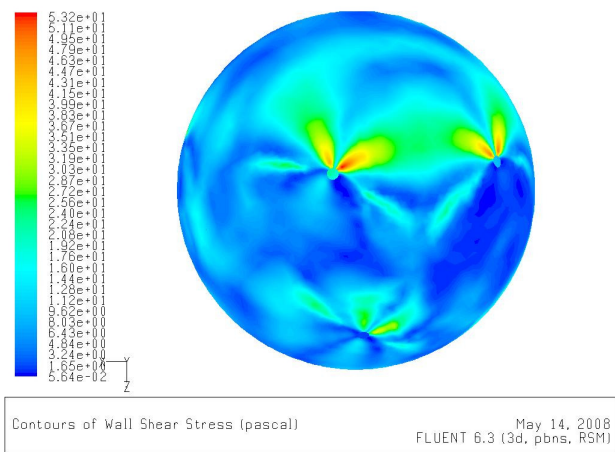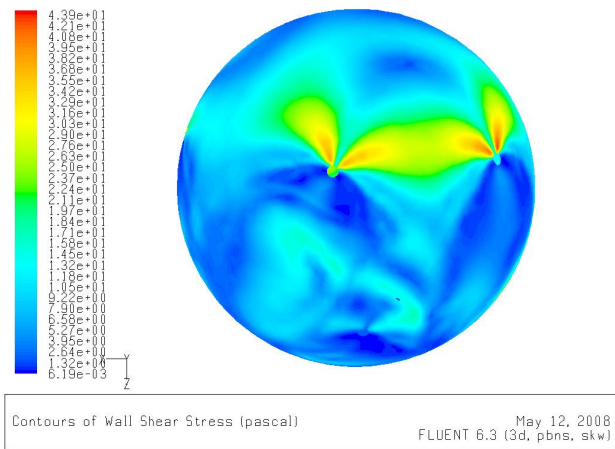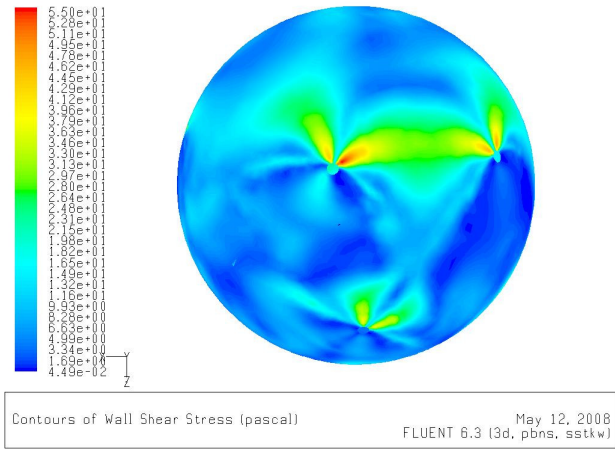
These figures show the same areas of high shear stress and the general shear stress distribution are predicted by each turbulence model. There are some minor variations in the shear stress distribution between the turbulence models.

I.1.9 Using a Smoothly Varying Power Distribution

The first two CFD studies use a smoothly varying power distribution where the actual power distribution in the core is composed of pebbles with discrete randomly varying power levels. The impact of this type of power distribution is assessed in the final CFD study documented in Section 10.6.

The analysis done in Section 10.6 uses a random power distribution with some constraints, which addresses one of the identified modeling errors of Section 10.5. With a more random distribution of pebble powers it does appear that the model has produced reasonable results, which removes the source of one of the potential modeling errors in Section 10.5. It should be noted though that the constraints applied to the power distribution may have introduced addition modelling errors, but this has not been examined fully in the current work.

I.2 Discretization Errors

Discretization errors are the result of attempting to solve for a continuous function using a discrete number of evaluation points. Discretization error also includes the errors such as numerical diffusion.

Discretization error can be formally estimated using a grid convergence index (GCI). A GCI can be calculated by solving an identical problem on at least 3 grids with different resolutions. The grid should be uniformly refined for proper estimation of this index. For the current analysis several unique meshing challenges were encountered, which led to a meshing strategy that required very fine meshes to resolve the boundary layer and the region near the contact between two touching pebbles. In order to uniformly increase the resolution of the grid a prohibitively large computational problem would be produced.

For the current analysis the discretization error was estimated producing a second grid using adaptive grid refinement. The original grid was refined in regions of high shear stress gradients and high pressure gradients. The resulting grid contains approximately 50% more cells than the original mesh. The solution was then found on this mesh for the 150 kg/s flow rate using an SST turbulence model. The pressure drop prediction for the original and refined model is shown in Figure I.2.1.

Figure I.2.1: Pressure Drop Prediction for Nominal Grid and Adaptively Refined Grid
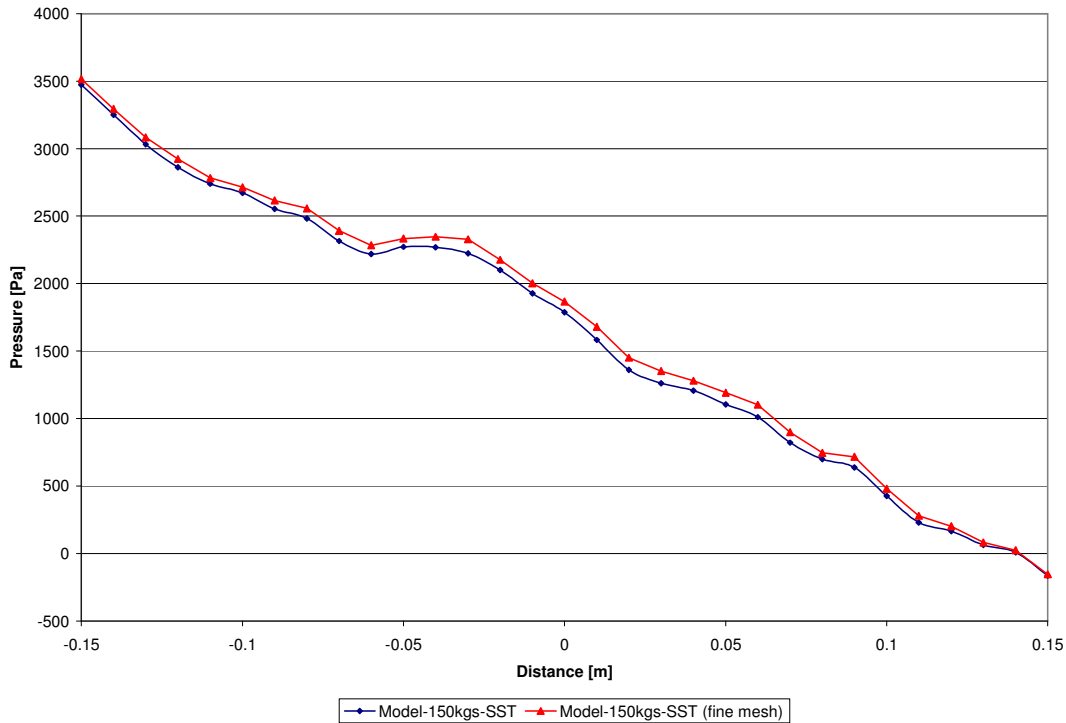
In Section 10.3.7 it was also indicated that Reference I.6 believed that 187,500 nodes per pebble would produce a grid independent solution and the model in this work uses approximately 160, 000 nodes per pebble. Because the current mesh density is close to the recommended value estimated for a grid independent solution and the pressure drop results between the nominal and refined models are very similar there is reasonable confidence that the discretization error will be low.

All analysis results in this document use second order discretization except for the solution of "omega" in the k-omega model (for solution stability). The use of second order discretizations are known to significantly reduce numerical diffusion on tetrahedral meshes.

Additional descritization errors are introduced with the use of thin shell elements for the analysis of pebbles adjacent to the reflector. The thin shell elements can only support a linear temperature variation through their thickness, which would be consistent with heat conduction through a plane wall. The current analysis applies these elements to curved walls which will not be completely accurate. The goal of this analysis was not however to examine the detailed temperature variation within a pebble or the reflector hence these errors are accepted as being reasonable.

I.3 Round-Off Errors

All simulations used in this document were solved in single precision. Single precision numbers are limited to 8 significant figures. Numbers in this simulation that are 8 orders of magnitude

smaller than the maximum value in the simulation are not considered valid. Round-off errors are considered to have a negligible impact on reported results in the current work.

I.4   Solution/Convergence Errors for Flow Solution of Pebble Assembly Remote from the Reflector

CFD simulations form very large non-linear (non-constant coefficient) matrices to solve discrete governing equations for desired variables. The direct inversion of a non-linear matrix is not possible so as an alternative the coefficients in the matrix are calculated at frozen values using an initial guess (or current solution). The matrix may then be inverted and the coefficients updated based on the new solution.[3] The process is repeated until the updated system of equations agrees with the current solution. The measure of the difference between the updated system of equations and the current solution is called a residual.

In FLUENT residuals are normalized such that the residual at the first iteration is 1.0. If a good initial guess is given the residuals may not decrease much or at all, and the converse situation is also true. It is not sufficient to monitor residuals only in FLUENT because of this unique definition so flow variables must also be monitored. For the current work the area weighted average pressure at the inlet to the solution domain and the integral of shear stress over all completely interior pebbles are monitored. When these flow variables stabilize on a "steady" value and the residuals are also not changing the solution is considered converged.

It was found that in all simulations performed that the monitored data never settles on a singular value, but rather they vary slightly. Figure I.4.1, Figure I.4.2 and Figure I.4.3 show the variation of the area averaged inlet pressure with solver step after the solution residuals have stopped decreasing significantly.

---

[3] The direct inversion of these matrices is prohibitively computationally expensive; hence approximate iterative methods that are computationally cheap (relatively) are used. Convergent iterative methods come closer and closer to the exact solution of a matrix with an increasing number of iterations. It is not possible to solve iterative equations for an infinite number of iterations so; the analyst must decide a sufficient level of convergence.

Figure I.4.1: Pressure Fluctuation in Converged Solution – 15 kg/s Core Coolant Flow Rate
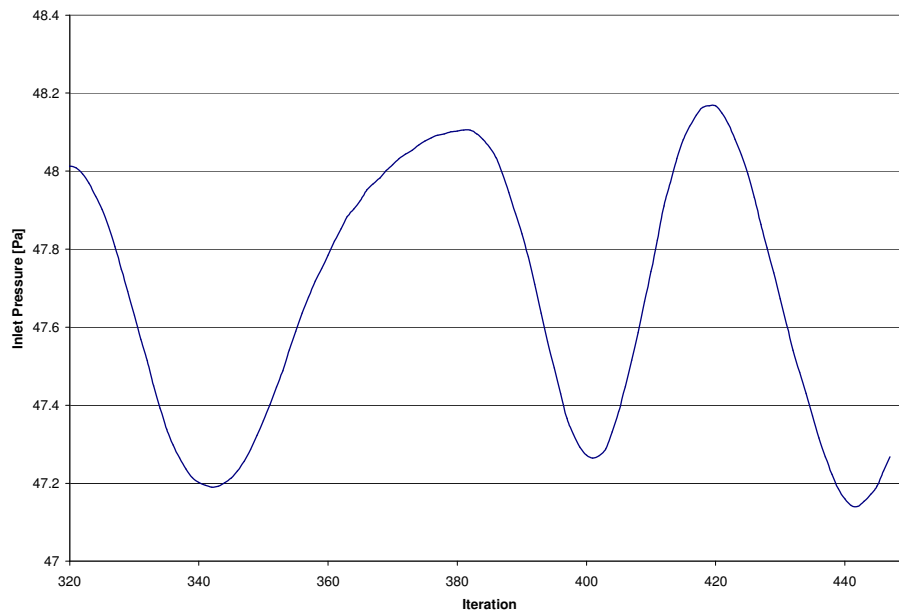
Figure I.4.2: Pressure Fluctuation in Converged Solution – 75 kg/s Core Coolant Flow Rate
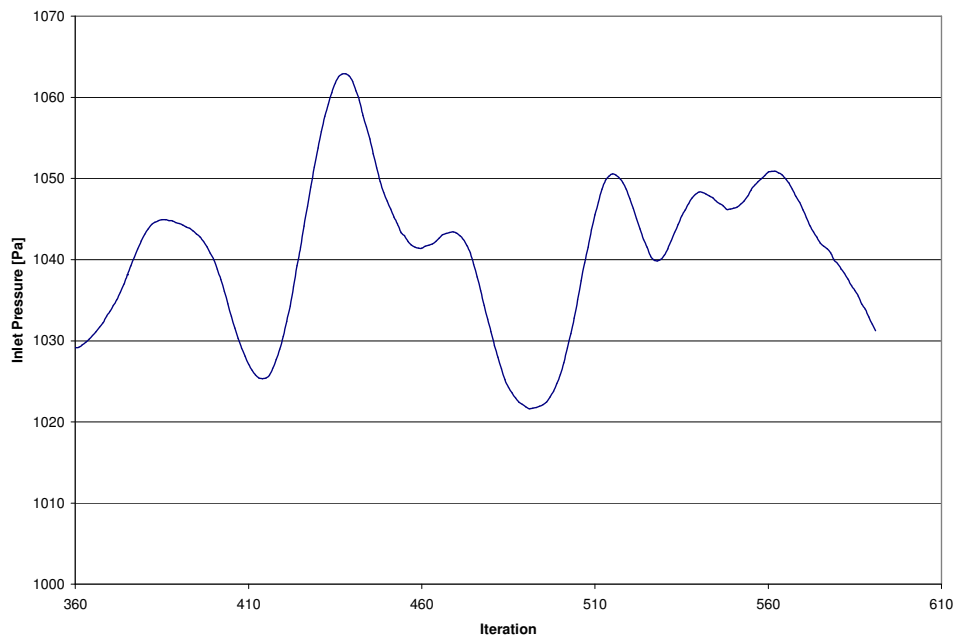
Figure I.4.3: Pressure fluctuation in converged solution – 150 kg/s Core Coolant Flow Rate
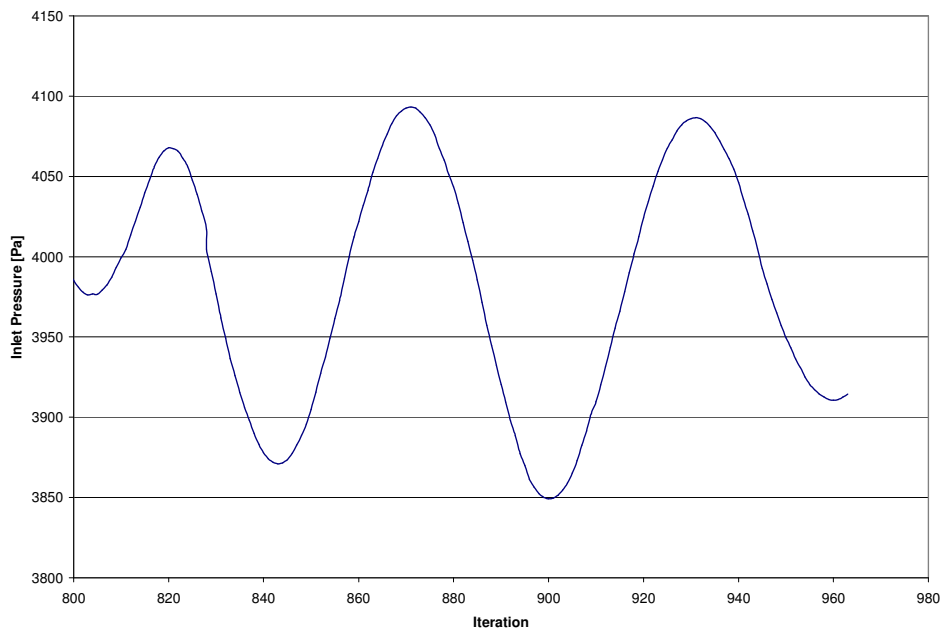
Figure I.4.4 shows the variation of the integrated wall shear stress (for the 150kg/s case only) over pebbles that are totally contained within the solution domain with solver step after the solution residuals have stopped decreasing significantly.

Figure I.4.4: Integrated Shear Stress Fluctuation in Converged Solution – 150 kg/s Core Coolant Flow Rate
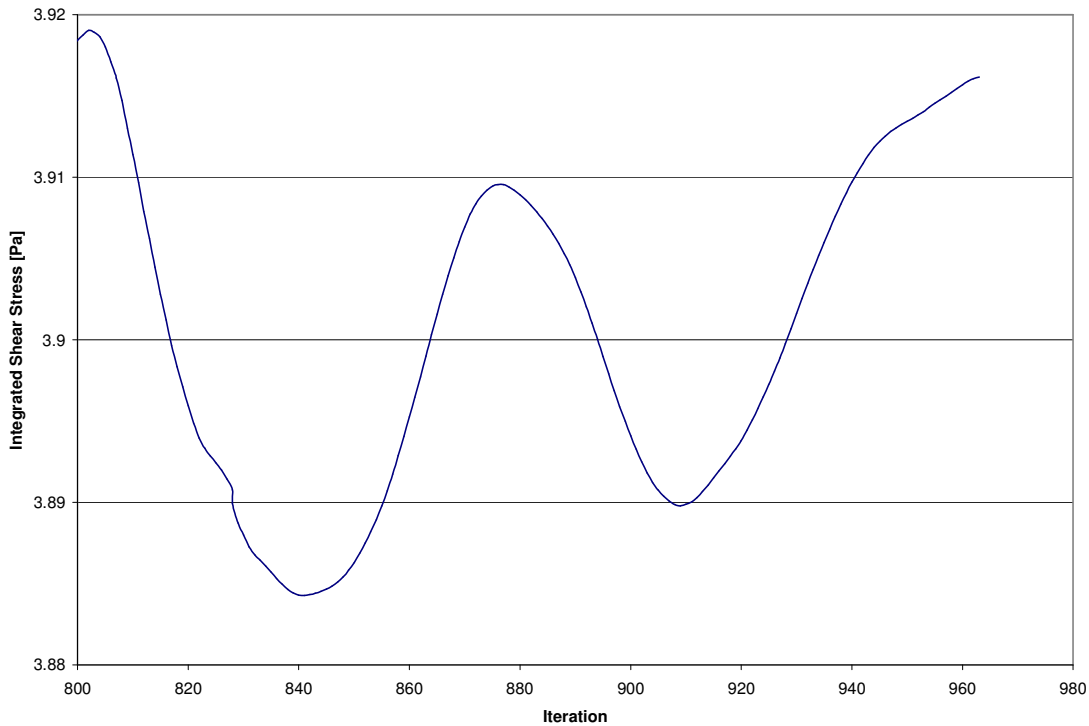
To quantify the variations shown in Figure I.4.1 to Figure I.4.4 the total variation (maximum – minimum) over the range shown in the figures was calculated and then divided by the average value over this range. These values are taken to represent the convergence error and are reported in Table I.4.1.

Table I.4.1: Convergence Error in the Solution

Simulation flow	Maximum Variation in Inlet Average Pressure (%)	Maximum Variation in Integrated Shear Stress (%)
150 kg/s	6.1	0.9
75 kg/s	4.0	1.5
15 kg/s	2.2	0.9

It should be noted that this variation in the converged solution may be a physical phenomenon. This variation is an indication that the solution may be transient in nature. If increased accuracy is required in future work it is recommended that a transient solution be created. The time averaged quantities from the transient can then be calculated as a more representative value for pressure drop and shear stress.

I.5   Solution/Convergence Errors for Pebble Assembly Adjacent to the Reflector

The convergence errors in the simulation were discussed in Section 10.5 and only estimates of these errors are presented in this section. Estimates of convergence error are calculated for the average pebble surface temperature, the average inlet pressure and the integrated shear stress on the pebble surfaces. The convergence error estimates were calculated by taking the range of each quantity (maximum subtract minimum) divided by the average of that quantity over the last 50 iterations of the solution. The convergence error estimates are provided in Table I.5.1.

Table I.5.1: Convergence Error in the Solution

Simulation flow	Maximum Variation in Average Surface Temperature (%)	Maximum Variation in Inlet Average Pressure (%)	Maximum Variation in Integrated Shear Stress (%)
150 kg/s	0.09%	1.30%	0.54%
75 kg/s	0.05%	1.56%	0.26%
15 kg/s	0.02%	0.69%	0.30%

Figure I.5.1 show the convergence history for average inlet pressure for the 150 kg/s case only.

Figure I.5.1: Inlet Pressure Convergence for 150 kg/s Core Coolant Flow Rate
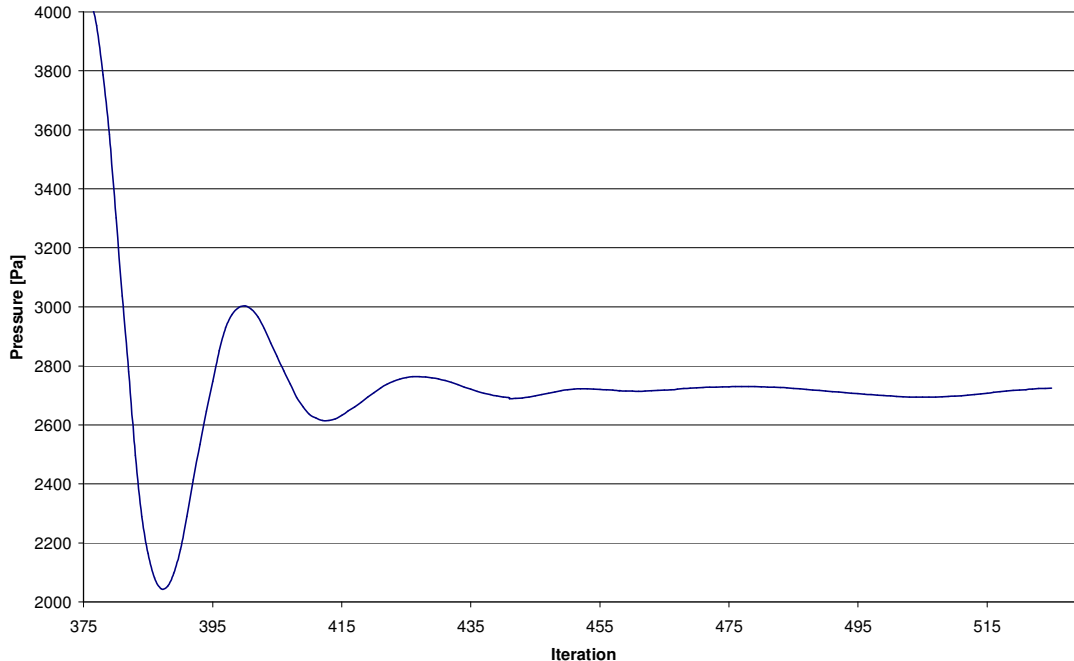
I.6 Unexpected Turbulence Intensity

During the examination of the results from the various models created in this work it was noted that the turbulence intensity produced by several of the models was significantly higher than expected. In many cases the turbulence models predicted fluctuation velocities greater than the mean flow velocity. Table I.6.1 shows a summary of the volume weighted average turbulence intensity for each model in this work.

Table I.6.1: Volume Weighted Average Turbulence Intensity

Model	Turbulence intensity (%)
15kg/s flow – SST turbulence model	20
75kg/s flow – SST turbulence model	98
150kg/s flow - SST turbulence model	200
150kg/s flow – k-omega turbulence model	254
150kg/s flow – Reynolds stress turbulence model	18

The results of Table I.6.1 show that the k-omega and SST turbulence models predict significantly different turbulence intensities than the RSM. The RSM intensity values appear much more reasonable than the other turbulence models. This is an unexpected result; however, the pressure drop and shear predictions from the RSM are similar to the SST and k-omega results. This effect is simply noted at this point and it is recommended that the turbulence quantities from the SST models in this simulation not be considered accurate, even though the remainder of the solution appears reasonable.

I.7 References

I.1   "Evaluation of High Temperature Gas Cooled Reactor Performance- Benchmark analysis related to the PBMR-400, PBMM, GT-MHR, HTR-10 and the ASTRA Critical Facility", IAEA-TECDOC-TBD DRAFT, September 2006.

I.2   The Nuclear Safety Standards Commission (KTA), "KTA Program of Standards (14.04.2008), Reactor Core Design for High-Temperature Gas-Cooled Reactor, Part 3: Loss of Pressure through Friction in Pebble Bed Cores", KTA Standard 3102.3, March 1981. URL <http://www.kta-gs.de/common/regel_prog.htm>.

I.3   G. Yesilyurt, "Numerical Simulation of Flow Distribution for Pebble Bed High Temperature Gas Cooled Reactors", Texas A&M University, May 2003.

I.4   The Nuclear Safety Standards Commission (KTA), "KTA Program of Standards (14.04.2008), Reactor Core Design for High-Temperature Gas-Cooled Reactor, Part 2: Heat Transfer in Spherical Fuel Elements", KTA Standard 3102.2, June 1983. URL <http://www.kta-gs.de/common/regel_prog.htm>.

I.5   F. Incropera, D. DeWitt, "Fundamentals of Heat and Mass Transfer 5th Ed.", 2002.

I.6   R. Hill, D. Koch, A. Ladd, "Moderate-Reynolds-number flows in ordered and random arrays of spheres", Journal of fluid Mechanics, Vol. 448, pp. 243-278, 2001.

APPENDIX J PROCESS TO CREATE LARGE PEBBLE BED GRIDS

J.1   Introduction

The purpose of this section is to describe a generic process in which one may create a volumetric mesh suitable for CFD simulations for a section of a packed bed.

J.1.1   Domain Definition

Prior to beginning the mesh generation process the domain being modeled must first be defined. This section deals with a solution domain that is a slice of an annular packed bed (Figure J.1.1). Figure J.1.1 and Figure J.1.2 show the definitions of several parameter that need to be determined prior to beginning the mesh generation process.

Figure J.1.1: Large Solution Domain Methodology, Domain Definitions - 1
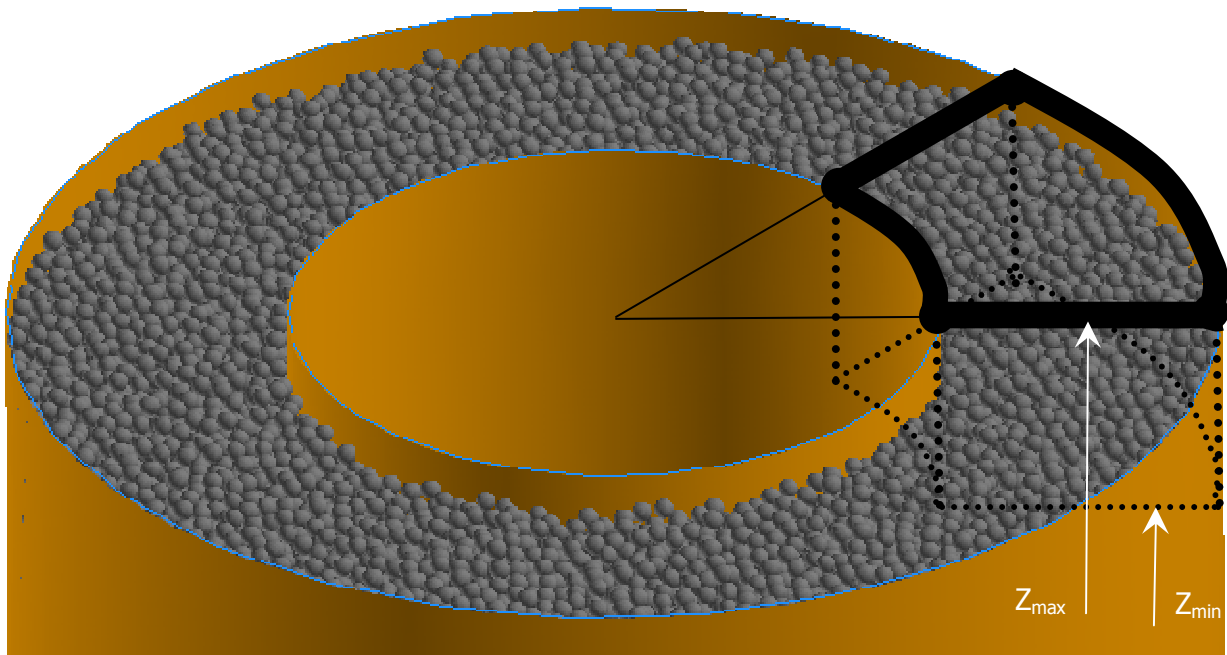
Figure J.1.2: Large Solution Domain Methodology, Domain Definitions - 2
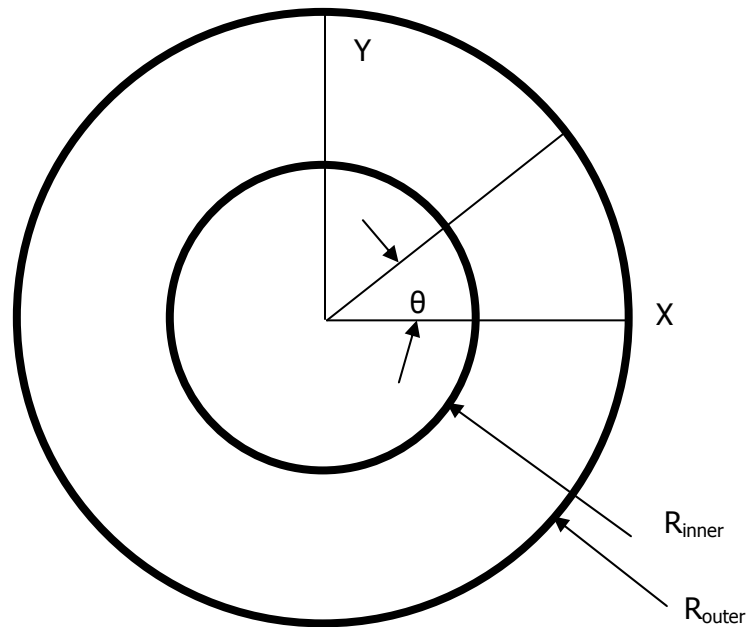
J.1.2 Assumptions

The following assumptions are made:

1. A data set exist which specifies the X,Y,Z coordinates of a set of pebble centroids within an annular region. The pebble centroid positions can be generated by the simulations of the PEBS code (see Appendix D). A sample dataset for an annular region with R_{inner} equal to 1.0 m and R_{outer} equal to 1.85 m has been provided as part of the work described in Appendix D.

2. A piece of software is available that can perform the following tasks:

    a. Generate prismatic elements.

    b. Generate hexahedral, tetrahedral and pyramid type elements within a single mesh.

    c. Can receive input through a scripting language

3. The software and hardware do not have any mesh size limitations. For most practical purposes 64bit software/hardware satisfies this criterion. ANSYS GAMBIT (32bit software) can not generate more than approximately 20 million mesh volumes.

J.1.3 Process Overview

The process for creating a volumetric mesh for a packed bed can be accomplished by the following general steps.

1. Create the CAD (computer aided design) geometry for the mesh.

2. Create the CAD geometry for the pebble contact points.

3. Split the CAD geometry. This operation divides the geometry up into regions "near" the pebble contact points and regions "far" from the pebble contact points.

4. Apply a surface mesh to the physical surfaces of the "near" regions.

5. Apply a triangular surface mesh to the physical surfaces of the "far" region.

    a. Examine the quality of the mesh. Definitions of quality are software dependent; however the quality must be "high".

6. Apply prismatic layers to the surfaces in the "far" region.

7. Apply a quadrilateral mesh to the "near" regions of the CAD geometry.

8. Apply a triangular tetrahedral/pyramid mesh to the "far" region of the CAD geometry.

J.2 Mesh Generation Details

J.2.1 Create the CAD Geometry for the Mesh

The arrangement of pebbles within a packed bed does not conform to any ordered packing arrangement, which limits the methods available to represent it as CAD geometry. Constructive solid geometry was the only method available to generate this geometry. The following process is used to create the CAD geometry for a packed bed.

1. Define the extents of the solution domain (Z_{min}, Z_{max}, θ (See Figure J.1.2 and Figure J.2.1))

2. Read the locations of the pebble centroids from a file.

3. Determine if the pebble makes contact with the solution domain. If a pebble does contact the solution domain the X,Y,Z coordinates should be stored in an array $X_{inc}(i),Y_{inc}(i),Z_{inc}(i)$.

4. Create the CAD geometry that represents the solution domain, which can be referred to as "DOMAIN" (i.e. an annular slice of the core). This region should span from (Z_{min}-tolerance) to (Z_{max}+tolerance). The "tolerance" must be greater than 1 pebble diameter.

5. Create the CAD geometry for the entire core, which can be referred to as "CORE". The "CORE" object must span a range of z-coordinates that is encompasses the "DOMAIN" object.

6. Create the CAD geometry for each pebble that touches the solution domain.

J.2.2 Create the CAD Geometry for the Pebble Contact Points

The contact points between pebbles can be represented by a cylindrical region. The following process is used to create the cylinders that represent the contact points.

1. Determine the radius of the contact using a stress analysis (e.g. Hertz contact analysis).

2. For each sphere in the domain, search for another sphere that has a centroid within 1 pebble diameter plus a small tolerance. A tolerance of 0.05 cm is reasonable for pebbles with a diameter of 6 cm. If another sphere is within this distance a contact set is formed.

3. If the contact set is close to the boundary of the solution domain (within distance "A") then proceed to Process B, otherwise use Process A. If a contact is very close to the boundary of the domain a degenerate geometric definition can be formed (See Figure J.2.3).

Process A

1. Create a cylinder between the centroids of each contact set with the contact radius.

2. Create a second cylinder between the centroids of each contact set with a larger radius (the radius should be equal to distance "A").

Process B

1. Delete the pebble that is furthest out of the domain and recreate it with a smaller radius (97% of original radius for example).

2. Do not create any contact object.

J.2.2.1   Reflector Contact Points

It is also possible for pebbles to make contact with the inner and outer reflector. In the case that a pebble does make contact with a reflector the following process should be followed.

1. For each pebble in the solution domain determine if it has a centroid that is within 1 pebble diameter plus a small tolerance (0.05 cm is reasonable) from the reflector. If this condition is satisfied then the pebble contacts the reflector.

2. If the contact is close to the boundary of the solution domain (within distance "A") then proceed to Process D, otherwise use Process C.
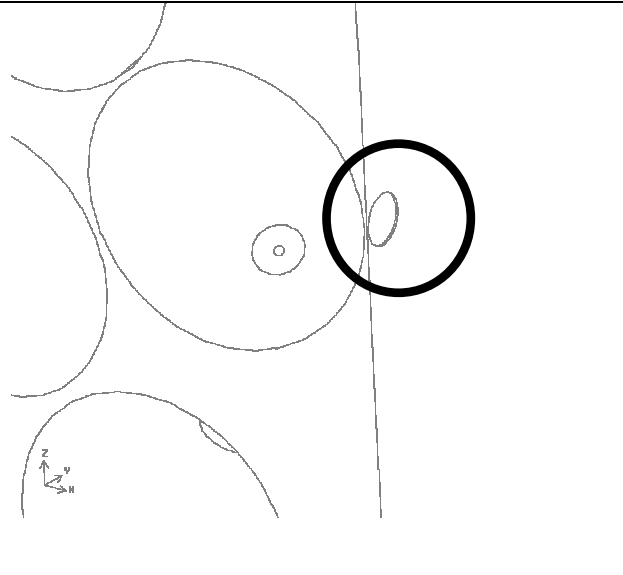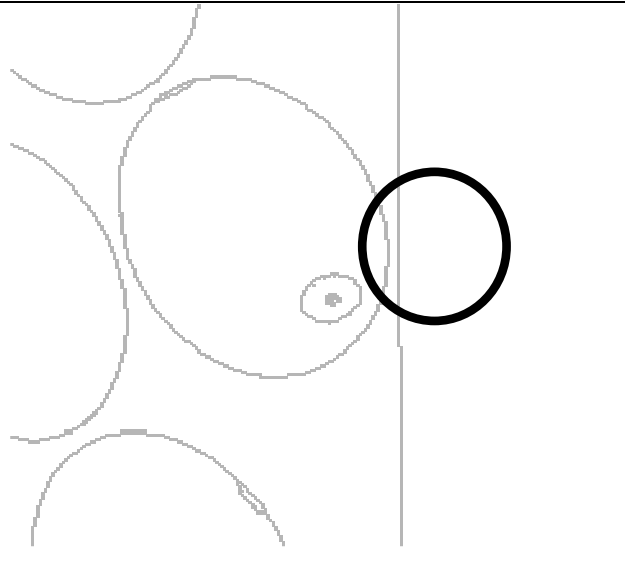
<u>Process C</u>

1. Create a cylinder that extends from the pebble centroid perpendicular to the reflector. The radius of this cylinder is determined from a contact stress analysis.

2. Create a second cylinder with a radius equal to distance "A" along the same vector as the cylinder created in the previous step.

<u>Process D</u>

1. Delete the pebble and recreate it with a smaller radius (97% of original radius for example).

2. Do not create any contact object.

Figure J.2.1: Large Solution Domain Methodology, Reflector Contact Issue and Resolution

Degenerate contact is created if the cylindrical cutting object is near the boundary of the solution domain	Solved by shrinking the problem pebble slightly and not including the cutout (Processes B and D).

J.2.2.2   Cleanup

In the event a sphere is located well within the solution domain but the surface of the sphere barely touches the solution domain a sharp edged piece of geometry will be created as shown in the figure below.

Figure J.2.2: Large Solution Domain Methodology, Domain Boundary Contact Issue

Sharp Angle
Created
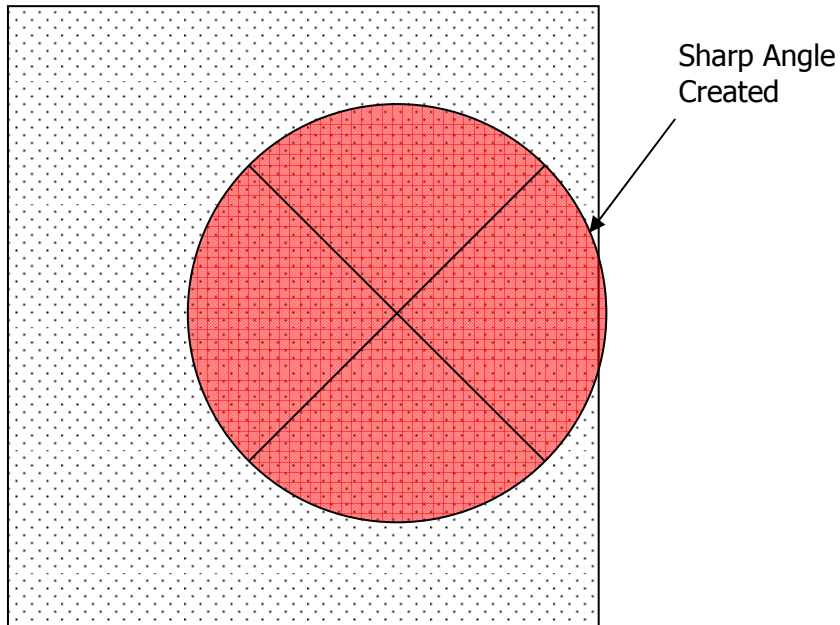
In this situation a cylinder should be created that is perpendicular to the solution domain boundary and extending from the center of the sphere. This cylinder should be treated the same as the contact point cylinders in the following steps. The images below show the cleanup operation performed.

Figure J.2.3: Large Solution Domain Methodology, Domain Boundary Contact Issue - Resolution

Material is removed eliminating sharp angles
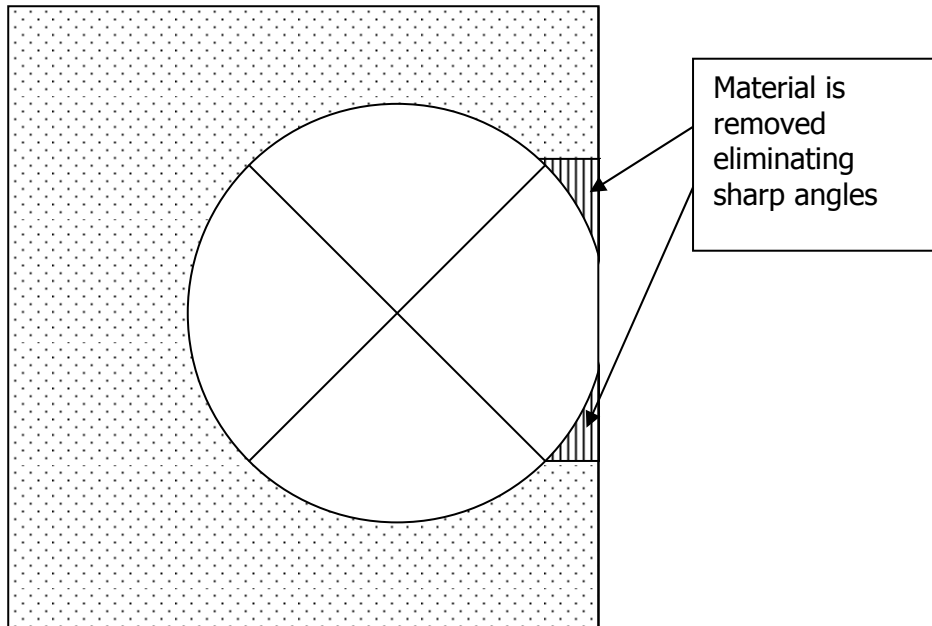
Figure J.2.4: Large Solution Domain Methodology, Domain Boundary Contact Issue – Resolution

Internal Pebble only touches boundary slightly	A cutout is used to correct this problem
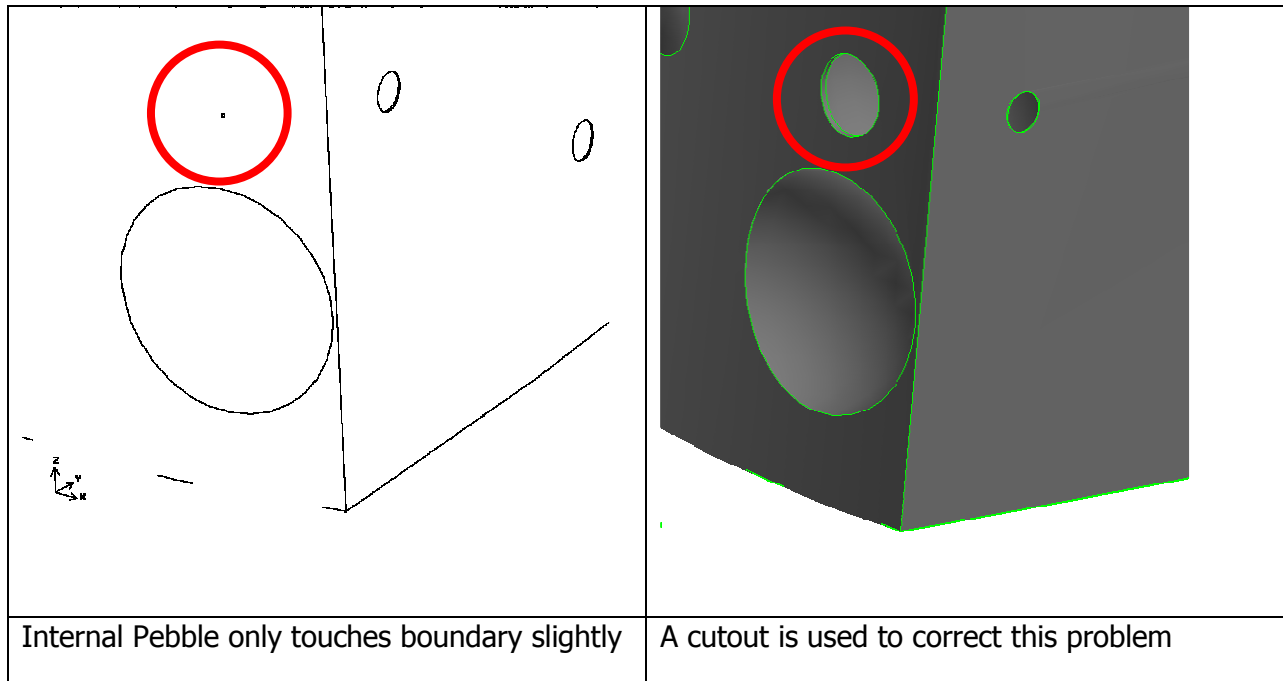
J.2.3 Split the CAD Geometry

The next step of the geometry generation process is to split the "near" pebble region from the "far" pebble region. The following steps are required to complete this process.

1. Subtract all cylinders representing pebble contacts and all cleanup cylinders from the "CORE" object. This step creates a single object (which will be referred to as "CORE CUT") that represents the annulus with the pebbles and pebble cutouts removed.

2. Split this new "CORE CUT" object using the larger cylinders created in Section J.2.2 and J.2.2.1. This operation separates the "near" and "far" regions of the geometry.

J.2.4 Apply a Surface Mesh to the Physical Surfaces of the "Near" Regions

In this step a surface mesh is applied to one surface of each "near" pebble contact point region. A sample mesh is shown in Figure J.2.5.

Figure J.2.5: Large Solution Domain Methodology, Sample of "Near" Pebble Contact Region

Apply mesh to top surface
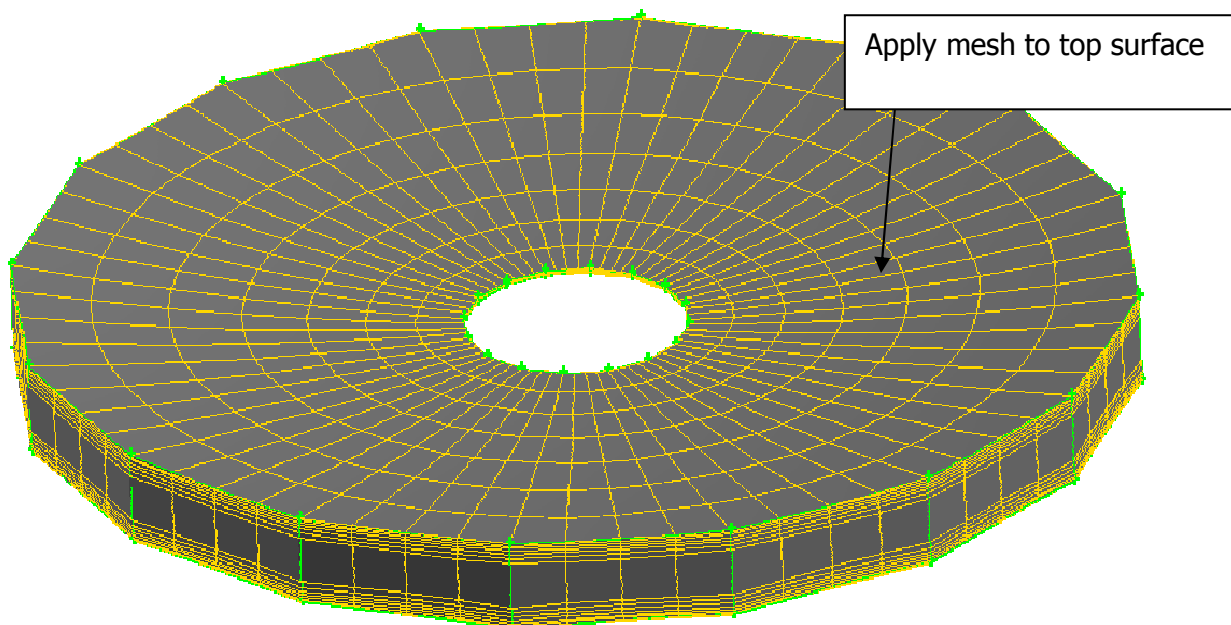
J.2.5 Apply Triangular Surface Mesh to the Physical Surfaces of the "Far" Region

The next step in the process is to apply a triangular mesh to the physical surfaces of all objects in the "far" region. There are some "non-physical surfaces" that form the boundary between

the "near" and "far" regions; however these are not meshed at this stage. An example of a surface mesh in the "far" region is shown in Figure J.2.6.

Figure J.2.6: Large Solution Domain Methodology, Triangular Surface Mesh in "Far" Region
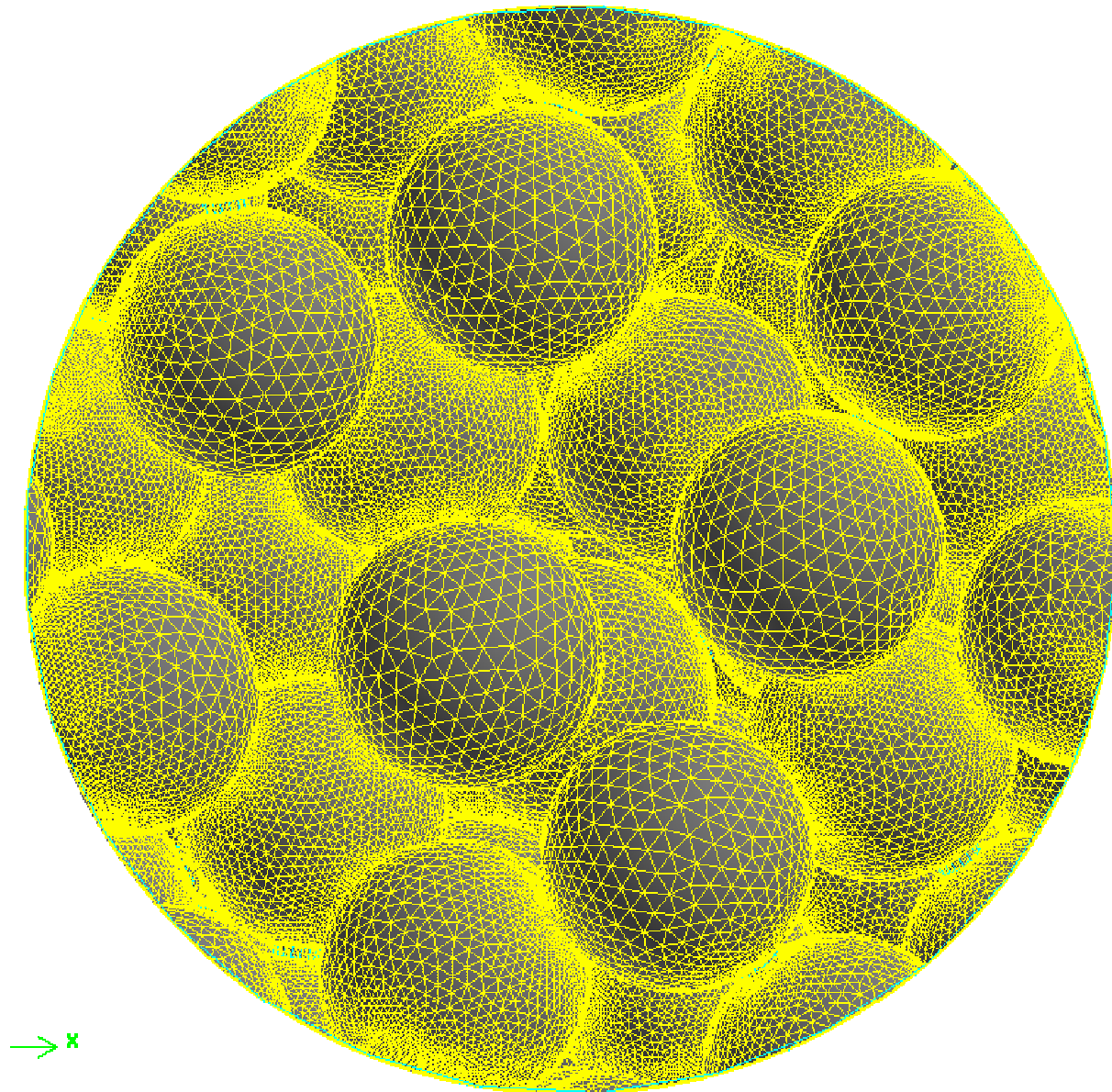
After a surface mesh has been created it is critical to examine the quality of the mesh. Highly skewed or inverted surface elements will not facilitate the creation of an acceptable surface

mesh. Highly skewed elements must be removed from the mesh and replaced with high quality elements. This is generally a manual process, and is different each time a mesh is generated.

J.2.6 Apply Prismatic Layers to the Surfaces in the "Far" Region

The modeling of viscous flows requires that a large number of elements be placed near the surface of objects. This is accomplished by extruding the surface mesh into the solution domain. It is recommended that at least 6 layers be created and the first layer thickness should be approximately 2×10^{-3} cm thick.

J.2.7 Volumetric Mesh Generation

The volumetric mesh generation fills in the gaps between the surface mesh (and outer prismatic layer) with 3 dimensional elements. The "near" regions should be filled with high quality quadrilateral elements (See Figure J.2.5). The "far" region should be filled with tetrahedral and pyramid type elements.

APPENDIX K EVALUATION OF MULTI-BATCH HEAT TRANSFER COEFFICIENTS

A model to describe heat transfer and temperature variations between PBR fuel elements of different powers within a pebble bed core has been described in Section 8. However, the values for certain coefficients used within the multi-batch model were not specified within this reference. The purpose of the current calculation note is to determine, from a literature search and hand calculations, approximate forms for the coefficients in the multi-batch model. The model will then be applied to a specific test case, and the batch surface temperatures evaluated for comparison with CFD results.

K.1 Summary of the Steady State Multi-batch Fuel Model

A pebble bed is considered to consist of a number of batches of pebbles, each of which releases a different amount of power. The heat generated within a computational cell by pebbles from batch i, $\dot{q}_{gen}^{i}$, will balance heat loss from the pebbles surfaces in steady state. The heat losses may be categorised as:

- Heat transferred to the coolant gas by convection, $\dot{q}_{conv}^{i}$
- Heat transferred to pebbles in neighbouring cells, $\dot{q}_{cond}^{i}$
- Heat transferred to neighbouring pebbles belonging to different batches, $\dot{q}_{batch}^{i}$

The heat balance for batch i within a computational cell, described in Figure K.1, therefore requires:

$$\dot{q}_{gen}^{i} = \dot{q}_{conv}^{i} + \dot{q}_{cond}^{i} + \dot{q}_{batch}^{i} \, .$$

The heat flux to pebbles in neighbouring cells is denoted $\dot{q}_{cond}^{i}$, since this transfer appears as a conductive term within a whole core porous medium model of the pebble bed. However, in reality this term represents a combination of two heat transfer processes:

- Radiation between pebble surfaces
- Heat conduction through pebble to pebble contacts

Similarly, the inter-batch heat fluxes, $\dot{q}_{batch}^{i}$, represent a combination of several constituent heat fluxes.

The model derived in Section 8 provides the following forms for the constituent heat fluxes in the multi-batch fuel temperature model:

- Heat transfer to the gas is determined by a heat transfer coefficient[4], h, and the surface area of batch i pebbles within the computational cell, $A^i = A_{peb} \cdot m_i$:

$$\dot{q}_{conv}^i = h \cdot A^i \cdot (T_{surf}^i - T_{gas})$$

- Batch to batch heat transfer within a cell is governed by the difference between the batch i temperature surface temperature and the average pebble surface temperature within the computational cell:

$$\dot{q}_{batch}^i = \frac{m_i}{m} C \cdot (T_{surf}^i - \overline{T}_{surf}) \; .$$

where

m_i = number of pebbles from batch i in cell,

m = total number of pebbles within the cell.

as detailed in Section 8.2.3.1.

- Heat transfer to pebbles in neighbouring computational cells, with index k, is governed by the temperature difference between the surface temperature of batch i in the cell, and the average pebble temperature in cell k:

$$\dot{q}_{cond,k}^i = \frac{m_i}{m} \cdot B_k \cdot (T_{surf}^i - \overline{T}_{surf,k})$$

where

m_i = number of pebbles from batch i in cell,

m = total number of pebbles within the cell.

as detailed in Section 8.2.4.

---

[4] In Section 8, the heat transfer coefficient is denoted by the symbol λ. In this document the symbol h is used to avoid confusion with expressions for thermal conductivity quoted from other sources.

Figure K.1: Inter-Pebble Heat Fluxes
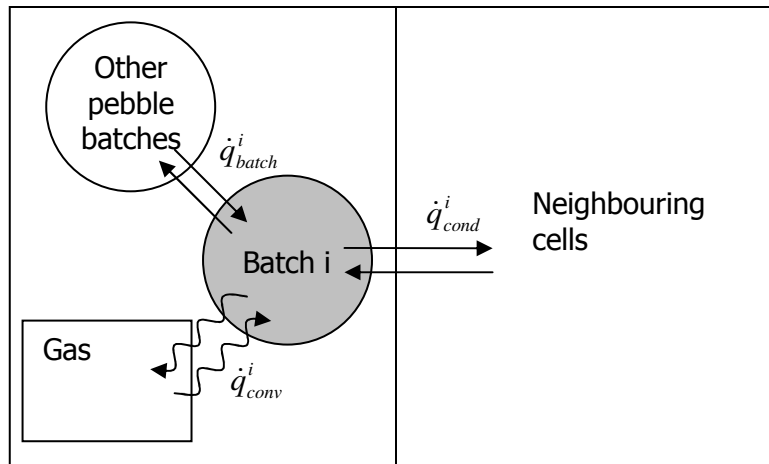
K.2 Published Correlations for Pebble Bed Heat Transfer

A range of experimental studies have been conducted to examine heat transfer within a pebble bed (see Reference K.2 and K.3 and references therein). These studies examine heat transfer across a uniform pebble bed. However, the correlations described still provide useful information to assist with the evaluation of the multi-batch model coefficients λ, B_k and C.

K.2.1 Heat Transfer from the Pebbles to the Coolant Gas

The KTA rules (Reference K.1 recommends that the heat transfer coefficient, h, at the pebble surface within a packed pebble bed should be determined by the following expression:

$$h = \frac{Nu \cdot \lambda_{gas}}{d}, \qquad \text{where} \quad Nu = 1.27 \cdot \frac{\text{Pr}^{1/3}}{\phi^{1.18}} \text{Re}^{0.36} + 0.033 \cdot \frac{\text{Pr}^{1/2}}{\phi^{1.07}} \text{Re}^{0.86}$$

where the Reynolds number is evaluated using the superficial velocity within the pebble bed:

$$\text{Re} = \frac{\dot{m} \cdot d}{\mu \cdot A}$$

and:

A Total (unoccupied) cross section area of pebble bed

ϕ Void fraction in pebble bed

Pr   Prandtl number of coolant gas

$\dot{m}$ Mass flow rate through pebble bed

μ Dynamic viscosity of coolant gas

d Pebble diameter

λ_{gas} Thermal conductivity of the coolant gas

This correlations is stated to be valid for the following range of parameter values:

Reynolds number Re $100 < Re < 10^5$

Porosity of the bed $0.36 < \varepsilon < 0.42$

Pebble diameter   d < 1/20 of pebble bed diameter

Height of bed H   H > 4 d

The restriction on the pebble diameter is stated not to apply if local values are used instead of the porosity values averaged over the cross section of the vessel.

K.2.2 Conduction and Radiation Transfer Between Pebbles

Zehner and Schlünder developed a model for heat transfer through a evacuated pebble bed, reported in English in Reference K.2. This model accounts for radiation between pebble surfaces and heat conduction through pebbles. The Zehner-Schlünder correlation takes the form of an effective pebble bed conductivity:

$$\lambda_{eff}^{Z-S} = \left\{ \frac{\left[1-(1-\phi)^{1/2}\right]\cdot\phi}{2/\varepsilon-1} + \frac{(1-\phi)^{1/2}}{2/\varepsilon-1}\cdot\frac{B_z+1}{B_z}\cdot\frac{1}{1+\dfrac{1}{(2/\varepsilon-1)\Lambda}} \right\}\cdot 4\cdot\sigma\cdot T^3\cdot d$$

Where:

$$B_z = 1.25\cdot\left(\frac{1-\phi}{\phi}\right)^{10/9}$$

and

ϕ Void fraction of pebble bed

d Pebble diameter (m)

T Pebble bed temperature (K)

ε Pebble surface emissivity

σ Stefan Boltzmann constant (5.67×10^{-8} W m^{-2} K^4)

λ_{peb} Thermal conductivity of the pebbles (W m^{-1} K^{-1})

$\Lambda = \lambda_{peb} / (4 \cdot \sigma \cdot T^3 \cdot d)$ Ratio of particle conductivity to effective black body radiation conductivity

The correlation is based on the analysis of a 'unit cell', as shown in Figure K.2. Within this expression, it is stated in Reference K.2 that the first term within the brackets represents direct radiative heat transfer across the bed, whilst the second term represents combined conduction through, and radiation between, pebbles within the bed.

Breitbach and Barthels Reference K.2 found improved agreement with a range of experimental data by modifying the first term in the above expression, leading to the modified Zehner Schlünder correlation:

$$\lambda_{eff}^{r} = \left\{ \left[1 - (1-\phi)^{1/2} \right] \cdot \phi + \frac{(1-\phi)^{1/2}}{2/\varepsilon - 1} \cdot \frac{B_z + 1}{B_z} \cdot \frac{1}{1 + \dfrac{1}{(2/\varepsilon - 1)\Lambda}} \right\} \cdot 4 \cdot \sigma \cdot T^3 \cdot d$$

Breitbach and Barthels modification treats the unoccupied sections of the base areas of the unit cell (see Figure K.2) as black surfaces, whereas Zehner and Schlünder originally treated these as grey surfaces with the same emissivity as the pebble surfaces.

Figure K.2: The Unit Cell Considered by Zehner and Schlünder

"Base areas" partly covered by pebble cross section

Unoccupied section of base treated as grey (emissivity ε) by Z&S. Modified to black by B&B to improve fit with experimental data.

Pebble surface emissivity ε

Pebble conductivity λ_{peb}

Heat paths across cell:

(a) Conduction – radiation - conduction

(b) Direct radiation across entire cell
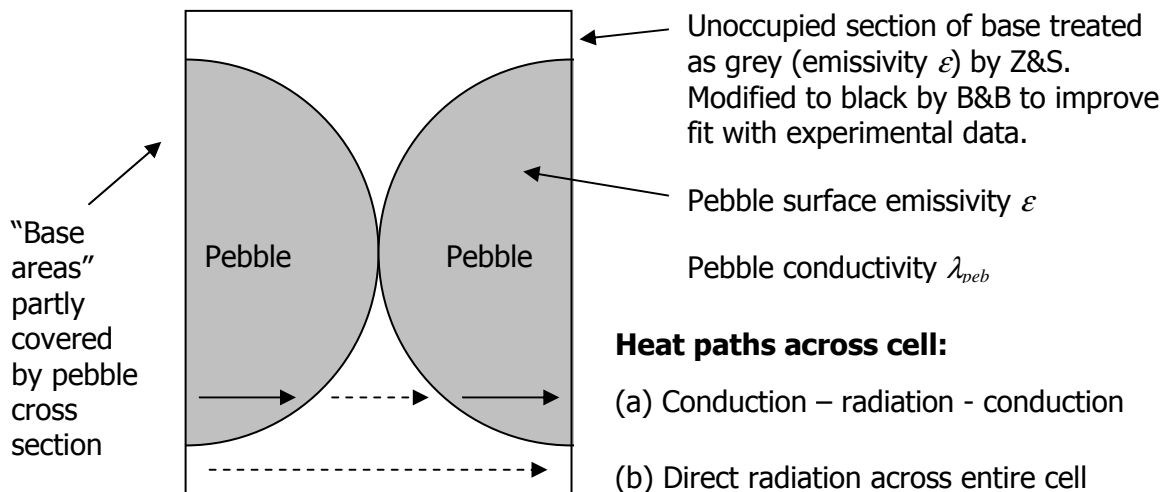
K.2.3 Conduction Between Pebbles to Pebble to Pebble Contact

Inter-pebble forces cause pebbles to deform slightly where they contact one another, leading to a non-zero contact area. The contact area depends on the material properties and the magnitude of the inter-pebble forces. Heat may pass between adjacent pebbles by conduction across these contact areas. The effective conductivity of the pebble bed is dependent on both the size of the contact area and the number of contact points between pebbles.

A correlation for the effective pebble bed conductivity resulting from pebble to pebble conduction due to Chen and Tien is quoted in Reference K.4[5]. The effective conductivity is presented as a fraction of the pebble graphite conductivity, λ_{peb}:

$$\lambda_{eff}^c = \lambda_{peb} \cdot \left[\frac{3 \cdot \left(1 - \mu_p^2\right)}{4 \cdot E_s} \cdot f \cdot R \right]^{1/3} \cdot \frac{1}{0.531 \cdot S} \left(\frac{N_A}{N_L} \right)$$

where

$$f = p_{peb} \cdot \frac{S_F}{N_A}$$

and

		Representative values for simple cubic packing (Reference K.4)
μ_p	Poisson ratio of the pebble material	0.136
E_s	Young's modulus of the pebble material	9.0×10^9 N m^{-2}
R	Pebble radius	0.03 m
N_L	Number of pebbles per unit length	$1/(2R) = 16.67$ m^{-1}
N_A	Number of pebbles per unit area	$1/(4R^2) = 278$ m^{-1}
S	Parameter describing packing	1
S_F	Parameter describing packing	1
p_{peb}	External pressure acting on pebbles	

The pressure p_{peb} can be estimated from the weight of the pebble bed. However, from the Hertzian contact theory, it may be noted that the expression in square brackets is equal to the

---

[5] The original reference could not be obtained in time for the current work.

cube of the radius of the contact area between two identical elastic spheres in contact. Thus, the correlation presented above may be understood as

$$\lambda_{eff}^c = \lambda_{peb} \cdot \frac{a}{0.531 \cdot S} \left(\frac{N_A}{N_L} \right)$$

where a is the radius of the pebble-pebble contacts predicted by Hertzian contact theory.

K.2.4 Heat Transfer Across the Pebble Bed due to the Coolant Gas

The presence of the coolant gas in the pebble bed facilitates heat transfer even in the absence of forced cooling. This due to heat conduction through coolant gas and the bodies of the pebble fuel element, together with localised convection currents.

Zehner and Schlünder published a correlation for the effective thermal conductivity of a saturated pebble bed, which is reported in Reference K.3. The correlation states:

$$\lambda_{eff}^g = \lambda_{gas} \cdot \left\{ 1 - (1-\phi)^{1/2} + \frac{2 \cdot (1-\phi)^{1/2}}{1 - \gamma \cdot B} \left[\frac{(1-\gamma)B}{(1-\gamma B)^2} \ln\left(\frac{1}{\gamma B} \right) - \frac{B+1}{2} - \frac{B-1}{1-\gamma B} \right] \right\}$$

where

$$\gamma = \frac{\lambda_{gas}}{\lambda_{peb}}, \qquad \text{and} \qquad B = 1.25 \left(\frac{1-\phi}{\phi} \right)^{10/9}$$

and

ϕ	Void fraction of pebble bed
λ_{peb}	Thermal conductivity of the pebbles (W m^{-1} K^{-1})
λ_{gas}	Thermal conductivity of the coolant gas (W m^{-1} K^{-1})

This correlation was compared to experimental test data by Prasad et al. (Reference K.3). Good agreement between the experimental data and the Zehner-Schlünder correlation was found for combinations of materials satisfying the condition $\gamma < 1$, i.e. where the thermal conductivity of the solid material is greater than the conductivity of the surrounding gas. This condition is satisfied by the materials present in a PBR core.

K.3 Derivation of Expressions for Heat Fluxes in the Multi-Batch Model

Based on the correlations described above, together with suitable approximate models, the coefficients B_k and C which form part of the multi-batch model can be evaluated.

K.3.1 Inter-Batch Heat Transfer Within a Cell

The inter-batch heat transfer is composed of two constituent terms, due to conduction across pebble contact areas and radiation between pebble surfaces:

$$\dot{q}^i_{batch} = \dot{q}^{i,(conduction)}_{batch} + \dot{q}^{i,(radiation)}_{batch}$$

K.3.1.1 Evaluating $\dot{q}^{i,(radiation)}_{batch}$

In order to generate a simple model for $\dot{q}^{i,(radiation)}_{batch}$, heat transfers to and from an individual pebble at temperature T^i_{surf} is considered. The pebble exchanges heat by radiation with a large number of surrounding pebbles. It is not in general possible to quantify the radiation view factors to all surrounding pebbles. Therefore, an approximation is used to simplify the problem:

- Radiation exchange between the batch *i* pebble and it's immediate neighbours is modelled explicitly.

- Radiation exchange between the pebble and it more distant neighbours is approximated by the use of a black enclosure. This is justified by the assumption that rays which travel beyond the initial neighbours will enter a labyrinthine path, in which reflections are unlikely to return them to the original emitting pebble.

This is illustrated in Figure K.3 and Figure K.4. A radiation network model describing the simplified model is shown in Figure K.5. This may be altered to the equivalent circuit shown in Figure K.6, which is simpler to analyse, as may be seen from the re-drawn version displayed in Figure K.7. Using the standard rules for the combination of resistances arranged in parallel and in series, the network shown in Figure K.7 is found to be equivalent to a single resistance, R_{Total}, with value:

$$R_{Total} = R_{i,surf} + \left\{ \frac{1}{R_{i,enc}} + \left[R_{i,av} + \left(\frac{1}{R_{av,surf}} + \frac{1}{R_{enc,av}} \right)^{-1} \right]^{-1} \right\}^{-1}$$

Therefore the heat flux from a single pebble in batch *i* to the surrounding average pebbles is:

$$q^{i,(radiation)}_{peb} = \frac{E^b_i - E^b_{av}}{R_{Total}} = \frac{\sigma}{R_{Total}} \cdot \left(T^4_i - T^4_{av} \right)$$

Figure K.3: Radiation Model Centred on a Pebble from Batch i

Radiation to first ring of pebbles (indicated by green arrows) assumes grey surface, and sphere to sphere view factors

Rays passing first ring of pebbles (shown red) assumed to escape and are assumed to be absorbed.

$2\ r_{peb}$ r_{peb}
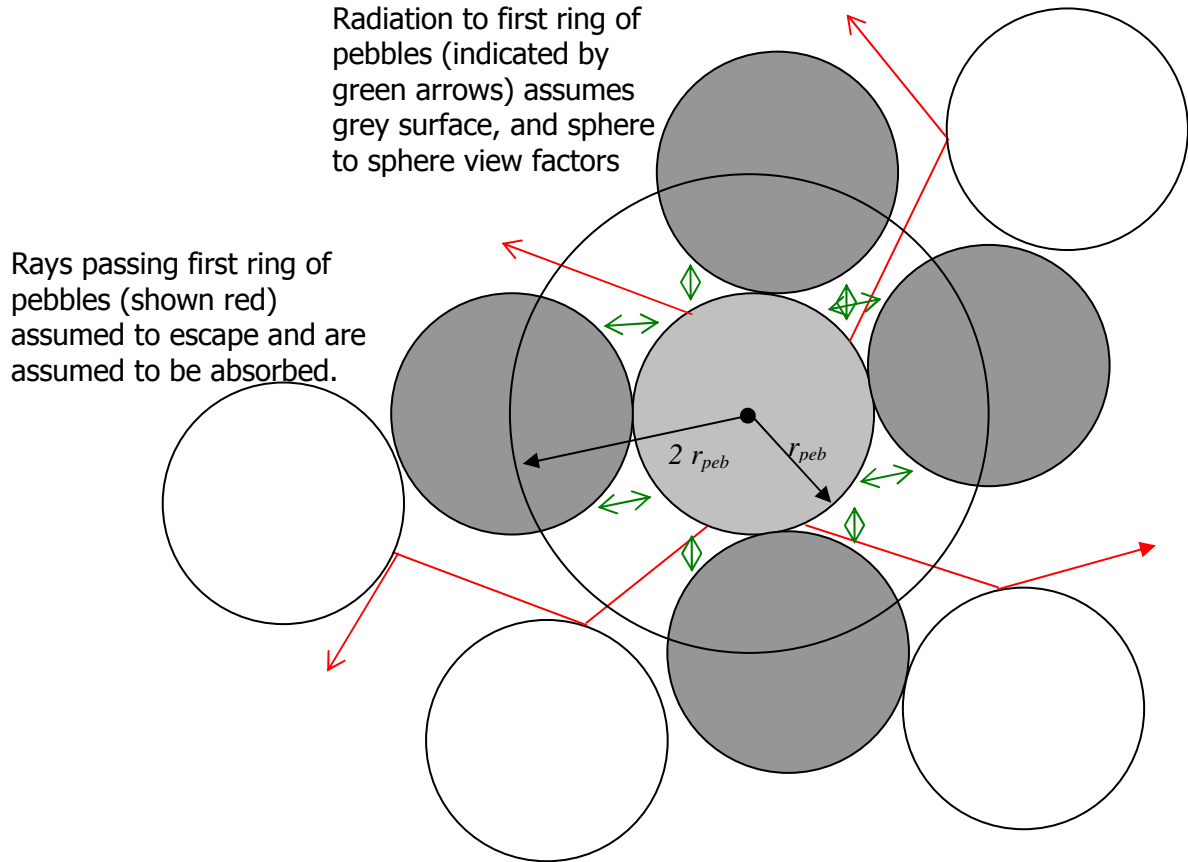
Figure K.4: Simplified Model of the Assembly Shown in Figure K.3

Thick red line indicates area modelled as black enclosure

Dark grey pebbles represent average pebbles, modelled directly
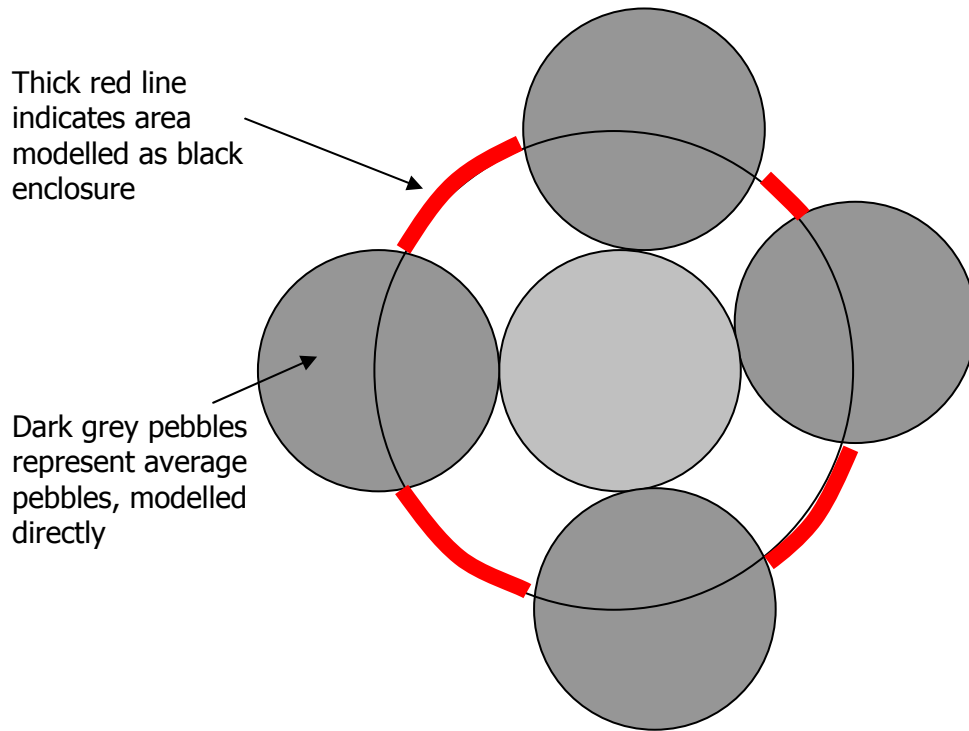
Figure K.5: Radiation Network for Radiation Transfer from a Batch *i* Pebble

Average pebbles E^b_{av}

$R_{av,surf}$

$q_{av,surf}$

J_{av}

$R_{enc,av}$ $q_{enc,av}$ Enclosure E^b_{av}

$R_{i,av}$ $q_{i,av}$

$R_{i,enc}$ $q_{i,enc}$

J_i

$R_{i,surf}$

$q_{i,surf}$

Pebble from batch E^b_i
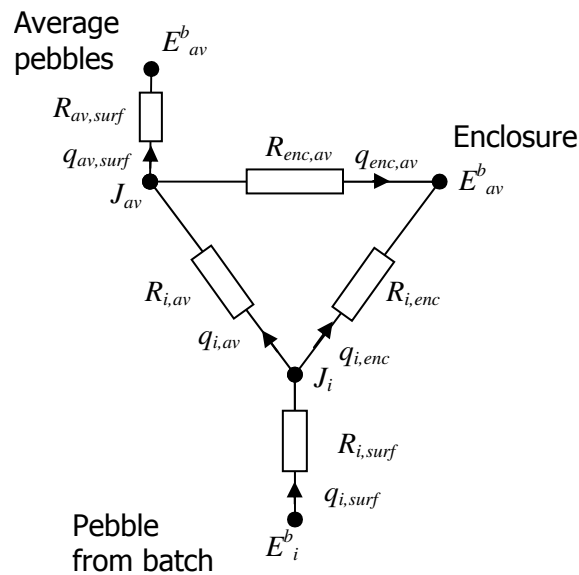
Figure K.6: Equivalent Circuit to Figure K.5, Formed by Adding a Zero-Resistance Link Between Two Nodes with an Identical Specified Potential
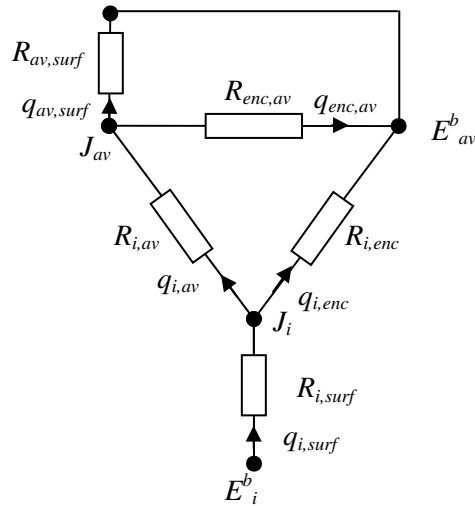
To complete the analysis, the values of the surface and spatial resistances must be determined, to allow the evaluation of R_{Total}. In order to estimate the view factors associated with the average pebbles, the number of 'average' pebbles immediately surrounding the batch i pebble must be estimated, together with the pebble to pebble radiation view factors.

The immediate neighbours are assumed to be in contact with the batch i pebble. The number of pebbles can be estimated by assessing the number of pebbles, n_{pebs}, required to achieve the nominal pebble bed packing fraction within a sphere of radius $2 \cdot r_{peb}$:

Figure K.7: The Circuit Shown in Figure K.6, Re-Drawn to Show its Structure
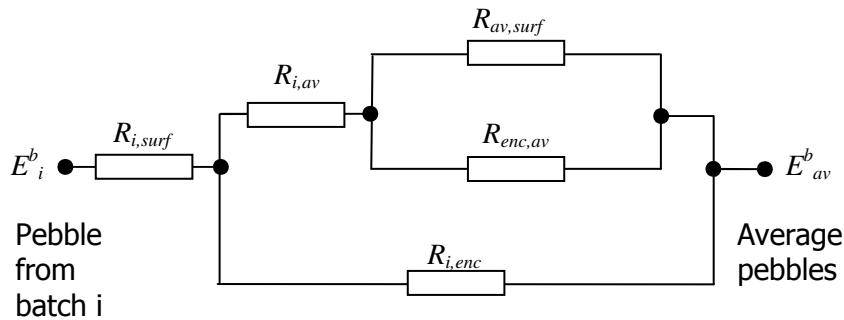
$$n_{pebs} = \frac{V_{occupied}}{V_{peb}} = \frac{(1-\phi) \cdot V_{sphere}}{V_{peb}} \frac{(1-\phi) \cdot \left[4 \cdot \pi \cdot \left(2 \cdot r_{peb}\right)^3 / 3\right]}{4\pi \cdot r_{peb}^3 / 3} = 8 \cdot (1-\phi)$$

The value of n_{Pebs} includes the central batch i pebble. Thus the number of average pebble volumes within the sphere is $n_{pebs} - 1 = 8 \cdot (1 - \phi) - 1 = 7 - 8 \cdot \phi$. Approximately half of each pebble surrounding the batch i pebble lies within the $2 \cdot r_{peb}$ sphere (more detailed calculations indicate that $122/256 = 0.48$ of the surrounding pebble volume lies within the sphere). Thus $2 \cdot (7 - 8 \cdot \phi)$ average spheres should be in contact with the batch i pebble to achieve the correct pebble packing fraction within the spherical region of radius $2 \cdot r_{peb}$. For a typical PBR pebble bed void fraction of $\phi = 0.39$, this gives $2 \cdot (7 - 8 \cdot \phi) = 7.76$ pebbles in contact with the central batch i pebble. It may be noted that for a set of hexagonally close packed pebbles (or equivalently, face centred cubic pebbles) for which $\phi \sim 0.25952$, each pebble would be in contact with 12 distinct neighbouring particles. For simple cubic packing, for which $\phi \sim 0.4764$, each pebble would be in contact with 6 neighbours. Thus the above estimate of 7.76 contacting neighbours appears realistic for a typical pebble bed packing of $\phi = 0.39$.

The spatial resistances depend on the view factors between the components. The view factor for two equal spheres in contact is given by Reference K.5, from a table of numerical values, to be $F_{sphere} = 0.0762$.

Thus the view factor from the batch i pebble to the surrounding $2 \cdot (7 - 8 \cdot \phi)$ identical average pebbles is:

$$F_{i,av} = 2 \cdot (7 - 8 \cdot \phi) \cdot F_{sphere} = 2 \cdot (7 - 8 \cdot \phi) \cdot (0.0762) = 1.0668 - 1.2192 \cdot \phi$$

The remaining view factor from the batch i pebble is assigned to the black enclosure which occupies the gaps between the average pebbles. View factor arithmetic shows:

$$F_{i,av} + F_{i,enc} = 1.0,$$

which implies

$$F_{i,enc} = 1.0 - F_{i,av} = 1.0 - (1.0668 - 1.2192 \cdot \phi) = 1.2192 \cdot \phi - 0.0668$$

To complete the evaluation of the spatial resistances, the view factor must be determined. To a first approximation, it may be assumed that since the pebble bed is homogeneous, and therefore the view factor from an average pebble to the enclosure is equal to the view factor from the batch i pebble to the enclosure. The surface resistances, $R_{av,surf}$ and $R_{i,surf}$ depend on the pebble emissivity and radiating areas, as described in Reference K.6. No surface resistance is associated with the black enclosure. The values of the radiation resistances are summarised in the following table.

$R_{av,surf}$	Surface resistance of average pebbles	$\dfrac{1-\varepsilon}{\varepsilon \cdot A_{av}}$
$R_{i,surf}$	Surface resistance of pebble from batch i	$\dfrac{1-\varepsilon}{\varepsilon \cdot A_{peb}}$
$R_{i,av}$	Spatial resistance from pebble in batch i to average pebbles	$\dfrac{1}{A_{peb} \cdot F_{i,av}} = \dfrac{1}{A_{peb} \cdot (1.0668 - 1.2192 \cdot \phi)}$
$R_{i,enc}$	Spatial resistance from pebble in batch i to black enclosure	$\dfrac{1}{A_{peb} \cdot (1 - F_{i,av})} = \dfrac{1}{A_{peb} \cdot (1.2192 \cdot \phi - 0.0668)}$
$R_{av,enc}$	Spatial resistance from average pebbles to black enclosure	$\dfrac{1}{A_{av} \cdot (1.2192 \cdot \phi - 0.0668)}$

The overall heat transfer from batch i to other batches within the cell may be computed by multiplying the single pebble flux by the number of batch i pebbles within the cell:

$$q_{batch}^{i,(radiation)} = m_i \cdot q_{peb}^{i,(radiation)}$$
$$= \frac{m_i \cdot \sigma}{R_{Total}} \cdot \left(\left(T_{surf}^i \right)^4 - \left(\overline{T}_{surf} \right)^4 \right)$$

If the temperature difference is much smaller than the absolute temperature value, as is usual in reactor conditions, then it may be seen that

$$\left(T_{surf}^i \right)^4 - \left(\overline{T}_{surf} \right)^4 \sim 4 \cdot \left(\overline{T}_{surf} \right)^3 \cdot \left(T_{surf}^i - \overline{T}_{surf} \right)$$

and hence the flux may be approximated by

$$q_{batch}^{i,(radiation)} = \frac{4 \cdot m_i \cdot \sigma \cdot \left(\overline{T}_{surf} \right)^3}{R_{Total}} \cdot \left(T_{surf}^i - \overline{T}_{surf} \right).$$

K.3.1.2 Evaluating $\dot{q}_{batch}^{i,(conduction)}$

In this section, the conductive heat transfer, $\dot{q}_{batch}^{i,(conduction)}$, between an individual pebble at temperature T_{surf}^i and surrounding average pebbles is considered. The thermal resistance associated with pebble-pebble contacts is determined by four factors (Reference K.7):

1. Thermal constriction resistance: The heat flux lines converge on approach to the contact point, and diverge as they pass from the contact point into the bulk of the second body

(see Figure K.8). This results in a thermal resistance due to the meso-scale geometry

2. Roughness of the surface: Roughness of the pebble surfaces causes the contact between the two pebbles to take the form of a large number of microscopic contacts, rather than a single perfect contact. Thermal constriction creates further thermal resistance at each micro-contact.

3. Emissivity of the pebble surfaces: Imperfect contact between the pebbles, due to roughness, results in a inter-pebble gap. Heat may be transferred across this gap by thermal radiation.

4. Conductivity of the gas surrounding the pebbles: Imperfect contact between the pebbles, due to roughness, results in a inter-pebble gap. Heat may be transferred across this gap by conduction through the inter-pebble gas.

Item 1 is a meso-scale resistance due to the meso-scale geometry of the bodies, whereas items 2-4 described microscopic resistances at the gap. The total gap resistance is the sum of the micro- and meso-scale resistances. Due to the absence of information about pebble roughness, etc. the pebbles are assumed to be in perfect contact, such that the microscopic contact resistance is zero, and only the meso-scale thermal constriction resistance is considered in this current work.

Inter-pebble forces cause elastic deformation of the pebbles, leading to a non-zero contact are between adjacent pebbles. The magnitude of the contact area may be estimated by Hertzian contact. The meso-scale thermal constriction resistance for two contacting spheres of conductivity λ_{peb}, with a circular contact region of radius a, assuming an isothermal boundary at the contact, is given by the expression (Reference K.7):

$$R_{contact} = \frac{1}{2 \cdot \lambda_{peb} \cdot a}$$

The assumption of a uniform heat flux across the contact area, in lieu of an isothermal contact, alters this result by just 8% (Reference K.7).

As described in Section K.3.1.1, the batch i pebble may be assumed to be in contact with $2 \cdot (7 - 8 \cdot \phi)$ surrounding average temperature pebbles. Thus the heat flux between a single pebble from batch i and the surrounding average pebbles is

$$\dot{q}_{peb}^{i,(conduction)} = 2 \cdot (7 - 8 \cdot \phi) \cdot \frac{\left(T_{surf}^i - \overline{T}_{surf} \right)}{R_{conatct}} = 4 \cdot (7 - 8 \cdot \phi) \cdot \lambda_{peb} \cdot a \cdot \left(T_{surf}^i - \overline{T}_{surf} \right)$$

The net conductive flux from batch i pebbles to other batches within the cell may be computed by multiplying the single pebble flux by the number of batch i pebbles within the cell:

$$\dot{q}_{batch}^{i,(conduction)} = m_i \cdot \dot{q}_{peb}^{i,(conduction)} = 4 \cdot \left(7 - 8 \cdot \phi \right) \cdot m_i \cdot \lambda_{peb} \cdot a \cdot \left(T_{surf}^i - \overline{T}_{surf} \right).$$

Figure K.8: Diagram Illustrating Thermal Constriction Resistance (diagram taken from Reference K.7)
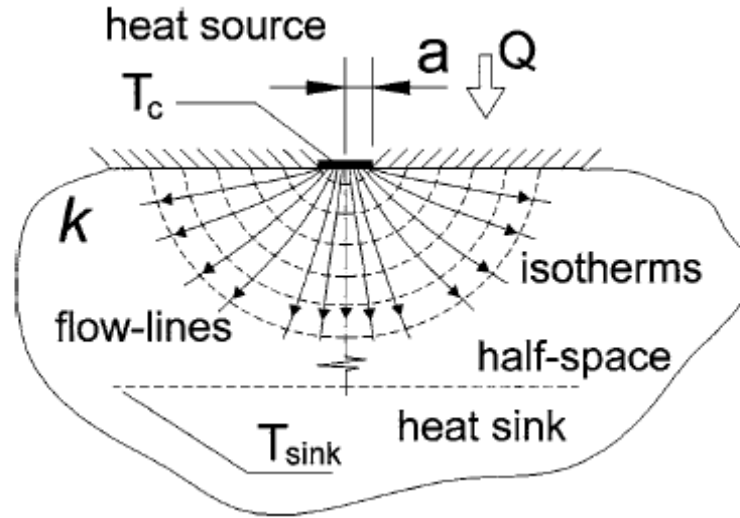
K.3.1.3 Comparison of Radiation and Conduction Fluxes for Inter-Batch Heat Transfer

The thermal resistances for heat transfer from a single batch *i* pebble to the surrounding average pebbles are evaluated for representative conditions in Table K.1 and Table K.2. Within this calculation, a pebble Hertzian contact radius of 1 mm is assumed, based on the values computed in support of the work documented in Section 10.3. The results show that at representative PBR conditions, radiative heat transfer between pebbles is approximately 5 times greater than pebble to pebble conduction.

K.3.2 Evaluating the Overall Inter-Batch Heat Flux

The overall inter-batch heat transfer is the sum of the radiation and contact conduction contributions, as described in Section K.3.1. Thus, combining the results presented in Section K.3.1.1 and K.3.1.2, it is found that:

$$
\dot{q}_{batch}^{i,(conduction)} = 4 \cdot (7 - 8 \cdot \phi) \cdot m_i \cdot \lambda_{peb} \cdot a \cdot \left(T_{surf}^i - \overline{T}_{surf} \right) + \frac{m_i \cdot 4 \cdot \sigma \left(\overline{T}_{surf} \right)^3}{R_{Total}} \cdot \left(T_{surf}^i - \overline{T}_{surf} \right)
$$

$$
= m_i \cdot \left(4 \cdot (7 - 8 \cdot \phi) \cdot \lambda_{peb} \cdot a + \frac{4 \cdot \sigma \cdot \left(\overline{T}_{surf} \right)^3}{R_{Total}} \right) \cdot \left(T_{surf}^i - \overline{T}_{surf} \right) .
$$

Therefore, the coefficient C in the multi-batch model can be evaluated by comparing the expression for $\dot{q}_{batch}^i$ described in Section K.1 with the above expression, which shows that

$$\frac{m_i}{m} \cdot C = m_i \cdot \left(4 \cdot (7 - 8 \cdot \phi) \cdot \lambda_{peb} \cdot a + \frac{4 \cdot \sigma \cdot \left(\overline{T}_{surf} \right)^3}{R_{Total}} \right),$$

and hence

$$C = m \cdot \left(4 \cdot (7 - 8 \cdot \phi) \cdot \lambda_{peb} \cdot a + \frac{4 \cdot \sigma \cdot \left(\overline{T}_{surf} \right)^3}{R_{Total}} \right).$$

K.4 Evaluating Multi-Batch Fuel Temperatures

Section 8 provides the following expression for the evaluation of pebble surface temperatures in a multi-batch pebble bed:

$$T_{surf}^i = \overline{T}_{surf} + \frac{\dfrac{m}{m_i} \dot{q}_{gen}^i - \dot{q}_{gen}}{h \cdot A + C + \overset{neighbours}{\underset{k}{\sum}} B_k}$$

If the pebble bed is treated as a single large computational cell, the sum of B_k over neighbouring cells may be neglected, such that the expression reduces to:

$$T_{surf}^i = \overline{T}_{surf} + \frac{\dfrac{m}{m_i} \dot{q}_{gen}^i - \dot{q}_{gen}}{h \cdot A + C}.$$

The above expression has been used to evaluate the expected pebble surface temperatures for the 3 batch model used within the CFD analysis of multi-batch temperatures, described in Section 10.7. The following inputs were used within the calculation:

- The coefficient C describing the inter-batch heat transfer has been evaluated based on the theory described in Section K.3, as described in Table K.2.

- The radius of the pebble to pebble contact areas has been set to 1 mm, equal to the value derived from considerations of inter-pebble loads within a pebble bed core (Section 10.3) and equal to that used in CFD models of a multi-batch PBR core described in Section 10.7.

- Three pebble batches were assumed, with equal populations within each batch. This is based on the multi-batch CFD model, which contains 39 pebbles divided equally between 3 batches. The batch powers were assumed to produce 50%, 100% and 150% respectively of the average power output of a PBMR fuel pebble (see Section 10.7). The pebble powers used were:

Batch:	Cool batch	Average batch	Hot batch
Power:	443 W / pebble	886 W / pebble	1329 W / pebble

- A packing fraction of 0.576 was used, equal to the packing fraction obtained in the CFD model of the pebble bed (see Section 10.7).

- The heat transfer coefficient at the pebble surface, h, is evaluated from the KTA rules (described in Section K.2.1) as shown in Table K.3.

- The average gas temperature and pressure are taken to be 1043.5 K and 89.1 bar, based on the values used in the multi-batch CFD model, which are representative of PBR reactor core conditions.

The model parameters and resulting fuel temperatures are shown in Table K.4. The results indicate that there will be a 11.2°C difference between surface temperatures of the cool and average pebbles. An 11.2°C temperature difference is also predicted between the surface temperatures of the average and hot fuel batches.

The effects of inter-pebble radiation and conduction may be suppressed by setting the value of the coefficient C to zero. In this case, the batch surface temperatures are given by the expression

$$T_{surf}^i = \overline{T}_{surf} + \frac{\frac{m}{m_i}\dot{q}_{gen}^i - \dot{q}_{gen}}{h \cdot A},$$

which may be evaluated from the 'intermediate values' presented in Table K.4. This shows that in the absence of inter-batch heat transfer, the surface temperature differences between the hot and average, and cool and average, batches will rise to 12.0 K. Thus inter-batch heat transfer results in a temperature differential of just 0.8 K.

K.4.1 Evaluation of Batch Surface Temperatures for a Lower Pebble to Gas Heat Transfer Coefficient Value

Evidence gathered from CFD simulations reported in Section 10.4 indicates significant differences may exist between heat transfer coefficients predicted by CFD modelling and the KTA rules. Work performed during the multi-batch CFD model study reported in Section 10.7 indicates that the CFD models (presented in Section 10.4.6.2) predict a heat transfer coefficient of 2187 W m^{-2} K^{-1} at the pebble surface. This value is just 67% of the value predicted by the KTA rules (shown in Table K.3).

In order to permit comparison between the analytical model of multi-batch fuel temperatures described in this model, and the CFD results described in Section 10.7, the pebble surface temperatures have been re-evaluated, based on a pebble to gas heat transfer coefficient of 2187 W m^{-2} K^{-1}. The results, shown in Table K.5, indicate that there will be a 16.1°C difference between surface temperatures of the cool and average pebbles. An 16.1°C temperature

difference is also predicted between the surface temperatures of the average and hot fuel batches.

The effect of inter-batch heat transfer is again assessed by setting the coefficient C to zero and re-evaluating the pebble surface temperatures. This shows that in the absence of inter-batch heat transfer, the surface temperature differences between the hot and average, and cool and average, batches will rise to 17.9 K. Thus inter-batch heat transfer results in a temperature differential of just 17.9 K − 16.1 K = 1.8 K in this case.

It may be noted that the influence of inter-batch heat transfer on the pebble surface temperatures will increase if the heat transfer coefficient is lowered further, as would occur if the forced flow rate through the reactor is decreased.

K.5 References

K.1   KTA Safety Standard, 'Reactor Core Design of High-Temperature Gas-Cooled Reactors. Part 2: Heat Transfer in Spherical Fuel Elements', KTA 3102.2, Issue 06/83, Nuclear Safety Standards Commission (KTA), Federal Republic of Germany, June 1983.

K.2   G. Breitbach and H. Barthels, 'The radiant heat transfer in the HTR core after failure of the afterheat removal systems', Nuclear Technology, Vol 49 Issue 3, pp 392-399, August 1980.

K.3   V. Prasad, N. Kladias, A. Bandyopadhaya and Q. Tian, 'Evaluation of correlations for stagnant thermal conductivity of liquid-saturated porous beds of spheres', Int. J. Heat and Mass Transfer, Vol 32, Issue 9, pp1793-1796, September 1989.

K.4   'INET analysis of SANA-1 experiment benchmark problems', published within 'Heat transport and afterheat removal for gas cooled reactors under accident conditions', IAEA-TECDOC 1163, IAEA, January 2001.

K.5   Campbell, J.P. and McConnell, D.G., 'Radiant-interchange configuration factors for spherical and conical surfaces to spheres' NASA TN D-4457,1968.

K.6   Holman, J.P., 'Heat Transfer', 9th edition, McGraw Hill, 2002.

K.7   Bahrami M., Culham J.R., Yananovich M.M. and Schneider G.E., 'Review of Thermal Joint Resistance Models for nonconforming Rough Surfaces', Applied Mechanics Reviews, Vol 59 Issue 1, January 2006.

Table K.1: Computation of Thermal Resistances for a Single Pebble in Batch *i*, at a Typical Pebble Bed Packing Fraction, ϕ=0.39

Quantity	Symbol	Value	Units
Pebble radius	r_{peb}	0.03	m
Pebble surface area	A_{peb}	0.011309734	m^2
Pebble volume	Vol_{peb}	8.4823E-05	m^3
Pebble bed void fraction	ϕ	0.39	-
Pebble packing fraction	$(1-\phi)$	0.61	-
Pebble emmisivity	ε	0.8	-
Pebble conductivity	λ_{peb}	30	W/m/K
Number of contacts per pebble (see calc note for details)	$N_{contact}$	7.76	-
Assumed radius of Hertzian contact regions (based on CFD work)	a	0.001	m
Surface area of average pebbles	A_{av}	0.087763532	m^2
Average pebble surface temperature	T^{av}_{surf}	1065.44	K
Stefan-Boltzmann constant	σ	5.67E-08	W m^{-2} K^{-4}

Radiation view factors

Quantity	Symbol	Value	Units
View factor for one pebble to single contacting pebble	F_{sphere}	0.0762	-
View factor for average pebbles from batch i pebble	$F_{i,av}$	0.591312	-
View factor for black enclosure from batch i pebble	$F_{i,enc}$	0.408688	-
View factor for black enclosure from average pebble	$F_{av,enc}$	0.408688	-

(note these multiply black body emmisive power differences, not temperature differences)

Radiation network resistances

Quantity	Symbol	Value	Units
Surface radiation resistance of average pebbles	$R_{av,surf}$	2.848563558	m^{-2}
Surface radiation resistance of pebble from batch i	$R_{i,surf}$	22.10485321	m^{-2}
Spatial radiation resistance from pebble in batch i to average pebbles	$R_{i,av}$	149.5308954	m^{-2}
Spatial radiation resistance from pebble in batch i to black enclosure	$R_{i,enc}$	216.3494226	m^{-2}
Spatial radiation resistance from average pebbles to black enclosure	$R_{av,enc}$	27.88008023	m^{-2}
Total radiation resistance from pebble in batch i to average pebbles	R_{Total}	111.4215976	m^{-2}

$$R_{Total} = R_{i,surf} + \left\{ \frac{1}{R_{i,enc}} + \left[R_{i,av} + \left(\frac{1}{R_{av,surf}} + \frac{1}{R_{enc,av}} \right)^{-1} \right]^{-1} \right\}^{-1}$$

Quantity	Symbol	Value	Units
Effective thermal resistivity equivalent to R$_{Total}$	$R_{Total} / (\sigma (T_{surf}^{av})^3)$	0.406168792	K/W

Conduction across Hertzian contacts

Quantity	Symbol	Value	Units
Thermal resistance of a single contact between two pebbles	$R_{contact} = 1/(2 \lambda_{peb}\ a)$	16.66666667	K/W
Thermal resistance between batch i pebble and average pebbles	$R_{Contact,peb}$	2.147766323	K/W

Comparison of conduction and radiation resistances

Quantity	Symbol	Value	Units
Ratio of conduction resistance to radiation thermal resistance		5.287866434	-

Table K.2: Computation of Thermal Resistances for a Single Pebble in Batch i, at a Pebble Bed Packing Fraction Representative of the CFD Model Geometry, ϕ=0.424

Quantity	Symbol	Value	Units
Pebble radius	r_{peb}	0.03	m
Pebble surface area	A_{peb}	0.011309734	m^2
Pebble volume	Vol_{peb}	8.4823E-05	m^3
Pebble bed void fraction	ϕ	0.424	-
Pebble packing fraction	$(1-\phi)$	0.576	-
Pebble emmisivity	ε	0.8	-
Pebble conductivity	λ_{peb}	17.5	W/m/K
Number of contacts per pebble (see calc note for details)	$N_{contact}$	7.216	-
Assumed radius of Hertzian contact regions (based on CFD work)	a	0.001	m
Surface area of average pebbles	A_{av}	0.081611037	m^2
Average pebble surface temperature	T^{av}_{surf}	1067.54	K
Stefan-Boltzmann constant	σ	5.67E-08	$W\ m^{-2}\ K^{-4}$

Radiation view factors

Quantity	Symbol	Value	Units
View factor for one pebble to single contacting pebble	F_{sphere}	0.0762	-
View factor for average pebbles from batch i pebble	$F_{i,av}$	0.5498592	-
View factor for black enclosure from batch i pebble	$F_{i,enc}$	0.4501408	-
View factor for black enclosure from average pebble	$F_{av,enc}$	0.4501408	-

(note these multiply black body emmisive power differences, not temperature differences)

Radiation network resistances

Quantity	Symbol	Value	Units
Surface radiation resistance of average pebbles	$R_{av,surf}$	3.063311143	m^{-2}
Surface radiation resistance of pebble from batch i	$R_{i,surf}$	22.10485321	m^{-2}
Spatial radiation resistance from pebble in batch i to average pebbles	$R_{i,av}$	160.8037345	m^{-2}
Spatial radiation resistance from pebble in batch i to black enclosure	$R_{i,enc}$	196.4261245	m^{-2}
Spatial radiation resistance from average pebbles to black enclosure	$R_{av,enc}$	27.22091526	m^{-2}
Total radiation resistance from pebble in batch i to average pebbles	R_{Total}	111.350391	m^{-2}

$$R_{Total} = R_{i,surf} + \left\{ \frac{1}{R_{i,enc}} + \left[R_{i,av} + \left(\frac{1}{R_{av,surf}} + \frac{1}{R_{enc,av}} \right)^{-1} \right]^{-1} \right\}^{-1}$$

Quantity	Symbol	Value	Units
Effective thermal resistivity equivalent to R_{Total}	$R_{Total} / (\sigma (T^{av}_{surf})^3)$	0.403515797	K/W

Conduction across Hertzian contacts

Quantity	Symbol	Value	Units
Thermal resistance of a single contact between two pebbles	$R_{contact} = 1/(2\ \lambda_{peb}\ a)$	28.57142857	K/W
Thermal resistance between batch i pebble and average pebbles	$R_{Contact,peb}$	3.959455179	K/W

Comparison of conduction and radiation resistances

Quantity	Symbol	Value	Units
Ratio of conduction resistance to radiation thermal resistance		9.812392	-

Table K.3: Evaluating the KTA Pebble Bed Heat Transfer Coefficient for Conditions Representative of the CFD Model

Quantity	Symbol	Value	Units
Pebble radius	r_{peb}	0.03	m
Pebble surface area	A_{peb}	0.011309734	m^2
Pebble volume	V_{peb}	8.4823E-05	m^3
Pebble bed void fraction	ϕ	0.424	-
Pebble packing fraction	$(1-\phi)$	0.576	-
Flow rate through PBMR core	mdot	150	kg/s
Pressure	p	8.91E+06	Pa
Average gas temperature	T_{gas}	1043.5	K
Density of helium at specified T and p	ρ	4.0718E+00	kg/m^3
Dynamic viscosity at specified T	μ	4.76523E-05	Pa s
Thermal conductivity at specified T and p	λ_{gas}	3.76E-01	W/m/K
Prandtl number of helium	Pr	0.66	-
Outer pebble bed diameter	D_{out}	3.7	m
Inner pebble bed diameter	D_{in}	2.00E+00	m
PBMR Pebble bed cross sectional area	A	7.61E+00	m^2
Pebble bed Reynolds number	Re = mdot (2 r_{peb})/(A μ)	2.48E+04	-
Nusselt number	Nu	5.20E+02	-

$$Nu = 1.27 \cdot \frac{Pr^{1/3}}{\phi^{1.18}} Re^{0.36} + 0.033 \cdot \frac{Pr^{1/2}}{\phi^{1.07}} Re^{0.86}$$

Quantity	Symbol	Value	Units
Heat transfer coefficient	h=Nu λ_{gas} / (2 r_{peb})	3258.158272	$W/m^2/K$

Table K.4: Evaluation of the Pebble Surface Temperatures, for the 3 Batch Model used in the CFD Calculations using the KTA Value of the Heat Transfer Coefficient

Quantity	Symbol	Value	Units
Pebble radius	r_{peb}	0.03	m
Pebble surface area	A_{peb}	0.011309734	m²
Pebble volume	V_{peb}	8.4823E-05	m³
Pebble bed void fraction	ϕ	0.424	-
Pebble packing fraction	$(1-\phi)$	0.576	-
Pebble surface emissivity	ε	0.8	-
Pebble thermal conductivity	λ_{peb}	17.5	W/m/K
Stefan-Boltzmann constant	σ	5.67E-08	W m^{-2} K^{-4}
Radius of pebble-pebble contact areas	a	1.00E-03	m
Gas pressure	p	8.91E+06	Pa
Average gas temperature	T_{gas}	1043.5	K
Density of helium at specified T and p	ρ	4.0718E+00	kg/m³
Dynamic viscosity at specified T	μ	4.76523E-05	Pa s
Thermal conductivity at specified T and p	λ_{gas}	3.76E-01	W/m/K
Batch 1 pebble power		443.0	W
Batch 2 pebble power		886.0	W
Batch 3 pebble power		1329.0	W
Batch fraction of batch 1	m_1/m	0.333333333	-
Batch fraction of batch 2	m_2/m	0.333333333	-
Batch fraction of batch 3	m_3/m	0.333333333	-
Number of pebbles	m	39	-
Number of batch 1 pebbles	m_1	13	-
Number of batch 2 pebbles	m_2	13	-
Number of batch 3 pebbles	m_3	13	-
Total power generated by batch 1	q^1_{batch}	5.76E+03	W
Total power generated by batch 2	q^2_{batch}	1.15E+04	W
Total power generated by batch 3	q^3_{batch}	1.73E+04	W
Total pebble surface area	A	4.41E-01	m²
Total pebble power (generated by all batches)	q_{gen}	3.46E+04	W
Heat transfer coefficient (obtained from heat transfer coefficient sheet)	h	3258.2	W/m²/K
Estimate of average surface temperature from q_{gen}, T_{gas}, A and h	T_{surf}^{av}	1067.5	K
Coefficient for inter-batch heat transfer	C	1.0650E+02	W/K

$$C = m \cdot \left(15.52 \cdot \lambda_{peb} \cdot a + \frac{4 \cdot \sigma \cdot \left(T_{surf}^{av}\right)^3}{R_{Total}} \right)$$

Intermediate values used in calculations:

		T	Value	h*A	h*A+C	m*q$_{batch}$/m$_i$	m*q$_{batch}$/m$_i$-q$_{gen}$
Surface temperature of batch 1 - Average surface temperature	$T_1 - T_{surf}^{av}$		-11.2	1.44E+03	1.54E+03	1.73E+04	-1.73E+04
Surface temperature of batch 2 - Average surface temperature	$T_2 - T_{surf}^{av}$		0.0	1.44E+03	1.54E+03	3.46E+04	0.00E+00
Surface temperature of batch 3 - Average surface temperature	$T_3 - T_{surf}^{av}$		11.2	1.44E+03	1.54E+03	5.18E+04	1.73E+04

$$T_{surf}^i = \overline{T}_{surf} + \frac{\frac{m}{m_i}\dot{q}_{gen}^i - \dot{q}_{gen}}{hA + C} \quad \text{which implies:} \quad T_{surf}^i - \overline{T}_{surf} = \frac{\frac{m}{m_i}\dot{q}_{gen}^i - \dot{q}_{gen}}{hA + C}$$

Table K.5: Evaluation of the Pebble Surface Temperatures, for the 3 Batch Model Used in the CFD Model, Based on a Pebble-Gas Heat Transfer Coefficient of 2187 W/m

Quantity	Symbol	Value	Units
Pebble radius	r_{peb}	0.03	m
Pebble surface area	A_{peb}	0.011309734	m^2
Pebble volume	V_{peb}	8.4823E-05	m^3
Pebble bed void fraction	ϕ	0.424	-
Pebble packing fraction	$(1-\phi)$	0.576	-
Pebble surface emissivity	ε	0.8	-
Pebble thermal conductivity	λ_{peb}	17.5	W/m/K
Stefan-Boltzmann constant	σ	5.67E-08	$W\ m^{-2}\ K^4$
Radius of pebble-pebble contact areas	a	1.00E-03	m
Gas pressure	p	8.91E+06	Pa
Average gas temperature	T_{gas}	1043.5	K
Density of helium at specified T and p	ρ	4.0718E+00	kg/m^3
Dynamic viscosity at specified T	μ	4.76523E-05	Pa s
Thermal conductivity at specified T and p	λ_{gas}	3.76E-01	W/m/K
Batch 1 pebble power		443.0	W
Batch 2 pebble power		886.0	W
Batch 3 pebble power		1329.0	W
Batch fraction of batch 1	m_1/m	0.333333333	-
Batch fraction of batch 2	m_2/m	0.333333333	-
Batch fraction of batch 3	m_3/m	0.333333333	-
Number of pebbles	m	39	-
Number of batch 1 pebbles	m_1	13	-
Number of batch 2 pebbles	m_2	13	-
Number of batch 3 pebbles	m_3	13	-
Total power generated by batch 1	q^1_{batch}	5.76E+03	W
Total power generated by batch 2	q^2_{batch}	1.15E+04	W
Total power generated by batch 3	q^3_{batch}	1.73E+04	W
Total pebble surface area	A	4.41E-01	m^2
Total pebble power (generated by all batches)	q_{gen}	3.46E+04	W
Heat transfer coefficient (obtained from heat transfer coefficient sheet)	h	2187.0	$W/m^2/K$
Estimate of average surface temperature from q_{gen}, T_{gas}, A and h	T_{surf}^{av}	1079.3	K
Coefficient for inter-batch heat transfer	C	1.0973E+02	W/K

$$C = m \cdot \left(4 \cdot (7 - 8 \cdot \phi) \cdot \lambda_{peb} \cdot a + \frac{4 \cdot \sigma \cdot \left(T_{surf}^{av}\right)^3}{R_{Total}} \right)$$

Intermediate values used in calculations:

h*A	h*A+C	$m*q_{batch}/m_i$	$m*q_{batch}/m_i$-q_{gen}
9.65E+02	1.07E+03	1.73E+04	-1.73E+04
9.65E+02	1.07E+03	3.46E+04	0.00E+00
9.65E+02	1.07E+03	5.18E+04	1.73E+04

Surface temperature of batch 1 - Average surface temperature	T_1-T_{surf}^{av}	-16.1
Surface temperature of batch 2 - Average surface temperature	T_2-T_{surf}^{av}	0.0
Surface temperature of batch 3 - Average surface temperature	T_3-T_{surf}^{av}	16.1

$$T_{surf}^i = \overline{T}_{surf} + \frac{\frac{m}{m_i}\dot{q}_{gen}^i - \dot{q}_{gen}}{hA + C} \qquad \text{which implies:} \qquad T_{surf}^i - \overline{T}_{surf} = \frac{\frac{m}{m_i}\dot{q}_{gen}^i - \dot{q}_{gen}}{hA + C}$$

APPENDIX L: UNDERSTANDING FLUENT RADIATION MODELING

This Appendix discusses several models that were created to understand some unexpected behaviour observed by FLUENT radiation models in stagnant flows.

L.1   Follow-up Attempts to Resolve Slow Convergence Issues

To address some of the initial issues that were postulated with the simulation a second model of the pebble bed was created. This test model used the identical geometry as presented in this report however the grid resolution was lowered. The test model contains approximately 2 million computational cells which is a significant reduction from the original 13 million cell mesh.

Figure L.1: View of Outer Surface of Assembled Mesh to Calculate Effective Thermal Conductivity
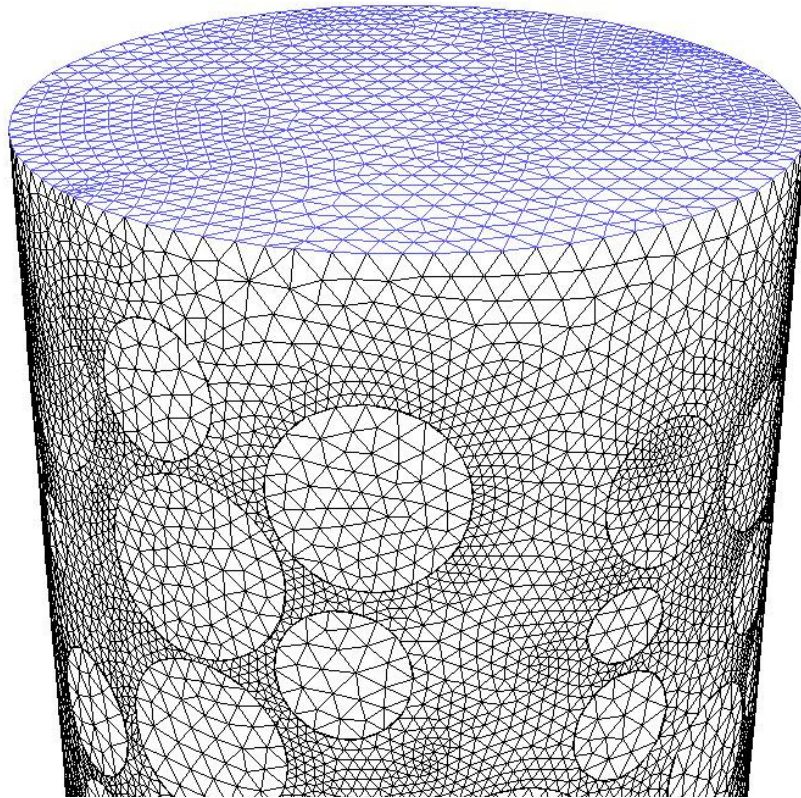
The coarse test model was used to test various solution strategies. None of the strategies were successful, hence only a brief description of each is presented.

1.   Solve the model utilizing the P-1 radiation model.

    This method produces a solution for the model, however the solution is very similar for all temperatures and the results are not reasonable. This result was not

unexpected as the P-1 radiation model is not intended for use with optically thin materials.

2. Set the conductivity of the coolant equal to the effective conductivity as predicted by the Breitbach effective thermal conductivity correlation (Reference L.1). Solve the model to convergence to achieve an initial guess for the solution. With the initial guess introduce the discrete ordinates radiation model and reduce the thermal conductivity of the helium to its appropriate value from Table 11.2.2.

    When the radiation model is introduced there is a sharp rise in the energy entering the system (2 to 3 orders of magnitude). The solution begins to converge upon the expected solution however convergence is extremely slow as indicated by the original fine grid model. The problem was allowed to run for several hundred iterations however at that time convergence was not close to being achieved and this solution approach was abandoned.

3. From the initial condition proposed in point 2 above, gradually increase the radiation emissivity from 0.1 to 0.8 and gradually decrease helium conductivity from the effective conductivity to its actual thermal conductivity.

    Immediately upon introducing the radiation model the energy flowing into the system changes by several orders of magnitude and the same slow approach to a converged solution is observed.

4. From the initial condition proposed in point 2 above, introduce the radiation model using an emissivity of 1.0.

    Immediately upon introducing the radiation model the energy flowing into the system changes by several orders of magnitude and the same slow approach to a converged solution is observed.

5. From the initial condition proposed in point 2 above, change the Multigrid smoother from Gauss Seidel to Incomplete LU and increase the number of smoothing sweeps.

    This solution technique offered no significant improvements in the convergence behaviour of the problem.

6. Change the temperature difference from inlet to outlet to 20ºC, instead of the usual 200ºC. Obtain an initial guess using the methodology from point 2 above, then introduce the discrete ordinates radiation model.

    This solution technique exhibited the same jump in energy input to the system as previous cases.

7. Start the problem with a uniform temperature field, with no temperature difference between the inlet and outlet.

    The result of this experiment was surprising. Even though the exact solution was given as the initial condition there was still a large spike in the system energy imbalance. The solution was run for several iterations however only a slow approach to a model with energy conservation was achieved.

L.2   Radiation within a Cylinder

The first model created was a single cylinder with a single constant property fluid contained within it. The properties of the fluid were set to the properties of helium at 1873 K. The top and bottom flat surfaces of the cylinder were set to temperatures of 1773 K and 1973 K respectively. The curved wall of the cylinder was set to be an adiabatic wall with a surface emissivity of zero. The cylinder has a radius of 0.12 m and a height of 0.42 m. This simulation was solved with 4 different radiation models and the results are presented in Table L.1.

Table L.1: Radiation Fluxes Reported for Radiation within an Empty Cylinder

Radiation Model	Inlet/Outlet Emissivity	Wall Treatment	Total Heat Flux In (W)	Total Heat Flux Out (W)	Total Radiation Heat Flux In (W)	Total Radiation Heat Flux Out (W)
Discrete Ordinates	1.0	Wall, 0 emissivity	-5210.4023	5210.4023	-5198.3491	5198.3491
S2S	1.0	Wall, 0 emissivity	-5399.5144	5407.9227	-5387.4611	5395.8694
DTRM	1.0	Wall, 0 emissivity	-5186.4783	5309.3463	-5174.425	5297.293
P-1	1.0	Wall, 0 emissivity	-12696.683	14048.398	-12670.184	14022.099

In FLUENT the total heat flux is defined as the sum of the heat flux from convective heat transfer and radiation heat transfer. This problem has no advection; hence the total heat transfer is the sum of conduction heat transfer and radiation heat transfer.

It is observed that only the Discrete Ordinates model strictly conserves energy. The S2S and DTRM models may be able to achieve better energy conservation with higher levels of discretization; however this effect was not studied here. All other models result in similar heat fluxes as the DO model except for the P-1 model which is known to produce significant errors for optically thin materials. Each of these problems was solved until residuals stopped changing entirely.

It was initially believe that this problem would be similar to the radiation between two infinite parallel plates. The curved wall of the cylinder must only reflect radiation (since it cannot absorb or emit radiation)[1]. The analytical result indicates that the radiation would be approximately 13,500 W, however this solution is only reflected by the P-1 model. Further

---

[1] This would be a good approximation had the test problem used a specular reflective boundary rather than a diffuse reflective wall. The infinte parallel plates analogy is only true if the reflection is specular. Diffuse reflection reflects some of the incident photons, received by the reflector, back in the direction of the emitting surface. Specular reflection reflects the incident photons from the emmiting plate in the direction of the collecting plate - therefore the thermal resistance with a diffuse reflector is higher and the radiative heat flux has to be lower than in the parallel plate assumption.

testing was done using the P-1 model and it was found that the results from the model are almost invariant with temperature changes. The problem is clearly not being solved as anticipated.

L.3 Radiation within a Cylinder Containing 1 Pebble Including Internal Geometry (Conformal Interface)

A second test model was created identical to the first one except that a single pebble was placed inside the cylinder. The cylinder is 0.42 m high and has a radius of 0.12 m. The pebble inside of the cylinder is located at the centroid of the cylinder and has a radius of 0.03 m. A mesh was created for this geometry and thus shared the same nodes on the surface of the pebble (i.e. this is a conformal interface). The properties of the pebble are set to the values provided in Table L.2. The emissivity on the surface of the pebble was set to a value of 1.0. The sensitivity case performed on this model involves changing the emissivity of the top and bottom faces of the cylinder (i.e. inlet and outlet) from a value of 1.0 to a value of 0.0.

Table L.2: Radiation and Total Heat Flux Imbalances for Radiation within a Cylinder Containing a Single Pebble				
Radiation Model	Inlet/Outlet Emissivity	Wall Treatment	Total Heat Flux In - Total Heat Flux Out (W)	Total Radiation Heat Flux In − Total Radiation Heat Flux Out (W)
Discrete Ordinates	0.0	Wall, 0 emissivity	?	?
Discrete Ordinates	1.0	Wall, 0 emissivity	-2.24737e-13	7.1e-05

The solution to this problem was obtained in approximately 1200 iterations for the case with the inlet and outlet emissivity equal to 1.0. This model produced a total heat flow through the system of 4591 W, which is comparable to the value calculated for the empty cylinder in Appendix L.2.

The case that had the inlet and outlet emissivity set equal to zero did not converge in 3000 iterations. A monitor of the total energy imbalance of the system indicated that the solution may reach a converged solution in approximately 10 000 iterations. An unusual feature of the solution is that the solution initially shows rapid residual reductions until the residual stops decreasing completely. After the residual stops changing the solution continues to evolve slowly towards a converged solution.

The target models in this report take approximately 5-30 minutes to solve one iteration. Assuming 3500 iterations is sufficient to reach a converged solution this will take between 10 and 75 days to achieve a converged solution for a single case. This time estimate is based on the assumption that the complex pebble bed model will converge at the same rate as this simple model containing only one pebble. The actual pebble bed geometry contains additional complexities (such as non-conformal interfaces) that are not considered in this model hence, these estimates may not be accurate.

L.4 References

L.1   G. Breitbach and H. Barthels, "The radiant heat transfer in the HTR core after failure of the afterheat removal systems," Nuclear Technology, Vol 49 Issue 3, pp 392-399, August 1980.

APPENDIX M: DETAILS OF THE FUEL TEMPERATURE SUB-MODEL WITHIN THE WHOLE CORE CFD MODEL

In a whole core CFD model it is not possible to include enough geometric resolution to adequately model micro and meso-scale phenomenon as it would require too fine of a mesh. Therefore, an analytical model is implemented in FLUENT to take the pebble surface temperatures calculated by FLUENT and calculate other quantities of interest.

M.1 Temperature Distributions within a Pebble

The meso-scale temperature profile within a pebble is computed using a spherically symmetric heat conduction model. The pebble is divided into two zones: the outer unfuelled graphite shell and the central fuelled pebble zone. The nuclear heating is assumed to be uniformly distributed over the central core region, and non-local heating due to gamma rays, etc. are not modelled.

The temperature within a fuel pebble is governed by the heat conduction equation:

$$-\nabla \cdot \left(k \cdot \nabla T_M \right) = \dot{q}''' \; , \tag{1}$$

which, under the assumption of spherical symmetry, reduces to:

$$-\frac{1}{r^2}\frac{d}{dr}\left(r^2 \cdot k(r) \cdot \frac{dT_M}{dr} \right) = \begin{cases} 0 & for \quad r_{fuelz} < r < r_{peb} \\ \overline{q}''' & for \quad \;\;\; 0 < r < r_{fuelz} \end{cases} , \tag{2}$$

where $\overline{q}'''$ represents the power density within the fuelled zone of the pebble element and:

Symbol	Description	Value	Units	Data source
r_{fuelz}	Radius of the fuelled zone within a pebble	0.025	m	Reference M.1
r_{peb}	Outer radius of a pebble	0.030	m	Reference M.1

The conduction equation is subject to the boundary condition:

$$T_M \left(r_{peb} \right) = T_{surf} \; .$$

To simplify the solution of this equation, the conductivity k is assumed to be constant within each of the two regions of the pebble, taking values k_{shell} and k_{fuelz} in the shell and fuelled core region respectively. The conduction equation for the temperature of batch i fuel pebbles can be solved analytically, with solution:

$$
T_M(r) = \begin{cases} T_{surf} + \dfrac{\overline{q}''' \cdot r_{fuelz}^3}{3 \cdot k_{shell}}\left(\dfrac{1}{r} - \dfrac{1}{r_{peb}}\right) & for \quad r_{fuelz} < r < r_{peb}, \\[4mm] T_{surf} + \dfrac{\overline{q}''' \cdot r_{fuelz}^3}{3 \cdot k_{shell}}\left(\dfrac{1}{r_{fuelz}} - \dfrac{1}{r_{peb}}\right) + \dfrac{\overline{q}'''}{6 \cdot k_{fuelz}}\left(r_{fuelz}^2 - r^2\right) & for \quad 0 < r < r_{fuelz}. \end{cases}
\tag{4}
$$

Typically, the model must report the average temperatures of the pebble components together with the maximum (pebble centre) values back to the CFD code. The average temperature of the pebble shell and core are computed by volume weighted averaging:

$$
\overline{T}_{Mshell} = \frac{\displaystyle\int_{r_{fuelz}}^{r_{peb}} T_M(r) \cdot r^2 \cdot dr}{\displaystyle\int_{r_{fuelz}}^{r_{peb}} r^2 \cdot dr} = \frac{\displaystyle\int_{r_{fuelz}}^{r_{peb}} T_M(r) \cdot r^2 \cdot dr}{(r_{peb}^3 - r_{fuelz}^3)/3}\ ,
\tag{5}
$$

$$
\overline{T}_{Mfuelz} = \frac{\displaystyle\int_{0}^{r_{fuelz}} T_M(r) \cdot r^2 \cdot dr}{\displaystyle\int_{0}^{r_{fuelz}} r^2 \cdot dr} = \frac{\displaystyle\int_{0}^{r_{fuelz}} T_M(r) \cdot r^2 \cdot dr}{r_{fuelz}^3/3}\ .
\tag{6}
$$

Evaluating these integrals shows that:

$$
\begin{aligned}
\overline{T}_{Mshell} &= T_{surf} + \frac{\overline{q}''' \cdot r_{fuelz}^3}{k_{shell}} \cdot \frac{\left(\dfrac{r_{peb}^2}{6} - \dfrac{r_{fuelz}^2}{2} + \dfrac{r_{fuelz}^3}{3 r_{peb}}\right)}{(r_{peb}^3 - r_{fuelz}^3)} \\[4mm]
&= T_{surf} + \frac{\overline{q}''' \cdot r_{fuelz}^2}{k_{shell}} \cdot \frac{\left(\dfrac{\gamma^2}{6} - \dfrac{1}{2} + \dfrac{1}{3\gamma}\right)}{\gamma^3 - 1}, \qquad where \quad \gamma = \frac{r_{peb}}{r_{fuelz}},
\end{aligned}
\tag{7}
$$

and

$$
\overline{T}_{Mfuelz} = T_{surf} + \frac{\overline{q}''' \cdot r_{fuelz}^3}{3 \cdot k_{shell}} \cdot \left(\frac{1}{r_{fuelz}} - \frac{1}{r_{peb}}\right) + \frac{\overline{q}'''}{k_{fuelz}} \cdot \frac{r_{fuelz}^2}{15}\ .
\tag{8}
$$

The graphite temperature at the centre of the pebble is:

$$
T_{M\,max} = T_{surf} + \frac{\overline{q}''' \cdot r_{fuelz}^3}{3 \cdot k_{shell}}\left(\frac{1}{r_{fuelz}} - \frac{1}{r_{peb}}\right) + \frac{\overline{q}'''}{6 \cdot k_{fuelz}} r_{fuelz}^2\ .
\tag{9}
$$

M.2 Fuel Particle Packing within the Pebbles

The central fuelled region of each pebble contains N_{part} = 15,000 fuel particles of radius r_{part} = 4.6×10^{-4} m (from Reference 0). Assuming the particles are uniformly distributed within the matrix graphite, each particle may be associated with a representative volume, V_{av}, of the matrix graphite, equal to the volume of the fuelled region of the pebble, $V_{fuelz} = 4\pi \cdot r_{fuelz}^3 / 3$, divided by N_{part}. This corresponds to a representative region of graphite surrounding each particle with radius:

$$r_g = \sqrt[3]{\frac{3 \cdot V_{av}}{4 \cdot \pi}} = \sqrt[3]{\frac{3 \cdot V_{fuelz}}{4 \cdot \pi \cdot N_{part}}} \ . \tag{10}$$

Evaluating r_g, using r_{fuelz} = 0.025 m, N_{part} = 15000, shows that

$$r_g = 1.01 \times 10^{-3} \text{ m} = 2.2 \cdot r_{part} = r_{part} + 1.2 \cdot r_{part}$$

This shows that the fuel particles are quite closely packed within the fuel pebble core, with a distance of approximately 1.2 particle diameters ($2.4 \cdot r_{part}$) between the surfaces of neighbouring fuel particles.

M.3 Fuel Particle Temperatures

The perturbation from the meso-scale temperature profile within each particle is represented by the micro-scale temperature field T_μ as described in Section 5.0.

A micro-sphere consisting of fuel kernel surrounded by its coatings and its share of surrounding graphite is shown in Figure M.3.1. This figure defines the radial extent of the layers and the various interface temperatures used in the following derivation for the particle temperature distribution. The one–dimensional steady-state micro-scale conduction equation in spherical coordinates is:

$$\frac{1}{\hat{r}^2} \frac{d}{d\hat{r}}\left(\hat{r}^2 k(\hat{r}) \frac{dT_\mu}{d\hat{r}} \right) = \begin{cases} \overline{q}''' & for & r_{CI1} < \hat{r} < r_g \\ -\hat{q}''' & for & 0 < \hat{r} < r_{CI1} \end{cases} . \tag{11}$$

Where the micro-scale perturbation to the power density is:

$$\hat{q}''' = \dot{q}''' - \overline{q}''' , \tag{12}$$

as defined in Section 5.0. The solutions of this equation within the kernel, the four layers of the coating and the particle's share of the surrounding graphite are derived below.

Figure M.3.1: Schematic Diagram of a Micro-Sphere Identifying the Interface Positions and Temperatures
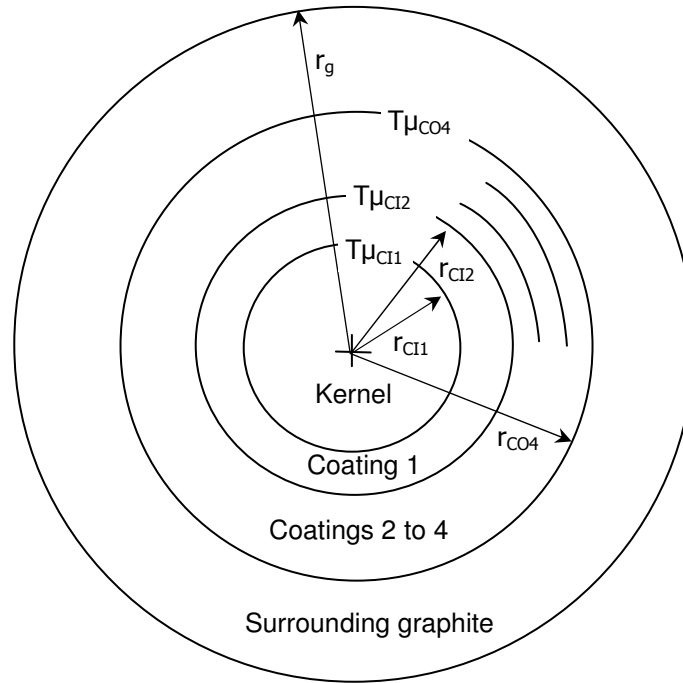
Kernel

Within the kernel, the 1D steady-state conduction equation is:

$$\frac{1}{\hat{r}^2}\frac{d}{d\hat{r}}\left(\hat{r}^2 k_k \frac{dT_{\mu k}}{d\hat{r}}\right) = -\hat{q}''' . \tag{13}$$

Integrating once gives:

$$k_k \frac{dT_{\mu k}}{d\hat{r}} = -\frac{\hat{q}'''\hat{r}}{3} + \frac{c_1}{\hat{r}^2} . \tag{14}$$

The symmetry condition at the centre of the kernel is;

$$\frac{dT_{\mu k}}{d\hat{r}} = 0 \text{ at } \hat{r} = 0 \Rightarrow c_1 = 0 .$$

Therefore, a second integration yields:

$$T_{\mu k} = -\frac{\hat{q}'''r^2}{6k_k} + c_2 .$$

When $\hat{r} = r_{CI1}$; $T_{\mu k} = T_{\mu CI1}$, where $T_{\mu CI1}$ is the temperature on the inner surface of the first coating, allowing the constant c_2 to be determined, giving the temperature profile in the kernel as:

$$T_{\mu k} = T_{\mu CI1} + \frac{\hat{q}'''}{6k_k}\left(r_{CI1}^2 - \hat{r}^2\right) . \tag{15a}$$

The maximum fuel temperature occurs at the centre of the kernel and is, therefore:

$$T_{\mu k\,max} = T_{\mu CI1} + \frac{\hat{q}''' r_{CI1}^2}{6k_k} . \tag{15b}$$

Coatings

For a general coating i, the 1D steady-state conduction equation is:

$$\frac{1}{\hat{r}^2}\frac{d}{d\hat{r}}\left(\hat{r}^2 k_{Ci}\frac{dT_{\mu Ci}}{d\hat{r}}\right) = \overline{q}''' . \tag{16}$$

For the first (innermost) coating, integration of (16) gives:

$$k_{C1}\frac{dT_{\mu C1}}{d\hat{r}} = \frac{\overline{q}'''\hat{r}}{3} + \frac{c_1}{\hat{r}^2} .$$

Continuity of heat flow through the inner surface of the first coating yields:

$$k_{C1}\frac{dT_{\mu C1}}{d\hat{r}}\bigg|_{r_{CI1}} = \frac{\overline{q}''' r_{CI1}}{3} + \frac{c_1}{r_{CI1}^2} = k_k\frac{dT_{\mu k}}{d\hat{r}}\bigg|_{r_{CI1}} = -\frac{\hat{q}''' r_{CI1}}{3} , \tag{17}$$

thus, for the constant c_1:

$$c_1 = \left(-\hat{q}''' - \overline{q}'''\right)\frac{r_{CI1}^3}{3} . \tag{18}$$

A further integration yields:

$$T_{\mu C1} = \frac{\overline{q}'''\hat{r}^2}{6k_{C1}} - \left(-\hat{q}''' - \overline{q}'''\right)\frac{r_{CI1}^3}{3k_{C1}\hat{r}} + c_2 .$$

When $\hat{r} = r_{CI2}$; $T_{\mu C1} = T_{\mu CI2}$, where $T_{\mu CI2}$ is the temperature on the inner surface of the second coating giving the constant c_2 as:

$$c_2 = T_{\mu CI2} - \frac{\overline{q}''' r_{CI2}^2}{6k_{C1}} + \left(-\hat{q}''' - \overline{q}'''\right) \frac{r_{CI1}^3}{3k_{C1} r_{CI2}} .$$

Thus, the temperature profile within the first coating is:

$$T_{\mu C1} = T_{\mu CI2} - \frac{\overline{q}'''}{6k_{C1}}\left(r_{CI2}^2 - \hat{r}^2\right) + \left(-\hat{q}''' - \overline{q}'''\right) \frac{r_{CI1}^3}{3k_{C1}}\left(\frac{1}{r_{CI2}} - \frac{1}{\hat{r}}\right).$$ (19)

For the second coating, continuity of heat flow through the surface between this and the first coating yields:

$$k_{C2} \frac{dT_{\mu C2}}{d\hat{r}}\bigg|_{r_{CI2}} = \frac{\overline{q}''' r_{CI2}}{3} + \frac{c_1}{r_{CI2}^2} = k_{C1} \frac{dT_{\mu C1}}{d\hat{r}}\bigg|_{r_{CI2}} = \frac{\overline{q}''' r_{CI2}}{3} + \left(-\hat{q}''' - \overline{q}'''\right) \frac{r_{CI1}^3}{3r_{CI2}^2} ,$$

giving the constant c_1 to be:

$$c_1 = \left(-\hat{q}''' - \overline{q}'''\right) \frac{r_{CI1}^3}{3} ,$$ (20)

i.e., the same as for the first coating.

So a further integration yields the temperature profile in the second coating:

$$T_{\mu C2} = T_{\mu CI3} - \frac{\overline{q}'''}{6k_{C2}}\left(r_{CI3}^2 - \hat{r}^2\right) + \left(-\hat{q}''' - \overline{q}'''\right) \frac{r_{CI1}^3}{3k_{C2}}\left(\frac{1}{r_{CI3}} - \frac{1}{\hat{r}}\right).$$

This implies that in general for the second and subsequent coatings:

$$T_{\mu Ci} = T_{\mu CI(i+1)} - \frac{\overline{q}'''}{6k_{Ci}}\left(r_{CI(i+1)}^2 - \hat{r}^2\right) + \left(-\hat{q}''' - \overline{q}'''\right) \frac{r_{CI1}^3}{3k_{Ci}}\left(\frac{1}{r_{CI(i+1)}} - \frac{1}{\hat{r}}\right).$$ (21)

For the outermost coating $T_{\mu CI(i+1)}$ is replaced by $T_{\mu CI(i+1)} = T_{\mu COi}$, where $T_{\mu CO4}$ is the temperature on the outer surface of the outermost coating:

$$T_{\mu C4} = T_{\mu CO4} - \frac{\overline{q}'''}{6k_{C4}}\left(r_{CO4}^2 - \hat{r}^2\right) + \left(-\hat{q}''' - \overline{q}'''\right) \frac{r_{CI1}^3}{3k_{C4}}\left(\frac{1}{r_{CO4}} - \frac{1}{\hat{r}}\right)$$ (22)

Surrounding graphite

Within the surrounding graphite, the 1D steady-state conduction equation is:

$$\frac{1}{\hat{r}^2} \frac{d}{d\hat{r}}\left(\hat{r}^2 k_g \frac{dT_{\mu g}}{d\hat{r}}\right) = \overline{q}''' .$$ (23)

Integration gives:

$$k_g \frac{d\,T_{\mu g}}{d\,\hat{r}} = \frac{\overline{q}'''\hat{r}}{3} + \frac{c_1}{\hat{r}^2} \ .$$

But the boundary condition on the outer surface of the micro-scale domain is a zero gradient boundary, so $\frac{dT_{\mu g}}{d\hat{r}} = 0$ when $\hat{r} = r_g$, therefore:

$$c_1 = -\frac{\overline{q}'''r_g^3}{3} \ .$$

A further integration gives:

$$T_{\mu g} = \frac{\overline{q}'''\hat{r}^2}{6k_g} + \frac{\overline{q}'''}{3k_g}\frac{r_g^3}{\hat{r}} + c_2 \ .$$

But, $T_{\mu g} = T_{\mu CO4}$ when $\hat{r} = r_{CO4}$, so:

$$c_2 = T_{CO4} - \frac{\overline{q}'''}{6k_g}\left(r_{CO4}^2 + 2\frac{r_g^3}{r_{CO4}} \right) \ .$$

So the temperature profile within the surrounding graphite is:

$$T_{\mu g} = T_{CO4} - \frac{\overline{q}'''}{6k_g}\left(r_{CO4}^2 - \hat{r}^2 + 2r_g^3\left(\frac{1}{r_{CO4}} - \frac{1}{\hat{r}} \right) \right) \ . \tag{24}$$

Evaluation of the coating temperature profiles at the interface layers between the coatings gives for the interface temperatures:

$$T_{\mu CI4} = T_{\mu CO4} - \frac{\overline{q}'''}{6k_{C4}}\left(r_{CO4}^2 - r_{CI4}^2 \right) + \left(-\hat{q}''' - \overline{q}''' \right)\frac{r_{CI1}^3}{3k_{C4}}\left(\frac{1}{r_{CO4}} - \frac{1}{r_{CI4}} \right) = T_{\mu CO4} + \lambda_4$$

$$T_{\mu CI3} = T_{\mu CI4} - \frac{\overline{q}'''}{6k_{C3}}\left(r_{CI4}^2 - r_{CI3}^2 \right) + \left(-\hat{q}''' - \overline{q}''' \right)\frac{r_{CI1}^3}{3k_{C3}}\left(\frac{1}{r_{CI4}} - \frac{1}{r_{CI3}} \right) = T_{\mu CI4} + \lambda_3 \tag{25}$$

$$T_{\mu CI2} = T_{\mu CI3} - \frac{\overline{q}'''}{6k_{C2}}\left(r_{CI3}^2 - r_{CI2}^2 \right) + \left(-\hat{q}''' - \overline{q}''' \right)\frac{r_{CI1}^3}{3k_{C2}}\left(\frac{1}{r_{CI3}} - \frac{1}{r_{CI2}} \right) = T_{\mu CI3} + \lambda_2$$

$$T_{\mu CI1} = T_{\mu CI2} - \frac{\overline{q}'''}{6k_{C1}}\left(r_{CI2}^2 - r_{CI1}^2 \right) + \left(-\hat{q}''' - \overline{q}''' \right)\frac{r_{CI1}^3}{3k_{C1}}\left(\frac{1}{r_{CI2}} - \frac{1}{r_{CI1}} \right) = T_{\mu CI2} + \lambda_1 \ ,$$

where the λ_i are simply collections of the terms which do not contain the interface temperatures.

The layer mean temperatures are determined by integrating the temperature profiles over each layer and dividing by the layer volume. In practice the micro-scale domain mean internal energy is determined by taking the volume-weighted average of the layer mean temperature and volumetric heat capacity products. Therefore it is simply sufficient to integrate the temperature profiles over each layer without dividing by the layer volumes.

Kernel

$$\overline{T}_{\mu k} = \frac{4\pi}{Vol_k} \int_0^{r_{CI1}} T_{\mu k} r^2 dr \quad .$$

When multiplied by the kernel volume this is:

$$\tilde{T}_{\mu k} = Vol_k \overline{T}_{\mu k} = 4\pi \int_0^{r_{CI1}} T_{\mu k} \hat{r}^2 d\hat{r} \ .$$

Integration gives:

$$\tilde{T}_{\mu k} = \frac{4\pi\, r_{CI1}^3}{3} T_{CI1} + \frac{4\pi r_{CI1}^5 \hat{q}'''}{45 k_k} = Vol_k T_{CI1} + \alpha_k , \tag{26}$$

where

$$\alpha_k = \frac{4\pi r_{CI1}^5 \hat{q}'''}{45 k_k} \quad .$$

Coatings

The integral of the temperature profile over coating i is:

$$\tilde{T}_{\mu Ci} = Vol_{Ci} \overline{T}_{\mu Ci} = 4\pi \int_{r_{CIi}}^{r_{CI(i+1)}} T_{\mu Ci} \hat{r}^2 d\hat{r} \quad .$$

Integration yields:

$$\tilde{T}_{\mu Ci} = \frac{4\pi\left(r_{CI(i+1)}^3 - r_{CIi}^3\right)}{3} T_{\mu CI(i+1)} - \frac{4\pi \overline{q}'''}{6 k_{Ci}}\left(\frac{2 r_{CI(i+1)}^5}{15} - \frac{r_{CI(i+1)}^2 r_{CIi}^3}{3} + \frac{r_{CIi}^5}{5}\right)$$
$$- \frac{4\pi\left(-\hat{q}''' - \overline{q}'''\right) r_{CI1}^3}{3 k_{Ci}}\left(\frac{r_{CI(i+1)}^2}{6} + \left(\frac{r_{CIi}}{3 r_{CI(i+1)}} - \frac{1}{2}\right) r_{CIi}^2 \right) = Vol_{Ci} T_{\mu CI(i+1)} + \alpha_{Ci} \quad , \tag{27}$$

where,

$$\alpha_{Ci} = -\frac{4\pi \overline{q}'''}{6k_{Ci}} \left(\frac{2r_{CI(i+1)}^5}{15} - \frac{r_{CI(i+1)}^2 r_{CIi}^3}{3} + \frac{r_{CIi}^5}{5} \right) - \frac{4\pi (-\hat{q}''' - \overline{q}''')r_{CI1}^3}{3k_{Ci}} \left(\frac{r_{CI(i+1)}^2}{6} + \left(\frac{r_{CIi}}{3r_{CI(i+1)}} - \frac{1}{2} \right) r_{CIi}^2 \right) \quad .$$

Surrounding graphite

The integral of the temperature profile over the surrounding graphite is:

$$\tilde{T}_{\mu g} = Vol_g \overline{T}_{\mu g} = 4\pi \int_{r_{CO4}}^{r_g} T_{\mu g} \hat{r}^2 d\hat{r} \quad .$$

Integration yields:

$$\tilde{T}_{\mu g} = \frac{4\pi (r_g^3 - r_{CO4}^3)}{3} T_{\mu CO4} - \frac{4\pi \overline{q}'''}{6k_g} \left(\left(-\frac{2r_{CO4}^5}{15} + \frac{r_{CO4}^2 r_g^3}{3} - \frac{r_g^5}{5} \right) + 2r_g^3 \left(\frac{r_g^3}{3r_{CO4}} - \frac{r_g^2}{2} + \frac{r_{CO4}^2}{6} \right) \right) \quad (28)$$

$$= Vol_g T_{\mu CO4} + \alpha_g \quad ,$$

where,

$$\alpha_g = -\frac{4\pi \overline{q}'''}{6k_g} \left(\left(-\frac{2r_{CO4}^5}{15} + \frac{r_{CO4}^2 r_g^3}{3} - \frac{r_g^5}{5} \right) + 2r_g^3 \left(\frac{r_g^3}{3r_{CO4}} - \frac{r_g^2}{2} + \frac{r_{CO4}^2}{6} \right) \right) \quad .$$

The zero mean internal energy condition within micro-scale domain is expressed as:

$$\rho_k c_{Vk} Vol_k \overline{T}_{\mu k} + \sum_{i=1}^{4} \rho_{Ci} c_{VCi} Vol_{Ci} \overline{T}_{\mu Ci} + \rho_g c_{Vg} Vol_g \overline{T}_{\mu g} = 0 ,$$

or,

$$\rho_k c_{Vk} \tilde{T}_{\mu k} + \sum_{i=1}^{4} \rho_{Ci} c_{VCi} \tilde{T}_{\mu Ci} + \rho_g c_{Vg} \tilde{T}_{\mu g} = 0 . \quad (29)$$

Defining:

$$\beta_k = \rho_k c_{Vk} Vol_k$$
$$\beta_{Ci} = \rho_{Ci} c_{VCi} Vol_{Ci} \quad (for\ i = 1\ to\ 3)$$
$$\beta_{C4g} = \rho_{C4} c_{VC4} Vol_{C4} + \rho_g c_{Vg} Vol_g \quad ,$$

and,

$$\gamma_k = \rho_k c_{Vk} \alpha_k$$
$$\gamma_{Ci} = \rho_{Ci} c_{VCi} \alpha_{Ci} \quad (for \ i = 1 \ to \ 4)$$
$$\gamma_g = \rho_g c_{Vg} \alpha_g \quad ,$$

the above definitions together with Equations (26), (27) and (28), allow (29) to be expressed as:

$$\beta_k T_{\mu CI1} + \sum_{i=1}^{3} \beta_{Ci} T_{\mu CIi+1} + \beta_{C4g} T_{\mu CO4} + \gamma_k + \sum_{i=1}^{4} \gamma_{Ci} + \gamma_g = 0 \,. \tag{30}$$

By successive substitution, (25) can be re-arranged to eliminate all but the temperatures of the inner surface of the inner coating and outer surface of the outer coating:

$$T_{\mu CO4} = T_{\mu CI4} - \lambda_4$$
$$\vdots \tag{31}$$
$$T_{\mu CO4} = T_{\mu CI1} - \lambda_1 - \lambda_2 - \lambda_3 - \lambda_4 \quad .$$

Substituting (25) into (30) gives:

$$\beta_{C4g} T_{\mu CO4} = -\beta_{C3}(T_{\mu CI3} - \lambda_3) - \beta_{C2}(T_{\mu CI2} - \lambda_2) - \beta_{C1}(T_{\mu CI1} - \lambda_1) - \beta_k T_{\mu CI1} - \left(\gamma_k + \sum_{i=1}^{4} \gamma_{Ci} + \gamma_g\right) \tag{32}$$

then, using (31) to eliminate all but two of the unknowns, gives:

$$\beta_{C4g} T_{\mu CO4} = (-\beta_{C3} - \beta_{C2} - \beta_{C1} - \beta_k) T_{\mu CI1}$$
$$+ \beta_{C3}(\lambda_1 + \lambda_2 + \lambda_3) + \beta_{C2}(\lambda_1 + \lambda_2) + \beta_{C3}\lambda_1 - \left(\gamma_k + \sum_{i=1}^{4} \gamma_{Ci} + \gamma_g\right) \quad . \tag{33}$$

Grouping the coefficients into:

$$A = -(\beta_{C3} + \beta_{C2} + \beta_{C1} + \beta_k) / \beta_{C4g} \,,$$
$$B = \frac{1}{\beta_{C4g}} \left(\beta_{C3}(\lambda_1 + \lambda_2 + \lambda_3) + \beta_{C2}(\lambda_1 + \lambda_2) + \beta_{C3}\lambda_1 - \left(\gamma_k + \sum_{i=1}^{4} \gamma_{Ci} + \gamma_g\right) \right),$$
$$C = -(\lambda_1 + \lambda_2 + \lambda_3 + \lambda_4),$$

allows (33) and the last equation of (31) to be expressed as a simple pair of simultaneous equations:

$$T_{\mu CO4} = A T_{\mu CI1} + B \,,$$
$$T_{\mu CO4} = T_{\mu CI1} + C \,,$$

the solution to which is:

$$T_{\mu CO4} = \frac{-AC + B}{1 - A} \quad .$$

(34)

The remaining interface temperatures, $T_{\mu CI1}$ to $T_{\mu CI4}$, are obtained from back-substitution in (25).

M.4 Implementation of Analytical Solution

The above solution was implemented into a C subroutine to test the model. The subroutine first solves the macro-scale equations to compute the pebble temperature profile and then uses this profile to calculate the micro-scale temperature profile within a particle. The routine adds the temperature fields together to get the maximum kernel temperature in the centre of the pebble and the average kernel temperature within the pebble. Average moderator, fuelled graphite, and average shell graphite temperatures are also calculated. The maximum fuel temperature is obtained by adding equations (9) and (15b), while the average temperature of all kernels in a pebble is obtained by adding equation (8) to equation (26) (or specifically equation (26) divided by the volume of a kernel).

M.5 Comparison with the Finite Difference Solutions

The results of the analytical solution are compared with the finite difference solutions documented in Section 5.0. Two separate tests are performed. In the first, only the micro-scale part of the solution was tested in isolation. The combined micro and meso-scale solutions were tested by comparing the maximum (pebble centre) values obtained from the finite difference solution with the analytical values.

Agreement between the two solution methods is very good. Differences, expressed as a percentage of the centre-to-edge temperature difference on each length scale respectively, are of the order of 0.3 %. Clearly, this percentage difference is much more noticeable in the meso-scale solution, giving rise to a discrepancy of just under $1^{o}C$ for the high power case, out of an overall, centre-to-edge, temperature difference of $280^{o}C$.

M.6 Implementation in FLUENT

The validated analytical model in the C code was coded into the FLUENT UDF routine used to calculate scalars quantities. For this model there was no need to solve the solutions for the scalars as they are simply a post-processed quantity based on the pebble surface temperature predicted by the code. As discussed in Section 12.3.7 since the FLUENT porosity model used for this work is a homogeneous equilibrium model the pebble temperature is equal to the fluid temperature predicted by the solver. At the end of each iteration the UDF was called to calculate the additional temperatures for each cell in the core and these values are then stored as User Defined Scalars that can be post-processed using the FLUENT GUI. Although internally FLUENT does all calculations in Kelvin these additional scalar fields were written out in degrees Celsius so as to be more easily compared to the benchmark values. The temperature scalars stored in the FLUENT results file and the names of the scalars and their meaning are as follows:

- Ave_Moderator_T_degC – This is the average moderator temperature in each cell in Celsius. This field is volume averaged over the core region to calculate the average moderator temperature in IAEA CRP-5 Case T-1.

- Ave_Fuel_T_degC – This is the average fuel temperature in each cell in Celsius. This field is volume averaged over the core region to calculate the average fuel temperature in Case T-1.

- Max_Fuel_T_degC – This is the maximum fuel temperature in each cell in Celsius. The maximum value of this field is determined and compared to the previous predictions for Case T-1.

In addition to these scalars, a Custom Field Function is also created to calculate the temperature in Celsius. This value is volume averaged over the core in order to compare the model predictions to the previous results for Case T-1.

M.7 References

M.1   OECD NEA/NSC/Doc(2005)xxx Draft V-03, "PBMR Coupled Neutronics/Thermal Hydraulics Transient Benchmark The PBMR-400 Core Design", September 2005.